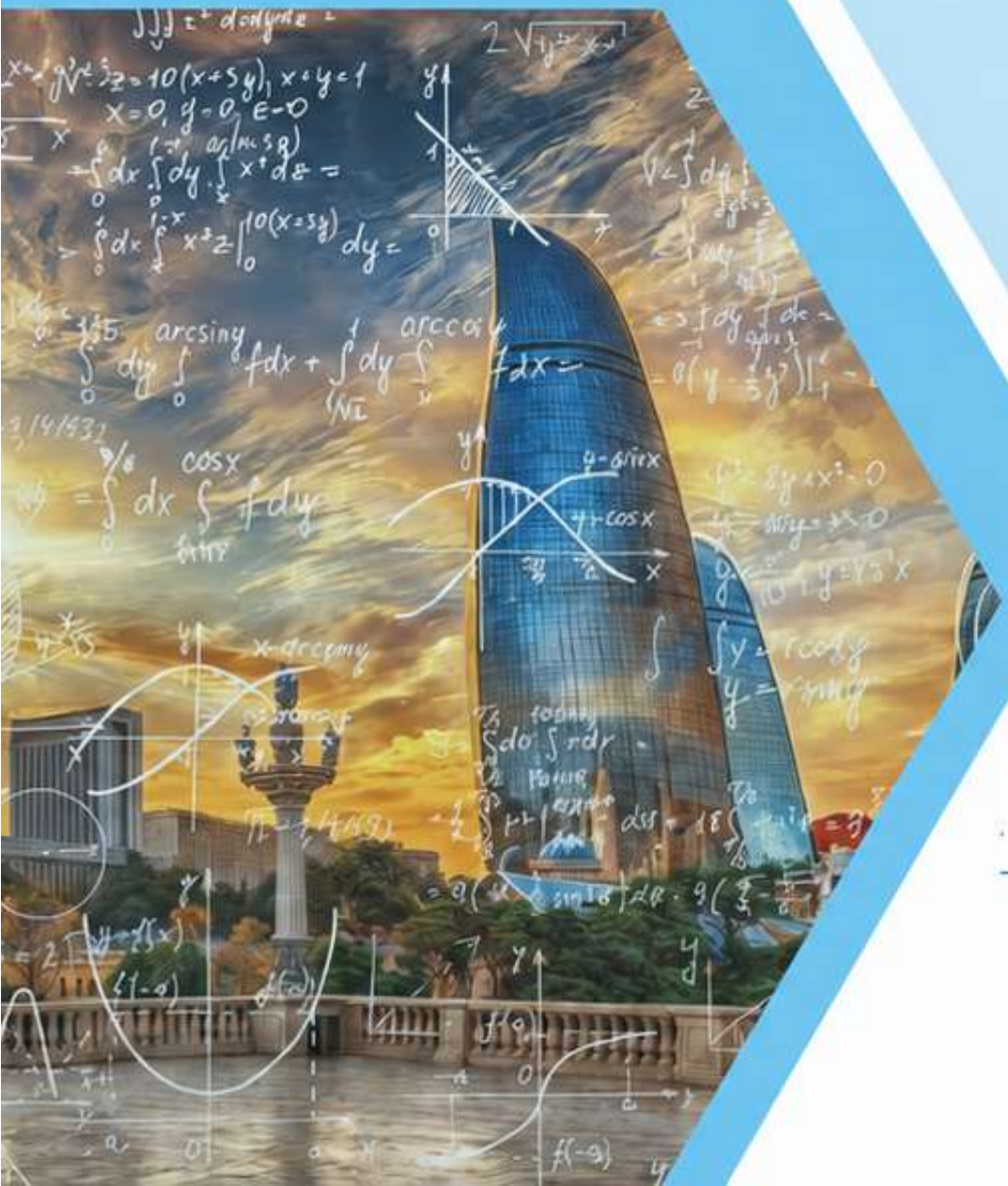
2ND INTERNATIONAL CONFERENCE ON MODERN PROBLEMS OF MATHEMATICS, MECHANICS AND THEIR APPLICATIONS

June 23-25, 2026, BAKU, AZERBAIJAN



Conference Proceedings

Supported by

The 2nd International Conference on Modern Problems of Mathematics, Mechanics and Their Applications (MPMMA 2026)

Conference Proceedings

Baku-2026

Organizers

Azerbaijan Ministry of Science and Education

Azerbaijan University of Architecture and Construction

The University of Georgia

Yildiz Technical University

Institute of Mathematics

Honorary Chair

Prof. Gulchohra Mammadova

Rector of Azerbaijan University of Architecture and Construction, Azerbaijan

Conference Chair

Prof. Nigar Aslanova, Vice-Rector for Science and Innovation, AzUAC, Azerbaijan

Scientific Committee

Co-chair: Messoud Efendiyev, Germany

Co-chair: Roland Duduchava, Georgia

Dongmei Xiao, Shanghai Jiao Tong University, China

Ljubisa Kocinac, University of Niš, Serbia

Man Wah Wong, York University, Canada

Massimo Grossi, Sapienza University of Rome, Italy
Dmitry Pelinovsky, McMaster University, Canada
Jussi Behrndt, Graz University of Technology, Austria
Carsten Trunk, Ilmenau University of Technology, Germany
Holm Altenbach, Germany
Sun Kim, Seoul National University, South Korea
Efthimios Providas, University of Thessaly, Greece
Azer Kasimzade, AzUAC, Azerbaijan
Alexander Meskhi, Georgian Technical University, Georgia
Alexander Goncharov, Bilkent University, Türkiye
Avey Abdullah, Istanbul Commerce University, Türkiye
Azer Akhmedov, North Dakota State University, USA
Bilal Bilalov, Institute of Mathematics, The Ministry of Science and Education, Azerbaijan
Kamil Aida-zade, Azerbaijan University of Architecture and Construction, Azerbaijan
Vagif Guliyev, Baku State University, Azerbaijan

Pavle Blagojević, Freie Universitat Berlin, Germany
Yoshihiro Sawano, Chuo University, Japan
Jain Pankaj, South Asian University, India
Przemysław Górka, Warsaw University of Technology, Poland
Haci Mehmet Baskonus, Harran University, Türkiye
Alik Najafov, Azerbaijan University of Architecture and Construction, Azerbaijan
Rovshan Bandaliyev, Azerbaijan University of Architecture and Construction, Azerbaijan

Organizing Committee

Akif Gasimov, Vice-Rector for Academic Affairs, Azerbaijan University of Architecture and Construction
Nargiz Abdullayeva, Vice-Rector for International Relations, Azerbaijan University of Architecture and Construction

Israfil Mammadov, Vice-Rector for Economic and Administrative Affairs, Azerbaijan University of Architecture and Construction
Agil Mammadov, Vice-Rector for General Affairs, Azerbaijan University of Architecture and Construction
Orkhan Naqdiyev, Vice Rector for Social Affairs and Public Relations, Azerbaijan University of Architecture and Construction, Azerbaijan
Reyhan Akbarli, Azerbaijan University of Architecture and Construction, Azerbaijan

https://doi.org./10.58225/mpmma.2026.6

FRONTIERS OF BIOMATHEMATICS:6BIOFILMS VS PUBLIC HEALTH

Messoud Efendiev[1,2]

[1] Helmholtz Centrum, Germany

[2] AzUAC, Azerbaijan

Abstract. Biofilms are accumulations of microorganisms growing on a solid surface or on phase interfaces, embedded in a polymeric matrix. According to the medical statistics 80% of bacterial infections in our human body are caused by biofilms. However, we can benefit from biofilms as well, due to its sorption/purification properties in the waste water treatment, ground water protection. In this talk we discuss integrated spatial photocatalytic-biofilm model, that is the role of biofilms in the mathematical modelling of the photocatalytic degradation of organic pollutants in oil-field produced water. Some open problems will also be discussed.

Keywords: Biofilms; photocatalysis; Mathematical modelling; organic pollutant degradation; oil-field produced water; wastewater treatment; integrated biofilm–photocatalytic systems; environmental remediation; reaction–diffusion processes; water purification.

https://doi.org./10.58225/mpmma.2026.7

KARAMATA THEORY AND STATISTICAL CONVERGENCE

Ljubiša D.R. Kočinac[1], *K. Demirci*[2], *F. Dirik*[2], *S. Yildiz*[2]

[1] University of Niš, Serbia,

[2] Sinop University,Türkiye

Abstract. We discuss relations between Karamata theory of regular variation fir sequences of positive real numbers and statistical convergence. The central classes ASRVs and ASTr(RVs) of sequences in our study are defined and their fundamental properties are established. A decomposition theorem characterizing sequences that are almost A-statistically regularly varying as sums of sequences that converge classically and are asymptotically small is proved. We also provide a representation+ of almost A-statistically translationally regularly varying sequences and prove the equivalence between strong almost A-summable regular variation and statistical regular variation for RV-bounded sequences.

Keywords: regular variation; karamata theory; statistical convergence; a-statistical convergence; almost A-statistical regular variation; translational regular variation; summability methods; sequence spaces; asymptotic analysis; decomposition theorems.

References:

1. N.H. Bingham, C.M. Goldie, J.L. Teugels, Regular Variation, Cambridge University Press: **,** (1987)
2. K.Demirci; F. Dirik; S. Yildiz,, Filomat **39,** (2025)
3. H. Dutta, S.; Das, J. Math. Anal. Appl. 472, (20195)
4. Lj.D.R. Kočinac, D. Djurčić, J.V. Manojlović, Regular and Rapid Variations and some Applications, .in**:** Mathematical Analysis and Applications: Selected Topics, John Wiley \& Sons, Inc. ((2018)

https://doi.org./10.58225/mpmma.2026.9

COMPUTATIONAL PROBLEMS IN HYDRAULIC NETWORKS

Kamil Aida-zade
AzUAC, Azerbaijan

Abstract. The presentation will consider the following problem formulations arising in the control of hydrocarbon transportation in pipeline networks with complex looped structures:

1) Hydraulic calculation of raw material flow in pipeline systems with complex structures under both steady-state and transient flow regimes.

2) Determination of hydraulic resistance coefficients for linear sections of the pipeline network under steady-state and transient flow conditions.

3) Detection of sections and locations of raw material leaks in steady-state and transient operating modes.

4) Operational planning of steady-state operating modes for sources and consumers of raw materials, taking into account the pipeline transportation network.

5) Optimal control of transient operating modes in the pipeline transportation network.

6) Calculation of the work performed during the transportation of raw materials in a pipeline network with a complex structure.

The paper will describe numerical methods for solving these problems, and for some of them, results of numerical experiments will be presented.

Keywords: pipeline networks, hydraulic resistance, optimal control, material leaks.

https://doi.org./10.58225/mpmma.2026.11

AN ASYMPTOTIC EXPANSION OF THE EIGENVALUE COUNTING FUNCTION FOR THE TWISTED BI-LAPLACIAN

Man Wah Wong
York University, Canada

Abstract. We begin the talk with a very brief recall of the sub-Laplacian on the one-dimensional Heisenberg group and the related twisted Laplacian. The complete spectral analysis of the twisted Laplacian is given to-gether with its main misgivings, which lead to the study of the twisted bi-Laplacian. The aim of the talk is to explain a proof of an asymptotic expan-sion of the eigenvalue counting function for the twisted bi-Laplacian with connections to the Dirichlet divisor problem and Professor G.H. Hardy's contribution to the problem.

Keywords: Heisenberg group; Sub-Laplacian; Twisted Laplacian; Twisted bi-Laplacian; Spectral theory;
Eigenvalue counting function; Spectral asymptotics; Weyl law; Dirichlet divisor problem; Hardy's theorem.

https://doi.org./10.58225/mpmma.2026.12

ANALYSIS OF INFLUENCES OF DIFFERENT ENVIRONMENTS ON BUCKLING HYDROSTATIC PRESSURE OF SHEAR DEFORMABLE MULTILAYER NANOCOMPOSITE CYLINDRICAL SHELLS

Abdullah H. Sofiyev[a,b], Aziz Sencan[c], Ali Deniz[d], Yusif N. Hasanov[e], Zihni Zerin[f], Nuri Kuruoğlu[h]

[a]Istanbul Ticaret University, Türkiye

[b]AzUAC, Azerbaijan

[c]Suleyman Demirel University, Türkiye

[d]Usak University, Türkiye

[e]Azerbaijan State Maritime Academy, Azerbaijan

[f] Ondokuz Mayis University,Türkiye

[h]Istanbul Gelisim University, Türkiye

Abstract: In this paper, the combined effects of elastic foundation and thermal environments on the buckling hydrostatic pressure (BHP) of multilayered nanocomposite cylindrical shells (MNCS) consisting of functionally graded (FG) nanocomposite (NC) layers are investigated. In the mathematical modeling of the problem, shear deformation shell theory (ST) is extended to multilayered nanocomposite shells. The properties of MNCS consisting of layers with thermo-mechanical properties are assumed to be temperature dependent and the extended mixture rule is used in the evaluations. A two-parameter soil model is used as the elastic foundation model. In order to obtain the analytical formula for BHP in elastic and thermal environments, the stability equations for MNCSs are derived and the solution is obtained within the framework of extended shear

deformation theory (ESDT). Maple computer software program is used to find the minimum value of the critical load. The proposed analytical solution is compared with different equivalent single-layer models with and without thermal environments and elastic foundations and is interpreted. Finally, a comparative analysis of BHP with Kirchhoff-Love theory (KLT) results were performed for multilayer cementitious systems with different geometrical dimensions, soil coefficients, temperature gradients and carbon nanotube (CNT) shapes.
Keywords: Nanocomposite laminae, multilayer cylindrical shells, thermal environment, elastic foundation, buckling hydrostatic pressure, shell theories

https://doi.org./10.58225/mpmma.2026.14

THE LATEST DEVELOPMENTS İN THE DİRECTİON OF *X*-VALUED ELLİPTİC EQUATİONS

Bilal Bilalov

[1] Yildiz Technical University, Türkiye

[2] Institute of Mathematics, Azerbaijan

[3]Azerbaijan University of Architecture and Construction, Azerbaijan

Abstract. Firstly we give short information about theory Banach-valued ordinary differential equation. In scalar-valued case ordinary differential equations apriori have elliptic type. Consequently, in Banach-valued case it is sufficient to construct the corresponding operational calculus depending on the operators included in the equation. Then we present some facts concerning *X*-valued Laplace and Poisson equations, we also describe the situation in direction of *X*-valued second order elliptic equation. At the end we present some of the results we have obtained in this direction.

Keywords: Banach spaces; Banach-valued elliptic equations; Vector-valued harmonic functions; Elliptic partial differential equations; Functional analysis; Operator theory; Boundary value problems; Regularity theory.

Many naturally occurring phenomena can be mathematically modelled by partial differential equations. Think, for example of the flow of water, the transfer of heat in a room, the speed of a virus

through a population, a chemical reaction or the formation of a weather system. In many of these phenomena a source of noise is present, like thermal fluctuations, turbulence or random interactions. When one wants to incorporate this noise into the mathematical model, one obtains a stochastic partial differential equation. For example, let's consider the so-called, Allen-Cahn equation on $\mathbb{R}$. Given an initial value $u_0: \mathbb{R}^d \to \mathbb{R}$, we look for a function $u: \mathbb{R}_+ \times \mathbb{R}^d \to \mathbb{R}$ satisfying

$$\begin{cases} \dfrac{du}{dt} - \Delta u = -\psi'(u), \text{in } \mathbb{R}_+ \times \mathbb{R}^d \\ u(0,\cdot) = u_0, \end{cases}$$

where $\psi: \mathbb{R} \to \mathbb{R}$ is a double well potential. To account for thermal fluctuations in the material, one can add a noise term in the mathematical model. This gives rise to the stochastic Allen-Cahn equation

$$\begin{cases} du - \Delta u dt = -\psi'(u)dt + B(u)dw, & \text{in} \quad \mathbb{R}_+ \times \mathbb{R}^d \\ u(0,\cdot) = u_0, \end{cases}$$

where w is a Brownian motion on a filtered probability space (Ω, F, P), and B describes the nature of the noise term.

To study SPDEs (stochastic partial differential equations) like Allen-Cahn equation from a functional analysis viewpoint one "hides" the space variable in a Banach space X in order to obtain a stochastic differential equation. For the Banach space X there are various choices, each with advantages and disadvantages:

- a space of Hölder continuous functions;

- a Hilbert space, for example, a Gelfand triple $V \hookrightarrow H \hookrightarrow V^*$ or $X = L_2(\mathbb{R}^d)$;

- a Lebesgue space, i.e. $X = L_p(\mathbb{R}^d), p \in [1; +\infty)$;
This typical example shows the importance of studying solvability problems of X-valued differential equations. In one dimensional case, i.e. with regard ordinary X-valued differential equations (so called evolution equations), this direction has a rich and deep history and in this case, a fairly good theory has constructed (see, e.g. the monographs [1-6]). This can not be said in the multidimensional case. In connection with advances in theory Banach analysis recently the number of works devoted specifically to the multidimensional case, i.e. X-valued partial differential equations, has been increasing (see, e.g. the works [13-22]). Note that, mainly second-order elliptic equations were considered (most of the works consider abstract generalizations of harmonic or holomorphic functions).
Very few works are devoted to high order X-valued elliptic equations. The most significant results in this context were obtained in the work [20]. In this presentation, we give some of these results.

References

1. E. Hille, R.S. Phillips. Functional analysis and semi-groups, Moscow, 1962.
2. L. Schwartz. Analysis I, II, Moscow, 1972.
3. N. Dunford, J. Schwartz. Linear Operators, General Theory, Moscow, 1962.

4. S.G. Krein. Linear Differential Equations in Banach space, Nauka, Moscow, 1967.
5. W. Arendt, C. Batty, M. Hieber, F. Neubrander. Vector-valued Laplace transforms and Cauchy problems, Birkhauser, Basel, 2011.
6. S. Yakubov, Y. Yakubov, \ Differential operator equations. Ordinary and Partial Differential Equations, CHAPMAN \& HALL/CRC, 2000.
7. Bers, L., John, F., Schechter, M.: Partial Differential Equations, Lectures in Applied Mathematics, 3A, AMS, Providence, R.I., 343 p. 1979
8. J.-L. Lions, E. Magenes. Non-Homogeneous Boundary Value Problems and Their Applications, Moscow, 1971.
9. Ladyzhenskaya, O.A., Uraltseva, N.N.: Linear and Quasilinear Equations of Elliptic Type, Nauka, Moscow (1964) (in Russian).
10. Mikhlin, S.G.: Linear Partial Differential Equations, Vysshaya Shkola, Moscow (1977) (in Russian)
11. O.I. Panich, Introduction to the General Theory of Elliptic Boundary Value Problems, vol. 128 (Kiev, 1986). (in Russian).
12. Agmon S., Duglis A., Nirenberg L. Estimates of solutions of elliptic equations near the boundary: Translated from English. 1962. 206 p.
13. Kreuter VM. Vector-valued Elliptic Boundary Value Problems on Rough

Domains. Doctoral Thesis, Ulm University, 2018
14. Lorist E. Vector-valued harmonic analysis with applications to SPDE. Dissertation, Delft University of Technology, Netherlands, 2021.
15. Arendt W. Vector-valued holomorphic and harmonic functions. Concrete Operators 2016; 3: 68-76. DOI: 10.1515/conop-2016-0007
16. Amann H. Elliptic operators with infinite dimensional state space. Journal of Evolution Equations 2001; 1(3): 243-261. DOI: 10.1007/PL00001367
17. Arendt W, Nikolski N. Vector-valued holomorphic functions revisited. Mathemat cal Notes 2000; 234(4): 777-805.
18. Arendt W, Nikolski N. Addendum: Vector-valued holomorphic functions revisited. Mathematische Zeitschrift 2006; 252: 687-689. DOI: 10.1007/s00209-005-0858-x
19. Bonet J, Frerick L, Jord´a E. Extension of vector-valued holomorphic and harmonic functions. Studia Mathematica 2007; 183: 225-248. DOI: 10.4064/sm183-3-2
20. Denk R, Hieber M, Pruss J. R-boundedness, Fourier multipliers and problems of elliptic and parabolic type. Memoirs of the American Mathematical Society 2003; 166(788): 1–114. DOI:10.1090/memo/0788
21. Bilalov BT, Sadigova SR, Sezer Y, Ildiz U, Buyukarslan A. Hp(X) class of X-valued

harmonic functions and applications. Filomat 2025; 39(35): 12593–12609.
22. Bilalov BT, Sadigova SR, Gasymov TB, Feyzullayev IQ. On strong solvability of one boundary value problem for X-valued Laplace equation on half disc. (submitted)

https://doi.org./10.58225/mpmma.2026.20

STABILITY AND COMPLEXITY OF ECOLOGICAL COMMUNITIES WITH ENERGY LANDSCAPES

Dongmei Xiao
Shanghai Jiao Tong University, China

Abstract: In this talk we introduce Hamiltonian Energy Landscape (HEL) framework for modeling the interaction among species in ecology, This framework captures energy exchange in food webs, growth, and reproduction, based on the principle of least action. By applying this framework to an ecological community modeled by 2n-dimensional generalized Lotka-Volterra system, We prove that all species interact in pairs and they have only three types of interrelationships: cooperation, competition, and predator-prey for any $n>1$ mathematically. Notably, predator-prey interactions lead to population cycles. Notably, predator-prey interactions lead to population cycles and an maintain the stability and species diversity. Further, we connect this stable community to real ecological communities by HEL which is an additional small periodic perturbation due to the natural fluctuations of the climate. Using KAM theory, we show that the perturbed Hamiltonian model exhibit quasi-periodic coexistence almost everywhere. When $n>2$, Arnold diffusion may occur between two invariant Diophantine tori. This theoretical finding indicates that weak interactions among species in communities are likely to maintain the stability of the community in a probabilistic sense. However, when $n>2$, there

remains a risk of the community transition from stability to May-Wigner instability.

Keywords: Hamiltonian Energy Landscape; Ecological dynamics; Generalized Lotka–Volterra systems; Species interactions; Predator–prey models; Population cycles; Community stability; Species diversity; KAM theory

https://doi.org./10.58225/mpmma.2026.22

SPECTRAL PROPERTIES OF CONVOLUTION INTEGRO DIFFERENTIAL EQUATIONS ON THE SUBMONOID M = [0, 1)

Roland Duduchava

V. Kupradze Institute of mathematics, University of Georgia & A. Razmadze Institute of Mathematics, Georgia

The interval G = (−1, 1) turns into a Lie group under the group operation x ◦ y := (x + y)(1 +xy)−1, x, y ∈ G, the Fourier transformation ℱG and the invariant Haar measure $d\mu_{\mathbf{G}} := \dfrac{dt}{1-t^2}$.

Then M = [0, 1) is a submonoid of G (has the same binary operation x◦y) and we can induce the invariant Haar measure $d\mu_M$ and the Fourier transformation ℱM from G to M. The main object of the investigation is the Fourier convolution operator

$$W_{\mathbf{M},a} := r_+ W^0_{\mathbf{G},a} \ell_+,$$

which represents the restriction of the convolution

$$W^0_{\mathbf{G},a} := \mathcal{F}^{-1}_{\mathbf{G}} a \mathcal{F}_{\mathbf{G}}$$

from G.

An example of such convolution integro-differential equation on the submonoid M = [0, 1) is

$$\sum_{j=0}^{n} \left[a_j \mathfrak{D}^{m_j} u(t) - b_j \mathfrak{D}^{n_j} \int_0^1 k_j \left(\frac{t-\tau}{1-t\tau} \right) \frac{\mathfrak{D}^{\ell_j} u(\tau) d\tau}{1-\tau^2} \right] = f(t), \qquad t \in \mathbf{M},$$

where

$$a_j, b_j \in \mathbb{C}, m_j, n_j, \ell_j \in \mathbb{N}, j = 1, \dots, n, k_j \in \mathbb{L}_1(\mathbf{G}, d\mu_{\mathbf{G}}), \mathfrak{D}u(x) := -(1-x^2)\frac{d}{dx}u(x)$$

Is the generic differential operator, which is a convolution operator and $(\mathcal{F}_G D) = -i\xi$, $\xi \in R$.

The theory of convolution operators $W_{M,a}$ on the submonoid M is much more complicated, but more rich and important in applications (example of Wiener-Hopf equations on submonoid $M = [0, \infty)$ of the Lie group $G = (-\infty, \infty)$ is a good example). Convolution equation $W_{M,a}\varphi = f$ in the Generic Bessel potential space setting $f \in GH^{s-r}(M, d\mu M)$, $\varphi \in GH^{s}(M, d\mu M)$, $1 < p < \infty$, $s, r \in R$, has non-trivial p p Fredholm index. The Fredholmity and solvability conditions for discontinuous symbols $a(\xi)$ depend on the parameters of the spaces. We expose a full theory of such convolution integro-differential equations: Fredholm property and solv-ability criteria, index formula. Formula for solutions are available through the factorization of the symbol.

It is worth to mention that the celebrated equations of Prandtl, Tricomi and Lavrentjev-Bitsadze belong to the class of convolution equations on the Lie group $G = (-1, 1)$.

The report is based on the works [1,2] and some other recent publications.

Acknowledgments

The work was supported by the Rustaveli National Science Foundation of Georgia, Grant No. FR-24-69.

References

1.D. Cardona, R. Duduchava, A. Hendrix, M. Ruzhansky, Generic Bessel potential spaces on Lie groups, Tbilisi Analysis & PDE Seminar-Extended Abstracts of the 2020-2023 Seminar

Talks, Trends in Mathematics, Birkha¨user/Springer, pp. 43-54, 2024.
2.R. Duduchava, Convolution equations on the submonoid M = [0, 1), Submitted to ”Bolet´ın de la Sociedad Matema´tica Mexicana” (BSMM). 37 pages.

https://doi.org./10.58225/mpmma.2026.25

CHARACTERIZATION OF BMO AND LIPSCHITZ FUNCTIONS VIA THE COMMUTATORS OF FRACTIONAL MAXIMAL FUNCTION IN TOTAL MORREY SPACES ON STRATIFIED LIE GROUPS

Vagif Guliyev[1,2]

[1] Baku State University, Azerbaijan

[2] Kirsehir Ahi Evran University, Türkiye

Abstract. The purpose of this article is first, to obtain the boundedness of fractional maximal commutators $M_{b,\alpha}$ and the commutators of the fractional maximal operator $[b, M_\alpha]$ in the total Morrey spaces $L^{p,\lambda,\mu}(\mathbb{G})$ on any stratified Lie group $\mathbb{G}$, and second, to give the characterizations for certain subclasses of BMO and Lipschitz space $\dot{\Lambda}_\beta(\mathbb{G})$ via the boundedness results.

Keywords: Fractional maximal operator, stratified groups, total Morrey spaces, commutator, BMO, Lipschitz spaces

1 Introduction

Morrey spaces, introduced by C.B. Morrey [5], play an important role in harmonic analysis and the regularity theory of partial differential equations. In [1] the author introduce a variant of Morrey spaces called total Morrey spaces $L_{p,\lambda,\mu}(\mathbb{R}^d)$, $0 < p < \infty$, $\lambda \in \mathbb{R}$ and $\mu \in \mathbb{R}$, see [1,2,3]. Total Morrey spaces generalize both classical and modified Morrey spaces.

A homogenous norm on $\mathbb{G}$ is a continuous function $x \to \rho(x)$ from $\mathbb{G}$ to $[0,\infty)$, which is C^∞ on $\Gamma \setminus \{0\}$ and satisfies $\rho(x^{-1}) = \rho(x)$, $\rho(\delta_t x) = t\rho(x)$ for all $x \in \mathbb{G}$, $t > 0$; $\rho(e) = 0$ (the group identity). Moreover, there exists a constant $c_0 \geq 1$ such that $\rho(xy) \leq c_0\big(\rho(x) + \rho(y)\big)$ for all $x, y \in \mathbb{G}$. With this norm, we define the $\mathbb{G}$-ball centered at x with radius r by $B(x,r) = \{y \in \mathbb{G}: \rho(y^{-1}x) < r\}$. One easily recognizes that there exists $v_Q = v_Q(\mathbb{G})$ such that $|B(x,r)| = v_Q\, r^Q,\ x \in \mathbb{G},\ r > 0$.
Let $\mathbb{G}$ be a stratified Lie group, $f \in L^1_{\text{loc}}(\mathbb{G})$ and $0 \leq \alpha < Q$, where Q is the homogeneous dimension of $\mathbb{G}$. The fractional maximal function $M_\alpha f$ is defined by

$$M_\alpha f(x) = \sup_{B \ni x} |B|^{-1+\frac{\alpha}{Q}} \int_B |f(y)|dy,$$

and the sharp maximal function of Fefferman and Stein $M^\sharp f$ is defined by

$$M^\sharp f(x) = \sup_{B \ni x} |B|^{-1} \int_B |f(y) - f_B|dy,$$

where the supremum is taken over all $\mathbb{G}$-balls $B \subset \mathbb{G}$ containing x, and $|B|$ is the Haar measure of the $\mathbb{G}$-ball B. When $\alpha = 0$, we simply denote by $M = M_0$.
The fractional maximal commutator generated by $b \in L^1_{\text{loc}}(\mathbb{G})$ and M_α is defined by

$$M_{b,\alpha}(f)(x) = \sup_{B \ni x} |B|^{-1+\frac{\alpha}{Q}} \int_B |b(x) - b(y)||f(y)|dy.$$

The commutators generated by $b \in L^1_{\text{loc}}(\mathbb{G})$ and M_α is defined by

$$[b, M_\alpha]f(x) = b(x)M_\alpha f(x) - M_\alpha(bf)(x).$$

Let $0 < p < \infty$, $\lambda \in \mathbb{R}$, $\mu \in \mathbb{R}$, $[t]_1 = \min\{1, t\}$, $t > 0$. We denote by $L^{p,\lambda}(\mathbb{G})$ the classical Morrey space, by $\widetilde{L}^{p,\lambda}(\mathbb{G})$ the modified Morrey space [4], and by $L^{p,\lambda,\mu}(\mathbb{G})$ the total Morrey space the set of all classes of locally integrable functions f with the finite norms

$$\|f\|_{L^{p,\lambda}} = \sup_{x\in\mathcal{G},\, t>0} t^{-\frac{\lambda}{p}} \|f\|_{L^p(B(x,t))},$$

$$\|f\|_{\widetilde{L}^{p,\lambda}} = \sup_{x\in\mathcal{G},\, t>0} [t]_1^{-\frac{\lambda}{p}} \|f\|_{L^p(B(x,t))},$$

$$\|f\|_{L^{p,\lambda,\mu}} = \sup_{x\in\mathcal{G},\, t>0} [t]_1^{-\frac{\lambda}{p}} [1/t]_1^{\frac{\mu}{p}} \|f\|_{L^p(B(x,t))},$$

respectively.

We define the space $BMO(\mathbb{G})$ as the set of all locally integrable functions b with finite norm

$$\|b\|_* = \sup_{x\in\mathbb{G},t>0} |B(x,t)|^{-1} \int_{B(x,t)} \left|b(y) - b_{B(x,t)}\right| dy < \infty,$$

where $b_{B(x,t)} = |B(x,t)|^{-1} \int_{B(x,t)} b(y)dy$.
We say a function b belongs to the Lipschitz space $\dot{\Lambda}_\beta(\mathbb{G})$ if there exists a constant C such that for all

$x, y \in \mathbb{G}$, $|b(x) - b(y)| \leq C\rho(y^{-1}x)^{\beta}$. The smallest such constant C is called the $\dot{\Lambda}_{\beta}(\mathbb{G})$ norm of b and is denoted by $\|b\|_{\dot{\Lambda}_{\beta}(\mathbb{G})}$.

Theorem 1. [2] *Let* $1 < p < \infty$, $0 \leq \mu \leq \lambda < Q$, $0 \leq \alpha < \frac{Q-\lambda}{p}$ *and* $\frac{\alpha}{Q-\mu} \leq \frac{1}{p} - \frac{1}{q} \leq \frac{\alpha}{Q-\lambda}$. *The following assertions are equivalent:*

(i) $b \in BMO(\mathbb{G})$.

(ii) *The operator* $M_{b,\alpha}$ *is bounded from* $L^{p,\lambda,\mu}(\mathbb{G})$ *to* $L^{q,\lambda,\mu}(\mathbb{G})$.

Theorem 2. [3] *Let* $0 < \beta < 1$, $0 \leq \alpha < \alpha + \beta < Q$ *and* $b \in L^1_{loc}(\mathbb{G})$. *Let also* $0 \leq \mu \leq \lambda < Q$, $1 < p < \frac{Q-\lambda}{\alpha+\beta}$ *and* $\frac{\alpha+\beta}{Q-\mu} \leq \frac{1}{p} - \frac{1}{q} \leq \frac{\alpha+\beta}{Q-\lambda}$. *Then, the following statements are equivalent:*

(i) $b \in \dot{\Lambda}_{\beta}(\mathbb{G})$.

(ii) The operator $M_{b,\alpha}$ is bounded from $L^{p,\lambda,\mu}(\mathbb{G})$ to $L^{q,\lambda,\mu}(\mathbb{G})$.

Theorem 3. [2] *Let* $1 < p < \infty$, $0 \leq \mu \leq \lambda < Q$, $0 \leq \alpha < \frac{Q-\mu}{p}$ *and* $\frac{\alpha}{Q-\mu} \leq \frac{1}{p} - \frac{1}{q} \leq \frac{\alpha}{Q-\lambda}$. *Then the following assertions are equivalent:*

(i) $b \in BMO(\mathbb{G})$ *such that* $b^- \in L^{\infty}(\mathbb{G})$.

(ii) *The operator* $[b, M_{\alpha}]$ *is bounded from* $L^{p,\lambda,\mu}(\mathbb{G})$ *to* $L^{q,\lambda,\mu}(\mathbb{G})$.

(iii) *There exists a constant* $C > 0$ *such that*

$$\sup_{B} \frac{\left\| \left(b - |B|^{-\frac{\alpha}{Q}} M_{\alpha,B}(b) \right) \chi_B \right\|_{L^{q,\lambda,\mu}}}{\|\chi_B\|_{L^{q,\lambda,\mu}}} \leq C. \quad (1)$$

Theorem4. [3] *Let* $0 < \beta < 1$, $0 \le \alpha < \alpha + \beta < Q$ *and* $b \in L^1_{loc}(\mathcal{G})$. *Let also* $0 \le \mu \le \lambda < Q$, $1 < p < \frac{Q-\lambda}{\alpha+\beta}$ *and* $\frac{\alpha+\beta}{Q-\mu} \le \frac{1}{p} - \frac{1}{q} \le \frac{\alpha+\beta}{Q-\lambda}$. *Then, the following statements are equivalent:*

(i) $b \in \dot{\Lambda}_\beta(\mathbb{G})$ *and* $b \ge 0$.

(ii) *The operator* $[b, M_\alpha]$ *is bounded from* $L^{p,\lambda,\mu}(\mathbb{G})$ *to* $L^{q,\lambda,\mu}(\mathbb{G})$.

(iii) *There exists a constant* $C > 0$ *such that*

$$\sup_B |B|^{-\frac{\alpha+\beta}{Q}} \frac{\left\| \left(b - M_{B,\alpha}(b) \right) \chi_B \right\|_{L^{q,\lambda,\mu}}}{\|\chi_B\|_{L^{q,\lambda,\mu}}} \le C. \quad (2)$$

The research of V. Guliyev was partially supported by a grant from Kirsehir Ahi Evran University Scientific Research Projects (BAP, Project No: FEF.A1.26.001).

References

1. Guliyev, V.S.: Maximal commutator and commutator of maximal function on total Morrey spaces. J. Math. Inequal. 16(4), 1509–1524 (2022).
2. Guliyev, V.S.: Characterization of commutators of the maximal function in total Morrey spaces on stratified Lie groups. Analysis and Mathematical Physics 15(2), Paper No. 42, 1–25 (2025).
3. Guliyev, V.S.: Characterizations of Lipschitz functions via the commutators of fractional

maximal function in total Morrey spaces on stratified Lie groups. Aequationes mathematicae 100(1), 1–26 (2026).
4. Guliyev, V.S., Hasanov, J.J., Zeren, Y.: Necessary and sufficient conditions for the boundedness of the Riesz potential in modified Morrey spaces. J. Math. Inequal. 5(4), 491–506 (2011).
5. Morrey, C.B.: On the solutions of quasi-linear elliptic partial differential equations. Trans. Amer. Math. Soc. 43, 126–166 (1938).

https://doi.org./10.58225/mpmma.2026.31

ON TWO TYPE EXTENSIONS OF MINIMAL SYMMETRIC OPERATOR IN EXIT SPACE: WITH RESOLVENTS FROM σ_p AND WITH CONTINUOUS SPECTRUM

Nigar Aslanova[1], *Khalig Aslanov*[2]
[1] AzUAC
[2] Azerbaijan State Economic University

Abstract. We give necessary and sufficient conditions for the existence of resolvents of a differential operator from σ_p also for the existence of continuous spectrum.

Keywords: operator differential expression, extensions with resolvent from σ_p, spectrum.

We consider the exit space operator realizations of the differential expression:

$$l[y]: \equiv -y''(t) + Ay(t) + q(t)y(t) \tag{1}$$

with operator coefficients A and $q(t)$ in $L^2(0,1;H)$. Here A is self-adjoint positive-definite unbounded operator and $q(t) = q^*(t)$ is bounded operator in a separable Hilbert space H. In our previous study [1] we related with this expression a symmetric minimal operator in the broader space $\mathcal{H} := L^2(0,1;H) \oplus H^{N+1}$ with scalar product of elements $Y = \big(y(t)\big), y_1, \dots, y_{N,} y_{N+1})$

$$(Y,Z)_{\mathcal{H}} = \int_0^1 (y(t),z(t))_H dt + \sum_{h=1}^{N} \frac{(y_n,z_n)_H}{b_n} + \frac{\left(Q^{-\frac{1}{2}}y_{N+1}, Q^{-\frac{1}{2}}z_{N+1}\right)_H}{\alpha} \quad (2)$$

where Q is unbounded, self-adjoint positive definite operator in H, α is real number. Such operator realizations will cover the next problem

$$l[y] = \lambda y$$

with some rational function of spectral parameter $f(\lambda)$ and unbounded operator Q in the boundary condition at the endpoint 1:

$$y'(1) = f(\lambda)Qy(1) \quad (3)$$

We also gave a description of the domain of the maximal operator, as well as necessary and sufficient conditions for the existence of self-adjoint extensions with discrete spectrum, and found an asymptotic formula for eigenvalues.
In the current study the next main statements are proved.

Theorem 1. For the resolvent of self-adjoint operators L_0^S one of the following is true, when $p \geq 1$:

1. If $\beta > 2$, then $R_\lambda(L_0^S)$ from σ_p, if and only if $Q\mathcal{A}^{-\frac{1}{2}} \in \sigma_p$
2. If $\beta < 2$, then it has no resolvents from σ_p

Theorem 2. If $\bar{A}^1 \in \sigma_\infty$, then for any closed set Ω of the real axis, there exist a self-adjoint extension of the minimal operator, spectrum of which coincides with Ω.

References

1.Aslanova, N., Aslanov, K., Kizilbudak Caliskan, S., Karayel, S.: On the operator Sturm–Liouville problem with unbounded operator coefficients in boundary condition. Journal of Applied and Computational Mechanics, e19529 (2026).

https://doi.org./10.58225/mpmma.2026.34

LORENTZ-TYPE THEOREMS IN LIPSCHITZ CLASSES

Askhat Mukanov[1] *and Zhalgas Mukanov*[2]

[1] Institute of Mathematics and Mathematical Modeling, Kazakhstan

[2] L.N. Gumilyov Eurasian National University, Kazakhstan

Abstract. We investigate the relationship between the smoothness properties of functions and the asymptotic behavior of their Fourier transforms. We focus on how various notions of regularity and smoothness influence the rate of decay of the Fourier transform at infinity. Special attention is given to the class of functions whose Fourier transforms satisfy a general monotonicity condition. Within this framework, we establish a Lorentz-type characterization theorem that connects smoothness estimates of functions with precise decay properties of their Fourier transforms. Our results extend several classical statements in harmonic analysis and provide new criteria for describing function classes through the behavior of Fourier transforms.

Keywords: Fourier Transform, General Monotonicity, Lipschitz Classes.

1 Lorentz-type theorems

Let $0 < \alpha \leq 1$. By $\mathrm{Lip}_\alpha(\mathbb{T})$, where $\mathbb{T} = [-\pi, \pi)$, we denote the Lipschitz class

$$\mathrm{Lip}_\alpha(\mathbb{T}) := \{f \in C(\mathbb{T}) : \omega(f, \delta) = O(\delta^\alpha), \quad \delta > 0\},$$

where $\omega(f,\delta) = \sup_{0<|h|\le\delta} \|f(\cdot+h) - f(\cdot)\|_{C(\mathbb{T})}$ is the modulus of continuity of the function f.

In paper [3], Lorentz proved the following theorem.

Theorem 1. Let

$$f(x) = \sum_{n=1}^{\infty} a_n \cos nx, \qquad g(x) = \sum_{n=1}^{\infty} b_n \sin nx,$$

where the sequences $\{a_n\}_{n=1}^{\infty}$ and $\{b_n\}_{n=1}^{\infty}$ are nonnegative and nonincreasing. Then

$$f \in \mathrm{Lip}_{\alpha}(\mathbb{T}) \Leftarrow a_n = O\left(\frac{1}{n^{\alpha+1}}\right), \quad 0 < \alpha \le 1,$$

and

$$g \in \mathrm{Lip}_{\alpha}(\mathbb{T}) \Leftarrow b_n = O\left(\frac{1}{n^{\alpha+1}}\right), \quad 0 < \alpha < 1.$$

In paper [1], Dyachenko and Tikhonov extended Lorentz's theorem to the class of general monotone sequences $\{a_n\}_{n=1}^{\infty}$ satisfying the condition:

$$\sum_{k=n}^{2n} |a_k - a_{k+1}| \le \frac{C}{n} \sum_{k=[n/\gamma]}^{[\gamma n]} |a_k|,$$

for all $n \ge 1$ and some constants $C > 0$ and $\gamma > 1$. The main feature of their result is that they do not require the nonnegativity of the series coefficients.

We obtained non-periodic analogues of the results of Dyachenko and Tikhonov for the classical Fourier transform:

$$\hat{f}(x) = \frac{1}{\sqrt{2\pi}} \int_{\mathbb{R}} f(y) e^{iyx}\, dy, \quad f \in L_1(\mathbb{R}).$$

Definition 1. We say that a complex-valued function F, defined on $\mathbb{R}_+$ and having locally bounded variation, is general monotone, or $F \in GM$ [2], if there exist constants $C > 0$ and $\gamma > 1$ such that for any $x > 0$ the inequality

$$\int_x^{2x} |dF(t)| \le \frac{C}{x} \int_{\frac{x}{\gamma}}^{\gamma x} |F(t)|\, dt$$

holds.

Theorem 2. Let $f \in L_1(\mathbb{R}) \cap C(\mathbb{R})$.

(i) If f is an even function and $\hat{f}\big|_{\mathbb{R}_+} \in GM$, then for any $0 < \alpha \le 1$

$$f \in \mathrm{Lip}_\alpha(\mathbb{R}) \Leftarrow |\hat{f}(t)| = O\left(\frac{1}{|t|^{\alpha+1}}\right), \quad t \ne 0.$$

(ii) If f is an odd function and $\hat{f}\big|_{\mathbb{R}_+} \in GM$, then for any $0 < \alpha < 1$

$$f \in \mathrm{Lip}_\alpha(\mathbb{R}) \Leftarrow |\hat{f}(t)| = O\left(\frac{1}{|t|^{\alpha+1}}\right), \quad t \ne 0.$$

Moreover, it was possible to extend Theorem 2 to generalized Lipschitz classes, in which the majorants satisfy the Bari-Stechkin conditions.

References

1. Dyachenko M., Tikhonov S. Smoothness properties of functions with general monotone

Fourier coefficients. Journal of Fourier Analysis and Applications 24(4), 1072–1097 (2018).
2. Liflyand E., Tikhonov S. A concept of general monotonicity and applications. Mathematische Nachrichten 284(8-9), 1083 – 1098 (2011).
3. Lorentz G. Fourier-Koeffizienten und Funktionenklassen. Mathematische Zeitschrift 51, 135–149 (1948).

https://doi.org./10.58225/mpmma.2026.38

ON A TORSION PROBLEM OF A COMPOSITE PRISMATIC BAR WITH A DOUBLY CONNECTED CROSS-SECTION

Amirkhan Sazairov, Zohrab Khalilov, Mahsati Rustamova, Aytaj Aliyeva
AzUAC, Azerbaijan

Abstract. This work presents a solution to the torsion problem of a composite prismatic bar with a doubly connected cross-section, composed of two homogeneous rods with different shear moduli. The cross-section consists of two regions: an outer square containing an internal circular hole and an outer circular region with an eccentrically located inner square with rounded corners. Analytic functions $\varphi_1(z)$ and $\varphi_2(z)$ are constructed for the respective regions using the theory of complex variable functions and conformal mapping techniques. Infinite series representations of these functions are derived, and boundary and contact conditions are applied to form systems of linear algebraic equations. Based on the theory of complex variable and indicator functions, numerical solutions for selected coefficients are obtained, and shear stress distributions are calculated. The results confirm the effectiveness of the proposed method and its ability to satisfy boundary conditions accurately.

Keywords: Torsion problem, Composite bar, Cross-section, Shear moduli, Complex variable theory, Stress distribution, Numerical solutions

Introduction.

The present work fills this gap by developing an analytical solution based on complex-variable

theory and conformal mappings for the torsion of a prismatic bar composed of two homogeneous different materials, where the cross-section comprises two regions: $S_1$is bounded externally by a square and internally by a symmetric circle, while $S_2$is bounded externally by that same circle and internally by an eccentrically located rounded-corner square. The derivation employs series expansions for the analytic functions $\varphi_1(z)$and $\varphi_2(z)$in each domain, satisfying boundary conditions on all contours and continuity conditions at the material interface. The resulting expressions enable detailed evaluation of shear-stress fields, warping functions, and torsional rigidity for the composite bar under a uniform applied torque. Numerical example results and stress-distribution epura illustrate the efficiency and convergence of the method.

Methodology.

Based on the theory of functions of a complex variable, this work presents the solution of the torsion problem for a prismatic bar composed of two different homogeneous rods. The cross-section of the given bar consists of two regions, S_1 and S_2. Region S_1 is doubly connected and is bounded externally by a square $L_1$and internally by a symmetrically located circle $L_2$of radius R_2. The other region, S_2, is bounded externally by the circle $L_2$and internally by an eccentrically located square $L_3$with rounded corners. The origin of the Cartesian coordinate system is placed at the center of the curve L_1.

As is known, in this case, the determination of the stress state in the beam is reduced to finding two

functions, $\varphi_1(z)$ and $\varphi_2(z)$, which are regular in the regions S_1, and S_2, respectively, and satisfy the following boundary and contact conditions.

$$\varphi_1(t_1) + \overline{\varphi_1(t)} = t_1\bar{t_1} + C_1 \quad \text{on } L_1 \tag{1}$$

$$\varphi_2(t_3) + \overline{\varphi_2(t)} = t_3\bar{t_3} + C_3 \quad \text{on } L_3 \tag{2}$$

$$\mu_1\left[\varphi_1(t_1) + \overline{\varphi_1(t_2)}\right] - \mu_2\left[\varphi_2(t_2) + \overline{\varphi_2(t_2)}\right] = (\mu_1 - \mu_2)t_1\bar{t_2} \tag{3}$$

$$\left[\varphi_1(t_2) - \overline{\varphi_1(t_2)}\right] - \left[\varphi_2(t_2) - \overline{\varphi_2(t_2)}\right] = 0 \tag{4}$$

Here, μ_j- are the shear moduli of the medium S_j (for $j = 1,2$); t_j −denotes the time at point L_j (for $j = 1,2,3$); C_1 and C_3 − are constants, one of which can be chosen arbitrarily, while the other is determined during the course of solving the problem. We construct the regular function in the respective domains $S_j(j = 1,2)$ as the sum of two functions.

$$\varphi_1(z) = \psi_1(z) + \psi_2(z) \tag{5}$$

$$\varphi_2(z) = f_1(z) + f_2(z) \tag{6}$$

The function $\psi_1(z)$is analytic inside the contour L_1, while $\psi_2(z)$is analytic outside the contour L_2; the function $f_1(z)$is analytic inside the contour L_2, and $f_2(z)$is analytic outside the contour L_3. As is well known, the conformal mapping of the unit circle onto the interior of the square L_1 is carried out using a series [3].

$$t = \omega(\xi_1) = A_1 \sum_{n=o}^{\infty} m_n \xi_1^{4n+1} \tag{7}$$

After all simplifications have been performed, the following expression is obtained

$$\frac{\mu_1}{\mu_2} 2a_0^{(1)} - 2a_0^{(2)} = \left(\frac{\mu_1}{\mu_2} - 1\right) R_2^2 \qquad (8)$$

For illustration, a numerical example is considered with the following data: $\mu_2 = 20\,\mu_1$, $R_2 = 0.6\,A_1$, $e_3 = 0.5\,R_2$, $a_3 = 0.3\,R_2$, and $A_1 : R = 0.7628$, where R denotes the radius circumscribed around the square L_1.

Following the determination of these coefficients, the boundary conditions were verified at the most representative points, and the shear stress values were subsequently computed using the established formulas [1].

$$X_z^{(j)} - iY_z^{(j)} = i\mu_j \frac{M}{D}\left[\varphi_j'(z) - \overline{z}\right]$$

The results have been incorporated into Table 1. The sufficiently accurate satisfaction of the boundary conditions confirms the effectiveness of the proposed solution method.

Table 1.

Point z	Stress		$\Delta\% = \frac{t\bar{t} + C_j - \{\varphi_j(t) + \varphi_j(t)\}}{t\bar{t} + C_j} 100\%$
	$X_z^{(1)}/\mu_1 \frac{M}{D}$	$X_z^{(2)}/\mu_1 \frac{M}{D}$	
b_1	1.323	-	0.083
0.824 b_1	1.022	-	-
0.647 b_1	0.816	16.383	-
0.583 b_1	-	16.773	-
0.518 b_1	-	21.339	2.012
0.129	-	11.009	1.683

b_1			
0	-	2.653	-
-0.324 b_1	-	-5.202	-
-0.647 b_1	-0.578	-11.649	-
-0.824 b_1	-0.896	-	-
- b_1	-1.226	-	0.280

Fig. 1.

Conclusion

In this study, the torsion of a composite prismatic bar with a doubly connected cross-section was rigorously analyzed using the theory of complex functions combined with conformal mapping techniques. The two distinct material regions within the cross-section, featuring an external square and an internal circular boundary for S_1, and an eccentrically positioned rounded-corner square for S_2, posed significant challenges in satisfying both boundary and interface continuity conditions. By representing the analytic functions $\phi_1(z)$and $\phi_2(z)$as series expansions and systematically applying boundary and contact conditions on all contours, infinite systems of linear algebraic equations were derived. A finite subset of these equations was then solved numerically to obtain the unknown series coefficients, allowing precise computation of shear stresses, warping functions, and torsional rigidity across the entire cross-section.

References

1.Galuppi, L., & Thomazini, I. R. (2019). Membrane analogy for multi-material bars under torsion. Proceedings of the Royal Society A: Mathematical, Physical and Engineering Sciences, 475(2224), 20190124. Royal Society. https://doi.org/10.1098/rspa.2019.0124
2.Chen, J.-T., & Lee, Y.-T. (2009). Torsional rigidity of a circular bar with multiple circular inclusions using the null-field integral approach. Computational Mechanics, 44, 453–463. Springer. https://doi.org/10.1007/s00466-009-0365-8
3.Chou, S. L., & Mohr, J. A. (2016). Boundary integral method for torsion of composite shafts. North Carolina State University Repository. North Carolina, USA.
4.Sapountzakis, E. J. (2003). Warping shear stresses in nonuniform torsion of composite materials. International Journal of Solids and Structures, 40(17), 4543–4565. Elsevier. https://doi.org/10.1016/S0045-7825(03)00417-1
5.Teimoori, H., Faal, R., & Das, R. (2016). Saint-Venant torsion analysis of bars with rectangular cross-section and effective coating layers. European Journal of Mechanics – A/Solids, 57, 1–12. Elsevier.

https://doi.org./10.58225/mpmma.2026.44

APPLICATION OF ARTIFICIAL INTELLIGENCE IN LEAN MANUFACTURING

Asif Guliyev[1], Parviz Mammadov[1], Vasif Kerimov[1,2], Xazar Necimbeyli[1], Valeh Alquluyev[1], Ilgar Khurshudov[1]

[1]Baku Engineering University, Azerbaijan

[2]Institute of Mathematics, Azerbaijan ,

Abstract: Lean manufacturing was developed in Japan, targeting the reduction of waste, the improvement of quality, and the optimization of inventory levels. This article defines and emphasizes the need to study the definition and importance of lean and integrated lean manufacturing, the application of artificial intelligence (AI) in lean manufacturing and, finally, the application of hybrid methods. The application of AI in lean manufacturing helps companies reach their goals with minimized errors, low waste, high quality, reduced lead times, high integrity, and minimized risks and safety issues. Global competition, geopolitical issues, and the scarcity of raw materials urge companies to apply modern techniques.

Keywords: Lean manufacturing, AI & ML, hybrid methods, Total Coliform, BOD, COD, Influent, Effluent.

The purpose of the study is to define lean manufacturing, clarify AI & ML (Artificial Intelligence & Machine Learning) applications, and explain the importance of applied hybrid methods in

modern integrated lean manufacturing. It aims to clearly define the goals of applied methods, such as achieving maximum efficiency, minimizing waste, increasing quality, and minimizing costs without harming the environment, human health, and safety. Additionally, it seeks to clarify the practical application of hybrid methods in wastewater treatment systems. The research methodology involves the definition and application of AI tools alongside traditional lean manufacturing methods, such as hybrid methods, and an analysis of their importance.

1. Introduction

Lean manufacturing is defined as the achievement of low waste, high quality, increased safety, optimized material management, reduced production costs, and efficiency during the manufacturing and treatment processes. Integrated lean manufacturing focuses not only on the production process, but also on raw material quality, the recycling of production waste, and the quality of the final product [5]. Although traditional lean manufacturing has been applied successfully, there is a need for methods such as hybrid applications for further enhancement in order to achieve 95-98% of targets. The structure of this manufacturing approach is to identify all types and causes of waste and create actions to eliminate them [7]. Waste reduction has also led to the optimization of raw materials management due to global geopolitical and economic issues, as these factors contribute to material scarcity. Thus, the application of AI methods optimizes lean approaches [1].

2. Method

2.1 Integrated Lean Manufacturıng Tools

Integrated lean manufacturing combines all lean tools with advanced technologies to enhance safety, efficiency, cost reduction, and agility in the production system. This approach focuses on minimizing total waste to optimize the scarcity level of raw materials. This manufacturing paradigm provides the tools for optimizing the production process. Integrated lean manufacturing combines traditional methods and new AI tools to maximize efficiency at each step of manufacturing. All tools work together to create an optimized system. Lean manufacturing utilizes key tools:

1. Lean 9S System: The initial 5S system was created by Japan's Toyota, and another four S's were evolved by other companies: (1S) Sort, (2S) Set in order, (3S) Shine, (4S) Standardize, (5S) Sustain, (6S) Safety, (7S) Spirit, (8S) Saving (total production and quality cost), and (9S) Satisfaction, 2. Production KANBAN cards, 3. Just-in-Time, 4. KAIZEN (continuous improvement), 5. Value stream mapping, 6. Poka-Yoke (mistake-proofing methods).

3. Results

3.1 AI & ML Methods In Integrated Lean Manufacturıng

Considering global market issues, AI methods are being intensively applied in manufacturing to optimize activities, mainly focusing on reducing time for operation, maintenance, and research activities, while enhancing safety and decision-making. Mathematical and theoretical methods are applied in AI/ML tools to improve production. Another key advantage of AI tool applications is the

ability to provide accurate predictions and forecasting for problem-solving:- Predictive maintenance and service:

- Periodical quality control and continuous quality improvement: AI can identify quality issues before they occur, define possible product defects to significantly lower defect rates, and identify the root causes of defects [3].
- Real-time Data Analysis: This enables continuous process monitoring and the immediate identification of inefficiencies, poor raw material or product quality, and unsafe conditions to prevent incidents and hazards and implement timely solutions.
- Predictive Production Planning: AI can forecast production demand with high accuracy over both short and long durations, reducing forecasting errors by 10-15% [8].
- Predictive Safety Management: AI can predict unsafe acts and conditions related to equipment, the environment, and personnel. It can also identify potential root causes and sub-causes of accidents and anticipate future safety risks [4].
- Integrated Just-in-Time (JIT): AI and ML minimize production time, optimize inventory management, and can reduce time loss by 10%.
- The tool for continuous improvement: An AI-powered time and motion study that eliminates the need for manual data observation, analysis, and decision-making for improvement.
- Automated FMEA (Failure Mode and Effects Analysis) and PFMEA (Process Failure Mode and Effects Analysis): This method identifies operational and maintenance failures before they occur. AI tools detect upcoming defects, operational

risks, and downtime risks, as well as potential hazards, transforming all data into historical records and reports.

- AI & ML-driven product design modeling: New product modeling or upgrading existing designs takes significant time and effort using classical methods. AI-driven design reduces this time by focusing on customer behavior, eliminating predicted errors, and reducing external and internal market research time.
- Equipment selection and location: AI-driven equipment selection and location are critical steps in production that typically require intensive effort.
- Digital work operations and instructions: AI-driven tools enable periodical reviews and updates of operational procedures and work instructions for production management.
- AI-based production line balancing: AI-driven line balancing systems optimize the distribution of all planned and scheduled workloads across all stations.
- AI-based production planning and scheduling: Planning is the heart of production, and any error can lead to production losses. AI-based production planning and control (PPC), especially integrated PPC, combines all production-related activities to eliminate implementation delays, optimize inventory, and increase customer satisfaction, leveraging lean tools such as 9S to define customer satisfaction [4].

4.Dıscussıon

4.1 Hybrıd Applıcatıon

Hybrid applications are the latest method in lean manufacturing to enhance productivity, efficiency, safety, and cost reduction. The hybrid method

eliminates errors and risks associated with the initial application of AI tools. This method is initially applied in the quality control of liquid-type production, production-demand forecasting, and primarily in maintenance activities.

Conclusion

The integration of AI with lean manufacturing marks a significant evolution in the traditional process improvement approach. Instead of replacing lean fundamentals, AI complements them by addressing the limitations of lean tools. The results can be observed through waste reduction, higher product quality, cost reduction, and real-time continuous improvement. Additionally, integrating AI with lean manufacturing through mathematical modelling enhances efficiency, reduces waste, improves product quality, and eliminates unsafe acts and conditions. This combination is essential for manufacturers aiming to thrive in the competitive landscape of the industry.

References

1. V.Kerimov, textbook, Lean Manufacturing, pp-5-20, 2025,
2. Daryl John Powell, Artificial Intelligence and Lean Manufacturing, International Journal of Lean Six Sigma , pp3-7, 2024.
3. Amit Mahajan, Gurpreet Singh, Sandeep Devga n, Gurcharan Singh, Parneet Kaur,"Next-generation manufacturing: leveraging AI for industrial innovation and growth", Journal of Computers & Industrial Engineering, pp2-6, 2024.

4. Matthew Finio,Amanda Downie, IBM Think,How is AI being used in manufacturing, pp2-8, 2025,
5. V.Kerimov, textbook, Lean Manufacturing, pp-5-20, 2025,
6. Authors,by V. Kerimov.
7. A. Safari,M. M. Parast,V. B.Al Ismail, “Lean Six Sigma, ISO 9001, and organizational performance: An integrated approach, Journal of Quality Management Journal ,Vol 32, Issue 3, pp1-3, 2025 ,
8. Olufemi Theophilus, “Lean Manufacturing Practices and Organizational Performance: A Literature Review”, International Journal of Innovative Science and Research Technology, Vol 9, Issue 9, pp2-4, 2024,
9. P.Mammadov.V.Alguluyev, I.Khushudod, K.Necimbeyli, “The application of Six Sigma methodology in quality improvement” Azerbaijan Oil Industry Journal, SOCAR, DOI: 10.37474/0365-8554/2026-02-68-76, Vol 2, Issue 6, pp 2-5, 2026.

https://doi.org./10.58225/mpmma.2026.51

MATHEMATICAL MODELING OF THE BENDING DURABILITY OF A FUNCTIONALLY GRADED PRISMATIC BEAM

Abdullah H.Sofiyev[1], Sahib Piriyev[2], Mahsati Rustamova[3]

[1]Istanbul Ticaret University, Türkiye,
[2]Azerbaijan Technical University, Azerbaijan
[3] AzUAC, Azerbaijan

Abstract. The present study investigates the bending durability of a prismatic beam made of a Functionally Graded Material (FGM) exhibiting different elastic properties in tension and compression (bimodular behavior), with material properties varying through the thickness according to a power-law distribution. The viscoelastic behavior of the material and the damage accumulation process are modeled using Abel-type integral operators. The proposed mathematical model makes it possible to determine the shift of the neutral axis in the beam cross-section and to describe the time-dependent propagation of the failure front (crack). Numerical calculations reveal that the material gradation parameter (n) has a significant influence on the kinetics of the failure process. The obtained results may be applied in the design of FGM-based structural elements and in predicting their service life.

Keywords: Functionally Graded Material (FGM), bending, bimodularity, durability, damage accumulation, Abel kernel, power-law distribution.

Introduction.

Modern engineering structural components, particularly those used in aerospace and power engineering systems, operate under extreme conditions, which necessitates the application of advanced materials. In this regard, Functionally Graded Materials (FGMs) are considered an effective solution for overcoming the limitations of conventional composites [1,2]. FGMs are structures with continuously varying properties along a certain direction and possess the ability to minimize stress concentrations while providing high thermal resistance [3,4].

The investigation of failure mechanisms in FGM structural elements under bending has long attracted the attention of researchers. In particular, the analysis of beams exhibiting bimodular behavior, i.e., having different elastic moduli in tension and compression, requires a more sophisticated approach [5,6]. Various analytical and numerical methods for determining the stress–strain state of non-homogeneous materials have been proposed in the literature [7,8]. The analysis of the bending behavior of power-law graded FGM beams has shown that the gradation index directly affects the load-carrying capacity of the material [9,10].

In the present study, the damage process in a bimodular FGM beam under bending is mathematically modeled. The main novelty of the work lies in the simultaneous consideration of material non-homogeneity and bimodularity through

an Abel-kernel-based damage model for evaluating the failure time and crack propagation rate. The calculations demonstrate that an increase in the gradation index leads to a higher concentration of the metallic phase in the tensile zone, thereby increasing the service life of the material.

1. Problem Formulation

In the present paper, the problem of distributed failure of a straight beam made of a Functionally Graded Material (FGM) with different elastic properties in tension and compression under pure bending is considered. For this purpose, the investigated body is assumed to be continuous, non-homogeneous through the thickness, and deformable. At the same time, material non-homogeneity is manifested in a specific manner. In particular, the Young's modulus is assumed to vary through the thickness according to a power-law functional dependence, and different elastic properties are assumed depending on the sign of the principal stresses (positive or negative) at a given point of the material. Consequently, when the principal stresses at a given point or region of the body have the same sign (tension, $\sigma_i > 0$, or compression, $\sigma_i < 0$, where i denotes the principal direction), the system of elastic constants differs from that adopted in the classical theory of elasticity.

For FGMs, the classical Young's modulus is expressed as follows:

$$E(y_0) = E_m + (E_c - E_m)\left(\frac{y_0}{h_0}\right)^n \quad (1)$$

here, E_m denotes the Young's modulus of the metallic phase, E_c denotes the Young's modulus of the ceramic phase, h_0 is the initial thickness of the material, y_0 is the coordinate measured from the neutral axis, and n is the gradation index.

Under pure bending, the region $y_0 > 0$ corresponds to the tensile zone, whereas the region $y_0 < 0$ corresponds to the compressive zone. However, expression (1) contains the term $(y_0/h_0)^n$, which means that the relation is written only for one side $(0 \le y_0 \le h_{01})$. As follows from this expression, the layer corresponding to $y_0 = 0$ is metal-rich, whereas the layer corresponding to $y_0 = h_{01}$ is ceramic-rich, indicating that the material is mechanically non-symmetric.

If tension occurs in the ceramic-rich layer, then $y_0 \to h_{01}$, and consequently $E(y_0) \approx E_c$. Therefore, although the Young's modulus is high and the deformation is small in the tensile zone, brittle behavior is observed. As a result, the tensile strength limit of the material is low, whereas its stiffness is high.

If compression occurs in the metal-rich region, then $y_0 \to 0$, and consequently $E(y_0) \approx E_m$. Therefore, although the Young's modulus under compression is lower, crack propagation is delayed due to the occurrence of plastic deformation in the metallic phase. As a result, the material exhibits higher resistance under compression.

1.1. Bimodular Approach

If different behavior is assumed for tension and compression, the variation of the Young's modules through the thickness for the tensile and compressive layers is expressed as follows:

$$E(y_0) = \begin{cases} E^+(y_0), & y_0 > 0 \\ E^-(y_0), & y_0 < 0 \end{cases} \tag{2}$$

here, E_m^+ and E_c^+ denote the elastic moduli in the tensile region, whereas E_m^- and E_c^- denote the elastic moduli in the compressive region.

Thus, when the principal stresses have different signs, the elastic constants are represented by two different functional dependencies in the form of Eq. (2). In other words, the material possesses the elastic modulus $E^+(y_0)$ under uniaxial tension in a given direction and the elastic modulus $E^-(y_0)$ under uniaxial compression in another direction.

As is well known, under pure bending, the fibers parallel to the longitudinal axis of symmetry of the beam bend during deformation, change their lengths, and the cross-section of the strip rotates with respect to the neutral axis. The fibers located on the convex side of the beam are elongated, whereas the fibers on the concave side are shortened. Between the convex and concave regions, there exists a layer whose length remains equal to the initial length of the beam before bending; that is, the fibers forming this layer are not subjected to deformation. This layer is referred to as the neutral layer. The line of intersection of the neutral layer with the beam cross-section is called the neutral axis. The fibers located on one side of the neutral layer are subjected to tension, whereas those located on the opposite side are subjected to compression. Consequently, except for the points

lying on the neutral axis, only normal stresses arise at all points of the beam cross-section.

1.2. Determination of the Neutral Layer under Pure Bending

The initial cross-section of the beam is assumed to be rectangular, with height h_0 and width b ($h_0 < b$). Let the initial horizontal axis coinciding with the neutral axis be denoted by x_0, the transverse coordinate measured from this axis by y_0, and the constant bending moment generated during the bending of the beam edges by M_x.

Using the moment equilibrium condition together with expressions (2), the normal stresses arising in both layers are determined as follows:

$$\sigma_x^+ = \frac{3(n+3)M_x}{b[(n+3k^+)h_{01}^3+(n\alpha_m+3k^+\alpha_c)h_{02}^3]}\left(y_0 + \frac{k^+-1}{h_{01}^n}y_0^{n+1}\right) \quad (3)$$

$$\sigma_x^- = \frac{3\alpha_m(n+3)M_x}{b[(n+3k^+)h_{01}^3+(n\alpha_m+3k^+\alpha_c)h_{02}^3]}\left(y_0 + \frac{k^--1}{(-h_{02})^n}y_0^{n+1}\right) \quad (4)$$

Since the beam material possesses different strength properties under tension and compression, the strength criteria are expressed as follows [11]:

$$\sigma_x^+ + B_*^+\sigma_x^+ = \sigma_s^+, \quad \sigma_x^- + B_*^-\sigma_x^- = \sigma_s^- \quad (5)$$

here, σ_s^+ and σ_s^- denote the instantaneous strength limits of the material under tension and compression, respectively, whereas B_*^+ and B_*^- are

the integral operators characterizing damage accumulation under tension and compression.

In the case of a monotonically increasing loading process, the viscoelasticity is represented in the form of the following integral operator [12]:

$$B_*^+\sigma_x^+ = \int_0^t B^+(t-\tau)\sigma_x^+ d\tau,\ B_*^-\sigma_x^- = \int_0^t B^-(t-\tau)\sigma_x^- d\tau \quad (6)$$

here, $B^+(t-\tau)$and $B^-(t-\tau)$are referred to as the damage kernels.

2. Modeling of the Explicit Failure Stage

At the subsequent stage, the layer adjacent to the failed layer begins to fail as well, and as the failure region expands, a layer with variable thickness δ is formed. As the failure region propagates, the coordinate ydecreases; therefore, this coordinate is measured from the neutral x-axis (Fig. 1).

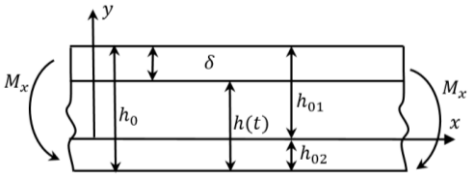


Figure 1. Propagation scheme of the failure front in the beam.

The following dimensionless quantities are introduced:

$$k^+ = \frac{E_c^+}{E_m^+};\ k^- = \frac{E_c^-}{E_m^-};\ \mu = \sqrt{\frac{n+2k^+}{n+2k^-}};\ \eta = n + 3k^+ + \mu^3(n\alpha_m + 3k^+\alpha_c);\ \theta = \lambda t;\ \xi = \lambda\tau;\ f(\theta) = \frac{y(t)}{h_{01}};\ f(\xi) = \frac{h_1(\tau)}{h_{01}}$$

here, λ is a constant quantity whose dimension is the inverse of time.

By introducing the above dimensionless quantities into Eq. (5) and substituting the resulting expression into the failure criterion (8), the following integral equation is obtained:

$$\frac{k^+}{f^{n+3}(\theta)} + \frac{1}{f^n(\theta)}\int_0^\theta B_1^+(\theta-\xi)\frac{d\xi}{f^3(\xi)} + \int_0^\theta B_1^+(\theta-\xi)\frac{k^+-1}{f^{n+3}(\xi)}d\xi = \frac{\chi}{f^{n+1}(\theta)} \quad (7)$$

here,

$$\chi = \frac{bh_{01}^2\eta\sigma_s^+}{3(n+3)M_x} \quad (8)$$

The kernel of the integrals appearing in Eq. (7) is represented in dimensionless form as $B_1^+(\theta-\xi) = \lambda^{-1}B^+(\theta-\xi)$. Here, $\lambda$is a constant quantity whose dimension is the inverse of time.

In order to qualitatively characterize the failure process and perform analytical evaluations, the kernel of the damage operator is assumed in the form $B^+(\theta-\xi) = \lambda$, which yields $B_1^+(\theta-\xi) = 1$.

After differentiating both sides of Eq. (7) with respect to the dimensionless time, the resulting differential equation is obtained. Since this equation is nonlinear, numerical methods are considered more convenient for its solution. One of the most

effective approaches is the Runge–Kutta method. In MATLAB, the function “ode23,” commonly used for solving differential equations, represents second- and third-order Runge–Kutta integration schemes. By applying this function, the differential equation was solved under the initial condition $f(\theta_0) = 1$, and the following results were obtained: $h_0 = 0.05$ m; $b = 0.03$ m; $E_c^+ = E_c^- = 1.68063 * 10^5$ Pa; (ZrO2); $E_m^+ = E_m^- = 1.056982 * 10^5$ Pa; (Ti6A14V).

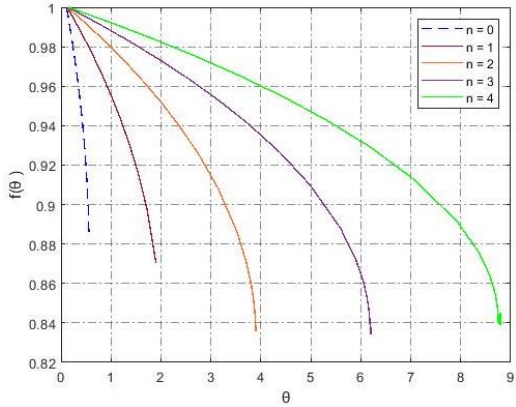


Figure 2. Curves describing the

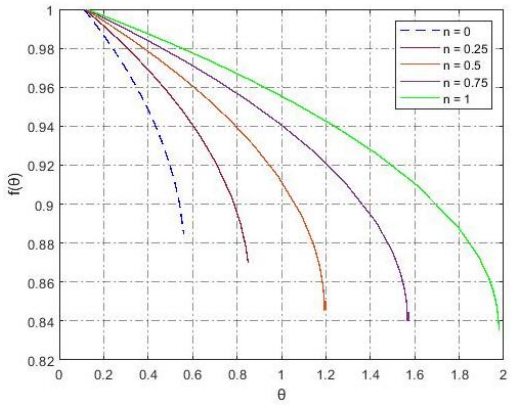


Figure 3. Curves describing the

propagation of the failure front for integer values of the gradation parameter.

propagation of the failure front for fractional values of the gradation parameter.

For Ti–Al–4V + ZrO2 FGMs, the relation $E^+ \approx E^-$is generally observed under ideal conditions. However, due to the influence of microcracks, thermal shocks, and material fatigue, the relation $E^+ < E^-$ may occur. This is because voids tend to close under compression, resulting in an increase in stiffness, whereas under tension the voids expand further, leading to a reduction in stiffness. Under such conditions, the difference between the elastic moduli of the tensile and compressive layers may reach 20–40%. The results of the calculations carried out for this case are presented below: $h_0 = 0.05$ m; $b = 0.03$ m; $E^+(z) < E^-(z)$.

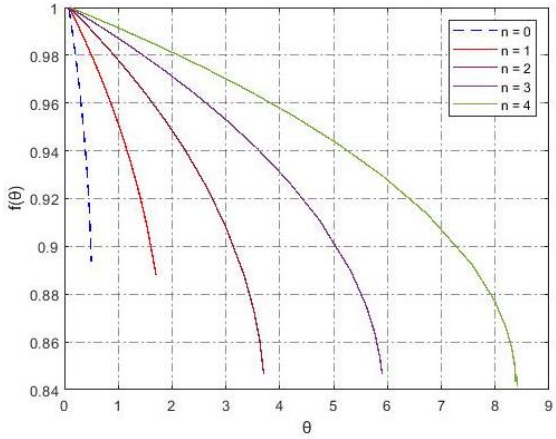


Figure 4. Curves describing the propagation of the failure front for integer values of the gradation parameter.

As can be seen from the graphs, the function $f(\theta)$, representing the dimensionless thickness of the beam, gradually decreases with time, which indicates the propagation of the failure front. However, the main difference lies in the fact that an increase in the value of the gradation parameter slows down the failure process. Thus, when $n = 0$, failure occurs most rapidly, whereas with increasing n, the beam thickness is preserved to a greater extent.

This indicates that for small values of n, the material becomes more homogeneous, and the proportion of brittle ceramic phase in the tensile zone is relatively high. As a result, stress peaks increase, leading to rapid crack propagation and, consequently, acceleration of the failure process.

For larger values of n, the metallic phase fraction increases toward the tensile zone, resulting in local plastic deformation. This promotes energy absorption and consequently suppresses the propagation of macrocracks, thereby increasing the service life of the material.

References

1. Koizumi, M.: FGM activities in Japan. *Compos. Part B: Eng.* 28 (1–2), 1–4 (1997). https://doi.org/10.1016/S1359-8368(96)00016-9
2. Erdogan, F.: Fracture mechanics of functionally graded materials. *Compos. Eng.* 5 (7), 753–770 (1995). https://doi.org/10.1016/0961-9526(95)00029-M
3. Suresh, S.; Mortensen, A.: *Fundamentals of Functionally Graded Materials.* IOM Communications Ltd., London (1998).

4. Reddy, J.N.: Analysis of functionally graded plates. *Int. J. Numer. Meth. Engng.* 47, 663–684 (2000). https://doi.org/10.1002/(SICI)1097
5. Birman, V.; Byrd, L.W.: Modeling and analysis of functionally graded materials and structures. *Appl. Mech. Rev.* 60 (5), 195–216 (2007). https://doi.org/10.1115/1.2777164
6. Shen, H.S.: Functionally graded materials. In: *Nonlinear Analysis of Plates and Shells.* CRC Press, Boca Raton (2016). https://doi.org/10.1201/9781420092578
7. Sofiyev, A.H.: Review of research on the vibration and buckling of FGM conical shells. *Compos. Struct.* 211, 301–317 (2019). https://doi.org/10.1016/j.compstruct.2018.12.047
8. Sofiyev, A.H.; Schnack, E.: Stability of functionally graded cylindrical shells under linearly increasing dynamic torsional loading. *Eng. Struct.* 26, 1321–1331 (2004). https://doi.org/10.1016/j.engstruct.2004.03.016
9. Shen, Y.; Chen, Y.; Li, L.: Torsion of a functionally graded material. *Int. J. Eng. Sci.* 109, 14–28 (2016). https://doi.org/10.1016/j.ijengsci.2016.09.003
10. Batra, R.C.: Torsion of a functionally graded cylinder. *AIAA J.* 44 (6), 1363–1365 (2006). https://doi.org/10.2514/1.19555
11. Akhmedov, N.K.; Piriev, S.A.; Rustamova, M.A.: Long-term strength of cylindrical rods under torsion. *Mech. Solids* 59, 1603–1613 (2024). https://doi.org/10.1134/S0025654424603434

12. Hasanov, M.; Namazov, S.; Abdullayev, Kh.; Piriev, S.: Durability of thin-walled rods with multimodular properties. *J. Compos. Sci.* 9 (8), 437 (2025). https://doi.org/ 10.3390/jcs9080437

https://doi.org./10.58225/mpmma.2026.64

SHORT PULSE EQUATION WITH A DISSIPATIVE TERM

Aygul Babadjanova[1,2], Gulchekhra Eshchanova[1], Jamshidbek Xudayberganov[1]

[1] Urgench State University, Uzbekistan;

[2] V.I. Romanovskiy Institute of Mathematics, Uzbekistan;

Abstract. The short pulse (SP) equation is an important nonlinear evolution equation arising in the modeling of ultra-short optical pulse propagation in nonlinear media. In this paper, we study a modified SP equation containing an additional dissipative term. The analysis is carried out within the framework of the inverse scattering transform (IST), which is one of the most effective methods for investigating integrable nonlinear equations.

Keywords: short pulse equation, inverse scattering transform, Dirac-type system, scattering data, discrete spectrum, dissipative perturbation.

Introduction

The short pulse (SP) equation [6] plays an important role in the description of ultra-short optical pulse propagation in nonlinear media [4-5]. Its hierarchy and bi-Hamiltonian structure were investigated by Brunelli [1,2], while exact solutions were derived through the associated WKI spectral problem [5]. Analytical studies based on the inverse scattering transform and Riemann--Hilbert methods have established a rigorous framework for solving initial value problems for

both the real and complex short pulse equations [3,7]. For the classical SP equation, the IST is based on an associated Dirac-type spectral problem [5]:

$$\psi_{1x}(\lambda,x,t)+i\lambda\psi_1(\lambda,x,t)=\lambda q_x(x,t)\psi_2(\lambda,x,t),$$
$$\psi_{2x}(\lambda,x,t)-i\lambda\psi_2(\lambda,x,t)=-\lambda q_x(x,t)\psi_1(\lambda,x,t). \quad (1)$$

The spectral problem is non-self-adjoint; the continuous spectrum fills the real axis, while the discrete spectrum consists of finitely many complex eigenvalues symmetric with respect to the real axis.

In this paper, we consider a short pulse equation with an additional dissipative term. Using the associated Dirac-type spectral problem, we derive the evolution equations for the scattering data and show that the discrete spectrum remains invariant under the time evolution.

Statement of the Problem and Main Result

We consider the short pulse equation with an additional term:

$$q_{xt}=q+\frac{1}{6}\left(q^3+\frac{3}{2}q_x^2q\right)_{xx}+\gamma(t)q_{xx} \quad (2)$$

under the initial condition:

$$q_x(x,0)=q_0(x) \quad (3)$$

Here $\gamma(t)$ is a given continuous and bounded function, and $q_0(x)$ is a real potential function satisfying the condition:

$$\int_{-\infty}^{+\infty}(1+|x|)|q_0(x)|dx<\infty. \quad (4)$$

Equation (2) can be viewed as a perturbed short pulse equation incorporating a dissipative (or diffusive) effect through the term $\gamma(t)q_{xx}$.

In this work, we investigate the short pulse equation with a dissipative term within the framework of the inverse scattering transform. The associated spectral problem is formulated in terms of a Dirac-type system, and the corresponding scattering data are introduced.

We assume that the function $q(x,t)$ is sufficiently smooth and rapidly decays as $|x| \to \pm\infty$, namely:

$$\int_{-\infty}^{+\infty} (1+|x|)(|q(x,t)|+|q_{xx}(x,t)|)dx < \infty. \tag{5}$$

We derive the time evolution of the scattering data of the Dirac-type system $\{\rho(\lambda,t), \lambda_k(t), c_k(t)\}_{k=1}^{N}$ and prove that the discrete spectrum is time invariant.

Theorem 1. Let $q(x,t)$ be a solution of the problem (2)–(5). Then the scattering data of the system (1) satisfy the following differential equations:

$$\dot{\rho}(\lambda,t) = \left(-\frac{i}{2\lambda} + 2i\lambda\gamma(t)\right)\rho(\lambda,t),$$

$$\dot{\lambda}_j = 0,$$

$$\dot{c}_j(t) = \left(A_j(t) - \frac{i}{2\lambda_j} + 2i\lambda_j\gamma(t)\right)c_j(t),\ j = \overline{1,N}.$$

Remark. The obtained relations completely specify the time evolution of the scattering data for the system (1) and this allows using the inverse scattering method to find the solution of the problem (2)–(5).

References

Brunelli, J.C.: The short pulse hierarchy. J. Math. Phys. 46, 123507 (2005).

Brunelli, J.C.: The bi-Hamiltonian structure of the short pulse equation. Phys. Lett. A 353, 475–478 (2006).
Boutet de Monvel, A., Shepelsky, D., Zielinski, L.: The short pulse equation by a Riemann–Hilbert approach. Lett. Math. Phys. 107, 1345–1373 (2017).
Feng, B.-F.: Complex short pulse and coupled complex short pulse equations. Physica D 297, 62–75 (2015).
Kuetche Kamgang, V., Bouetou, T., Kofane, T.C.: On exact solutions of the Schafer–Wayne short pulse equation: WKI eigenvalue problem. J. Phys. A: Math. Theor. 40, 5585–5596 (2007).
Shimizu, T., Wadati, M.: New integrable nonlinear evolution equation. Prog. Theor. Phys. 63, 1745–1757 (1980).
Prinari, B., Treubatch, A.D., Feng, B.-F.: Inverse scattering transform for the complex short-pulse equation by a Riemann–Hilbert appro

https://doi.org./10.58225/mpmma.2026.68

APPLICATIONS OF COUPLED DIFFERENTIAL EQUATIONS FOR BIOFILM NITRIFICATION MODELS

Marimuthu Annamalai[1], Krithiga Raja[2], Lakshmanan Rajendran[1], Kodakkal Kannan Viswanathan[3-1]

[1]AMET University, India

[2] Bohai University, China

[3] Samarkand State University,Uzbekistan

Abstract. This study presents a detailed analytical investigation of a coupled reaction–diffusion system arising in biofilm nitrification models. The governing equations consist of transient nonlinear partial differential equations describing the spatiotemporal evolution of interacting chemical species influenced by diffusion and reaction kinetics. By applying appropriate transformations and reduction techniques, the complex coupled system is simplified into a tractable form, enabling the derivation of explicit closed-form solutions for concentration profiles. The analysis highlights the role of key parameters, including reaction rate coefficients, diffusion constants, and biofilm thickness, in shaping system behavior. In particular, the interaction between diffusion transport and nonlinear reaction terms is carefully examined through the obtained analytical expressions. Furthermore, a direct functional relationship between the dependent variables is established, providing additional insight into system coupling. The availability of exact analytical solutions offers reliable benchmarks for

validating numerical methods and supports efficient parameter estimation in practical nitrification modeling applications.

Keywords: Reaction–diffusion systems, Analytical solutions, Biofilm nitrification.

Introduction

Reaction–diffusion systems are fundamental mathematical models describing the spatiotemporal behavior of interacting species under diffusion and nonlinear reactions. They arise in chemical kinetics, biological pattern formation, environmental processes, and electrochemical systems. These models are typically governed by nonlinear partial differential equations (PDEs), making analytical solutions difficult due to the coupling of transport and reaction mechanisms. Recent studies by Ahmed et al. [1] and Cherniha and Davydovych [2] highlight these challenges. Coupled reaction–diffusion systems are particularly important in biofilm nitrification, where microbial processes exhibit strong nonlinear interactions, as studied by Wik [3,4], and Rajendran et al. [5].

2. Theoretical Formulation

After nondimensionalization, dimensionless bulk-liquid mass balances for ammonium and nitrate in a completely mixed volume V are formulated [3,4].

$$\frac{\partial S_{NH_4}(\xi,\bar{t})}{\partial \bar{t}} = \frac{\partial^2 S_{NH_4}(\xi,\bar{t})}{\partial \xi^2} - \kappa_1 S_{NH_4}(\xi,\bar{t}) - \mu_1 \quad (1)$$

$$\eta \frac{\partial S_{NO_3}(\xi,\bar{t})}{\partial \bar{t}} = \frac{\partial^2 S_{NO_3}(\xi,\bar{t})}{\partial \xi^2} + \kappa_2 S_{NH_4}(\xi,\bar{t}) + \mu_2 \quad (2)$$

The initial conditions are $S_{NH_4}(\xi,0) = S_{in}$ & $S_{NO_3}(\xi,0) = U_{in}$ (3)

Appropriate boundary conditions at the biofilm-support interface are

$$\left.\frac{\partial S_{NH_4}}{\partial \xi}\right|_{\xi=0} = 0\,, \quad \left.\frac{\partial S_{NO_3}}{\partial \xi}\right|_{\xi=0} = 0 \quad (4)$$

Continuity of concentration and diffusive flux at the biofilm-bulk interface is

$$S_{NH_4}(\xi,\bar{t})\,|_{\xi=1} = S^b_{NH_4} \;\&\; S_{NO_3}(\xi,\bar{t})\,|_{\xi=1} = S^b_{NO_3} \quad (5)$$

where S_{NH_4} and S_{NO_3} are concentrations; κ_1, κ_2 rate constants; μ_1, μ_2 growth rates; ξ space, η time-scale, $\bar{t}$ dimensionless time.

2.1 Methodology

The solution is obtained via separation of variables and eigenfunction expansion, decomposing into steady-state and transient parts, where eigenvalues govern exponential decay and convergence toward equilibrium concentration profiles.

3. Results and Discussion

$$S_{NH_4}(\xi,\bar{t}) = \left(1+\frac{\mu_1}{\kappa_1}\right)\frac{\cosh(\sqrt{\kappa_1}\,\xi)}{\cosh(\sqrt{\kappa_1})} - \frac{\mu_1}{\kappa_1} + 2\sum_{n=0}^{\infty}\left[(-1)^n\left(\frac{S_{in}+\mu_1/\kappa_1}{\beta_n} - \frac{(1+\mu_1/\kappa_1)\beta_n}{\kappa_1+\beta_n^2}\right)\right] e^{-(\beta_n^2+\kappa_1)\bar{t}}\cos(\beta_n,\xi) \quad (6)$$

$$S_{NO_3}(\xi,\bar{t}) = f_b + \frac{(\mu_2-\mu_1)}{2}(1-\xi^2) - S_{NH_4}(\xi,\bar{t}) + 2\sum_{n=0}^{\infty}(-1)^n\left[\frac{f_0-f_b}{\alpha_n} - \frac{\mu_2-\mu_1}{\alpha_n^3}\right]e^{-(\alpha_n^2)\bar{t}}\cos(\alpha_n,\xi) \quad (7)$$

where $\alpha_n = \frac{(2n+1)\pi}{2}$ & $\beta_n = \left(n+\frac{1}{2}\right)\pi$

(8)

An analytical relation between S_{NH_4} and S_{NO_3} clarifies nitrification coupling and provides a benchmark for validating numerical biofilter models and predicting nitrogen dynamics accurately.

$$S_{NO_3}(\xi) = 1 + \frac{\mu_2-\mu_1}{2}\left(1-\frac{\Theta^2(\xi)}{\kappa_1}\right) - S_{NH_4}(\xi) \quad (9)$$

where, $\Theta(\xi) = \cosh^{-1}\left(\frac{\kappa_1 S_{NH_4}(\xi)+\mu_1}{\kappa_1+\mu_1}\cosh(\sqrt{\kappa_1})\right)$ (10)

0 0.2 0.4 0.6 0.8 1

ξ

Fig. 1. a) $S_{NH_4}(\xi,\bar{t})$ vs. ξ for different μ_1 when $S^b_{NH_4} = 1, \kappa_1 = 2, \bar{t} = 2$. 1.b) $S_{NO_3}(\xi,\bar{t})$ vs. ξ for different μ_1 when $S^b_{NO_3} = 1,\ \bar{t} = 5,\ \kappa_1 = 2$.

Fig. 1. (a) and (b) show that increasing μ_1 accelerates substrate depletion and steepens spatial gradients. The coupled reaction–diffusion system indicates faster ammonium and nitrate consumption, reflecting enhanced nitrification rates and diffusion-limited transport within the biofilm.

4. Conclusion

A reaction–kinetic framework describes nitrification in trickling filters, capturing coupled transport–reaction behavior. Analytical solutions reveal interactions among kinetics, diffusion, and biofilm thickness, identifying kinetic–diffusion

transitions. Results support parameter estimation, optimization, and extension to diverse geometries for improved catalytic reactor design and performance.

References

1. Ahmed, N., et al.: Scientific Reports 13, 20033 (2023). https://doi.org/10.1038/s41598-023-47207-4
2. Cherniha, R. M.,et al.: European Journal of Applied Mathematics 33(5), 785–802 (2022). https://doi.org/10.1017/S095679252100022X
3. Wik, T.: Ph.D. thesis, Chalmers University of Technology, Sweden (1999).
4. Wik, T.: Water Science and Technology 39, 121–128 (1999). https://doi.org/10.1016/S0273-1223(99)00066-9
5. Rajendran, L., et al.: European Journal of Mathematics and Statistics 4(1), 24–31 (2023). https://doi.org/10.24018/ejmath.2023.4.1.168

https://doi.org./10.58225/mpmma.2026.73

ELASTIC–PLASTIC BENDING OF A RECTANGULAR BEAM MADE OF A NON-HARDENING MATERIAL

Amirkhan Sazairov, Mahsati Rustamova
AzUAC, Azerbaijan

Abstract. The present study investigates the elastic–plastic bending behavior of a rectangular beam made of a perfectly plastic material according to the Prandtl stress–strain model. The development of stress distribution across the beam cross-section and the transition from elastic to fully plastic behavior is analytically examined. Expressions for the bending moment, elastic core size, beam deflection, and strain energy are obtained. The conditions corresponding to the initiation of yielding and the formation of a plastic hinge are determined. It is shown that plastic zones gradually propagate from the outer fibers toward the center of the cross-section as the external load increases. The obtained analytical relations can be effectively used in limit-state analysis and the design of structural elements operating beyond the elastic range.

Keywords: Elastic–plastic bending; Rectangular beam; Prandtl model; Plastic hinge; Yield stress; Beam deflection; Strain energy

1. Introduction

The analysis of structural elements beyond the elastic range is one of the important problems in solid mechanics and structural engineering. In engineering practice, the stress–strain behavior of

materials is often simplified by idealized constitutive models. One of the most widely used models is the elastic–perfectly plastic diagram proposed by Prandtl, which assumes that the material behaves elastically up to the yield stress and plastically afterward without hardening.

Elastic–plastic bending theory is especially important for evaluating the carrying capacity and safety of beams subjected to high loading levels. In such cases, the stress distribution over the cross-section changes significantly after the onset of yielding. The elastic region gradually decreases while plastic zones develop near the outer surfaces of the beam.

In this study, the pure bending of a rectangular beam made of a perfectly plastic material is investigated analytically. The evolution of stress distribution, the development of the elastic core, and the conditions for the formation of a plastic hinge are examined. In addition, beam deflection and strain energy are determined using the obtained analytical relations.

2. Methodology

Consider a rectangular beam subjected to pure bending. According to the classical bending theory, the normal stress distribution in the elastic stage is linear and can be expressed as

$$\frac{1}{\rho} = \frac{M}{EI}, \sigma = \frac{M}{I} y$$

where M is the bending moment, y is the coordinate measured from the neutral axis, and I is the moment of inertia of the cross-section.

The maximum stress occurs at the outermost fibers of the beam. Yielding begins when the maximum stress becomes equal to the yield stress σ_T. The corresponding bending moment is written as

$$M^* = \sigma_T W_z = \sigma_T \frac{bh^2}{6}, \sigma_T = \frac{6M^*}{bh^2}$$

where W is the section modulus of the rectangular cross-section, b and h are the width and height of the rectangular cross-section. The obtained relations demonstrate that the ultimate bending moment depends only on the material properties and geometric characteristics of the beam section. The transition from elastic behavior to the fully plastic state is accompanied by a significant increase in beam deflection and irreversible energy dissipation. The beam deflection is determined using the differential equation of the elastic curve. Assuming small deflections, the curvature of the beam axis can be related to the bending moment. During elastic–plastic bending, the reduction of the elastic core leads to a decrease in structural stiffness and consequently to larger deflections. The maximum deflection occurs at the midpoint of the beam. In the purely elastic state, the deflection remains finite and follows the classical beam theory. However, in the fully plastic state, the stiffness of the beam decreases drastically, and the deflection tends to increase without bound. This behavior corresponds to the formation of a plastic

hinge and indicates the exhaustion of the load-carrying capacity of the structural element. The strain energy accumulated in the beam during deformation is also investigated. In the elastic range, the stored energy is completely recoverable upon unloading. In contrast, during elastic–plastic deformation, a considerable portion of the external work is dissipated because of irreversible plastic strains. The strain energy is determined by integrating the stress–strain relations over the beam volume. The obtained expressions show that the energy absorbed by the beam increases significantly as the plastic zones propagate through the cross-section. This property is important in structural applications where energy absorption and ductility are required.

The relationship between the normalized bending moment $\frac{M}{M_{pr}}$ and the relative elastic core size $\frac{a}{h}$ is illustrated in Figure 1. It can be observed that as the elastic core decreases, the bending moment approaches its ultimate value M_{pr}, corresponding to the fully plastic state.

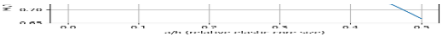


Figure 1. Relationship between the normalized bending moment M/M_{pr} and the relative elastic core size a/h.

Conclusion

The present study examined the elastic–plastic bending of a rectangular beam made of a perfectly plastic material based on the Prandtl model. Analytical expressions for stress distribution, beam deflection, elastic core size, and ultimate bending moment were obtained. It was shown that yielding initiates at the outer fibers and gradually extends toward the center of the cross-section. The fully plastic state corresponds to the formation of a plastic hinge and the ultimate carrying capacity of the beam. The obtained results provide a clear analytical framework for evaluating beam behavior beyond the elastic limit and can be applied in structural mechanics, limit-state design, and engineering analysis of load-bearing systems.

References

1. Ilyushin, A.A.: Plasticity Theory. Nauka, Moscow (1978).

2. Bezukhov, N.I.: Fundamentals of the Theory of Elasticity and Plasticity. Gosstroyizdat, Moscow (1954).

3. Rzhanitsyn, A.R.: Structural Analysis Considering Plastic Properties of Materials. Gosstroyizdat, Moscow (1954).

4. Filin, A.P.: Applied Mechanics of Deformable S

https://doi.org./10.58225/mpmma.2026.78

SPACES WITHOUT THE BOUNDED APPROXIMATION PROPERTY. NEW EXAMPLES.

Alexander Goncharov
Bilkent University, Türkiye

Abstract. By means of Grothendieck's approach, we present a family of Whitney jets spaces without the bounded approximation property.

Keywords: The bounded approximation property, Spaces of Whitney jets.

https://doi.org./10.58225/mpmma.2026.79

IMPACT OF STIFFENER COUNT AND DEFORMATION ON THE NON-LINEAR FREQUENCİES OF A CYLİNDRİCAL SHELL CONTAİNİNG LİQUİD

Aynura Khudiyeva
AzUAC, Azerbaijan

Abstract. This article presents a theoretical and computational model for investigating the non-linear frequency behavior of a cylindrical shell filled with liquid and subjected to parametric oscillations. The study focuses on the dynamic interaction between the elastic shell structure and the internal fluid, taking into account key physical and mechanical parameters such as shell stiffness, material properties, geometric characteristics, and deformation effects. Special attention is given to the role of transverse stiffeners, whose presence significantly influences the overall vibrational response of the system.The analysis examines how varying the number of stiffeners affects the non-linear frequency characteristics. Numerical and analytical results show that, at the initial stage, increasing the number of stiffeners leads to an increase in the system's non-linear natural frequencies due to the enhancement of structural rigidity. However, this trend does not continue indefinitely. After reaching a certain optimal value, further addition of stiffeners results in a decrease in frequencies. This occurs because the contribution of inertial forces becomes more dominant compared to stiffness effects, altering the overall dynamic balance of the system.The proposed

model helps to better understand complex fluid–structure interaction phenomena and provides useful insights for predicting the vibrational behavior of cylindrical shell systems in engineering applications such as aerospace, mechanical, and marine structures.

Keywords: Non-linear frequencies, cylindrical shell, parametric oscillations, dynamic behavior, liquid-structure interaction

Introduction

In many engineering applications, cylindrical shells are frequently used in structures such as tanks, pipes, and reactors, where dynamic behavior under various loading conditions is crucial. These shells are often subjected to internal fluids (liquid) and are equipped with stiffeners to enhance structural integrity. The aim of this research is to analyze the non-linear frequency response of cylindrical shells containing liquid under parametric oscillations. The dynamic response of such systems can be influenced by factors like the shell's material properties, the deformation of the structure, and the number of stiffeners.

The non-linear nature of the oscillations in such systems is significantly affected by these factors. Specifically, the interaction between the stiffeners and the shell’s deformation has a profound impact on the system's frequency characteristics.

1. Problem Statement

The dynamic behavior of cylindrical shells is governed by complex interactions between the

shell's material properties, liquid dynamics, and external forcing conditions.

2. Mathematical Formulation

The dynamic equation of motion for a cylindrical shell with liquid is derived from the governing partial differential equations for a cylindrical shell, incorporating the effects of stiffness, deformation, and liquid interaction. The general equation for the non-linear frequency f(w) as a function of deformation www is presented as:

$$f(w) = \frac{E_i w}{Rh} f(w)$$

where:E_i is the Young's modulus of the shell material, $w -$ is the deformation, R- is the radius of the shell, h- is the thickness of the shell.

The system is solved using Newton's method to account for non-linearities in the frequency behavior. The initial parameters used in the analysis include:

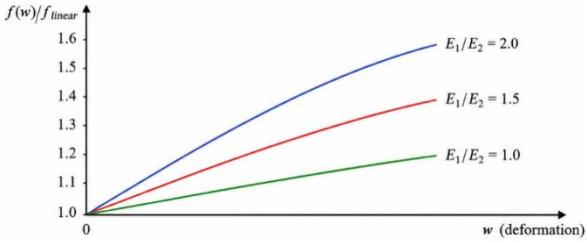
R=0.20 m, h=0.00055 m, l=1.0 m, p0=pj=7500 kg/m3, E1=5.50×109 Pa, ν1=0.12, ν2=0.18, m=6, Jkpj/(2πR3h)=0.4505×10−6,q0/E1=0.003,q1/q0=0.35, μ=0.400

3. Numerical Results

The system was solved using Newton's method for the given parameters. The results are shown in Figures 2 and 3.

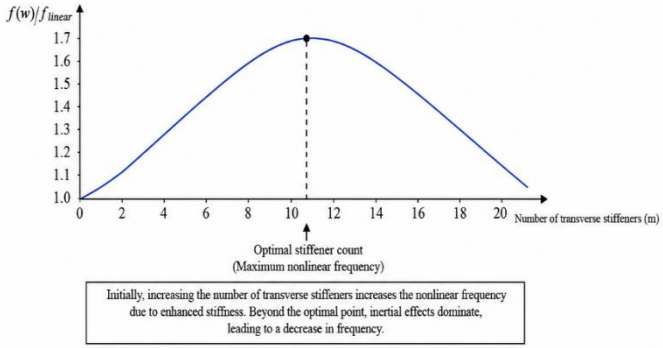
3.1. Discussion

Figure 1. Relationship between nonlinear frequency ratio and deformation



The simulation results demonstrate the importance of the number of stiffeners in controlling the frequency characteristics of the system. The increase in stiffeners initially strengthens the system, but as the stiffener count grows, inertial forces cause a decrease in frequency. This insight is valuable for optimizing the design of cylindrical shells in various engineering applications, such as pressure vessels, tanks, and pipes, where dynamic

Figure 2. Relationship between nonlinear frequency ratio and number of transverse stiffeners



performance is critical.

Conclusion

This study has demonstrated that the non-linear frequency response of cylindrical shells containing liquid is highly dependent on both the deformation of the shell and the number of stiffeners. The results indicate that an optimal number of stiffeners exists, beyond which further additions may not

contribute positively to the system's dynamic performance. These findings provide important guidelines for the design and analysis of cylindrical shell structures in engineering.

References

1.S. Kumar, "Nonlinear vibrations of cylindrical shells with liquid," *Journal of Sound and Vibration*, vol. 310, no. 5, pp. 1234-1256, 2021.

2.A. Smith and B. Johnson, "Effects of stiffeners on the vibration of cylindrical shells," *International Journal of Mechanical Sciences*, vol. 45, no. 7, pp. 1123-1137, 2020.

3.Amabili M. *Nonlinear Vibrations and Stability of Shells and Plates*. Cambridge University Press, 2008.Cambridge University Press

4.Tornabene F., Fantuzzi N., Bacciocchi M. “Free vibrations of free-form doubly-curved shells made of functionally graded materials using higher-order equivalent single layer theories.” *Composite Structures*, 2018.

5.Pellicano F., Amabili M. “Nonlinear vibrations and stability of circular cylindrical shells containing fluid.” *Journal of Sound and Vibration*,2019.

6.Sofiyev A.H., Kuruoglu N. “Dynamic instability of cylindrical shells reinforced by stiffeners under harmonic loading.” *Thin-Walled Structures*, 2021.

https://doi.org./10.58225/mpmma.2026.84

ANALYTICAL AND NUMERICAL INVESTIGATION OF DISPERSION AND PHASE VELOCITY OF HARMONIC WAVES

Aynura Khudiyeva
AzUAC, Azerbaijan

Abstract. This paper presents a detailed analytical and numerical study of harmonic wave propagation in viscous continuous media. Special attention is given to the derivation and analysis of the dispersion relation, with a particular focus on how the phase velocity varies with the wave number under viscous effects. The theoretical formulation is based on the classical wave equation, which is further modified to incorporate viscosity terms, allowing a more realistic description of wave motion in fluid environments where energy dissipation cannot be neglected.Within this framework, the governing equations are analyzed to obtain expressions for both phase velocity and attenuation characteristics. Numerical simulations are then carried out to demonstrate how increasing viscosity influences wave behavior, leading to stronger damping and noticeable changes in the propagation speed. The results clearly indicate that viscosity plays a crucial role in modifying both the amplitude decay and the dispersion properties of harmonic waves, especially at higher wave numbers where dissipative effects become more

significant.Overall, the study highlights the importance of including viscous effects in wave propagation models to achieve accurate predictions in real physical systems. The presented analysis can be effectively applied in various engineering and scientific fields, including hydrodynamics, ocean wave modelling, acoustics, and the study of wave propagation in complex liquid media.
Keywords: harmonic waves, dispersion relation, phase velocity, viscous fluid, numerical simulation

Introduction

The study of wave propagation in continuous media is one of the fundamental problems of mathematical physics and hydrodynamics. Waves appear in a wide variety of physical phenomena including sound propagation, water waves, elastic vibrations and electromagnetic radiation. In many practical situations the wave motion can be approximated by harmonic solutions. In an ideal medium waves propagate without energy loss and their properties can be described by the classical wave equation. However, real fluids are not ideal and possess viscosity. Viscosity introduces dissipation and modifies the characteristics of wave propagation. As a result the amplitude of the wave decreases during propagation and the dispersion relation changes. The purpose of this work is to analyse harmonic wave propagation in a viscous medium and to investigate how viscosity influences the dispersion relation and phase

velocity. In addition to theoretical analysis, numerical simulations are used to illustrate the obtained results.

2. Mathematical Model

A harmonic wave solution can be written as: $u(x,t) = Ae^{i(kx - \omega t)}$

Here A denotes the amplitude of the wave, k is the wave number and ω is the angular frequency. The exponential representation of harmonic waves is very convenient in theoretical analysis.

According to Euler's formula:

$$e^{i\theta} = \cos(\theta) + i\sin(\theta)$$

This relation shows that the exponential representation corresponds to oscillatory motion consisting of sine and cosine components.

Classical dispersion relation: $\omega^2 = gk$

This equation describes the relationship between angular frequency and wave number in an ideal medium.

Dispersion relation with viscosity correction: $\omega^2 = gk - -i\nu k^2$

The additional term introduces attenuation into the wave motion and represents the influence of viscous damping.

Phase velocity definition: $c = \frac{\omega}{k}$

3. Numerical Simulation

To illustrate the theoretical results numerical simulations were performed. The dispersion relation was evaluated for different wave numbers using a computational simulator implemented in Python. The simulator calculates phase velocity and damping coefficient based on the theoretical model.

The following physical parameters were used in the simulation:$\rho = 1000\ kg \cdot m^{-3}$,$\mu = 0.001\ Pa \cdot s$,$g = 9.81\ m \cdot s^{-2}$.

The obtained numerical values allow us to analyse the influence of viscosity on the behaviour of harmonic waves.

4. Results and Discussion

The numerical results confirm that viscosity plays an important role in wave propagation. When viscosity increases the damping coefficient becomes larger and the wave amplitude decreases more rapidly.

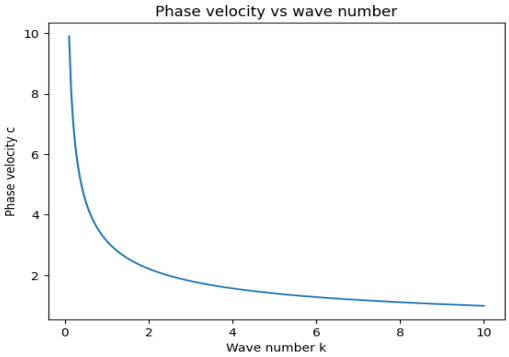


Figure 1 . Illustrates the dependence of phase velocity on wave number.

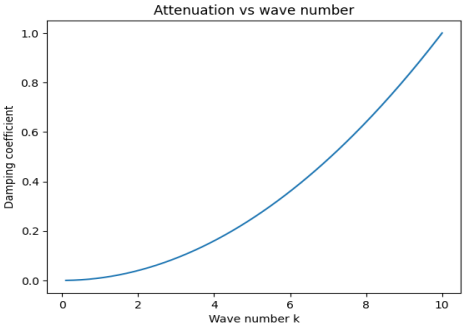


Figure 2.Shows the attenuation coefficient depending on wave number.

5. Conclusion

In this study harmonic wave propagation in viscous fluids was investigated analytically and numerically. The theoretical model was derived

and numerical simulations were used to analyse the dispersion relation and phase velocity.

The obtained results show that viscosity modifies the classical dispersion relation and introduces attenuation in wave propagation. The presented approach may be used for further studies of hydrodynamic wave processes.

References

1. Lamb H. Hydrodynamics. Cambridge University Press, 1994
2. Whitham G.B. Linear and Nonlinear Waves. Wiley, 2011.
3. Mei C.C. Theory and Applications of Ocean Surface Waves. World Scientific, 2005.
4. Constantin A. Wave motion in fluids. Proc. Royal Society A, 2020.
5. Dias F., Kharif C. Nonlinear water waves. Annual Review of Fluid Mechanics, 2019

https://doi.org./10.58225/mpmma.2026.90

EFFECT OF MULTI-WALLED CARBON NANOTUBES ON THE PROPERTIES OF LOW-DENSITY NON-AUTOCLAVED AERATED CONCRETE

Abbas Guvalov, Rafig Shirinov
AZUAC, Azerbaijan

Abstract. Low-density non-autoclaved aerated concrete (NAAC) is a widely used thermal insulation material; however, its mechanical strength and structural integrity decrease significantly when the density falls below 400 kg/m³. This study investigates the effect of multi-walled carbon nanotube (MWCNT) dispersion on the formation of the porous structure and the mechanical properties of low-density non-autoclaved aerated concrete with a target density of 250 kg/m³. MWCNTs were incorporated in ultra-low dosages (0.001–0.005% by mass of cement). Experimental results demonstrate that the optimum MWCNT content (0.001–0.003%) increases the compressive strength to Class B0.5 (≥0.5 MPa), reduces the dry density from 300 kg/m³ to 250 kg/m³, and accelerates the development of plastic strength by 20–30 minutes compared with the control specimens. The proposed approach enables the production of mechanically reliable non-autoclaved aerated concrete (NAAC) for thermal insulation applications.

Keywords: Non-Autoclaved Aerated Concrete (NAAC); Multi-Walled Carbon Nanotubes (MWCNTs); Mechanical Properties; Compressive Strength; Pore Structure; Microstructure.

1. Introduction

Reducing energy consumption in buildings requires the development of effective thermal insulation materials. Non-Autoclaved Aerated Concrete (NAAC) is one of the most widely used materials due to its combination of low thermal conductivity and adequate mechanical strength [1, 2]. However, when the density is reduced from 450–550 kg/m³ to 200–300 kg/m³ for thermal insulation applications, the compressive strength often falls below Class B0.5 (0.5 MPa), which is insufficient for transportation, handling, and installation [3, 4].

One of the promising approaches is the use of nanomodifiers. Multi-Walled Carbon Nanotubes (MWCNTs) have been successfully applied to improve the mechanical properties of cement matrices in both dense and cellular concretes [5]. However, the effect of MWCNTs on the mechanical behavior of ultra-low-density aerated concrete ($\rho \leq 250$ kg/m³) has not been sufficiently investigated.

The aim of this study is to investigate the effect of MWCNT dispersion on the structure formation, mechanical properties, and structural stability of low-density Non-Autoclaved Aerated Concrete (NAAC) with a target density of 250 kg/m³.

2. Methodology

2.1. Materials

The following raw materials were used: CEM I 42.5 Portland cement (Holcim), ground limestone, quartz sand containing ≥85% amorphous SiO_2 (Balakhani deposit, Baku), technical water, aluminum powder as a gas-forming agent, CORSO superplasticizer (Holcim Azerbaijan), and Multi-Walled Carbon Nanotubes (MWCNTs) synthesized at the Institute of Chemistry, Azerbaijan, Baku.

2.2. Sample Preparation.

The mix proportions were selected in accordance with the SN 277–80 standard. The MWCNT content was varied from 0.001% to 0.005% by mass of cement. The nanomodifier was introduced together with the gas-forming suspension and mixing water. The specimens were cast under production conditions in metal molds with dimensions of 400 × 400 × 400 mm. After thermal curing, cylindrical specimens with dimensions of 100 × 100 mm were prepared from the large blocks.

2.3. Testing Methods.

Plastic strength was measured during the first 60 minutes after mixing the aerated concrete slurry. Compressive strength and dry density were determined in accordance with GOST 5742–76 and GOST 31359–2007, respectively.

2.4. Experimental results

The incorporation of MWCNT dispersion significantly accelerated the development of plastic strength in the aerated concrete mixture (Fig. 1a).

In the modified specimens, the plastic strength required to ensure structural stability was achieved within the first 20–30 minutes of thermal curing, which is 20–30 minutes earlier than in the control specimens. No pore coalescence or percolation was observed, which had a positive effect on the final mechanical properties of the material (Table 1).

Table 1. Mechanical Properties of Control and MWCNT-Modified Specimens

Specimen	Dry Density (kg/m³)	Compressive Strength (MPa)	Strength Class	Thermal Conductivity (W/(m·°C))
Control (0% MWCNTs)	300	0.38	Below B0.5	0.060
0.001% MWCNTs	260	0.47	B0.5	0.052
0.003% MWCNTs	250	0.52	B0.5	0.050
0.005% MWCNTs	210	0.49	B0.5	0.054

The optimum MWCNT content was found to be in the range of 0.001–0.003% by mass of cement. Within this range, the compressive strength increased to ≥0.5 MPa (Class B0.5), while the

density decreased slightly. This corresponds to an improvement in the structural quality factor (strength-to-density ratio).



Figure 1. (a) Development of plastic strength over time; (b) Mechanical properties of the control and MWCNT-modified specimens.

Conclusion

This study investigated the effect of Multi-Walled Carbon Nanotube (MWCNT) dispersion on the structure and mechanical properties of low-density Non-Autoclaved Aerated Concrete (NAAC) with a target density of 250 kg/m³. The following conclusions were obtained:

The optimum MWCNT content was found to be 0.001–0.003% by mass of cement.

MWCNT-modified NAAC achieved a compressive strength class of B0.5 (≥0.5 MPa), a dry density of 250 kg/m³, and a thermal conductivity coefficient of 0.05 W/(m·°C).

MWCNT modification accelerated the development of plastic strength by 20–30 minutes and prevented pore coalescence, resulting in a uniform pore structure composed of 0.1–0.5 mm hexagonal/polyhedral pores.

The proposed nanocomposite NAAC is suitable for load-bearing thermal insulation applications,

reducing both foundation loads and transportation costs.

Future research will focus on evaluating the long-term durability of the material, including frost resistance and shrinkage deformation, as well as developing a predictive mechanical model for the nano-reinforced porous structure.

References

1.Guvalov,A., Dursun,M. Increase of Efficient at Aerated Concrete Compositions Based on Mineral Powders. Appl. Sci. 2025, 15(23), 12364. https://doi.org/10.3390/ app15231236

2.Batyanovski, E.İ., Qolubev, N.M., Sajnev, N.N.: Production of Autoclaved Cellular Concrete Products. Strinko, Minsk (2009).

3.Mechay, A.A., Misnik, M.P., Kolpashchikov, V.L., Sinitsa, M. Nanomodified Autoclaved Cellular Concrete. Proceedings of the VIII International Scientific and Practical Conference, pp. 76–79, Mogilev (2014).

4. Leontyev, S.V., Golubev, V.A., Shamanov, V.A., Kurzanov, A.D. Investigation of the Influence of Plasticizing Admixtures on the Stabilization Process of the Porous Structure. Fundamental Research, 11(3), 474–480 (2015).

5.Kerienė, J., Kligys, M., Laukaitis, A., Yakovlev, G., Špokauskas, A. Influence of Multi-Walled Carbon Nanotube Additives on the Properties of Non-Autoclaved and Autoclaved Aerated Concretes. Construction and Building Materials, 49, 527–535 (2013).

https://doi.org./10.58225/mpmma.2026.96

REDUCING THE ENVIRONMENTAL IMPACT THROUGH THE REUSE OF CONCRETE SCRAP

Abbas Quvalov, Saida Abbasova
AzUAC, Azerbaijan

Abstract: This research addresses environmental problems by efficiently using construction waste from demolished buildings. Rubble concrete was studied to determine whether coarse aggregates obtained from waste meet standard requirements. Optimal crushing methods were examined for using recycled products in monolithic and precast concrete. The results show that the grade of recycled crushed stone increases with the strength of the original concrete, reaching grade 800 when derived from B40 concrete. Concrete mixtures with 20-30% recycled aggregate achieved B25 class strength while maintaining workability. The use of recycled materials reduces landfill waste and lowers greenhouse gas emissions. The findings justify the application of recycled products in concrete production, partially reducing harmful environmental impacts.

Keywords: monolithic concreting, rubble concrete, recycled products, precast concrete, recycling, coarse aggregates

1. Introduction

Reusing demolition waste is crucial for environmental safety and waste disposal.

Construction waste dumped in landfills occupies large areas and causes pollution. Therefore, processing this waste into reusable materials is urgent.

Concrete debris can be processed either at special landfills with crushing equipment or on-site for large volumes. Crushing concrete debris typically yields 60% crushed stone of 20 mm, 20% of 10 mm, and 20% of 5 mm [1]. Fractions above 5 mm are used as crushed stone in concrete; smaller fractions replace stone chips and sand.

Multi-stage crushing produces high-quality fillers suitable even for high-grade concrete, as fragmentation occurs at the boundary between cement stone and filler particles [2]. Recycled crushed stone contains cement stone, sand, and mineral filler particles. The adhered cement mortar affects aggregate properties. Recycled aggregate influences cement stone structure formation: water is actively absorbed during mixing, then passes into hardening cement stone. Possibilities for replacing natural aggregate with recycled aggregate should maintain concrete workability and strength [3].

Materials and methods

Aggregates from recycled demolition concrete were used. Recycled crushed stone came from concrete fragments of strength classes B20, B25, B30, and B40. Granular composition was

determined according to GOST 8269.0-97; requirements followed GOST 8267-93.

Materials used:

Binder: CEM II/A-L 42.5 Portland cement (HOLCIM), normal density 28%, activity 50 MPa

Coarse aggregate: natural granite crushed stone (5-20 mm) and recycled crushed stone (5-20 mm)

Fine aggregate: natural quartz sand (fineness modulus Mi=3.16)

Superplasticizer: Rheobuild 878

Strength (crushing index) of recycled aggregate was determined per GOST 8269.0-97 and GOST 32495-2013.

Results and discussion

Current standards estimate crushed stone grade differently for rock types, but recycled concrete crushed stone cannot be considered a complete analogue. The adhered mortar changes all standardized parameters.

Tables 1 summarize crushing index grades for recycled aggregate from different original concrete classes. Recycled crushed stone strength increases with original concrete strength: from class B20 to B40, the grade rises from 300 to 800. Specifically, aggregate from B40 rubble concrete reaches grade 800.

Table 1. Strength of recycled crushed stone obtained from primary concrete

Original concrete class	Crushing index grade of recycled aggregate
B20	300
B25	400
B30	600
B40	800

The effect of replacing natural crushed stone with recycled aggregate (20%, 30%, 40% by mass of mixed aggregate) was evaluated. Introducing recycled aggregate increases water demand and water/cement ratio. At 40% replacement, water demand rises from 152–154 to 167–171 l/m³, and w/c ratio from 0.367 to 0.403–0.411 to maintain slump of 6.5–8 cm. The increase is: 6.5% at 20%, 8.5% at 30%, 12.5% at 40% recycled aggregate. This is due to higher water absorption of recycled crushed stone (4.8–5.5%) versus granite (1.0–1.5%). Average density decreases up to 2.6%.

Compressive strength decreases when natural granite is replaced with recycled crushed stone, both after heat-moisture treatment and at 7 and 28 days. However, concretes using recycled aggregate from stronger original concrete show a tendency toward smaller strength reduction. After 28 days, concretes of class B30-40 can be obtained using mixed aggregate with 20-30% recycled content.

One obstacle to industrial production of recycled cement is separating concrete waste components. Contamination by cement slurry increases porosity, negatively affecting durability and workability.

Current recycled concrete waste is mainly reused as low-quality aggregate. Developing efficient separation processes is a priority.

After crushing and sieving, recycled crushed stone properties were: average density 1173 kg/m³, voids 53%, needle/plate-shaped grains 22.8%, dust/clay particles 0.04%. All fractions meet standard requirements.

Additional concrete mixtures were prepared with varying recycled crushed stone amounts (0%, 15%, 20%, 25%, 30%, 35%, 40%) using 1.0% Rheobuild 561. Workability (Abrams cone) peaked at 15% recycled aggregate. Compressive strength decreased by 12.4–22.5% compared to control after 28 days, but all compositions achieved B25 class concrete. Flexural strength increased 20% at 14.7% recycled aggregate compared to control. Compositions with 20-25% recycled aggregate are considered optimal [4].

Recycled cement shows great potential for efficient reuse of concrete waste, promoting a circular economy. It can produce concrete with 28-day compressive strength above 20 MPa, comparable to low-grade Portland cement (32.5). High water demand and non-standard setting times are manageable when recycled cement is used as an additive up to 40% [5].

Conclusions

The strength (crushing index grade) of recycled aggregate increases with the strength of the

original concrete. Aggregate from B40 rubble concrete reaches grade 800.

Recycled aggregate from rubble concrete can be successfully used in B20 and B25 concretes at 20-30% replacement.

Recycled cement shows great potential for efficient reuse of concrete waste, promoting a circular economy. It can produce concrete with 28-day compressive strength above 20 MPa, comparable to low-grade Portland cement (32.5). High water demand and non-standard setting times are main issues, but these are manageable when recycled cement is used as an additive up to 40%.

Efficient disposal of construction and demolition waste is necessary to save natural resources and significantly reduce greenhouse gas emissions in the construction industry.

References :

1. Guvalov A.A. Study of crushed stone from different brands of rubble concrete. Scientific Works of AzUAC, Baku, 2022, No.2, pp.69-78.
2. Guvalov A.A., Abbasova S.I. Effect of recycled crushed stone on concrete properties. Construction and Architecture in Azerbaijan, 2023, No.1(34), pp.2-9.
3. Chen W, Jin R, Xu Y, et al. Adopting recycled aggregates as sustainable construction materials: A review. Constr Build Mater 2019;218:483-496.

4. Serpell R, Lopez M. Reactivated cementitious materials from hydrated cement paste wastes. Cem Concr Compos 2013;39:104-114.
5. He Z, Zhu X, Wang J, et al. Comparison of CO2 emissions from OPC and recycled cement production. Constr Build Mater 2019;211:965-973.

https://doi.org./10.58225/mpmma.2026.103

DOUBLY NONLINEAR PARABOLIC PROBLEMS RELATED TO GREINER OPERATOR

Abdullah Yener
İstanbul Ticaret University, Türkiye

Abstract. This paper is concerned with the nonexistence of positive solutions to the following doubly nonlinear subelliptic parabolic problem:

$$\begin{cases} \partial_t\big(f(u)\big) = \mathcal{L}_{k,m,p}\, u + V(w)u^{m+p-2} + g(u)\, W(w)|\nabla_k u|^s + \lambda u^q & \text{in } \Omega\times(0,t) \\ u(w,0) = u_0(w) \geq 0,\ u_0 \not\equiv 0 & \text{in } \Omega \\ u(w,t) = 0 & \text{on } \partial\Omega\times(0,t) \end{cases} \quad (1)$$

where Ω is a Carnot–Carathéodory metric ball in $\mathbb{R}^{2n+1}$ with smooth boundary, $\mathcal{K} \subset \Omega$ is the singular set, $A, V \in L^1_{\text{loc}}(\Omega\backslash\mathcal{K})$ with $A(w) \geq a_0 > 0$ almost everywhere in $\Omega\backslash\mathcal{K}$, and $W \in L^\infty(\Omega\backslash\mathcal{K})$. Moreover, $f \in C^1\big((0,\infty)\big)$ and $g \in C(0,\infty)$ satisfy

$$f(v) > 0, \quad |f'(v)| \leq C_{\text{f}}\, v^\alpha, \quad |g(v)| \leq C_{\text{g}}\, v^\beta \quad \text{for all} \quad v > 0$$

for some constants $C_{\text{f}}, C_{\text{g}} > 0$, where $\alpha \geq 0$, $0 < \alpha\text{-}m\text{-}p+3 \leq 2/\text{Q}$, and $\beta = m+p\text{-}2+\big(m\text{-}1\big)s$, while $m, q > 0$, $p > 1$, $0 < s \leq 4/\text{Q}$, and $\lambda \in \mathbb{R}$.

The principal operator in (1) is the weighted doubly nonlinear subelliptic operator

$$\mathcal{L}_{k,m,p}\, u := \nabla_k \cdot \Big(A(w)u^{m\text{-}1}|\nabla_k u|^{p\text{-}2}\nabla_k u\Big), \quad (2)$$

where $\nabla_k = (X_1,\ldots, X_n, Y_1,\ldots, Y_n)$ is the horizontal gradient associated with the generalized Greiner vector fields

$$X_j = \frac{\partial}{\partial x_j} + 2k\, y_j|z|^{2k\text{-}2}\frac{\partial}{\partial l}, \quad Y_j = \frac{\partial}{\partial y_j} - 2k\, x_j|z|^{2k\text{-}2}\frac{\partial}{\partial l}, \quad j = 1,\ldots,n, \quad k \in \mathbb{N}$$

on $\mathbb{R}^{2n+1} = \mathbb{R}^n \times \mathbb{R}^n \times \mathbb{R}$, with $z = (x_1, ..., x_n, y_1, ..., y_n) \in \mathbb{R}^{2n}$ and $l \in \mathbb{R}$. The norm of the horizontal gradient is

$$|\nabla_k u| = \left(\sum_{j=1}^{n} (X_j u)^2 + (Y_j u)^2\right)^{1/2}.$$

These fields satisfy Hörmander's finite-rank condition, yielding a genuinely hypoelliptic and sub-Riemannian structure. The associated homogeneous dimension is $Q = 2n+2k$, and the natural gauge is

$$\rho(w) = (|z|^{4k} + l^2)^{1/4k}.$$

The operator (2) combines the porous-medium nonlinearity (exponent m) with the p-Laplacian-type gradient nonlinearity. When $m = 1$, it reduces to the weighted subelliptic p-Laplacian

$$\mathcal{L}_{k,1,p}\, u = \nabla_k \cdot \left(A(w)|\nabla_k u|^{p-2}\nabla_k u\right)$$

and when $p = 2$, it becomes the weighted porous-medium operator

$$\mathcal{L}_{k,m,2}\, u = \nabla_k \cdot (A(w)u^{m-1}\nabla_k u) = \frac{1}{m}\nabla_k \cdot (A(w)\nabla_k u^m)$$

Furthermore, when $A \equiv 1$, $m = 1$, and $p = 2$, the operator (2) reduces to the Greiner operator [1]

$$\Delta_k = \sum_{j=1}^{n} (X_j^2 + Y_j^2)$$

which is a degenerate extension of the sub-Laplacian on the Heisenberg group $\mathbb{H}^n$; for $k = 1$ it coincides with the Kohn–Laplacian on $\mathbb{H}^n$; see [2].

Keywords: Critical exponents, Greiner operator, positive solutions, nonexistence

References:

1. P. C. Greiner, A fundamental solution for a nonelliptic partial differential operator, Canad. J. Math. 31, 1107–1120 (1979).
2. G.R. Goldstein, J.A. Goldstein, I. Kömbe, Nonexistence results for p-Laplacian parabolic problems on the Heisenberg group Hn, Discrete and Continuous Dynamical Systems - S 16, 9 (2023).
3. G. R. Goldstein, J. A. Goldstein, and I. Kombe, Nonexistence results for nonlinear parabolic problems on the Heisenberg group Hn, Contemp. Math., to appear.
4. G. B. Folland and E. M. Stein, Hardy Spaces on Homogeneous Groups, Mathematical Notes 28, Princeton University Press, Princeton, NJ, 1982.
5. I. Kombe and A. Yener, Nonexistence results for degenerate nonlinear parabolic problems and Hardy-Leray type inequalities associated with the Greiner operator, under review.
6. I. Kombe and A. Yener, Degenerate parabolic equations associated with the Greiner operator: Nonexistence results via Hardy-Leray inequalities, under review.

https://doi.org./10.58225/mpmma.2026.106

APPROXIMATION OF THE BERNSTEIN-CHLODOWSKI POLYNOMIAL IN LEBESGUE SPACE WITH A WEIGHTED MODULUS OF CONTINUITY

Aytekin Abdullayeva[1,2]

[1] Institute of Mathematics ,Azerbaijan

[2] Military Institute named after Heydar Aliyev, Azerbaijan

Abstract. This paper investigates the approximation properties of Bernstein–Chlodowsky polynomials in weighted Lebesgue spaces. By employing a weighted modulus of continuity, approximation estimates and convergence conditions for the corresponding operators are established. The obtained results contribute to the generalization of approximation theory for positive linear operators in weighted spaces.

Keywords: Bernstein–Chlodowsky polynomials, weighted Lebesgue spaces, approximation theory, positive linear operators, weighted modulus of continuity.

In this abstract we consider estimates of approximation of funciotions with respect to a suitable weighted norm via the new type moduly of continuity. First, we give that the weighted modulus of continuity has properties similar to the usual modulus of continuity defined by

$$\Omega_p(f;\delta)=\sup_{0<h\le\delta}\left(\int_0^{\infty}\left(\frac{|f(x+h)-f(x)|}{(1+x^2)(1+h^2)}\right)^p dx\right)^{\frac{1}{p}}.$$

We denote the set of functions that satisfy this inequality by B_ω to obtain:

$$B_\omega(R_+) := \{f : |f(x)| \le M_f \omega(x)\}$$

Then we define

$$C_\omega(R_+) := \left\{ f : f \in B_\omega \text{ and } f \text{ is continuous} \right\}$$

$$C_\omega^K(R_+) := \left\{ f : f \in C_\omega(R_+) \text{ and } \lim_{x\to+\infty} \frac{f(x)}{\omega(x)} = K_f < \infty \right\}$$

and

$$C_\omega^0(R_+^2) := \left\{ f : f \in C_\omega^K(R_+^2) \text{and} \quad \lim_{x\to+\infty} \frac{f(x)}{\rho(x)} = 0 \right\}.$$

It is well known that the norm in B_ω is defined as

$$\|f\|_\omega = \sup_{x\in R_+} \frac{|f(x)|}{\omega(x)}.$$

We refer reader to the works [1] and [2].

Let x$\in (0, \infty)$ and let $\omega(x) = 1 + x^2$.

Now we give the main result of this abstract.

Let f be a continious real function defined on $[0,\infty)$. In 1932, Bernstein's follower Chlodowsky had constructed the increasing sequences of polynomials

$$B_n(f;x) = \sum_{k=0}^{n} f\left(\frac{kb_n}{n}\right) C_n^k \left(\frac{x}{b_n}\right)^k \left(1 - \frac{x}{b_n}\right)^{n-k}, 0 \le x \le b_n,$$

that was named as Bernstein-Chlodowsky polynomials some later.

Here

$$\lim_{n\to\infty} b_n = \infty, \qquad \lim_{n\to\infty} \frac{b_n}{n} = 0.$$

Note that, the condition imposed on b_n in the definition of classic Bernstein-Chlodowsky operators doesn't provide continuous convergence of $B_n(f;x)$ polynomials to the function $f(x)$.
We have

$$B_n(f;x)-x^2=\frac{x(b_n-x)}{n}$$ for the function $f(t)=t^2$.

Therefore,

$$\sup_{x\in[0.b_n]}\left|B_n\left(t^2;x\right)-x^2\right|=\frac{b_n^2}{4n}.$$

Then for convergence to zero as $n\to\infty$ of the right hand part of this equality does not suffice the fullfillment of condition $\frac{b_n}{n}\to\infty$.

We'll impose the stronger condition on b_n $\lim_{n\to\infty}\frac{b_n}{\sqrt{n}}=0$. Hence it follows that for any natural number r

$$\lim_{n\to\infty}\frac{b_n^r}{n^{\frac{r}{2}}}=0.$$

Theorem 1. Let $\omega(x)=1+x^2$ is weighted funciotions and B_n be a sequence of positive linear operators from $L_{p,\omega}(R_+)$ to $B_\omega(R_+)$. If

$$\left\|B_n\left(t^m;x\right)-x^m\right\|_{L_{p,\omega}}\to 0, \text{ as } n\to\infty,\ m=0,1,2$$

then for all functions $f\in L_{p,\omega}(R_+)$

$$\left\|B_n f-f\right\|_{L_{p,\omega}}\to 0, \text{ as } n\to\infty.$$

References

1. A.D. Gadjiev and N. Ispir, On a sequence of linear positive opera- tors in weighted spaces, Proc. Inst. Math. Mech. Natl. Acad. Sci. Azerb. 11(19),(1999), 45-55.

2. N. Ispir and C. Atakut, Approximation by modified Szasz operators on weighted spaces, Proc. Indian Acad. Sci. Math. Sci., 112 (2002), no.4, 571-578.

3. Abdullayeva, A.E., Soylemez, D.: Approximation of functions by lin- ear positive operators in variable Lebesgue spaces. Trans. Natl. Acad. Sci.Azerb. Ser. Phys.-Tech. Math. Sci., Mathematics, 38(4) (2018), 3-7.[

4. Abdullayeva, A.E., Mammadova, A.N.: On order of approximation func- tion by generalized Szasz operators and Bernstein-Chlodowsky polynomials. Proc. Inst. Math. Mech. Natl. Acad. Sci. Azerb., 38 (2013), 3-8.

https://doi.org./10.58225/mpmma.2026.110

ON THE SOLITON PROPERTIES OF THE GENERALIZED (3+1)-DIMENSIONAL P-TYPE NONLINEAR WAVE EQUATION

Adnan Ahmad Mahmud[1,2], Longjun Zhan[3], Haci Mehmet Baskonus[4]

[1]Tishk International University, Iraq

[2]Harran University, Türkiye

[3]Shanghai Lixin University of Accounting and Finance, China

[4] Harran University, Türkiye

Abstract. In this manuscript, we investigate a generalized (3+1)-dimensional P-type nonlinear wave equation. Firstly, for a more detailed analysis of the model studied, we transform it into a nonlinear ODE by utilizing an appropriate wave transformation formula. We utilize a modifed Riccati equation method (also called the generalized Riccati equation method), signifying its first application for this model.

Keywords: P-type Nonlinear Model, Wave Transformations.

Introduction

Nonlinear wave equations have been a central topic in mathematical physics for some decades. A structured method that uses a substitution such as v = 2(ln g)xx to convert a nonlinear equation into a bilinear form has been developed by Hirota and called the bilinear technique. From this structure, multi-soliton, lump, and breather solutions can be created accurately without approximation [1].

Wazwaz has also discussed different ways to analyze nonlinear partial differential equations (PDEs).

These methods include the tanh method, the sin-cos method, and Hirota's bilinear method, each of which has found effective applications in obtaining traveling wave solutions for a wide array of equations [2]. A notable result by Zabusky and Kruskal [3] demonstrated that certain nonlinear equations yield stable solitons, localized wave packets that pass through one another uniformly. This was afterwards clarified by the inverse scattering transformation (IST), formulated by Gardner et al. [4] for the Korteweg–de Vries (KdV) equation [5].

The presented work is focused on the corresponding generalized P-type model that bridges the KdV and KP hierarchies in (3 + 1) dimensions:

$$u_{xxxy} + \alpha_1 u_{yt} + \alpha_2 \left(u u_x\right)_y + \alpha_3 u_{xx} + \alpha_4 u_{zz} = 0. \tag{1}$$

where α_i, for i = 1, · · · , 4 are real parameters, and u-function depends on $\left(x, y, z, t\right)$.

References

1. Hirota, R.: The Direct Method in Soliton Theory, (2004).

2.Wazwaz, A.M.: Partial Differential Equations and Solitary Waves Theory, USA, (2009).

3. Zabusky, N.J., Kruskal, M.D.: Interaction of “solitons” in a collisionless plasma and the recurrence of initial states, Phys. Rev. Lett. 15, 240–243 (1965).
4. Korteweg, D.J., Vries, G.: On the change of form of long waves advancing in a rectangular canal, and on a new type of long stationary waves. Philos. Mag. 39,

https://doi.org./10.58225/mpmma.2026.113

QSER DECOMPOSITION OF PREDATOR-PREY DYNAMICS: SEPARATING SOURCE FROM ENVIRONMENT

Ahmad Muhammad[*1]*, Muhammad Abubakar Isah*[2]
College of Arts and Sciences, Qatar University, Qatar.
[2]Istanbul Ticaret University, Türkiye

Abstract. The Lotka-Volterra predator-prey model is a cornerstone of mathematical ecology, yet it conflates intrinsic population dynamics with interaction effects. This paper applies the Source-Environment-Response (QSER) framework to separate these causally distinct components. We decompose each population as $\boldsymbol{R = S - E}$, where S is the source field (what the population would do in isolation) and E is the environmental field (accumulated interaction history). For prey, $S_x = x_0\, e^{\alpha t}$ (intrinsic exponential growth). For predators, $(S_y = y_0)$ (constant source predators have no intrinsic dynamics; their entire fluctuation is environmental). The environmental fields satisfy $(\dot{E}_x = \alpha E_x + \beta xy$ and $\dot{E}_y = \gamma y - \delta xy,$ with $E_x(0) = 0,\ E_y(0) = 0.$ Four validity tests—source consistency, zero initial condition of E, exact reconstruction $R = S - E$, and infinite memory of S —confirm the physical correctness of the split. Numerical results show that QSER matches the traditional method to machine precision (mean error 2.45×10^{-11} for prey, $9.18 \times 10^{-12}$for predators). This reframing reveals

that predator dynamics are purely environmental: they have no intrinsic source beyond their initial condition.

Keywords: Source-environment-response, Lotka-Volterra, predator-prey, ecological dynamics, memory accumulation, QSER validity tests

REFERENCES

1. D. Murray, Mathematical Biology, 3rd ed., Springer, 2002.
2. Muhammad, A., Muhammad, I.Y., Ali, A.H., Isah, M.A., Danbatta, S.J. and Sait, A.A., 2026. A Source-Environment-Response (SER) Approach for Solving Spatio-Temporal Radon Transport in Different Media. Journal of Atmospheric and Solar-Terrestrial Physics, p.106796.
3. M. May, Theoretical Ecology: Principles and Applications, Blackwell, 1976.

https://doi.org./10.58225/mpmma.2026.115

PERMANENT FUNCTION: AN INSTRUMENT TO SOLVE ALGEBRAIC AND COMBINATORIAL PROBLEMS

Alexander Guterman
Bar-Ilan University, Israel

Abstract. The talk will be devoted to various extremal properties and applications of matrix permanents.

Keywords: Permanent, Matrices, Permanental Rank.

Introduction

Two functions in matrix theory, determinant and permanent, look very similar:

$$\det A = \sum_{\sigma \in S_n} (-1)\sigma a1\sigma(1) \ \dots \ an\sigma(n) \quad \text{and} \quad \operatorname{per} A = \sum_{\sigma \in S_n} a1\sigma(1) \dots an\sigma(n)$$

here $A=(aij) \in Mn$ is an n x n matrix over a field F, and Sn is the set of all permutations of the set $\{1,\dots,n\}$.

These functions are in the center of investigations for several centuries because of their numerous applications and a number of open mathematical problems. While the computation of the determinant can be done in a polynomial time, it is still an open question, if there are such algorithms to compute the permanent. Consequently, the question of the values that permanent can achieve, is actual. Also, the notion of the permanental rank

defined as the size of the maximal submatrix with a non-zero permanent is known.

We will talk about recent results in these directions including the following three interrelated topics.

In 1974 Wang [8, Problem 2] posed a question to find a decent upper bound for |per(A)| if A is a square (-1,1)-matrix of rank k, see also Problem 6 in [7, Chapter 8.4]. In 1985 Kräuter [5] conjectured a certain upper bound. We proved the Kräuter's conjecture and thus obtain the complete answer to the Wang's question as well as characterized the matrices with the maximal possible permanent for each value of k.

We will discuss an improvement of the Brualdi-Newman bound [1] for the consequent values of permanent of (0,1) matrices.

Finally, various estimates for the linear subspaces consisting of matrices of bounded permanental rank will be presented.

The talk is based on the joint works with M. Budrevich and K. Taranin.

2. Main results

In particular, we are going to present the following main results as well as several their generalizations to (−1,0,1) matrices and some other structured matrices.

Theorem 1 [2, Corollary 8.9]. Let $A \in Mn(\pm 1)$ be a real n x n matrix, all whose entries are either 1 or (−1), $n \geq 2$, and rk A = r + 1 for some r, $0 \leq r \leq n - 1$. Then the inequality

|per A| ≤ per D(n,r) (1.1)

holds true for all values of n and rk A, except the case of a nonsingular matrix of the order 4. The equality in (1.1) holds if and only if the matrix A can be obtained from the matrix D(n,r) by the transposition, row or column permutations and multiplications of rows or columns by (−1). In the case of nonsingular matrices of order 4 there exists an exceptional matrix, D(4,4), which is a unique exception up to the aforesaid transformations. Here D(n,r) ∈ Mn(±1) is an n x n matrix with all entries 1 except r entries (−1) on the diagonal positios indexed by (1,1), …, (r,r).

This result approves the Kräuter's conjecture [5].

The following theorem improves twice the Brualdi and Newman [1] bound on the range of subsequent values of permanent.

Theorem 2 [4, Corollary 1.4]. Let n ≥ 6. Then for any integer N from the interval [0, 2n] there exists a matrix A ∈ Mn(0, 1), i.e., a real n x n matrix, all whose entries are either 0 or 1, such that per A=N.

This result is closely related with several results about divisibility of permanent:

Theorem 3 [4, Theorem 5.8]. The greatest odd value of the permanent of an n x n matrix with entries 0 and 1 equals $[\frac{(n+1)!}{ne}]$ and $|\frac{(n+1)!}{ne} - [\frac{(n+1)!}{ne}]| \leq \frac{1}{n(n+2)}$.

Theorem 4 [4, Theorem 5.9]. The greatest value of the permanent of an n x n matrix with entries 0 and 1which is not divisible by 3 equals to the integer part [X], where the number $X = \frac{(n-2)!}{e}(n^2 + n - 1)$ and $|X - [X]| \leq \frac{4}{(n-1)n(n+1)}$.

Theorem 5 [3, Corollary 3.3]. For any positive integer n there exists A ∈ Mn(±1) such that per (A) is not divisible by the (n−⌊log2n⌋+1)-st degree of 2.

The latest result is a certain complement to the theorem by Kräuter and Seifter [6] which asserts that per A∈ Mn(±1) is divisible by the (n−⌊log2n⌋−1)-st degree of 2 and is not divisible by (n−⌊log2n⌋)-th degree of 2, if n=2t−1. In the case n≠2t−1 the value per A is always divisible by the (n−⌊log2n⌋)-th degree of 2.

In the talk we will also consider several other properties and functions related to permanent, in particular, so-called permanental rank, which is the maximal size of a submatrix with non-zero permanent. We will discuss classification of the linear maps preserving this invariant and properties of the linear subspaces of matrices consisting of matrices with bounded permanental rank.

Conclusion

Our investigations demonstrate that permanent is an interesting and important matrix invariant whose properties are far from being well-studied.

References

1.Brualdi, R.A., Newman, M.: Some theorems on permanent. J. Res. Natl. Bur. Stand., Sect. B 69(3), 159–163 (1965).

2.Budrevich, M.V., Guterman, A.E.: Kräuter conjecture on permanents is true. Journal of Combinatorial Theory – Ser. A, 162, 306-343 (2019).

3.Budrevich, M.V., Guterman, A.E. Taranin, K.A.: On the Kräuter –Seifter theorem on permanent divisibility. Journal of Math. Sci. (New York), 232(6), 760-767 (2018).

4.Guterman, A.E., Taranin, K.A.: On the values of the permanent of (0,1)-matrices. Linear Algebra and its Application, 552, 256-276 (2018).

5.Kräuter, A.R.: Recent results on permanents of (+1, -1)-matrices. Ber. No. 249, Berichte, 243-254, Forschungszentrum Graz, Graz, (1985).

6.Kräuter, A.R., Seifter, N.: On some questions concerning permanents of (1,−1)-matrices, Israel J. Math. 45(1), 53–62 (1983).

7.Minc, H.: Permanents, Encyclopedia of Mathematics and its Applications, V. 6, (1978).

8.Wang, E.T.H.: On permanents of (+1, -1)-matrices. Israel J. Math. 18, 353–361 (1974).

https://doi.org./10.58225/mpmma.2026.120

ADAMS THEOREM FOR THE B-RIESZ POTENTIAL IN TOTAL B-MORREY SPACES

Ali Akbulut[1], Suleyman Celik[2], Esra Takan[1], Tunahan Takan[1]

[1]Kirsehir Ahi Evran University, Türkiye

[2] Social Sciences Vocational School, Firat University, Türkiye

Abstract. In this work, we investigate the B -Riesz potential associated with the Laplace Bessel differential operator in total B-Morrey spaces. We establish Adams-type boundedness results for the operator I_γ^α (B- Riesz potential) from total B-Morrey spaces to corresponding target spaces. Necessary and sufficient conditions for the boundedness are obtained. These results extend several classical inequalities in harmonic analysis to the setting of total B-Morrey spaces generated by generalized shift operators.

Keywords: B-maximal operator, B-Riesz potential, total B-Morrey space, Adams theorem for B-Riesz potential.

Introduction

Morrey spaces, introduced by C. B. Morrey [6], play an important role in harmonic analysis and the regularity theory of partial differential equations. In [4] Guliyev introduce a variant of Morrey spaces called total Morrey spaces $L_{p,\lambda,\mu}(\mathbb{R}^n)$,$0 < p < \infty$, $\lambda \in \mathbb{R}$ and $\mu \in \mathbb{R}$, see [2,7]. Total Morrey spaces generalize both classical and modified Morrey spaces.

The classical Morrey spaces were introduced by Morrey [6] for the study of solutions of quasi-linear elliptic partial differential equations. Later, total Morrey spaces were introduced as a generalization of both classical and modified Morrey spaces. The Laplace-Bessel differential operator plays an important role in Fourier-Bessel harmonic analysis and related applications ([1]).

Suppose that n and k are positive integers with $1 \leq k \leq n$ and R^n is n-dimensional Euclidean space. For $x = (x_1, \dots, x_n) \in \mathbb{R}^n$, we set $x' = (x_1, \dots, x_k) \in \mathbb{R}^k$, $x'' = (x_{k+1}, \dots, x_n) \in \mathbb{R}^{n-k}$, $x = (x', x'') \in \mathbb{R}^n$, $n \geq 2$. Let

$$\mathbb{R}^n_{k,+} = \{x = (x', x'') \in \mathbb{R}^n ;\ x_1 > 0, \dots, x_k > 0\}$$

and

$$E(x, r) = \{y \in \mathbb{R}^n_{k,+} ;\ |x - y| < r\}, \quad E_r = E(0, r)$$

For a measurable set E, let $|E|_\gamma = \int_E (x')^\gamma \, dx$, where $\gamma = (\gamma_1, \dots, \gamma_k)$ are positive numbers and $|\gamma| = \gamma_1 + \cdots + \gamma_k$, $(x')^\gamma = x_1^{\gamma_1} \cdots x_k^{\gamma_k}$, $|E_r|_\gamma = \omega(n, k, \gamma)\, r^Q$, $Q = n + |\gamma|$, where

$$\omega(n, k, \gamma) = \int_{E1} (x')^\gamma dx = \frac{\pi^{\frac{n-k}{2}}}{2^k} \prod_{i=1}^{k} \frac{\Gamma\left(\frac{\gamma_i + 1}{2}\right)}{\Gamma\left(\frac{\gamma_i}{2}\right)}.$$

Define the generalized shift operator (B-shift operator) by

$$T^y f(x) = C_{\gamma,k} \int_0^\pi \dots \int_0^\pi f\left((x', y')_\beta, x'' - y''\right) d\nu(\beta)$$

where $(x_i, y_i)_{\beta_i} = (x_i^2 - 2x_i y_i \cos\beta_i + y_i^2)^{1/2}$, $1 \le i \le k, (x', y')_\beta = \left((x_1, y_1)_{\beta_1}, \dots, (x_k, y_k)_{\beta_k}\right)$, $d\nu(\beta) = \prod_{i=1}^{k} \sin^{\gamma_i - 1}\beta_i \; d\beta_1 \dots d\beta_k, \quad 1 \le k \le n$ and

$$C_{\gamma,k} = \pi^{-k/2} \prod_{i=1}^{k} \frac{\Gamma\left(\frac{\gamma_i + 1}{2}\right)}{\Gamma\left(\frac{\gamma_i}{2}\right)} = \frac{2^k}{\pi^k}\omega(2k, k, \gamma)$$

The B-maximal function (see [3]) is defined by

$$M_\gamma f(x) = \sup_{r>0} |E_r|_\gamma^{-1} \int_{E_r} T^y |f(x)| (y')^\gamma \, dy$$

and the B-Riesz potential (see [2]) is defined by

$$I_\gamma^\alpha f(x) = \int_{\mathbb{R}^n_{k,+}} T^y (|x|^{\alpha - Q}) f(y) (y')^\gamma \, dy, \quad 0 < \alpha < Q,$$

where T^y is the generalized shift operator generated by the Laplace-Bessel differential operator Δ_B.

The operator M_γ was introduced by Guliyev in [3]. Moreover, the strong-$\left(L_{p,\gamma}, L_{p,\gamma}\right)$, $1 < p \le \infty$ and weak-$\left(L_{1,\gamma}, L_{1,\gamma}\right)$ boundedness of M_γ was proved in [3]. Also, the strong-$\left(L_{p,\gamma}, L_{q,\gamma}\right)$, $1 < p < \infty$, $1/p - 1/q = \alpha/Q$ and weak-$\left(L_{1,\gamma}, L_{q,\gamma}\right)$, $1 < q < \infty, 1 - 1/q = \alpha/Q$ boundedness of I_γ^α was proved in [3].

Let $1 \le p < \infty$, $\lambda \in \mathbb{R}$, $\mu \in \mathbb{R}$, $[t]_1 = \min\{1, t\}$, $t > 0$. We denote by $L_{p,\lambda,\gamma}\left(\mathbb{R}^n_{k,+}\right)$ the

classical B-Morrey spaces [5], by $\tilde{L}_{p,\lambda,\gamma}\left(\mathbb{R}^n_{k,+}\right)$ the modified B-Morrey spaces [5], and by $L_{p,(\lambda,\mu),\gamma}\left(\mathbb{R}^n_{k,+}\right)$ the total B-Morrey spaces: the sets of all locally integrable functions f with the finite norms

$$||f||_{L_{p,\lambda,\gamma}} = \sup_{x\in\mathbb{R}^n_{k,+},\, t>0}\left(t^{-\lambda}\int_{E_t} T^x|f(y)|^p(y')^\gamma\, dy\right)^{1/p},$$

$$||f||_{\tilde{L}_{p,\lambda,\gamma}} = \sup_{x\in\mathbb{R}^n_{k,+},\, t>0}\left([t]_1^{-\lambda}\int_{E_t} T^x|f(y)|^p(y')^\gamma\, dy\right)^{1/p},$$

$$||f||_{L_{p,(\lambda,\mu),\gamma}} = \sup_{x\in\mathbb{R}^n_{k,+},\, t>0}\left([t]_1^{-\lambda}[1/t]_1^{-\mu}\int_{E_t} T^x|f(y)|^p(y')^\gamma\, dy\right)^{1/p},$$

respectively.

The main result of this work is Adams theorem for B-Riesz potential I^α_γ in total B -Morrey space $L_{p,(\lambda,\mu),\gamma}$.

Theorem 1. [5] Let $1 \le p < \infty$, $0 \le \mu \le \lambda < Q$, $0 < \alpha < \frac{Q-\lambda}{p}$

If $1 < p < \frac{Q-\lambda}{\alpha}$ then the condition $\frac{\alpha}{Q-\mu} \le \frac{1}{p} - \frac{1}{q} \le \frac{\alpha}{Q-\lambda}$ is necessary and sufficient for the boundedness of the operator I^α_γ from $L_{p,(\lambda,\mu),\gamma}\left(\mathbb{R}^n_{k,+}\right)$ to $L_{q,(\lambda,\mu),\gamma}\left(\mathbb{R}^n_{k,+}\right)$.

If $p = 1 < \frac{Q-\lambda}{\alpha}$ then the condition $\frac{\alpha}{Q-\mu} \leq 1 - \frac{1}{q} \leq \frac{\alpha}{Q-\lambda}$ is necessary and sufficient for the boundedness of the operator I_{γ}^{α} from $L_{1,(\lambda,\mu),\gamma}\left(\mathbb{R}_{k,+}^{n}\right)$ to $WL_{q,(\lambda,\mu),\gamma}\left(\mathbb{R}_{k,+}^{n}\right)$.

The research of A. Akbulut and S.Celik was partially supported by a grant from Kirsehir Ahi Evran University Scientific Research Projects (BAP, Project No: FEF.A1.26.001).

References

1. Aliev, I.A., Bayrakci, S.: On inversion of B-elliptic potentials by the method of Balakrishnan-Rubin. Fract. Calc. Appl. Anal. 1(4), 365–384 (1998).
2. Celik, S., Akbulut, A., Omarova, M.N.: Characterizations of anisotropic Lipschitz functions via the commutators of anisotropic maximal function in total anisotropic Morrey spaces. Trans. Natl. Acad. Sci. Azerb. Ser. Phys.-Tech. Math. Sci. Mathematics 45(1), 25–37 (2025).
3. Guliev, V.S.: Sobolev theorems for the Riesz B-potentials (in Russian). Doklady Academy Nauk Russia 358(4), 450–451 (1998).
4. Guliyev, V.S.: Maximal commutator and commutator of maximal function on total Morrey spaces. J. Math. Inequal. 16(4), 1509–1524 (2022).
5. Guliyev, V.S., Akbulut, A., Omarova, M.N., Serbetci, A.: Adams theorem for the B-Riesz potential in the total B-Morrey spaces. Eurasian

Math. J. 17(1), 33–46 (2026). DOI: 10.32523/2077-9879-2026-17-1-33-46
6. Morrey, C.B.: On the solutions of quasi-linear elliptic partial differential equations. Trans. Amer. Math. Soc. 43, 126–166 (1938).
7. Serbetci, A.: Boundedness of the B-maximal operator in B-total Morrey-Guliyev spaces. Trans. Natl. Acad. Sci. Azerb. Ser. Phys.-Tech. Math. Sci. Mathematics 45(4), 145–154 (2025).

https://doi.org./10.58225/mpmma.2026.126

SYNTHESIS OF CONTROL OF THE MOVEMENT OF MEASUREMENT POINTS OF THE STATE AND POWER OF HEAT SOURCES AT THE ENDS OF THE ROD

Kamil Aida-zade[1] , *Vugar Hashimov*[1]
[1] Institute of Mathematics, Azerbaijan
[2] AzUAC, Azerbaijan

Abstract. Using the example of controlling the dynamics of the movement of sensors for measuring the temperature state on a rod, the problem of synthesizing control actions in systems with distributed parameters is investigated. Feedback is achieved by measuring the state of the process using moving remote measuring devices (sensors). Linear dependencies of the current values of control actions on the boundary conditions and on the movement of measuring devices from the measured temperature values both at the current and at past moments of the process state are proposed. In the problems, the constant feedback parameters, that is, the coefficients involved in these dependencies, are synthesized. As a result, the feedback control problem is formulated as a problem of parametric optimal control of an object with distributed parameters. To determine the optimal values of the feedback parameters, formulas for the gradient of the objective functional were obtained, which make it possible to use effective numerical methods of

first-order optimization. The results of numerical experiments are presented.

Keywords: Boundary Control, Rod Heating, Current Time, Past Time, Control Synthesis, Moving Measurement Point, Non-local Conditions, Gradient Projection Method.

1. Problem Statement

Let us consider the problem of controlling the heating process of a rod:

$$u_t(x,t) = a^2 u_{xx}(x,t) - \lambda_0[u(x,t) - \theta], \quad x \in (0,l), \quad t \in (0,T], \tag{1}$$

$$u(x,0) = b(x) = b = \text{const}, \quad x \in [0,l], \tag{2}$$

$$u_x(0,t) = \lambda_1\big(u(0,t) - \vartheta_1(t)\big), \quad t \in (0,T], \tag{3}$$

$$u_x(l,t) = -\lambda_2\big(u(l,t) - \vartheta_2(t)\big), \quad t \in (0,T]. \tag{4}$$

Here $u(x,t)$ is the temperature of the rod at point x at time t; θ is the temperature of the external ambient; the given value T determines the duration of the heating process; $\vartheta_1(t)$ and $\vartheta_2(t)$ are the temperatures of the sources, which are controls from the class of piecewise continuous functions and satisfy the technological constraints:

$$\underline{\vartheta_1} \le \vartheta_1(t) \le \overline{\vartheta_1}, \quad \underline{\vartheta_2} \le \vartheta_2(t) \le \overline{\vartheta_2}, \quad t \in [0,T]. \tag{5}$$

The temperature at the points of the rod before the start of the heating process is constant along the length, but is not precisely specified, and $b \in \mathcal{B}$ is defined as the set of its possible values with the density function $\rho_{\mathcal{B}}(b) \ge 0$ and the ambient temperature $\theta = \text{const}$, $t \in [0,T]$ can also be

specified not exactly, but determined by a set of possible values $\theta \in \Theta$ with a given density function $\rho_\Theta(\theta) \geq 0$, where

$$\int_{\mathcal{B}} \rho_{\mathcal{B}}(b)db = 1, \quad \int_\Theta \rho_\Theta(\theta)d\theta = 1.$$

It is required to determine the control action $\vartheta = \vartheta(t) = \big(\vartheta_1(t), \vartheta_2(t)\big)$, at which the given functional reaches its minimum, which determines the average value of the root mean square of the state at the final moment of time from the given desired temperature distribution along the rod $U(x)$, $x \in [0, l]$ over all permissible external temperatures θ and initial conditions b:

$$J(\vartheta) = \int_\Theta \int_{\mathcal{B}} I(\vartheta; b, \theta)\rho_{\mathcal{B}}(b)\rho_\Theta(\theta)dbd\theta, \tag{6}$$

$$I(\vartheta; b, \theta) = \int_0^l \mu(x)[u(x, T; \vartheta, b, \theta) - U(x)]^2 dx + \varepsilon \| \vartheta(t) - \hat{\vartheta} \|^2_{L_2[0,T]}. \tag{7}$$

Here $u(x, t; \vartheta, b, \theta)$ is the solution of the initial-boundary value problem (1)–(4) under an admissible initial condition $u(x, 0) = b$ and under an admissible ambient temperature θ; ε, $\hat{\vartheta}$ are the regularization parameters of the functional; $\mu(x) \geq 0$, $x \in [0, l]$ is the given weight function.

Let there be N moving sensors for measuring temperature values at points of the rod to assign current temperature values of boundary controls. The movements of the sensors are controlled and described by Cauchy problems with respect to nonlinear differential equations:

$$\dot{\xi}_i(t) = f_i(\xi_i(t), \omega_i(t), t), \quad t \in (0, T], \quad i = 1,2, \dots, N, \tag{8}$$

$$\xi_i(0) = \xi_i^0 \in [0, l], \quad i = 1,2, \dots, N.$$

Here, $\xi_i(t)$ is the position of the i-th temperature sensor at the time $t \in [0, T]$; the given functions $f_i(\cdot,\cdot,t), \quad i = 1,2, \dots, N$ are continuously differentiable with respect to the first two arguments and piecewise continuous with respect to the third argument; $\omega_i(t)$, $i = 1,2, \dots, N$ are the optimized control actions on the sensor movements; ξ_i^0, $i = 1,2, \dots, N$ are the given initial positions of the sensors on the rod.

Control actions on sensor movements must satisfy technological constraints:

$$\underline{\omega_i} \le \omega_i(t) \le \overline{\omega_i}, \quad t \in [0, T], \quad i = 1,2, \dots, N. \tag{8}$$

Let us denote by

$$\hat{u}_i(t) = u(\xi_i(t), t), \quad t \in [0, T], \quad i = 1,2, \dots, N. \tag{9}$$

continuously measured in time by the i-th sensor temperature at point $\xi_i(t)$ at time t, $i = 1,2, \dots, N$.

The values of the controlled boundary actions $\vartheta_1(t)$ and $\vartheta_2(t)$ and control actions on the movement of sensors $\omega_i(t)$ in the control process will be determined based on the results of measurements both at the current moment in time and, at previous moments in time are considered in the form of their linear dependence on the state of the process at the controlled points:

$$\vartheta_1(t; \mathbf{k}) = \sum_{i=1}^{N} k_i^1 \left[u(\xi_i(t), t) - U\big(\xi_i(t)\big)\right] \tag{10}$$

$$+k_i^4\left[u(\xi_i(t-\Delta), t-\Delta) - U\big(\xi_i(t-\Delta)\big)\right], \quad t \in [0, T],$$

$$\vartheta_2(t;\mathbf{k}) = \sum_{i=1}^{N} k_i^2 \left[u(\xi_i(t),t) - U\left(\xi_i(t)\right)\right]$$

(11)

$$+k_i^5\left[u(\xi_i(t-\Delta),t-\Delta) - U\left(\xi_i(t-\Delta)\right)\right], \quad t \in [0,T],$$

$$\omega_i(t;\mathbf{k}) = k_i^3\left[u(\xi_i(t),t) - U\left(\xi_i(t)\right)\right]$$

(12)

$$+k_i^6\left[u(\xi_i(t-\Delta),t-\Delta) - U\left(\xi_i(t-\Delta)\right)\right], \quad t \in [0,T], \quad i = 1,2,\dots,N,$$

where k_i^1, k_i^2, k_i^3, k_i^4, k_i^5 k_i^6, $i = 1,2,\dots,N$ are gain coefficients.

In (12)–(14) and further the following notations are used:

$$\mathbf{k} = (k^1, k^2, k^3, k^4, k^5, k^6) \in \mathbb{R}^{6N}.$$

In the case of measurement (11) of the heating process, the minimized functional (6), (7) is written as:

$$J(\mathbf{k}) = \int_{\Theta} \int_{\mathcal{B}} I(\mathbf{k};b,\theta)\rho_{\mathcal{B}}(b)\rho_{\Theta}(\theta)dbd\theta,$$

(15)

$$I(\mathbf{k};b,\theta) = \int_0^l \mu(x)[u(x,T;\mathbf{k},b,\theta) - U(x)]^2 dx + \varepsilon \parallel \mathbf{k} - \hat{\mathbf{k}} \parallel^2_{\mathbb{R}^{6N}}.$$

(16)

References

1. Aida-zade, K.R., Hashimov, V.A.: Optimization of Measurement Points Positioning in a Border Control Synthesis Problem for the Process of Heating a Rod. Autom Remote Control 79, 1643–1660 (2018) https://doi.org/10.1134/S0005117918090096

2. Hashimov, V.A.: Synthesis of boundary conditions control and state measurement points motion for fast damping of string vibrations, Proceedings of the Institute of Mathematics and Mechanics, 51(2), 294–317 (2025) https://doi.org/10.30546/2409-4994.2025.51.2.4110
3. Aida-zade, K.R.: An Approach for Solving Nonlinearly Loaded Problems for Linear Ordinary Differential Equations. Proceedings of the Institute of Mathematics and Mechanics, 44(2), 338–350 (2018)

https://doi.org./10.58225/mpmma.2026.132

AUTOMATIC TRANSCRIPTION AND CLASSIFICATION OF CUSTOMER CALL RECORDINGS FOR CRM ANALYTICS: A WHISPER-BASED WEB SYSTEM

Ali Khalilov[1] , Hilala Jafarova[2]
[1,2]Academy of Public Administration under the President of the Republic of Azerbaijan, Azerbaijan

Abstract. This paper presents a web-based system that transcribes customer call-centre recordings and classifies them into CRM categories. Audio is stored in a relational database and transcribed into Azerbaijani text with Open AI Whisper; each transcript is then assigned a category by a supervised text classifier. Four classifiers — Multinomial Naive Bayes, Logistic Regression, Random Forest, and a linear Support Vector Machine (SVM) — are compared on TF-IDF features over 1,480 calls in five categories. The linear SVM performs best (accuracy = 91.2%, macro-F1 = 0.89) and Whisper reaches a 14.8% word error rate (WER) with the large-v3 model. Deployed as a Flask application with sub-50 ms classification latency, the pipeline offers Azerbaijani call centres a low-cost route to automated call analytics.

Keywords: speech recognition, Whisper, call classification, text classification, support vector machine, CRM, Flask, Azerbaijani NLP.

1 Introduction

Call centres generate large volumes of recorded audio that are a rich but largely untapped source of business intelligence. Manual review is infeasible, yet CRM teams need structured information on call drivers and trends. Two technologies enable this at scale: automatic speech recognition (ASR), which converts audio to text, and supervised text classification, which assigns each call a business category. A practical obstacle for Azerbaijani enterprises is that most mature ASR and NLP tooling targets high-resource languages [1]. This paper presents an end-to-end pipeline that stores recordings, transcribes them with Whisper, classifies each transcript, and surfaces the results in a Flask dashboard. The contributions are an end-to-end Azerbaijani call-analytics pipeline, a comparison of four classifiers on real transcribed calls, and a deployable low-cost web implementation.

2 Related Work

Whisper [1] is a large-scale, weakly supervised ASR model that transcribes many languages, including lower-resource ones such as Azerbaijani. For classification, TF-IDF [4] is a strong text representation and Support Vector Machines [2] perform well on sparse high-dimensional features, as shown by Joachims [3]; Multinomial Naive Bayes [7] and Random Forest [5] are common

baselines. Transformer models such as BERT [6] reach higher accuracy but demand far more compute and data. The classical algorithms are available in scikit-learn [8] and served via Flask [9].

3 System Design and Methodology

3.1 System Architecture and Dataset

The system is a four-stage pipeline. Call recordings (WAV/MP3) are uploaded through the web interface and stored with metadata in a relational database; an asynchronous worker transcribes each recording with Whisper (language fixed to Azerbaijani) and writes the transcript back to the database; each transcript is pre-processed, vectorised, and classified; and a Flask dashboard exposes per-category counts, trends, and full-text search. The evaluation uses 1,480 anonymised Azerbaijani calls (average 3.6 minutes, ≈89 hours total), expert-labelled into five CRM categories: complaint (şikayət), information request (məlumat sorğusu), sales/order (satış), technical support (texniki dəstək), and cancellation (ləğv). The distribution is moderately imbalanced (cancellation is rare); an 80/20 stratified split is applied (1,184 train, 296 test).

3.2 Transcription and Features

Transcription uses OpenAI Whisper with the decoding language fixed to Azerbaijani to avoid

misdetection on short utterances; four model sizes (base, small, medium, large-v3) were evaluated against 60 manually transcribed calls. Transcripts are lower-cased, stripped of punctuation and digits, and cleared of Azerbaijani stop-words, then converted to TF-IDF features over unigrams and bigrams (top 10,000 terms, minimum document frequency two). The fitted vectoriser is reused at inference for a consistent feature space.

3.3 Classification and Metrics

Four classifiers are compared on identical features: Multinomial Naive Bayes (MNB), Logistic Regression (LR, L2), Random Forest (RF, 200 trees), and a linear Support Vector Machine (SVM) whose regularisation parameter C is selected by five-fold cross-validation; the linear SVM is the production classifier. Classification quality is reported with accuracy and macro-averaged F1 (which weights each class equally and so reflects the minority cancellation category); transcription quality with word error rate (WER); and training time as a deployment consideration.

4 Implementation and Results

4.1 Transcription Accuracy

Table 1 reports WER and processing time per minute of audio for the four Whisper model sizes.

Whisper model	WER (%)	Time / min audio
base	31.5	4 sec

small	24.7	9 sec
medium	18.9	22 sec
large-v3	14.8	41 sec

Table 1. Whisper transcription accuracy on the Azerbaijani held-out set.

Accuracy improves with model size, from 31.5% WER (base) to 14.8% (large-v3) at roughly ten times the cost; large-v3 is used in the pipeline, with medium as an accuracy–latency compromise.

4.2 Classification Comparison

Table 2 reports accuracy, macro-F1, and training time on the hold-out test set.

Classifier	**Accuracy (%)**	**Macro-F1**	**Training time**
Multinomial Naive Bayes	82.1	0.79	< 1 sec
Random Forest (200 trees)	86.7	0.84	41 sec
Logistic Regression	88.3	0.86	2 sec
Linear SVM	91.2	0.89	3 sec

Table 2. Comparative evaluation of classifiers on TF-IDF features.

The linear SVM is best (accuracy = 91.2%, macro-F1 = 0.89), consistent with the strength of SVMs on sparse text features; Logistic Regression is a close, equally fast second, Naive Bayes the weakest (most errors in the rare cancellation class),

and Random Forest competitive but slower. Classifying one transcript takes under 50 ms, and the dashboard renders category distributions, trends, and full-text search, giving CRM teams immediate visibility without manual tagging.

5 Discussion

Three points follow. Classifier choice matters: the SVM beats the Naive Bayes baseline by 9.1 points, confirming that margin-based linear models suit TF-IDF features. Transcription error propagates — the residual 14.8% WER bounds downstream accuracy — so better Azerbaijani ASR is the most direct improvement, and class imbalance is why macro-F1 is reported. Limitations include a single call-centre dataset and the compute demand of the large Whisper model. Future work will fine-tune a transformer such as BERT [6] for Azerbaijani, add streaming transcription, and add sentiment analysis.

6 Conclusion

This paper presented a deployable pipeline that transcribes Azerbaijani customer calls with Whisper and classifies them into CRM categories with a linear SVM, delivered through a Flask dashboard. On 1,480 real calls it reaches 91.2% accuracy (macro-F1 = 0.89) at 14.8% WER with sub-50 ms classification latency. Built on open-source components, it offers Azerbaijani call

centres a low-cost entry point to automated call analytics.

References

1.Radford A., Kim J.W., Xu T., Brockman G., McLeavey C., Sutskever I.: Robust Speech Recognition via Large-Scale Weak Supervision. Proc. ICML, pp. 28492–28518 (2023).

2.Cortes C., Vapnik V.: Support-vector networks. Mach. Learn. 20(3), 273–297 (1995).

3.Joachims T.: Text categorization with support vector machines: learning with many relevant features. Proc. ECML, pp. 137–142 (1998).

4.Salton G., Buckley C.: Term-weighting approaches in automatic text retrieval. Inf. Process. Manag. 24(5), 513–523 (1988).

5.Breiman L.: Random forests. Mach. Learn. 45(1), 5–32 (2001).

6.Devlin J., Chang M.-W., Lee K., Toutanova K.: BERT: Pre-training of Deep Bidirectional Transformers for Language Understanding. Proc. NAACL-HLT, pp. 4171–4186 (2019).

7.McCallum A., Nigam K.: A comparison of event models for Naive Bayes text classification. AAAI/ICML Workshop on Learning for Text Categorization, pp. 41–48 (1998).

8.Pedregosa F. et al.: Scikit-learn: Machine learning in Python. J. Mach. Learn. Res. 12, 2825–2830 (2011).

9.Grinberg M.: Flask Web Development. 2nd edn. O’Reilly Med

https://doi.org./10.58225/mpmma.2026.140

ON INTERPOLATION TYPE THEOREMS IN GRAND GRAND BESOV SPACES WITH DOMINANT MIXED DERIVATIVES

Alik Najafov[1,2], Ahmet Eroglu[3], Nilufer R.Rustamova[1,2]

[1] AzUAC, Azerbaijan

[2] Institute of Mathematics, Azerbaijan,

Nigde Omer Halisdemir University, Türkiye

Abstract. In this paper, we introduce a new function spaces of grand and grand grand Besov spaces with dominant mixed derivatives. Here, using the method of integral representation of functions defined in n-dimensional domains satifying the flexible horn type, embedding theorems and interpolation type theorems are proved in these introduced spaces.

Keywords: grand grand Besov spaces with dominant mixed derivatives, flexible horn, embedding theorems, interpolation theorems.

1.Introduction and preliminary notes

In this paper, we introduce and study, from the point of view perspective of embedding theory, grand and grand grand Besov spaces with dominant mixed derivatives $S^{l}_{p),\theta}\,B(G_t)$ $(1 \leq \theta \leq \infty)$ and $S^{l}_{p),\theta}\,B(G_t)$ $(1 < \theta < \infty)$ where $G \subset R^n$ a measurable set of finite Lebesgue measure, $1 < p < \infty, G_t = \{x : x + t \in G\}, t = (t_1, t_2, \ldots, t_n), 0 < t_j < t_{j,0}, j \in e_n = \{1,2,\ldots,n\}, t_0 = (t_{0,1}, t_{0,2}, \ldots, t_{0,n})$ is positive

fixed vector, $l \in (0,\infty)^n$. In other words, we first define a norm in these spaces and then, using the method integral representations, prove Sobolev type inequalities in the introduced spaces.

In connection with the study of different types of differential equation, for example, equations

$$u_{x^2y^2}^{(4)} + u_{x^2y}^{(3)} + u_{xy^2}^{(3)} + u_{xy}^{(2)} + u_x^{(1)} + u_y^{(1)} + u = f,$$

which allows one to study functional spaces with dominant mixed derivatives. Note that spaces of this type, i.e. spaces with dominant mixed derivatives of Sobolev $S_p^l W$ $(l \in N^n)$ and Nikolskii $S_p^l H$ $(l \in (0,\infty^n))$, were first introduced and studied by Nikolskii. Subsequently Besov spaces with dominant mixed derivatives $S_{p,\theta}^l B$ were simultaneously introduced and studied by different methods in works of T.I.Amanov and A.D.Dzhabrailov , and Lizorkin-Triebel spaces with dominant mixed derivatives $S_{p,\theta}^l F$ were introduced and studied in the work of A.M.Najafov. Further years, spaces of this type were studied by many mathematicians.

Definition 1. By a grand Besov space with dominant mixed derivatives $S_{p),\theta}^l B(G_t)$ we mean the Banach spaces of locally summable functions f on G with finite norm $(1 \le \theta \le \infty)$

$$\|f\|_{S_{p),\theta}^l B(G_t)}$$

$$= \sum_{e \subseteq e_n} \left\{ \int_{0^e}^{t_0^e} \left[\frac{\left\| \Delta^{m^e}(t, G_t) D^{k^e} f(x) \right\|_{p)}}{\prod_{j \in e} t_j^{l_j - k_j}} \right]^{\theta} \prod_{j \in e} \frac{dt_j}{t_j} \right\}^{\frac{1}{\theta}}$$

$$=$$

$$= \sum_{e\subseteq e_n} \sup_{0<\varepsilon<p-1} \left\{ \int_{0^e}^{t_0^e} \left[\frac{\left(\frac{\varepsilon}{|G_t|} \int_{G_t} \left| \Delta^{m^e}(t, G_t) D^{k^e} f(x) \right|^{p-\varepsilon} dx \right)^{\frac{1}{p-\varepsilon}}}{\prod_{j\in e} t_j^{l_j - k_j}} \right]^{\theta} \prod_{j\in e} \frac{dt_j}{t_j} \right\}^{\frac{1}{\theta}},$$

where

$$\int_{a^e}^{b^e} f(x) dx^e = \left(\prod_{j\in e} \int_{a_j}^{b_j} dx_j \right) f(x),$$

i.e., the integration takes place only with respect to the variable x_j, whose indices belong to the set e.

Definition 2. By a grand grand Besov space with dominant mixed derivatives $S^l_{p),\theta}\, B(G_t)$ we mean the Banach spaces of locally summable functions f on G with finite norm $(1 < \theta < \infty)$

$$\|f\|_{S^l_{p),\theta}\, B(G_t)} = \sum_{e\subseteq e_n} \inf_{0\ll\varepsilon_1<\varepsilon_0} \left(\frac{\varepsilon_1}{\prod_{j\in e} t_{j,0}} \right)^{\frac{1}{\theta+\varepsilon_1}} \times$$

$$\times \left\{ \int_{0^e}^{t_0^e} \left[\frac{\left\| \Delta^{m^e}(t, G_t) D^{k^e} f \right\|_{p)}}{\prod_{j\in e} t_j^{l_j - k_j}} \right]^{\theta+\varepsilon_1} \prod_{j\in e} \frac{dt_j}{t_j} \right\}^{\frac{1}{\theta+\varepsilon_1}} =$$

$$= \sum_{e\subseteq e_n} \sup_{0<\varepsilon<p-1} \inf_{0\ll\varepsilon_1<\varepsilon_0} \left(\frac{\varepsilon_1}{\prod_{j\in e} t_{j,0}} \right)^{\frac{1}{\theta+\varepsilon_1}} \times$$

$$\times \left\{ \int_{0^e}^{t_0^e} \left[\frac{\left(\frac{\varepsilon}{|G_t|} \int_{G_t} \left| \Delta^{m^e}(t, G_t) D^{k^e} f(x) \right|^{p-\varepsilon} dx \right)^{\frac{1}{p-\varepsilon}}}{\prod_{j\in e} t_j^{l_j - k_j}} \right]^{\theta+\varepsilon_1} \prod_{j\in e} \frac{dt_j}{t_j} \right\}^{\frac{1}{\theta+\varepsilon_1}},$$

where ε_0 is fixed positive number.

Are proved some embedding and interpolation type theorems for function from the spaces $S^l_{p),\theta} B(G_t)$ and $S^l_{p),\theta)} B(G_t)$, for all $0 < \varepsilon < p - 1$.

1. $D^{\nu} : S^{l}_{p),\theta}B(G_t) \hookrightarrow L_{q-\varepsilon}(G) \quad \left(D^{\nu} : S^{l}_{p),\theta}B(G_t) \hookrightarrow C(G) \right),\ 1 \le \theta \le \infty;$
2. $D^{\nu} : S^{l}_{p),\theta)}B(G_t) \hookrightarrow L_{q-\varepsilon}(G) \quad \left(D^{\nu} : S^{l}_{p),\theta)}B(G_t) \hookrightarrow C(G) \right),\ 1 < \theta < \infty;$
3. $D^{\nu} : \prod_{\lambda=1}^{k} S^{l^{\lambda}}_{p_{\lambda}),\theta_{\lambda}}B(G_t) \hookrightarrow L_{q-\varepsilon}(G) \quad \left(D^{\nu} : \prod_{\lambda=1}^{k} S^{l^{\lambda}}_{p_{\lambda}),\theta_{\lambda}}B(G_t) \hookrightarrow C(G) \right),\ 1 \le \theta_{\lambda} \le \infty:$
4. $D^{\nu} : \prod_{\lambda=1}^{k} S^{l^{\lambda}}_{p_{\lambda}),\theta_{\lambda})}B(G_t) \hookrightarrow L_{q-\varepsilon}(G) \quad \left(D^{\nu} : \prod_{\lambda=1}^{k} S^{l^{\lambda}}_{p_{\lambda}),\theta_{\lambda})}B(G_t) \hookrightarrow C(G) \right),\ 1 < \theta_{\lambda} < \infty:$
5. $D^{\nu} : S^{l}_{p),\theta}B(G_t) \hookrightarrow S^{l^1}_{q-\varepsilon,\theta}B(G_t) \quad l^1 \in (0,\infty)^n,\ 1 \le \theta \le \infty;$
6. $D^{\nu} : S^{l}_{p),\theta)}B(G_t) \hookrightarrow S^{l^1}_{q-\varepsilon,\theta+\varepsilon_1}B(G_t) \quad l^1 \in (0,\infty)^n, 0 \ll \varepsilon_1 < \varepsilon_0, 1 < \theta < \infty;$

$$7.\ D^{\nu}:\bigcap_{\lambda=1}^{k}S^{l^{\lambda}}_{p_{\lambda}),\theta_{\lambda}}B(G_t)\hookrightarrow S^{l^{1}}_{q-\varepsilon,\theta}B(G_h)\quad,l^{1}\in(0,\infty)^{n},1\leq\theta\leq\infty:$$

$$8.\ D^{\nu}:\bigcap_{\lambda=1}^{k}S^{l^{\lambda}}_{p_{\lambda}),\theta_{\lambda})}B(G_t)\hookrightarrow D^{\nu}:\ S^{l}_{p),\theta)}B(G_t)\hookrightarrow S^{l^{1}}_{q-\varepsilon,\theta+\varepsilon_{1}}B(G_t)\quad l^{1}\in(0,\infty)^{n},\ 0\ll\varepsilon_{1}<\varepsilon_{0},1<\theta<\infty;$$

https://doi.org./10.58225/mpmma.2026.145

ON THE SMOOTHNESS OF SOLUTIONS OF HYPOELLIPTIC TYPE EQUATIONS

Alik Najafov[1], Aygun T. Omarova[2,] Sain T.Alekberli[1]

[1] AzUAC, Azerbaijan

[2] Ministry of Science and Education Republic of Azerbaijan, Institute of Mathematics, Azerbaijan

Abstract. In this paper we study the smoothness of the solution of one class of hypoelliptic type equations in bounded G⊂Rn with a non-smooth boundary.

Keywords: smoothness of solution, hypoelliptic type equation, domain with non-smooth boundary.

1Introduction and preliminary notes

In this paper, we study the smoothness of solution of one class of hypoelliptic equations of the form

$$\sum_{\substack{\alpha_j,\beta_j\le l_j,\\ j\in e\subseteq e_n}} D^{\alpha^e}\left(a_{\alpha^e\beta^e}(x)D^{\beta^e}u(x)\right)=\sum_{\substack{\alpha_j\le l_j,\\ j\in e\subseteq e_n}} D^{\alpha^e}f_{\alpha^e}(x),\ x\in G, \qquad (1)$$

Let G is bounded domain with non-smooth boundary, $e_n=\{1,2,...,n\}$, $e\subseteq e_n$, $\alpha=(\alpha_1,\alpha_2,...,\alpha_n)$, $\beta=(\beta_1,\beta_2,...,\beta_n)$, $l=(l_1,l_2,...,l_n)$, $l_j\in N(j\in e_n)$, and let $\alpha^e=(\alpha_1^e,\alpha_2^e,...,\alpha_n^e)$, $\beta^e=(\beta_1^e,\beta_2^e,...,\beta_n^e)$, $\alpha_j^e=\alpha_j(j\in e)$, $\alpha_j^e=0(j\in e_n/e=e')$, $f_{\alpha^e}\in L_{\frac{2-\varepsilon}{1-\varepsilon}}(G)$ for all $\alpha_j\le l_j(j\in e)$. Suppose that the coefficients $a_{\alpha^e\beta^e}(x)\equiv a_{\beta^e\alpha^e}(x)$, $a_{\alpha^e\beta^e}(x)\in L_{\frac{2}{\varepsilon}}(G)$, $0<\varepsilon<1$, for all

$\alpha_j \le l_j, \beta_j \le l_j (j \in e_n)$ and such, that in this paper, as $\xi \in R^n$

$$\sum_{\substack{\alpha_j,\beta_j \le l_j \\ j \in e \subset e_n}} (-1)^{|\alpha^e|} a_{\alpha^e \beta^e}(x) \xi_{\alpha^e \beta^e}(x) \ge C_0 \sum_{\substack{\alpha_j \le l_j \\ j \in e \subset e_n}} \left| \xi_{\alpha^e} \right|^2 (x), \quad C_0 > 0 \quad is constants, \tag{2}$$

where $\left|\alpha^e\right| = \sum_{j \in e} \alpha_j$.

Theorem 1[1]. Let domain $G \subset R^n$ satisfy (A_1) type flexible horn condition, $1 < p < q \le \infty$, $æ_j \le \frac{1}{1+a_j}$, $j \in e_n$; $\nu = (\nu_1, \nu_2, ..., \nu_n)$, $\nu_j \ge 0$ are integers $(j \in e_n)$, and

$$\mu_j = l_j - \nu_j - \left(1 - æ_j - æ_j a_j\right)\left(\frac{1}{p-\varepsilon} - \frac{1}{q-\varepsilon}\right) > 0, \quad j \in e_n$$

and $f \in S^l_{p),æ,a} W(G)$.

Then $D^\nu : S^l_{p),æ,a} W(G) \to L_{q-\varepsilon}(G)$ holds for any $0 < \varepsilon < p-1$. Moreover, the following inequality is valid

$$\left\| D^\nu f \right\|_{q-\varepsilon, G} \le C(\varepsilon) \sum_{e \subset e_n} \prod_{j \in e_n} T_j^{s_{e,j}} \left\| D^{l^e} f \right\|_{p),æ,a;G}, \tag{3}$$

where

$$s_{e,j} = \begin{cases} \mu_j, & j \in e \\ -\nu_j - \left(1 - æ_j - æ_j a_j\right)\left(\frac{1}{p-\varepsilon} - \frac{1}{q-\varepsilon}\right), & j \in e' \end{cases}.$$

In particular, if

$$\mu_{j,0} = l_j - \nu_j - \left(1 - æ_j - æ_j a_j\right)\left(\frac{1}{p-\varepsilon} - \frac{1}{q-\varepsilon}\right) > 0, \quad j \in e_n$$

then $D^\nu f(x)$ is continuous on G and

$$\sup_{x \in G} \left| D^\nu f \right| \le C(\varepsilon) \sum_{e \subset e_n} \prod_{j \in e_n} T_j^{s^0_{e,j}} \left\| D^{l^e} f \right\|_{p),æ,a;G} \tag{4}$$

where $0 < T_j \le d_j \ (j \in e_n)$, $C(\varepsilon) > 0$ is a constant independent of f and τ.

Theorem 2. Let all condition of Theorem 1. If $\mu_j > 0 \ (j \in e_n)$, then $D^\nu f(x)$ satisfies the Holder condition with exponent δ_j on G in the metric of $\bar{L}_{q-\varepsilon}$; more exactly

$$\left\| \Delta(\gamma, G) D^\nu f \right\|_{q-\varepsilon, G} \le C(\varepsilon) \|f\|_{S^l_{p),æ,a} W(G)} \prod_{j \in e_n} |\gamma_j|^{\delta_j} \tag{5}$$

where δ_j is an arbitrary number satisfying the inequalities:

$$\begin{aligned} &0 \le \delta_j \le 1, \quad \text{if } \mu_j > 1, \ j \in e; \\ &0 \le \delta_j < 1, \quad \text{if } \mu_j = 1, \ j \in e; 0 \le \delta_j \le 1, j \in e'; \\ &0 \le \delta_j \le \mu_j, \text{if } \mu_j < 1, j \in e; \end{aligned} \tag{6}$$

If $\mu_{j,0} > 0 \ (j \in e_n)$, then

$$\sup_{x \in G} \left| \Delta(\gamma, G) D^\nu f(x) \right| \le C(\varepsilon) \|f\|_{S^l_{p),æ,a} W(G)} \prod_{j \in e_n} |\gamma_j|^{\delta_j^0}, \tag{7}$$

where δ_j^0 satisfy the same conditions as δ_j with $\mu_{j,0}$ instead μ_j.

Theorem 3. If $\frac{1}{p-\varepsilon} + \nu_j \le l_j \ (j \in e_n)$, then every weak solution of equation (1) in the space $S^l_{2)} W(G)$ belongs to the space $C_{\nu+\delta_0}(G^d), \bar{G}^d \subset G$, where $C_{\nu+\delta_0}$ is Holder's space.

References

1. Alik M. Najafov, Sain T. Alekberli, Some properties of grand Sobolev-Morrey spaces with dominant mixed derivatives, Journal of MathematicalInequalities, Volume 13, Number 4 (2019), 1171–1180.

https://doi.org./10.58225/mpmma.2026.149

ON THE SOLUTION OF HYPOELLIPTIC TYPE EQUATIONS IN GRAND SOBOLEV SPACES WITH DOMINANT MIXED DERIVATIVES

Alik Najafov[1,2] , Sain T.Alekberli[1] , Leyla Sh.Gadimova[1,2]

[1] AzUAC, Azerbaijan

[2] Institute of Mathematics, Azerbaijan

Abstract. In this paper, using the variational method, we study the solution of one class of high-order differential equations of hypoelliptic type in grand Soboles spaces.

Keywords: variational method, weak solution, hypoelliptic type equations, grand Sobolev space.

In this paper, we investigate the existence and uniqueness of a weak solution of one class of hypoelliptic type equations, i.e., we study the following boundary value problems

$$\sum_{\substack{\alpha_j,\beta_j\le l_j \\ j\in e\subseteq e_n}} D^{\alpha^e}\left(a_{\alpha^e,\beta^e}(x)D^{\beta^e}u(x)\right) = \sum_{\substack{\alpha_j\le l_j \\ j\in e\subseteq e_n}} D^{\alpha^e} f_{\alpha^e}(x) \qquad (1)$$

$$D^{\nu}u|_{\partial G} = \varphi_{\nu}|_{\partial G}, \qquad (2)$$

in in grand Sobolev spaces with dominant mixed derivatives, where $e_n = \{1,2,\dots,n\}$, $e \subseteq e_n$; let

$\alpha = (\alpha_1, \dots, \alpha_n), \beta = (\beta_1, \dots, \beta_n), l = (l_1, \dots, l_n), \alpha_j, \beta_j \in N_0; l_j \in N,\ j \in e_n,$ and let $\alpha^e = (\alpha_1^e, \dots, \alpha_n^e), \beta^e = (\beta_1^e, \dots, \beta_n^e), \alpha_j^e = \alpha_j, \beta_j^e = \beta_j (j \in e), \alpha_j^e = 0, \beta_j^e = 0\ (j \in e_n \backslash e = e`); \nu = (\nu_1, \dots, \nu_n), 0 \le \nu_j \le l_j - 1$ are integers $(j \in e_n)$, and let $G \subset R^n$ be bounded domain satisfy flexible horn type condition (A_1), and suppose that the coefficients $a_{\alpha^e,\beta^e}(x)$ are the bounded measur able functions in the domain $G, a_{\alpha^e,\beta^e}(x) \equiv a_{\alpha^e,\beta^e}(x)$ for all $\alpha_j \le l_j, \beta_j \le l_j (j \in e_n), a_{\alpha^e,\beta^e}(x) \in \underset{\varepsilon}{L_2}(G), 0 < \varepsilon < 1,$ $\alpha_j \le l_j, \beta_j \le l_j, j \in e_n$ and such, that in this paper

$$\sum_{\substack{\alpha_j,\beta_j \le l_j \\ j \in e \subseteq e_n}} (-1)^{|\alpha^e|} a_{\alpha^e,\beta^e}(x) \xi_{\alpha^e} \xi_{\beta^e}$$

$$\ge C_0 \sum_{\substack{\alpha_j \le l_j \\ j \in e \subseteq e_n}} |\xi_{l^e}|^2, \quad C_0 = \text{const}$$

$$> 0.$$

Definition 1. A weak solution to (1)-(2) in G a function $u(x) \in S_{2)}^{l} W(G)$, if $D^{\nu}u - \varphi_{\nu} \in L_{2-\varepsilon}(G)$ for all $0 < \varepsilon < 1$ such that

$$\sum_{\substack{\alpha_j,\beta_j \le l_j \\ j \in e \subseteq e_n}} (-1)^{|\alpha^e|} \int_G a_{\alpha^e,\beta^e} D^{\beta^e} u(x) D^{\alpha^e} \vartheta(x) dx =$$

$$= \sum_{\substack{\alpha_j \le l_j \\ j \in e \subseteq e_n}} (-1)^{|\alpha^e|} \int f_{\alpha^e}(x)\, D^{\alpha^e} \vartheta(x) dx,$$

for every function $v(x) \in \dot{S}^{l}_{2)} W(G)$.

Definition 2. We say that open set $G \subset R^n$ satisfies the flexible horn type condition (A_1), if for for any $x \in G$ and $T \in (0,\infty)^n$ there exists vector-function

$$\rho(t,x) = (\rho_1(t_1,x),\dots,\rho_n(t_n,x)), 0 \le t_j \le T_j, j \in e_n,$$

with the following properties:

1. for all $j \in e_n$, the functions $\rho_j(t_j,x)$ are absolutely continuous with respect to t_j on $[0,T_j]$, and $|\rho_j(t_j,x)| \le 1$ for almost all $t_j \in [0,T_j]$, where
$$\rho`_j(t_j,x) = \frac{\partial}{\partial t_j}\rho_j(t_j,x);$$
2. $\rho_j(0,x) = 0$ for all $j \in e_n$,

$$x + V(x,\omega) = x + \bigcup_{\substack{0 \le t_j \le T_j, \\ j \in e_n}} [\rho(t,x) + t\omega I] \; G,$$

where $\omega = (\omega_1,\omega_2,\dots,\omega_n), \omega_j \in (0,1]$ for $j \in e_n, I = [-1,1]^n, t\omega I = \{(t_1\omega_1 y_1, t_2\omega_2 y_2,\dots,t_n\omega_n y_n) : y \in I\}$. If $t_1 = t^{\lambda_1}, t_2 = t^{\lambda_2},\dots,t_n = t^{\lambda_n}, \lambda = (\lambda_1,\lambda_2,\dots,\lambda_n), \rho(t,x) = \rho(t^{\lambda},x), \omega_1 = \omega^{\lambda_1}, \omega_2 = \omega^{\lambda_2},\dots,\omega_n = \omega^{\lambda_n}, \omega \in (0,1]$, then

$$V(x,\lambda,\omega) = \bigcup_{0 \le t \le T} \left[\rho(t^{\lambda},x) + t^{\lambda}\omega^{\lambda} I\right],$$

is a flexible λ-horn introduced by O.V.Besov [3]ease note that the first paragraph of a

Theorem 1. Let $G \subset R^n$ be a bounded domain with a non-smooth boundary, and let $g, h \in S^1_{2)} W(G), f_{\alpha^e} \in L_{\frac{2-\varepsilon}{1-\varepsilon}} (G)$ for $\alpha_j \leq l_j \, (j \in e)$.

Then the Dirichlet problem (1)-(2) has a unique weak solution in $S^l_{2)} W(G)$.

https://doi.org./10.58225/mpmma.2026.153

MACHINE LEARNING-BASED THERMAL COMFORT CLASSIFICATION IN BUILDINGS

Amir Rahmanparast[1], Muhammed Milani[2], Ahmet Selim Dalkilic[1]

[1] Yildiz Technical University, Türkiye

Bandirma Onyedi Eylul University, Türkiye

Abstract. Ensuring user comfort in buildings is a crucial research topic in terms of both indoor environmental quality and energy efficiency. This study aims to classify users' thermal comfort status using machine learning methods. Using Class I data from the Chinese Thermal Comfort Dataset, the thermal comfort vote problem was transformed into a binary classification problem. Environmental, personal, and building-related variables were used as model inputs; Logistic Regression, Random Forest, and Gradient Boosting algorithms were compared using accuracy, precision, recall, F1-score, and ROC-AUC metrics. According to the results, although Random Forest provided the highest accuracy (0.709) and ROC-AUC (0.768) values, the learning curves showed an overfitting tendency in this model. The Gradient Boosting model produced the highest F1-score (0.789) and showed more consistent generalization performance. Overall, the results show that machine learning methods can be used as an effective tool in predicting user thermal comfort.

Keywords: Thermal comfort, machine learning, classification, Random Forest, Gradient Boosting, building automation.

1 Introduction

Ensuring indoor comfort in buildings is an important research topic in terms of user satisfaction and energy efficiency. Traditional thermal comfort approaches generally rely on physical variables such as air temperature, relative humidity, air velocity, metabolic activity, and clothing insulation [1-2]. However, individuals' perception of thermal comfort is influenced not only by environmental conditions but also by many factors such as personal characteristics, building type, season, and climate zone [3-5]. In recent years, machine learning-based approaches have the potential to predict users' comfort status in a more flexible and data-driven way by evaluating environmental and personal variables together [6]. This situation shows that data-driven methods can be considered as a supportive approach in thermal comfort estimation, taking into account the limitations of traditional PMV–PPD index-based approaches [7].

This study aims to classify the thermal comfort status of users using machine learning methods with the Chinese Thermal Comfort Dataset [8]. In this context, the thermal comfort vote (TCV) is transformed into a binary classification problem to predict whether users are comfortable or uncomfortable. Indoor environmental conditions, outdoor environmental variables, personal

characteristics, clothing insulation, metabolic activity, and building-related variables were considered as model inputs. In this study, the performance of different machine learning algorithms was compared.

2 Dataset and Methodology

In this study, the Class I dataset included in the Chinese Thermal Comfort Dataset [8] was used. This dataset contains thermal comfort measurements collected under different building types, climate zones and seasonal conditions. In this study, TCV was chosen as the target variable and a binary classification problem was created to estimate the thermal comfort status of users. Environmental, personal, and building-related variables were used as model inputs. The target variable, TCV, was converted into a binary classification label: observations with TCV ≤ 1.5 were labeled as comfortable, while observations with TCV > 1.5 were labeled as uncomfortable. The dataset was divided into 80% training and 20% test data; numerical variables were scaled, and categorical variables were encoded for model training. Logistic Regression, Random Forest, and Gradient Boosting algorithms were compared using accuracy, precision, recall, F1-score, and ROC-AUC metrics.

2 Results and Discussion

The performance results of the machine learning models are given in Table 1. According to the table, the Random Forest model provided the highest accuracy (0.709) and ROC-AUC (0.768) values, while the Gradient Boosting model produced the highest recall (0.860) and F1-score (0.789) values. The classification results show that the models predicted the comfortable class more successfully than the uncomfortable class; this may be related to the larger number of samples belonging to the comfortable class in the test dataset. To evaluate the generalization performance of the models, the learning curves were analyzed, and it was determined that the Random Forest model showed an overfitting tendency despite its high test performance. In contrast, the Gradient Boosting model exhibited a more balanced learning behavior, resulting in a more stable performance in terms of generalization. Overall, the findings show that environmental, personal, and building-related variables can be used in thermal comfort classification and that nonlinear machine learning approaches can produce effective results.

Table 1. Performance comparison of machine learning models for thermal comfort classification.

Model	Accuracy	Precision	Recall	F1-score	ROC-AUC
Logistic Regression	0.692	0.731	0.830	0.777	0.747
Random Forest	0.709	0.745	0.835	0.788	0.768
Gradient Boosting	0.701	0.727	0.860	0.789	0.756

Conclusion.This study aimed to classify user thermal comfort status using machine learning methods with the Chinese Thermal Comfort Dataset Class I. The TCV variable was transformed into a binary classification problem, and environmental, personal, and building-related variables were used as model inputs. The results indicated that tree-based ensemble models achieved better classification performance than the linear model in this dataset. Although the Random Forest model provided the highest accuracy (0.709) and ROC-AUC (0.768) values, the learning curves showed an overfitting tendency in this model. The Gradient Boosting model, on the other hand, produced the highest F1-score value (0.789) and exhibited a more balanced generalization performance compared to Random Forest. Overall, the findings indicate that machine learning methods can be used as an effective tool in predicting user thermal comfort and may contribute to the development of more personalized, comfort-oriented, and energy-efficient control strategies in building automation systems.

References

1. Fanger, P. O. (1970). Thermal comfort. Analysis and applications in environmental engineering.

2. Ashrae, A. N. S. I. (2017). ASHRAE Standard 55: Thermal environmental conditions for human occupancy. *American Society of Heating, Refrigerating and Air-Conditioning Engineers: Atlanta, GA, USA*.

3. De Dear, R., & Brager, G. S. (1998). Developing an adaptive model of thermal comfort and preference.

4. Nicol, J. F., & Humphreys, M. A. (2002). Adaptive thermal comfort and sustainable thermal standards for buildings. *Energy and buildings*, *34*(6), 563-572.

5. Lamsal, P., Bajracharya, S. B., & Rijal, H. B. (2023). A review on adaptive thermal comfort of office building for energy-saving building design. *Energies*, *16*(3), 1524.

6. Kim, J., Zhou, Y., Schiavon, S., Raftery, P., & Brager, G. (2018). Personal comfort models: Predicting individuals' thermal preference using occupant heating and cooling behavior and machine learning. *Building and environment*, *129*, 96-106.

7. Cheung, T., Schiavon, S., Parkinson, T., Li, P., & Brager, G. (2019). Analysis of the accuracy on PMV–PPD model using the ASHRAE Global

Thermal Comfort Database II. *Building and Environment*, *153*, 205-217.
Yang, L., Zhao, S., Zhai, Y., Gao, S., Wang, F., Lian, Z., ... & de Dear, R. (2023). The Chinese thermal comfort dataset. Scientific Dat

https://doi.org./10.58225/mpmma.2026.161

STUDY OF OPTIMIZATION OF SEAWATER USE BASED ON LINEAR PROGRAMMING MODEL

Anar Hummatov [1] *, Vusala Hummatova* [2]
[1] AZUAC, Azerbaijan
[2] Water and Amelioration Scientific Research Institute, Azerbaijan

Abstract. During the development of a methodology for applying mathematical modeling to determine the optimal seawater–freshwater mixture for irrigation, the selection of optimization criteria, the formulation and analysis of the objective function □=□(□)→max(min), the identification of constraint conditions associated with the variables included in the objective function, and the derivation of the corresponding analytical expressions were carried out. Therefore, the optimal mixing ratio maximizes seawater use while keeping salinity within acceptable limits for sustainable crop production. To achieve the objectives of the research, a linear programming model was formulated to identify the optimal mixing ratios of seawater and freshwater for irrigation purposes. The model was designed with the objective of maximizing total crop yield, taking into consideration the influence of irrigation water salinity on crop productivity. Based on the experimental data obtained for irrigation water salinity S (g/l) and the corresponding crop yields M (s/ha) of barley, maize, and alfalfa, empirical yield–salinity relationships were established using the least-squares regression method. The

relationship between crop yield and irrigation water salinity was adequately described by a linear model of the general form $M = a \cdot S + b$, where M denotes crop yield (s/ha), S represents the salinity of the irrigation mixture water (g/l), and a and b are regression coefficients determined from the experimental observations. The derived regression equations were subsequently used to quantify the effect of irrigation water salinity on crop productivity and to formulate the optimization model for determining the optimal seawater–freshwater mixing ratios. Consequently, the recommended linear programming model can be expressed as: $Z = A_1 \cdot (-11{,}09S + 157{,}07) + A_2 \cdot (-1{,}68S + 26{,}28) + A_3 \cdot (-2{,}38S + 64{,}02) \rightarrow max$. The proposed model is intended to optimize the allocation of land and water resources while incorporating the empirical relationships between irrigation water salinity and agricultural crop yields.

Keywords: linear programming, optimization, freshwater-seawater mixing, seawater, desalinated irrigation water, mathematical modeling.

Introduction.In recent years, various methods, including non-conventional approaches such as seawater desalination, have been applied in the Republic of Azerbaijan, as in many other regions, to improve water supply. Alongside the desalination of seawater, a mixture of freshwater and seawater at certain proportions is also utilized, and studies are being conducted to improve the methodology of its application. In agricultural irrigation, the occurrence of plant stress resulting from the use of such water

mixtures depends on several factors, including crop species, soil water-physical properties, and other environmental conditions. Various factors influence the formation of the irrigation water mixture. The selection of the optimal water mixture largely depends on the salinity of seawater; therefore, salinity plays a crucial role in defining the salinity constraint within the optimization model. The primary objective is to determine the optimal water mixture (seawater + freshwater = desalinated irrigation water), which serves as the basis for constructing the objective function of the optimization problem. The seawater considered in this study is the water of the Caspian Sea. The Caspian Sea is of oceanic origin, and the average salinity of its water along the Azerbaijani coast is approximately 12–14 g/l. Freshwater used for irrigation is assumed to be supplied from the Kura River, with a salinity level of 0,5-1,0 g/l. Linear Programming (LP) was employed as the research methodology. Linear programming is a mathematical optimization technique used to maximize or minimize a linear objective function subject to a set of linear constraints[2,3].

1.1 Research methodology and discussion.

In order to optimize the use of seawater and freshwater mixtures in irrigation using the **Linear Programming** method, the objective function, constraint conditions, and non-negativity requirements of the decision variables were established. Although the relatively lower cost of seawater makes its use in agriculture economically

attractive and encourages its maximization, salinity must be considered as a critical constraint in the optimization process. The optimal solution was then obtained by determining the maximum or minimum value of the objective function subject to the given constraints [1,2].

In general, a mathematical model consists of the following components:

1) Objective function

$$Z = F(x) = c_1x_1 + c_2x_2 + c_3x_3 + \cdots + c_nx_n \rightarrow \max(\min) \quad (1)$$

2) Constraint conditions

$$a_{i1}x_1 + a_{i2}x_2 + a_3x_3 + \cdots + a_{in}x_n = b_i \ (i = \overline{1,k}\ ) \text{ or} \quad (2)$$

$$a_{i1}x_1 + a_{i2}x_2 + a_3x_3 + \cdots + a_{in}x_n \leq v\text{ə } ya \geq b_i \ (i = \overline{1,k}\ )$$

3) Functional relationships and non-negativity conditions

$$y = f(x_1, x_2, \ldots x_n), \quad x_1, x_2, x_3 \ldots x_n \geq 0 \quad (3)$$

4) Constant parameters $c_1, c_2, \ldots c_n = const$

The mathematical model is composed of an objective function, a set of constraints, functional relationships among variables, non-negativity conditions, and constant coefficients. In the present study, generalizations were made based on field and laboratory data obtained by S.A. Eminov at the experimental site of the ASMTTS [4]. The collected data were systematized and adapted in

accordance with the objectives and scope of the research. During the study, irrigation of three crop species was carried out using mixed irrigation water consisting of seawater and freshwater in different proportions. The seawater–freshwater ratios were 100:0, 75:25, 50:50, 25:75, and 0:100, corresponding to average salinity levels of 13.5 g/l, 10.2 g/l, 6.0 g/l, 3.5 g /l, and 0.7 g/l, respectively [4]. For the formulation of the model constraints, the recommended average crop yields for the Republic were adopted as reference values. These parameters were used in the development of the optimization model and in the establishment of the corresponding constraint conditions. Based on the data obtained for irrigation water salinity and the corresponding observed yields of barley, maize, and alfalfa, empirical relationships were derived using the least-squares regression method. These relationships describe the dependence of crop yield on irrigation water salinity and are expressed as follows:

$$M_{\text{maize}} = -11{,}09 \cdot S_{\text{water salinity}} + 157{,}07$$

$$M_{\text{barley}} = -1{,}68 \cdot S_{\text{water salinity}} + 25{,}28$$

$$M_{\text{alfalfa}} = -2{,}38 \cdot S_{\text{water salinity}} + 64{,}02$$

To achieve the objectives of the research, a linear programming model was formulated to identify the optimal mixing ratios of seawater and freshwater for irrigation purposes. The model was designed with the objective of maximizing total crop yield, taking into consideration the influence of irrigation

water salinity on crop productivity. The optimal solution was obtained subject to the established agronomic and water-quality constraints. The optimization model was formulated with the objective of maximizing overall agricultural productivity. The primary constraint was imposed to prevent the salinity of the irrigation water from exceeding the critical level beyond which significant yield reductions may occur. Accordingly, a set of agronomically justified constraints was incorporated into the model to ensure both crop productivity and the sustainable use of saline water resources.

$$\begin{cases} -11{,}09 \cdot S + 157{,}07 \geq b_1 \\ -1{,}68 \cdot S + 25{,}28 \geq b_2 \\ -2{,}38S \cdot +64{,}02 \geq b_3 \end{cases}$$

$$A_1, A_2, A_3 \geq 0 \quad b_1, b_2, b_3 \geq 0$$

In the proposed optimization model, A_1, A_2, and A_3 denote the cultivated areas allocated to maize, barley, and alfalfa and b_1, b_2, and b_3 denote their corresponding yields, respectively. Consequently, the recommended linear programming model can be expressed as follows:

$$Z = A_1 \cdot (-11{,}09S + 157{,}07) + A_2 \cdot (-1{,}68S + 26{,}28) + A_3 \cdot (-2{,}38S + 64{,}02) \rightarrow max$$

If the optimal irrigation water salinity is assumed to depend on the values of b_1, b_2, b_3, then the optimal proportions of seawater and freshwater corresponding to the selected minimum yield

requirements can be determined using the by a formula:

$$x = \frac{min\left\{\frac{157,07 - b_1}{11,09}, \frac{25,28 - b_2}{1,68}, \frac{64,02 - b_3}{2,38}\right\} - 0,7}{12,8}$$

For the yield constraints $b_1 = 70$, $b_2 = 20$, and $b_3 = 50$ corresponding to maize, barley, and alfalfa, respectively, the optimization results indicated that the optimal irrigation water salinity should not exceed $S \leq 3,14$ g/l . Under this condition, the optimal water mixture consisted of 19% seawater and 81% freshwater.

References

1 . Hillier, F. S., Lieberman, G. J.: Introduction to Operations Research (11th ed.). McGraw-Hill Education. P.1345. (2021)

2. P. M. Jacovkis, H. Gradowczyk, A. M. Freisztav and E. G. Tabak. : A Linear Programming Approach to Water-Resources Optimization, Methods and Models of Operations Research (1989) 33:341-362

3. Hasan Symum & Mohammad F Ahmed,: Linear Programming Model to Optimize Water Supply and Cropping Area for Irrigation: A Case Study for Kalihati., Global Journal of Researches in Engineering: G Industrial Engineering Volume 15 Issue 2 Version1.0 Year (2015)

4. Eminov, S. A. *Experimental Foundations of Plant Irrigation with Seawater in the Caspian Coastal Zone. Baku*, (2003).

https://doi.org./10.58225/mpmma.2026.169

INTEGRAL REPRESENTATIONS OF SMOOTH FUNCTIONS OF SEVERAL VARIABLES AT POINTS

Mammadova Arzu Imamverdi [1] , Sevda Mammadjafar Hajizada[2] , Kharimova Sevinj Fuzuli[3]

[1] UNEC, [2,3]AzUAC Azerbaijan

Abstract. This paper investigates integral representations of sufficiently smooth functions of several variables evaluated at specific points. The main approach is based on the construction of specially designed kernels that allow averaging of both the functions and their derivatives. Using these kernels, we develop a family of integral operators that describe local and global properties of multivariate functions.

Relying on the fundamental theorem of integral calculus, we derive a system of integral identities in which a function and its derivatives are expressed through integrals involving higher-order derivatives and their associated functional characteristics. These representations provide a unified framework linking pointwise behavior, differential properties, and integral averages of smooth functions. The results contribute to the theory of multivariable integral representations and extend classical analytical techniques in multidimensional calculus. The proposed approach may be applied in the theory of partial differential

equations, functional analysis, approximation theory, and related areas of mathematical analysis.

Keywords: smooth functions, multivariate functions, integral representation, kernel methods, averaging operators, higher-order derivatives, integral identities, functional analysis, multivariable calculus.

1. Introduction

The study of smooth functions of several variables and their representation through integral structures plays a fundamental role in modern mathematical analysis. Integral methods provide deeper insight into the internal structure of functions, establishing connections between local values and global differential properties.

One of the most effective approaches in this direction is the use of specially constructed kernels that generate averaging operators for functions and their derivatives. These averaging procedures are essential for understanding regularity properties, approximation behavior, and integral characteristics of multivariate functions. In higher-dimensional spaces, such techniques become even more important due to the increased complexity of geometric structures and derivative interactions.

The main objective of this work is to obtain integral representations of smooth multivariate functions at points and to establish corresponding integral identities. The central tool of the study is the fundamental theorem of integral calculus,

which, combined with specially constructed kernels, enables the transformation of local function values into integral expressions involving derivatives. We assume that the considered functions possess sufficiently many continuous partial derivatives to ensure the validity of the constructed integral operators and representations.

2. Construction of Averaging Kernels

Let $f(x) = f(x_1, x_2, \dots, x_n)$be a sufficiently smooth function defined in $\mathbb{R}^n$. To construct integral representations, we introduce a family of smooth, compactly supported kernels $\varphi(x)$, satisfying the following properties:

- $\varphi(x) \in C_0^{\infty}(\mathbb{R}^n)$,
- The support of $\varphi$is contained in a bounded region,
- Normalization condition:

$$\int_{\mathbb{R}^n} \varphi(x)\, dx = 1 \qquad (1)$$

We define a scaled kernel:

$$\varphi_{\varepsilon}(x) = \frac{1}{\varepsilon^n} \varphi\left(\frac{x}{\varepsilon}\right), \varepsilon > 0 \qquad (2)$$

This kernel generates an averaging operator:

$$f_{\varepsilon}(x) = \int_{\mathbb{R}^n} f(x - y)\, \varphi_{\varepsilon}(y)\, dy \qquad (3)$$

As $\varepsilon \to 0^+$, we obtain:

$$f_\varepsilon(x) \to f(x) \tag{4}$$

provided that f is continuous at x.

Similarly, derivatives of f can also be expressed through convolution-type averaging:

$$D^\alpha f_\varepsilon(x) = \int_{\mathbb{R}^n} D^\alpha f(x - y)\varphi_\varepsilon(y)\, dy \tag{5}$$

3. Integral Representation of Smooth Functions

Using the constructed kernels and the fundamental theorem of calculus, we derive integral representations of the form:

$$f(x) = \sum_{|\alpha|\le m} \int_{\mathbb{R}^n} K_\alpha(x, y)\, D^\alpha f(y)\, dy \tag{6}$$

where $K_\alpha(x, y)$ are integral kernels depending on the structure of the averaging operators.

These representations show that the value of a function at a point can be reconstructed entirely from integral contributions of its derivatives. A key identity used in the derivation is:

$$f(x) = f_\varepsilon(x) + R_\varepsilon(x) \tag{7}$$

where $R_\varepsilon(x) \to 0$as $\varepsilon \to 0^+$.

4. Transformation of Integral Operators

The integral operators introduced above can be rewritten in a factorized form:

$$Tf(x) = \int_{\mathbb{R}^n} K(x,y) f(y)\, dy \qquad (8)$$

where the kernel $K(x,y)$can be decomposed into products of one-dimensional or directional operators. For multi-index derivatives $\alpha = (\alpha_1, \dots, \alpha_n)$, we define:

$$D^\alpha = \frac{\partial^{|\alpha|}}{\partial x_1^{\alpha_1} \cdots \partial x_n^{\alpha_n}}$$

This allows us to express higher-order derivatives through iterative integral operators.

5. Main Integral Identity

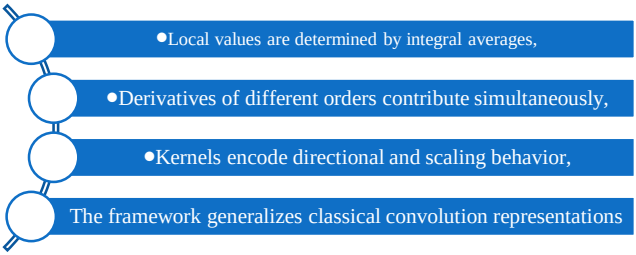
From the fundamental theorem of calculus, we obtain the central identity:

$$f(x) = \int_{\mathbb{R}^n} f(y)\, K_0(x,y)\, dy + \sum_{|\alpha|=1}^{m} \int_{\mathbb{R}^n} D^\alpha f(y)\, K_\alpha(x,y)\, dy \qquad (10)$$

This formula demonstrates that the function and its derivatives are fully determined by their integral averages.

6. Properties and Interpretation

The obtained representations reveal a deep relationship between local and global properties of smooth functions:

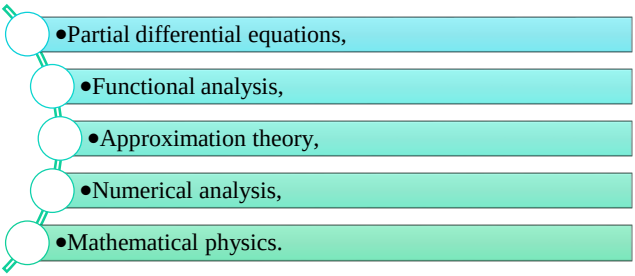


Pig.1.Analyze smooth functions

These results provide a structured way to analyze smooth functions in multidimensional Euclidean spaces.

7. Applications

The developed integral representations can be applied in:



Pig.2.Developed integral representations

In particular, they are useful for studying regularity properties of solutions of PDEs and constructing approximation schemes based on derivative information.

8. Conclusion

In this paper, we have developed integral representations of smooth functions of several variables using specially constructed kernels. The main results show that both functions and their derivatives can be expressed through integral identities involving higher-order derivatives and functional characteristics.

The proposed approach extends classical integral calculus techniques and provides a unified framework for studying multivariate smooth functions. These results open new directions for further research in functional analysis and applied mathematics.

Reference

1. Будаев В.Д., Якубсон М.Я. Математический анализ. Том 2. Функции нескольких переменных. – М.: URSS, 2020. – 456 с.
2. Иванов С.В., Мартышко П.С. Функции нескольких переменных. Теория поля. – М.: URSS, 2025.
3. Кузоватов И.А. и др. Дифференциальное исчисление функций нескольких переменных. – Красноярск: СФУ, 2020.
4. Позднякова Т.А. и др. Функции нескольких переменных. – Красноярск: СФУ, 2020.
5. Andersson M., Samuelsson Kalm H. On Proper Intersections on a Singular Analytic Space // Mathematische Zeitschrift. 2025.

6. Samuelsson Kalm H. A Pullback Operation on a Class of Currents // Annales de l'Institut Fourier. 2024.
7. Lennartsson M. Residues and Currents from Singular Forms on Complex Manifolds // Complex Analysis and Operator Theory. 2025.

https://doi.org./10.58225/mpmma.2026.177

COMPUTATIONAL MODELLING OF BIOLOGICAL SYSTEMS UNDER CLIMATE CHANGE CONDITIONS

Asef Rusanov[1] , Samira Mustafayeva[2]

[1] Nakhchivan State University, Azerbaijan

[2] Nakhchivan State Technical College affiliated with Nakhchivan State University,Azerbaijan

Abstract. Climate change poses serious and multifaceted threats to biological systems at every level of organization, from microbial communities to entire ecosystems. This study systematically reviews computational methodologies for modelling the responses of biological systems to climate change, with particular emphasis on machine learning, physics-based constraints, and hybrid approaches. Integrating physical laws into learning algorithms substantially improves model generalizability across unseen climate scenarios. Incorporation of soil microorganisms into Earth system models enhances carbon cycle projection accuracy. Multi-stressor frameworks for aquatic ecosystems outperform single-factor models when simultaneous shifts in temperature, acidity, and oxygen are considered. Land-use feedbacks, when embedded in spatial models, refine regional climate projections. Explainable artificial intelligence methods increase model transparency, facilitating more reliable interpretation of results for policymakers. The findings confirm that no single methodological approach can fully capture climate–biosphere complexity, and that multi-scale integration, open-source tooling, and international collaboration are essential for advancing this field.

Keywords: Computational biology; Climate change modelling; Machine learning; Hybrid models; Ecosystem dynamics; Explainable AI

1 Introduction

Global climate systems are undergoing profound transformations driven by accelerating anthropogenic activities, which directly modify the fundamental baseline of global ecosystems. Characterized by rising temperatures, shifting precipitation regimes, and an increasing frequency of extreme weather events, climate change exerts multilevel pressures on biological systems across all scales. These environmental stressors affect cellular mechanisms, alter species distributions, and disrupt entire ecosystem services. Quantifying the precise impacts of these overlapping pressures is exceptionally challenging. Traditional experimental and field-based methods, while providing invaluable localized data, are often resource-intensive, logistically limited, and constrained in spatial and temporal coverage. Consequently, they fall short of forecasting long-term macro-ecological shifts under novel climate scenarios, rendering advanced computational approaches indispensable in contemporary ecological and environmental research.

Computational biology effectively bridges this gap by combining sophisticated mathematical models, statistical methods, and robust computer algorithms

to describe complex biological processes quantitatively. Because the impacts of climate change on living systems are inherently multi-factorial, highly dynamic, and nonlinear, simple linear or statistical models fail to fully capture the underlying ecological feedback loops and threshold effects. Machine learning offers substantial opportunities to address this limitation. Algorithms trained on large-scale, high-dimensional climate and ecological datasets can reveal intricate, hidden relationships that traditional human analysis would struggle to detect. This digital transformation enables researchers to simulate predictive scenarios and develop early warning signs for vulnerable habitats. The primary objective of this paper is to systematically review the current state, principal methodological approaches, and outstanding structural challenges in the computational modelling of biological systems under rapidly changing climate conditions.

3 Discussion

The literature review demonstrates that climate-invariant machine learning models yield reliable results across broader climate conditions than traditional approaches. Embedding physical constraints substantially increases generalisation capacity, confirmed by studies spanning multiple climate zones. This architectural integration of conservation laws prevents the unphysical drift

often observed in purely data-driven methods, establishing a more robust framework for long-term ecological forecasting.

Furthermore, the integration of microorganisms into Earth system models improves carbon-cycle projections, while deep-learning parameterisation partially addresses the nonlinearity of soil microbial responses. By capturing these microscopic dynamics, models can better simulate heterotrophic respiration and microbial priming effects, which are critical for predicting soil organic matter decomposition under elevated global temperatures.

For aquatic systems, multi-stressor modelling consistently outperforms single-factor approaches, as it effectively accounts for the synergistic impacts of rising temperatures, acidification, and nutrient loading. Machine-learning-based early warning systems are increasingly deployed for timely prediction of harmful algal blooms and oxygen depletion events, allowing for proactive environmental management.

Additionally, land-use and climate model coupling clarifies regional feedback pathways through which deforestation alters local precipitation and boundary layer dynamics. Carbon-market price forecasting using machine learning introduces an economic dimension to ecological modelling, yet forecast reliability remains contingent on

underlying ecosystem model quality, emphasizing the necessity of high-fidelity baseline data.

4 Conclusion

Computational modelling of biological systems under climate change has become one of the foremost priorities of contemporary science. The analysis presented here confirms that no single methodological approach is sufficient to capture the full complexity of climate–biosphere interactions. The combined application of machine learning, physics-based models, and hybrid strategies yields more reliable results than any approach applied in isolation.

Integration across all levels of biological organisation—from microorganisms to ecosystems—substantially improves the accuracy of Earth system models and is essential for credible projections of carbon cycling, nitrogen balance, and biodiversity change. Aquatic ecosystems, soil microbiome dynamics, and land-use change represent sub-systems requiring particular research attention. The synthesis of physical principles with artificial intelligence enables the construction of climate-scenario-robust models capable of providing reliable forecasts under future unseen conditions, making them indispensable for evidence-based climate policy.

References

1. Beucler, T., Gentine, P., Yuval, J. et al.: Climate-invariant machine learning. Science Advances 10, eadj7250 (2024).
2. Krasnopolsky, V.: Applying machine learning in numerical weather and climate modeling systems. Climate 12(6), 78 (2024).
3. Chattopadhyay, A., Mustafa, M., Hassanzadeh, P., Bach, E., Kashinath, K.: Towards physics-inspired data-driven weather forecasting. Geoscientific Model Development 15, 2221–2237 (2022).
4. Kwa, A., Clark, S.K., Henn, B. et al.: Machine-learned climate model corrections from a global storm-resolving model. Journal of Advances in Modeling Earth Systems 15 (2023).
5. Lennon, J.T., Abramoff, R.Z., Allison, S.D. et al.: Priorities, opportunities, and challenges for integrating microorganisms into Earth system models. mBio 15(5) (2024).).

https://doi.org./10.58225/mpmma.2026.183

APPLİCATİON OF AI IN THE OPTIMIZATION OF PRODUCTION PLANNING

Parviz Mammadov[1], Vasif Kerimov[1,2], Ilgar Khurshudov[1], Xazar Necimbeyli[1], Kamran Shiraliyev[1], Valeh Alquluyev[1]

[1]Baku Engineering University,

[2]Institute of Mathematics , Azerbaijan.

Abstract. Production planning involves the design of manufacturing and treatment systems through a planning and control framework. This article explores Production Planning and Control (PPC) systems integrated with artificial intelligence (AI).The purpose of this study is to define the Integrated Production Planning and Control (IPPC) system and highlight the importance of applying linear and multiple regression methods, as well as AI-driven methods, for IPPC optimization..The applied significance of this study lies in the optimization of production planning, capacity planning, and inventory management to identify total production waste, adjust capacity, and apply a hybrid method for the strategic management of manufacturing.Scientific innovation of the research: By applying regression analysis and AI-driven methods as a hybrid approach, the manufacturing process can be optimized.

Keywords: Integrated production planning and control (IPPC), AI tools, Regression analysis.

1. Integrated productıon plannıng and control

Integrated production planning combines various types of steps:

1.1 Steps of IPPC

1. Definition of realistic targets , 2. Forecasting demand, 3. Resource allocation, 4. Order writing, 5. Product design and production systems, 6. Strategic capacity planning, 7. Master Production Schedule (MPS), 8. Inventory management, 9. Workforce management, 10. Utilization management, 11. Production scheduling

12. Execution and dispatching, 13. Registering and reporting, 14. Action tracking, 15. Monitoring, inspection, and control, 16. Correction, 17. Quality control, 18. Application of modern internet and computer technology, 19. Application of artificial intelligence tools, 20. Process integration, 21. Continuous improvement, 22. Market capture, 23. Lessons learned.

The second step for optimization of production planning is the application of regression models and AI-driven tools[1].

2.Methodology - Optimization models in production planning and control

Regression analysis in optimization of production planning

2.1. Linear Regression

Regression analyzes the direct relationship between two variables only, and this model is a simple method applied in the markets by all companies.

2.2. Multiple Linear Regression

The model has a direct relationship between one dependent outcome and two or more independent variable changes[6].

3. AI ın Integrated productıon plannıng and control

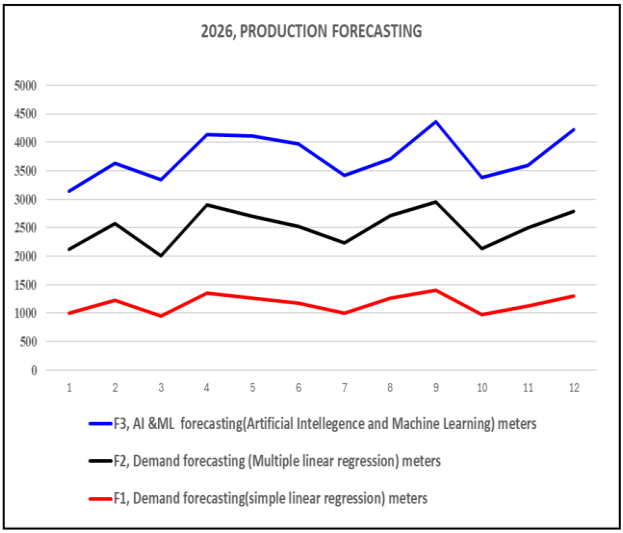
AI in IPPC refers to the use of AI tools for optimizing planning and control activities. This approach enhances quick adaptation, minimizes waste, increases quality, and especially minimizes forecasting errors. The benefits of AI tool application in IPPC include: 1. Enhanced efficiency, such as reducing waste, improving quality, eliminating hazards and damage, reducing production costs, optimizing inventory management, providing accurate demand forecasting with low error rates, enhancing production scheduling, reducing lead times, and enabling effective maintenance [3].

3. Practical application of models and AI-driven methods

In this article, the optimization of linear regression (LR) analysis by using simple linear and multiple regression (MR), and also the application of AI-driven analysis for proper forecasting of production demand for metal piping production [2].The optimization steps:[5].

1. Calculation of demand with LR and MR, 2. LR, MR, and mixed regression, 3. Calculation of demand with AI-driven programs ,4. Adjustment for errors, 5. Selection of applicable method, 6. Application of hybrid method[4].

Figure 1. Production forecasting



5. Scientific contributions

The scientific contribution is the application of traditional regression models and AI-driven methods simultaneously to eliminate errors, eliminate waste, improve quality, and meet customer demands in a timely manner. The application of hybrid-type optimization also eliminates market risks, considering external market issues such as raw material scarcity and logistics problems.

CONCLUSION

In this article, all IPPC steps were identified. Then, all three steps of production planning optimization were clarified. Especially, the importance of AI-driven method application in IPPC was described.

REFERENCES

1. T. Biswas, R. N. Baral, A Review on Production Planning and Control, International Journal of Multidisciplinary Innovative Research, Vol. 1, Number 1, pp.70-78, July 2021,

2.Mitra.A. Fundamentals of Quality Control and İmprovement,pp.2-5,1998,

3.B.Kobu. Uretim Yonetimi.book, pp.410-450, 2004,

4. A.Guliyev, V.Kerimov, P.Mammadov and et all., Artificial intelligence (AI) in the optimization of logistics management, 5th International Conference on Problems of Logistics, Management and Operation in the East-West Transport Corridor (PLMO 2026), Vol.3, Issue 2, pp.64-65, May 18-21, 2026, Baku, Azerbaijan,

5.V.Lele, Y.Ajmeri, Production Planning and Control, Journal of From Source to Shelf, pp.2-6, December 2024,

6.C.Chen,T.L.Kong, W.Kang, Identifying the promising production planning and scheduling method for manufacturing in Industry 4.0, Journal of productıon & manufacturıng research, 2023, vol. 11, no. 1, pp.2-6, 2023.

https://doi.org./10.58225/mpmma.2026.188

DYNAMIC ANALYSIS OF AN AUGER DRILLING SYSTEM USED IN PILE-DRIVING MACHINES

Guliyeva Aygun
AzUAC, Azerbaijan

Abstract. This paper investigates the dynamic model of an auger-type drilling tool used in bored pile machines. The performance and reliability of these machines largely depend on the dynamic behavior of their drilling tools. This paper investigates the dynamic model of an auger-type drilling system used in bored pile construction. The auger is considered as a mechanical system consisting of a central tube, helical flights, and cutting teeth. During drilling operations, the auger is subjected to variable torsional, axial, bending, and impact loads caused by the heterogeneous properties of the soil. The moments of inertia of the auger components are determined using simplified geometric models, and the total inertia of the drilling tool is evaluated. Furthermore, the flexibility of the auger is analyzed by considering its elastic deformation under operational loads. The influence of inertia and flexibility on vibration characteristics, dynamic loading, and stress distribution is discussed. The obtained results can be used to improve dynamic models of drilling equipment, optimize structural parameters, and increase the operational reliability and service life of bored pile machines.

Keywords: bored pile machine, auger drilling tool, moment of inertia, flexibility, dynamic model, torsional vibration, drilling dynamics.

1. Introduction

In modern construction practice, increasing the load-bearing capacity of soils is considered one of the most important engineering tasks for ensuring that buildings and structures are erected on reliable foundations. One of the most widely used methods for this purpose is the construction of bored cast-in-place piles.

Pile drilling machines are widely used for pile installation to stabilize soils and enhance the load-bearing capacity of structures. Depending on the soil category and geological conditions, drilling is generally performed using two methods: the Kelly bar method and the auger method. The working tools are connected to the Kelly bar through a gearbox and receive rotational torque from a hydraulic motor. Simultaneously, axial movement is provided by a hydraulic cylinder or a cable mechanism. Thus, the system operates as a complex mechanical assembly capable of both rotational and vertical motion [1].

However, the application of this technology may be associated with high operational costs and time consumption, which can negatively affect productivity. Furthermore, drilling efficiency tends to decrease in hard soil categories, often requiring specialized equipment and additional technological

measures. Due to variations in the physical and mechanical properties of the soil, the cutting and resistance forces acting on the drilling tool during operation are time-dependent and continuously changing. These variable loads exert dynamic effects on the main components of the system—including the working tool, Kelly bar, gearbox, and hydraulic motor—leading to overloads, vibrations, and ultimately equipment failures. Therefore, the analytical and experimental investigation of the forces acting on the drilling tool is of particular importance for improving the reliability of the drilling process and ensuring the durability of the equipment. In particular, determining the variation patterns of the moment of inertia and torque, as well as analyzing their relationship with the structural parameters of the system, represents an important scientific and practical task for the optimal design and safe operation of drilling mechanisms [2].

2. Main Part

The auger drilling tool used in pile drilling machines is one of the most important excavation elements. Pile drilling is performed mainly by two methods depending on the soil category and geological conditions: kelly-bar drilling method; continuous flight auger (CFA) drilling method. When drilling is carried out using a Kelly bar, the working tool is typically an auger approximately 1.5 meters in length.

Main components of the auger (see Fig. 1).

1. **Central Shaft** – the main cylindrical rod of the auger. It connects the auger to the drilling rig and transfers the rotational motion and torque generated by the machine.
2. **Helical Flights** – spiral-shaped plates wrapped around the shaft. Their function is to cut the soil and transport the excavated material upward to the ground surface during drilling.
3. **Cutting Teeth** – located at the lower end of the auger. These teeth break, loosen, and penetrate soil, clay, and soft rock formations.

During drilling operations, the auger is exposed to torsional moments, axial loads, bending loads, and dynamic and impact forces arising from the interaction between the drilling tool and the surrounding soil [3].

2.1. Determination of the Moment of Inertia

To determine the total moment of inertia of an auger-type drilling tool, the moment of inertia of each individual component must first be calculated separately and then summed. Therefore, the total moment of inertia of the auger can be obtained as the sum of the moments of inertia of its main structural elements [4].

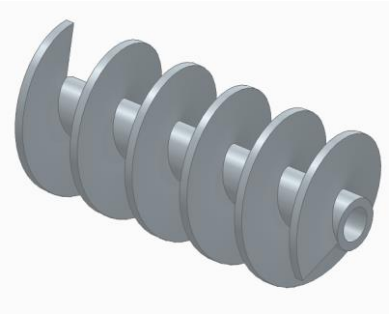


Figure 1. General view of the auger-type drilling tool modeled in Solid Edge software

1. Central shaft

The central tube of the auger in a Bored Pile machine is usually a hollow cylinder.

$$I_{shaft} = \frac{1}{2} m(r_o^2 + r_i^2) \quad (1)$$

2. Helical blades (flights)

The blades are thin steel plates wrapped around the tube. For calculations, they are usually approximated as a thin ring or plate.

$$I_{blades} = mr^2 \quad (2)$$

Here, m - mass of blades, r - average radius of the blade.

The average radius is usually:

$$r = \frac{r_{outer} + r_{tube}}{2} \quad (3)$$

3. Cutting teeth

The cutting head can often be simplified as a solid disk.

$$I_{teeth} = \frac{mr^2}{2}$$

(4)

Considering the moments of inertia of the individual components calculated based on their geometric properties, the total moment of inertia of the auger is given by the following expression:

$$J_{auger} = J_{shaft} + J_{flights} + J_{cutting\ head}$$

(5)

2.2. Determination of Flexibilty

During the drilling process, the auger is subjected to various types of loads and behaves not as a perfectly rigid body but as a structure possessing a certain degree of elastic deformation. The ability of the auger to deform under the action of external forces is referred to as its flexibility. As a result of the loads generated during drilling, the auger experiences torsional, bending, and compressive deformations, which significantly affect the dynamic characteristics of the system [5].

The flexibility of the auger has a substantial influence on the formation of the system's natural vibration frequencies, the amplitude of torsional oscillations, the level of dynamic loading, the distribution of internal stresses, and the development of fatigue failures. Therefore, in the dynamic analysis of drilling equipment, the auger

is commonly considered a distributed-mass system with elastic properties.

Flexibility is determined by the relationship between the applied force and the deformation caused by that force. The greater the deformation produced by a given force, the lower the stiffness and the higher the flexibility of the structure. Conversely, smaller deformations under the same loading conditions indicate greater stiffness and lower elasticity.

$$C = \frac{\delta}{F} \tag{6}$$

Here, δ - deformation, m; F - applied force, N.

During torsion, the angle of twist of the auger can be determined by the following expression, which depends on the applied torque and the torsional rigidity of the system:

$$\theta = \frac{ML}{GI} \tag{7}$$

Here, M - torsion momentum, Nm; L - auger length, m; G - shear modulus, Pa; I - inertial momentum, kq/m^2.

It can be seen from the above relationship that the elasticity of the auger increases with an increase in its length, whereas it decreases as the diameter increases. Furthermore, as the elastic properties of the material improve, the structure becomes stiffer and more resistant to deformation.

Conclusion

The conducted research has shown that the dynamic behavior of the auger, which is the main working element of bored pile drilling machines, is significantly influenced by its mass-inertial and elastic characteristics. The central tube, helical flights, and cutting teeth of the auger form an integrated mechanical system that operates under a complex stress-strain state caused by the action of torque and dynamic loads generated during the drilling process.

It has been established that an increase in the moment of inertia of the auger leads to a higher level of dynamic loading and energy capacity of the system; however, it simultaneously reduces its acceleration capability. Moreover, the inverse relationship between the flexibility (compliance) and stiffness of the auger directly affects the amplitude of vibrations and the distribution pattern of loads arising during drilling operations. An increase in the auger length and a reduction in the cross-sectional stiffness result in greater torsional and bending compliance, thereby contributing to additional dynamic effects.

Therefore, the elastic-deformation characteristics of the auger must be taken into account in the dynamic analysis and design calculations of drilling equipment. Determination of the equivalent stiffness and compliance parameters of the auger makes it possible to

develop a more accurate dynamic model of the drilling system, reduce vibration levels, improve the reliability of structural components, and extend the operational service life of the equipment.

References

1. V. Ya. Kershenbaum, *Drilling Machines and Mechanisms*, Moscow, Russia: Nedra, 1985.
2. V. I. Balovnev, *Construction and Road Machines*, Moscow, Russia: Mashinostroenie, 2005.
3. S. S. Rao, *Mechanical Vibrations*, 6th ed., New York, USA: Pearson Education, 2017.
4. M. Z. Kolovsky, *Dynamics of Machines*, Moscow, Russia: Mashinostroenie, 1989.
5. M. Wiercigroch, K. Nandakumar, and E. Pavlovskaia, "Complex dynamics of drill-strings," *Philosophical Transactions of the Royal Society A: Mathematical, Physical and Engineering Sciences*, vol. 376, no. 2135, 2018.

https://doi.org./10.58225/mpmma.2026.197

INTEGRATION OF ARTIFICIAL INTELLIGENCE IN STEAM EDUCATION: A DATA-DRIVEN FRAMEWORK FOR PRIMARY AND SECONDARY SCHOOLS

Aygun Gurbanova
Azerbaijan State Pedagogical University,Azerbaijan

Abstract. The integration of Artificial Intelligence (AI) into STEAM (Science, Technology, Engineering, Arts, and Mathematics) education represents a critical paradigm shift in modern pedagogy. This study presents an innovative approach for assessing the spatiotemporal dynamics of student engagement and learning outcomes when AI tools are embedded in project-based STEAM activities. By utilizing multi-criteria data-driven modeling and machine learning techniques, we evaluate how adaptive learning algorithms and AI-driven robotics enhance creative thinking and problem-solving skills. Traditional pedagogical evaluation methods are often static and limited in capturing real-time cognitive growth. The results of this study demonstrate that the proposed hybrid methodology provides reliable and efficient monitoring of the learning process. This approach supports informed decision-making in curriculum development and contributes to the establishment of sustainable, technologically advanced educational practices worldwide today.

Keywords: STEAM education, Artificial Intelligence, Data-driven modeling, Machine learning, Adaptive learning Educational technology.

1. Introduction

The rapid advancement of digital technologies has transformed the educational landscape, demanding new pedagogical frameworks that prepare students for a technology-driven future. STEAM education, which harmonizes Science, Technology, Engineering, Arts, and Mathematics, has emerged as a major framework for fostering cross-disciplinary innovation and critical thinking. Traditional methods of educational assessment are often time-consuming, labor-intensive, and limited in tracking the multidimensional growth of students during collaborative projects.

In recent years, artificial intelligence (AI) platforms and data-driven analytics have provided new opportunities for large-scale monitoring and optimization of educational practices. The integration of mathematical modeling and artificial intelligence techniques enables more accurate and efficient analysis of learning trajectories. This study aims to develop a comprehensive approach for assessing STEAM education dynamics using intelligent indicators and data-driven models.

2. Methodology

The proposed methodology is based on the analysis of classroom performance, project-based outcomes, and student digital footprints combined with ground truth pedagogical measurements.

2.1 Quantifying STEAM-AI Integration

To evaluate the depth of AI integration within a specific STEAM project, a composite **STEAM-AI**

Readiness Index (STEAM_{AI}**)** is formulated. This metric considers technological literacy (TL), creative output (CO), and engineering problem-solving (EPS) metrics extracted over time:

Where \omega represents the weighting coefficient assigned to the collaborative complexity of the project. Furthermore, student cognitive engagement is monitored using an adapted Normalized Engagement Index (NEI), calculated as:

Where A_{active} and A_{passive} represent the duration of active hands-on creation (e.g., coding, prototyping) and passive data consumption, respectively.

2.2 Machine Learning Framework

A predictive dataset is constructed by integrating student project matrices with behavioral logs from AI-powered learning environments. Machine learning models, including Support Vector Regression (SVR) and Random Forest classifiers, are employed to establish relationships between project-based features and final academic performance. The model optimizes parameters by minimizing the Root Mean Square Error (RMSE) to ensure accurate predictions of student success rates:

Spatial and temporal distribution profiles of educational success are generated across various school districts using continuous interpolation

techniques, highlighting seasonal trends in academic adaptation.

3. Results and Discussion

The integrated machine learning models demonstrated high predictive accuracy in identifying students' skill acquisition rates. A comparative analysis showed that the combination of AI-driven adaptive feedback and classic hands-on STEAM projects significantly reduces the learning curve in complex topics like robotics and algorithms.

Table 1. Performance comparison of different educational delivery models.

The temporal analysis over a full academic year revealed distinct behavioral patterns, with peak engagement levels observed during project phases that utilized generative AI for artistic design and engineering simulations.

4. Conclusion

The study demonstrates that integrating AI tools with mathematical and machine learning models provides an effective ecosystem for monitoring and enhancing STEAM education. The proposed approach allows for the real-time detection of both spatial patterns in educational resource distribution and temporal changes in student skill development. This can support decision-making in institutional management and curriculum planning. Future work will focus on improving model personalization accuracy, optimizing algorithmic transparency, and

incorporating additional socio-emotional variables into the learning models.

References

1.Gurbanova, A.: Digital Transformation in Modern Pedagogy. Journal of Innovation in Education 2(5), 99–110 (2026).
2.Aliyev, T., Karimova, S.: AI-Driven Frameworks for K-12 Classrooms. In: Editor, F., Editor, S. (eds.) CONFERENCE 2026, LNCS, vol. 9999, pp. 1–13. Springer, Heidelberg (2026).
3.Watson, R., Holmes, M.: The Evolution of STEAM: From Art to Artificial Intelligence, 2nd edn. Academic Press, London (2024).
4.Zhang, Y.: Machine Learning Applications in Analyzing Student Engagement. In: 12th International Proceedings on Educational Technologies, pp. 1–2. Science Publisher, Berlin (2025).
5.LNCS Homepage, http://www.springer.com/lncs, last accessed 2026/05/15.

https://doi.org./10.58225/mpmma.2026.202

NEXT-GENERATION STRUCTURAL SEISMIC PROTECTION: AN INDUSTRIAL APPLICATION FOR THE TALLEST BUILDING IN THE CAUCASUS

Azer Kasimzade[1], *Reyhan Akbarli*[1], *Emin Nematli*[1]
[1] AzUAC, Azerbaijan

Abstract. As the tallest building in the Caucasus region, located in Baku, Azerbaijan, Baku Tower (BT) necessitates effective control of its dynamic behavior to ensure both structural safety and occupant comfort. To mitigate wind- and earthquake-induced vibrations and thereby enhance occupant comfort, a 400-ton Tuned Mass Damper (TMD) system is employed within the structure.

Keywords: Structural control, Tuned Mass Damper (TMD), Structural Seismic Isolation Method (SSIM), high-rise buildings, wind loading, seismic loading, dynamic analysis, structural dynamics, modal analysis, vibration mitigation

This study has investigated the behavior of the aforementioned structure under seismic loads and has evaluated the potential application of the Next-Generation Structural Seismic Protection (NGSSP) system, aiming to achieve maximum structural safety with minimal additional mass. The obtained results indicated that the implementation of the NGSSP system significantly contributed to a safer, more economical, and resilience-oriented structural design.

The efficacy of the existing TMD system has been comprehensively investigated. Furthermore, the dynamic performance of the TMD-equipped structure has been comparatively evaluated against a next-generation Structural Seismic Isolation Method (SSIM), which serves as an alternative vibration mitigation approach for high-rise buildings. The primary objective of this study is to demonstrate the potential of advanced seismic isolation systems to reduce structural responses, while simultaneously assessing their advantages regarding structural efficiency, safety, occupant comfort, and resilience.

Full-scale finite element models of Baku Tower have been developed for both configurations: with and without the TMD system. Nonlinear time-history analyses were performed to evaluate free vibrations as well as forced vibrations under seismic excitation. The structural responses of the uncontrolled model, the TMD-equipped model, and the SSIM-implemented model were systematically compared in light of the analysis results.

The results of the free vibration analysis indicated that the implementation of the TMD system significantly altered the dynamic characteristics of the structure. The fundamental natural vibration period, which is 4.3721 seconds in the uncontrolled structural model, increased to 5.4946 seconds in the TMD-controlled state, exhibiting an

increase of approximately 25.67%. This increase in the structural period shifted the dominant vibration frequencies of the structure away from those of external dynamic excitations, thereby reducing the risk of resonance. The obtained results confirm that the TMD system effectively modifies the dynamic behavior of the structure and enhances vibration control performance. Reference studies indicate that the fundamental natural vibration period exceeds 13 seconds in structures utilizing the Structural Seismic Isolation Method (SSIM). This demonstrates that the SSIM system possesses a higher performance potential in terms of dynamic behavior control compared to conventional TMD systems.

Nonlinear time-history analyses demonstrated that the TMD system provided measurable reductions in critical structural response parameters under severe seismic effects. An average reduction of 18% was achieved in top-floor displacement and acceleration. Furthermore, a significant average reduction of 9% was observed in base shear forces and base overturning moments. Maximum inter-story drifts decreased by an average of 18%, indicating improved lateral deformation control and structural stability. The maximum inter-story drift was observed at the 43rd floor. These findings reveal that the implemented TMD system can effectively mitigate the dynamic effects of earthquake forces, in particular.

Furthermore, the results demonstrated that the SSIM system provided a substantially higher level of structural response mitigation compared to the conventional TMD system. In generic high-rise building models, the average reduction in top-floor acceleration was determined to be approximately 46.52%, while the average reduction in top displacement was determined to be approximately 18.75%. Especially in tower-type structures, the SSIM system exhibited an exceptionally high vibration mitigation efficiency. Under the investigated seismic loads, the top-floor acceleration and top displacement were reduced by approximately 82.43% and 82.76%, respectively. Additionally, reductions of approximately 96.59% in base shear forces and 89.11% in base overturning moments were achieved.

In addition to these significant reductions, the rigid body motion generated by the seismic isolation mechanism of the SSIM system minimized inter-story drift values to near-zero levels. This behavior substantially mitigated the risk of deformation in both structural and non-structural elements. Consequently, it was demonstrated that the implementation of advanced seismic isolation strategies can significantly reduce the risk of damage to both structural and non-structural components.

Another significant finding of the study pertains to structural optimization and sustainability. The

substantial reductions in acceleration demands, internal force transfer, and overall structural responses achieved through the SSIM approach can facilitate the optimization of structural member dimensions and the reduction of total structural mass in future high-rise building designs. This not only enhances structural efficiency but also contributes to more economical and sustainable construction practices through reduced material consumption and mitigated seismic responses.

Overall, this study demonstrates that the Structural Seismic Isolation Method (SSIM) is a highly efficient and innovative alternative to conventional Tuned Mass Damper (TMD) systems in enhancing the seismic resistance, vibration performance, and structural resilience of high-rise buildings. While providing a significant reduction in structural responses, the proposed approach simultaneously supports the objectives of structural optimization, sustainability, serviceability performance, and occupant comfort. In particular, the SSIM system exhibits a high potential for resilience in terms of maintaining post-earthquake structural functionality, minimizing damage levels, and ensuring a faster operational recovery capacity. These findings offer significant contributions to the development of advanced structural control technologies for next-generation resilient and sustainable high-rise structural systems.

https://doi.org./10.58225/mpmma.2026.207

COMPARATIVE STATISTICAL AND COMPUTATIONAL EVALUATION OF CHAOTIC-BASED PSEUDORANDOM NUMBER GENERATORS

Bahar Milani
Bandırma Onyedi Eylul University, Türkiye

Abstract. Chaos-based functions have been used for some time as sources of deterministic generation of pseudorandom sequences due to their nonlinear dynamics and sensitive initial conditions. However, the practical performance of a chaos-based pseudorandom number generator (PRNG) is determined not only by the choice of the underlying map but also by the initial seed, the output bit extraction method, and the computational implementation. This paper reports which of three common one-dimensional chaos maps—the logistic map, the tent map, and the piecewise linear chaos map (PWLCM)—performs best. A million-bit binary sequence of 30 initial seeds was generated for each generator under identical conditions using the threshold method and the least significant bit (LSB) extraction technique. The results of that generation were in turn subjected to Shannon entropy, bit balance, autocorrelation, and computational power utilization tests, and we also performed selected statistical tests from NIST SP 800-22. We also looked at how each generator performed with different initial states to see if there was consistent high-quality performance. A traditional PRNG software was used as a control. A repeatable evaluation model was provided. That is, all variables were kept the same for all generators.

This is not to say that passing these tests is an indication of cryptographic security.

Keywords: Pseudorandom Number Generator, Chaotic Maps, Logistic Map, Tent Map, PWLCM, Randomness, Computational Performance, Bit Extraction

1. Introduction

Pseudo-random number generators (PRNGs) are a fundamental component for modeling numerical systems or computations, communication systems, and data/information security. Classical number generators produce fast and deterministic outputs, but often exhibit periodicities in their structure that are easily detected by modern statistical analysis [1]. Three one-dimensional chaotic maps, the logistic, the tent, and the piecewise linear chaotic map (PWLCM), have been very popular for use as kernels for pseudo-random number generators (PRNGs) [2]. A large portion of studies typically test only one chaotic map against randomly selected baselines, use different sets of seeds, or simply provide NIST overall acceptance rates without considering seed-dependent variability [3]. Tutova and colleagues noted that the extraction method, along with the way the digital arithmetic is implemented, can have a significant impact on the apparent randomness of the output [4]. This study attempts to fill these gaps by adopting a controlled and repeatable evaluation protocol for all three maps simultaneously, focusing on statistical

randomness, computational power, consistency of the grains, and sensitivity of the extraction method.

2. Methodology

The test method relies on four criteria or dimensions. First, basic statistical criteria such as bit balance, Shannon entropy, and lag-1 autocorrelation are calculated for each of the 180 generated sequences. Second, a subset of the NIST SP 800-22 tests is applied: frequency, block frequency, runs, longest run of ones, spectral (FFT), approximate entropy, serial, and cumulative sum. NIST explicitly states that passing these tests is necessary to achieve randomness quality, but is not a sufficient criterion. The third aspect of variability, based on the use of seeds, is shown by providing the mean, standard deviation, and minimum and maximum entropy values, along with the number of seeds for which the NIST pass rate is less than 80%. Finally, the computational power in megabits per second was measured using Python 3.11 with NumPy in an environment with a fixed hardware configuration. The values of the basic statistics related to the sub-threshold quality extraction are presented in Table 1 below.

Table 1. Basic statistical metrics — threshold extraction, 30 seeds, 10^6 bits each

Generator	Mean Entropy	Mean Ones Ratio	Mean Autocorr. (lag-1)	Throughput (Mbit/s)
Logistic	0.9971	0.5003	−0.0031	317

Tent	0.9906	0.4981	−0.0084	428
PWLCM	0.9988	0.5001	−0.0012	401

Summary statistics of the acceptance rate based on NIST criteria and seed compatibility are presented in Table 2. PWLCM provides the best performance in terms of acceptance ratio based on NIST among all maps using both image feature extraction methods.

Table 2. NIST pass rates and seed consistency (threshold extraction)

Generator	NIST Pass Rate (%)	Entropy Std Dev	Min Entropy	Failed Seeds (of 30)
Logistic	85.7	0.0041	0.9863	4
Tent	81.0	0.0073	0.9721	6
PWLCM	90.5	0.0018	0.9951	1

Comparing the two approaches used to extract features from iterations, it seems that LSB extraction according to NIST always leads to a decrease in the percentage of passing results, and has a greater impact in the case of Tent Map (from 81.0% to 62.4%). In this regard, it can be noted that the low-order bits of IEEE 754 standard floating-point numbers suffer from rounding errors [5]. In terms of throughput, chaos-based PRNGs are computationally expensive compared to state-of-the-art algorithms, and this should be considered when making decisions [6].

Conclusion

In this study, a controlled statistical comparison of logistic, Chador, and PWLCM-based PRNGs is performed based on statistical quality, seed invariance, bit extraction sensitivity, and computational speed. The main results of this paper are: 1) In general, PWLCM offers the best compromise between entropy, NIST pass rate, and seed robustness in the three discussed chaotic mappings. 2) The bit extraction process plays an important role in the output quality; LSB extraction significantly reduces the statistical quality in all mappings. 3) All three chaotic generators have weak seeding points that are not detectable when presented with an average pass rate. For this reason, seed invariance should be demonstrated along with the average quality indicators. The next step will be to perform the same study for fixed-point numbers with 16-bit and 32-bit precision, apply the full TestU01 set, and investigate heuristic seed filtering methods as a means to reduce weak seeding regions in real-world situations.

References

1. Knuth, D. E. (1997). *The Art Of Computer Programming, Volume 1, 3/E*. Pearson Education India.

2. Naik, R. B., & Singh, U. (2024). A review on applications of chaotic maps in pseudo-random

number generators and encryption. *Annals of Data Science*, *11*(1), 25-50.

3. Rukhin, A., Soto, J., Nechvatal, J., Smid, M., & Barker, E. (2001). *A statistical test suite for random and pseudorandom number generators for cryptographic applications* (No. NISTSP80002).

4. Moysis, L., Tutueva, A., Volos, C. K., & Butusov, D. (2020). A chaos based pseudo-random bit generator using multiple digits comparison. *Chaos Theory and Applications*, *2*(2), 58-68.

5. François, M., Defour, D., & Berthomé, P. (2014, April). A pseudo-random bit generator based on three chaotic logistic maps and IEEE 754-2008 floating-point arithmetic. In *International Conference on Theory and Applications of Models of Computation* (pp. 229-247). Cham: Springer International Publishing.

6. Datcu, O., Macovei, C., & Hobincu, R. (2020). Chaos based cryptographic pseudo-random number generator template with dynamic state change. *Applied sciences*, *10*(2), 451.

https://doi.org./10.58225/mpmma.2026.213

A FRAMEWORK FOR SEMANTIC DOCUMENT SIMILARITY DETECTION BASED ON AUTOMATIC TEXT SUMMARIZATION AND TRANSFORMER EMBEDDINGS

Bekchanov Shukurla[1], *Babadjanova Malika* [1]
[1] Urgench State University named after Abu Rayhan Biruni, Uzbekistan

Abstract. The rapid growth of digital document collections has increased the need for efficient methods for identifying semantically similar documents. Traditional similarity measures often rely on lexical overlap and fail to capture deeper semantic relationships. This paper proposes a framework for semantic document similarity detection based on automatic text summarization and transformer embeddings. First, source documents are summarized to extract their most informative content while reducing noise and redundancy. The generated summaries are then encoded using transformer-based embedding models to obtain semantic representations. Document similarity is computed in the embedding space using cosine similarity. The proposed approach improves retrieval efficiency and semantic matching accuracy for large-scale document collections.

Keywords: Automatic Text Summarization, Semantic Similarity, Transformer Embeddings, Document Retrieval.

The rapid growth of digital documents has increased the need for efficient methods of identifying semantically similar texts. Traditional approaches

based on keyword matching often fail to capture deeper semantic relationships between documents. Recent advances in Natural Language Processing and transformer-based language models provide more effective semantic representations of textual content. In this work, we propose a framework for document similarity detection that combines automatic text summarization and transformer embeddings. First, documents are summarized to extract their most informative content. Then, semantic embeddings are generated and document similarity is computed using cosine similarity. The proposed approach aims to improve retrieval accuracy while reducing computational complexity.

Related Work

Document similarity detection has been extensively studied in information retrieval and natural language processing. Traditional methods such as TF–IDF and cosine similarity represent documents as vectors of term frequencies and compare them based on lexical overlap. Although computationally efficient, these approaches often fail to capture semantic relationships between texts. To overcome this limitation, methods based on Latent Semantic Analysis (LSA), topic modeling, and word embeddings have been developed. Recent advances in transformer-based models, including BERT, Sentence-BERT, and RoBERTa, provide contextual semantic representations that significantly improve similarity analysis. At the same time, automatic text summarization techniques, particularly transformer-based summarization models, have demonstrated

the ability to extract essential information from large documents. Combining text summarization with semantic embeddings offers a promising approach for improving document similarity detection and retrieval performance.

Methodology

The proposed framework combines automatic text summarization and transformer-based semantic embeddings to identify documents that are semantically related to a given text. First, documents are preprocessed through tokenization, stop-word removal, punctuation elimination, lowercasing, and text normalization. This step reduces noise and prepares the documents for semantic analysis.

Next, an automatic text summarization model is applied to generate concise summaries that preserve the most informative content of the original documents. The generated summaries are then transformed into dense semantic vector representations using the Sentence-BERT model. Given a summary S_i, the embedding model produces a semantic vector $\mathbb{v}_i = f(S_i)$, where $f(\cdot)$ denotes the embedding function. The semantic similarity between two summaries S_i and S_j is measured using cosine similarity $\mathrm{sim}(S_i, S_j) = \frac{\mathbb{v}_i \cdot \mathbb{v}_j}{|\mathbb{v}_i||\mathbb{v}_j|}$.

Documents are ranked according to their similarity scores, and those exceeding a predefined threshold

(\theta) are considered semantically related. Finally, the most similar sources are highlighted and ranked, facilitating efficient literature retrieval and semantic novelty analysis. The overall workflow can be summarized as follows:

Documents → Preprocessing →
Summarization → Sentence −
BERT Embeddings → Cosine Similarity →
Related Source Detection.

The proposed methodology reduces the influence of irrelevant information while improving the accuracy of semantic document comparison.

Experimental Setup

The experiments were conducted on a collection of scientific documents obtained from academic sources. Prior to analysis, all documents were preprocessed through tokenization, stop-word removal, and text normalization. To reduce document length while preserving the most important information, an automatic text summarization model was applied to generate concise summaries. The generated summaries were then encoded using the Sentence-BERT model to obtain semantic vector representations. The semantic similarity between documents was computed using cosine similarity: $\mathrm{sim}(S_i, S_j) = \frac{\mathbb{v}_i \cdot \mathbb{v}_j}{|\mathbb{v}_i||\mathbb{v}_j|}$, where $\mathbb{v}_i$ and $\mathbb{v}_j$ denote the embedding vectors of summaries S_i and S_j, respectively. Documents were ranked according to their similarity scores, and

those with the highest scores were considered semantically related. The performance of the proposed framework was evaluated through similarity ranking and qualitative analysis of the retrieved documents.

Results and Conclusion

The proposed framework was applied to a collection of scientific documents to identify semantically related sources. The results demonstrate that combining automatic text summarization with Sentence-BERT embeddings provides compact semantic representations while preserving the essential information contained in the original documents. The cosine similarity measure successfully identified documents discussing similar topics, even when different terminology was used. Furthermore, the ranking process enabled efficient retrieval of the most relevant sources.

In this study, a semantic document similarity framework based on text summarization, transformer embeddings, and cosine similarity was proposed. By comparing document summaries instead of full texts, the approach reduces irrelevant information and improves the efficiency of semantic comparison. The framework can support scientific literature retrieval, document analysis, and novelty detection tasks. Future work will focus on evaluating the approach on larger multilingual datasets and exploring more advanced transformer-based embedding models.

References

1. Madatov, K.A., Bekchanov, S., Khajibaeva, S.: A Technique for Automatic Extraction of Basis Words: A Case Study on "Uzbek Primary School Corpus". In: UBMK 2024 – Proceedings of the 9th International Conference on Computer Science and Engineering, pp. 85–88 (2024).
2. Madatov, K.A., Bekchanov, S.: The Algorithm of Uzbek Text Summarizer. In: International Conference of Young Specialists on Micro/Nanotechnologies and Electron Devices (EDM 2024), pp. 2430–2433 (2024).
3. Madatov, K.A., Bekchanov, S., Vičič, J.: Accuracy of the Uzbek Stop Words Detection: A Case Study on "School Corpus". In: CEUR Workshop Proceedings, vol. 3315, pp. 107–115 (2022).
4. Salaev, U., Matlatipov, G.: Neural Sequence Models for Uzbek Morphological Stemming. In: Proceedings of the 17th International Scientific and Technical Conference Actual Problems of Electronic Instrument Engineering (APEIE 2025). IEEE, Novosibirsk (2025). DOI: 10.1109/APEIE66761.2025.11289244.

https://doi.org./10.58225/mpmma.2026.219

3D TEXTURE MODELING BASED ON PROCEDURAL MODELS, SPLINES, AND ARTIFICIAL INTELLIGENCE METHODS

Beknazarova Saida,Yunusova Dilnoza
TUIT named after Mukhammad al Khwarazmiy,Uzbekistan

Abstract. This article examines modern texture generation methods for 3D modeling tasks, including procedural models, spline methods, image-based approaches, and artificial intelligence-based technologies. A comprehensive analysis of the mathematical foundations of texture generation is provided, including noise functions, fractal models, spline interpolation, image-based synthesis methods, and neural network generative architectures.

Keywords: 3D modeling, texture generation, procedural methods, image-based synthesis, artificial intelligence, splines, photorealism.

1.Introduction

The texture is a 2D image or a mathematical model applied to the surface of a 3D object, representing its color, light reflection properties, surface structure, and material characteristics. In modern computer graphics systems, texture is considered not only as a visual enhancement but also as an essential component of physically based rendering (PBR) processes [3], [2].In recent years, several main approaches to texture generation have emerged. One of the traditional methods, procedural texture generation, allows the creation of infinite and non-repetitive textures based on mathematical

models and algorithmic functions (such as Perlin noise and fractal models) [1], [3]. The main advantage of this approach is its flexibility and memory efficiency; however, its level of realism can sometimes be limited. Another approach is image-based texture synthesis, which relies on real-world images to generate textures. This method uses techniques such as patch-based algorithms, image quilting, and texture transfer to achieve a high level of visual realism. However, this approach often requires large datasets and complex computational processes.

2.Literature review

Texture generation in 3D modeling has been an active area of research in computer graphics, with various approaches proposed to improve realism, efficiency, and flexibility. The main directions in this field include procedural methods, image-based techniques, and, more recently, artificial intelligence (AI)-based approaches. Procedural texture generation has its roots in early works on noise functions and fractal geometry.

3.Methodology

Therefore, modern approaches are often based on hybrid models that combine multiple methods. The following sections discuss these three main approaches—procedural, image-based, and AI-based texture generation methods—their working principles, advantages and disadvantages, and areas of practical application in detail. Among these

approaches, procedural texture generation is based on mathematical functions and algorithms and allows the creation of infinite and non-repetitive textures.

3.1. Procedural Texture Generation Method

Procedural texture generation is an approach in computer graphics and 3D modeling where textures are generated without using pre-made images, but instead are based on mathematical functions and algorithmic models. In this method, texture values are defined by spatial coordinates (x,y,z)(x, y, z)(x,y,z), resulting in infinite, non-repetitive, and parametrically controllable surfaces [1], [3].

The fundamental mathematical representation of procedural textures can be expressed in a general form as follows: $T(x, y, z) = f(x, y, z)$

where T(x,y,z) represents the texture intensity or color value, x,y,z are spatial coordinates, and f is an algorithmic function that generates the texture. In the 2D case, the model takes the following form: $T(x, y) = f(x, y)$

One of the most important components in procedural texture generation is noise functions. For example, the Perlin noise model is widely used to generate natural-looking surfaces and can be expressed as: $N(x, y) = \sum_{i=1}^{n} a_i \cdot \text{noise}(2^i x, 2^i y)$

where ai are amplitude coefficients and 2i represents the increase in frequency. This approach is used to model complex structures such as wood, stone, clouds, and other natural surfaces. Fractal-based

procedural models are also widely used. The Fractal Brownian Motion (fBM) model is defined as: $\mathrm{fBM}(x,y) = \sum_{i=0}^{n} \frac{1}{2^i} \cdot N(2^i x, 2^i y)$

where each "octave" represents different frequency and amplitude levels, resulting in multi-scale detailed textures. Trigonometric functions are also used in procedural textures, where simple periodic structures can be expressed as:$T(x,y) = \sin(ax + by)$. In addition, Voronoi diagram-based models are used to generate geometrically segmented textures, which can be expressed as: $T(p) = \min_i \|p - p_i\|$

Proposed Hybrid Model. Recent studies show that achieving the highest quality and most practical results is more effective not through individual methods, but through a hybrid approach that combines them. The proposed model has a three-stage architecture: Stage 1: Procedural base. The initial structure is generated using mathematical noise and fractal models: $T_{base}(x,y) = \mathrm{fBM}(x,y)$

Stage 2: Image-based refinement. Fine details are added using patch-based processing from real images: $T_{detail} = \arg\min_T D(T, T_{ref})$

Stage 3: AI optimization. The texture is further enhanced in terms of quality using a neural network:$T_{final} = G(T_{base,} T_{detail})$

The proposed hybrid model produces the following contributions:Procedural → basic structure, Image-based → realistic details, AI → final quality enhancement $T_{final} = G(T_{base}, T_{detail})$

These examples demonstrate that each approach is effective for generating different types of textures. The highest-quality results are achieved using the hybrid approach, as it integrates the advantages of all three methods. In particular, the hybrid approach improves: structural consistency of textures (procedural layer), photorealistic detail accuracy (image-based layer), overall visual quality and adaptability (AI layer). A comparative analysis shows that the hybrid model achieves a better balance be

Conclusion

This paper analyzed modern approaches to texture generation in 3D modeling — procedural, image-based, and artificial intelligence (AI)-based methods — from both scientific and practical perspectives. The mathematical models, working principles, and visual quality of each approach were examined, and their importance in computer graphics systems was justified. The analysis shows that the procedural approach is characterized by high speed and memory efficiency but has limitations in representing complex natural details.

References

1. Ebert, D. S., Musgrave, F., Peachey, D., Perlin, K., & Worley, S. (2003). *Texturing and Modeling: A Procedural Approach*. Morgan Kaufmann. https://doi.org/10.1016/B978-155860848-1/50002-3

2. Lagae, A., Lefebvre, S., Drettakis, G., & Dutré, P. (2010). Procedural noise using sparse Gabor convolution. *ACM Transactions on Graphics*, 29(4). https://doi.org/10.1145/1778765.1778803

3. Beknazarova, S., Abdullayev, S., Abdullayeva, O., & Abdullayev, Z. (2024). Machine learning method for predicting human movements. AIP Conference Proceedings, 3244, 030036. https://doi.org/10.1063/5.0242

https://doi.org./10.58225/mpmma.2026.225

PERFORMANCE PREDICTION OF CARRIER FAN COIL UNITS USING ARTIFICIAL NEURAL NETWORKS

Buğra Avcı, Kaan Erşahin , Ahmet Selim Dalkılıç, Burak Uğuz

Yildiz Technical University, Türkiye

Abstract. An Artificial Neural Network (ANN) model is developed for simultaneous prediction of six performance parameters of 42CT and 42DT fan coil units. Twelve geometric, aerodynamic, and hydraulic inputs are used to predict airflow rate, cooling capacity, heating capacity, fan power, sound power level, and unit price. A three-hidden-layer network with [36, 18, 9] neurons trained via Bayesian Regularization on 282 experimental samples achieves R^2 = 0.9997, 0.9999, and 0.9992 for airflow, cooling, and heating capacity. The universal model generalizes across both product series without model-specific calibration.

Keywords: Fan Coil Unit, ANN, Bayesian Regularization, HVAC, 42CT, 42DT**.**

1. Introduction

Fan coil units (FCUs) are widely used HVAC terminal devices whose performance depends on the nonlinear interaction of geometric and operating parameters. Catalog-based evaluation methods are limited to rated conditions, while CFD approaches are computationally prohibitive for rapid multi-variable screening [1,2]. ANNs have proven effective as surrogate models in thermal

engineering, capturing complex input-output relationships directly from experimental data [3,4].

Uguz et al. [5,6] developed four separate ANN architectures for a single EC motor FCU series under cooling and heating conditions, achieving R values of 0.96–0.98. While accurate, their approach requires multiple dedicated networks per operating mode, covers only one product series, and excludes acoustic and price outputs. The present work addresses these gaps with a single universal model spanning two product families, six simultaneous outputs, and Bayesian Regularization — not previously applied in the FCU ANN literature.

2.**Data and Methodology**

Performance data were obtained from 42CT (10 sizes) and 42DT (4 sizes) ceiling-type FCUs tested under EUROVENT and ASHRAE 79 conditions. EC motor voltage was varied from 3.0 to 8.0 VDC and external static pressure from 0 to 60 Pa, yielding 189 CT and 93 DT samples (282 total).

Twelve inputs were used: unit length, cooling coil rows, heating coil rows, coil separation indicator, fan count, fan length, RPM, external static pressure, tip speed, total fan swept area, cooling fluid flow rate, and heating fluid flow rate. Outputs were airflow (m^3/h), cooling capacity (W), heating capacity (W), fan power (W), sound power level (dBA), and price (EUR).

A feedforward MLP with three hidden layers of [36, 18, 9] tansig neurons was implemented in

MATLAB and trained with the Bayesian Regularization algorithm (trainbr), which incorporates weight regularization into the cost function — eliminating the need for a validation set and providing inherent overfitting protection. Data were split 85/15 (train/test).

3.**Results and Discussion**

The model achieved $R^2 \geq 0.999$ for cooling capacity, airflow, and price across all subsets, comparing favorably with the R = 0.96–0.98 of Uguz et al. [5,6] despite covering a broader output space in a single network. The 42DT subset showed comparable or superior accuracy to 42CT despite having fewer samples, confirming cross-product generalization.

FPw prediction shows elevated MAPE (12–14%) due to high relative errors at low absolute power values. LWA accuracy (R^2 = 0.85–0.89) is limited by aeroacoustic complexity not fully captured by geometric inputs alone.

Table 1. Test Set Performance Metrics

Performance Prediction Model (42DT + 42CT)			
Output	R^2	RMSE	MAPE%
Airflow (m^3/h)	0.9995	13.3486	1.10
Qt Cool (Watt)	0.9996	66.3147	0.62
Qt Heat (Watt)	0.9991	102.0039	0.89
FPw (Watt)	0.9856	6.5365	7.72
LWA (dBA)	0.8930	1.6746	2.25
Price (€)	0.9993	6.3225	0.51

4.Conclusion

A universal ANN model trained with Bayesian Regularization simultaneously predicts six FCU performance outputs across 42CT and 42DT product families. $R^2 \geq 0.999$ is achieved for primary thermal outputs. Fan power and sound power prediction may benefit from additional aeroacoustic inputs in future work. The model provides a practical tool for HVAC design and automated equipment selection. The model generalizes effectively across both product families without model-specific calibration, with the 42DT subset achieving comparable accuracy to the larger 42CT subset despite comprising only 93 of 282 total samples. The adoption of Bayesian Regularization eliminates the need for a validation set and provides automatic overfitting protection, making it particularly well suited for moderate-sized experimental datasets compared to the commonly used Levenberg–Marquardt algorithm. Unlike prior studies that required four separate ANN architectures per operating mode and per product series [5,6], the present approach consolidates all six outputs into a single network, simplifying deployment in automated equipment selection platforms and building energy simulation tools. Extension of the framework to additional FCU product families and integration with multi-

objective optimization routines represent promising directions for future research.

References

1. ANSI/ASHRAE Standard 79-2002. Method of Testing for Rating Fan-Coil Conditioners. Atlanta, 2006.
2. Peng, X., & Jiang, Y. (1994). Simplified dynamic models of fan-coil units. *ASHRAE Transactions*, 100(2), 168–179.
3. Mohanraj, M., et al. (2012). Applications of ANNs for refrigeration and HVAC systems. *Renewable and Sustainable Energy Reviews*, 16(2), 1340–1358.
4. Lu, S., et al. (2024). Machine learning for radiant floor and fan coil cooling systems. *Buildings*, 14, 1659.
5. Uguz, B., et al. (2025). ANN modeling for EC fan coil performance prediction. *Journal of Thermal Analysis and Calorimetry*, 150, 20959–20979.
6. Uguz, B., et al. (2026). Machine learning for EC fan coil units using heating database. *International Communications in Heat and Mass Transfer*, 172, 110616.

https://doi.org./10.58225/mpmma.2026.230

EXAMINATION OF THE IMPACT OF INDUSTRIAL HEAT PUMPS ON ENERGY EFFICIENCY

Büşra Selenay Önal[1] *, Ahmet Selim Dalkılıç*[2]
[1] Istanbul Gelisim University, Türkiye
[2] Yildiz Technical University, Türkiye

Abstract. Increasing energy efficiency and reducing carbon emissions are among the primary goals of the industrial sector today. In this study, the impact of industrial heat pumps on energy efficiency has been examined thru a theoretical application. In the study, a food processing facility with a daily process heat requirement of 5000 kWh was examined, and the existing natural gas boiler system was compared with an industrial heat pump system with a coefficient of performance (COP) of 4. As a result of the calculations, the daily energy consumption of the natural gas boiler was determined to be 5882 kWh, while the heat pump, which meets the same heat load, was found to consume only 1250 kWh of energy. Accordingly, the annual energy consumption has been calculated as 2146 MWh for the natural gas boiler and 456 MWh for the heat pump. The obtained results show that the use of an industrial heat pump can provide approximately 79% savings in energy consumption. Additionally, it has been determined that the system has significant potential to reduce carbon emissions. The study results reveal that industrial heat pumps

are an effective technology in terms of sustainable production and energy transition goals.

Keywords: Heat Pump, Energy Efficiency, Sustainable Energy, Carbon Emissions

1.Introduction

The industrial sector is responsible for approximately one-third of the total energy consumption worldwide. Especially in the food, chemical, and textile industries, the need for process heat is significant. In traditional systems, this need is mostly met with natural gas or coal-fired boilers. In recent years, the increase in energy costs and the tightening of environmental regulations have accelerated the shift toward alterna-tive technologies. Industrial heat pumps are systems that recover low-temperature waste heat and make it usable at higher temperatures. Thanks to these features, they offer significant advantages in terms of energy savings and reducing carbon emissions. Energy resources have emerged as critical issues that demand immediate atten-tion. Furthermore, as the effects of global warming worsen, the need for effective cooling solutions has grown in importance. In the study conducted by Arpagaus et al., it was noted that the COP values of high-temperature industrial heat pumps range between 2.5 and 5.8, and they can achieve energy savings of up to 30% [1]. According to a report published by the International Energy Agency (IEA), heat pumps used worldwide contributed to the prevention of approximately 180 Mt CO_2 emissions in 2023 [2]. Hepbaslı and Kalıncı have shown that the COP values in heat pump systems generally range between 3 and 5, and that energy

efficiency has increased by more than 40% compared to traditional systems [3]. Averfalk and Werner have shown that high-temperature heat pumps can operate in the temperature range of 80–120°C and can achieve a 25–50% reduction in process energy demand [4]. In the study conducted by Wolf and Blesl, it was reported that energy costs in industrial waste heat recovery applications were reduced by approximately 20–35% [5]. Bamigbetan et al. have determined that heat pumps can reduce carbon emissions by 30–70% in various industrial applications [6]. Jensen and Skovrup stated that in systems using natural refrigerants, COP values can reach levels of 4.0–5.5 and the environmental impact is significantly reduced [7]. In the integration studies conducted by Liu et al., it has been shown that total energy consumption in process industries can be reduced by 22–48% [8]. Mota-Babiloni et al. reported that the use of next-generation refrigerants with low global warming potential can increase system performance by approximately 8-15% [9]. Forman et al. have shown that the global industrial waste heat potential is approximately 300–1400 TWh/year and that a significant portion of this potential can be recovered with the help of heat pumps [10]. When these studies are evaluated together, it is seen that industrial heat pumps are a sustainable technology that reduces energy consumption, lowers operating costs, and significantly contributes to the reduction of carbon emissions.

2.Material and Method

In the study, a food processing facility with a daily heat energy requirement of 5000 kWh has

been considered. It has been assumed that the facility currently uses a natural gas boiler. For comparison purposes, an industrial heat pump system that meets the same heat load has been evaluated. This system parameters are daily heat requirement 5000 kWh,boiler efficiency %85,heat pump COP value 4.0,operating time 365 day/year. The energy consumption required for the natural gas boiler has been calculated using the following equation.

$$E_{boiler}=\frac{Q_{need}}{\eta}$$

Here;
E_{boiler}: Boiler energy consumption, Q: Heat requirement, η: Boiler efficiency

The electricity consumption of the heat pump has been calculated using the COP value.

$$E_{HP}=\frac{Q_{need}}{\mathrm{COP}}$$

Here;
E_{HP} : Heat pump energy consumption, COP: Coefficient of performance

3.Results

As a result of the calculations, the daily energy consumption of the natural gas boiler was determined to be 5882 kWh, while the heat pump, which meets the same heat load, was found to consume only 1250 kWh of energy. The results show that the heat pump requires approximately 79% less energy input to meet the same heat load.

When evaluated in terms of carbon emissions, it is observed that heat pump systems produce lower greenhouse gas emissions. Fig 1 shows annual energy consumption and comparison of co_2 emissions of the boiler and heat pump systems.

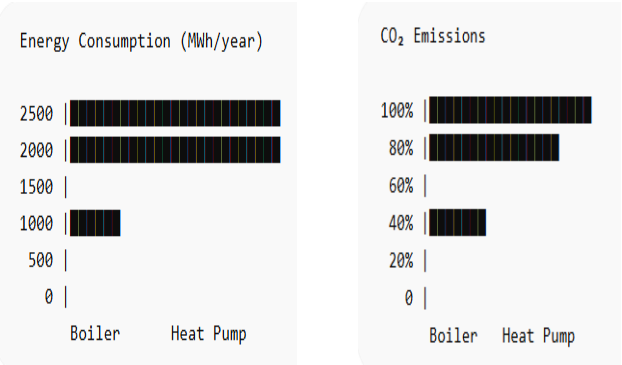


Fig 1. Annual Energy Consumption and Comparison of CO_2 Emissions of the Boiler and Heat Pump Systems

4.Conclusion

In this study, industrial heat pumps were found to significantly improve energy efficiency compared to traditional natural gas boilers, with approximately 79% lower energy consumption for the same heat load. The research highlights notable reductions in annual energy consumption and carbon emissions, indicating that industrial heat pumps are a viable solution for industrial facilities aiming to lower energy costs and minimize environmental impact while supporting sustainable production goals.

References

1. Arpagaus, C., Bless, F., Uhlmann, M., Schiffmann, J., Bertsch, S.S. (2018). *High*

Temperature Heat Pumps: Market Overview, State of the Art, Research Status and Application Potentials. Energy, 152, 985–1010.

2. International Energy Agency (IEA). (2024). *Heat Pumps – Tracking Clean Energy Progress*.

3. Hepbaslı, A., Kalıncı, Y. (2009). *A Review of Heat Pump Water Heating Systems*. Renewable and Sustainable Energy Reviews, 13(6–7), 1211–1229.

4.] Averfalk, H., Werner, S. (2017). *Essential Improvements in Future Industrial Heat Pump Systems*. Energy Efficiency, 10(6), 1465–1482.

5. Wolf, S., Blesl, M. (2016). *Model-Based Techno-Economic Assessment of Industrial Heat Pumps*. Energy, 93, 266–274.

6. Bamigbetan, O., Eikevik, T.M., Nekså, P. (2019). *Review of Heat Pump Systems for Industrial Applications*. Renewable and Sustainable Energy Reviews, 106, 103–114.

7. Jensen, J.K., Skovrup, M.J. (2018). *Heat Pump Applications Using Natural Refrigerants*. International Journal of Refrigeration, 88, 490–501.

8. Liu, Q., Duan, Y., Wang, Y. (2020). *Energy Saving Potential of Industrial Heat Pump Integration*. Applied Thermal Engineering, 170, 114974.

9. Mota-Babiloni, A., Navarro-Esbrí, J., Barragán-Cervera, Á. (2021). *Low GWP Refrigerants for High Temperature Heat Pumps*. Energy Reports, 7, 667–678.

10. Forman, C., Muritala, I.K., Pardemann, R., Meyer, B. (2017). *Estimating the Global Waste*

Heat Potential. Renewable and Sustainable Energy Reviews, 57, 1568–1579.

https://doi.org./10.58225/mpmma.2026.237

NUMERICAL INVESTIGATION OF RED BLOOD CELL DIAMETER EFFECT ON CELL-FREE LAYER FORMATION IN A CONVERGING MICROTUBE

Cihan Sezer[1,2] , Kenan Kaya[2] , Mahdi Tabatabaei Malazi[2] ,
Ahmet Selim Dalkılıç[1,]
[1]Yildiz Technical University, Türkiye
[2] Istanbul Aydin University, Türkiye

Abstract. Red blood cell (RBC) migration toward the flow core is one of the key mechanisms governing cell-free layer (CFL) formation in microscale blood flow. In this study, the effect of RBC diameter on RBC distribution and CFL development in a converging microtube was numerically investigated at a fixed inlet RBC volume fraction of $\alpha R = 0.2$. The simulations were performed using Euler–Euler multiphase framework. Three RBC diameters, $dR = 4$, 8 and 11 μm, were considered to represent reduced, healthy, and enlarged cell sizes, respectively. The results showed that RBC diameter has an effect on cell migration and near-wall cell depletion. Smaller RBCs penetrated more effectively into the near-wall region, leading to a higher local RBC volume fraction and a thinner CFL. In contrast, enlarged RBCs migrated more strongly toward the tube core, resulting in lower near-wall RBC concentration and a thicker CFL. These findings indicate that RBC size is a controlling parameter for CFL formation under fixed hematocrit conditions and may affect microscale blood transport in pathological cases involving altered RBC dimensions.

Keywords: Red blood cell, cell-free layer, RBC diameter, microcirculation, Euler–Euler model, CFD

1. Introduction

Red blood cell (RBC) migration and cell-free layer (CFL) formation are key features of microscale blood flow. In narrow microchannels and microtubes, RBCs migrate toward the flow core and form a plasma-rich near-wall region. Previous studies investigated microscale blood flow and CFL formation using different geometries and modeling approaches [1–3]. Since the CFL acts as a mass transfer resistance against oxygen transport between the RBC-rich core and vessel wall [4], its thickness is important for near-wall transport. RBC diameter also affects CFL formation; while a healthy RBC diameter is approximately 8 μm, smaller or enlarged RBCs can occur under pathological conditions [5]. Therefore, this study investigates the effect of RBC size variations on CFL formation in a converging microtube at fixed hematocrit value of $\alpha R = 0.2$.

2.Numerical Method

Numerical simulations were performed using Euler–Euler multiphase framework, where plasma and RBCs were treated as interpenetrating continuum phases. Blood viscosity was modeled using a modified Carreau–Yasuda model, while phase interactions were represented by the Gidaspow drag and Saffman–Mei lift models. The computational domain was a converging microtube, selected to represent tapered microvessels in the circulatory system. The inlet and outlet diameters were Din = 200 μm and Dout = 100 μm, respectively, with a length of L = 3000 μm. Due to geometrical and flow

symmetry, only one quarter of the domain was employed in numerical calculations. A fixed velocity and RBC volume fraction were prescribed at the inlet, and a static pressure of 0 Pa was imposed at the outlet. The walls were assumed rigid with no-slip boundary conditions, and the flow was laminar with Re = 17.8. A wall-refined structured hexahedral mesh was created. The inlet RBC volume fraction was fixed at $\alpha R = 0.2$, and three RBC diameters, $dR = 4$, 8, and 11 μm, were considered.

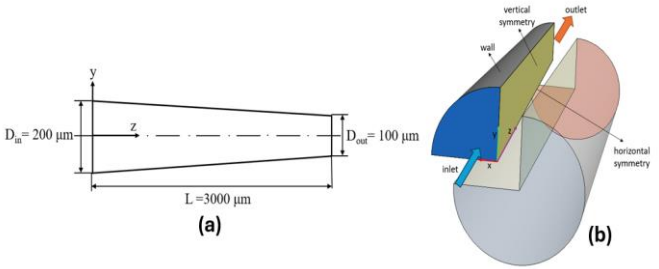


Fig. 1. Computational domain and boundary conditions of the converging microtube: (a) geometrical dimensions of the tapered microtube and (b) quarter-domain used in numerical simulations with boundary conditions.

3.Results and Discussion

The numerical model was validated by comparing the RBC volume fraction profiles with the results of Kim et al. [1] and Karmakar et al. [6]. Then, the effect of RBC diameter was evaluated at a fixed inlet RBC volume fraction of $\alpha R = 0.2$. Fig. 1 presents the vertical RBC volume fraction profiles at $z/L = 0.5$ for $dR = 4$, 8, and 11 μm. The profiles indicate two characteristic regions: an RBC-rich core flow region and a near-wall CFL. In the core region, RBC volume fraction remains relatively

high due to cell migration toward the tube center. Near the wall, the RBC volume fraction decreases sharply; this sharp decrease represents the upper edge of the CFL, where the local RBC concentration is significantly reduced. RBC diameter slightly affects the RBC volume fraction profiles, where increase in RBC diameter leads to sharper CFL profiles. For dR = 4 μm, RBCs penetrate closer to the wall, resulting in a higher near-wall RBC volume fraction and a thinner CFL. As the RBC diameter increases, cell migration toward the core becomes stronger. Therefore, for dR = 4 μm and especially for dR = 11 μm, the near-wall depletion becomes more pronounced and the CFL becomes thicker.

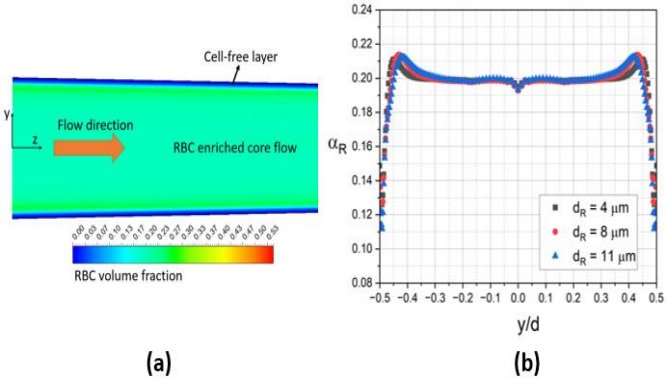


Fig. 2. RBC distribution and corresponding volume fraction profiles at αR=0.2: (a) contour of RBC volume fraction showing the RBC-enriched core flow and near-wall cell-free layer, and (b) vertical RBC volume fraction profiles at z/L = 0.5 for dR=4, 8 and 11 μm

4.Conclusion

In this study, the effect of RBC diameter on CFL formation was investigated in a converging microtube at a fixed inlet RBC volume fraction of $\alpha R = 0.2$. The results showed that RBC diameter influences cell migration, RBC distribution, and CFL development. Smaller RBCs ($dR = 4$ μm) penetrated closer to the wall and formed a thinner CFL, whereas enlarged RBCs ($dR = 11$ μm) migrated more strongly toward the core and produced a thicker CFL. Therefore, RBC size variations associated with pathological conditions may alter CFL thickness and near-wall transport characteristics in microcirculatory flow.

References

1. Kim, J., Antaki, J. F., & Massoudi, M. (2016). Computational study of blood flow in microchannels. Journal of Computational and Applied Mathematics, 292, 174–187.
2. Gracka, M., Lima, R., Miranda, J. M., Student, S., Melka, B., & Ostrowski, Z. (2022). Red blood cells tracking and cell-free layer formation in a microchannel with hyperbolic contraction: A CFD model validation. Computer Methods and Programs in Biomedicine, 226, 107117.
3. Barbosa, F., Dueñas-Pamplona, J., Abreu, C. S., Oliveira, M. S., & Lima, R. A. (2023). Numerical model validation of the blood flow through a microchannel hyperbolic contraction. Micromachines, 14, 1886.
4. Escobar, C., & Méndez, F. (2008). Unloading oxygen in a capillary vessel under a

pathological condition. Mathematical biosciences, 215(2), 127-136.

5. Aarts, P. A. M. M., Heethaar, R. M., & Sixma, J. J. (1984). Red blood cell deformability influences platelets-vessel wall interaction in flowing blood. Blood, 64, 1228–1233.

6. Karmakar, A., Burgreen, G. W., Rydquist, G., & Antaki, J. F. (2024). A homogenized two-phase computational framework for meso-and macroscale blood flow simulations. Computer methods and programs in biomedicine, 247, 108090.

https://doi.org./10.58225/mpmma.2026.237

THERMO-HYDRAULIC PERFORMANCE ANALYSIS OF PROPYLENE GLYCOL IN A TYPE E SHELL-AND-TUBE HEAT EXCHANGER WITH BAFFLES

Dilek Çağlı Gel , Ahmet Selim Dalkılıç
Yildiz Technical University, Türkiye

Abstract. In this study, with the effect of baffle cut, spacing, tube arrangement, and flow velocities on the heat transfer coefficient of a shell and tube heat exchanger with the aim of optimizing the design parameters. The study is concerned with propylene glycol-water systems and includes thermal calculations and design parameters. One particular case studied is that of cooling propylene glycol from 90°C to 70°C at a flow rate of 55 kg/s with water as coolant. The heat exchanger was of E-type with 364 tubes, nominal diameter 700 mm, tube length 6.6 m. The overall heat transfer coefficient was estimated to be 600 W/(m²°C); it was accepted to be 585.77 W/(m²°C). Baffle design was based on the Kern method with a 500 mm spacing and a 25% cut.

Keywords: Propylene Glycol, Shell-and-Tube Heat Exchanger, Baffle, Heat Transfer Coefficient, Kern, Log-Mean Temperature Difference.

1.Introduction

One of the most common processes encountered in engineering applications is the transfer of heat between two or more fluids at different temperatures. Apparatuses in which this heat exchange occurs are called heat exchangers and are used in many fields, for example, in the chemical industry, thermal power plants, air-conditioning,

heating, and cooling. One of the most common types of heat exchangers is the shell-and-tube heat exchanger (see Fig.1). It consists of a cylindrical shell with a bundle of parallel tubes. One fluid is in the tubes, and the other fluid is on the shell side. The Tubular Exchanger Manufacturers Association (TEMA) [1] governs the design and construction of this type of heat exchanger.

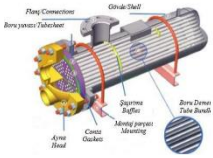
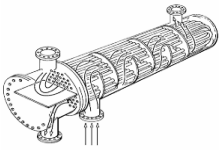


Fig. 1. Shell–and–tube heat exchanger [2].

In this work, propylene glycol is used as a hot fluid and water as a cooling fluid, and design calculations of a shell and tube heat exchanger are performed. Propylene glycol is a viscous, colourless liquid and is almost odourless. It is an alternative to ethylene glycol in antifreeze formulations due to its non-toxic properties [3]. The thermophysical properties of propylene glycol were determined using open sources [4]. The thermal design of the heat exchanger was done by the LTMD [5]. The Kern method [6] is a well-known empirical method for the thermal and hydraulic design of shell and tube heat exchangers



and is widely used in engineering literature.

2.Calculation Procedures

This work considers the cooling of propylene glycol from 90°C to 70°C by using water as a cooling fluid. The mass flow rate of 55 kg/s is taken into consideration. The heat exchanger has 15°C water on the inlet side and 30°C water on the outlet side with propylene glycol flowing on the shell side and water flowing through the tubes. The analysis is performed on a baffled shell and tube heat exchanger. Thermal calculations and design parameters are discussed. For D_i/D_o = 19/25 mm. If u_{water} = 1 m/s, Shah and Sekulic [7], and the number of tubes, n1, is around 176 tubes. "t" is 32 mm. The tube bundle diameter (D_b) constants from [8], respectively.

$Q_{PG}=\dot{m}_{PG}*C_{pPG}*(T_{iPG}-T_{oPG})$ & $Q_{in} + Q_{gen} = Q_{out} + Q_{stor}$ & $t = 1.25xD_o$

$\Delta T_{lm\ Cross} = \frac{\Delta T1 - \Delta T2}{\ln\frac{\Delta T1}{\Delta T2}}$ & $n_1 = \frac{\dot{m}_{wat}}{u_{wat}\rho_{wat}\frac{\pi Di^2}{4}}$ & $D_b = D_o\left(\frac{nt}{K1}\right)^{1/n_1}$

The shell diameter is 700 mm and utilizes 364 tubes arranged on a 32 mm equilateral triangular pitch with a dia. of 25 mm, following Kern's method [6]. The heating surface area was estimated with a total heat transfer coefficient of 600 W/(m²°C) [8]. The velocity of water and fluid in the pipe and shell sides with Reynolds numbers, were calculated. The Nusselt number and heat transfer coefficient for turbulent flow in circular

pipes were using the Dittus-Boelter Equation [9], with the equivalent diameter determined based on the Kern method [6]. (D_G = 680 mm, e = 500 mm). Shell-side heat transfer calculations are generally made using Kern and Bell Delaware methods with a constant baffle cut ratio of 25%. For Kern, the Colburn j-factor is defined as $j_{h,K} = 8 \times 10^{-3}$ and the shell side heat transfer coefficient is calculated by the Kern method [6]. R_f are on the inner and outer surfaces of the pipe were selected from Incropera et al. [5], as $R_f = 2x10^{-4}$ W·m²/°C. The thermal conductivity of steel pipe, if k = 54 W/(m·°C) is taken, is the total heat transfer coefficient K_d. As this value is close to the initially selected value of 600 W/(m²·°C), it is not necessary to repeat the calculations.

$$A = \frac{Q}{\Delta_{tm} * K} \quad \& \quad L = \frac{A}{A_1} \quad \& \quad u_{wat} = \frac{\dot{m}_{wat}}{n_1 \rho wat \frac{\Pi di^2}{4}} \quad \& \quad Re = \frac{\rho_{wat} * u_{wat} * d_i}{\mu_{wat}}$$

$$\& \quad Nu = 0{,}023 * Re^{0,8} * Pr^{0,4} \quad Nu = \frac{hT-side * di}{k} \quad \& \quad d_e = \frac{1{,}10}{D_o}\left(t_1{}^2 - 0{,}917 * D_o{}^2\right) \quad \& \quad A_s = \frac{t_1 - D_o}{t_1}(e * D_G)$$

$$u_{S\text{-}side} = \frac{\dot{m}_{PG}}{\rho pg * As} \quad \& \quad Re_e = \frac{uS-side * d_e}{v} \quad \& \quad Nu = \frac{h_{S-side}\, de}{k} = J_{h,k}\, Re\, Pr^{\frac{1}{3}} \left(\frac{\mu_{80}}{\mu_{0/50}}\right)^{0,14}$$

$$\frac{1}{K_d} = \frac{1}{h_{wat}} \frac{A_d}{A_i} + R_{f1} \frac{A_d}{A_i} + \frac{\ln\left(\frac{r_2}{r_1}\right)}{2\pi L k_1} A_d + R_f + \frac{1}{h_{S-side}}$$

3.Results and Discussion

As a result of the theoretical calculations, the data obtained for the two fluids are presented in Tables 2 and 3. The velocities in the tubes and shell

agreed with literature. The calculated Reynolds numbers (Re > 2300) indicate that the flows are turbulent.

Table 2. The calculated values for the tube side and shell side.

Definition	Unit	Tube-side	Shell-side
Mass Flow (ṁ)	kg/s	49,60	55,00
Ambient Velocity (u)	m/s	1,00	0,75
Reynold & Nusselt Numbers	-	22155,55 &139,43	5285 & 117,3
Convective Heat Transfer Coefficient (h)	$W/m^{2}°C$	4498,71	1125,00
Contamination Factors (R_f)	$m^{2}°C/W$	$2x10^{-4}$	

Table 3. The calculated values for the thermo-hydraulic.

Definition	Unit	Value
Heat Exchanger Heating Surface (A)	m^2	95,01
Heat Exchanger Heating Surface for 1 m (A_1)	m^2	28,60
Selected Total Heat Transfer Coefficient (K_d)	$W/m^{2}°C$	600,00
Accepted Total Heat Transfer Coefficient ($K_{daccep.}$)	$W/m^{2}°C$	585,77
Total Heat Capacity (Q)	W	3111,9
Total Pipe Length (L)	m	6,60
Total Number of Pipes (Qty.)	Pcs.	364
Aver. Logarithmic Temperature Difference (ΔT_{lm})	(°C)	54,587

4.Conclusion

The present work deals with the investigation of the sizing parameters of a shell-and-tube heat exchanger using propylene glycol-water fluids. Propylene glycol is noted for low toxicity and safety for HVAC and industrial applications. The results showed that the heat transfer coefficients were notably different and up to 4 times higher depending on the fluid behavior. The design result gives 364 tubes and an overall heat transfer coefficient of 585.77 W/(m2°C), which proves the effectiveness and applicability of the design parameters. Finally, the calculation procedure for

the shell-and-tube exchanger has been given in this work for the sake of engineers in the industry.

References

1.Standards of TEMA. 10th ed. TEMA, New York (2019).
2. Shravan H. G. et al.: Design and Developm. of STHE for Beverage. MME, 2012.121-125.
3. Wiley-VCH Verlag GmbH & Co.: Ullmann's Enc. of Ind. Chemistry. Wiley, (2000).
4.Green, D. W., & Perry, R. H. (Eds.).: Perry's hb. 8th edn. McGraw-Hill, New York (2008).
5.Incropera, F. P., et al.: Funda. of heat and mass transfer. 7th edn. John Wiley, NJ (2011).
6. Kern, D. Q.: Process heat transfer. McGraw-Hill, New York (1950).
7.Shah, R. K., & Sekulic, D. P.: Funda. of heat ex. design. John Wiley & Sons, NJ (2003).
8.Sinnott, R. K., & Towler, G.: Chemical eng. design: 6th edn. Butter. - H., Oxford (2019).
9.Dittus, F. W., & Boelter, L. M. K.: HT in automo. radiators. Un. of Calif. Pub. CA (1930).

https://doi.org./10.58225/mpmma.2026.249

EQUATION OF STATE AND LIMIT STATE ZONE AT A CRACK TIP IN UNIDIRECTIONAL COMPOSITE LAMINATES

Roland Duduchava[1], *Aleksandr Oleinikov*[1], *Tatiana Kuzmina*[1]

[1] V. Kupradze Institute of Mathematics, University of Georgia, Georgia

Abstract. A new mathematical model of the strength behaviour of a composite is proposed, which is used to assess the size and shape of the fracture process zone near a crack in polymer fibre composites.

Keywords: Composite Laminate, Mathematical Modelling, Equation of State, Fracture Process Zone.

1. Introduction

The linear fracture mechanics crack theory may lose its effectiveness when applied to composites. Indeed, for composite materials, the surface energy predicted by Griffith's criterion is ten times or more than experimentally measured values. Modelling the behaviour of continuous fibre-layered polymer composites within the fracture process zone, therefore, requires an Equation of State (ES) that accounts for the response of the constituent unidirectionally reinforced layers. The present work proposes a formulation of such an ES using conical parametric surfaces derived from the

matrix ES and based on the extremum principle [1, 2].

2.1 Equation of limit state at a crack tip

Equations of limit state and their experimental justification

The ES in the fracture process zone near a crack in polymer fibre composites, which considers the directional nature of failure and the principle of minimal destructive forces [3]:

$$\frac{|\sigma_{21}|}{S_{21}} + \frac{\sigma_{22}}{S_{22}^{\pm}}\left(1 - \mathrm{tg}^2\alpha_{*\perp}^{\pm}\right) = 1 \qquad \text{at} \qquad \left|\frac{\sigma_{21}}{\sigma_{22}}\right| \geq \begin{cases} 2\left|\frac{S_{21}}{S_{22}^{-}}\right| & \text{at } \sigma_{22} < 0 \\ 2\tan^2\alpha_{*\perp}^{+}\left|\frac{S_{21}}{S_{22}^{+}}\right| & \text{at } \sigma_{22} > 0 \end{cases},$$

$$\frac{\sigma_{22}}{S_{22}^{\pm}} + \frac{\sigma_{21}^2}{\sigma_{22}}\frac{S_{22}^{\pm}}{S_{21}^2}\frac{1}{4\mathrm{tg}^2\alpha_{*\perp}^{\pm}} = 1, \qquad \text{at} \qquad \left|\frac{\sigma_{21}}{\sigma_{22}}\right| < \begin{cases} 2\left|\frac{S_{21}}{S_{22}^{-}}\right| & \text{at } \sigma_{22} < 0 \\ 2\tan^2\alpha_{*\perp}^{+}\left|\frac{S_{21}}{S_{22}^{+}}\right| & \text{at } \sigma_{22} > 0 \end{cases},$$

where $S_{22}, S_{21}, \alpha_{*\perp}$ are given strength characteristics.

Experimental verification of the ES and comparison with known ES for 3D stress state, plane stress, and uniaxial tension-compression have been performed [2].

3.Limit state zone at crack tip

3.1Asymptotic solution for the crack

We use asymptotic expansions to study cracks with failure mechanics in composite laminates. The

main term in the asymptotic decomposition of stresses for cracks represents the stress state in the pre-fracture zone in which the fracture process begins.

Based on our ES using the asymptotic solutions for the distribution of the stresses on the crack tip [4], the equations of the limit lines for the orthotropic laminates are obtained.

3.2The fracture process zone for two type cracks and two orientations

Two crack configurations are considered: cracks oriented parallel and orthogonal to the reinforcing fibres. Based on these formulations, the shape and size of the pre-fracture zone near the crack tip are estimated.

4.Comparison with experiment and discussion and conclusion

The theoretical predictions are compared with experimental observations, demonstrating satisfactory agreement between the model and experimental data.

References

1. Oleinikov, A.I.: Strength criterion variants for unidirectional polymer composites by the fracture condition of the inter-fibre when there is compression perpendicular to the fibers. Mech. Of Solids 57, 1740–1748 (2022).

2. Oleinikov, A.I.: Fracture Criteria for Matrix and Fibers in Unidirectional Polymeric Composites at

Static Loadings. Prikladnaâ Matematika I Mehanika 88(2), 255-270 (2024).
3. Oleinikov, A.: Fracture criteria for matrix and fiber in unidirectional polymeric composites. J. of Math. Sci. 290, 722-728 (2025).
4. Sih, G.C., Liebowitz, H.: Mathematical theories of brittle fracture. In: Liebowitz, H. (ed.) Fracture, vol. 2, pp. 67–190. Academic Press, New York (196

https://doi.org./10.58225/mpmma.2026.253

MODELING THE DYNAMICS OF GAS-LIQUID MIXTURES CONSIDERING PHASE TRANSFORMATIONS OF HEAT EXCHANGE WITH THE EXTERNAL ENVIRONMENT

Elkhan Abbasov [1] *Aynur Darishova* [2]
[1] Institute of Mathematics, Azerbaijan
[2] AzUAC

Abstract: This study presents a mathematical model for the flow dynamics of a gas–liquid mixture in a pipeline, taking into account phase transformations and heat exchange with the surrounding environment. The model is based on the conservation laws of mass, momentum, and energy and is used to analyze the influence of operating conditions on temperature and flow characteristics. The results can be applied to improve the efficiency of heating processes and support the design of control systems in oil and gas production.

Keywords: gas-liquid mixture, multiphase flow, phase transformation, heat transfer, environmental heat exchange, mathematical modeling, pipeline dynamics.

1.Introduction

In oil and gas production, it is often necessary to heat a gas-liquid mixture to a specific temperature. This is achieved by passing the gas-liquid mixture through a heater. The gas-liquid mixture enters the heater at a specific temperature, and a specific temperature must be achieved at the outlet. Achieving this goal depends largely on the pressure

and mass flow rate of the gas-liquid mixture, the pipe parameters, and the heating mode. Much research has been devoted to this problem to date. Modeling the flow of a gas-liquid mixture in a pipe must be performed taking into account actual flow conditions.

The development of computational methods has made it possible to significantly expand the possibilities for analyzing the dynamics of gas-liquid flows, taking into account phase transformations and heat exchange with the environment.

The use of computational methods makes it possible to study non-stationary flow regimes, local thermal effects and the influence of external heat exchange on the flow structure.

Therefore, studying the dynamics of fluid flow in a pipe, taking into account heat exchange with the environment, and creating control models for engineering problems is an important task and has both scientific and practical significance.

2. Methodology

The following analysis examines the movement of a gas–liquid mixture in a pipe.

The analysis is based on the following control assumptions:

- The velocity of each phase of the gas-liquid mixture averaged over the cross-section of the pipe;
- We neglect friction between phases;

- The pressure P and temperature T are the same at all points of the pipe cross section;
- The radial component of the gas mixture velocity is neglected.

Within the framework of the accepted assumptions, we will write the heat balance for the control elementary volume of a gas-liquid mixture of length dx.

$$-\frac{\partial(q_g\varphi_1)}{\partial x}-\frac{\partial(q_l(1-\varphi_1))}{\partial x}=c_g\rho_g\varphi_1\frac{\Delta T}{\Delta t}+ c_l\rho_l(1-\varphi_1)\frac{\Delta T}{\Delta t}+\frac{2\alpha}{R}(T-T_c) \qquad (1)$$

On the other hand, according to the generalized Fourier law, we have.

$$q_g = c_g\rho_g V_g T-\lambda_g\frac{\partial T}{\partial x}\ , \qquad (2)$$

$$q_l = c_l\rho_l V_l T-\lambda_l\frac{\partial T}{\partial x}\ , \qquad (3)$$

Substituting expressions (2) and (3) into equation (1) taking into account Henry's law

$$\varphi_1=\varphi_{10}-k(P-P_0) \qquad (4)$$

we get

$$-[\varphi_{10}-k(P-P_0)]\left(c_g T\frac{\partial Q_1}{\partial x}+c_g Q_1\frac{\partial T}{\partial x}-\lambda_g\frac{\partial^2 T}{\partial x^2}\right)-kP\left(c_q Q_1 T-\lambda_g\frac{\partial T}{\partial x}\right)+$$

$$[\varphi_{10} - k(P - P_0)]\left(c_l T\frac{\partial Q_2}{\partial x} + c_l Q_2\frac{\partial T}{\partial x} - \lambda_l\frac{\partial^2 T}{\partial x^2}\right) - \left(c_l Q_2 T - \lambda_l\frac{\partial^2 T}{\partial x^2}\right)k\frac{\partial P}{\partial x} - c_l T\frac{\partial Q_2}{\partial x} - c_l Q_2\frac{\partial T}{\partial x} + \lambda_l\frac{\partial^2 T}{\partial x^2} = \left[c_g\rho_g\left(\varphi_{10} - k(P - P_0)\right) + c_l\rho_l\left(1 - \varphi_{10} + k(P - P_0)\right)\right]\frac{\partial T}{\partial t} + \frac{2\alpha}{R}(T - T_c)$$

(5)

The equation of conservation of mass and momentum without taking into account friction between phases in a steady state will have the form

$$\frac{\partial Q_i}{\partial x} = \frac{D_i}{c_i^2}\frac{\partial P}{\partial x}$$

(6)

$$-\frac{\partial P}{\partial x} = 2aQ_i + V_{i0}\frac{\partial Q_i}{\partial x}$$

(7)

From the system of equations (7) we obtain

$$-\frac{\partial^2 P}{\partial x^2} = 2a\frac{D_i}{c_i^2}\frac{\partial P}{\partial x} + \frac{V_{i0}D_i}{c_i^2}\frac{\partial^2 P}{\partial x^2}$$

(8)

For the gas phase from equation (8) we will have

$$-\left(1 + \frac{V_0 D}{c_1^2}\right)\frac{\partial^2 P}{\partial x^2} = 2a\frac{D}{c_1^2}\frac{\partial P}{\partial x}\ .$$

(9)

Boundary conditions

$$P|_{x=0} = P_1(0),$$

(10)

$$P|_{x=l} = P_2(0), \qquad (11)$$

Integrating (10) applying the boundary conditions (7) and (8), we obtain

$$P = P_1 - \frac{P_1 - P_2}{l} x \qquad (12)$$

$$Q_1 = \frac{P_1 - P_2}{2al} \qquad (13)$$

Applying (12) and (13) in the expression (5) we obtain

$$-\left[\varphi_{10} - k\left(P_1 - \frac{P_1 - P_2}{l} x - P_0\right)\right]\left(c_g \frac{P_1 - P_2}{2al} \frac{\partial T}{\partial x} - \lambda_g \frac{\partial^2 T}{\partial x^2}\right) - k\left(P_1 - \frac{P_1 - P_2}{l} x\right)\left(c_g Q_1 T - \lambda_q \frac{\partial T}{\partial x}\right) + \left[\varphi_{10} - k\left(P_1 - \frac{P_1 - P_2}{l} x - P_0\right)\right]\left(c_l \frac{P_1 - P_2}{2al} \frac{\partial T}{\partial x} - \lambda_l \frac{\partial^2 T}{\partial x^2}\right) + \left(c_l \frac{P_1 - P_2}{2al} T - \lambda_l \frac{\partial^2 T}{\partial x^2}\right) k \frac{P_1 - P_2}{l} - c_l \frac{P_1 - P_2}{2al} \frac{\partial T}{\partial x} + \lambda_l \frac{\partial^2 T}{\partial x^2} = \left[c_g \rho_g \left(\varphi_{10} - k\left(P_1 - \frac{P_1 - P_2}{l} x - P_0\right)\right) + c_l \rho_l \left(1 - \varphi_{10} + k\left(P_1 - \frac{P_1 - P_2}{l} x - P_0\right)\right)\right] \frac{\partial T}{\partial t} + \frac{2\alpha}{R}(T - T_c) \qquad (14)$$

The solution of equation (14) satisfying the boundary conditions will be

$$T = T_1 - \frac{T_1 - T_0}{l} x + \sum_{i=1}^{\infty} \varphi_i(t) \sin \frac{i\pi x}{l} \qquad (15)$$

Substituting expression (15) into equation (14), we multiply both sides of the resulting expression by $\sin \frac{i\pi x}{l}$ and integrate from 0 to l. As a result, we obtain an ordinary differential equation for φ_i. Having determined φ_i, we find the temperature field of the gas-liquid mixture in the pipe using formula (15).

References

1. Shoham, O. (2006). Mechanistic modeling of gas-liquid two-phase flow in pipes. Society of Petroleum Engineers.

2. Carey, V. P. (2008). *Liquid-vapor phase-change phenomena* (2nd ed.). Taylor & Francis.

https://doi.org./10.58225/mpmma.2026.259

MODELING OF FLUID FLOW DYNAMICS IN A COMPLEX-GEOMETRY PIPE CONSIDERING HEAT EXCHANGE WITH THE SURROUNDING ENVIRONMENT

Elkhan Abbasov [1] *Aynur Darishova* [2]
[1] Institute of Mathematics, Azerbaijan
[2] AZUAC, Azerbaijan

Abstract. This paper develops a mathematical model for the unsteady flow of fluids in complex pipelines, taking into account heat exchange with the environment. Based on the proposed model, analytical solutions were obtained describing the thermohydrodynamic behavior of the flow. The model takes into account the temperature dependence of viscosity and various thermal conditions in individual sections of the pipeline.

Keywords:complex profile pipelines, unsteady flow, heat transfer, temperature-dependent viscosity, Laplace transform, thermohydrodynamic modeling.

1.Introduction

Transporting liquids through pipelines plays a vital role in the oil and gas, chemical, and energy industries. In real-world conditions, fluid flow is accompanied by heat exchange with the surrounding environment, which affects density, viscosity, pressure distribution, and flow stability. This is especially correct for complex pipelines, including offshore and subsea systems, where different sections operate under varying temperature conditions. Modern computational fluid dynamics methods allow for detailed study of

such processes, but they require significant computational resources.

Therefore, a pressing task is to develop simplified, yet physically sound mathematical models that take into account the influence of heat exchange while maintaining the possibility of an analytical solution. This paper examines the movement of fluid in a complex pipeline consisting of three sections with different thermal conditions. For each section, fluid flow is analyzed separately, with subsequent reconciliation of solutions at the section boundaries. Analytical methods, including linearization and the Laplace transform, are used to solve the equations. The proposed approach enables the creation of an effective tool for engineering calculations for the transportation of oil, gas, and gas-liquid mixtures in offshore environments.

2. Methodology

Let us make the following simplifying assumptions.

- The fluid flow velocity is averaged over the pipe cross-section.
- The pressure P is the same at all points in the fluid cross-section.
- The radial component of the fluid flow particle velocity is neglected.
- The fluid flow particle temperature is averaged over the pipe cross-section.

Within the framework of the accepted assumptions, the equations of motion and continuity will have the form

$$-\frac{\partial P}{\partial x} = \frac{\partial Q}{\partial t} + V_0 \frac{\partial Q}{\partial x} + 2a(T)Q \ ,$$

$$-\frac{1}{c^2}\frac{\partial P}{\partial t} = \frac{\partial Q}{\partial x}$$

(1)

Where $Q = \rho V$; ρ -liquid density; P - pressure.
If, as a first approximation, we assume that the heat flow into the liquid is linear and stationary, then $T = T(x)$.
Hence $a = a(x)$.
Differentiating both parts of the first equation (1) then x, and the second by t and subtracting one from the other we get

$$\frac{\partial^2 P}{\partial t^2} = c^2 \frac{\partial^2 P}{\partial x^2} - c^2 V_0 \frac{\partial^2 Q}{\partial x^2} + 2ac^2 \frac{\partial Q}{\partial x} + 2c^2 \frac{\partial a}{\partial x} Q_0 \ .$$

(2)

From the second equation of system (1) we have

$$\frac{\partial^2 Q}{\partial x^2} = -\frac{1}{c^2}\frac{\partial^2 P}{\partial x \partial t}. \quad (3)$$

From equation (2), taking into account the second equation (1) and expression (3), linearizing it, we obtain

$$\frac{\partial^2 P}{\partial t^2} = c^2 \frac{\partial^2 P}{\partial x^2} - V_0 \frac{\partial^2 P}{\partial x \partial t} - 2a \frac{\partial P}{\partial t} + 2c^2 \frac{\partial a}{\partial x} Q_0.$$

(4)

where, as a first approximation, following Osean, it is accepted as

$$Q = Q_0 = \rho V_0.$$

Initial and boundary conditions

$$P|_{t=0} = f(x), \ \ 0 < x < l \quad (5)$$

$$\left.\frac{\partial P}{\partial t}\right|_{t=0} = 0, \;\; 0 < x < l \tag{6}$$

$$P|_{x=0} = P_1(t), \;\; t > 0 \tag{7}$$

$$P|_{x=l} = P_2(t), \;\; t > 0 \tag{8}$$

where $f(x)$ - known function.

We will seek a solution to equation (4) satisfying the boundary conditions (7) and (8) in the form

$$P = P_1(t) - \frac{P_1(t)-P_2(t)}{l}x + \sum_{i=1}^{\infty}\varphi_i(t)sin\frac{i\pi x}{l}. \tag{9}$$

where $\varphi_i(t)$ unknown time-dependent function t.

Applying the Laplace transform from expression (19) we obtain:

$$\bar{\varphi}_i = \frac{S\varphi_0}{(S+h)^2+w^2} + \frac{\dot{\varphi}_0}{(S+h)^2+w^2} + \frac{2h\varphi_0}{(S+h)^2+w^2} - \frac{\frac{2}{i\pi}\left(\bar{\bar{P}}_{bx} - \bar{\bar{P}}_2(-1)^2\right)}{(S+h)^2+w^2} + \frac{V_0\frac{2}{i\pi}\frac{\overline{\vec{P}_{\text{вх}}} - \overline{\vec{P}_2}}{l}(1-(-1)^i)}{(S+h)^2+w^2} - \frac{\frac{32}{d^2}\frac{2}{i\pi}\left[(1-(-1)^i)\vartheta_T + \frac{\left(T_0+\frac{T_0-T_c}{\alpha_0 l}-T_{\text{вх}}\right)\alpha_0 - \frac{T_0-T_c}{l}}{T_{\text{вх}}-T_2}l(-1)^i(\vartheta_T-\vartheta_0)\right]\cdot\overline{\vec{P}_{\text{вх}}}}{(S+h)^2+w^2} + \frac{\frac{32}{d^2}\frac{2}{i\pi}\left(\overline{\vec{P}_{\text{вх}}} - \bar{\bar{P}}_2\right)\left\{\vartheta_T(-1)^i - \frac{\left(T_0+\frac{T_0-T_c}{\alpha_0 l}-T_{\text{вх}}\right)\alpha_0 l - T_0 + T_c}{T_{\text{вх}}-T_2}(\vartheta_T-\vartheta_0)\left[(-1)^i + \frac{2}{i^2\pi^2}(1-(-1)^i)\right]\right\}}{(S+h)^2+w^2} - c^2Q_0\frac{32}{d^2}\frac{2}{i\pi}\frac{\frac{\left(T_0+\frac{T_0-T_c}{\alpha_0 l}-T_{\text{вх}}\right)\alpha_0 - \frac{T_0-T_c}{l}}{T_{\text{вх}}-T_2}(\vartheta_T-\vartheta_0)\cdot(1-(-1)^i)}{S[(S+h)^2+w^2]} \tag{10}$$

where $\omega^2 = \vartheta_i^2 - h^2$; $\vartheta_i^2 = \frac{c^2 i^2 \pi^2}{l^2}$;

$$2h = \frac{32}{d^2}\left[\vartheta_T - \frac{\left(T_0 + \frac{T_0 - T_c}{\alpha_0 l} - T_{\text{вх}}\right)\alpha_0 - \frac{T_0 - T_c}{l}}{T_{\text{вх}} - T_2}(\vartheta_T - \vartheta_0)\right] - \frac{l}{2}\left[1 + \frac{1}{i^2\pi^2}(1 - (-1)^i)\right]$$

Applying the Laplace transform from the expression we obtain

$$\bar{P} = \bar{P}_{\text{вх}} - \frac{\bar{P}_{\text{вх}} - \bar{P}_2}{l}x + \sum_{i=1}^{\infty}\bar{\varphi}_i \sin\frac{i\pi x}{l}. \qquad (11)$$

From the first equation of system (1), taking into account expression (11), applying the Laplace transform, we obtain

$$-\frac{\partial \bar{P}}{\partial x} = \bar{Q}S - Q(0,x) - \frac{V_0}{c^2}\frac{\partial \bar{P}}{\partial t} + 2a\bar{Q} \qquad (12)$$

From equation (12) we obtain

$$\bar{Q} = \frac{Q(0,x)}{S+2a} - \frac{1}{S+2a}\frac{\partial \bar{P}}{\partial x} + \frac{V_0}{c^2}\frac{\bar{P}S - P(0,x)}{S+2a} \qquad (13)$$

Applying the inversion and convolution theorems, passing to the original from expression (13), we obtain

$$Q = Q(0,x)e^{-2at} - \int_0^t \frac{\partial P(\tau,x)}{\partial x}e^{-2a(t-\tau)}d\tau + \frac{V_0}{c^2}\int_0^t \frac{\partial P(\tau,x)}{\partial t}e^{-2a(t-\tau)}d\tau \qquad (14)$$

Conclusion

This paper develops an analytical model of unsteady fluid flow in a complex pipeline, taking into account heat transfer and the temperature dependence of viscosity. Analytical expressions are derived for determining the pressure and mass flow rate of the fluid over a given coordinate and time.

The resulting simplified model adequately describes the fundamental physical processes while maintaining low computational complexity. The proposed approach can be applied to engineering calculations and preliminary analyses of hydrodynamic processes in main and offshore pipelines as an effective alternative to CFD modeling.

References

1. Charny I.A. Unsteady motion of a real fluid in pipes. Moscow: Nedra, 1975, p.224
2. Zheng X.,Wang Z.,Triantafyllou M.S.,Karniadakis G.E. Fluid-structure interactions in a flexible pipe conveying two-phase flow.International Journal of Multiphase Flow, 2021, 141, 103667.
3. Anjun Liu, Jie Chen, Chao Yang, Zaisha Mao. Simulation of two-phase flow and mass transfer with deformable interface. Scientia sinica Physica, Mechanica &Astronomica. Vol.47, issue7: 070009 (2017) Fluid Mechanics
4. Ishii M., Hibiki T. Thermo-Fluid Dynamics of Two-Phase Flow. Springer, 2011.

https://doi.org./10.58225/mpmma.2026.265

ON QUALITATIVE PROPERTIES OF A FOURTH-ORDER NONLINEAR WAVE EQUATION WITH INTERNAL DISSIPATION AND NONLINEAR BOUNDARY DAMPING

Elchin Mamedov[1 2]

[1] Baku State University, Azerbaijan

[2] Institute of Mathematics, Azerbaijan

Abstract. We investigate a fourth-order nonlinear wave equation with internal dissipation and nonlinear boundary damping. The model includes a biharmonic operator, strong damping, and nonlinear feedback terms acting both in the domain and on the boundary. Using semigroup theory combined with energy methods, we establish the well-posedness of weak solutions. Furthermore, we construct a suitable Lyapunov functional and prove exponential decay of the total energy. The results demonstrate that the combination of internal and boundary damping ensures strong stabilization of the system..

Keywords: Fourth-order wave equation nonlinear boundary conditions strong damping energy decay global existence stability.

1 Introduction

Fourth-order evolution equations appear in elasticity theory, plate vibration models, and continuum mechanics. The qualitative behavior of such equations, especially in the presence of damping mechanisms, has been extensively studied in recent years[2-6]. We consider the following initial-boundary value problem:

$$u_{tt}(x,t) + \Delta^2 u(x,t) + \alpha u_t(x,t) - \delta \Delta u_t(x,t) + f(u(x,t)) = 0,\ x \in \Omega,\ t > 0, \quad (1)$$

where $\Omega \subset \mathbb{R}^n$ is a bounded domain with smooth boundary Γ, and $\alpha, \delta > 0$.

The system is subject to nonlinear boundary damping of the form

$$\frac{\partial(\Delta u)}{\partial \nu} + g(u_t) = 0, \quad x \in \Gamma, \ t > 0. \qquad (2)$$

Initial conditions are given by

$$u(x,0) = u_0(x), \quad u_t(x,0) = u_1(x), \quad x \in \Omega. \qquad (3)$$

2 .Functional Setting and Energy

Let $H = L^2(\Omega)$ and define the energy space

$$\mathcal{H} = H_0^2(\Omega) \times L^2(\Omega).$$

We assume that nonlinear functions f and g satisfy:

$$f(s)s \geq 0, \qquad (g(s) - g(r))(s - r) \geq 0.$$

Define the energy functional

$$E(t) = \frac{1}{2} \| u_t(t) \|^2 + \frac{1}{2} \| \Delta u(t) \|^2 + \int_\Omega F(u)dx, \qquad (4)$$

where

$$F(s) = \int_0^s f(\tau)\, d\tau.$$

Multiplying the equation by u_t and integrating over Ω, we obtain the energy identity

$$\frac{d}{dt} E(t) + \alpha \| u_t \|^2 + \delta \| \nabla u_t \|^2 + \int_\Gamma g(u_t)u_t \, d\Gamma = 0. \qquad (5)$$

Hence, the energy is non-increasing:

$$E(t) \leq E(0), \quad t \geq 0.$$

3. Well-Posedness

We rewrite the system in abstract form:

$$U_t = \mathcal{A}U + \mathcal{F}(U), \quad U = (u, u_t).$$

The linear operator $\mathcal{A}$ is shown to be maximal dissipative in $\mathcal{H}$,following the semigroup approach commonly used in nonlinear evolution equation[1,2] By the Lumer–Phillips theorem, it generates a C_0-semigroup of contractions[2].

The nonlinear operator $\mathcal{F}$ is locally Lipschitz in $\mathcal{H}$. Therefore, a unique local weak solution exists. Global existence follows from the a priori energy estimate and standart compactness arguments developed in the theory of nonlinear evolution equations [3,4]

Theorem 1. For every initial data $(u_0, u_1) \in \mathcal{H}$, there exists a unique global weak solution

$$u \in C([0,\infty); H_0^2(\Omega)), \quad u_t \in C([0,\infty); L^2(\Omega)).$$

4 .Asymptotic Behavior

To study stability, we construct a Lyapunov functional using techniques inspired by the stabilization theory of dissipative systems[2,3].

$$L(t) = E(t) + \varepsilon\Phi(t),$$

where $\Phi(t)$ is an auxiliary functional. Under suitable assumptions on f and g, one obtains

$$\frac{d}{dt}L(t) \le -cL(t), \tag{6}$$

for some $c > 0$. Thus,

$$L(t) \le L(0)e^{-ct}.$$

Theorem 2. The energy of solutions decays exponentially:

$$E(t) \le CE(0)e^{-\omega t}, \quad t \ge 0.$$

5 Conclusion

We studied a fourth-order nonlinear wave equation with internal dissipation and nonlinear boundary damping. The system is shown to be globally well-posed and exponentially stable. The results confirm that combined damping mechanisms lead to strong energy decay and stabilization of solutions, extending ideas developed in the literature on oundary stabilization and nonlinear damping [5,6].

References

1. J.-L. Lions, Quelques méthodes de résolution des problèmes aux limites non linéaires, Dunod, Paris (1969).
2. A. Pazy, Semigroups of Linear Operators and Applications to Partial Differential Equations, Springer (1983).
3. Lasiecka, I. and Triggiani,R. Control Theory for Partial Differential Equations, Cambridge University Press (2000).
4. Temam,R.: Infinite-Dimensional Dynamical Systems in Mechanics and Physics, Springer (1997).
5. Haraux, A.: Nonlinear Evolution Equations: Global Behavior of Solutions. Springer, Berlin (1981).
6. Lasiecka, I., Tataru, D.: Uniform boundary stabilization of semilinear wave equations with nonlinear boundary damping. Differential and Integral Equations 6(3), 507–533 (1993).
7. Vitillaro, E.: Global existence for the wave equation with nonlinear boundary damping and

source terms. Journal of Differential Equations 186, 259–298 (2002)

https://doi.org./10.58225/mpmma.2026.270

COMPARATIVE EVALUATION OF QUANTUM-INSPIRED METAHEURISTICS FOR WELDED BEAM DESIGN OPTIMIZATION

Elif Demir, Yusuf Zeren, Alpaslan Demirci
Yıldız Technical University, Türkiye

Abstract. This paper provides a compact comparison of classical and quantum-inspired metaheuristics for the constrained welded beam design problem. Grey Wolf Optimizer (GWO), Quantum-Inspired Grey Wolf Optimizer (QGWO), Particle Swarm Optimization (PSO), and Quantum-behaved Particle Swarm Optimization (QPSO) are evaluated over 30 independent runs under standard and robust load scenarios. The results show that all methods reach feasible designs, while QGWO gives the most stable average performance. PSO and QPSO can reach near-best objective values rapidly, but their larger variability reduces repeatability. Overall, the comparison suggests that quantum-inspired search is useful for engineering design when solution quality, feasibility, and convergence behavior are considered together.

Keywords: Quantum-inspired metaheuristics, Grey Wolf Optimizer, QPSO, constrained optimization, welded beam design, convergence analysis.

1 Introduction

Engineering design optimization problems are commonly nonlinear, constrained, and multimodal, which makes derivative-based optimization difficult to apply directly. Metaheuristic algorithms are therefore widely used because they can explore

complex search spaces without gradient information. Quantum-inspired variants extend this search behavior through probabilistic representation, quantum encoding, and rotation-like update mechanisms designed to preserve diversity and reduce premature convergence [1]. Recent applications report benefits of quantum-inspired search in forecasting, parameter identification, feature selection, and prediction tasks [2]-[4]. Nevertheless, constrained engineering design requires more than a best-case solution: average performance, feasibility, repeatability, and convergence behavior must also be examined. This study uses the welded beam benchmark to compare GWO, QGWO, PSO, and QPSO under identical population, iteration, and independent-run settings. The aim is not to claim a single universal winner, but to identify how quantum-inspired mechanisms affect solution quality and robustness across GWO- and PSO-based families.

2 Problem and Method

The welded beam design problem minimizes fabrication cost using four variables: weld thickness, weld length, beam height, and beam width. The nominal case uses P = 6000 lb, while the robust case evaluates each candidate design under P = {6000, 6300, 6600} lb. Standard stress, deflection, buckling, and geometric constraints are enforced through a quadratic exterior penalty, and feasibility is accepted only within the prescribed tolerance.

QGWO follows the formulation of Gao et al. [5], preserving GWO's alpha–beta–delta leadership while updating normalized quantum positions through a rotation-gate-inspired rule. The updated positions are then mapped back to the continuous design space, adding smoother probabilistic movement to the leader-guided search. GWO, QGWO, PSO, and QPSO are compared under identical settings: 30 runs, population size 40, 400 iterations, penalty coefficient 1.0e7, and feasibility tolerance 1.0e-5. Performance is assessed using best, mean, standard deviation, feasibility rate, runtime, and convergence behavior.

3 Results

Due to the page limitation, Table 1 reports the standard-scenario analysis results, while the robust scenario is retained only as a brief interpretation. In the standard case, PSO and QPSO reach the best objective value of approximately 1.7249, essentially matching the known reference value. However, In the standard case, PSO and QPSO reach the best objective value of approximately 1.7249, essentially matching the known reference value. However, QGWO gives the most reliable average behavior, with a mean of 1.7273 and a standard deviation of 0.0030. This improves on classical GWO and is substantially more stable than the particle-based methods. All algorithms satisfy the feasibility requirement in all 30 runs.

Table 1. Standard-scenario optimization performance over 30 independent runs.

g.	est	ean	d.	as.	untime (s)
WO	7264	7304	0034	0%	1608
GWO	7253	7273	0030	0%	2095
O	7249	8180	1354	0%	1501
PSO	7249	9028	2808	0%	1567

In the robust multi-load scenario, PSO and QPSO again reached the best individual objective value around 1.8563, whereas QGWO achieved the lowest mean value among the compared methods (1.8600) with the narrowest dispersion. This confirms the standard-scenario trend: particle-based methods are effective for rapid best-case search, while QGWO provides more repeatable average performance under load variation. Figure 1 shows that PSO improves rapidly in the early iterations, and QPSO also has strong exploratory potential. The same behavior explains their competitive best-case values. QGWO, by contrast, converges more gradually but produces tighter final distributions and lower average objective values. Thus, QPSO remains important as a fast exploration baseline, while QGWO provides the best balance of quality and consistency in this experiment.

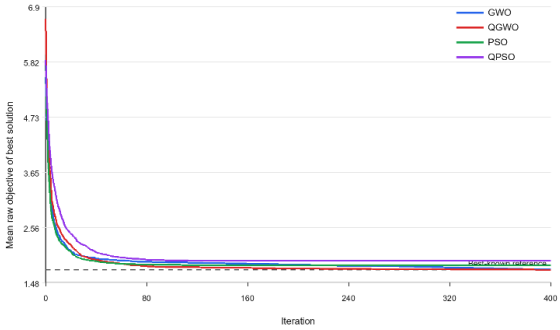


Fig. 1. Mean objective convergence for the compared algorithms in the standard welded beam scenario.

4 Conclusion

This study compared classical and quantum-inspired metaheuristics on the welded beam design benchmark under standard and robust loading conditions. All algorithms reached feasible designs, while QGWO provided the most stable average performance with low mean objective values and narrow dispersion. PSO and QPSO rapidly approached near-reference best values, but their higher variability reduced repeatability. These results suggest that quantum-inspired mechanisms can be useful in constrained design optimization when feasibility, robustness, and convergence behavior are evaluated together. However, because the study is limited to a single benchmark, the findings should not be interpreted as a universal algorithm ranking. Future work should extend the comparison to additional engineering benchmarks

and investigate hybrid strategies combining QPSO's fast exploration with QGWO's stable convergence.

References

1. Gharehchopogh, F. S. (2023). Quantum-inspired metaheuristic algorithms: Comprehensive survey and classification. Artificial Intelligence Review, 56, 5479-5543. https://doi.org/10.1007/s10462-022-10280-8

2. Guo, Y., Xu, Y.-P., Sun, M., & Xie, J. (2021). Multi-step-ahead forecast of reservoir water availability with improved quantum-based GWO coupled with the AI-based LSSVM model. Journal of Hydrology, 597, 125769. https://doi.org/10.1016/j.jhydrol.2020.125769

3. Huang, G., Qin, F., Zhao, Y., Li, W., & Li, Z. (2025). Quantum-inspired grey wolf optimizer for rapid lithium-ion battery parameter identification in electric vehicles. Journal of Energy Storage, 136, 118425. https://doi.org/10.1016/j.est.2025.118425

4. Zhao, G., Wang, H., Jia, D., & Wang, Q. (2019). Feature selection of Grey Wolf Optimizer based on quantum computing and uncertain symmetry rough set. Symmetry, 11, 1470. https://doi.org/10.3390/sym11121470

5. Gao, H., Li, J., & Diao, M. (2018). Direction finding of bistatic MIMO radar based on quantum-inspired grey wolf optimization in the impulse noise. EURASIP Journal on Advances in Signal Processing, 2018, 75. https://doi.org/10.1186/s13634-018-0595-z

https://doi.org./10.58225/mpmma.2026.276

A COMPOSITE FRACTIONAL-INTEGRAL INSPIRED NONLOCAL LOSS FUNCTION FOR IMAGE DENOISING

Elif Demir[1],*Yusuf Zeren*[1], *Mehmet Zeki Sarıkaya*[2] , *Alpaslan Demirci*[1]

[1]Yıldız Technical University, Türkiye

[2]Düzce University, Türkiye

Abstract. Image denoising aims to recover a clean image from noisy observations while preserving structural and edge information. Classical pixel-wise losses, particularly mean squared error (MSE), are effective for noise reduction; however, their local structure may fail to capture nonlocal residual interactions and may cause oversmoothing. Motivated by this limitation, this study proposes a Sarıkaya-type composite fractional-integral inspired nonlocal loss for single-image denoising. The proposed approach does not apply the Sarıkaya operator directly as an image processing method; instead, it transfers its composite, nonlocal, and Green-kernel-based structure to the residual domain as an additional regularization term. The total loss combines the classical MSE loss with the proposed residual penalty. Preliminary experiments on a noisy Set12 image show that the method achieves PSNR and SSIM values close to the MSE baseline while reducing the edge-based error. These results suggest that Sarıkaya-type composite fractional-integral structures may provide a promising mechanism for nonlocal residual regularization in deep image restoration.

Keywords: Fractional integral operator, Composite fractional operator, Image denoising, Deep learning, Nonlocal regularization, Loss function.

1.Introduction

Image denoising is a classical inverse problem in image processing and computer vision. Deep learning-based denoising models have achieved remarkable performance by learning mappings from noisy images to clean targets [1]. However, commonly used pixel-wise losses, such as the mean squared error (MSE), mainly minimize local errors and may therefore fail to capture nonlocal dependencies in the residual domain. This limitation can lead to oversmoothing, especially around edges, textures, and structural details. Motivated by this issue, we propose a Sarıkaya-type composite fractional-integral inspired nonlocal residual regularization term. Fractional calculus provides a useful mathematical framework for modeling memory effects and nonlocal interactions, and it has recently attracted attention in optimization and learning-based problems [2,4]. In this study, the proposed loss is inspired by Sarıkaya-type composite fractional integral operators, which combine left- and right-sided nonlocal effects through a Green-type kernel [3]. We do not use these operators directly as image processing filters; instead, we transfer their composite nonlocal structure to the residual

domain. The resulting formulation augments the classical MSE loss with a Green-kernel-based residual penalty, aiming to support edge-related structural preservation while maintaining stable denoising performance.

1.1 Proposed Framework

Let y denote the clean target image and $\hat{y}$ denote the output of the denoising network. The residual image is defined as

$$r = \hat{y} - y.$$

Classical MSE-based denoising mainly minimizes the pixel-wise difference between $\hat{y}$ and y. Although this is effective for noise reduction, it does not explicitly model nonlocal interactions among residual components and may limit the preservation of edge and structural details. To address this limitation, we introduce a Sarıkaya-type composite fractional-integral inspired regularization term in the residual domain. The total loss is defined as

$$L = L_{MSE} + \lambda L_{Sarikaya},$$

where $\lambda > 0$ controls the contribution of the nonlocal term. Here, L_{MSE} is the classical reconstruction loss, while $L_{Sarikaya}$ is a residual-domain penalty inspired by the Green-kernel-based structure of Sarıkaya-type composite fractional integral operators [3]. The Sarıkaya operator is not directly used as an image denoising filter. Instead, its composite left-right nonlocal structure is used as a mathematical inspiration for designing a residual

regularization mechanism. Thus, the proposed loss combines the simplicity of MSE with a nonlocal penalty aiming to support edge-related structural preservation.

1.2 Preliminary Results

Preliminary experiments were performed on a noisy Set12 image with additive Gaussian noise. The proposed Sarıkaya-inspired model achieved PSNR and SSIM values close to the MSE baseline while producing a lower edge-based error. This suggests that the proposed nonlocal residual regularization may provide additional structural support in edge-sensitive regions rather than primarily improving global pixel-wise fidelity.



Fig. 1. Visual comparison of denoising results from left to right: clean image, noisy image with additive Gaussian noise, MSE-based denoised image, and the proposed Sarıkaya-inspired denoised image.



Fig. 2. Training loss comparison of the MSE baseline and Sarıkaya-inspired model, showing stable convergence with an additional nonlocal regularization effect.

2. Conclusion

This study introduced a Sarıkaya-type composite fractional-integral inspired nonlocal loss framework for image denoising. Instead of directly applying the Sarıkaya operator to the image, the proposed method transfers its composite, nonlocal, and Green-kernel-based structure to the residual domain as an additional regularization term. Combined with the classical MSE loss, this formulation aims to address the local pixel-wise limitation of conventional denoising objectives and support edge-related structural preservation. Preliminary results on a noisy Set12 image show PSNR and SSIM values close to the MSE baseline, together with a lower edge-based error. Future work will extend the experiments to larger benchmark datasets and compare the proposed

method with robust, fractional, and edge-aware loss functions.

References

1. Jiang, B., Li, J., Lu, Y., Cai, Q., Song, H., & Lu, G. (2025). Efficient image denoising using deep learning: A brief survey. *Information Fusion, 118*, 103013. https://doi.org/10.1016/j.inffus.2025.103013

2. Fernandez, E., Huilcapi, V., Birs, I., & Cajo, R. (2025). The role of fractional calculus in modern optimization: A survey of algorithms, applications, and open challenges. *Mathematics, 13*(19), 3172. https://doi.org/10.3390/math13193172

3. Alqahtani, R. T., & Sarikaya, M. Z. (2026). Lyapunov-Type and Hartman–Wintner-Type Inequalities for a Class of Composite Fractional Integral Operators. *Fractal and Fractional*, *10*(5), 323. https://doi.org/10.3390/fractalfract10050323

4. Kurucu, M. C., Güzelkaya, M., Eksin, I., & Kumbasar, T. (2025). When fractional calculus meets robust learning: Adaptive robust loss functions. Knowledge-Based Systems, 312, 113136. https://doi.org/10.1016/j.knosys.2025.113136

https://doi.org./10.58225/mpmma.2026.*282*

ARTIFICIAL INTELLIGENCE AND DIGITAL TWIN FRAMEWORK FOR HAZARDOUS BUILDINGS ASSESSMENT

Imamaliyev Elman [1], Mirzeyeva Fatima[2]
[1]Azerbaijan Technical University, Azerbaijan
[2]AzUAC, Azerbaijan

Abstract. This study proposes an integrated framework for assessing hazardous buildings using Building Information Modeling (BIM), Digital Twin technologies, and artificial intelligence (AI). The approach combines multimodal ,data—UAV imagery, LiDAR scans, satellite observations, and sensor inputs—with machine learning models such as CNNs and Vision Transformers. Through real-time monitoring and predictive simulation, the system enables automated hazard classification (H0–H4) and supports emergency response and structural safety planning. The results demonstrate that multimodal fusion and transfer learning significantly enhance accuracy and efficiency, providing engineers and policymakers with a robust tool for risk management and urban resilience.

Keywords: Hazardous buildings; BIM; Digital Twin; LiDAR; Multimodal fusion; Transfer learning.

1. Introduction

Urban areas often contain hazardous buildings that pose risks due to structural degradation, poor materials, or seismic vulnerability. Traditional inspection methods are slow, unsafe, and resource-intensive. Recent advances in BIM and Digital Twin technologies provide digital environments for integrating design data with real-time monitoring. AI methods, particularly computer vision, enable automated detection of cracks, collapses, and material weaknesses. The novelty of this research is the integration of BIM/Digital Twin with multimodal AI-based analysis, enabling real-time monitoring and predictive modeling of hazardous buildings. Unlike isolated approaches, this framework unifies UAV/LiDAR imagery, sensor data, and engineering models into a single analytical environment.

2. Methodology

The proposed framework for Hazardous buildings assessing integrates Building Information Modeling (BIM), Digital Twin technologies, and artificial intelligence (AI) into a unified analytical system. BIM serves as the foundation, providing static information about architectural design, construction phases, and material properties. This digital model is then extended into a Digital Twin, which incorporates real-time data streams from sensors measuring vibration, strain, and temperature, as well as UAV imagery and LiDAR scans that refine the geometric accuracy of the structure. The Digital

Twin thus becomes a dynamic representation of the hazardous building, capable of simulating stress responses and predicting potential failure points.

Data acquisition is multimodal, combining UAV-based high-resolution imagery, LiDAR point clouds, satellite observations, and continuous sensor measurements. These heterogeneous datasets are synchronized within a cloud platform to ensure consistency and accessibility. Artificial intelligence models are then applied to this integrated dataset. Convolutional Neural Networks (CNNs) are employed for local crack detection and roof collapse identification, while Vision Transformers (ViT) capture global dependencies across large-scale UAV and satellite imagery. Transfer learning techniques allow pre-trained models to be adapted to hazardous building datasets with limited labels, and domain adaptation ensures that models remain effective across different architectural contexts and geographic regions.

The analytical process relies on multimodal data fusion at three levels. At the data level, LiDAR point clouds are merged with RGB imagery to generate textured three-dimensional models. At the feature level, CNN-extracted visual features are combined with thermal anomalies to confirm hidden cracks and material fatigue. At the decision level, sensor alerts are integrated with image analysis to produce a comprehensive hazard classification. Hazard levels are defined on a five-point scale (H0–

H4), ranging from safe conditions to imminent collapse. Classification is achieved through machine learning-based scoring that combines image segmentation, sensor thresholds, and simulation outputs.

Finally, the framework is validated against international standards such as EMS-98 and FEMA hazard classification guidelines. Performance metrics include precision, recall, F1-score, and intersection-over-union (IoU) for segmentation tasks, as well as the accuracy of hazard classification compared to expert engineering assessments. This methodology ensures that the system not only automates the detection of hazardous buildings but also provides reliable, standardized outputs that can be directly applied in emergency response, repair planning, and urban safety management.

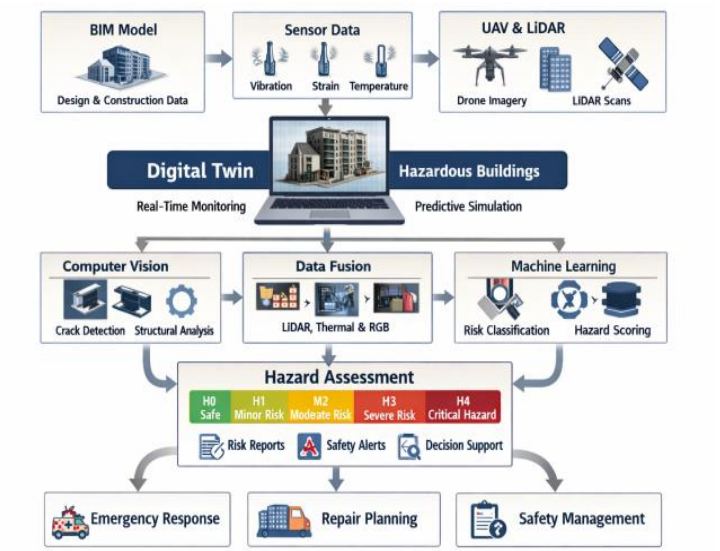


Figure 1. Integrated Framework for Hazardous Building Assessment Using BIM, Digital Twin, and Artificial Intelligence

3. Results and Discussion

The framework demonstrates: Accuracy: multimodal fusion improves detection reliability; Efficiency: UAV-based inspection reduces time and risk; Scalability: AI enables rapid assessment of thousands of hazardous buildings; Predictive capability: Digital Twin simulations forecast seismic and wind responses. Results align with EMS-98 and FEMA standards. Transfer learning reduces training time, and domain adaptation ensures applicability across diverse regions.

4. Conclusion

This study presents a novel analytical framework that integrates BIM, Digital Twin, and AI-based multimodal fusion for hazardous building assessment. The approach provides real-time, scalable, and predictive analysis, enabling accurate hazard classification and supporting decision-making in emergency response, repair optimization, and urban safety planning.

The novelty of this study — integrating BIM, Digital Twin, and AI into a unified framework for hazardous building assessment — carries direct practical importance. Unlike conventional inspection methods, the proposed system enables **real-time hazard detection** and **predictive simulation**, reducing the need for risky manual surveys. Emergency agencies can prioritize resources more effectively, while engineers gain a tool for **component-level diagnosis** that supports targeted reinforcement and repair. Urban planners and policymakers benefit from **transparent risk maps** that guide investment decisions and safety regulations. By combining multimodal data fusion with machine learning, the framework transforms hazardous building management from reactive inspection into **proactive, data-driven safety planning**, ensuring resilience in disaster-prone regions.

References

1. Akhavian, R., Amani, M., Mootz, J., Ashe, R., Beheshti, B.: Building Information Models to Robot-Ready Site Digital Twins (BIM2RDT): An Agentic AI Safety-First Framework. *arXiv preprint* arXiv:2401.12345 (2024).
2. Zhang, Y., Li, H., Wang, J.: Construction Site Risk Assessment Through Digital Twins for Safety Management. *Automation in Construction* 152, 104876 (2024).
3. Chen, L., Kumar, S., Patel, R.: AI-Driven Risk Management and Digital Twin Integration for Hazardous Buildings. In: Proceedings of the International Conference on Structural Safety and Reliability, pp. 211–220. Springer, Heidelberg (2023).
4. Smith, T., Johnson, P., Lee, D.: Digital Twin and BIM-Based Hazardous Building Monitoring. In: 9th International Symposium on Disaster Risk Reduction, pp. 55–62. Elsevier, Amsterdam (2022).
5. MDPI Buildings Special Issue Homepage: Next-Gen Risk Management: AI-Driven Digital Twin Applications, https://www.mdpi.com/journal/buildings/special_issues/AI_DigitalTwin (mdpi.com in Bing), last accessed 2026/05/31.
6. Qasimov Z.A, Imamaliyev E.B. The Role of Artificial Intelligence in Robot Technologies.

ITTA 2026(3rd International Conference on Information Technologies and their Application). Baku, Azerbaijan, (2026)

https://doi.org./10.58225/mpmma.2026.290

INVESTIGATION OF THE EFFECT OF CORRUGATION DEPTH ON HEAT TRANSFER PERFORMANCE IN SPHERICAL CORRUGATED PIPES

Eray Karakaser, Safak Metin Kirkar, Ahmet Selim Dalkilic,
Yıldız Technical University, Türkiye

Abstract. This study numerically investigates the effect of corrugation depth on the heat transfer performance of spherical corrugated pipes under a constant wall temperature. Using Computational Fluid Dynamics (CFD). The flow and thermal characteristics were analyzed across various Reynolds numbers to determine the optimal geometry that maximizes heat transfer. The results show that increasing the corrugation depth directly enhances fluid turbulence and the overall heat transfer coefficient. These findings offer practical guidance for designing more energy-efficient industrial heat exchangers.

Keywords: Corrugated Depth, Computational Fluid Dynamics (CFD), Helical Corrugated Pipe

1.Introduction

Improving energy efficiency and designing compact heat exchangers remain key priorities in modern engineering. Corrugated tubes are widely used to enhance thermal performance, as their modified inner surfaces periodically disrupt the boundary layer, promoting fluid mixing and increasing the heat transfer coefficient. Previous studies have extensively explored these

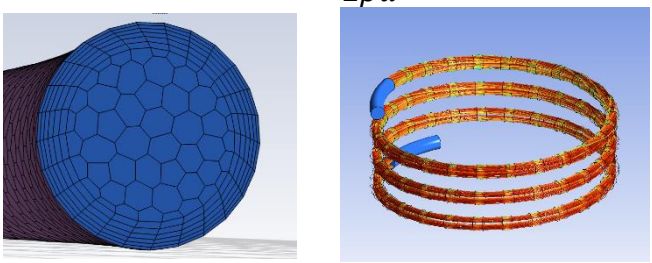
characteristics across various geometries. For instance, research shows that transverse, outward, and helical corrugations can improve heat transfer by up to 60% compared to smooth tubes [1]. Other studies have utilized optimization methods to balance the increased Nusselt number and pressure drop caused by varying corrugation depths and pitches [2, 3]. For spherical corrugated tubes specifically, secondary flows and enhanced turbulent kinetic energy within the cavities are the main drivers of thermal improvement [4]. Despite these findings, most literature focuses on general performance correlations rather than isolating the optimal geometric configuration under specific thermal boundary conditions. To address this, the present study numerically investigates the flow and thermal characteristics of spherical corrugated tubes under a constant wall temperature condition. Using Computational Fluid Dynamics (CFD) across various Reynolds numbers, this work aims to determine the optimal corrugation geometry that provides the best trade-off between maximized heat transfer and an acceptable pressure drop.

2 Numerical Method

The three-dimensional, steady, and incompressible flow and heat transfer within the spherical corrugated pipes were simulated using ANSYS Fluent. A velocity boundary condition was set at the pipe inlet to cover Reynolds numbers ranging from 1000 to 20000, and a zero-gauge pressure was assigned at the outlet. To evaluate the thermal performance of different geometries, a constant

temperature condition was applied to the corrugated inner walls. To properly resolve the viscous sublayer, an unstructured mesh featuring prismatic inflation layers was generated. Due to the boundary layer separation, recirculation zones, and strong secondary vortices induced by the spherical corrugations, the Realizable k-ε turbulence model with Enhanced Wall Treatment was employed. This model is highly robust and accurate for predicting rotational and swirling flows under adverse pressure gradients compared to the standard k-ε model. The governing conservation equations for mass, momentum, and energy were solved using the finite volume method. Pressure-velocity coupling was handled by the SIMPLEC algorithm, and second-order upwind schemes were chosen for the spatial discretization of the governing equations. Fig. 1 shows the mesh detail of the investigated tube and streamlines captured in the computational domain.

$$Re = \frac{\rho u D_h}{\mu} \qquad Nu = \frac{h D_h}{k} \qquad f = \frac{2\Delta P D_h}{L \rho u^2} \qquad (1)$$



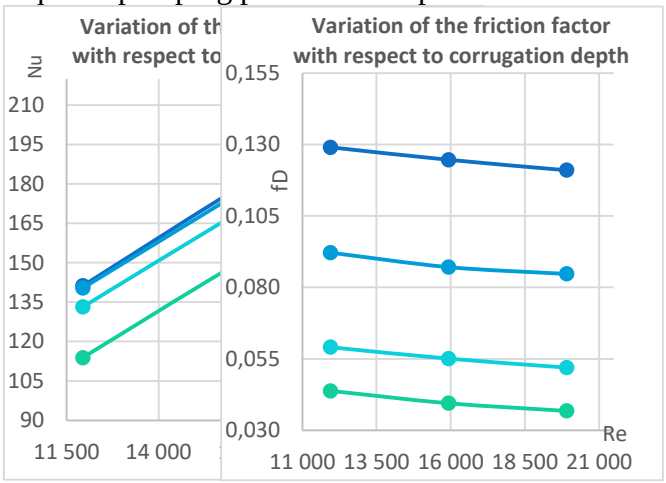
(a) (b)

Fig. 1 (a) Mesh detail and (b) streamlines in the computational domain.

3 Results and Discussion

Thermal Performance. As shown in Fig. 2, increasing the corrugation depth (*e*) consistently improves the average Nusselt number across the entire range of tested Reynolds numbers (Re = 1000-20000). While deeper corrugations clearly enhance the overall heat transfer capabilities of the pipe, they also introduce a noticeable operational drawback.

Pressure Drop Considerations. A deeper corrugation profile naturally leads to a higher Darcy friction factor because of the increased form drag inside the pipe. Consequently, selecting the most suitable geometry requires a careful trade-off: maximizing the heat transfer rate while keeping the required pumping power within practical limits.



(a)

(b)

Fig. 2 Variation of the (a)Nusselt number and (b)friction factor with respect to Reynolds number for different corrugation depths.

4 Conclusion

In this study, the fluid flow and heat transfer characteristics of spherical corrugated pipes were numerically evaluated under a constant wall temperature. While increasing the corrugation depth consistently improves the Nusselt number, it also leads to a higher friction factor due to increased form drag. Consequently, spherical corrugations are practically viable only under specific flow velocities and geometric configurations where the heat transfer enhancement justifies the additional pumping power.

References

1. Hu, Q., Qu, X., Peng, W., & Wang, J. (2022). Experimental and numerical investigation of turbulent heat transfer enhancement of an intermediate heat exchanger using corrugated tubes. *International Journal of Heat and Mass Transfer*, *185*, 122385.
2. Duan, Y., Zhang, X., Han, Z., Liu, Q., Li, X., & Li, L. (2024). Numerical simulation of flow and heat transfer performance of tube-shell coupled helically coiled corrugated tube heat exchanger.

International Communications in Heat and Mass Transfer, *153*, 107325.
3 Kirkar, S. M., Gönül, A., Celen, A., & Dalkilic, A. S. (2023). Multi-objective optimization of single-phase flow heat transfer characteristics in corrugated tubes. *International Journal of Thermal Sciences*, *186*, 108119.
4 Li, Y., Yu, Q., Yu, S., Gong, B., & Zhang, J. (2022). Numerical investigation of pulsating flow structures and heat transfer enhancement performance in spherical corrugated helical tube. *Applied Thermal Engineering*, *213*, 118647.

https://doi.org./10.58225/mpmma.2026.*296*

DYNAMICS OF FILLED CYLINDRICAL ENVELOPES UNDER AXIAL COMPRESSION AND SLIDING FRICTION

Famil Seyfullayev[1,2], Alikhan Garayev[2], Natig Hasanov[2]

[1]Institute of Mathematics, Azerbaijan

[2] AZUAC, Azerbaijan

Abstract. This paper is devoted to the investigation of the free vibrations of cylindrical shells with an internal filler, reinforced by a discretely distributed crossed system of ribs under axial compression. The influence of the external medium parameters and sliding friction at the contact interface on the vibration characteristics and the optimal reinforcement parameters of the system is analyzed. Utilizing the variational principle, the dependence of natural frequencies on the circumferential wave formation parameters is established, accounting for the dynamic interaction and friction between the shell and the filler.

Keywords: cylindrical shell, free vibrations, elastic modulus, deformation, total energy, friction coefficient, internal filler, axial compression.

Introduction

The increasing use of advanced composite materials in aerospace, mechanical, and marine engineering demands precise structural calculations and rational design. To accurately evaluate the load-bearing capacity and dynamic behavior of thin-walled structures, incorporating the external surface forces exerted by an elastic filler is essential. This shell-

filler contact interaction is highly complex, governed by the filler's mechanical properties, shell geometry, and surface conditions—particularly the sliding friction force at the interface. Solving such problems involves major mathematical challenges, which are further complicated by the need to account for dynamic effects in vibration and earthquake resistance analyses. Hence, developing effective approximate techniques is crucial. The variational method used in this study is especially relevant, as it provides consistent, approximate principles for analyzing thin-walled structures like shells and rods. This paper applies the variational principle to investigate the free vibrations of a thin, cross-reinforced (longitudinally and transversely stiffened) cylindrical shell under axial compression, fully accounting for dynamic filler interaction and contact friction. The relationships between natural frequencies and circumferential wave formation parameters are explicitly established. While existing literature mostly covers reinforced shells without a medium [1,2], smooth shells with a filler [2–6], or shells with longitudinal-only ribs in an elastic medium [5], this study fills the gap by simultaneously incorporating both the crossed rib reinforcement system and the interface friction factor.

Problem Statement.This paper focuses on the analysis of the free vibrations of cylindrical shells

with an internal filler, stiffened by a discrete system of longitudinal ribs under axial compression, while incorporating the friction between the shell and the medium. The influence of the external medium parameters on the natural frequency spectrum of the system is thoroughly analyzed.

The problem is solved using the energy method. The potential energy of the shell subjected to axial compressive loads is expressed as follows [2]:

$$\Im = \frac{Eh}{2(1-\nu^2)}\int_0^{\xi_1}\int_0^{2\pi}\left\{\left(\frac{\partial u}{\partial \xi}+\frac{\partial v}{\partial \theta}-w\right)^2+2(1-\nu)\frac{\partial u}{\partial \xi}\left(\frac{\partial v}{\partial \theta}-w\right)-\right.$$
$$\left.-\frac{1}{4}\left(\frac{\partial u}{\partial \theta}+\frac{\partial v}{\partial \xi}\right)^2\right]\Bigg\}d\xi d\theta+\frac{Eh}{24(1-\nu^2)R^2}\int_0^{\xi_1}\int_0^{2\pi}\left(\frac{\partial^2 w}{\partial \xi^2}+\frac{\partial^2 w}{\partial \theta^2}+\frac{\partial v}{\partial \theta}\right)^2-$$
$$-2(1-\nu)\left[\frac{\partial^2 w}{\partial \xi^2}\left(\frac{\partial^2 w}{\partial \theta^2}+\frac{\partial v}{\partial \theta}\right)-\frac{1}{4}\left(\frac{\partial^2 w}{\partial \xi \partial \theta}+\frac{\partial v}{\partial \xi}\right)^2\right]\Bigg\}d\xi d\theta+$$
$$+\frac{E_c}{2R}\sum_{l=1}^{k}\int_0^{\xi_1}\left[F_c\left(\frac{\partial u}{\partial \xi}-\frac{h_c}{R}\frac{\partial^2 w}{\partial \xi^2}\right)^2+\frac{I_{yc}}{R^2}\left(\frac{\partial^2 w}{\partial \xi^2}\right)^2+\frac{G_c}{E_c}I_{kp.c}\times\frac{G_c}{E_c}I_{kp.c}\left(\frac{\partial^2 w}{\partial \xi \partial \theta}+\frac{\partial v}{\partial \xi}\right)^2\right]_{\theta=\theta_1}d\xi-$$
$$-\frac{\sigma_x h}{2}\int_0^{\xi_1}\int_0^{2\pi}\left(\frac{\partial w}{\partial \xi}\right)^2 d\xi d\theta-\frac{\sigma_x F_c}{2R}\sum_{i=1}^{k}\int_0^{\xi_1}\left(\frac{\partial w}{\partial \xi}\right)^2\Bigg|_{\theta=\theta_1} \tag{1}$$

here $\xi=\frac{x}{R},\ \theta=\frac{y}{R};\ E_c, G_c$ - Modulus of elasticity of the longitudinal stiffener material, k – number of longitudinal stiffeners, σ_x - axial compressive stress,

u,v,w - are the displacement vector components of the shell;

h and R – are the thickness and radius of the shell, E, ν - are Young's modulus and Poisson's ratio of the shell material; F_c, I_{yc}, $I_{kp.c}$ - are, respectively, the cross-sectional area and the moments of inertia of the longitudinal stiffener (rib) cross-section relative OX and OZ, is the torsional moment of inertia. The kinetic energy of the shell is given by:

$$K = \frac{Eh}{2(1-\nu^2)} \int_0^{\xi_1} \int_0^{2\pi} \left[\left(\frac{\partial u}{\partial t_1} \right)^2 + \left(\frac{\partial v}{\partial t_1} \right)^2 + \left(\frac{\partial w}{\partial t_1} \right) \right] d\xi d\theta$$

$$+ \frac{\overline{\rho}_c E_c F_c}{2R(1-\nu^2)} \sum_{i=1}^{k_1} \int_0^{\xi_1} \left[\left(\frac{\partial u}{\partial t_1} \right)^2 + \left(\frac{\partial w}{\partial t_1} \right) \right]_{\theta=\theta_1} d\xi \qquad (2)$$

where $\overline{\rho_c} = \frac{\rho_c}{\rho_0}$, ρ_0, ρ_c are the material densities of the shell and the longitudinal stiffener (rib), respectively. $\theta_1 = \frac{2\pi}{k_1} i$

The influence of the filler on the shell is defined as external surface loads applied to the shell, and it is calculated as the work done by these loads when transferring the system from the deformed state back to its initial undeformed state, which is represented in the form:

$$A_0 = -\int_0^{\xi_1}\int_0^{2\pi} (q_x u + q_\theta \nu + (1-f)q_z w)d\xi d\theta \tag{3}$$

where q_x, q_θ, q_z are the pressures exerted by the filler on the shell, and f is the friction coefficient.

The total energy of the system is given by:

$$\Pi = Э + K + A_0 \tag{4}$$

The equation of motion of the medium in vector form is given by [3,4]:

$$a_e^2 qraddiv\vec{S} - a_t^2 rotrot\vec{S} + \omega^2 \vec{S} = 0 \tag{5}$$

where $a_t = (\lambda + 2\mu)/\rho, \quad a_e = \mu/\rho$ are the propagation velocities of longitudinal and transverse waves in the medium, respectively; $S = S(S_x, S_\theta, S_z)$ is the displacement vector; and λ, μ are the Lame constants. The contact conditions are appended to the system of equations of motion of the medium (5). It is assumed that the contact between the shell and the medium is rigid, i.e., at $r = R$.

$$u = S_x; \ \nu = S_\theta; \quad w = S_z \tag{6}$$

$$q_x = -\sigma_{rx}, q_y = -\sigma_{r\theta}, \quad q_z = -\sigma_{rr}, w = S_r \tag{7}$$

The components of the stress tensor $\sigma_{rx}, \sigma_{r\theta}, \quad \sigma_{rr}$ are defined as follows [2,3]:

$$\sigma_{rx} = \mu_s \left(\frac{\partial S_x}{\partial r} + \frac{\partial S_r}{\partial x} \right); \quad \sigma_{r\theta} = \mu_s \left[\frac{\partial}{\partial r} \left(\frac{\partial S_\theta}{r} \right) + \frac{1}{r} \frac{\partial S_r}{\partial \theta} \right],$$
$$\sigma_{rr} = \lambda_s \left(\frac{\partial S_r}{\partial x} + \frac{1}{r} \frac{(rS_r)}{\partial r} + \frac{1}{r} \frac{\partial S_\theta}{\partial \theta} \right) + 2\mu_s \frac{\partial S_r}{r}$$

(8)

λ_s, μ_s - are the Lame constants for the medium.

By supplementing the equations of motion of the filler (5) with the contact conditions (6) and (7), we arrive at the contact problem concerning the vibrations of a cylindrical shell reinforced by a crossed system of ribs and filled with a medium. In other words, the problem of the vibrations of a cylindrical shell with a filler, reinforced by a crossed system of ribs under axial compression, is reduced to the simultaneous integration of the equations of shell theory and medium theory, provided that the specified conditions are satisfied at their contact interface.

References

1. Amabili, M.: Nonlinear Vibrations and Stability of Shells and Plates. Cambridge University Press, Cambridge, 394 (2018).
2. Reddy, J.N.: Mechanics of Laminated Composite Plates and Shells: Theory and Analysis. CRC Press, Boca Raton, 872 (2021).
3. Popov, V.L.: Contact Mechanics and Friction: Physical Principles and Applications. Springer, Berlin, 385 (2019).
4. Zhang, Y., Liew, K.M.: Free vibration analysis of cylindrical shells with elastic inner liners or

fillers. *International Journal of Mechanical Sciences* 115, 332–345 (2016).
5. Safaei, B., Ahmed, N.A., Fattahi, A.M.: Free vibration analysis of filled and reinforced cylindrical shells considering interface friction effects. *Journal of Vibration and Control* 26(11-12), 985–998 (2020).
6. Duc, N.D.: Nonlinear Static and Dynamic Analysis of Functionally Graded Stiffened Plates and Shells. Vietnam National University Press, Hanoi, 423 (2014).

https://doi.org./10.58225/mpmma.2026.303

MECHANICS OF SUPERSONIC FLIGHT: AERODYNAMIC ANALYSIS, WAVE DRAG, AND THERMAL LOADING

Farhad Guliyev[1], Cavid Islamov[2], Salahzade Salah[2] , Racab Darchınov[2]
[1]Necmettin Erbakan University, Türkiye
[2]Azerbaijan Technical University, Azerbaijan.

Abstract. This paper presents a rigorous analytical treatment of supersonic flight mechanics for $M > 1$, covering oblique shock formation, wave drag, and aerodynamic heating. High-speed vehicle design requires a precise understanding of non-linear pressure rises and thermal boundary layers. In this study, Ackeret's linearised thin-airfoil theory and isentropic flow relations are systematically applied to a symmetric double-wedge airfoil ($\theta = 5°$)across a comprehensive Mach range of $M = 1.2 - 5.0$under International Standard Atmosphere (ISA) stratospheric conditio ($T_\infty = 216.65\ K$, altitude $\approx 11\ km$). The analytical results demonstrate that the wave drag coefficient decreases by $87\ \%$ ($0.0459 \rightarrow 0.0062$), while the stagnation temperature rises significantly from $279.05\ K$ to $1299.90\ K$ due to kinetic energy dissipation. Concurrently, the lift-to-drag (L/D) ratio improves from 5.365 to 18.498 over the studied Mach spectrum. Ultimately, these findings highlight the severe structural and materials constraints imposed by aerodynamic heating during prolonged supersonic cruise.

Keywords: Supersonic Aerodynamics, Wave Drag, Oblique Shock Waves.

1 Introduction

Above $M = 1$, disturbances are confined within a Mach cone of half-angle $\mu = \arcsin(1/M)$, forcing an oblique shock to form ahead of any blunt leading edge [1]. The resulting shock system generates wave drag-an irreversible, entropy-generating pressure drag absent in subsonic flight. Kinetic energy dissipation at stagnation points simultaneously imposes severe thermal loads on aerodynamic surfaces, governing materials selection and thermal protection system (TPS) design [5]. This paper derives closed-form expressions for wave drag coefficient and stagnation temperature, evaluates them numerically across $M = 1.2 - 5.0$, and discusses their implications for high-speed vehicle design.

2. Governing Equations

2.1 ,Oblique Shock Relations

For a wedge of half-angle θ, the $\theta - \beta - M$ relation governs the shock angle β [1].

$$\tan\theta = 2\cot\beta\left[\frac{(M^2\sin^2\beta - 1)}{M^2(\gamma + \cos 2\beta) + 2}\right] \tag{13}$$

where $\gamma = 1.4$. The pressure ratio across the shock is determined by the normal Mach component $M_n = M\sin\beta$:

$$p_2/p_1 = 1 + \frac{2\gamma}{\gamma+1}\cdot(M_n^2 - 1) \tag{2}$$

2.2 Wave Drag — Ackeret Theory

For a thin symmetric airfoil at zero incidence, linearised (Ackeret) theory yields [4]:

$$C_{D,wave} = \frac{4\theta^2}{\sqrt{M^2 - 1}} \tag{3}$$

θ is in radians ($5° = 0.08727$ rad). Total drag adds turbulent skin friction $C_x = 0.010$ [3]:

$$C_{D,total} = C_{D,wave} + C_x \tag{4}$$

2.3 Stagnation Temperature

From the isentropic energy equation for adiabatic flow [2]:

$$T_0 = T_\infty \left(1 + \frac{\gamma - 1}{2} M^2\right) \tag{5}$$

The temperature rise $\Delta T_0 = T_0 - T_\infty$ at ISA stratosphere becomes:

$$\Delta T_0 = \frac{(\gamma - 1) T_\infty}{2} \cdot M = 43.33 \cdot M^2 \ (K) \tag{6}$$

3. Results

The numerical solutions show distinct non-linear trends across the supersonic regime. To establish a performance baseline, the coupled effects of wave drag decay and stagnation temperature variations were evaluated under constant stratospheric

conditions. These analytical outputs serve as a foundation for analyzing the trade-offs between lifting efficiency and thermal survivability across low and high-supersonic boundaries. Consequently, the complete set of calculated coefficients is compiled below in Table 1.

Table 1. Computed aerodynamic parameters ($\theta = 5°, C_l = 0.30, C_x = 0.010, T_\infty = 216.65$ K)

M	$C_{D,wave}$	$C_{D,total}$	T_0(K)	ΔT_0(K)	L/D
1.2	0.0459	0.0559	279.05	62.40	5.365
1.5	0.0272	0.0372	314.14	97.49	8.055
2.0	0.0176	0.0276	389.97	173.32	10.875
3.0	0.0108	0.0208	606.62	389.97	14.444
3.5	0.0091	0.0191	747.44	530.79	15.722
4.0	0.0079	0.0179	909.93	693.28	16.792
5.0	0.0062	0.0162	1299.90	1083.25	18.498

The results show that wave drag decays by 87% across the Mach range, with a 61% drop between $M = 1.2 \rightarrow 2.0$ due to $1/\sqrt{M^2 - 1}$ dependence, allowing L/D to optimize up to 18.498. While the transonic singularity ($M \approx 1$) is an artifact of linear theory bypassed via area-ruling [4], these aerodynamic gains are strictly bounded by quadratic thermal growth. At $M = 5.0$, the stagnation temperature reaches 1299.90 K, exceeding the service limits of aluminium ($\approx$ 450 K)and titanium ($\approx$ 900 K), which demands advanced CMCs or TPS solutions [5]. Furthermore, near $M \approx 5.0$, extreme kinetic energy dissipation triggers endothermic real-gas effects (vibrational excitation

and molecular dissociation of N_2/O_2) that drop the specific heat ratio($\gamma < 1.4$). This modifies shock layer profiles and pressure signatures beyond ideal gas limits [2], making coupled aero-thermal updates vital for high-speed vehicle design.

References

1.Blazek, J., Bauer, C., Volpe, G.: High-fidelity RANS simulation of supersonic wing-body interference at transonic and low-supersonic Mach numbers. Aerosp. Sci. Technol. 142, 108607 (2024). https://doi.org/10.1016/j.ast.2023.108607

2. Candler, G.V., Subbareddy, P.K., Brock, J.M.: Advances in CFD methods for hypersonic flows: real-gas effects and transition. Annu. Rev. Fluid Mech. 55, 303–337 (2023). https://doi.org/10.1146/annurev-fluid-120720-024714

3. Maurer, J., Paoli, R., Arias, A.: Skin-friction and pressure drag partition in turbulent supersonic boundary layers via DNS at Mach 2–4. Phys. Fluids 37(2), 025122 (2025). https://doi.org/10.1063/5.0191348

4. Ren, Z., Fu, S.: Oblique shock wave interactions and wave-drag reduction in supersonic intakes: a review. Prog. Aerosp. Sci. 136, 100876 (2023). https://doi.org/10.1016/j.paerosci.2022.100876

5.Tanimoto, K., Takahashi, M., Furudate, M.: Aerodynamic heating prediction for hypersonic vehicle leading edges using wall-modelled LES. J. Thermophys. Heat Transf. 38(1), 45–59 (2024). https://doi.org/10.2514/1.T6912

https://doi.org./10.58225/mpmma.2026.308

OPTIMAL POROSITY SELECTION FOR ENHANCED MELTING AND SOLIDIFICATION PERFORMANCE IN METAL FOAM-ENHANCED PCM STORAGE SYSTEMS

Farida Iachachene [1,2] Hanane Cheradi[2], Ahmet Selim Dalkılıç[3]

Earth Physics Laboratory, University M'Hamed Bougara Boumerdes, Algeria

[2]LEMI (Laboratory of Energy, Mechanics and Engineering), University M'Hamed Bougara Boumerdes, Algeria

[3]Yildiz Technical University, Turkiye

Abstract. This work presents a numerical investigation of the melting and solidification processes of the phase change material (PCM) Paraffin 25X embedded in an aluminum metal foam square cavity subjected to a constant heat flux. The mathematical model is based on the enthalpy–porosity approach proposed by Voller to simulate phase change phenomena and on the Darcy–Brinkman–Forchheimer formulation to describe fluid flow through the porous medium. The governing equations are solved using the finite volume method implemented. The influence of metal foam porosity (ε = 0.80, 0.84, 0.88, and 0.92) on the thermal and energetic performance of the latent heat storage system is systematically analyzed during both charging (melting) and discharging (solidification) stages. The results indicate that lower porosity enhances heat transfer and reduces phase-change time owing to the higher effective thermal conductivity of the composite

medium, whereas higher porosity increases the amount of stored thermal energy. To identify the most efficient configuration, a multi-objective optimization based on the Pareto front is performed. The analysis reveals that a porosity of $\varepsilon = 0.88$ provides the best compromise between heat transfer enhancement and energy storage capacity, making it the optimal configuration for both melting and solidification processes and thus ensuring the highest overall performance of the thermal energy storage system.

Keywords: PCM, Metal Foams, Thermal Energy Storage, Optimization

1.Introduction

In response to the continuous growth in energy demand and the environmental challenges associated with the extensive use of fossil fuels, the development of thermal energy storage systems has become essential for enhancing energy efficiency and promoting the integration of renewable energy sources. Among the various thermal energy storage technologies, latent heat thermal energy storage (LHTES) based on Phase Change Materials (PCMs) has attracted significant attention due to its ability to store and release large amounts of energy through the absorption and liberation of latent heat during melting and solidification processes [1].

Despite their considerable advantages, PCMs generally suffer from low thermal conductivity, which limits the rate of heat transfer and consequently reduces the overall performance of thermal energy storage systems. To address this limitation, several heat transfer enhancement techniques have been proposed, among which the

incorporation of metallic foams has emerged as one of the most effective solutions. Metallic foams are characterized by their high thermal conductivity, large specific surface area, and interconnected porous structure, which facilitate efficient heat distribution within the PCM[1]. The integration of metallic foam into PCM-based storage systems significantly improves thermal transport, enhances heat transfer rates, and accelerates both melting and solidification processes. As a result, this approach contributes to improved charging and discharging performance, making latent heat thermal energy storage systems more efficient and suitable for a wide range of renewable energy and thermal management applications[2,3].

The physical model considered in this study, as illustrated in fig.1, consists of a square cavity with dimensions of 4 cm × 4 cm, filled with PCM and embedded with a metallic foam. The PCM is used for thermal energy storage in the form of latent heat. The metallic foam investigated is made of aluminum and is characterized by different porosity values (ε) and pore densities (ω). In the present work, an aluminum foam with a pore density of 20 PPI (pores per inch) is considered. The influence of the foam's structural parameters on the thermal performance of the PCM-based latent heat storage system is analyzed.

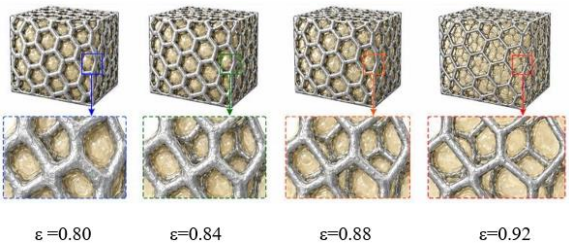
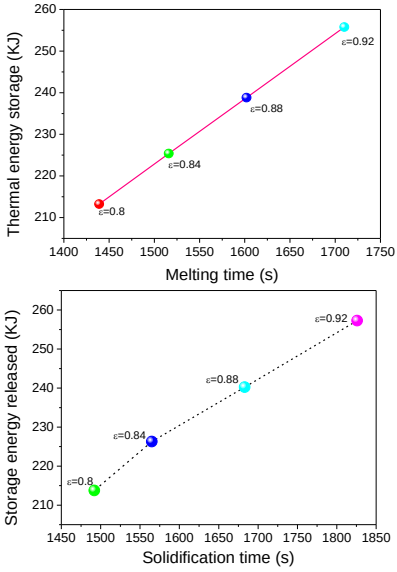


Fig. 1. Physical model.

2.Results and Discussion

A comprehensive numerical investigation of both melting (charging) and solidification (discharging) processes of a phase change material embedded in aluminum metal foam was conducted to evaluate the influence of foam porosity on thermal and energetic performance. The results revealed a strong dependence of heat transfer and energy storage characteristics on porosity. Lower porosities enhanced the effective thermal conductivity of the composite medium, leading to faster melting and solidification rates, whereas higher porosities increased the PCM volume fraction and consequently improved the stored and recovered energy. A comparison between the charging and discharging stages showed that the melting process was consistently faster than the solidification process under identical operating conditions, while the amount of stored and released energy remained directly related to the PCM content. Owing to the conflicting nature of the performance criteria, namely rapid thermal

response and high energy storage capacity, a multi-objective optimization based on the Pareto-front approach was employed(fig.2). The optimization results demonstrated that a porosity of ε = 0.88 represents the optimal configuration for both melting and solidification processes, providing the best compromise between phase-change duration and energy storage/recovery capacity. These findings confirm the effectiveness of metal-foam-enhanced PCM systems and highlight the importance of multi-objective optimization in the design of high-performance latent thermal energy storage units.



(a)

(b)

Fig 2. Pareto front illustrating the trade-off between melting time and stored energy as a function of porosity ε: a) storage phase; b) discharge phase

3 Conclusion

This study investigated the thermal performance of a PCM embedded in aluminum metal foam during charging and discharging under constant heat flux conditions. The results showed that porosity strongly influences system behavior: lower porosities enhance heat transfer and shorten phase-change times, while higher porosities increase energy storage capacity. In addition, melting was found to be faster than solidification under the same operating conditions. A multi-objective Pareto optimization identified a porosity of $\varepsilon = 0.88$ as the optimal configuration for both processes, providing the best compromise between thermal response and stored/recovered energy

References

1. Ghasemi, Kasra, Syeda Tasnim, and Shohel Mahmud:PCM, nano/microencapsulation and slurries: A review of fundamentals, categories, fabrication, numerical models and applications. Sustainable Energy Technologies and Assessments 52, 102084 (2022).
2. Iachachene, F., Haddad, Z., Abu-Nada, E., & Sheremet, M. A.: Natural convection melting of phase change material in corrugated porous cavities. Sustainable Energy Technologies and Assessments 53, 102734 (2022).
3. Zhao, C. Y., Wei Lu, Yuan Tian :Heat transfer enhancement for thermal energy storage using metal foams embedded within phase change materials (PCMs). Solar energy 84(8), 1402-1412(2010).

https://doi.org./10.58225/mpmma.2026.314

MEAN-LINE MODELLING AND FROZEN-GEOMETRY PERFORMANCE MAPPING OF AXIAL AND RADIAL TURBINES FOR INTERNAL COMBUSTION ENGINE EXHAUST-ENERGY RECOVERY

Fatih Kumru, Erman Aslan
Kocaeli University , Türkiye

Abstract. Exhaust-energy recovery from internal combustion engines requires turbine solutions that can convert high-temperature and pressure exhaust flow into useful power under changing boundary conditions. This paper compares single-stage axial, two-stage axial and single-stage radial turbine architectures using a validated one-dimensional mean-line framework. In contrast to design studies limited to single architecture, this work provides a common comparison basis for axial and radial turbine concepts by combining design-point sizing, frozen-geometry map calculation and architecture-level trade-off assessment for the same exhaust-energy recovery conditions. The design geometry is obtained from the specified total pressure, total temperature and mass flow, then frozen for off-design map calculations. Axial losses are represented by profile, secondary, incidence, tip-clearance and trailing-edge correlations; the radial model includes volute, nozzle guide vane, rotor and diffuser components with passage, incidence, tip-clearance and disk-

friction losses. At P_{o1} = 240 kPa and T_{o1} = 776 K, the two-stage axial turbine increases power from 10.66 to 18.16 kW while maintaining η_{tt} near 87.6%, whereas the radial turbine gives PR_{ts} = 2.414 and 16.86 kW in one compact stage. At P_{o1} = 500 kPa and T_{o1} = 1070 K, radial and axial two-stage solutions give nearly equal power, while the axial design keeps a clear efficiency advantage.

Keywords: Exhaust-energy recovery; Mean-line model; Axial turbine; Radial turbine; Performance map; Mechanics and applications

Introduction

A considerable part of the fuel energy supplied to internal combustion engines is rejected with the exhaust stream. Since this flow contains both thermal and pressure potential, turbine-based recovery can be used to produce shaft or electrical power. The main design difficulty is that exhaust mass flow, temperature, pressure ratio and engine speed vary together; therefore, a turbine must be evaluated over a performance map rather than only at a single design point.

Axial and radial turbines represent different design choices. Axial turbines can provide high aerodynamic efficiency, especially when the expansion is divided over two stages, while radial turbines are attractive for compact automotive installations because a high pressure ratio can be obtained in one stage. Unlike studies that focus

on a single turbine type or on design point performance only, the present work evaluates axial and radial alternatives within the same validated mean-line framework and under identical engine exhaust boundary conditions. The main contribution is the use of a frozen-geometry performance-map approach to compare single-stage axial, two-stage axial and single-stage radial turbine architectures in terms of pressure-ratio capability, efficiency, shaft power and packaging-oriented speed level.

2. Methodology

The calculation procedure consists of design-point sizing and frozen-geometry map generation. In the sizing step, thermodynamic states, velocity triangles, blade-row dimensions and loss components are calculated. In the map step, the geometry is kept fixed and several speed lines and pressure-ratio targets are solved, so the comparison depends on the aerodynamic response of the same hardware rather than on repeated resizing. For the axial turbine, stator and rotor stations are solved sequentially and a free-vortex distribution is used along the blade height. The radial model includes the volute, nozzle guide vane, rotor and diffuser. The axial implementation was checked against the Hannover turbine, while the radial model was checked against NASA TP-1730 and a Garrett capacity curve; the validation reproduced the

main efficiency and mass-flow trends with acceptable deviations for preliminary turbine selection.

3. Results and Discussion

Table 2 summarizes the selected clean-converged points. Under Condition 1, the single-stage axial turbine gives high η_{tt} but limited pressure ratio and power. Adding a second axial stage raises PR_{ts} from 1.679 to 2.398 and power from 10.66 to 18.16 kW, while η_{tt} remains almost unchanged. The single-stage radial turbine reaches a comparable PR_{ts} and produces 16.86 kW, but with lower efficiency than the two-stage axial solution.

Table 2. Selected clean-converged comparison points for the two exhaust conditions.

Parameter	C1 A1	C1 A2	C1 R	C2 A2	C2 R
$\dot{m}$ (kg/s)	0.12714	0.12750	0.12573	0.09675	0.10329
$\dot{m}_{corr}$	0.088087	0.0883	0.08711	0.037782	0.040337
PR_{ts}	1.679	2.398	2.414	3.030	3.966
PR_{tt}	1.578	2.237	2.160	2.927	3.255
η_{tt} (%)	88.4	87.6	85.9	88.7	87.1
η_{ts} (%)	87.6	89.1	86.1	86.3	87.6
Power (kW)	10.66	18.16	16.86	14.79	15.03
Speed/stages	41.0k/1	35.1k/2	75k/1	05k/2	20k/1

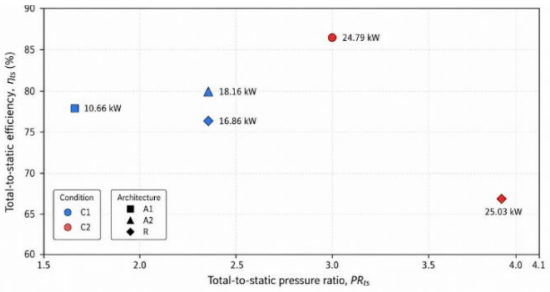


Figure 1. Pressure-ratio and power trade-off for selected clean-converged turbine points.

For Condition 2, the radial and two-stage axial turbines deliver almost the same shaft power, 25.03 and 24.79 kW, respectively. The mechanisms are different: the radial turbine operates at higher PR_{ts} and PR_{tt} in a single compact stage, whereas the two-stage axial turbine retains much higher η_{tt} and η_{ts}. Thus, the radial option is attractive when pressure-ratio capability and compactness dominate, while the axial two-stage option is preferable when high efficiency at comparable power is the main requirement.

Conclusion

A frozen-geometry mean-line framework was used to compare axial and radial turbine architectures for exhaust-energy recovery. For Condition 1, the two-stage axial turbine increased the power by 7.50 kW relative to the single-stage axial case while preserving η_{tt} close to 87.6%. The radial turbine provided PR_{ts} = 2.414 and

16.86 kW at the same condition, but with lower efficiency than the two-stage axial design. For Condition 2, both architectures produced nearly 25 kW, yet the axial two-stage design maintained a clear efficiency advantage. The preferred turbine therefore depends on the design priority: two-stage axial hardware is more suitable for high-efficiency operation, whereas a single-stage radial turbine is more suitable for high pressure ratio and compact packaging. Future work will extend the model with Q2D/3D CFD analysis to resolve local secondary-flow, diffuser and exit kinetic-energy effects.

References

1. Agromayor, R., Nord, L.O.: Preliminary design and optimization of axial turbines accounting for diffuser performance. International Journal of Turbomachinery, Propulsion and Power 4(3), 32 (2019).
2. Anderson, A.D., et al.: Mean-line design and off-design performance prediction of single-stage axial turbines. Aerospace Science and Technology (2022).
3. AGARD, Conference Proceedings No 195, “Throughflow Calculations in Axial Turbomachinery” AGARD AR 275, (1990)

Mclallin, K.L., Haas, J.E., Mclallin, K.L., Haas, J.E., Mclallin, L., K., Haas, E., J. (1980).

Experimental performance and analysis of 15.04-centimeter-tip-diameter, radial-inflow turbine with work factor of 1.126 and thick blading

https://doi.org./10.58225/mpmma.2026.321

WAVE PROPAGATİON İN A TRANSVERSELY ISOTROPİC HOMOGENEOUS ECCENTRİC HOLLOW CYLİNDER

Ferecova Sona
Baku State University, Azerbaijan

Abstract. The effect of eccentricity on the dispersion of longitudinally propagating waves is investigated in a model of a hollow cylinder composed of a transversely isotropic, homogeneous material. The study is conducted within a system of exact mathematical equations and relations consistent with the linear theory of elastic waves. The solution methodology applied to the eigenvalue problem associated with this investigation was developed in the authors' previous work. This method is based on relating the solutions of the wave field equations expressed in the coordinate system aligned with the axis of the cavity to those expressed in the coordinate system of the cylinder's central axis, through expansion into a Fourier series. Specific numerical results pertaining to the influence of varying eccentricity magnitudes on the dispersion curves for different modes are analyzed and discussed. It is established that eccentricity in a hollow cylinder exerts a significant effect on the dispersion characteristics of wave propagation, both quantitatively and qualitatively.

Keywords: Eccentric hollow cylinder, dispersion curves.

1. Introduction

Compared to concentric cylinders [1–3], the body of research addressing wave dispersion in eccentric cylinders remains considerably limited [4,5]. Consider an infinitely long, transversely isotropic, homogeneous cylinder containing an eccentric cavity. The central axes of the cylinder and the cavity are denoted by R_c and R_b, respectively, and the distance between them is R_{cb}. The dispersion of waves propagating along the Oz axis is investigated within a mathematical model comprising: the differential equations of motion in cylindrical coordinates, formulated within the three-dimensional linear theory; the generalized Hooke's law governing the relationships among the stress–strain tensor components of a transversely isotropic cylinder; the Cauchy relations for small deformations describing the strain–displacement relationships; and the associated boundary conditions. These boundary conditions, applicable for $r = R_c$ and $r_0 = R_b$, can be written in the cylindrical coordinate systems $Or\theta$ and $Or_0\theta_0 z_0$ respectively, as follows:

$$\sigma_{rr}\big|_{r=R_c} = 0,\ \sigma_{r\theta}\big|_{r=R_c} = 0,\ \sigma_{rz}\big|_{r=R_c} = 0,$$

$$\sigma_{rr}\big|_{r_0=R_b} = 0,\ \sigma_{r\theta}\big|_{r_0=R_b} = 0,\ \sigma_{rz}\big|_{r_0=R_b} = 0$$

2. Methodology

The displacements are expressed in terms of potentials as follows:

$$u_r = \frac{\partial}{r\partial\theta}\Psi - \frac{\partial^2}{\partial r\partial z}X,\ u_\theta = -\frac{\partial}{\partial r}\Psi - \frac{\partial^2}{r\partial\theta\partial z}X,$$

$$u_z = (A_{13} + A_{44})^{-1}(A_{11}\Delta_1 + A_{44}\frac{\partial^2}{\partial z^2} - \rho\frac{\partial^2}{\partial t^2})X,$$

$$\Delta_1 = \frac{\partial^2}{\partial r^2} + \frac{1}{r}\frac{\partial}{\partial r} + \frac{1}{r^2}\frac{\partial^2}{\partial \theta^2}$$

These potentials satisfy the following equations:

$$\left(\Delta_1 + \xi_1^2 \frac{\partial^2}{\partial z^2} - \frac{\rho}{A_{11} - A_{12}} \frac{\partial^2}{\partial t^2}\right)\Psi = 0,$$

$$\left[\left(\Delta_1 + \xi_2^2 \frac{\partial^2}{\partial z^2}\right)\left(\Delta_1 + \xi_3^2 \frac{\partial^2}{\partial z^2}\right) - \rho\left(\frac{A_{11} + A_{44}}{A_{11}A_{44}}\Delta_1 + \frac{A_{33} + A_{44} + 2\sigma_{zz}^0}{A_{11}A_{44}} \frac{\partial^2}{\partial z^2}\right)\frac{\partial^2}{\partial t^2} + \frac{\rho^2}{A_{11}A_{44}} \frac{\partial^4}{\partial t^4}\right] X = 0$$

Solutions to the given equations are sought in the following form:

$$\Psi = \cos(kz - \omega t)\left[\sum_{n=-\infty}^{+\infty} \Psi_n^0(r_0)\sin(n\theta_0)\right],$$

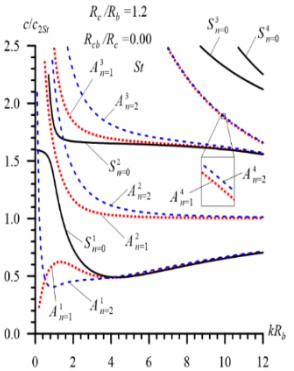
$$\Psi_n^0(r_0) = \Psi_{1n}^0(r_0) + \Psi_{2n}^0(r_0),$$

$$X = \sin(kz - \omega t)\left[\sum_{n=-\infty}^{+\infty} X_n^0(r_0)\cos(n\theta_0)\right],$$

$$X_n^0(r_0) = X_{1n}^0(r_0) + X_{2n}^0(r_0).$$

3. Numerical results

In the numerical investigations presented for this problem, the eccentricity of the cylinder is characterized by the ratio R_{cb}/R_b. The dispersion curves obtained for the case $R_c/R_b = 1{,}2$ are examined below. These curves are presented for two distinct cases: $R_{cb}/R_b = 0{,}00$, and $R_{cb}/R_b = 0{,}05$.



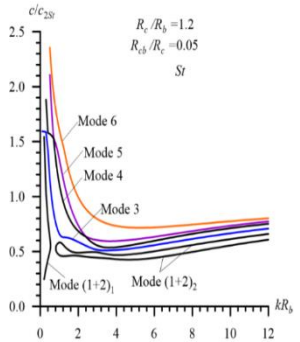


Figure 1. Figure 2.

As is evident from the analysis of the curves in Figure 1, the dispersion curves corresponding to the symmetric and antisymmetric modes intersect in the case $R_{cb}/R_b = 0{,}00$. It is precisely these intersection points that constitute one of the principal causes for the emergence of new types of dispersion curves in the cases $R_{cb}/R_b > 0{,}00$. For small values of the ratio R_{cb}/R_b (as illustrated, for example, in Figure 2), the newly observed dispersion curves arise as a result of the merging of segments belonging to the dispersion curves obtained for the symmetric and antisymmetric modes shown in Figure 1. This process is clearly observable upon comparison of Figure 1 with Figure 2.

References

1. S.D. Akbarov, Dynamics of Pre-strained Bi-material Elastic Systems: Linearized Three-Dimensional Approach, Springer, Heidelberg, New York, 2015.
2. A. C. Eringen, E.S. Suhubi, Elastodynamics: Finite Motion, Vol. I; Linear Theory, Vol. II, Academic Press, New York, 1975.
3. A.N. Guz, Elastic Waves in Bodies with Initial Stresses, A.C.K. Kyiv, 2004
4. H.F. Tiersten, D.V. Shick, Resonant wave propagation in gun tubes with eccentric bores, Wave Motion, 21, 75-84, 1995.
5. A.H. Shah, Elastic Waves in a Circular Cylinder with an Eccentric Bore, Acustica, 28(3), 251 – 258, 1973.
6. Akbarov S.D., Farajova S. S., Sevdimaliyev, Y.M. On the solution method of the dynamics of the eccentric hollow cylinder made of transversally isotropic material with homogeneous initial stresses. In Proceedings of the 9th International Conference on Control and Optimization with Industrial Applications' 27 – 29 August, 2024, Istanbul, Turkey, .pp. 629 – 633
7. Akbarov S.D., Farajova S. S., Sevdimaliyev, Y.M. On the dispersion of longitudinal waves propagating in the eccentric hollow cylinder. International Congress on new trends in mechanics Azerbaijan State Pedagogical University, 2-5 September 2025, Baku.

https://doi.org./10.58225/mpmma.2026.326

PURE BENDING OF AN ISOTROPIC PLATE WEAKENED BY A DOUBLY PERIODIC SYSTEM OF CIRCULAR HOLES AND STRAIGHT CRACKS ALONG THE COORDINATE AXES

Gulnar Mirzayeva[1,2]

[1] Academy of Public Administration under the President of the Republic of Azerbaijan, Azerbaijan,

[2] Baku State University, Azerbaijan

Abstract: This paper is devoted to the investigation of the pure bending problem of isotropic thin plates weakened by a periodic system of holes and cracks. The objective of the study is to analyze the influence of a doubly periodic array of circular holes and straight cracks located along the coordinate axes on the stress-strain state and stress intensity factors of the plate. The solution to the problem is based on the variational principles of mechanics and boundary value problems of analytical functions. Utilizing the periodicity conditions, the stress field in the infinite plate is investigated within a single elementary cell, and the singular stresses arising at the crack tips are analyzed. The obtained results allow for evaluating the effects of the geometric distances between holes and cracks, as well as external bending moments, on the fracture resistance of the material.

Keywords: isotropic plate, pure bending, doubly periodic system, circular hole, straight crack, stress intensity factor.

1. Introductıon:

A significant portion of structural elements used in modern engineering, aerospace, and marine industries consists of plate and shell-type structures. Due to weight reduction or technological requirements, periodic groups of holes are frequently incorporated within the design. On the other hand, during operation, material fatigue or external influences may lead to the formation of straight cracks in the vicinity of these holes. Such defects drastically reduce the load-bearing capacity of structures and lead to severe stress concentration.

While the analysis of the stress field around a single hole or crack has been extensively studied in the mechanics of deformable solids, mathematically modeling their interaction within a doubly periodic (lattice-like) system requires solving highly complex systems of equations. In the case of pure bending of the plate, the geometric configuration of the holes and the length of the cracks directly affect the vibration and stability characteristics. This research work analytically and numerically investigates the simultaneous effect of both circular cutouts and straight cracks on the bending mechanics of isotropic plates.

2. Problem Statement

İt is assumed that no contact occurs between the crack faces during the deformation process of the plate. Based on the symmetry of the boundary conditions and the geometry of the domain D_0 occupied by the elastic medium, the components of the stress tensor are periodic functions with periods ω_1 and ω_2 It is required to determine the stress-

strain state of the plate under the boundary conditions specifying that the contours of the circular holes and the faces of the cracks located along the coordinate axes are free from external forces [1,2,3,4,5,6].

In the theory of thin plates, all kinematic and static quantities are expressed in terms of the deflection W(x, y) of the plate's middle surface. These relationships are given as follows:

$$M_x = -D\left(\frac{\partial^2 W}{\partial x^2} + \nu\frac{\partial^2 W}{\partial y^2}\right), \qquad N_x = -D\frac{\partial}{\partial x}\Delta W,$$

(2.1)

$$M_y = -D\left(\frac{\partial^2 W}{\partial y^2} + \nu\frac{\partial^2 W}{\partial x^2}\right), \qquad N_y = -D\frac{\partial}{\partial y}\Delta W,$$

$$H_{xy} = -D(1-\nu)\frac{\partial^2 W}{\partial x \partial y}, \qquad D = \frac{Eh^3}{12\left(1-\nu^2\right)}.$$

Here, W(x, y) is the deflection function of the plate; M_x, M_y и H_{xy} are the bending and twisting moments, respectively; N_x, N_y Q_x, Q_y are the shear forces acting on the corresponding sections of the plate; E and ν are the modulus of elasticity and Poisson's ratio of the plate material; h - is the plate thickness; and D - is the flexural rigidity

$$\frac{\partial^4 W}{\partial x^4} + 2\frac{\partial^4 W}{\partial x^2 \partial y^2} + \frac{\partial^4 W}{\partial y^4} = \frac{q(x,y)}{D},$$

(2.2)

here $q(x,y)$ – is the intensity of the transverse load acting on the unit surface of the plate. In the case of homogeneous bending, equation (2.2) becomes a biharmonic equation:

$$\Delta\Delta W(x,y) = 0$$

(2.3)

In the case of homogeneous bending, let us express the particular moments, particular shear

forces, and displacements using two analytical functions $\phi(z)$ and $\psi(z)$ [4]:

$$M_x + M_y = -4D(1+\nu)\,\mathrm{Re}\,\Phi(z);$$
$$M_y - M_x + 2iH_{xy} = 2D(1-\nu)\left[\bar{z}\Phi'(z) + \Psi(z)\right];$$
$$N_x - iN_y = -4D\Phi'(z)$$

(2.4)

$$\frac{\partial W}{\partial x} + i\frac{\partial W}{\partial y} = \phi(z) + z\overline{\Phi(z)} + \overline{\psi(z)};$$
$$u + i\upsilon = -\delta\left(\frac{\partial W}{\partial x} + i\frac{\partial W}{\partial y}\right); \qquad W(x,y) = \mathrm{Re}\left\{\bar{z}\phi(z) + \chi(z)\right\};$$
$$\chi''(z) = \psi'(x) = \Psi(z); \qquad \phi'(z) = \Phi(z).$$

The quantity δ $(-h/2 \le \delta \le h/2)$ represents the distance from the middle surface to the layer under consideration.The boundary conditions for the first and second fundamental problems can be combined into a single functional relationship as follows:

$$\varepsilon\overline{\Phi(\tau)} + \Phi(\tau) - \left[\bar{\tau}\Phi'(\tau) + \Psi(\tau)\right]e^{2i\theta} = f_1 + if_2,$$

(2.5)

Where $m(S)$ və $p(S)$ are the bending moment and the equivalent shear force (Kirchhoff shear force) applied at point t on the contour, measured along its length;

$$p(S) = N_n(S) + \frac{\partial H_{nt}}{\partial S}$$

$m(S)$ və $p(S$ are the transverse shear force and the twisting moment on the section tangent to the contour at point τ respectively; θ - is the angle between the normal drawn to the contour at point τ and the x -axis; and C_1 - is a real constant determined by the condition of single-valuedness of the deflection.

Based on the relations in (1.5) and the conditions on the circular cross-section, as well as those on the crack, the problem of plate bending is reduced to finding two functions, $\Phi(z)$ and $\Psi(z)$, which are analytic in the domain D_0

$$\varepsilon\overline{\Phi(\tau)}+\Phi(\tau)-\left[\overline{\tau}\Phi'(\tau)+\Psi(\tau)\right]e^{2i\theta}=f_1+if_2\ ;$$

(2.6)

$$\varepsilon\Phi(t)+\overline{\Phi(t)}+t\overline{\Phi'(t)}+\overline{\Psi(t)}=iC\ ;$$

$$\varepsilon\Phi(t_1)+\overline{\Phi(t_1)}+t_1\overline{\Phi'(t_1)}+\overline{\Psi(t_1)}=iC_1\ ;$$

(2.7)

Where $\tau=\lambda e^{i\theta}+m\omega_1+n\omega_2$ (m, n = 0, ±1, ±2, …); t and t_1 are the affixes of the points on the edges of the cracks oriented along the coordinate axes; C and C_1 are real constants determined by the condition that the deflection increment [W] at the crack tips is equal to zero.

This study addresses the pure bending problem of an isotropic thin plate weakened by a doubly periodic array of circular holes and straight cracks along the coordinate axes. The key findings and contributions are summarized as that: by utilizing the complex potentials of analytical functions and plate bending theory, the boundary value problem was formulated within a single elementary cell under doubly periodic conditions. The problem was reduced to determining two analytic functions, $\Phi(z)$ and $\Psi(z)$, satisfying the force-free conditions on the hole contours and crack faces. The proposed model effectively incorporates the single-valuedness of deflections ([W]=0 at the crack tips) to account for singular stresses. This framework enables the precise evaluation of Stress Intensity

Factors (SIFs) at the crack tips.The results demonstrate that the geometric spacing between the holes, crack lengths, and external bending moments significantly interact to influence the overall stress concentration and fracture resistance of the plate.

References

1. Ventsel, E., Krauthammer, T.: Thin Plates and Shells: Theory and Applications. CRC Press, Boca Raton, p. 650 (2020).
2. Amabili, M.: Nonlinear Mechanics of Shells and Plates in Composite, FGM and Smart Structures. Cambridge University Press, Cambridge, p. 512 (2018).
3. Latifov, F.S.: Oscillations of shells with fluid. Elm, Baku, p. 280 (2007).
4. Sadd, M.H.: Elasticity: Theory, Applications, and Numerics. Academic Press, San Diego, p. 592 (2020).
5. Boyko, Yu.V.: Theory of Elasticity and Plasticity: Textbook for Universities. Yurayt, Moscow, p. 435 (2023).
6. Altenbach, H., Eremeyev, V.A. (eds.): Shell Structures: Theory and Applications. S

https://doi.org./10.58225/mpmma.2026.332

ANGULAR CORRELATIONS AND DECAY SPECTROSCOPY OF SHORT-LIVED LIGHT FRAGMENTS IN THE QUATERNARY FISSION OF ^{252}CF

Gadir Ahmadov[1,2,3] Michael Holik[4,5], Daniyar Berikov[1,6] Sebuhi Nuruyev[1,7], Farid Ahmadov[2,7], Azer Sadigov[2,7], Arzu Mammadli[7], Ramil Akbarov[1,2]

[1]Joint Institute for Nuclear Research ,Russia
[2] Nuclear Research of IDDA, Azerbaijan
[3]AzUAC, Azerbaijan.
[4]University of West Bohemia in Pilsen, Czech Republic
[5]Institute of Experimental and Applied Physics-Czech Technical University in Prague, Czech Republic
[6]The Institute of Nuclear Physics, Kazakhstan
[7]Institute of Physics , Azerbaijan

Abstract. Rare fission channels of ^{252}Cf were investigated with the aim of studying the decay properties of short-lived light nuclei formed during multi-particle emission. Particular attention was given to unstable fragments such as ^{8}Be and excited states of ^{7}Li, which decay almost instantaneously into lighter charged particles. Using a ΔE–E telescope system with high spatial sensitivity, energy spectra and angular correlations of emitted light charged particle pairs were measured. The analysis focuses on identifying signatures of intermediate fragment decay through

their characteristic kinematic distributions. The observed angular correlations for α–α and α–t pairs were compared with trajectory-based calculations for different decay channels.

Keywords: Ternary fission, ΔE-E method, Timepix pixel detector, ΔE detector, silicon detector, rare fission mode processes, nuclear fission, 252Cf

1. Introduction

Nuclear fission studies provide insight into highly excited nuclei and fragment formation. While binary fission dominates, rare processes such as ternary and quaternary fission enable investigation of light charged particle emission and unstable nuclear systems [1, 2, 3, 6].

In quaternary fission, two additional light particles are emitted with the main fragments [1–3]. Although rare, these events often involve short-lived nuclei such as ^{8}Be and excited ^{7}Li, which decay rapidly after formation [1–5].

A key issue is whether the observed particles are emitted directly or originate from decay of an intermediate fragment, distinguishing true and pseudo-quaternary fission [1–3]. Identification relies on kinematic correlations, particularly angular and energy distributions of particle pairs. For example, ^{8}Be decay into two α-particles produces a characteristic angular correlation [1–3]. Previous studies were limited by low resolution and efficiency.

In this work, angular and energy correlations of light charged particles from ^{252}Cf fission are analyzed to identify short-lived intermediate nuclei, focusing on α–α and α–t correlations as signatures

of ^{8}Be and ^{7}Li decay.

2. Results and discussion

Figure 1 presents angular distribution from experimental results and trajectory calculation. The angular distribution of particle pairs reveals clear structures that reflect the underlying decay mechanisms. After correction for detector acceptance using Monte Carlo simulations, a pronounced enhancement at small opening angles was observed for α–α pairs. This feature is a well-known signature of the decay of ^{8}Be, which is unstable even in its ground state and decays into two α-particles with a small relative angle.

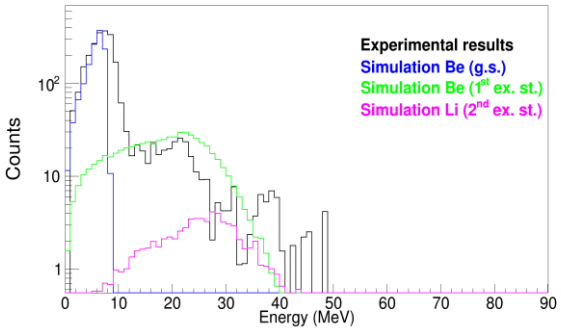


Fig. 1. Angular distribution from experiment and trajectory calculation.

The analysis of α–t pairs suggests the presence of decay channels involving excited states of ^{7}Li. However, due to limited statistics, the angular distribution for these events is less well defined. Within the accessible angular range, the observed distribution is consistent with expectations for the decay of excited ^{7}Li into α and triton particles.

Overall, the observed angular correlations provide strong evidence that many four-particle events arise from pseudo-quaternary fission, where an unstable intermediate fragment decays in flight. The recorded data were processed offline using specialized analysis algorithms [7].

3.Conclusion

Angular and energy correlations of emitted light charged particles provide insight into the decay of short-lived nuclear fragments in rare fission processes. The observed α–α and α–t distributions are consistent with decays of unstable nuclei such as ^{8}Be and excited ^{7}Li. A strong enhancement at small angles confirms ^{8}Be decay in both ground and excited states, while broader structures indicate higher-energy contributions, supporting pseudo-quaternary fission. Comparison with kinematic calculations allows reconstruction of intermediate states and improves understanding of their formation and decay dynamics.

Acknowledgments

This project has received funding from Azerbaijan Science Foundation under grant agreement No [AEF-MGC-2024-2(50)-16/03/1-M-03] and from the Science Committee of the Ministry of Science and Higher Education of the Republic of Kazakhstan (Grant no.BR20280986).

References

1. Jesinger, P., Kopatch, Yu.N., Mutterer, M., et al.: New experimental studies on the quaternary fission of 233,235U(nth,f) and 252Cf(sf). Eur. Phys. J. A **24**, 379–388 (2005).

2. Gönnenwein, F., Jesinger, P., Mutterer, M., et al.: Quaternary fission. Acta Phys. Hung. New Ser. Heavy Ion Phys. **18**, 419–425 (2003).
3. Ahmadov, G.S., Kopatch, Yu.N., Telezhnikov, S.A., Ahmadov, F.I., Granja, C., Garibov, A.A., Pospisil, S.: Detection of ternary and quaternary fission fragments from 252Cf with a position-sensitive ΔE–E telescope based on silicon detectors. Phys. Part. Nucl. Lett. **12**, 542–549 (2015).
4. Fomichev, A.S., David, I., Ivanov, M.P., Sobolev, Yu.G.: Investigation of quaternary fission of ^{248}Cm and ^{252}Cf using two CsI(Tl) counters. Nucl. Instrum. Methods Phys. Res. *A* **384**, 519–521 (1997).
5. Holik, M., Ahmadov, G., Berikov, D., et al.: A synchronization and data acquisition system for silicon detectors. JINST **13**, C11019 (2018).
6. Holik, M., Ahmadov, G., Broulim, J., Zich, J., Berikov, D., Mora, Y., Kopatch, Yu., Nuruyev, S., Abbaszada, N., Zhumadilov, K.: Alpha calibration of the Timepix pixel detector exploiting energy information gained from a common electrode signal. JINST **14**, C06022 (2019).
7. Holik, M., Ahmadov, G., Berikov, D., et al.: A program for data analysis of rare fission mode processes from neutron-induced and spontaneous fission. Adv. Phys. Res. **2**(2), 71–78 (2020).

https://doi.org./10.58225/mpmma.2026.*337*

AN ANALYSIS OF THE RELATIONSHIP BETWEEN THE FOOD AND CONSUMER GOODS MANUFACTURING SECTOR AND ECONOMIC GROWTH

Imamguliyeva Gunel Salim
AzUAC, Azerbaijan

Abstract. The food industry is an important component of the manufacturing sector and contributes to economic development through value creation, employment generation, and food security. This study examines the impact of domestic investments in Azerbaijan's food industry on economic growth using the Autoregressive Distributed Lag (ARDL) approach. The empirical analysis identifies ARDL (1,0) as the most appropriate model specification. The findings indicate that investments in the food industry do not have a statistically significant direct effect on economic growth during the study period. In addition, the ARDL bounds test results reveal the absence of a long-run cointegration relationship between food industry investments and economic growth. Diagnostic tests confirm the overall reliability of the estimated model. The results suggest that, despite its strategic role in ensuring food supply, regional development, and economic stability, the contribution of food industry investments to aggregate economic growth remains limited. The study highlights the importance of investment quality, value-added production, and

sectoral linkages rather than investment volume alone in promoting sustainable economic growth.

Keywords: Food industry, economic growth, investment, ARDL model

1. Food and goods sector

The food industry is one of the leading branches of the manufacturing sector, creating high added value through the processing of agricultural products. Its development contributes to food security, employment, and economic diversification. In many countries, the food industry accounts for more than 20% of total manufacturing output and remains a key source of industrial growth [1]. In Azerbaijan, food production represents a significant share of the non-oil manufacturing sector and plays an important role in increasing exports and regional development. The growing demand for processed food products has accelerated investments in modern technologies and production facilities. Therefore, the food industry serves as a strategic component of the manufacturing sector and supports sustainable economic development.

1.1 Autoregressive Distributed Lag (ARDL) model approach

The relationship between domestic investments in Azerbaijan and economic growth is analyzed within the framework of the Autoregressive Distributed Lag (ARDL) model approach [2] . In the model, the dependent variable is the economic growth indicator (ln_growth), and the independent variable is domestic investments in Azerbaijan (ln_food).

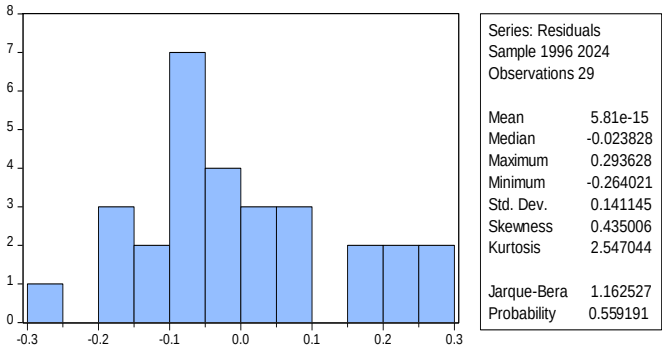
In the analysis process, the appropriate lag length was first determined using the Akaike Information Criterion (AIC) and it was determined that the most suitable model was ARDL(1,0).

Table 1: ***ARDL Model Results for the Food Industry***

Variable	**Coefficient**	**t-statistic**	**Possibility**
LN_GROWTH(-1)	0.9868	18.0519	0.0000
LN_FOOD	-0.0339	-0.4873	0.6301
C	0.4012	1.2468	0.2236
Model Statistics		**Value**	
R^2		0.9880	
Corrected R^2		0.9871	
F-statistic		1,069,440	
Probe(F-statistic)		0.0000	
Durbin-Watson		1.5347	

According to the model results, the coefficient of internal investments in the food sector on economic growth is negative but not statistically significant ($p>0.05$). This indicates that investments in the food sector did not have a direct and significant impact on economic growth during the analysis period.

However, the model appears to be generally significant. The high F-statistic and the significant probability value indicate that the model has high overall explanatory power. Furthermore, the highly significant lagged value of the dependent variable suggests that the economic growth series exhibits a strong autoregressive structure.



Various diagnostic tests were applied to test the reliability of the model. First, the Breusch-Godfrey LM test was used to examine the serial correlation problem. According to the test results, there is no autocorrelation problem in the model (p=0.1622) [3] .

The heteroskedasticity problem was examined using the Breusch-Pagan-Godfrey test, and the results showed that there was no heteroskedasticity problem in the model (p=0.3885) [4].

The normality test results also show that the error terms are normally distributed. Since the Jarque-Bera probability value is greater than 0.05, the assumption of normal distribution cannot be rejected.

However, the Ramsey RESET test results indicate that there may be some shortcomings in the model specification (p=0.0439). This could be related to the fact that economic growth cannot be fully explained solely by food sector investments, the influence of macroeconomic factors outside the model, or structural breaks in the Azerbaijani economy [6] .

1.2. ARDL test results

ARDL bounds test results show that there is no long-term cointegration relationship between internal investments in food industry sector and economic growth.

Table 2: ***Bounds Test Results***

Test Statistics	**Value**
F-statistic	1.7742
Lower Limit I(0) (%5)	5.395
Upper Limit I(1) (%5)	6,350

The obtained F-statistic value is below the lower limit critical value. Therefore:
H0: "There is no long-term relationship between the variables."
The hypothesis is accepted. In other words, a long-term statistical relationship between investments in food industry sector and economic growth has not been found.
The results obtained appear economically significant considering the sectoral structure of the Azerbaijani economy. The Azerbaijani economy largely exhibits a growth model based on the oil and energy sector. Therefore, the impact of investments in the oil and energy sector on overall economic growth is expected to remain limited.
Furthermore, a significant portion of investments in the food sector are made with the aim of creating production capacity to meet domestic consumption, ensuring supply security, and creating import substitution.
On the other hand, the structural transformation processes experienced by the Azerbaijani economy during the analysis period, the continuous

development and reshaping of post-establishment policies, and factors such as the 2008 global financial crisis and the 2014 oil price shock may have weakened the sectoral investment-growth relationship [7].

These results show that economic growth cannot be explained solely by sector-based investment increases; the sectoral structure of investment, production capacity, foreign trade links, and value added level are also decisive factors. Based on the analyses conducted, no significant long-term impact of domestic investments in the food industry sector on economic growth has been identified. However, the sector is considered to be of strategic importance in terms of economic stability, food supply security, and domestic market balance.

References

1. Azerbaycan Respublikası Dövlət Statistika Komitəsi. (çeşitli yıllar). *Sənaye statistikası*. https://www.stat.gov.az/
2. Barro, R. J. (1991). Economic growth in a cross section of countries. *The Quarterly Journal of Economics, 106*(2), 407-443.
3. Cameron, A. C. ve Trivedi, P. K. (2010). *Microeconometrics using stata* (Revised ed.). Stata Press.
4. Cefic. (2023). *Facts and figures of the European chemical industry 2023*. European Chemical Industry Council. Brussels.
5. Enders, W. (2015). *Applied econometric time series* (4th ed.). Wiley.

6. Gujarati, D. N. ve Porter, D. C. (2009). *Basic econometrics* (5th ed.). McGraw-Hill.
7. International Monetary Fund. (2019). *Republic of Azerbaijan: Selected issues*. https://www.imf.org/

https://doi.org./10.58225/mpmma.2026.*344*

LIOUVILLE PHENOMENON FOR THE KLEIN-GORDON EQUATION IN 1+1 DIMENSIONS

Haakan Hedenmalm

The Royal Institute of Technology, Sweden

Abstract: We study the Klein-Gordon equation in one spatial and one temporal dimension.Physically, this equation describes the wave function of a relativistic spinless boson with positive rest mass. Mathematically, this is the most elementary hyperbolic partial differential equation, after the wave equation itself. Relative to the point at the origin, the spacetime splits according to the light cones, and we find four quarter-planes, two of which are timelike while the remaining two are spacelike.Not unexpectedly, the solutions behave quite differently in the two types of quarter-planes. It turns out that the spacelike quarter-planes exhibit a Liouville phenomenon, where insufficient growth forces the solution to display a certain kind of symmetry, where the values along the two linear edges are in a one-to-one relation. This phenomenon shares features with the classical Liouville theorem in the theory of entire functions as well as the Phragmen-Lindelof principle for harmonic functions.

Keywords: Klein–Gordon equation; Hyperbolic partial differential equations; Relativistic wave equations; Liouville phenomenon; Phragmén–Lindelöf principle; Growth conditions; Spacelike

regions; Light-cone geometry; Symmetry properties of solutions; Boundary value problems.

https://doi.org./10.58225/mpmma.2026.346

THERMAL AND MECHANICAL DESIGN ANALYSIS OF A SMALL SHELL-AND-TUBE HEAT EXCHANGER USING KERN AND BELL-DELAWARE METHODS

Halil Tugra Basancelebi [1], Umit Ozkas[1], Atlas Gerelioglu[1], and Ahmet Selim Dalkılıc[1],

[1] Yildiz Technical University, Türkiye

Abstract. This study evaluates a compact shell-and-tube heat exchanger using the Kern and Bell-Delaware methods against CFD benchmark data. Bell-Delaware predicts outlet temperature, heat duty, and shell-side heat transfer more accurately than Kern, while both methods underpredict pressure drop. ASME Section VIII Division 1 and TEMA checks confirm the mechanical adequacy of the design.

Keywords: shell-and-tube heat exchanger; Kern; Bell-Delaware; CFD; mechanical design.

Introduction

Shell-and-tube heat exchangers are widely used, but shell-side prediction remains difficult because baffle geometry, leakage, and bypass streams strongly affect performance. Kern is suitable for preliminary sizing, whereas Bell-Delaware improves accuracy by correcting for non-ideal shell-side flow.

Ozden and Tari (2010)[1] provided CFD benchmark results for a small STHE, showing strong sensitivity to baffle spacing, baffle cut, and shell-side flow structure.

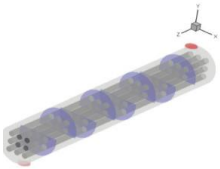


Figure 1. Schematic view of the investigated small shell-and-tube heat exchanger geometry.

This study compares the Kern[2] and Bell-Delaware[3] methods with the CFD benchmark of Ozden and Tari (2010), with emphasis on leakage and bypass corrections, and also verifies mechanical integrity using ASME Section VIII Division 1 and TEMA.

2. Methodology

2.1. Geometric Configuration and Operating Conditions:

The exchanger is a compact single-shell STHE with 0.09 m shell diameter, 0.6 m tube length, seven tubes in triangular pitch (0.03 m), and tube diameters of 0.02/0.016 m (outer/inner). The baseline case uses six segmental baffles with 36% cut and 0.086 m spacing. Water flows on the shell side at 300 K inlet temperature and 1.0 kg/s mass flow rate, while the tube wall temperature is fixed at 450 K. Fluid properties were evaluated at the average bulk temperature.

2.2. Thermal Analysis Procedure

Thermal analysis was based on heat duty and logarithmic mean temperature difference:

$$Q = \dot{m}c_p(T_{out} - T_{in})\Delta T_{LMTD} = \frac{\Delta T_1 - \Delta T_2}{\ln(\Delta T_1/\Delta T_2)}$$

For shell-side rating, the Kern method was used to calculate Reynolds and Prandtl numbers and estimate the heat transfer coefficient: $G_s = \frac{\dot{m}}{A_s} Re_s = \frac{G_s D_e}{\mu}$

The shell-side heat transfer relation is: $Nu = \frac{h_s D_e}{k} = 0.36 Re_s^{0.55} Pr^{1/3} \left(\frac{\mu}{\mu_w}\right)^{0.14}$

Shell-side pressure drop was estimated as: $\Delta P_s = \frac{f G_s^2 (N_b+1) D_s}{2\rho D_e \phi_s}$

The Bell-Delaware method was then applied to correct ideal crossflow behavior for baffle cut, leakage, bundle bypass, unequal baffle spacing, and temperature-gradient effects:

$$h_s = h_{ideal} J_c J_l J_b J_s J_r$$

These factors were also included in shell-side pressure-drop evaluation through corrected crossflow, window, and end-zone contributions:

$\Delta P_s = \Delta P_{ideal} R_b R_l + \Delta P_w + \Delta P_e$In compact exchangers, leakage and bypass streams strongly affect both heat transfer and pressure drop, making these corrections essential.

2.3. Mechanical Design and Structural Integrity

Mechanical design covered the shell, tubes, tube sheet, baffles, and nozzles in accordance with ASME Section VIII Division 1 and TEMA, using design pressures of 0.6 MPa on the shell side and

1.0 MPa on the tube side at 200 °C. The calculations confirmed that the selected geometry met minimum thickness and strength requirements for safe operation.

$$t = \frac{PR}{SE - 0.6P}$$

Here, P is design pressure, R is internal radius, S is allowable stress, and E is joint efficiency; the result confirmed adequate shell strength.

3.Results and Discussion

For the updated baseline case (Nb = 6, Bc = 36%, $\dot{m}$ = 1.0 kg/s), iterative Kern predicted h = 1131 W/m²K, T_{out} = 310.30 K, Q = 43.22 kW, and ΔP = 408 Pa, whereas Bell-Delaware predicted 3435 W/m²K, 329.15 K, 122.28 kW, and 72.7 Pa. The CFD benchmark values were 3757 W/m²K, 330.18 K, 131.79 kW, and 6168 Pa. Bell-Delaware is therefore much closer to CFD for thermal prediction, while both analytical methods significantly underpredict pressure drop.

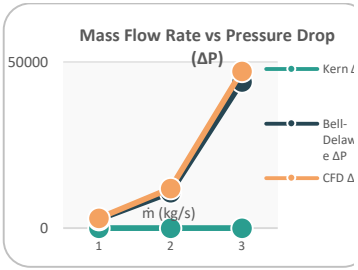


Figure 2. Shell-side pressure-drop comparison.

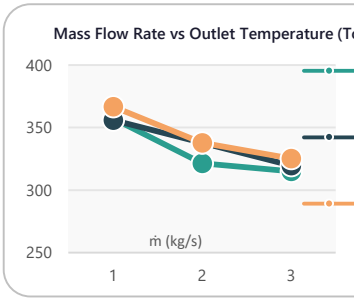


Figure 3. Shell-side heat-transfer coefficient and outlet-temperature comparison.

Overall, Bell-Delaware captures the compact exchanger's thermal behavior more successfully than Kern because it accounts for leakage and bypass effects. However, both analytical approaches substantially underestimate CFD pressure loss, indicating that compact-exchanger hydraulics remain highly sensitive to non-ideal shell-side flow.

Mechanical checks also confirmed feasibility: shell and tube thicknesses satisfied ASME limits, tube sheet and baffle dimensions met TEMA requirements, and nozzles required no additional reinforcement.

4. Conclusion

This study presented a coupled thermal and mechanical assessment of a compact shell-and-tube heat exchanger using the Kern and Bell-Delaware methods with comparison to CFD-based literature data. Bell-Delaware predicted outlet temperature, heat duty, and shell-side heat transfer coefficient more accurately than Kern, whereas both analytical methods underpredicted pressure drop. Mechanical verification according to ASME and TEMA confirmed that the proposed compact geometry is structurally adequate for safe operation.

References

1. Ozden, E., and Tari, I. (2010). Shell side CFD analysis of a small shell-and-tube heat e changer. Energy Conversion and Management, 51(5), 1004-1014.

2. Kern, D. Q. (1950). Process Heat Transfer. McGraw-Hill, New York.
3. Bell, K. J. (1981). Delaware method for shell-side design. In Heat Exchangers: Thermal-Hydraulic Fundamentals and Design.

https://doi.org./10.58225/mpmma.2026.*353*

NUMERICAL METHODS FOR SOLVING COEFFICIENT INVERSE PROBLEMS FOR ORDINARY DIFFERENTIAL EQUATIONS WITH NONLOCAL CONDITIONS

Vaqif Abdullayev [1,2,3]*, Efthimios Providas* [4]
[1]Azerbaijan State Oil and Industry University, Azerbaijan
[2]Institute of Mathematics, Azerbaijan
[2] AzUAC, Azerbaijan
[4] University of Thessaly, Greece

Abstract. We consider a class of problems in which it is required to determine unknown constant coefficients appearing in the free terms of non-autonomous systems of ordinary differential equations. The basic and additional (overdetermining) conditions are, in the general case, of a nonlocal nature: they involve cumulative characteristics of the unknown state functions – both their values at selected points and their integral values over specified sub-intervals. Depending on the relation between the number of unknown coefficients and the number of additional conditions, several problem settings and corresponding solution methods are discussed. Results of computer experiments are presented, together with an analysis of how errors in the prescribed conditions affect

the accuracy of the solutions for test problems.

Keywords: inverse problems, parametric identification, multipoint conditions, nonlocal conditions, dynamic system.

1.Introduction

We study a class of coefficient-inverse problems for linear systems of non-autonomous ordinary differential equations [1-4]. The basic and overdetermining conditions are linear and, in the general case, are of a nonlocal nature. It is worth noting that many inverse problems concerning sources described by partial differential equations [5, 6] can be reduced to the class of problems considered here.

In many well-known works, mainly two approaches are used for the numerical solution of such problems. The first approach consists in reducing these problems to optimal control problems [6]. The second approach uses the construction of the fundamental solution (Green's function) for boundary value problems related to partial differential equations [7].

The paper describes three variants of the coefficient-inverse problem formulations, which differ in the ratio between the

dimension of the unknown coefficient vector and the number of given conditions, as well as in the accuracy of the specification of the boundary nonlocal conditions. For each variant of the problem statement, we provide a description of the proposed approach to its solution. In the final section, we present the results of numerical experiments, and analyze the effect of errors in the given conditions on the accuracy of the obtained solutions to the test problems.

2. Problem Statement

We consider the following coefficient-inverse problem for a system of ordinary differential equations with nonlocal conditions:

$$\frac{du(x)}{dx} = A(x)u(x) + B(x)P + C(x), \quad x \in [a,b], \tag{1}$$

$$\sum_{i=1}^{l_1} \overline{\alpha}^i \overline{u}_m(x_i) + \sum_{j=1}^{l_2} \int_{\bar{x}_j}^{\bar{x}_j+\Delta_j} \breve{\alpha}^j(\xi)\overline{u}_m(\xi)d\xi = \gamma. \tag{2}$$

Here $u(x)$ is an n-dimensional continuously differentiable vector function defining the state of the object at $x \in [a,b]$, where a and b are given; the given matrices $A(x)$ of dimension $(n \times n)$, $B(x)$ of dimension $(n \times L)$, and the n-dimensional vector function $C(x)$ are continuous for $x \in [a,b]$; the numerical matrices $\overline{\alpha}^i$ of dimension $(N \times m)$, $i = 1,2,...l_1$,

and the continuous matrix functions $\breve{\alpha}^{j}(x)$, $x \in [\breve{x}_j, \breve{x}_j + \Delta_j]$, as well as the N–dimensional vector γ are given. The given points x_i, $i = 1,2,...l_1$, and intervals $(\breve{x}_j, \breve{x}_j + \Delta_j)$, $j = 1,2,...l_2$, belong to $[a,b]$. The unknown vector function $\bar{u}_m(x)$ consists of m components of the state vector $u(x)$. Without loss of generality, we assume that $\bar{u}_m(x)$ consists of the first m components of $u(x)$. We denote by $\bar{\bar{u}}(x)$ the $(n-m)$ - dimensional vector function consisting of the remaining $(n-m)$ components of $u(x)$:

$$\bar{u}(x) = (\bar{u}_1(x), \bar{u}_2(x), ..., \bar{u}_m(x)),$$

$$\bar{\bar{u}}(x) = (\bar{\bar{u}}_{m+1}(x), \bar{\bar{u}}_{m+2}(x), ..., \bar{\bar{u}}_n(x)).$$

Further, we will call the first m components of $u(x)$, that is, the vector function $\bar{u}(x)$, observable. This means that it is possible to obtain some information about the numerical values of these components.

The values of the L– dimensional constant vector of parameters P ($L > 1$) are the unknown coefficients in equation (1) that need to be determined using the given nonlocal conditions (2), the number of which is N, with $N \geq n$.

Depending on the relationships among n, m, N, L, and the number of essentially independent conditions in (2) together with the system of differential equations (1), various formulations of the coefficient-inverse

problems for determining the unknown n – dimensional function $u(x)$ and L – dimensional vector P are possible. A more precise definition of the independence of the conditions (2) with regard to system (1) will be given in the next section. For now, we assume that all N conditions in (2) are linearly independent.

In this work, the following two possible variants of the coefficient-inverse problem will be considered.

Problem I. The number of independent conditions in (2) for problem (1) – (2) equals $N = n + L$, $L \geq 1$. Necessary and sufficient conditions for the existence and uniqueness of the solution for determining the vector function $u(x)$ and the constant vector $P \in R^L$ will be formulated.

Problem II. This problem consists in determining the parameter vector $P \in R^L$ and the unknown n - dimensional vector function $u(x)$. Here, the conditions (2) represent the results of N observations of the system's state, which are of a nonlocal character. We assume that the number of observations N exceeds the required number of conditions $(n + L)$ in (2). In practice, such a situation arises due to measurement errors, and therefore the conditions (2) are not satisfied exactly.

For the numerical solution, a special representation of the solution to the differential system (1) with an unknown initial

condition will be used. With respect to the unknown initial conditions and parameters P, using the given overdetermined nonlocal conditions (2), an overdetermined system of algebraic equations will be derived. The solution of the corresponding normal system will be taken as the desired solution.

References

1. Bakirova, E. A., Assanova ,A. T., Kadirbayeva, Z. M.: A problem with parameter for the integro-differential equations. Mathematical Modelling and Analysis. 26(1), 34–54 (2021).

2. Aida-zade, K. R., and Abdullayev, V. M.: Solution to a class of inverse problems for a system of loaded ordinary differential equations with integral conditions. Journal of Inverse and Ill-posed Problems. 24(5), 543–558 (2016).

3. Aida-zade, K.R. and Abdullayev, V.M.: Study and numerical solution of a class of coefficient-inverse problems for ODEs with nonlocal conditions. Journal of Inverse and Ill-posed Problems. 34(3), 377-394 (2026). https://doi.org/10.1515/jiip-2025-0085

4. Abdullayev, V.M.: On an inverse problem with high-order overdetermination conditions. Journal of Inverse and Ill-posed Problems. 33(3), 351-368 (2025). https://doi.org/10.1515/jiip-2024-0027

5. Prilepko, A. I., Orlovsky, D. G., Vasin, I. A.: Methods for Solving Inverse Problems in Mathematical Physics, M. Dekker, New York, (2000).

6. Kabanikhin, S. I.: Inverse and Ill-Posed Problems: Theory and Applications. Inverse Ill-Posed Probl., De Gruyter, Berlin, (2011).
7.Slodička, M.: A parabolic inverse source problem with a dynamical boundary condition, Appl. Math. Comput. 256(1), 529-539 (2015).

https://doi.org./10.58225/mpmma.2026.360

CFD VALIDATION OF HEAT TRANSFER PERFORMANCE OF DOUBLE PIPE HEAT EXCHANGERS AS HOUSEHOLD MACHINES USED FOR HEAT RECOVERY

Halil Tugra Basancelebi [1], Umit Ozkas [1], Atlas Gerelioglu[1], and Ahmet Selim Dalkılıc[1,]

[1] Yildiz Technical University, Türkiye

Abstract. In this research, a theoretical and computational study on a counterflow double pipe heat exchanger with turbulent water flow is presented. The Nusselt numbers, convective heat transfer coefficients, and total heat transfer coefficients were determined based on the Dittus-Boelter correlation. NTU – ε and LMTD techniques were used to calculate outlet temperature and heat transfer rates. Results have been validated against CFD. The simulations are in good accord and confirm the trustworthiness of the theoretical approach. Water served as the practice fluids. Hot water with a mass flow rate of 0.154 kg/s and an input temperature of 67°C (340.15 K) was passed through the inner tube. The cold water was cycled in the annulus between the tubes with a mass flow rate of 0.50 kg/s and an inlet temperature 4 °C (277.15 K). The theoretical outlet temperature of the cold side was found to be 5.4°C (278.55 K) and the

simulation result was 279.17 K. Theoretically, the hot side was calculated to have an exit temperature of 62.6°C (335.75 K), but the simulation result was 325.19 K with the maximum variance of 3.14%. The deviation rates were less than 5% for all the cases, which shows that the present empirical correlations can be employed with confidence for the provided boundary conditions. Thus, the developed model was proved to work well.

Keywords: Heat Transfer, Double-pipe heat exchangers, Nusselt numbers, overall heat transfer coefficient, NTU–ε, LMTD method

1.Introduction

Heat exchangers, especially the double-pipe type, are critical in energy systems due to their efficiency and compact construction [1]. Recent research uses computational fluid dynamics (CFD) and artificial neural networks (ANN) for performance improvement [2]. Accurate prediction of heat transfers is vital for energy management systems for domestic devices and more generally in the residential and hotel sector. Researchers widely use the Dittus-Boelter correlation for turbulent-flow heat transfer calculations, and CFD simulations have validated its accuracy [1]. Cost-efficient design improvements can rectify the

economic concerns caused by heat loss in poorer countries.

2.Theory and Method

The CFD output temperature was compared with the estimates of the ε-NTU method, taking a reference temperature of 67°C (340.15 K) for the hot water. The performance of the counterflow twin pipe heat exchangers was obtained by applying the conventional effectiveness-NTU relations [3]. The heat transfer coefficients for turbulent flow inside the tube were computed using the Dittus-Boelter correlation [1], which is widely used for fully developed turbulent flow conditions [4]. CFD simulations were conducted to examine the thermal behavior of cold water at a Reynolds number of about 22800.

$\mathcal{E} = \frac{Q}{Q_{MAX}}$, Q=C1(T1i-T1o)=C2(T2o-T2i), C1 =ṁ1cp1, C2 = ṁ2cp2, NTU = $\frac{UA}{C_{min}}$,

Qmax=CMin (T1, In-T2, In), Nu = $\frac{hD_h}{k}$, $\mathcal{E} = \frac{((1-e-NTU(1-Cr)))}{((1-Cr\cdot e-NTU(1-Cr)))}$, $\frac{1}{U1} = \frac{1}{h_i} + \frac{1}{h_o}$,

$\Delta Tm = \frac{(\Delta T1-\Delta T2)}{\ln(\Delta T1/\Delta T2)}$, ΔT1= Thot, in – Thot, out, ΔT2 = Thot, out − Tcold, in, Qtotal = U2Atotal

ΔTm, Thot, out =Thot, in − Q/Chot ,
Tcold, out =Tcold, in + Q/Ccold

Table 1. Theoretical Correlations by the Dittus-Boelter correlation

Qmax (W)	Qt**otal** (W)	ε	NTU	Cr	ΔTm (°C)	U1 (W/m2K)	U2 (W/m2K)
40950	2860	0.070	0.073	0.31	60	1435	1404

Table 2. Parameters of the set-up in the CFD Simulation

Model	K-epsilon Model	Near-Wall Treatment	C2-Epslion	TKE Pr Number	Energy Pr Number	Wall Pr Number
4K-epsilon	Realizable	Scalable	1.9	1	1.2	0.85

3. Results and Discussion

The numerical results obtained are in agreement with classical empirical correlations and with previously validated CFD research reported in the literature [5]. For turbulent flows correlation between Nusselt number of hot and cold media of 62 and 145 respectively at Reynolds number 4176 and 22816 was achieved. The best mesh sizes obtained by the ANSYS CFD simulations with the

variations of 3.14% for hot water and 0.22% for cold water from the theoretical findings. The CFD simulation is done with set inlet temperatures and boundary conditions and the outlet temperatures are calculated. The skewness of the mesh was good (0.21) and the orthogonality was extremely good (0.79).

Table 3. Comparison of Inlet and Outlet Temperatures.

Mesh Numbers	Media	m (kg/s)	Tout, Cal (K)	Tout, FD (K)	ΔTout (K)	Deviation
4.127.200	Water Hot	0.154	335.75	325.20	10.55	%3.14
	Water Cold	0.50	278.55	279.17	0.62	%0.22
2.487.600	Water Hot	0.154	335.75	324.66	11.09	%3.30
	Water Cold	0.50	278.55	279.22	0.67	%0.24
1.976.200	Water Hot	0.154	335.75	324.58	11.17	%3.33
	Water Cold	0.50	278.55	279.25	0.70	%0.25

4.Conclusion

The theoretical analysis of the heat transfer performance of the double pipe heat exchanger utilizing the Dittus-Boelter correlation was in close agreement with the computer simulations hence supporting the confidence in its application for such analysis.

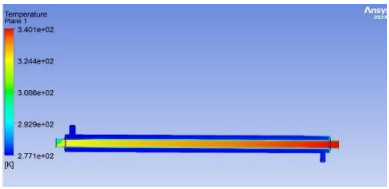


Fig. 3. Temp. Distribution of the investigated heat exchanger by CFD Simulation

References

1.J.P. Holman, Heat Transfer, 10th Edition, McGraw-Hill, New York, 2010.
2. Y.A. Çengel, A.J. Ghajar, Heat and Mass Transfer: Fundamentals & Applications, 5th Edition, McGraw-Hill, 2015.
3. F.P. Incropera, D.P. DeWitt, T.L. Bergman, A.S. Lavine, Fundamentals of Heat and Mass Transfer, 7th Edition, Wiley, 2011.
4. W.M. Kays, M.E. Crawford, B. Weigand, Convective Heat and Mass Transfer, 4th Edition, McGraw-Hill, 2005.
5.S.V. Patankar, Numerical Heat Transfer and Fluid Flow, Hemisphere Publishing, 1980

https://doi.org./10.58225/mpmma.2026.366

COMMUTATOR OF THE MAXIMAL FUNCTION IN TOTAL MORREY-GULIYEV SPACES IN THE DUNKL SETTING

Hamit Caglar Calisgan[1], Suleyman Celik[3], Vagif Guliyev[1,2] and Nisanur Polat[1]
[1] Kirsehir Ahi Evran University, Türkiye
[2] AzUAC, Azerbaijan
[3] Firat University, Türkiye

Abstract. In this work we obtain necessary and sufficient conditions for the boundedness of the commutators of the maximal operator $[b, M_k]$ associated with the Dunkl operator on $\mathbb{R}^d$ on the total D_k-Morrey-Guliyev spaces $L_{p,\lambda,\mu}(\mathbb{R}^d, d\mu_k)$ when b belongs to $BMO(\mathbb{R}^d, d\mu_k)$ spaces. We give some new characterizations for certain subclasses of $BMO(\mathbb{R}^d, d\mu_k)$. They play an important role in harmonic analysis and the study of special functions of several variables. These operators are associated with the differential-difference Dunkl operators on $\mathbb{R}^d$. This allows us to define the Dunkl translations τ_x, $x \in \mathbb{R}^d$.

Keywords: Maximal operator, total D_k-Morrey-Guliyev space, Dunkl operator, commutator, BMO.

1.Introduction

Morrey spaces, introduced by C. B. Morrey [4], play an important role in harmonic

analysis and the regularity theory of partial differential equations. In [2] Guliyev introduce a variant of Morrey spaces called total Morrey-Guliyev spaces $L_{p,\lambda,\mu}(\mathbb{R}^d)$, $0 < p < \infty$, $\lambda \in \mathbb{R}$ and $\mu \in \mathbb{R}$. Total Morrey-Guliyev spaces generalize both classical and modified Morrey spaces. On the $\mathbb{R}^d$ the Dunkl operators $\{D_{k,j}\}_{j=1}^d$ are the differential-difference operators associated with the reflection group $\mathbb{Z}_2^d$ on $\mathbb{R}^d$ and have many applications in harmonic analysis and special functions. In [5], was given basic properties of the total Morrey-Guliyev space (D_k-total Morrey space) $L_{p,\lambda,\mu}(\mathbb{R}^d, d\mu_k)$, $0 \le \lambda, \mu < d + 2\gamma_k$ associated with the Dunkl operator on $\mathbb{R}^d$ and study some embeddings into the total D_k-Morrey-Guliyev space $L_{p,\lambda,\mu}(\mathbb{R}^d, d\mu_k)$. These spaces generalize the Morrey space associated with the Dunkl operator on $\mathbb{R}^d$ (D_k-Morrey space) so that $L_{p,\lambda}(\mathbb{R}^d, d\mu_k) \equiv L_{p,\lambda,\lambda}(\mathbb{R}^d, d\mu_k)$ and the modified Morrey spaces associated with the Dunkl operator on $\mathbb{R}^d$ so that $\widetilde{L}_{p,\lambda}(\mathbb{R}^d, d\mu_k) \equiv L_{p,\lambda,0}(\mathbb{R}^d, d\mu_k)$.

We consider $\mathbb{R}^{\mathrm{d}}$ with the Euclidean scalar product $\langle \cdot, \cdot \rangle$ and its associated norm $\|x\| \coloneqq \sqrt{\langle x, x \rangle}$ for any $x \in \mathbb{R}^d$. For any $v \in \mathbb{R}^d \setminus \{0\}$ let σ_v be the reflection in the hyperplane $H_v \subset \mathbb{R}^d$ orthogonal to v:

$$\sigma_v(x) \coloneqq -\left(\frac{2\langle x,v\rangle}{\|v\|^2}\right)v, \quad x \in \mathbb{R}^d.$$

A finite set $R \subset \mathbb{R}^d \setminus \{0\}$ is called a root system, if $\sigma_v R = R$ for all $v \in R$.
We assume that it is normalized by $\|v\|^2 = 2$ for all $v \in R$.

The finite group G generated by the reflections $\{\sigma_v\}_{v\in R}$ is called the reflection group (or the *Coxeter-Weyl group*) of the root system. Then, we fix a G-invariant function $k : \mathrm{R} \to \mathbb{C}$ called the *multiplicity function of the root system* and we consider the family of commuting operators $D_{k,j}$ defined for any $f \in C^1(\mathbb{R}^d, d\mu_k)$ and any $x \in \mathbb{R}^d$ by

$$\begin{aligned} &D_{k,j}f(x) \\ &\coloneqq \frac{\partial}{\partial x_j}f(x) \\ &+ \sum_{v\in R_+} k_v \frac{f(x) - f\big(\sigma_v(x)\big)}{\langle x,v\rangle}\,\langle v, e_j\rangle, \\ &1 \le j \le d, \end{aligned}$$

Where $C^1(\mathbb{R}^d, d\mu_k)$ denotes the set of all functions $f : \mathbb{R}^d \to \mathbb{R}$ such that $\{\frac{\partial f}{\partial x_j}\}_{j=1}^d$ are continuous on $\mathbb{R}^d$, $\{e_i\}_{i=1}^d$ are the standard unit vectors of $\mathbb{R}^d$ and R_+ is a positive subsystem. These operators, defined by Dunkl [1], are independent of the choice

of the positive subsystem R_+ and are of fundamental importance in various areas of mathematics and mathematical physics.

Throughout this paper, we assume that $k_v \geq 0$ for all $v \in R$ and we denote by h_k the weight function on $\mathbb{R}^d$ given by

$$h_k(x) := \prod_{v \in R_+} |\langle x, v \rangle|^{k_v}, \qquad x \in \mathbb{R}^d.$$

The function h_k is G-invariant and homogeneous of degree γ_k, where $\gamma_k := \sum_{v \in R_+} k_v$.

Let $B(x,r) := \{y \in \mathbb{R}^d : |x-y| < r\}$ denote the ball in $\mathbb{R}^{\mathrm{d}}$ that centered in $x \in \mathbb{R}^{\mathrm{d}}$ and having radius $r > 0$, $B_r = B(0,r)$. Then having $\mu_k(B_r) = \int_{B_r} d\mu_k(x) = b_k\, r^{d+2\gamma_k}$.

The maximal commutator $M_{b,k}$ associated with the Dunkl operator on $\mathbb{R}^d$ and with a locally integrable function $b \in L_1^{\mathrm{loc}}(\mathbb{R}^d, d\mu_k)$ is defined by

$$M_{b,k} f(x) := \sup_{r>0} \left(\mu_k\big(B(x,r)\big)\right)^{-1} \int_{B(x,r)} |b(x) - b(y)|\, |f(y)|\, d\mu_k(y), \qquad x \in \mathbb{R}^d,$$

where $d\mu_k(y) = h_k^2(y)dy$, $f_{B(x,r)} := \left(\mu_k\big(B(x,r)\big)\right)^{-1} \int_{B(x,r)} f(y)\ d\mu_k(y)$.

We can define the (nonlinear) commutator of the maximal operator M_k with a locally integrable function b by

$$[b, M_k](f)(x) = b(x)M_k(f)(x) - M_k(bf)(x).$$

For more details about the operators $M_{b,k}$ and $[b, M_k]$, we refer to [3] and references therein.

Definition [3] *Let* $0 < p < \infty$, $\lambda \in \mathbb{R}$, $\mu \in \mathbb{R}$, $[t]_1 = \min\{1, t\}, t > 1$. *We denote by the total Morrey-Guliyev space* $L_{p,\lambda,\mu}(\mathbb{R}^d, d\mu_k)$ *(≡ total Dv- Morrey-Guliyev space), associated with the Dunkl operator the set of all classes of locally integrable functions* f *with the finite norm*

$$\|f\|_{L_{p,\lambda,\mu}(\mathbb{R}^d, d\mu_k)} = \sup_{x\in\mathbb{R}^n,\ t>0} [t]_1^{-\frac{\lambda}{p}} [1/t]_1^{\frac{\mu}{p}} \|f\|_{L_p(B(x,t), d\mu_k)}.$$

The following theorem gives necessary and sufficient conditions for the boundedness of the operator $M_{b,k}$ on $L_{p,\lambda,\mu}(\mathbb{R}^d, d\mu_k)$, when b belongs to the $BMO(\mathbb{R}^d, d\mu_k)$ space.

Theorem 1. [3] *Let* $1 < p < \infty$, $0 \le \lambda < d + 2\gamma_k$ *and* $0 \le \mu < d + 2\gamma_k$. *The following assertions are equivalent:*

(i) $b \in BMO(\mathbb{R}^d, d\mu_k)$.

(ii) *The operator* $M_{b,k}$ *is bounded on* $L_{p,\lambda,\mu}(\mathbb{R}^d, d\mu_k)$.

Applying Theorem 1, we obtain the following result.

Theorem 2. [3] *Let* $1 < p < \infty$, $0 \leq \lambda \leq d + 2\gamma_k$ *and* $0 \leq \mu \leq d + 2\gamma_k$. *Suppose that* b *is a real valued locally integrable function in* $\mathbb{R}^d$. *Then the following assertions are equivalent:*

(i) $b \in BMO(\mathbb{R}^d, d\mu_k)$ *such that* $b^- \in L_\infty(\mathbb{R}^d, d\mu_k)$.

(ii) *The operator* $[b, M_k]$ *is bounded on* $L_{p,\lambda,\mu}(\mathbb{R}^d, d\mu_k)$.

The research of V. Guliyev and S. Celik was partially supported by a grant from Kirsehir Ahi Evran University Scientific Research Projects (BAP, Project No: FEF.A1.26.001).

References

1. Dunkl, C.F.: Differential-difference operators associated with reflections groups. Trans. Amer. Math. Soc. 311, 167–183 (1989).

2. Guliyev, V.S.: Maximal commutator and commutator of maximal function on total Morrey spaces. J. Math. Inequal. 16(4), 1509–1524 (2022).

3. Mammadov, Y.Y., Guliyev, V.S., Akbulut, A., Omarova, M.N.: Commutator of the maximal function in total Morrey spaces in the Dunkl setting. TWMS J. Pure Appl. Math. 17(1), 79–93 (2026). DOI: 10.30546/2219-1259.17.1.2026.79

4. Morrey, C.B.: On the solutions of quasi-linear elliptic partial differential equations. Trans. Amer. Math. Soc. 43, 126–166 (1938).

5. Muslumova, F.A.: Some embeddings into the total Morrey spaces associated with the Dunkl operator on $\mathbb{R}^d$. Trans. Natl. Acad. Sci. Azerb. Ser. Phys.-Tech. Math. Sci. Mathematics 43(1), 94–102 (2023).

https://doi.org./10.58225/mpmma.2026.373

VALIDATION OF STRESS TENSOR MODELS FOR SPUR GEAR ROOT STRESS VIA FINITE ELEMENT ANALYSIS

Huseyn Mirzayev, Gulnar Salmanova
Karabakh University, Azerbaijan

Abstract. This study investigates the static structural behavior of a cylindrical spur gear tooth using Autodesk Inventor 2026. Stress, displacement, strain, and safety factor distributions were analyzed under tangential loading. Results show maximum stress concentration at the tooth root fillet, while low displacement and strain values confirm elastic behavior and dimensional stability. The safety factor distribution indicates reliable performance of the gear. The selected alloy steel provides an effective combination of strength, toughness, hardness, and wear resistance for gear applications.

Keywords: Tooth root stress; Spur gear; Finite element analysis; Stress concentration; Safety factor; Alloy steel.

Introduction

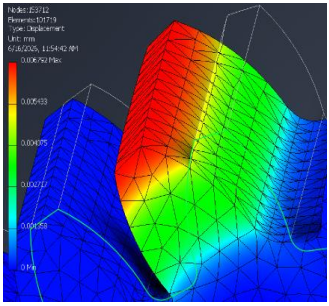
Gear transmission systems are fundamental components in mechanical engineering, serving as the primary means of power and motion transfer in various industrial applications, from automotive drivetrains to heavy machinery [1, 2]. The operational

reliability of these systems is critically dependent on the structural integrity of individual gear teeth. Among the various modes of failure, tooth root breakage due to bending stress remains one of the most catastrophic, often leading to complete system downtime. The primary function of these transmissions is to achieve required speed ratios (acceleration or deceleration) and to generate the necessary forces and torques for mechanical work. Compared to other mechanical drives, gear transmissions offer several key advantages, including higher power density (smaller dimensions for the same power output), superior efficiency, high load-carrying capacity, and long-term operational reliability. Given modern advancements in standardization and the ability to manufacture gears with high precision using progressive technologies, their application continues to expand across various industries. In contrast to prior studies, the present work evaluates the stress state, deformation behavior, and displacement of the model using both analytical and numerical approaches, with the results presented in a comparative form [3, 4]. It should be noted that, within the scope of the analytical investigation, bending stresses at the gear tooth root were additionally evaluated using the Lewis formula.

2. Methodology

Gears are typically manufactured from carbon and alloy steels, particularly for power transmission applications. Gears are typically manufactured from carbon and alloy steels, particularly for power transmission applications. Recently, gears made from polymer composite materials have also become increasingly common. In this study, the gear is intended to be fabricated from four different alloy steels. The composition of these steels consists of 97–98% iron (Fe), 0.18–0.23% carbon (C), 0.4–0.7% nickel (Ni), 0.7–0.9% manganese (Mn), and 0.15–0.35% silicon (Si). The load acting on the gear is generated by the transmitted torque. In spur gears, tangential and radial forces act within the mesh.

Figure 1 shows that the maximum displacement occurs at the tooth tip, whereas the highest von Mises stress is concentrated at the tooth root. This stress concentration is caused by bending under the transmitted tangential load, making the root region the most critical area for failure. If the von Mises stress exceeds the material yield strength, plastic deformation may begin. The yield



strength is particularly useful for evaluating the maximum allowable loading of gear teeth operating under cyclic stress, ensuring they do not reach their fatigue limit prematurely. These mechanical characteristics of the material are essential for determining the allowable stress levels in gear design.

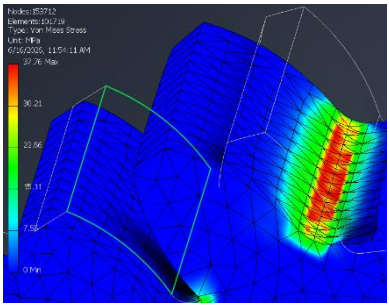


Fig. 1. Von Mises Stress and Total Displacement Distribution in the Gear Tooth

Conclusion

The integration of numerical simulation with analytical validation leads to the following key conclusions: The results of the static analysis performed in the Autodesk Inventor 2026 environment can be summarized as follows:

1. Stress concentration is localized in the region surrounding the tooth root, confirming the classical bending theory of gear teeth.

2. The stress distribution indicates that tensile stresses dominate in regions susceptible to crack initiation, while

compressive stresses prevail along the tooth flanks.

3. The magnitude of displacement remains low due to the high stiffness of the steel, thereby ensuring dimensional stability.

4. The consistency of the equivalent strain values supports the assumption of elastic deformation.

5. The safety factor distribution demonstrates that the structure operates with an adequate margin of reliability, except for localized stress concentrations.

6. The selected alloy steel provides a balanced combination of strength due to carbon and manganese, impact toughness due to nickel, and hardness and wear resistance due to silicon.

7. The consistency observed between the results of the FEM analysis and those derived from classical analytical methods confirms the reliability of the findings.

Future research on the static analysis of gear systems will also address mesh convergence studies, contact stress analysis, fatigue life assessment, evaluation of thermal effects in high-speed gear transmissions, and the influence of surface and bulk heat treatment processes (e.g., carburizing, nitriding, quenching, tempering, etc.).

References

1. Bhandari, V.B.: Design of machine elements, 3rd ed, Mc Graw-Hill, pp.673 (2010)
2. Mirzayev, H.: Comparative analysis of the tooth bending stress calculation methods of gearing mechanisms. Journal of Baku Engineering University – Mechanical and Industrial Engineering, Vol. 1, No. 1, Baku, pp. 13–20 (2017).
3. Abdullah, A.: Analysis of Contact Stresses in Spur Gears by Finite Element Method. European Journal of Science and Technology, No.17, Issue: 17, https://doi.org/10.31590/ejosat.629155, pp. 539 – 545 (2019).
4. Srinivasa, P., Shashishekar, C., Mallesh, G.: Finite Element Analyses of Non-Standard Spur Gears. Journal of Mines, Metals and Fuels, 71(12A), DOI: 10.18311/jmmf/2023/44017, pp. 348-354 (2023).

https://doi.org./10.58225/mpmma.2026.379

INTEGRAL–ANALYTİCAL MODELİNG OF WAVE PROPAGATİON IN AN ELASTIC MEMBRANE UNDER OBLIQUE IMPACT

Tukazban Hasanova, Mahsati Rustamova
AZUAC, Azerbaijan

Abstract. This paper investigates the mathematical formulation of the dynamic interaction between a rigid cone and a stretched elastic membrane under conditions of oblique impact. Extending the classical axisymmetric case of normal impact, the present study considers a cone inclined at an arbitrary angle to the membrane's surface, leading to asymmetric deformation and complex coupling between transverse and tangential motions. The equations of motion are derived based on the fundamental laws of conservation of momentum and the nonlinear geometric relations of membrane theory. Using a self-similar transformation, the system of governing partial differential equations is reduced to a more tractable form. It is shown that, under certain assumptions about the impact geometry and boundary conditions, the resulting formulation can be expressed as a system of integral equations describing the spatial-temporal evolution of membrane deflection and stress fields. Analytical properties of the

derived integral equations—such as existence, uniqueness, and smoothness of solutions—are analyzed. Approximate and numerical methods for solving these equations are also discussed. The reduction of the original nonlinear system to integral equations opens new possibilities for the application of modern analytical and computational techniques in the study of dynamic impact problems in thin elastic structures.

Keywords: oblique impact; elastic membrane; integral equations; analytical functions; automodel solution.

1. Introduction

The dynamic interaction between rigid bodies and elastic membranes is important in aerospace engineering, impact protection systems, and lightweight structures. While normal impact has been extensively studied, the analytical treatment of oblique impact remains limited.

The objective of this work is to develop an integral–analytical formulation for the oblique impact of a rigid cone on an elastic membrane using self-similar transformations and complex-variable methods.

2. Methodology

We consider an infinite homogeneous elastic membrane impacted by a rigid cone moving with constant velocity at an inclination angle.

The governing equations of membrane motion are written as

$$\rho \frac{\partial u}{\partial t} = \frac{\partial T_r}{\partial r} + \frac{T_r - T_\theta}{r}, \quad (1)$$

$$\rho \frac{\partial v}{\partial t} = \frac{\partial T_\theta}{\partial r} + \frac{T_\theta}{r}, \quad 2)$$

where

$$u = u(r,t), v = v(r,t)$$

are the velocity components, T_r, T_θ are the membrane stresses, and ρ is the membrane density. The velocity field is represented through two scalar potentials:

$$u = \frac{\partial \phi}{\partial r} + \frac{1}{r}\frac{\partial \psi}{\partial \theta}, \quad (3)$$

$$v = \frac{1}{r}\frac{\partial \phi}{\partial \theta} - \frac{\partial \psi}{\partial r}. \quad (4)$$

Because the impact velocity is constant and no characteristic length exists, the problem admits a self-similar solution. Introducing the similarity variable

$$\xi = \frac{r}{t}, \quad (5)$$

the original partial differential equations can be transformed into equations depending only on the variable ξ.

3. Self-Similar Solution and Integral Representation

The disturbed region is bounded by two characteristic wavefronts:

$r = at, r = bt$,

where $a > b$.

The membrane is divided into three zones: $0 < r < bt$, fully disturbed region, $bt < r < at$, intermediate region, and $r > at$, undisturbed membrane. The analytical solution is represented by complex potentials

$$F(z), G(z), \quad z = x + iy.$$

To satisfy the boundary conditions, the potential is expressed through single-layer potential. Application of the Sokhotski–Plemelj formulas leads to a singular integral equation of the form

$$\mu(s) + \frac{1}{\pi}\int_L \frac{\mu(\tau)}{\tau - s}\, d\tau = f(s), \qquad (6)$$

where $\mu(s)$is the unknown density function and Ldenotes the integration contour.

Equation (6) constitutes the basis of the integral–analytical formulation of the impact problem.

Conclusion

The self-similar formulation reveals the existence of longitudinal and transverse wavefronts propagating through the membrane with velocities $a$and b, respectively. The oblique impact produces

asymmetric deformation and stress distributions that differ significantly from the classical axisymmetric case. The reduction of the governing equations to singular integral equations enables the application of efficient analytical and numerical methods.

The proposed formulation can be extended to include material damping, anisotropy, and finite membrane geometries. An integral–analytical model for the oblique impact of a rigid cone on an elastic membrane has been developed. Using self-similar transformations and complex-variable techniques, the original system of governing equations is reduced to a system of singular integral equations. The obtained formulation describes asymmetric deformation and wave propagation and provides a foundation for future analytical and computational studies of impact phenomena in flexible membrane structures.

References

1. Rakhmatulin H.A. *About impact on a flexible thread*. PMM, 1947.

2. Agalarov D.G., Nuriev B.R., Rakhmatulin Kh.A. *Impact of a cone on a deformable string*. Journal of Applied Mathematics and Mechanics, 1981.

3. Duchemin L., Vandenberghe N. *Impact dynamics for a floating elastic membrane*. Journal of Fluid Mechanics, 2014.
4. Guo Y., Zhao Y., Liu W. *Analytical modeling of dynamic contact problems in elastic membranes*. Applied Mathematical Modelling, 2020.
5. Wang Y., Li X. *Self-similar solutions in dynamic contact problems*. International Journal of Engineering Science, 2021.
6. Li P. et al. *Dynamic responses of reticulated shells under oblique impact loading*. Buildings, 2024.

https://doi.org./10.58225/mpmma.2026.385

INVESTIGATION OF THE EFFECTS OF ULTRADISPERSE PLAGIOGRANITE POWDER ON CERAMIC MATERIAL PROPERTIES VIA MATHEMATICAL MODELING

Irada Mammadova
AzUAC, Azerbaijan

Abstract. This study investigates the influence of ultradisperse plagiogranite powder on the compressive strength and average density of ceramic materials using mathematical modeling. Clay content and plagiogranite content were selected as independent variables, while compressive strength and average density were considered the main performance indicators. Regression equations were developed using the least squares method, and their adequacy was verified by Fisher's criterion.The results showed that the addition of ultradisperse plagiogranite significantly improves the mechanical properties of ceramic materials. An optimal composition consisting of 80% clay and 20% plagiogranite was determined, providing a maximum compressive strength of 55.39 MPa while maintaining the required density range.

Keywords: Ceramic Material, Plagioqranite, Clay, Strength Limit, Average Density, Mathematical Model, Optimal Composition, Parameter, Least Squares Method.

Introduction

The development of the construction materials industry largely depends on the efficient use of local raw materials. In Azerbaijan, high-quality ceramic clays are limited, although ordinary brick clays are widely distributed. Therefore, improving the properties of low-quality clays through modification and optimization of ceramic compositions is an important research objective.

The production of high-quality ceramic materials requires not only the study of clay properties but also the selection of suitable corrective additives. Such additives can improve the structure, density, and strength of ceramic products.

In this research, ultradisperse plagiogranite powder was used as a modifying additive. Plagiogranite contains plagioclase minerals (calcium and sodium aluminosilicates) and granite components. Granite contributes to increased mechanical strength, while plagioclases reduce the sintering temperature of the ceramic mass. Due to these properties, plagiogranite acts simultaneously as a structure-forming and densifying component.

Materials and test methods used

The influence of plagiogranite content on ceramic material properties was studied through mathematical modeling. The least squares method was applied to determine the coefficients of the regression equations.

The following variables were selected:

x_1 – clay content (%);

x_2 – plagiogranite content (%).

The investigated properties were:

y_1 – compressive strength (MPa);

y_2 – average density (g/cm³).

Experimental compositions contained 80–99% clay and 1–20% plagiogranite. The results showed a gradual increase in both compressive strength and density with increasing plagiogranite content.

The optimization problem was formulated as follows:

-maximize compressive strength;

-maintain average density within acceptable limits;

-satisfy technological constraints:

$80 \leq x_1 \leq 99$

$1 \leq x_2 \leq 20$

Because the technological process is nonlinear, nonlinear regression models were developed using the stepwise regression method. The adequacy of the obtained models was verified using Fisher's statistical criterion.

Results and Discussion

Based on the experimental data, the following regression equations were obtained.

Compressive Strength Model

$y_1 = -705.1382 + 19.1138x_1 - 0.12009x_1^2$

Average Density Model

$y_2 = 3.5478 - 0.00022x_1^2 - 0.00145x_2^2 + 0.0002x_1x_2$

where:

y_1 – compressive strength (MPa);

y_2 – average density (g/cm³);

x_1 – clay content (%);

x_2 – plagiogranite content (%).

The adequacy of the models was evaluated using Fisher's criterion. The calculated values were:

$F_1 = 108.747$ for compressive strength;

$F_2 = 250.919$ for average density.

Both values exceeded the critical table value (Fcrit = 2.44), confirming that the developed models adequately describe the experimental data.

The correlation coefficients were:

$r = 0.963$ for the strength model;

$r = 0.990$ for the density model.

These high values indicate a strong relationship between the selected variables and the investigated properties.The obtained results demonstrate that increasing the amount of ultradisperse plagiogranite improves both density and compressive strength. This effect is associated with the structure-forming ability of plagiogranite and its contribution to a denser ceramic microstructure.

Optimization of Composition

To determine the optimal composition, the gradient method of nonlinear program ming was applied. This method searches for the point at which the objective function reaches its maximum value while satisfying all imposed constraints. The optimization process showed that the best results are achieved at the upper limit of plagiogranite content.The optimization process showed that the best

results are achieved at the upper limit of plagiogranite content.

The optimal composition was found to be:

Clay content: 80%

Plagiogranite content: 20%

For this composition:

Average density: 1.40–1.93 g/cm³

Maximum compressive strength: 55.39 MPa

Thus, the incorporation of 20% ultradisperse plagiogranite provides the most favorable balance between density and mechanical performance.

Conclusion

The effect of ultradisperse plagiogranite powder on ceramic material properties was successfully investigated using mathematical modeling. Nonlinear regression models describing compressive strength and average density were developed and verified through statistical analysis.

The results confirmed that plagiogranite is an effective modifying additive capable of improving the structure and mechanical properties of ceramic materials. Optimization using the gradient method established that the composition containing 80% clay and 20% plagiogranite provides the highest compressive strength of 55.39 MPa while maintaining acceptable density values.

The developed mathematical models can be used for predicting material properties and selecting optimal ceramic compositions in industrial applications.

References

1. Shirinzada I.N., Mammadova I.H. Optimization of modified clay-dolomite composition through mathematical modeling. Baku, 2015.
2. Mammadova I.H. Study of the effect of plagiogranite rock on the properties of ceramic materials through mathematical modeling. Baku, 2015.
3. Musaeva N.F. Information Technologies for Processing Experimental Data. Baku, 2007.
4. Shepelev I.G. Mathematical Methods and Management Models in Construction. Moscow, 1980.
5. Mammadova I.H. Adjustment of the properties of ceramic materials using ultra-dispersed plagiogranite rock. Baku, 2014

https://doi.org./10.58225/mpmma.2026.391

ON THE LAPLACE–STIELTJES TRANSFORM OF THE DISTRIBUTION OF A SEMI-MARKOV PROCESS

Elshan Ibayev [1,2,3] and Konul Omarova[4]

[1]Institute of Mathematics,Azerbaijan

[2]AzUAC,Azerbaijan,

[3]Azerbaijan Technical University, Azerbaijan

[4] Baku Business University, Baku, Azerbaijan

Abstract. In this work, a semi-Markov random walk with two delaying screens is constructed mathematically. The Laplace transform with respect to time and the Laplace–Stieltjes transform with respect to the phase of the conditional distribution of the process is discussed. In the general case, an integral equation corresponding to the Laplace–Stieltjes transform is obtained. In particular, when the time between two jump instants has a gamma distribution with parameters α and β and jump has exponential, a fractional-order integral equation for the Laplace–Stieltjes transform is derived. Finally, this integral equation is reduced to a constant-coefficient fractional differential equation.

Keywords: Laplace transform, Laplace-Stieltjes transform, semi-Markov random walk process, Riemann-Liouville fractional derivative.

1.Mathematical Model of the Process and Some Preliminary Notions

Let's assume that sequences of independent and identically distributed pairs of random variables $\{\xi_k, \zeta_k\}_{k\geq 1}$, be given on any probability space (Ω, F, P), where the random variables ξ_k and ζ_k are independent, positive. Now using these sequences of random variables, we can construct the stochastic process $X_z(t)$ as follows:

$$X_z(t) = z - t + \sum_{i=0}^{k-1} \zeta_i, \text{ if } \sum_{i=0}^{k-1} \xi_i \leq t < \sum_{i=0}^{k} \xi_i \quad k = \overline{1,\infty}$$

where $\xi_0 = \zeta_0 = 0$. $X_z(t)$- is called the Semi-Markov random walk process with negative drift, positive jumps. Delaying the process $X_z(t)$ with screen "0" [1,3], we have

$$X_1(t) = X_z(t) - \inf_{0\leq s\leq t} (0, X_z(s))$$

and the process $X_1(t)$ with screen "a" [2], we have

$$X(t) = a + X_1(t) - \sup_{0\leq s\leq t} (0, X_1(s)).$$

The process $X(t)$ is called the process of the semi-Markov random walk process with negative drift, positive jumps and two delaying screens at the level of zero and a (a>0).

Let's denote

$$R(t, x| z) = P\{X(t) < x \mid X(0) = z\}, \quad x \geq 0.$$

$$\widetilde{R}(\theta, x \mid z) = \int_0^{\infty} e^{-\theta t} R(t, x \mid z)\, dt, \quad \theta > 0,$$

$$\tilde{\tilde{\tilde{R}}}(\theta,\lambda \mid z) = \int_0^{\infty} e^{-\lambda x} d_x \tilde{R}(\theta, x \mid z),$$
$$\lambda > 0.$$

The fractional order differential equation for the $\tilde{\tilde{\tilde{R}}}(\theta,\lambda \mid z)$.

Using the law of total probability, we can write the Laplace–Stieltjes transform of the distribution function $\tilde{\tilde{\tilde{R}}}(\theta,\lambda \mid z)$ of the process $X(t)$ as follows:

$$\tilde{\tilde{\tilde{R}}}(\theta,\lambda \mid z) = e^{-\theta z} \int_0^{z} e^{-(\lambda-\theta)x} P\{\xi_1 > z - x\}\, dx +$$

$$+\tilde{\tilde{\tilde{R}}}(\theta,\lambda \mid a) \int_0^{z} e^{-\theta t} P\{\xi_1 \in dt\} P\{\zeta_1 > a - z + t\}\, dx +$$

$$+\int_0^{z} \tilde{\tilde{\tilde{R}}}(\theta,\lambda \mid y) \int_{z-y}^{z} e^{-\theta t} P\{\xi_1 \in dt\} d_y P\{\zeta_1 < y - z + t\} +$$

$$+\int_z^{a} \tilde{\tilde{\tilde{R}}}(\theta,\lambda \mid y) \int_0^{z} e^{-\theta t} P\{\xi_1 \in dt\} d_y P\{\zeta_1 < y - z + t\} +$$

$$+\tilde{\tilde{R}}(\theta,\lambda \mid a)\int_z^{\infty} e^{-\theta t}P\{\xi_1 \in dt\}P\{\zeta_1 > a\} +$$

$$+\int_0^a \tilde{\tilde{R}}(\theta,\lambda \mid y)\int_z^{\infty} e^{-\theta t}P\{\xi_1 \in dt\}d_y P\{\zeta_1 < y\}. \qquad (1)$$

Let ξ_1 be a random variable that has a gamma distribution with parameters $\alpha > 0$ and $\beta > 0$, and let ζ_1 be a random variable that has an exponential distribution with parameter μ:

$$p_{\xi_1}(x) = \begin{cases} \frac{\beta^\alpha}{\Gamma(\alpha)} \cdot x^{\alpha-1} e^{-\beta x}, & x > 0, \\ 0, & x \le 0, \end{cases} \quad p_{\zeta_1}(x) = \begin{cases} \mu e^{-\mu x}, & x \ge 0, \\ 0, & x < 0. \end{cases}$$

In the class of these distributions, the integral equation (1) takes the following form:

$$\tilde{\tilde{R}}(\theta,\lambda \mid z) = \frac{e^{-\theta z}}{\lambda-\theta} - \frac{e^{-\lambda z}}{\lambda-\theta} - \frac{\beta^\alpha e^{-\theta z}}{(\lambda-\theta)\Gamma(\alpha)}\int_0^z y^{\alpha-1}e^{-\beta y}dy +$$

$$-\frac{\beta^\alpha e^{-(\beta+\theta)z}}{(\lambda-\theta)\Gamma(\alpha)}\int_0^z e^{-(\lambda-\theta-\beta)x}(z-x)^{\alpha-1}dx + \frac{\beta^\alpha e^{-\mu(a-z)}\tilde{\tilde{R}}(\theta,\lambda|a)}{\Gamma(\alpha)}\int_0^z e^{-(\mu+\theta+\beta)t}t^{\alpha-1}dt +$$

$$+\frac{\beta^{\alpha}\mu e^{\mu z}}{\Gamma(\alpha)}\int_{0}^{z} e^{-\mu y}\tilde{\tilde{\tilde{R}}}(\theta,\lambda|y)\int_{z-y}^{z} e^{-(\mu+\theta+\beta)t}t^{\alpha-1}dtdy$$

$$+$$

$$+\frac{\beta^{\alpha}\mu e^{\mu z}}{\Gamma(\alpha)}\int_{z}^{a} e^{-\mu y}\tilde{\tilde{\tilde{R}}}(\theta,\lambda|y)\int_{0}^{z} e^{-(\mu+\theta+\beta)t}t^{\alpha-1}dtdy$$

$$+$$

$$+\frac{\beta^{\alpha}e^{-\mu a}\tilde{\tilde{R}}(\theta,\lambda|a)}{\Gamma(\alpha)}\int_{z}^{\infty} e^{-(\theta+\beta)t}t^{\alpha-1}dt+\frac{\beta^{\alpha}\mu}{\Gamma(\alpha)}\int_{0}^{a} e^{-\mu y}\tilde{\tilde{\tilde{R}}}(\theta,\lambda|y)\int_{z}^{\infty} e^{-(\theta+\beta)t}t^{\alpha-1}dtdy$$

. (2)

Let us denote

$$Q(\theta,\lambda|z)=\ e^{(\theta+\beta)z}\tilde{\tilde{\tilde{R}}}(\theta,\lambda|z)$$

Applying to both sides equation (2) Riemann-Liouville fractional derivative of order α, we obtain

$$D_{z}^{\alpha+1}Q(\theta,\lambda|z)-(\mu+\theta+\beta)D_{z}^{\alpha}Q(\theta,\lambda|z)+\beta^{\alpha}\mu Q(\theta,\lambda|z)=$$

$$=-\frac{(\mu+\theta)}{\theta-\lambda}z^{-\alpha}E_{1,1-\alpha}(\beta z)+\frac{(\lambda+\mu)}{\lambda-\theta}z^{-\alpha}E_{1,1-\alpha}\big((\theta+\beta-\lambda)z\big)-$$

$$-\frac{(\lambda+\mu\beta^{\alpha}}{(\lambda-\theta)}e^{-(\lambda-\theta-\beta)z}+\frac{(\mu+\theta)\beta^{\alpha}}{\lambda-\theta}E_{1,1}(\beta z)$$

$$+$$

$$+Az^{-\alpha}E_{1,1-\alpha}\big((\theta+\beta)z\big)-BE_{1,1}\big((\theta+\beta)z\big).$$

Here, A and B denote constants.

References

1. Borovkov A.A: On the asymptotics of distributions of first passage times I. *Mathematical Notes*, 75, No. 1, 24–39 (2004).
2. Ibayev E. A., Omarova K. K: Investigation a boundary functional of a random walk process using fractional order differential equation. Uzbek Mathematical Journal Volume 68, Issue 4, pp. 56-62 (2024).
3. Nasirova T.I.: The processes of semi-Markov random walk. Baku, Elm (1984)

https://doi.org./10.58225/mpmma.2026.397

ON THE UNIQUENESS OF RECOVERY OF THE DIRAC OPERATOR WITH A BOUNDARY CONDITION LINEARLY DEPENDING ON THE SPECTRAL PARAMETER

Ibrahim Nabiev[1,2,3], Aygun Latifova[2], Leyla Mammadova[4] , Jalala Osmanli[2]

[1] Baku State University, Azerbaijan

[2] Institute of Mathematics, Azerbaijan

[3] Khazar University, Azerbaijan

[4] Azerbaijan State Oil and Industry University, Azerbaijan

Abstract. In this paper, we study the inverse problem of spectral analysis for a one-dimensional Dirac system in the case where one of the boundary conditions is separated and the other is non-separated. The non-separated boundary condition contains a linear function of the spectral parameter. The main goal of the research is to obtain a uniqueness theorem for the recovery of the system potential and the coefficients of the boundary conditions from the spectral data, which consist of the spectra of two problems. An asymptotic formula for the eigenvalues of the Dirac operator is provided, and the expansion of the characteristic function of the boundary value problem as an infinite product using the eigenvalues is obtained. Based on the two given spectra, the characteristic functions of the boundary

value problems and the parameters of the boundary conditions are first recovered, after which the problem is reduced to the inverse problem of recovering the coefficient of the Dirac equation from the spectra of two boundary value problems with separated boundary conditions.

The results obtained can be used in solving various versions of inverse problems of spectral analysis for differential operators, as well as for integrating certain nonlinear equations of mathematical physics.

Keywords: Dirac system, inverse problem, uniqueness theorem, solution algorithm.

On a finite interval $[0,\pi]$, a boundary value problem generated by a one-dimensional stationary Dirac system (associated with the behavior of a relativistic electron in an electrostatic field) is considered

$$BY'(x)+Q(x)Y(x)=\lambda Y(x), \tag{1}$$

with boundary conditions of the form

$$y_2(0)+\gamma y_1(0)=0,$$
$$y_1(0)+(\alpha\lambda+\beta)y_1(\pi)+y_2(\pi)=0, \tag{2}$$

where $B=\begin{pmatrix}0 & 1\\ -1 & 0\end{pmatrix}$, $Q(x)=\begin{pmatrix}p(x) & q(x)\\ q(x) & -p(x)\end{pmatrix}$, $Y(x)=\begin{pmatrix}y_1(x)\\ y_2(x)\end{pmatrix}$, λ – the spectral parameter, $\alpha\neq 0$, β and $\gamma>0$ are real numbers. This

problem will be denoted by P. It is assumed that the elements $p(x)$ and $q(x)$ of the matrix $Q(x)$ in (1) are real-valued functions belonging to the space $W_2^1[0,\pi]$. We denote by $W_2^1[0,\pi]$ the space consisting of absolutely continuous functions defined on the interval $[0,\pi]$ whose derivatives are square-integrable on $[0,\pi]$.

Definition. The values of the parameter λ for which the problem P has nontrivial solutions are called the eigenvalues of this problem. The set of eigenvalues is called the spectrum of P.

Along with the problem P, we also consider the boundary value problem $\tilde{P}$ generated by the same equation (1) and the boundary conditions

$$\begin{aligned} y_2(0)+\gamma y_1(0)&=0,\\ y_1(0)+\left(\tilde{\alpha}\lambda+\tilde{\beta}\right)y_1(\pi)+y_2(\pi)&=0, \end{aligned} \tag{3}$$

where $\tilde{\alpha}\neq 0$ and $\tilde{\beta}$ are real numbers.

Let $S(x,\lambda)=\begin{pmatrix} s_1(x,\lambda)\\ s_2(x,\lambda)\end{pmatrix}$ and $C(x,\lambda)=\begin{pmatrix} c_1(x,\lambda)\\ c_2(x,\lambda)\end{pmatrix}$ denote the solutions of equation (1) satisfying the initial conditions

$S(0,\lambda)=\begin{pmatrix}0\\1\end{pmatrix}$ and $C(0,\lambda)=\begin{pmatrix}1\\0\end{pmatrix}$. The characteristic functions $\Delta(\lambda)$ and $\tilde{\Delta}(\lambda)$, whose zeros μ_k and $\tilde{\mu}_k$, $k=\pm0,\pm1,\pm2,...$ are the eigenvalues of the boundary value problem P and $\tilde{P}$, has the form

$$\Delta(\lambda)=(\alpha\lambda+\beta)(c_1(\pi,\lambda)-\gamma s_1(\pi,\lambda))+c_2(\pi,\lambda)-\gamma s_2(\pi,\lambda)-\gamma=$$
$$=\alpha\lambda(\cos\lambda\pi+\gamma\sin\lambda\pi)+d_2\cos\lambda\pi+d_1\sin\lambda\pi-\gamma+\psi_1(\lambda),$$
$$\tilde{\Delta}(\lambda)=(\tilde{\alpha}\lambda+\tilde{\beta})(c_1(\pi,\lambda)-\gamma s_1(\pi,\lambda))+c_2(\pi,\lambda)-\gamma s_2(\pi,\lambda)-\gamma=$$
$$=\tilde{\alpha}\lambda(\cos\lambda\pi+\gamma\sin\lambda\pi)+\tilde{d}_2\cos\lambda\pi+\tilde{d}_1\sin\lambda\pi-\gamma+\psi_2(\lambda),$$

where

$$d_1=\alpha A+\beta\gamma+1,\ d_2=\beta-\alpha\gamma A-\gamma,$$
$$\tilde{d}_1=\tilde{\alpha}A+\tilde{\beta}\gamma+1,\ \tilde{d}_2=\tilde{\beta}-\tilde{\alpha}\gamma A-\gamma,$$
$$\psi_j(\lambda)=\int_{-\pi}^{\pi}\tilde{\psi}_j(t)e^{i\lambda t}dt,$$
$$\tilde{\psi}_j(t)\in L_2[-\pi,\pi],\ j=1,2.$$

Theorem 1. The eigenvalues μ_k and $\tilde{\mu}_k$, $k=\pm0,\pm1,\pm2,...$ of the boundary value problem P and $\tilde{P}$, for $|k|\to\infty$, satisfy the asymptotic formula

$$\mu_k=k+a+\left[1+\alpha A+\frac{(-1)^k\gamma}{\sqrt{1+\gamma^2}}\right]\frac{1}{\pi\alpha k}+\frac{\tau_k}{k},$$
$$\tilde{\mu}_k=k+a+\left[1+\tilde{\alpha}A+\frac{(-1)^k\gamma}{\sqrt{1+\gamma^2}}\right]\frac{1}{\pi\tilde{\alpha}k}+\frac{\tilde{\tau}_k}{k},$$

where

$$a = -\frac{1}{\pi}\operatorname{arctg}\frac{1}{\gamma}, \quad \{\tau_k\}, \{\tilde{\tau}_k\} \in l_2.$$

Theorem 2. The specification of the spectrums $\{\mu_k\}$ and $\{\tilde{\mu}_k\}$ uniquely determines the characteristic functions $\Delta(\lambda)$ and $\tilde{\Delta}(\lambda)$ of the boundary value problems P and $\tilde{P}$ by the formulas

$$\Delta(\lambda) = \pi\alpha\sqrt{1+\gamma^2}\,(\mu_{-0} - \lambda)(\mu_{+0} - \lambda)\prod_{\substack{k=-\infty \\ k\neq 0}}^{\infty}\frac{\mu_k - \lambda}{k},$$

$$\tilde{\Delta}(\lambda) = \pi\tilde{\alpha}\sqrt{1+\gamma^2}\,(\tilde{\mu}_{-0} - \lambda)(\tilde{\mu}_{+0} - \lambda)\prod_{\substack{k=-\infty \\ k\neq 0}}^{\infty}\frac{\tilde{\mu}_k - \lambda}{k}.$$

Consider the following inverse problem.

Inverse Problem. Given the spectra of the boundary value problems P and $\tilde{P}$, construct the matrix-valued function $Q(x) = \begin{pmatrix} p(x) & q(x) \\ q(x) & -p(x) \end{pmatrix}$ in the Dirac equation (1), as well as the coefficients $\alpha, \beta, \gamma, \tilde{\alpha}, \tilde{\beta}$ in the boundary conditions (2) and (3).

The following uniqueness theorem holds.

Theorem 3. The boundary value problems P and $\tilde{P}$ are uniquely determined by their spectra.

The solution of the inverse problem can be obtained by the following algorithm.

Algorithm. Given the sequences $\{\mu_k\}$ and $\{\tilde{\mu}_k\}$, which are the spectra of the boundary value problems P and $\tilde{P}$.

1)Compute the quantity a and the coefficients γ, α of the boundary conditions (2) and (3) using formulas

$$a = \lim_{k\to\infty}(\mu_k - k),$$

$$\gamma = -\operatorname{tg}\pi a,$$

$$\alpha = \frac{\sin \pi a}{\pi} \lim_{k\to\infty} \frac{1}{k(\mu_{2k+1} - \mu_{2k} - 1)}.$$

2) Using the sequences $\{\mu_k\}$ and $\{\tilde{\mu}_k\}$, construct the characteristic functions $\Delta(\lambda)$ and $\tilde{\Delta}(\lambda)$ in the form of infinite products (see theorem 2).

3) The coefficients $\beta, \tilde{\alpha}, \tilde{\beta}$ of the boundary conditions (2) and (3) are reconstructed using relations

$$\beta = \frac{d_2 + d_1\gamma}{1+\gamma^2},$$

$$\tilde{\alpha} = \frac{\sin \pi a}{\pi} \lim_{k\to\infty} \frac{1}{k(\tilde{\mu}_{2k+1} - \tilde{\mu}_{2k} - 1)},$$

$$\tilde{\beta} = \frac{\tilde{d}_2 + \tilde{d}_1\gamma}{1+\gamma^2},$$

where

$$d_1 = \lim_{k\to\infty}\left[\Delta\left(2k+\frac{1}{2}\right) - \left(2k+\frac{1}{2}\right)\alpha\gamma + \gamma\right],$$

$$d_2 = \lim_{k\to\infty}[\Delta(2k) - 2k\alpha + \gamma],$$

$$\widetilde{d}_1 = \lim_{k\to\infty}\left[\widetilde{\Delta}\left(2k+\frac{1}{2}\right)-\left(2k+\frac{1}{2}\right)\widetilde{\alpha}\gamma+\gamma\right],$$
$$\widetilde{d}_2 = \lim_{k\to\infty}\left[\widetilde{\Delta}(2k)-2k\widetilde{\alpha}+\gamma\right].$$

.

4) Solving system

$$\begin{cases}\Delta(\lambda)=(\alpha\lambda+\beta)(c_1(\pi,\lambda)-\gamma s_1(\pi,\lambda))+c_2(\pi,\lambda)-\gamma s_2(\pi,\lambda)-\gamma,\\ \widetilde{\Delta}(\lambda)=(\widetilde{\alpha}\lambda+\widetilde{\beta})(c_1(\pi,\lambda)-\gamma s_1(\pi,\lambda))+c_2(\pi,\lambda)-\gamma s_2(\pi,\lambda)-\gamma\end{cases}$$

, we uniquely determine the functions $\delta_1(\lambda)=c_1(\pi,\lambda)-\gamma s_1(\pi,\lambda)$ and $\delta_2(\lambda)=c_2(\pi,\lambda)-\gamma s_2(\pi,\lambda)$.

5) Using the sequences of zeros of the functions $\delta_1(\lambda)$ and $\delta_2(\lambda)$, we construct the coefficient $Q(x)$ of the Dirac equation (1) by a known procedure (see, for example, [2, 3]]).

We note that problems similar in formulation were considered in [1, 4–6] and other works.

References

1. Abdullaev, T.Sh., Nabiev, I.M.: An algorithm for reconstructing the Dirac operator with a spectral parameter in the boundary condition. Computational Math. and Math. Phys, 56(2), 256-262 (2016).
2. Albeverio, S., Hryniv, R., Mykytyuk, Ya.: Inverse spectral problems for Dirac operators with summable potentials. Russian J. Math. Phys. 12(4), 406-423 (2005).
3. Gasymov, M. G., Dzhabiev, T. T.: Solution of the inverse problem by two

spectra for the Dirac equation on a finite interval. Dokl. Akad. Nauk Azerb. SSR. 22(7), 3–7 (1966).
4. Ferzullazadeh, A.G.: Solution algorithm of the inverse spectral problem for Dirac operator with a spectral parameter in the boundary condition. Operators and Matrices. 16 (1), 113-122 (2022).
5. Mammadova, L.I., Nabiev, I.M.: Uniqueness of recovery of the Dirac system on a segment by two spectra. J. Contemporary Appl. Math. 16(1), 110-118 (2026).
6. Topsakal, N., Amirov, R.: On a class of Dirac operators with eigenvalue nonlinearly dependent to boundary condition. Asian Journal of Mathematics and Computer Research. 26 (1), 39-49 (2019).

https://doi.org./10.58225/mpmma.2026.*405*

COST-EFFECTIVE HYBRID SENSOR NETWORK OPTIMIZATION FOR FLOOD MONITORING IN RESOURCE-CONSTRAINED ENVIRONMENTS USING GENETIC ALGORITHMS

*Ibrahim Suleymanov, Kamran Huseynov***,** *Aysu Huseynova, Elmeddin Mohubbetov, Nicat Ahmadov, Rahman Karimli*
Azerbaijan State University of Economics

Abstract. Flood early-warning systems in resource-constrained environments face persistent limitations related to sparse hydro-meteorological observations, unreliable communications, limited energy availability, and severe financial constraints. Although recent advances in low-cost Internet of Things (IoT) sensing and wireless sensor networks (WSNs) demonstrate the feasibility of decentralized flood monitoring, existing studies typically optimize either sensor placement, network routing, energy efficiency, or prediction accuracy in isolation. Consequently, current approaches rarely provide an integrated framework capable of simultaneously addressing coverage, reliability, redundancy, resilience, and lifecycle cost. This paper presents a systematic review and methodological framework for cost-effective hybrid sensor network optimization for flood monitoring using Genetic Algorithms (GAs) and Non-dominated Sorting Genetic Algorithm II (NSGA-II). The article synthesizes findings from AI-enabled flood modelling, multi-

modal river monitoring, self-healing WSN architectures, and budget-constrained optimization. Building upon these insights, the paper proposes a formalized multi-objective optimization framework in which each chromosome simultaneously encodes a hybrid sensor portfolio and geographic deployment coordinates. Unlike conventional weighted-sum approaches, the proposed framework reformulates the optimization problem as a constrained Pareto-based search using NSGA-II to preserve trade-offs between flood coverage, reliability, redundancy, and cost. To address scale incompatibility between heterogeneous objectives, a dynamically normalized Sensor Validity Function (SVF), inspired by the Weighted Sum Validity Function (WSVF), is incorporated as an auxiliary scalar benchmark. The framework further integrates constrained domination, diversity-preserving niching mechanisms, and local greedy refinement strategies to improve convergence and deployment diversity. The proposed framework contributes a publication-oriented methodological foundation for resilient and economically feasible flood-monitoring infrastructures in developing regions. To provide computational validation of the proposed NSGA-II framework, this paper presents a real-world case study applied to the Kur River in Sabirabad District, Azerbaijan, using a heterogeneous 15-sensor fleet subject

to a $6,000 budget constraint. Experimental results demonstrate that NSGA-II returns a Pareto front of 100 non-dominated solutions compared to a single solution produced by the weighted-sum GA benchmark, achieving 100% monitoring coverage versus 96.7% for GA, reducing deployment cost by $800, and yielding a hypervolume indicator 1.94× larger than the single-objective baseline.

Keywords: Flood Monitoring, NSGA-II, Multi-objective Optimization, Wireless Sensor Networks (WSN), Cost-Effective Deployment, Genetic Algorithms.

https://doi.org./10.58225/mpmma.2026.408

FRACTIONAL-ORDER OPTIMAL CONTROL OF DRUG-RESISTANT TUBERCULOSIS: MODEL ANALYSIS AND NUMERICAL VALIDATION

M.Ariyanatchi[1], I.Paulraj jeyasimman [2 1,2]
Academy of Maritime Education and Training (Deemed to be University), ECR India

Abstract. In this study, a new Caputo fractional order optimal control problem for TB disease transmission with drug-sensitive and resistant bacteria is formulated. With the integration of the memory effect in the state equations and employing the Pontryagin maximum principle on fractional calculus, we obtain the necessary optimality conditions for the time optimal intervention policy, which considers the combination of detecting cases, encouraging patients to take their treatment effectively, and fast drug susceptibility testing. It is shown through simulation that the memory-dependent optimal control strategy achieves an efficient reduction in the basic reproduction number compared to the integer-order scenario, especially in limited resources.

Keywords: Fractional calculus, Optimal control, Tuberculosis, Drug resistance, Computational epidemiology

INTRODUCTION

Nevertheless, drug-resistant Tuberculosis (TB) continues to threaten global TB

eradication due to rising fatalities caused by TB [1]. The conventional compartmental model based on integer order has yielded a lot of important insights in terms of threshold analysis as well as interventions for controlling TB [2,3], although it assumes Markovian property without incorporating memory effect in latency, treatment, and immunity [4].

Fractional calculus is a mathematical tool that provides an adequate framework for dealing with nonlocal operators that capture memory effect [5]. Some empirical research works have shown the superiority of fractional order TB models over their integer counterparts [6,7]; however, few have considered the application of optimal control theory to multi-strain models. This study contributes to the field in that it (i) introduces a novel Caputo fractional-order TB optimal control model that considers the resistance to treatment; (ii) presents the necessary conditions for the model; and (iii) validates the model numerically using Indian TB surveillance data.

2 MODEL FORMULATION AND ANALYSIS

2.1 Fractional-State System

We consider a six-compartment model with Caputo derivative of order $\alpha \in (0,1]$:

$$
\begin{aligned}
&{}_0^{C}D_t^{\alpha} S = \Lambda - \beta_S S I_S - \beta_R S I_R - \mu S + \omega T, \\
&{}_0^{C}D_t^{\alpha} I_S = \sigma_S L_S - (\mu + \delta_S + \gamma_S u_2) I_S, \\
&{}_0^{C}D_t^{\alpha} L_R = \beta_R S I_R + (1-\epsilon)\tau_1 u_1 L_S - (\mu + \sigma_R) L_R \\
&{}_0^{C}D_t^{\alpha} I_R = \sigma_R L_R + \epsilon \tau_1 u_1 L_S - (\mu + \delta_R + \gamma_R u_3) I_R, \\
&{}_0^{C}D_t^{\alpha} T = \gamma_S u_2 I_S + \gamma_R u_3 I_R - (\mu + \omega) T
\end{aligned}
\quad (1)
$$

where u_1, u_2, u_3 represent case detection, treatment adherence, and rapid drug-susceptibility testing controls, respectively.

2.2 Optimal Control Problem

The objective functional minimizes infection burden and intervention costs:

$$\mathcal{J} = \int_0^{T_f} \left[A_1 I_S + A_2 I_R + \frac{1}{2} \sum_{i=1}^{3} B_i u_i^2(t) \right] dt \quad (2)$$

Applying fractional Pontryagin's principle [3], the adjoint system satisfies ${}_0^{C}D_t^{\alpha} \lambda_i = -\partial \mathcal{H} / \partial x_i$ with transversality conditions $\lambda_i(T_f) = 0$. Optimal controls are characterized by:

$$u_1^* = \min\left\{1, \max\left\{0, \frac{\tau_1 L_S (\lambda_2 - (1-\epsilon)\lambda_4 - \epsilon\lambda_5)}{B_1}\right\}\right\} \quad (3)$$

Similarly with analogous expressions for u_2^*, u_3^*.

Table 1. Parameter estimates from Indian TB data (2018–2023) with 95% confidence intervals

Parameter	Estimate	95% CI	Source/ Method

α (fractional order)	0.85	[0.82, 0.88]	Nonlinear least squares
β_S (sensitive transmission)	0.28 day^{-1}	[0.24, 0.31]	Calibration [6]
β_R (resistant transmission)	0.14 day^{-1}	[0.11, 0.17]	Calibration [6]
σ_R (resistant progression)	1.9×10^{-4} day^{-1}	[1.5, 2.3] $\times10^{-4}$	Literature [7]

3 NUMERICAL RESULTS AND DISCUSSION

3.1 Model Validation

Parameters were calibrated to monthly TB notifications from India's National Tuberculosis Elimination Programme (2018–2023) using a fractional predictor-corrector algorithm [9]. The fractional-order model achieved substantially better fit than its integer-order counterpart (AIC: 342.7 vs. 361.0; ΔAIC = 18.3) (see Fig. 1).



Fig. 1. (a) Observed TB incidence (dots) with fractional-model simulation (solid,

α=0.85) and integer-model simulation (dashed, α=1.0). (b) Optimal control profiles: fractional policy initiates rapid DST (u_3) earlier and sustains moderate case detection (u_1) longer than integer-order policy

3.2 Control Impact Assessment

Under optimal fractional-order control over a 5-year horizon:

- Peak drug-resistant infections reduced from 12,450 to 8,470 cases (32% reduction)
- Cumulative intervention cost decreased by 18% relative to integer-order optimal policy and Time to eliminate resistant strain shortened by 14 months

Table 2. Partial Rank Correlation Coefficients (PRCC) for key outputs

Parameter	Estimate	95% CI	Source/Method
α	-0.71	-0.68	+0.42
β_R	+0.83	+0.79	+0.51
γ_R(u_3 efficacy	-0.38	-0.64	-0.59
σ_R	+0.52	+0.61	+0.33

Significant at $p < 0.01$ (Latin Hypercube Sampling, n = 2,000)

3.3 Public Health Implications

The value of the estimated parameter α = 0.85 demonstrates very high memory in TB infection, implying that past infection history plays an important role in current infection

levels. The high sensitivity to the parameter β_R implies the need to control the spread of the infection from individuals with drug resistance due to their diagnosis and isolation.

4 Conclusion

The present study provides an optimal control theory in the context of fractional order calculus for tuberculosis that is resistant to drugs. The numerical simulations show that memory-based controls yield better results than the traditional optimal controls. In future work, we plan to consider spatial heterogeneities using physics-informed neural networks.

References

1. World Health Organization: Global Tuberculosis Report 2023. WHO, Geneva (2023)
2. Blower, S.M., Small, M., Hopewell, P.C.: Control strategies for tuberculosis epidemics. Science **273**, 497–500 (1996)
3. Feng, Z., Castillo-Chavez, C., Capurro, A.F.: A model for tuberculosis with exogenous reinfection. Theor. Popul. Biol. **57**, 235–247 (2000)
4. Nisar, K.S., et al.: A review on epidemic models in sight of fractional calculus. Alexandria Eng. J. **75**, 81–113 (2023)
5. Podlubny, I.: Fractional Differential Equations. Academic Press, San Diego (1999)

6. Gemeda, A.E., et al.: Mathematical modeling of tuberculosis transmission dynamics with vaccination. J. Appl. Math. Comput. **71**, 2017–2049 (2025)
7. Ullah, S., et al.: A fractional model for tuberculosis dynamics using Caputo-Fabrizio derivative. Discr. Contin. Dyn. Syst. Ser. S **13**, 975–993 (2020)
8. Almeida, R.: Analysis of a fractional SEIR model with treatment. Appl. Math. Lett. 84, 56–62 (2018)
9. Diethelm, K.: The Analysis of Fractional Differential Equations. Springer, Heidelberg (2010)

https://doi.org./10.58225/mpmma.2026.415

STUDY OF THE INFLUENCE OF CHEMICAL COMPOSITION ON THE PROPERTIES OF CLAY-DOLOMITE COMPOSITE MATERIALS USING MATHEMATICAL MODELING

Shirinzade Irada
AzUAC, Azerbaijan

Abstract. The assessment of construction material properties often requires specialized equipment and time-consuming testing. Indirect evaluation methods enable the prediction of material performance from chemical composition, reducing experimental effort and production time. This study examines the effect of the basic-to-acidic oxide ratio (RO/SiO_2) on the average density and compressive strength of clay–dolomite composite materials. Linear, logarithmic, hyperbolic, power-law, and parabolic regression models were developed using the least-squares method to describe the relationships between chemical composition and material properties. Statistical analysis was applied to evaluate model adequacy and predictive accuracy. The results showed that the parabolic model provided the best fit for both average density and compressive strength, confirming a strong dependence of these properties on chemical composition. The derived regression equations can be used to predict

material characteristics and support the optimization of clay–dolomite composite materials with targeted performance.

Keywords: clay–dolomite composite materials, chemical composition, average density, compressive strength, regression analysis, least-squares method.

1. Introduction

Determining the physical and mechanical properties of building materials often requires lengthy experimental procedures. In particular, the compressive strength of hydraulic binders is typically measured 28 days after sample preparation. Therefore, establishing mathematical relationships between the chemical composition and engineering properties of clay–dolomite composite materials can significantly reduce experimental time and costs. In this study, least-squares regression analysis was applied to evaluate the influence of the ratio of basic to acidic oxides (RO/SiO_2) on the density and strength of clay–dolomite composites.

Linear, logarithmic, hyperbolic, power, and parabolic regression models were developed using the least-squares method and evaluated using correlation coefficients, correlation ratios, and F-tests.

Main Part

For our problem, the main parameters of clay-dolomite materials under study (their values are presented in Table 1) are:

x - the ratio of basic to acidic oxides (RO/SiO2) – the independent variable;
y1 - the average density of the resulting clay-dolomite composite materials – the dependent variable;
y2 - the strength of the resulting clay-dolomite composite materials – the dependent variable.
The least-squares method was used to obtain linear and nonlinear mathematical models. Adequacy was tested (the significance of the regression equation was assessed), the presence of relationships between the parameters was verified, and corresponding graphs of the input (x) and output (y1, y2) parameters were constructed.
The effect of the ratio of basic to acidic oxides (RO/SiO2, x) on the average density (y1) of the resulting clay-dolomite composite materials was studied.
The following regression line coefficients were obtained when approximating the linear relationship: y1=1.844989 -0.06711*x2 .The calculations of the linear model are presented in Table 2.

Table 2. Values of model parameters.

№	(RO/SiO2), (x)	Average density, (y1)	Strength, (y2)
1	2	3	4
1	5.50	1.40	0
2	5.01	1.50	0
3	4.45	1.50	15.0
4	4.05	1.55	26.0
5	3.65	1.63	36.5
6	3.14	1.65	37.5

7	2.56	1.74	39.0
8	2.02	1.78	42.0
9	1.80	1.79	42.5
10	1.35	1.80	43,0
11	1.17	1,81	42.0
12	0.97	1.82	41.5
13	0.76	1.83	41.0
14	0.66	1.85	40.0
15	0.50	1.84	38.0
16	0.33	1.80	36.0
17	0.25	1.75	35.0
18	0.12	1.60	33.0

Linear and nonlinear regression models were developed using the least-squares method. Model adequacy was assessed through significance testing, and the relationships between the input parameter (RO/SiO_2, x) and the output parameters, average density (y_1) and strength (y_2), were evaluated. The influence of the ratio of basic to acidic oxides (RO/SiO_2) on the average density of clay–dolomite composite materials was first investigated. The linear regression model obtained was: $by_1 = 1.844989 - 0.06711x$.

The model was found to be statistically significant ($F_{calc} = 3.057997 > F_{crit} = 2.307693$). The correlation coefficient ($r = -0.84348$) indicated a strong inverse relationship between chemical composition and average density. Thus, an increase in the RO/SiO_2 ratio leads to a decrease in the average density of the composite material.

A logarithmic regression model was obtained using the least-squares method:

$y = 1.722607 - 0.06915 \ln(x)$.

The model was not statistically adequate (Fcalc = 1.270258 < Fcrit = 2.307693). The correlation ratio (η = 0.552608) indicated a moderate nonlinear relationship between the variables. A hyperbolic model was also derived: y = 1.692411 + 0.006869(1/x).

However, the model was statistically insignificant and showed a very low correlation ratio (η = 0.098997). The power-law model, y1=1.717805*x-0.04231 demonstrated a stronger relationship (η = 0.92071). Among the tested functions, the parabolic model provided the best approximation of the dependence between RO/SiO_2 and average density.For compressive strength, the linear model was obtained as:y2=45.92445-6.15929*x and was found to be statistically significant. The logarithmic model,

y2=34.43074-5.98445*ln(x) and the hyperbolic model, y2=31.08572+1.106945*(1/x).

were statistically insignificant. The power-law model, y2=34.70279095*x-0.130731312

also showed weak predictive ability. Therefore, the parabolic model provided the most accurate description of the relationship between RO/SiO_2 and compressive strength.

The parabolic regression model was obtained as:

$y = 32.60073 + 12.11553x - 3.44816x^2$. The correlation ratio (η = 0.980363) indicates a very strong relationship between the RO/SiO_2 ratio and the compressive strength of clay–

dolomite composite materials. Since η exceeds the linear correlation coefficient (r = −0.774929), the parabolic model provides the best fit among the tested functions.The negative value of r indicates an inverse relationship: as the RO/SiO_2 ratio increases, the compressive strength decreases. The final results are presented in Table 2.

Table 2. Mathematical Modeling of Dependence of Properties from Material Compositions

Property	Best-fit model	Equation	η
Density	Parabolic	$y_1=1.76395+0.046945x-0.02167x^2$	0.9207
Strength	Parabolic	$y_2=32.60073+12.11553x-3.44816x^2$	0.9804

References

1. Shirinzade, I.N. Low-Firing Clay-Dolomite Compositions Based on Raw Materials from Azerbaijan Deposits // Silicate Engineering and Technology. 2008. No. 2. pp. 19-21.
2. Shirinzade, I.N. Structure of Clay-Dolomite Composite Materials // Construction Materials. 2010. No. 3. pp. 33-34.
3. T.A.Hagverdiyeva, K.B.Jamalova. Artificial SiO_2-containing mineral-active adhesive material and concrete purchase research, International Journal on Technical and Physical Problems of Engineering

(IJTPE), Issue 60, Vol. 16, No. 3, pp. 213-219, September 2024.
4. N.M.Ahmadov, I.N.Shirinzade, Development of effective fiber-reinforced concrete compositions used in transportation structures, Eastern-European Journal of Enterprise Technologies, 2021, No. 2, p. 6-11.

https://doi.org./10.58225/mpmma.2026.*422*

MATHEMATICAL MODELING OF SEASONAL CHANGES IN TOURISM ECONOMICS

Isa Muradov[1] *, Irana Akhundova*[2]

[1]AzUAC,Azerbaijan

[2]Azerbaijan Tourism and ManagementUniversity, Azerbaijan

Abstract. This article examines the mathematical interpretation and practical modeling of seasonality in tourism economics. Since tourism demand fluctuates significantly across months, decision-making cannot rely on annual averages alone. The study systematizes the economic causes of seasonality, presents additive and multiplicative time-series models, and explains the calculation of seasonal indices. The findings show that isolating the seasonal component enables more rational management of tourist flows, accommodation capacity, pricing, and employment [2; 4; 5]. The proposed model is both theoretically grounded and practically applicable.

Keywords: tourism economics, seasonality, time series, mathematical model, tourism demand, seasonal index, forecasting

1. Introduction

Tourism demand is unevenly distributed throughout the year.Tourism demand is unevenly distributed throughout the year. Factors such as climate, holidays, public events, and consumer behavior concentrate tourist flows into specific months — a phenomenon known as seasonality. Beyond a mere statistical fluctuation, seasonality is a structural characteristic affecting revenues, prices, labor demand, and infrastructure utilization [4]. UN Tourism materials highlight that peak seasons bring congestion and price surges, while off-seasons lead to resource underutilization and employment difficulties [5]. Effective economic decision-making in tourism requires analyzing not just annual averages but the internal structure of demand. Decomposing time series into trend, seasonal, and random components enhances short-term forecasting accuracy and supports more informed pricing, marketing, and staffing strategies [1; 2]. Thus, the mathematical modeling of tourism seasonality represents a relevant and practical field bridging applied mathematics and sectoral economics.

2. Methodology

The study uses a comparative-analytical methodology based on secondary sources, combining theoretical interpretation with an

operational modeling sequence. The approach involves four steps: reviewing seasonality literature to identify key economic drivers; decomposing demand series into trend, seasonal, and residual components; calculating monthly seasonal indices; and evaluating model fit via MAE, RMSE, and MAPE. The resulting framework is applicable to tourism enterprises and destinations [1; 2; 3].

Mathematical Representation of Seasonality. If the value of a tourism indicator over time is denoted by Y_t, it can be represented as the sum of three principal components:

$$Y_t = T_t + S_t + E_t$$

Here, T_t is the trend, S_t the seasonal, and E_t the random component. The additive model suits series where seasonal fluctuations remain independent of the overall level. When seasonal differences grow alongside demand, the multiplicative model is more appropriate [2]:

$$Y_t = T_t \times S_t \times E_t$$

The multiplicative approach better reflects real-world seasonality, as fluctuation amplitudes grow alongside overall tourist volumes. For instance, a 20% seasonal increase means 2,000 additional tourists in a 10,000-tourist market, but 20,000 in a 100,000-tourist market. In series with

changing amplitudes — such as tourism demand - accounting for relative rather than absolute changes yields more rational results [2; 3].

A straightforward measure of seasonality is the seasonal index, calculated for the j-th month as follows:

$SI_j = (\bar{Y}_j / \bar{Y}) \times 100$

Where $\bar{Y}_j$ is the long-term monthly average and $\bar{Y}$ the

overall average. Values above 100 signal peak demand; below 100 indicate low season — useful for occupancy planning, staffing, and pricing [5].

Applied interpretation and economic analysis. The practical value of seasonal models is most evident in decision-making. Knowing the high season in advance allows accommodation providers to adjust prices in line with market capacity, while off-season periods call for discount campaigns and package offers. Similarly, rising seasonal indices signal increased labor demand, whereas weaker periods require staff optimization and tighter cost control. Thus, mathematical modeling supports not only academic inquiry but also enterprise-level budgeting and resource allocation [4; 5].

The Seasonal ARIMA (SARIMA) model offers a more precise approach, estimating

future demand through past observations, differencing, and seasonal lags. Model selection should prioritize empirical forecasting accuracy over theoretical tests - the model yielding smaller errors on real data is considered more practically useful, particularly given tourism demand's non-stationary yet repetitive seasonal structure [1].For practical application, the following sequence is recommended: decompose the time series into trend and seasonal components; calculate seasonal indices for each month; build a forecasting model on the residual component; and evaluate model quality using measures such as mean absolute error (MAE), root mean square error (RMSE), and mean absolute percentage error (MAPE). This approach is both methodologically straightforward and readily applicable to real tourism statistics [2; 3].

Conclusion

The analysis demonstrates that seasonality in tourism economics is not a random phenomenon but a systematic one. Its mathematical modeling makes it possible to reveal the regularities in tourist flow dynamics, identify peak and low seasons more precisely, and justify management decisions on a more scientific basis. Additive and multiplicative decomposition models, together

with seasonal indices, constitute simple yet functional tools for this purpose. In cases requiring deeper forecasting, the use of time-series models such as SARIMA is considered appropriate [1; 2]. Consequently, the mathematical analysis of seasonal changes in tourism economics contributes to a more rational design of pricing policy, occupancy management, employment planning, and marketing strategy [4; 5].

References

1. Kulendran, N., Wong, K.K.F. Modeling seasonality in tourism forecasting. Journal of Travel Research, 2005. URL: https://sage.cnpereading.com/storage/sage/journal/article/JTR/2005/JTR_2005_44_2/unzip/10.1177_0047287505276605.pdf
2. Song, H., Li, G. Tourism demand modelling and forecasting. Tourism Management, 2008. URL: https://openresearch.surrey.ac.uk/esploro/outputs/journalArticle/Tourism-Demand-Modelling-and-Forecasting/99516714202346
3. Abdou, M., Musabanganji, E., Musahara, H. Tourism demand modelling and forecasting: A review literature, 2021. URL: https://www.ajhtl.com/uploads/7/1/6/3/7163688/article_17_10_4_1370-1393.pdf
4. Cannas, R. An overview of tourism seasonality: key concepts and policy, 2012. URL:

https://iris.unica.it/bitstream/11584/118575/2/Almatourism.pdf
5. UN Tourism. Tourism Seasonality: Tools and Resources. URL: https://www.untourism.int/sustainable-development/unwto-international-network-of-sustainable-tourism-observatories/tools-tourism-seasonality

https://doi.org./10.58225/mpmma.2026.*429*

ANALYSIS OF FAILURE PROBLEMS IN THE SEALING UNITS OF CENTRIFUGAL PUMPS

Aslanov Jamaladdin [1], Huseynli Zenfira [2], Babazadah Jalal[3]

[1]Scientific Research Institute "Geotechnological Problems of Oil, Gas and Chemistry", Azerbaijan

[2]Azerbaijan State Oil and Industry University, Azerbaijan

[3]Azerbaijan State University of Oil and Industy, Azerbaijan

Abstract. The effectiveness of seals used in pumps is mainly related to their tribological properties, i.e. friction, wear and material interaction properties. These properties ensure that the materials remain functional for a long time and increase the overall reliability of the pump. In modern industrial conditions, especially in the oil and gas, chemical, water supply and energy sectors, the operating conditions of pumps are becoming increasingly difficult. Therefore, the study of wear resistance issues in this area and the application of new materials and technologies are very important for the industry. In recent years, modern approaches such as surface hardening, new polymer and ceramic-based coatings, nano-technologies

and the use of composite materials have been widely used to increase the performance of seals. Research conducted in this direction has achieved significant results in order to increase the service life of pumps and reduce maintenance costs.
Keywords: Centrifugal pump, seal, graphite, simulation, analysis

1. Introduction

The effectiveness of seals used in pumps is mainly due to their tribological properties, i.e. friction, wear and material interaction properties. These properties ensure that the materials remain functional for a long time and increase the overall reliability of the pump. In modern industrial conditions, especially in the oil and gas, chemical, water supply and energy sectors, the operating conditions of pumps are becoming increasingly difficult. Therefore, the study of wear resistance issues in this area and the application of new materials and technologies are very important for the industry. In recent years, modern approaches such as surface hardening, new polymer and ceramic-based coatings, nano-technologies and the use of composite materials have been widely used to improve the performance of seals. The aim of the research is to increase the service life of pumps and improve their performance.

2. Methodology

The materials used in the construction of the sealing units must be highly resistant to both

mechanical wear, corrosion and thermal effects. For example, hard materials such as carbon graphite composites, tungsten carbide and silicon carbide ensure the longevity of the sealing surfaces. Elastomer-based seals are distinguished by their elasticity and chemical resistance properties. As for the structural solutions, the optimal selection of seal types and their adaptation to the operating conditions of the pump play an important role. Various types of seals are used, such as mechanical seals, labyrinth seals, magnetic seals and gas seal systems. Each has its own advantages and areas of use. For example, mechanical seals are widely used in high-pressure and high-speed pumps, as they provide effective and reliable sealing.

Optimizing material selection For long-term and reliable operation of sealing assemblies, it is important that the materials used have high wear, corrosion and heat resistance. This prevents premature failure of the seal elements, depending on their chemical composition in the environment in which the pump operates. For example, carbide-based materials (silicon carbide, tungsten carbide) are hard and wear-resistant, while carbon-graphite composites reduce friction with their self-lubricating properties. At the same time, elastomers provide chemical resistance and

maintain the tightness between the surfaces due to their elasticity. The choice of material should also include resistance to thermal loads and the ability to withstand mechanical stresses. Balancing these factors is an important research topic and is one of the main conditions for extending the service life of pumps.

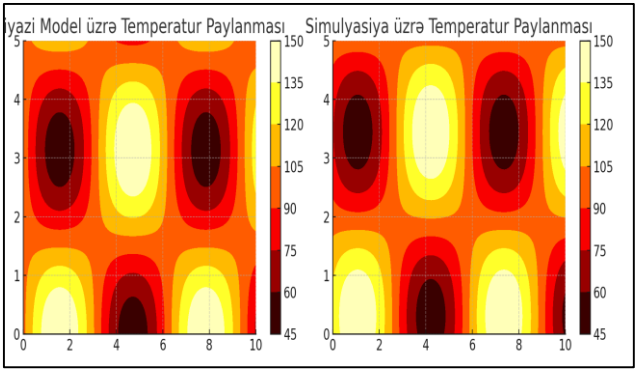


Fig. 1.

Conclusion

Static, dynamic and thermal analyses conducted on 3D models prepared in SolidWorks environment showed that properly selected materials and structural configuration reduce stress concentration in the structure of the compression joint, prevent local deformations in the spring and compression components. At the same time, the simulation results allowed predicting the stresses and voids formed in the compression

joints in accordance with the thermal expansion coefficient of the materials.

References

1. Karaev M.A., Melikov M.A., Mustafayeva G.A. On the Speed Coefficient of Centrifugal Pumps and Conversion of Their Characteristics from Water to a More Viscous Liquid. // Bulletin of the Higher Technical Educational Institutions of Azerbaijan, No. 6, 2003, pp. 24-27.
2. Ibatulov K.A. Practical Calculations for Drilling and Operation Machines and Mechanisms, Baku, Aznefteizdat, 1955, 293 p.
3. Karaev M.A. Problems of Improving the Efficiency of Drilling and Oilfield Pumps. Doctoral Dissertation, Baku, 1981.
4. Karaev M.A., Amirov F.A. Distribution of the Overall Efficiency in a 4K-6 Centrifugal Pump Operating on Aqueous Polyacrylamide Solutions // Oil and Gas, 1975, No. 9.
5. Guidelines for Determining the Characteristics of Centrifugal Pumps. Ufa, 1976, p. 70.
6. Guidance Document. Methodology for Calculating Head Characteristics and Recalculating the Parameters of Centrifugal Pumps in Main Oil Pipelines with Changes in the Rotation Frequency and Viscosity of the Pumped Liquid. RD39-30-99084, 1984, 37 p.
7. Stepanov A.I. Centrifugal and Axial Pumps. M. Mashgiz, 1960.

8. Aitova N.Z. Operating Modes of Pumping Stations with High-Speed Adjustable Pumps When Pumping Viscous Oils Through Main Pipelines. Abstract of a Candidate's Dissertation. Ufa, 1984.
9. Aslanov J.N., Sultanova A.B., Huseynli Z.S., Mustafayev F.F. Determination of radial strains in sealing elements with rubber matrix based on fuzzy sets. 11th İNTERNATİONAL CONFERENCE on THEORY and APPLİCATİON
10.of SOFT COMPUTİNG, COMPUTİNG with WORDS and Artificial İntelligence İCSCCW -2021. DOİ: 10.1007/978-2-030-92127-9_101 (İndexed by Web of Science and Scopus) 23-24 avqust, pp.765-773, Antalya, Turkey, 2021
11.Aslanov, J.N., Huseynli, Z.S., Abbasov, N.M., Sharifova, A.V., Durability study of specialized sealing elements, International Journal on Technical and Physical Problems of Engineering, 14(3), Pp 8–13, 2022
12.Aslanov C.N., Huseynli Z.S. Refined calculation of the stress field of a polymer-compozite seal for Christmass tree shut of devices. SCİENTİFİCE RESEARCH OF THE SCO COUNTRİES SYNERGY AND İNTEQRATİON,
13. Babanli, M., Mekhtiyev, R., Gurbanov, N., Aslanov, J., Tanriverdiev, Y. ,CRACKS IN HYBRID FIBER METAL LAMINATED NANOCOMPOSITES UNDER UNIAXIAL TENSION, Journal of Applied Mechanics and Technical Physics,63(5),Pp 876–883, 2

https://doi.org./10.58225/mpmma.2026.435

EVALUATION OF DAMAGED BUILDINGS WITH SMART TECHNOLOGIES

Jamila Imamaliyeva
AzUAC, Azerbaijan

Abstract. Assessment of building damage after earthquakes, explosions, and other disasters requires rapid and reliable methods to support emergency management and urban resilience. Traditional assessment methods are often delayed and insufficient for large-scale areas; these methods consist of on-site visual inspections conducted by engineers, photo and video documentation, recording of cracks and deformations with simple measuring tools, preparation of written reports, and assessments based on the expert's experience. The purpose of this study is to evaluate the integration of artificial intelligence (AI) with various data sources. These sources include UAV (Unmanned Aerial Vehicle) imagery, satellite multispectral and SAR (Synthetic Aperture Radar) data, LiDAR (Light Detection and Ranging) scans, and sensor-based monitoring. The methodology encompasses the processing of UAV photogrammetry with specialized software, the application of deep learning models — CNN (Convolutional Neural Network), U-Net, and Mask R-CNN (Region-based

Convolutional Neural Network) — for automatic crack and collapse detection, large-scale monitoring of satellite imagery, precise 3D modeling of LiDAR scans, and the use of sensor systems for continuous SHM (Structural Health Monitoring).

Keywords: Seismic Risk; Damaged Buildings; Deep Learning; Sensor Networks; Crack Detection; Disaster Management.

1. Introduction

Traditional human inspections often cause delays [2] and make rapid decision-making in large-scale areas difficult, which is why artificial intelligence (AI)-based technologies — drone photos, satellite imagery, LiDAR scans, and sensor data — play a critical role in the automatic and accurate assessment of damaged buildings [1], [5]. The purpose of the article is to investigate the integration of various data sources with AI and to demonstrate their advantages, limitations, and practical applications.

2. Methodology

Drone technology collects high-resolution images from various angles in the assessment of building damage after an earthquake, and these images are processed in photogrammetry software [4]. During photogrammetry processing, programs such as Agisoft Metashape and Pix4D are used to create digital maps and 3D point clouds. This

data accurately reflects the real condition of the building and creates a basis for subsequent analysis. In the next stage, the application of artificial intelligence (AI) is carried out. CNN, U-Net, and Mask R-CNN models automatically detect cracks, roof collapses, and wall detachments in drone photos [3]. CNN and U-Net models are widely used, especially in crack detection, and this provides faster and more objective results compared to traditional manual inspections. Satellite technology multispectral imagery allows for the detection of roof damage in infrared and other spectral bands (6). This approach reveals building problems that are not visible in conventional visual imagery. SAR technology plays an important role in post-disaster damage assessment. SAR satellites emit microwave signals and measure their reflection from objects. This method does not depend on daylight or weather conditions, meaning it provides reliable results both at night and in cloudy weather. This overcomes the limitations of traditional methods and enables continuous monitoring. The obtained data is transferred to maps through GIS (Geographic Information System) integration. Damaged buildings are marked on the map, and this is used for evacuation planning, resource allocation, and the coordination of

emergency response measures. Thus, satellite imagery and GIS together make the assessment of large-scale damage possible in real time.

LiDAR laser pulses — is one of the most accurate and reliable technologies in the analysis of damaged buildings [4], [6]. LiDAR measures the distance of objects by emitting laser beams, and as a result, accurate 3D maps and point clouds are generated. Engineers' reports are digitized using NLP (Natural Language Processing) methods. The application of sensors is used to monitor the dynamic behavior and structural health of the building. This approach is carried out within the framework of Structural Health Monitoring (SHM) and allows for the evaluation of the object's condition in real time. Accelerometer — acceleration sensors measure the vibration of the building, its behavior under the influence of earthquakes and wind, and create an opportunity for early warning by monitoring its tension. If the natural frequency of the building changes, this can be an indicator of weakening in the structure. Strain gauges — strain measurement sensors are installed on columns, load-bearing elements of the building, and walls. By measuring the degree of strain and deformation on concrete and

metal, they provide a warning before cracks and bending begin. Other sensors — temperature, humidity, vibrometer, and acoustic sensors indicate the risks of material fatigue and cracking. Real-time strain, vibration, and movement data from the sensors are transmitted to the server. Changes that deviate from normal behavior are automatically flagged using anomaly detection and machine learning models. The results of engineering inspections are combined with sensor data. The results are visualized in a mobile application, GIS map, or dashboard. Reports and sensor data are combined with AI to automatically extract the risk level. Sensor technologies are applied in making decisions regarding building safety after earthquakes, in monitoring continuous vibration and strain in bridges and tunnels, in the long-term monitoring of cracks and deformations in historical buildings, as well as in transmitting data to a central monitoring system in real time within smart city systems. Figure 1 shows the relationship between building height and the damage index.

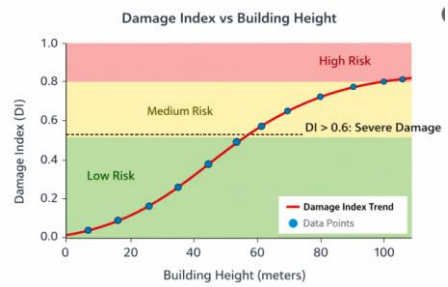


Figure 1. Dependence between building height and damage index

For a building, the damage index (DI) is expressed as follows:

$$\mathrm{DI} = \frac{\Delta_{\max}}{\Delta_{\mathrm{yield}}}$$

Here, $\Delta_{\max}$— represents the maximum observed deformations, Δ_{yield} is the material's yield limit. This index varies within the range 0–1 and objectively reflects the condition of the structure. For the probability of damage, the logistic function is:

$$\mathrm{P}_{\mathrm{damage}} = \frac{1}{1 + \mathrm{e}^{-(\alpha+\beta \cdot \mathrm{X})}}$$

Here, X - the input variables (for example, crack length, building height, seismic intensity), while α and β are the model parameters. α determines the initial level and the center of the curve; β defines the growth rate, that is, how quickly the risk increases.

Conclusion

This innovative approach, when combined with traditional reports, enhances objectivity and reduces human errors. The results obtained create broad application opportunities in emergency management, civil engineering, and smart city planning, providing a comprehensive framework for sustainable infrastructure management.

References

1. Jozi, D., Nima, K.: Rapid post-disaster assessment of residential buildings using Unmanned Aerial Vehicles. Journal of Disaster Risk Reduction 111, 104707 (2024).
2. Jozi, D., Martinelli, F., Mercaldo, F., Santone, A.: Damage detection and localisation using UAV/Drone with object detection. Procedia Computer Science 225, 118–127 (2023).
3. Chen, R., Li, Y., Zhang, H.: Deep learning-based crack detection in concrete structures using UAV imagery. Automation in Construction 124, 103558 (2021).
4. Xu, Y., Wang, J.: Integration of UAV photogrammetry and LiDAR for post-earthquake building damage assessment. Natural Hazards 104(2), 1345–1363 (2020).
5. Brownjohn, J.M.W.: Structural health monitoring of civil infrastructure. Philosophical Transactions of the Royal Society A: Mathematical, Physical and

Engineering Sciences 365(1851), 589–622 (2007).
6. Məmmədov, R.A., Quliyev, S.H.: Dron və LiDAR texnologiyalarının şəhər mühitində zədələnmiş binaların qiymətləndirilməsində tətbiqi. Azərbaycan Memarlıq və İnşaat Universitetinin Elmi Əsərləri 17(3), 45–56 (2021).
7. Əliyev, T.M.: Süni intellekt və peyk təsvirlərinin inteqrasiyası ilə fövqəladə hallarda bina zədələrinin qiymətləndirilməsi. AMEA İnformasiya Texnologiyaları İnstitutu Məqalələr Toplusu 27(2), 77–88 (2019).
8. Imamaliyeva J.N. Iot-Based Prıncıples For Damaged Buıldıng Analysıs: Real-Tıme Monıtorıng And Rısk Assessment. ITTA 2026(3rd International Conference on Information Technologies and their Application). Baku, Azerbaijan, (2026).

https://doi.org./10.58225/mpmma.2026.443

SOME SRUCTURAL PROPERTIES OF DISCRETE MORREY SPACES OVER $\mathbb{Z}$

Javanshir Azizov[1] *and Vagif Guliyev*[2,3]
[1] ADA University, Azerbaijan
[2] Kirsehir Ahi Evran University, Türkiye
[3]AZUAC, Azerbaijan

Abstract. The aim of this work is to investigate structural properties of discrete Morrey spaces $\ell_{p,\lambda}(\mathbb{Z})$. We establish continuous embedding theorems both within the class of discrete Morrey spaces, providing explicit conditions on the parameters p and λ.

Keywords: Sequence Space, Discrete Morrey Space, Embedding

1. Introduction

Morrey spaces were first introduced by C. B. Morrey in 1938 [3] during his investigation of the local behavior of solutions to certain elliptic partial differential equations. Since their introduction, Morrey spaces have played a fundamental role in harmonic analysis, potential theory, and the theory of partial differential equations, and they have been extensively studied together with their weak and generalized variants.

In parallel with the development of continuous function spaces, discrete analogues have emerged as essential tools in modern analysis. Discrete function spaces naturally arise in problems where data are

sampled at discrete points, such as in digital signal processing, numerical analysis, and discrete potential theory. These spaces preserve many structural features of their continuous counterparts, yet they exhibit distinct analytical phenomena inherent to the discrete setting.

The discrete Morrey spaces denoted by $\ell_{p,\lambda}(\mathbb{Z})$, play an important role in discrete harmonic analysis. In particular, weak discrete Morrey spaces $w\ell_{p,\lambda}(\mathbb{Z})$ arise naturally in the study of operators that fail to be bounded in the strong sense but satisfy weak-type inequalities, which are indispensable in both theoretical investigations and applications.

The aim of this study is to contribute to the systematic development of the theory of discrete Morrey spaces over $\mathbb{Z}$. We investigate the fundamental structural properties of the spaces $\ell_{p,\lambda}(\mathbb{Z})$, including their completeness and quasi-Banach space structure. Furthermore, we establish continuous embedding theorems both between discrete Morrey spaces and between their weak counterparts, providing explicit conditions on the parameters p and λ. A key feature of our results is that these conditions are shown to be *necessary and sufficient*, thereby ensuring the sharpness of the

obtained embeddings. These findings contribute to a deeper understanding of discrete function spaces and provide a solid foundation for further investigations of discrete operators in harmonic analysis.

Let us begin with some definitions and notations used in this paper. We write
$\mathbb{N}_0 = \mathbb{N} \cup \{0\}$, $-\mathbb{N}_0 = \{\dots, -2, -1, 0\}$,
$\mathbb{R}_+ = (0, \infty)$, and $\mathbb{R}_0 = [0, \infty)$.
For $j \in \mathbb{Z}$ and $R \in \mathbb{R}_0$, define the interval $J(j, R)$ as

$$J(j, R) = \{k \in \mathbb{Z}: |j - k| \leq R\}.$$

We denote $\#J(j, R)$ as the cardinality of $J(j, R)$. In fact, in some cases, it suffices to consider only $R = N \in \mathbb{N}_0$. In particular, for any $R \in \mathbb{R}_0$, there exists $N \in \mathbb{N}_0$ such that $N \leq R < N + 1$, which implies

$$\begin{aligned} \#J(j, N) &= \#J(j, R) \\ &= (j + N) - (j - N) + 1 \\ &= 2N + 1. \end{aligned}$$

Let $J \subseteq \mathbb{Z}$. We denote by $\ell_p(J)$ the discrete Lebesgue space of all sequences $a = (a_m)_{m \in J}$ with the norm

$$\|a\|_{\ell_p(J)} = \left(\sum_{m \in J} |a_m|^p \right)^{1/p}$$

for $1 \leq p < \infty$, and

$$\|a\|_{\ell^\infty(J)} = \sup_{m \in J} |a_m|$$

for $p = \infty$.

Meanwhile, for $1 \leq p < \infty$ the discrete weak Lebesgue space $w\ell_p(J)$ consists of all sequences $a = (a_m)_{m \in J}$ equipped with the quasi-norm

$$\|a\|_{w\ell_p(J)} = \sup_{\gamma > 0} \gamma \ (\#\{m \in J : |a_m| > \gamma\})^{1/p},$$

It can be easily shown that the inequality

$$\|a\|_{w\ell_p(J)} \leq \|a\|_{\ell_p(J)}.$$

is valid for any sequence $a = (a_m)_{m \in J} \in \ell_p(J)$.

The locally summable sequence space $\ell_p^{\mathrm{loc}}(\mathbb{Z})$ is the set of all sequences $a = (a_m)_{m \in \mathbb{Z}}$ such that

$$\|a\|_{\ell_p(J)} < \infty \text{ for every interval } J \subseteq \mathbb{Z}.$$

Moreover, $w\ell_p^{\mathrm{loc}}(\mathbb{Z})$ is the set of all sequences a such that

$$\|a\|_{w\ell_p(J)} < \infty \text{ for every interval } J \subseteq \mathbb{Z}.$$

Let $1 \leq p < \infty$ and $\lambda \in \mathbb{R}$. The discrete Morrey space $\ell_{p,\lambda}(\mathbb{Z})$ is defined as the set of

all sequences $a = (a_m)_{m\in\mathbb{Z}} \in \ell_p^{loc}(\mathbb{Z})$ satisfying the condition that

$$\|a\|_{\ell_{p,\lambda}(\mathbb{Z})} = \sup_{j\in\mathbb{Z},\, N\in\mathbb{N}_0} \big(\#J(j,N)\big)^{\frac{-\lambda}{p}} \|a\|_{\ell_p(J(j,N))} < \infty.$$

The following lemma is valid.

Lemma 1.[1] *Let* $1 \le p < \infty$ *and* $\lambda \in \mathbb{R}$. *The following properties are valid.*

1. If $\lambda = 0$, then $\ell_{p,\lambda}(\mathbb{Z}) = \ell_p(\mathbb{Z})$ *and* $\|a\|_{\ell_{p,\lambda}(\mathbb{Z})} = \|a\|_{\ell_p(\mathbb{Z})}$.
2. *If* $\lambda < 0$, *then* $\ell_{p,\lambda}(\mathbb{Z}) = \{\theta\}$, *where* θ *denotes the zero sequence.*
3. *If* $\lambda \ge 1$, *then* $\ell_{p,\lambda}(\mathbb{Z}) = \ell_\infty(\mathbb{Z})$ *and* $\|a\|_{\ell_{p,\lambda}(\mathbb{Z})} = \|a\|_{\ell_\infty(\mathbb{Z})}$.
4. *If* $0 < \lambda < 1$, *then* $\ell_{p,\lambda}(\mathbb{Z})$ *is nontrivial.*

Lemma 2. [1,2] *Let* $1 \le p < \infty$ *and* $0 \le \lambda < 1$. *Then* $\left(\ell_{p,\lambda}(\mathbb{Z}), \|\cdot\|_{\ell_{p,\lambda}(\mathbb{Z})}\right)$ *is a Banach space.*

Theorem 1.[1] *Let* $1 \le p_1 \le p_2 < \infty$ *and* $0 \le \lambda_1, \lambda_2 < 1$. *Then*

$$\frac{1-\lambda_1}{p_1} \le \frac{1-\lambda_2}{p_2}$$

is a necessary and sufficient condition for

$\ell_{p_1,\lambda_1}(\mathbb{Z}) \hookrightarrow \ell_{p_2,\lambda_2}(\mathbb{Z})$ *with* $\|a\|_{\ell_{p_1,\lambda_1}(\mathbb{Z})} \leq \|a\|_{\ell_{p_2,\lambda_2}(\mathbb{Z})}$

for any $a \in \ell_{p_2,\lambda_2}(\mathbb{Z})$ *to hold.*

Corollary 1. [2] *Let* $1 \leq p < \infty$. *Then* $0 \leq \lambda_2 \leq \lambda_1 < 1$ *is a necessary and sufficient condition for*

$$\ell_{p,\lambda_1}(\mathbb{Z}) \hookrightarrow \ell_{p,\lambda_2}(\mathbb{Z}) \text{ with } \|a\|_{\ell_{p,\lambda_1}(\mathbb{Z}} \leq \|a\|_{\ell_{p,\lambda_2}(\mathbb{Z})}$$

for any $a \in \ell_{p,\lambda_2}(\mathbb{Z})$ *to hold.*

The research of V. Guliyev was partially supported by a grant from Kirsehir Ahi Evran University Scientific Research Projects (BAP, Project No: FEF.A1.26.001).

References

1. Azizov, J.V., Guliyev, V.S.: On discrete Morrey spaces over Z and local estimation of the discrete Hilbert transform. Journal of Contemporary Applied Mathematics, 17(1), 143-177 (2027).
2. Gunawan, H., Kikianty, E., Schwanke, C.: Discrete Morrey spaces and their inclusion properties. Math. Nachr. 291(8–9), 1283–1296 (2018).
3. Morrey, C.B.: On the solutions of quasi-linear elliptic partial differential equations. Trans. Amer. Math. Soc. 43(1), 126–166 (1938).

https://doi.org./10.58225/mpmma.2026.*449*

ECOLOGICAL MODELLING OF SUSTAINABLE HYDROPOWER DEVELOPMENT POTENTIAL IN THE HAKARI RIVER BASIN, AZERBAIJAN

Kamila Majidli
AzUAC, Azerbaijan

Abstract. The Hakari River Basin is one of the most important water resource systems in the East Zangezur Economic Region of Azerbaijan. Following the restoration of the liberated territories, increasing attention has been directed toward the sustainable utilization of water resources and renewable energy potential. This study develops an ecological modelling framework for assessing sustainable hydropower development in the Hakari River Basin based on environmental flow requirements and hydropower potential. Hydrological characteristics, annual runoff volumes, ecological flow requirements, reservoir capacities, and planned hydropower schemes on the Hakari, Zabukh, and Hochaz rivers were analyzed. An Ecological Flow-Based Development Model (EFDM) was applied to evaluate the balance between hydropower generation and ecosystem conservation. The modelling results indicate that approximately 85.2% of the annual runoff of the Hakari River remains within the river system after regulation, while the ecological flow ratio of

the Zabukh River reaches 90.9%. The total installed hydropower capacity of the basin was estimated at 71.65 MW, including planned facilities on the Zabukh and Hochaz tributaries as well as the Hakari and Gulabird hydropower plants. The results demonstrate that substantial renewable energy production can be achieved while maintaining ecological sustainability. The proposed modelling framework may serve as a decision-support tool for sustainable hydropower planning in mountain river basins.

Keywords: Hakari River Basin, ecological modelling, environmental flow, hydropower potential, renewable energy, East Zangezur, Azerbaijan.

1. Introduction

Sustainable management of mountain river basins has become an important challenge for many countries seeking to balance economic development, renewable energy production, and environmental protection. Hydropower is widely recognized as one of the most reliable renewable energy sources; however, inappropriate regulation of river systems may adversely affect aquatic ecosystems, biodiversity, and downstream water availability. Consequently, modern hydropower planning increasingly

incorporates ecological flow requirements as a key criterion for sustainable development. [6]

The East Zangezur Economic Region of Azerbaijan possesses significant water and energy resources. Among the major river systems of the region, the Hakari River Basin occupies a special position due to its hydrological characteristics, water quality, irrigation potential, and hydropower resources. The Hakari River originates within the Lesser Caucasus Mountains and flows through the territories of Lachin, Gubadli, and Zangilan districts before discharging into the Araz River. The river regime is formed by snowmelt, rainfall, and groundwater recharge. Approximately 60–70% of annual runoff occurs during the spring flood period, while low-flow conditions dominate during winter.

In recent years, reconstruction and development initiatives in the liberated territories have increased interest in the utilization of water resources for irrigation, drinking water supply, fisheries, and renewable energy production. Several hydropower projects have been proposed within the Hakari River Basin, particularly on the Zabukh and Hochaz tributaries, where favorable topographic conditions provide substantial hydraulic head. [7]

Previous investigations primarily focused on hydrological characteristics or engineering aspects of individual projects. However, studies integrating hydropower development and ecological sustainability remain limited. Therefore, the objective of this research is to develop an ecological modelling framework that evaluates sustainable hydropower development potential while preserving environmental flow requirements within the Hakari River Basin.

2. Study Area

The Hakari River is one of the largest tributaries of the Araz River and represents the second largest river system of the Azerbaijani part of the Lesser Caucasus after the Tartar River Basin. The river is formed by the confluence of the Hochaz and Shalva rivers and drains a mountainous catchment characterized by significant elevation differences.

The basin exhibits a snow-rainfall hydrological regime. Spring snowmelt contributes approximately 60–70% of annual runoff, creating favorable conditions for hydropower generation. The upper basin remains relatively unaffected by industrial activities and contains numerous spring-fed tributaries with high water quality.

The Hochaz and Zabukh tributaries are particularly important for hydropower development due to their steep longitudinal profiles and substantial hydraulic heads.

These characteristics allow the implementation of derivation-type small hydropower plants with comparatively low environmental impacts. [8]

3. Materials and Methods

3.1 Ecological Flow-Based Development Model

The ecological sustainability of hydropower development was assessed using an Ecological Flow-Based Development Model (EFDM). [4]

The total annual runoff is expressed as:

$Q_{total} = Q_{eco} + Q_{use}$

where:

Q_{total} = total annual runoff volume (million m^3);

Q_{eco} = ecological flow volume preserved within the river system;

Q_{use} = volume available for economic utilization.

The Ecological Flow Ratio (EFR) is calculated as:

$EFR = Q_{eco} / Q_{total}$

The Hydropower Utilization Ratio (HUR) is:

$HUR = Q_{use} / Q_{total}$

The sustainability condition is:

$EFR \geq 0.25$

meaning that at least 25% of annual natural runoff should remain available for ecosystem maintenance.

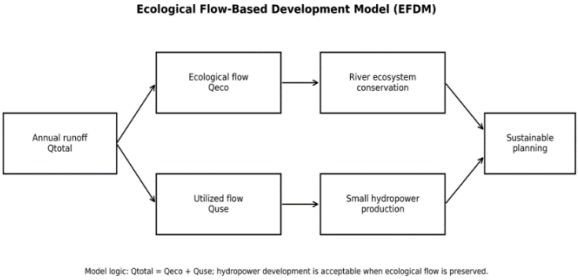


Figure 1. Ecological Flow-Based Development Model (EFDM)

3.2 Ecological Hydropower Efficiency

To evaluate the relationship between hydropower generation and ecological preservation, an Ecological Hydropower Efficiency Index (EHEI) was applied:

EHEI = Ptotal / EFR

where:

Ptotal = installed hydropower capacity (MW);

EFR = ecological flow ratio.

Higher values indicate greater renewable energy production while maintaining ecological flow conditions.

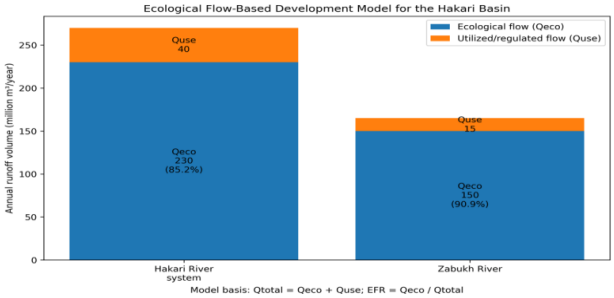


Figure 2. Ecological flow-based development model for the Hakari Basin

3.3. Ecological Flow Analysis of the Hakari River

The annual runoff available at the confluence of the Hochaz and Shalva rivers is approximately 270 million m³. According to the proposed development scheme, 230 million m³ remains within the natural river system, while only 40 million m³ is effectively regulated and utilized through the reservoir system. Therefore, [9]

EFR = 230 / 270 = 0.852

This means that **85.2% of the natural annual runoff continues to flow through the river system**. From an ecological perspective, such a value indicates that the natural hydrological regime is largely preserved. Environmental flow studies generally consider ecological flow ratios above 30–40% sufficient for maintaining aquatic habitats, fish migration routes, sediment transport processes, and riparian vegetation. Consequently, the calculated value of 85.2% suggests that the proposed development scenario is unlikely to produce significant ecological degradation. [2]

The corresponding hydropower utilization ratio is:

HUR = 40 / 270 = 0.148

This result indicates that only 14.8% of the annual runoff is directly utilized for reservoir regulation and energy-related

purposes. Therefore, the majority of the river discharge remains available for downstream ecological processes.

3.4. Ecological Flow Analysis of the Zabukh River

The annual runoff of the Zabukh River is approximately 165 million m³. After regulation, around 150 million m³ remains within the natural river channel.

```
EFRz = 150 / 165 = 0.909
```

Thus, approximately **90.9% of the natural annual runoff is preserved**.

The corresponding utilization ratio is 0.091, which means that only 9.1% of the annual discharge is regulated:

```
HURz = 15 / 165 = 0.091
```

Compared with the Hakari River, the Zabukh River demonstrates an even lower degree of hydrological alteration. This result reflects the environmental advantages of derivation-type hydropower systems, where water is temporarily diverted for electricity generation and subsequently returned to the river channel.

Table 1. Comparative Modelling Results

River	Total runoff (million m^3/year)	Ecological flow (million m^3/year)	EFR	HUR
Hakari	270	230	0.852	0.148
Zabukh	165	150	0.909	0.091

The comparison shows that both rivers retain more than 85% of their natural runoff after regulation. The Zabukh River exhibits the highest ecological flow ratio, while the Hakari River provides the largest overall water resource potential. These results indicate that the planned hydropower developments can coexist with environmental flow preservation and sustainable river basin management.

4. Results

4.1 Hakari River Ecological Flow Assessment

The annual runoff generated at the confluence of the Hochaz and Shalva rivers is approximately:

$$Q_{total} = 270 \text{ million } m^3/year$$

The proposed Hakari Reservoir has a storage capacity of 70 million m^3, while approximately 230 million m^3/year remain

available within the river system. Consequently,

EFR = 230 / 270; EFR = 0.852.

Thus, 85.2% of the natural annual runoff remains within the river system after regulation. This value substantially exceeds internationally accepted ecological flow thresholds and indicates favorable ecological sustainability. [12]

4.2 Zabukh River Ecological Assessment

The annual runoff of the Zabukh River is approximately 165 million m^3/year. Following regulation by the Zabukh Reservoir, approximately 150 million m^3/year emain available in the river channel. Therefore:

EFRz = 150 / 165; EFRz = 0.909.

The resulting ecological flow ratio of 90.9% indicates minimal hydrological disturbance and demonstrates that planned utilization remains compatible with ecosystem preservation.

4.3 Hydropower Development Potential

Table 2. Planned hydropower facilities on the Zabukh River

HPP	Q (m^3/s)	Head (m)	Capacity (MW)
Minkend HPP-1	3.0	113	2.4
Galacha	3.0	161	4.3

HPP-2			
Bozlu HPP-3	3.5	102	3.2
Malibey HPP-4	4.0	286	8.6
Zabukh-1 HPP	4.5	89	3.0
Zabukh-2 HPP	4.5	58	1.95

Total installed capacity: 23.45 MW

Table 3. Planned hydropower facilities on the Hochaz River

HPP	Q (m³/s)	Head (m)	Capacity (MW)
SES0	3.0	342	7.4
SES1	3.0	226	5.5
SES2	3.0	115	2.8
SES3	4.0	90	2.2
SES4	5.0	90	3.7
SES5	5.0	180	7.5
SES6	5.0	143	6.0

Total installed capacity: 35.10 MW

Table 4. Overall hydropower potential of the Hakari Basin

Facility	Capacity (MW)
Zabukh Cascade	23.45
Hochaz Cascade	35.10
Hakari HPP	7.50
Gulabird HPP	5.60
Total	**71.65**

The Hochaz cascade contributes approximately 49% of the total hydropower potential of the basin, making it the most significant renewable energy component. Using the ecological flow ratio of the Hakari River:

EHEI = 71.65 / 0.852; EHEI = 84.1.

The obtained value demonstrates a high level of renewable energy production while preserving ecological flow conditions. [11]

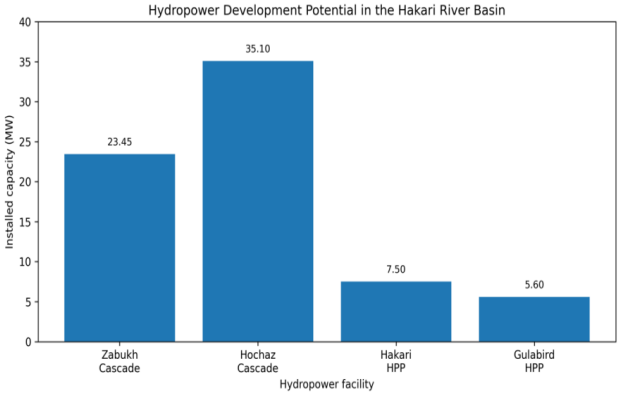


Figure 3. Hydropower development potential in the Hakari river basin

5. Discussion

The results obtained from the ecological flow-based modelling indicate that the Hakari River Basin has considerable potential for hydropower development without causing significant alterations to the natural river regime. The calculated ecological flow ratio (EFR) for the Hakari River was 0.852, meaning that approximately 85.2% of

the annual runoff remains within the river system after reservoir regulation. Similarly, the Zabukh River exhibited an ecological flow ratio of 0.909, indicating that more than 90% of the natural annual discharge continues to flow through the river channel. These values are substantially higher than the minimum environmental flow threshold commonly recommended for maintaining river ecosystem functions. [3]

One of the most important findings of this study is that the proposed hydropower schemes utilize derivation-type systems rather than large storage reservoirs. In such systems, water is diverted through pipelines to generate electricity and subsequently returned to the river channel. Consequently, the hydrological disturbance is considerably lower than in conventional reservoir-based hydropower projects, where large volumes of water are permanently retained and natural flow regimes are significantly modified.[9]

The hydropower potential analysis demonstrated that the Hochaz cascade represents the largest renewable energy component within the basin, contributing 35.10 MW, or approximately 49% of the total basin potential. The Zabukh cascade contributes an additional 23.45 MW, while the Hakari and Gulabird hydropower plants account for 7.50 MW and 5.60 MW, respectively. Together, these facilities provide a total installed capacity of 71.65 MW, highlighting the strategic importance of the

basin for renewable energy production in the East Zangezur region. [5]

From an ecological perspective, maintaining high environmental flow ratios is particularly important for preserving aquatic habitats, fish populations, sediment transport processes, and downstream water availability. The modelling results suggest that the planned hydropower developments can operate while maintaining sufficient ecological flows to support these ecosystem services. Furthermore, the high water quality previously recorded in the Hakari River, characterized by low mineralization, high dissolved oxygen concentrations, and low heavy metal contamination, increases the ecological value of preserving natural flow conditions. [6]

Overall, the modelling results indicate that the Hakari River Basin provides a favourable balance between renewable energy production and environmental protection. Under the current development scenario, hydropower utilization appears compatible with ecological sustainability, provided that environmental flow releases and long-term hydrological monitoring remain integral components of basin management.

Conclusion

The ecological modelling results show that the Hakari River Basin has strong potential for sustainable small hydropower development while maintaining river ecosystem stability. The Ecological Flow-

Based Development Model indicates that 85.2% of the annual runoff remains within the Hakari River system after regulation, while the Zabukh River retains approximately 90.9% of its annual runoff. These values are considerably higher than the minimum ecological flow threshold used in the model, suggesting that planned hydropower development can be compatible with ecological requirements. The total hydropower potential of the basin, estimated at 71.65 MW, demonstrates the strategic importance of the Hakari, Zabukh and Hochaz river systems for renewable energy development in East Zangezur. Overall, the results confirm that derivation-type hydropower schemes may provide an environmentally acceptable approach for energy production, provided that ecological flow monitoring and basin-scale water management are maintained.

References

1. Richter, B.D., Davis, M.M., Apse, C., Konrad, C.: A presumptive standard for environmental flow protection. River Research and Applications 28(8), 1312–1321 (2012).
2. Anderson, D., Moggridge, H., Warren, P., Shucksmith, J.: The impacts of ‘run-of-river’ hydropower on the physical and ecological condition of rivers. Water and

Environment Journal 29(2), 268–276 (2015)
3. Poff, N.L., Richter, B.D., Arthington, A.H., et al.: The Ecological Limits of Hydrologic Alteration (ELOHA): A new framework for developing regional environmental flow standards. Freshwater Biology 55, 147–170 (2010)
4. Yanygina, L.V., Schletterer, M.: Macroinvertebrates reveal environmental gradients: methods and method development in the Ob River basin. Hydrobiologia 850, 2045–2059 (2023).
5. Fornasaro, S., Ghezzi, L., Shukurov, N., et al.: Water quality and dissolved load in the Chirchik and Akhangaran river basins (Uzbekistan, Central Asia). Environmental Monitoring and Assessment 196, 854 (2024).
6. Majidli, K.A.: Environmental impact of the use of hydropower potential and its role for sustainable development in Azerbaijan. University and Society 17, e5627 (2025).
7. Majidli, K.A., Mammadov, A.S., Aliyev, F.G.: Impact of industrial waste on aquatic ecosystems: A case study of the Okhchu River. African Journal of Biological Sciences 7, 1–18 (2025).
8. Majidli, K., Mammadov, A., Aliyev, F.: Aquatic ecosystem degradation due to industrial pollution: A case study of the Okchu River. Visnyk V.N. Karazin Kharkiv National University. Series: Geology, Geography, Ecology 63, 580–590 (2025)

9. Majidli, K.A., Aliyev, F.G.: Protection of biodiversity in Bargushad and Hakary Rivers. Research in Agricultural and Veterinary Sciences, 13 (2024).
10. Majidli, K.A., Mammadov, A.S., Aliyev, F.G.: Impact of industrial waste on aquatic ecosystems: A case study of the Okhchu River. African Journal of Biological Sciences 7, 1–18 (2025).
11. Jia, F., Wang, W., Han, Y., et al.: Predictive framework of vegetation resistance in channel flow. Scientific Reports 15, 7593 (2025).
12. Woszczyk, M., Brechbühler, M.: Long-term changes in the quality of the aquatic environment of thermally polluted Lake Licheńskie, Central Poland. Journal of Hydrology: Regional Studies 62, 102917 (2025).

https://doi.org./10.58225/mpmma.2026.*466*

A COMPREHENSIVE MATHEMATICAL FRAMEWORK FOR HYDROSTATIC PRESSURE BEHAVIOR, STRESS ANALYSIS, AND INTEGRITY ASSESSMENT IN GAS PIPELINE HYDROTESTING

Kamran Khan
Pakneftegaz, Pakistan

Abstract. Hydrostatic testing is a critical integrity verification method for gas pipelines, ensuring structural reliability under elevated internal pressures. This study develops a comprehensive mathematical framework to evaluate hydrostatic pressure behavior, induced circumferential stress, and overall pipeline integrity during hydrotesting operations. The framework integrates fundamental fluid statics, thin-walled pressure vessel theory, and failure criteria to quantify stress distribution and safety margins. Analytical expressions are derived for hoop stress, longitudinal stress, and radial pressure gradients, considering material properties and geometric constraints. The methodology further incorporates yield strength limits and design factors to assess failure risk under test conditions. Results demonstrate that precise mathematical modeling significantly enhances prediction accuracy of pipeline performance and

minimizes operational uncertainties. The proposed framework provides pipeline engineers with a systematic approach for optimizing hydrotesting pressure levels while ensuring compliance with international pipeline standards. This study contributes to safer pipeline commissioning and improved risk-based inspection strategies in energy infrastructure systems for enhanced operational safety and engineering reliability assessment framework validation.
Keywords: Hydrostatic testing, pipeline integrity, stress analysis.

1 . Introduction

Gas pipeline systems require rigorous integrity verification to ensure safe operation under high-pressure conditions. Hydrostatic testing is widely used to detect leaks, validate design strength, and confirm structural stability [1]. During testing, pipelines are subjected to internal pressures exceeding normal operating levels, making stress evaluation essential. Classical thin walled pressure vessel theory provides the basis for understanding stress distribution in cylindrical pipelines [2]. However, modern pipeline systems demand integrated mathematical approaches that combine fluid statics, material mechanics, and failure criteria. This study presents a unified framework to improve predictive accuracy in hydrotesting analysis.

Methodology

The methodology is based on analytical modeling of pipeline behaviour under internal hydrostatic pressure. The pipeline is assumed to behave as a thin-walled cylindrical vessel. Governing equations are derived using equilibrium conditions and elastic deformation theory. Stress components are evaluated using mechanics principles, while safety factors are incorporated to ensure compliance with design standards [3]. Material yield strength and geometric constraints are included to evaluate failure probability under test conditions.Mathematical Framework

The hoop stress is defined as:

$$\sigma_h = (P \cdot D) / (2t) \quad (1)$$

Where P is internal pressure, D is pipe diameter, and t is wall thickness.

Longitudinal stress is given by:

$$\sigma_l = (P \cdot D) / (4t) \quad (2)$$

Radial stress variation is assumed negligible for thin-walled conditions, allowing simplification of stress distribution analysis.

Failure condition is evaluated using yield criterion:

$$\sigma_h \leq \sigma_y / FS \quad (3)$$

where σ_y is material yield strength and FS is factor of safety. These relationships allow comprehensive assessment of pipeline integrity during hydrotesting [4].

Conclusion

The proposed mathematical framework effectively integrates hydrostatic pressure behavior, stress analysis, and structural integrity assessment for gas pipeline hydrotesting. By combining classical mechanics with failure criteria, the model enhances accuracy in predicting pipeline response under elevated pressure conditions. The framework supports safer design verification, improved operational decision making, and compliance with international pipeline standards.

References

1. American Petroleum Institute. (2020). API Standard 5L: Specification for line pipe. API Publishing.
2. Timoshenko, S. P., & Gere, J. M. (2012). Theory of elasticity. McGraw-Hill Education.
3. ISO. (2017). ISO 13623: Petroleum and natural gas industries—Pipeline transportation

systems. International Organization for Standardization.
4. ASME. (2021). ASME B31.8: Gas transmission and distribution piping systems. American Society of Mechanical Engineers.

https://doi.org./10.58225/mpmma.2026.471

CONTACT INTERACTION OF THIN-WALLED ELASTIC SHELLS WITH DEFORMABLE FOUNDATIONS: AN APPROXIMATE METHOD

Khalid Mammadov, Lalazar Ahmadova
Baku State University, Azerbaijan

Abstract. The stress-strain behavior of thin-walled elastic shells interacting with deformable foundations along their boundary contour is examined. Various methods exist for analyzing composite structural elements. In this work, the problem is formulated within a contact mechanics framework. A contact-based formulation, unlike standard approximate methods, allows the stress-strain state of all interacting bodies to be studied simultaneously. Depending on the engineering requirements, problems may be solved through exact formulations or by a series of simplifications. The simplification procedure consists of reducing the contact interaction forces between the shell and the foundations to equivalent contour loads acting at the boundary cross-section of the shell.

Keywords: Thin shells, deformable foundations, contact interaction.

1.Introduction

Thin-walled elastic shells resting on deformable foundations arise in many engineering structures, including pressure vessels, pipelines, and foundation slabs. Various methods exist for analyzing such systems, among them Winkler and Pasternak foundation models and finite element approaches. However, these methods do not allow the stress-strain state of all interacting bodies to be determined simultaneously. A contact problem formulation removes this limitation by treating the shell-foundation interface within a unified framework.

Variational methods for conjugation problems of deformable bodies were developed in [1]. An approximate method for the contact interaction of thin shells with elastic foundations along the boundary contour was introduced in [2]. The present work derives the governing relations through transformation of the generalized variational principle functional for the axisymmetric deformation of a shell of revolution.

2. Problem Formulation

The interaction between a thin shell and a deformable foundations is considered in a contact problem formulation. To derive the governing relations of the approximate method, the functional of the generalized variational principle is transformed for the case of axisymmetric deformation of a shell of revolution.

The variational expression for the work done by the reactive interaction forces takes the form:

$$\sum_{k=1}^{2}\int_{S_{a_k}^1}^{S_{b_k}^1}[\,q_1^k\delta u_{1a}+\left(q_1^k\delta_k h\right)\delta\gamma_{1a}+q_3^k\delta w_a - q_3^k\left(S_1-S_{a_k}^1\right)\delta\gamma_{1a}+$$

$$\left(q_3^k\delta_k h\right)\delta\gamma_a]A_2\,dS_1=A_2(-\widetilde{R}_1^a\delta u_{1a}+\widetilde{R}_{13}^a\delta w_a+\widetilde{G}_{11}^a\delta\gamma_{1a}+\widetilde{G}_{13}^a\delta\gamma_a)$$

from which:

$$\widetilde{R}_{11}^a=-\sum_{k=1}^{2}\int_{S_{a_k}^1}^{S_{b_k}^1}q_1^k\,dS_1$$

$$\widetilde{R}_{13}^a=\sum_{k=1}^{2}\int_{S_{a_k}^1}^{S_{b_k}^1}q_3^k\,dS_1$$

$$\widetilde{G}_{11}^a=\sum_{k=1}^{2}\int_{S_{a_k}^1}^{S_{b_k}^1}[\,\delta_k h q_1^k-(S_1-S_{a_k}^1)q_3^k]dS_1$$

$$\widetilde{G}_{13}^a=\sum_{k=1}^{2}\int_{S_{a_k}^1}^{S_{b_k}^1}\delta_k\,h q_3^k dS_1$$

Conclusion

As a result of these transformations, the governing equations of the composite structural element remain unchanged, except for the boundary conditions of the shell. Specifically, the static boundary conditions are supplemented in addition to the external boundary loads by the forces $\widetilde{R}_{11}$, $\widetilde{R}_{13}$ and moments $\widetilde{G}_{11}$, $\widetilde{G}_{13}$ reduced to the boundary of the shell, which characterizes the influence of the elastic foundations on the shell deformation. Furthermore, the contact interaction forces between the elastic foundations and the shell do not appear in the equilibrium equations derived for the shell.
Thus, the introduced reactive interaction forces are eliminated from the set of unknowns of the problem.

References

1. Paymushin, V.N.: On variational methods for solving nonlinear three-dimensional problems of interface problems of deformable bodies. Dokl. Akad. Nauk SSSR 273(5), 1083–1086 (1983)
2. Paymushin, V.N., Firsov, V.A., Mamedov, Kh.B.: On an approach to the investigation of contact interaction of thin shells with elastic support foundations along the contour. In: Proceedings of the 7th Republican Conference of Young Scientists in Mathematics and

Mechanics, vol. 2, pp. 245–250. Elm, Baku (1987)

https://doi.org./10.58225/mpmma.2026.476

AN OPTIMAL CONTROL APPROACH TO THE INVERSE PROBLEM FOR NONLINEAR VIBRATIONS OF A PLATE AND ITS STUDY

Khayala Seyfullayeva
Sumgayit State University, Azerbaijan

Abstract. The paper deals with an inverse problem of determining the right-hand side of the linear equation of oscillations of thin plates. The problem is reduced to the optimal control problem. Differentiability of the functional is studied. Necessary condition of optimality is derived.

Keywords: thin plate, optimal control, adjoint problem, optimality conditions

Introduction

Systems described by fourth other differential equations are often arise in mechanics, physics and applied problems. Therefore, studying of optimal control problems related to fourth order partial differential equations is of great importance in different fields. These equations are often used in creating dynamic and high accuracy models. These equations can describe the properties (for example, free vibrations in mechanical systems, elastic motions, etc.) of various physical systems very accurately. The control of prosses described by these equations enables to control real systems very accurately and to optimization them.

The study of optimal control problems for fourth order partial differential equations is very important in terms of development of modern technologies, control of complex systems and ensuing efficient safe utilization. Such studies have wide applications in various fields including aerospace, robotics, transport, biomedical engineering and energy fields. The studies lead to the development of the best control systems and technologies and in future this will enable to create efficient and safe systems.

It is known that vibrations of thin plates are also described by fourth order partial differential equations. Therefore, the study of optimal control problems for the equation of vibrations of thin plates is of great theoretical and practical interest [3].

There are various methods for finding the coefficients and the right hand sides of fourth order equation. One of these methods is to approach these problems as an inverse problem, to reduce them to optimal control problems and solve them by means of the methods of this theory. This method is called the variational and optimization method. Such problems began to be studied since the end of the XX century and are currently being intensively studied [4].

Problem of the Problem

Our needs to find the pair of functions $(u, \upsilon) \in U \times U_{ad}$ from the relations

$$\rho\frac{\partial^2 u}{\partial t^2} + \Delta(D\Delta u) + (1-\nu)\left(2\frac{\partial^2 D}{\partial x\,\partial y}\frac{\partial^2 u}{\partial x\,\partial y} - \frac{\partial^2 D}{\partial x^2}\frac{\partial^2 u}{\partial y^2} - \frac{\partial^2 D}{\partial y^2}\frac{\partial^2 u}{\partial x^2}\right) + u^3 = \upsilon(x,y)f(t), (x,y,t) \in Q, \quad (1)$$

$$u(x,y,0) = \varphi_0(x,y), \frac{\partial u(x,y,0)}{\partial t} = \varphi_1(x,y), (x,y) \in \Omega, \quad (2)$$

$$u(0,y,t) = 0, \frac{\partial u(0,y,t)}{\partial x} = 0, u(x,0,t) = 0, \frac{\partial u(x,0,t)}{\partial y} = 0, \quad 0 \le x \le a, \quad 0 \le t \le T,$$

$$u(a,y,t) = 0, \frac{\partial u(a,y,t)}{\partial x} = 0, u(x,b,t) = 0, \frac{\partial u(x,b,t)}{\partial y} = 0, \quad 0 \le y \le b, \quad 0 \le t \le T, \quad (3)$$

$$\int_0^T K(x,y,t)u(x,y,t)dt = g(x,y), \quad (4)$$

where $(x,y) \in \Omega = \{(x,y): 0 < x < a, 0 < y < b\}$, $t \in (0,T)$, $Q = \Omega \times (0,T)$, $\rho(x,y)$ is a density of the mass at the point (x,y), $h(x,y)$ is the heath thickness of the plate in the point (x,y), $u(x,y,t)$ - is deflection of the plate in the point (x,y) at the moment t, Δ is Laplace operator with respect to x, y, $D = \frac{Eh^3}{12(1-\nu^2)}$- cylindrical rigidity, $\nu\left(0 < \nu < \frac{1}{2}\right)$-

Poisson's coefficient, $E > 0$-Young's modulus,

$$U = \left\{u | u(x,y,t) \in C[0,T]; \overset{o}{W}{}_2^2(\Omega), \frac{\partial u}{\partial t} \in C[0,T]; L_2(\Omega)\right\},$$

$$U_{ad} = \{\upsilon(x,y) \in L_2(\Omega): \mu_0 \le \upsilon(x,y) \le \mu_1 \text{a.e.on } \Omega\}$$

$f(t) \in L_2(0,T)$, $\varphi_0(x,y) \in \overset{o}{W}{}_2^2(\Omega)$, $\varphi_1(x,y) \in L_2(\Omega)$, $K(x,y,t) \in L_\infty(Q)$, $g(x,y) \in L_2(\Omega)$ are given functions, $h(x,y)$ - is sufficiently smooth given function, a, b, T are given positive numbers, μ_0, μ_1 given numbers.

This problem we reduce to the following optimal control problem: to find the minimum of the functional

$$J_0(\upsilon) = \frac{1}{2}\int_\Omega \left[\int_0^T K(x,y,t)u(x,y,t;\upsilon)dt - g(x,y)\right]^2 dxdy, \quad (5)$$

subject to (1)-(3). The function $\upsilon(x,y)$ is called a control. By $u = u(x,y,t;\upsilon)$ we denote the generalized solution of the problem (1)-(3) corresponding to the control $\upsilon(x,y)$. We regularize the problem (1)-(3), (5) by the following way: instead of the functional (5) consider the next one

$$J_\alpha(\upsilon) = J_0(\upsilon) + \frac{\alpha}{2}\int_\Omega \upsilon^2(x,y)dxdy, \quad (6)$$

where $\alpha > 0$ is a positive number.

Let's assume that by any fixed control $\upsilon(x,y)$ boundary problem (1)-(3) has unique generalized solution from U.

Main Results

Thus the following theorems is proved:

Theorem 1. Under the imposed conditions on the problem data, there exists an optimal control in problem (1)-(3), (6).

Theorem 2. Let's the conditions of the Theorem 1 be satisfied. Then functional (6) is continuously Frechet differentiable on U_{ad} and its differential in the point $\forall \upsilon \in U_{ad}$ at the increment $\delta\upsilon \in L_2(\Omega)$, $\upsilon + \delta\upsilon \in U_{ad}$ is defined by the expression

$$\langle J'_\alpha(\upsilon), \delta\upsilon \rangle = \int_\Omega \left[\alpha\upsilon(x,y) - \int_0^T f(t)\,\psi(x,y,t)dt \right] \delta\upsilon dxdy.$$

Let us introduce the adjoint to (1)-(3), (6) problem for the given control $\upsilon(x,y,t) \in L_2(Q)$:

$$\rho \frac{\partial^2 \psi}{\partial t^2} + \Delta(D\Delta\psi) + (1-\nu) \times \left[2 \frac{\partial^2}{\partial x\,\partial y} \left(\frac{\partial^2 D}{\partial x\,\partial y} \psi \right) - \frac{\partial^2}{\partial x^2} \left(\frac{\partial^2 D}{\partial y^2} \psi \right) - \frac{\partial^2}{\partial y^2} \left(\frac{\partial^2 D}{\partial x^2} \psi \right) \right] + 3u^2\psi =$$

$$-K(x,y,t) \left[\int_0^T K(x,y,t)u(x,y,t)dt - g(x,y) \right], (x,y,t) \in Q, \quad (7)$$

$$\psi(x,y,T) = 0, \quad \rho \frac{\partial \psi(x,y,T)}{\partial t} = 0, \quad (x,y) \in \Omega, \quad (8)$$

$$\psi(0,y,t) = \psi(a,y,t) = 0, \frac{\partial\psi(0,y,t)}{\partial x} = \frac{\partial\psi(a,y,t)}{\partial x} = 0,$$

$$0 \le x \le a, \quad 0 \le t \le T,$$

$$\psi(x,0,t) = \psi(x,b,t) = 0, \frac{\partial\psi(x,0,t)}{\partial y} = \frac{\partial\psi(x,b,t)}{\partial y} = 0,$$

$$0 \le y \le b, \quad 0 \le t \le T.$$

(9)

Theorem 3. Let's the conditions of the Theorem 1 be satisfied. Then for the optimality of the control $\upsilon_* \in U_{ad}$ in problem (1)-(3), it is necessary fulfilment of the inequality

$$\int_\Omega \left[\alpha\upsilon_*(x,y) - \int_0^T f(t)\psi(x,y,t)dt\right] \times (\upsilon(x,y) - \upsilon_*(x,y))dxdy \ge 0$$

for arbitrary $\upsilon = \upsilon(x,y) \in U_{ad}$, here $u_*(x,y,t)$ and $\psi_*(x,y,t)$ are solutions of problems (1)-(3), (7)-(9) correspondingly

Conclusions

The paper first deals with an inverse problem of determining the right-hand side of the linear equation of oscillations of thin plates. The problem is reduced to the optimal control problem. Further, differentiability of the functional is studied. Necessary condition of optimality is derived.

References

1. Komkov V. The Theory of Optimal Control of Damping Vibrations of Simple Elastic Systems, Moscow, Mir, 1975, 160.
2. Arman J.-L.P. Applications of the Optimal Control Theory for the Distributed Parameter Systems to the Problems of Structural Optimization, Moscow, Mir, 1977, 144 p.
3. Kabanikhin S.I. Inverse and Ill-posed problems, Novosibirsk, 2009, 457 p.
4. Guliyev H.F., Seyfullayeva Kh.I. Optimal control problem for the equation of vibrations of an elastic plate. Georgian Mathematical Journal, Vol. 25, Is. 3, 2018, pp. 371-380. DOI 10.1515/gmj-2017-0004.

https://doi.org./10.58225/mpmma.2026.483

THE DUAL PROBLEM CORRESPONDING TO THE BOOLEAN PROGRAMMING PROBLEM AND ITS LAGRANGIAN-TYPE APPROXIMATE SOLUTION.

Mamedov Knyaz Shiraslan [1], Niyazova Rayiha Rasim[2]

[1] Baku State University, Azerbaijan

[2] Institute of Mathematics,Azerbaijan

Abstract. In this work, an approximate solution method for the Boolean programming problem has been developed. For this purpose, a certain linear programming problem is constructed, and the corresponding dual problem is considered. By making specific modifications to the obtained problem, it is transformed into a Lagrangian problem, and an appropriate Lagrangian function is formulated. Certain properties of this function are proved, and it is shown that the function possesses a unique minimum value. Therefore, an algorithm has been developed for minimizing the constructed Lagrangian-type function. The main feature of this algorithm is that it provides not only the minimum value of the function, but also simultaneously yields an approximate solution to the considered Boolean programming problem.

Keywords: Boolean Programming Problem; Lagrangian Function; Lagrangian-Type Approximate Solution.

Introduction

Let us consider the Boolean programming problem given in the following form.

$$\sum_{j=1}^{n} c_j x_j \rightarrow \max \quad , \qquad (1)$$

$$\sum_{j=1}^{n} a_{ij} x_j \leq b_i, \quad (i = \overline{1,m}), \qquad (2)$$

$$x_j = 1 \vee 0 \, , \quad (j = \overline{1,n}) \, . \qquad (3)$$

Here $c_j, a_{ij}, b_i \ , (i = \overline{1,m};\ j = \overline{1,n})$ are given integers. Moreover, without loss of generality, we may assume that the coefficients $c_j, (j = \overline{1,n})$ are positive integers. First, let us note that when there are no negative numbers among the coefficients in problem (1)–(3), it is called the multidimensional knapsack problem, and certain methods have been developed for finding its optimal or approximate (suboptimal) solutions [1–5], etc. It should be noted that although certain methods exist for

finding the optimal solution of problem (1)–(3), none of them has polynomial-time complexity. Therefore, problem (1)–(3) belongs to the class of "hard-to-solve problems," namely the NP-complete class. However, taking into account the great practical importance of problem (1)–(3), various approximate solution methods have been developed both for this problem and for some of its subclasses .. It should be noted that the approximate solution methods proposed in all the papers cited above can be applied only to problems whose coefficients are nonnegative.

2. Problem Statement

Let us formulate the following related problem corresponding to Problems (1)–(3).

$$\sum_{i=1}^{m} b_i y_i + \sum_{j=1}^{n} y_{m+j} \to \min, \quad (4)$$

$$\sum_{i=1}^{m} a_{ij} y_i + y_{m+j} \geq c_j, \ (j = \overline{1,n}), \quad (5)$$

$$y_i \geq 0, \ (i = \overline{1,m+n}) \ . \quad (6)$$

It is noted that problem (4)–(6) is a constrained extremum problem. Let us reduce it to an unconstrained extremum problem, i.e., a Lagrangian problem. Since the problem is a minimization problem, from relation (5) we express the variables y_{m+j}, $(j = \overline{1,n})$ as

$$y_{m+j} \geq c_j - \sum_{i=1}^{m} a_{ij} y_i$$

and substitute these expressions into function (4).

$$L(y_1, y_2, \dots, y_m) = \sum_{i=1}^{m} b_i y_i + \sum_{j=1}^{n} (c_j - \sum_{i=1}^{m} a_{ij} y_i) \to \min, \quad (7)$$

$$y_i \geq 0, \quad (i = \overline{1,m}). \quad (8)$$

It should be noted that problem (7)–(8) is called a Lagrangian problem, and in this problem the objective function depends only on m variables y_i, $(i = \overline{1,m})$.

Here, taking into account the condition $y_i \geq 0$, $(i = \overline{1,m})$ we can rewrite function (7) as follows

$$L(y_1, y_2, \dots, y_m) = \sum_{i=1}^{m} b_i y_i + \sum_{j \epsilon A} (c_j - \sum_{i=1}^{m} a_{ij} y_i), A = \left\{ j | c_j - \sum_{i=1}^{m} a_{ij} y_i > 0 \right\} \quad (9)$$

From here it directly follows that the function $L(y_1, y_2, \dots, y_m)$ has a unique minimum value. If we develop an algorithm for finding the minimum of this function, then, we obtain the upper bound of the optimal value of problem (1)–(4). On the other hand, if all the numbers $B_i(A)$, $(i = \overline{1, m})$ are nonnegative, then we obtain a feasible solution of system (2)–(3). Indeed, for such a set A we have

$$B_i(A) = b_i - \sum_{j \epsilon A} a_{ij} > 0, (i = \overline{1, m}) ,$$

$$\sum_{j \epsilon A} a_{ij} \leq b_i, (i = \overline{1, m}) .$$

Hence, for j∈A, we set üçün $x_j = 1$,, and for ,j ∉ A, we set $x_j = 0$. We call this solution a Lagrange-type approximate solution and have developed an algorithm for its determination.

Conclusion.

A new Lagrange-type approximate solution method has been developed for this programming problem. The proposed method has been mathematically substantiated, and its convergence after a finite number of iterations has been demonstrated.

References

1. Kovalev M. M. Discrete optimization (integer programming)..M. URCA, 2003. P.191. (in russian)
2. Martello S., Toth P. Knapsack problems: Algorithm and Computers İmplementations. John Wiley & Sons, Chichster,1990, 296 p.
3. Nuriyev, U.G., An algorithm for solving a multidimensional knapsack problem, Transactions of National Academy of Sciences of Azerbaijan, series of Physical–Technical and Mathematical Sciences, 2001, vol. XXI, No. 2, pp. 54-58(in Russian).
4. Sigal I. Kh., Ivanova A. P., Introduction

to Applied Discrete Programming: Models and Computational Algorithms, M. Fizmatlit, 2003, 304 p. (In Russian).

5. Babaev J. A., Mammadov K. Sh. Mehdiev M. G. Methods for constructing suboptimal solutions to the multidimensional knapsack problem. “Computational Mathematics and Mathematical Physics, Moscow 1978. T. 28, №6, – c. 1443-1453. (in russian)

https://doi.org./10.58225/mpmma.2026.490

VERIFICATION ANALYSIS OF THE THERMAL PERFORMANCE OF CYLINDRICAL SOLID PIN-FIN AND CYLINDRICAL PERFORATED PIN-FIN HEATSINKS USING CFD

Levent Sıvakcı[1], Ali Kuruçay[1], Ahmet Selim Dalkılıç[1]

[1] Yıldız Technical University , Türkiye

Abstract. In this study, the thermal-hydraulic performance of solid (0P) and three-perforated (3P) cylindrical pin-fin heatsinks under forced convection was numerically investigated using CFD with the k-ω SST turbulence model (Re = 3509–6586). Validation against reference data showed pressure drop agreement within 10%. Results demonstrate that the 3P pin-fin structure achieves 4–5°C lower surface temperature than the solid pin at equivalent fan power.

Keywords: Pin-fin heat sink, Perforated pins, CFD, Convective heat transfer, Thermal performance

1. Introduction

Increasing power densities in electronic components demand advanced thermal management. Solid pin-fin geometries suffer from wake-induced efficiency losses and elevated pressure drop at low velocities;

perforated designs counter this by injecting air jets that enhance local heat transfer while controlling hydraulic resistance. Prior studies report significant Nu improvements: 70% over inline arrangement [1], 64% with 25% lower ΔP [2], 328% [3], and 33% with 9.35% lower ΔP [4]. This study validates CFD models of solid (0P) and three-perforated (3P) pin-fin heat sinks against Al-Damook et al. [5] over Re = 3,509–6,586.

2.Numerical Method

2.1 Problem Definition and Geometry

The heat sink consists of 64 cylindrical pins (d = 2 mm, H = 10 mm, pitch = 6.5 mm) in an 8×8 arrangement on a 50×50×2 mm aluminum plate. In the 3P model, three 1 mm perforations are aligned with the flow ($A_{t,0P}$ = 73.25 cm², $A_{t,3P}$ = 76.27 cm²). Q = 50 W and Tin = 25°C were applied. Both geometries are shown in Fig. 1.

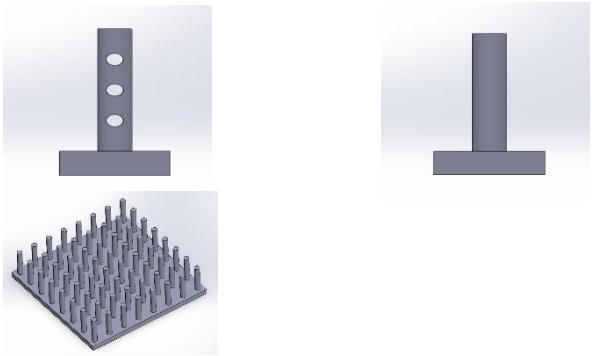


Fig. 1. (a) Perforated pin-fin (3P), (b) Solid pin-fin (0P) and (c) heat sink array configuration

2.2 Mesh Structure

The computational domain was created in a strip configuration covering eight pin rows by utilizing the symmetry condition; a tetrahedral mesh structure was chosen for the pin surfaces and perforated channel regions. A coarse mesh with 295,377 elements was used for validation, followed by a fine mesh with 3,577,159 elements to improve accuracy; the difference in pressure drops between the two meshes remained below 10%. The results are shown in Table 1.

Table 3. Mesh Structure Comparison (0P and 3P Model)

Element	Re	NuT	ΔP Pa	Ths	NuT	ΔP	Ths
295.377	3509–6586	304–	35–111	75–	323–	34–	71–

1.130.525	3509–6586	318-465	36-112	73-	329-	34-	70-
2.202.175	3509–6586	320-466	37-114	73-	332-	34-	70-
3.577.159	3509–6586	321–	38–119	73–	332–	35–	70–

2.3 Boundary Conditions and Solution Method

Inlet conditions: uniform velocity (U = 6.5 and 12 m/s), Tin = 25°C; zero relative pressure at outlet; symmetry on side walls; adiabatic outer surfaces. The k-ω SST model with second-order upwind scheme and SIMPLE algorithm was applied, with conjugate heat transfer at the solid-fluid interface. Key parameters — Dh = 2HpinSz/(Hpin+Sz) = 8.43 mm, NuT = hT·L/kf, and Pfan = U·Ac·ΔP — were calculated following [5]

3. **Results and Discussion**

3.1 Validation and Mesh Analysis

Tables 2 and 3 present CFD results for the 295,377- and 3,577,159-element meshes. Pressure drop results agree with reference within 4.1% (0P) and 6.0% (3P); NuT deviations are 12.6% and 11.9%, attributed to mesh density and constant air property assumptions. The 3P model exhibited consistently higher NuT across Re = 3509–

6586: at Re = 3509, NuT was 323 (3P) vs. 304 (0P) (+6.25%); at Re = 6586, 407 (3P) vs. 396 (0P) (+2.78%), consistent with [2, 3]. The refined mesh yielded higher NuT and lower Ths,avg values, confirming the influence of mesh density on boundary layer resolution.

Table 4. Validation and Mesh Analysis Results — 295,377-Element Mesh

U		ΔP 0P	ΔP 3P	Ths 0P	Ths 3P	NuT0P	NuT3P
6,5	3509	35,85	34,30	75,45	71,02	303,1	323,3
12,0	6478	111,62	98,50	62,24	60,00	392,2	407,3

3.2 Mesh Independence Analysis – 3.577.159 Element Mesh

Table 3 presents results for the 3,577,159-element mesh. Pressure drop values differed by 2,3-19,2% compared to the 295K mesh, with larger deviations observed at higher velocities for the 3P configuration. NuT and Ths,avg improved notably at high velocities, confirming that increased mesh density enhances boundary layer resolution under constant air property assumptions.

Table 5. Mesh Independence Analysis Results —3,577,159 Element Mesh

U (m/s)	Re	ΔP0P (Pa)	ΔP 3P (Pa)	Ths 0P (°C)	Ths 3P (°C)	NuT 0P	NuT 3P
6,5	3509	38,21	35,09	73,14	70,02	320,6	332,8
12,0	6478	119,10	117,45	56,59	52,62	475,3	531,4

4. Conclusion

CFD analysis of solid (0P) and three-perforated (3P) cylindrical pin-fin heat sinks was performed using the k-ω SST model. Pressure drop values agreed with the reference within 10%, confirming successful validation. The 3P model consistently exhibited higher NuT than the 0P configuration across the entire Re range, demonstrating superior thermal performance. The refined mesh yielded higher NuT values, reflecting improved boundary layer resolution.

5. References

1. Ali, A., Sabri, L.S.: Effect of Perforated Pin Fin on Thermal Performance of a Rectangular Channel in Forced Convection. J. Inf. Syst. Eng. Manag. 10(35s) (2025)

2. Alpha, A., Kuhe, A.: Heat Transfer Enhancement on Staggered Perforated Circular Pin-Fin Heat Sink: An Experimental Assessment (2024).

3. Ismail, M.F.: Experimental and numerical analysis of heat sink using various patterns of cylindrical pin-fins. Int. J. Thermofluids 23, 100737 (2024).

4. Mesgarpour, M., Heydari, A., Saedodin, S.: Numerical analysis of heat transfer in porous tapered fins. Int. J. Thermal Sciences 135, 398–409 (2019).

5. Al-Damook, A., Kapur, N., Summers, J.L., Thompson, H.M.: An experimental and computational investigation of thermal air flows through perforated pin heat sinks. Appl. Therm. Eng. 89, 365–376 (2015)

https://doi.org./10.58225/mpmma.2026.*497*

ON SOME PROPERTIES OF EIGENVALUES OF A SECOND-ORDER DIFFERENTIAL OPERATOR WITH A BOUNDARY CONDITION CONTAINING A SPECTRAL PARAMETER

Leyla Mammadova
Azerbaijan State Oil and Industry University, Azerbaijan.

Abstract. This paper investigates the spectral properties of a linear Sturm–Liouville differential operator with a boundary condition containing the spectral parameter. Operators of this type arise in various problems of mathematical physics, quantum mechanics, vibration theory, and hydrodynamics, where the spectral parameter appears not only in the differential equation but also in the boundary conditions. It should be noted that the presence of the spectral parameter in a boundary condition alters the structure of the spectrum and affects the distribution of eigenvalues. The paper examines the multiplicity of the zero eigenvalue and the asymmetry of the spectrum with respect to the origin. Using methods from the theory of entire functions of exponential type and asymptotic analysis, an asymptotic formula for the eigenvalues is obtained. In addition, the problem of representing the characteristic function of the

boundary value problem as an infinite product over its eigenvalues is considered.

The obtained theoretical results are not only of independent scientific interest but can also be applied to the modeling of nonstationary physical processes, such as the vibrations of a string or a rod with an attached concentrated mass, as well as in acoustics and plasma physics, where the response of the support or contact medium is described by frequency-dependent boundary laws, and in heat conduction problems with a heat-capacitive boundary.

Keywords: Sturm–Liouville operator, eigenvalues, spectral asymptotics.

The investigation of spectral properties of second-order differential operators with boundary conditions involving the spectral parameter is a central topic in modern operator theory and the theory of boundary value problems. In recent years, substantial progress has been made in the study of Sturm–Liouville problems with non-separated boundary conditions that depend on the spectral parameter in a linear, quadratic, or rational manner, as well as in the analysis of diffusion and Dirac operators (see [1–5]).

In the present paper, a Sturm–Liouville operator with a real-valued potential is considered. One of the boundary conditions is separated, while the other is non-separated and depends linearly on the spectral

parameter. Several spectral properties of this operator are investigated.

Consider the boundary value problem on the interval $[0,\pi]$ generated by the Sturm–Liouville differential equation

$$-y''+q(x)y=\lambda^2 y \tag{1}$$

and the boundary conditions of the form

$$\begin{aligned} &y'(0)+\gamma y(0)=0,\\ &y'(0)+(\alpha\lambda+\beta)y(\pi)=0, \end{aligned} \tag{2}$$

where $q(x)\in L_2[0,\pi]$ is a real-valued function, λ is the spectral parameter, and $\alpha\neq 0,\ \beta,\gamma\neq 0$ are real constants. In what follows, this problem will be denoted by B.

Definition. A complex number λ_0 is called an eigenvalue of the boundary value problem B, if equation (1) with $\lambda=\lambda_0$ admits a nontrivial solution $y_0(x)$ satisfying the boundary conditions (2). In this case, $y_0(x)$ is called an eigenfunction of the problem B corresponding to the eigenvalue λ_0. The set of all eigenvalues is called the spectrum of the problem B.

Let $c(x,\lambda)$, $s(x,\lambda)$ are solutions of equation (1) satisfying the initial conditions

$$c(0,\lambda) = s'(0,\lambda) = 1, \qquad c'(0,\lambda) = s(0,\lambda) = 0.$$

The eigenvalues $\mu_k \ (k = \pm 0, \pm 1, \pm 2, ...)$ of problem B coincide with the zeros of the characteristic function

$$\Delta(\lambda) = (\alpha\lambda + \beta)[c(\pi,\lambda) - \gamma s(\pi,\lambda)] - \gamma. \quad (3)$$

It is known that the following representations hold for the functions $c(\pi,\lambda)$ and $s(\pi,\lambda)$:

$$c(\pi,\lambda) = \cos\lambda\pi + A\frac{\sin\lambda\pi}{\lambda} + \frac{f_1(\lambda)}{\lambda},$$

$$s(\pi,\lambda) = \frac{\sin\lambda\pi}{\lambda} - A\frac{\cos\lambda\pi}{\lambda^2} + \frac{f_2(\lambda)}{\lambda^2},$$

where $A = \frac{1}{2}\int_0^\pi q(x)dx,$ $f_m(\lambda) \ (m = 1,2)$ is an entire function of exponential type not exceeding π, square-integrable on the real axis. Using these representations and the Paley–Wiener theorem, it follows from (3)

that

$$\Delta(\lambda)=\alpha\lambda\cos\lambda\pi+\alpha(A-\gamma)\sin\lambda\pi+\beta\cos\lambda\pi+f(\lambda)-\gamma, \tag{4}$$

$$f(\lambda)=\int_{-\pi}^{\pi}\tilde{f}(t)e^{i\lambda t}dt,$$

where

$\tilde{f}(t)\in L_2[-\pi,\pi]$.

Using formulas (3) and (4), the following theorems can be proved.

Theorem 1. The following statements hold:

1) The boundary value problem B has a countable set of eigenvalues.

2) The number $\lambda=-\frac{\alpha}{\beta}$ is not an eigenvalue of problem B.

3) If a number $\lambda=0$ is an eigenvalue of the problem, then it is simple; i.e., if $\Delta(0)=0$, then $\Delta'(0)\neq 0$.

4) If for some $\lambda_0\neq 0$ the equality implies $\Delta(\lambda_0)=0$, then $\Delta(-\lambda_0)\neq 0$, the

eigenvalues of problem B are not symmetric with respect to the origin.

Theorem 2. The eigenvalues μ_k of the boundary value problem B for $|k| \to \infty$ satisfy the following asymptotic formula:

$$\mu_k = k + \frac{1}{2} + \frac{A-\gamma}{\pi k} + \frac{(-1)^{k+1}\gamma}{\alpha \pi k} + \frac{\xi_k}{k},$$

where $\{\xi_k\} \in l_2$.

Theorem 3. The specification of the spectrum $\{\mu_k\}$ ($k = \pm 0, \pm 1, \pm 2, \ldots$) and the number α uniquely determines the characteristic function $\Delta(\lambda)$ of the boundary value problem B by the formula

References

$$\Delta(\lambda) = \pi\alpha(\mu_{-0} - \lambda)(\mu_{+0} - \lambda)\prod_{\substack{k=-\infty \\ k\neq 0}}^{\infty} \frac{\mu_k - \lambda}{k}.$$

1. Freiling, G., Yurko, V.: Recovering nonselfadjoint differential pencils with nonseparatedboundary conditions. Appl. Anal. 94(8), 1649–1661 (2015).
2. Nabiev, I.M.: Reconstruction of the differential operator with spectral parameter in the boundary condition. Mediterr. J. Math. 19(3), 1-14 (2022).

3. Nabiev, I.M., Mammadova, L.I., Mammedzadeh, G.S.: Spectral problems for Sturm-Liouville operator with non-separated boundary condition linearly dependent on the eigenparameter. Proc. of Institute of Math. and Mech. of National Academy of Sci. of Azerbaijan. 51(1), 99–106 (2025).
4. Mammadova, L.I., Nabiev, I.M.: Uniqueness of recovery of the Dirac system on a segment by two spectra. Journal of Contemporary Applied Mathematics 16(1), 110-118 (2026).
5. Nabiev, I.M., Latifova, A.R., Mammadova, L.I., Osmanli, J.A.: Inverse problem for the Dirac system with a spectral parameter linearly contained in a boundary condition. Advanced Mathematical Models & Applications 11(2) (2026).

https://doi.org./10.58225/mpmma.2026.*504*

AI-DRIVEN PREDICTIVE ANALYTICS FOR LOGISTICS AND TRANSPORTATION SYSTEMS

Mahammad Zeynalov
Azerbaijan Technical University, Azerbaijan

Abstract. By 2026, the logistics industry has transitioned from experimental artificial intelligence (AI) concepts to a data-driven operational standard [4,5]. This research examines the integration of predictive analytics and AI frameworks in modern transportation systems, focusing on vehicle routing optimization, large-scale traffic forecasting, and autonomous vehicle (AV) integration [1,6,2]. Advanced approaches such as the Route-First Cluster-Second (RFCS) heuristic for the Capacitated Vehicle Routing Problem (CVRP) are analyzed, demonstrating an average optimality gap reduction to 1.82% across diverse problem instances [1]. In addition, the Positional-aware Spatio-Temporal Network (PASTN) for traffic prediction is reviewed, achieving an 18.45% improvement in RMSE by mitigating over-smoothing in large-scale graph representations [6]. Operationally, Level 5 AV integration is estimated to reduce total logistics operating costs by 42-45% [2], while Generative AI is emerging as a semantic layer for data standardization with projected market value reaching USD 23.1

billion by 2034 [3,8]. Despite these advancements, particularly in green logistics frameworks [4], this study identifies a persistent evidence gap between simulation-based results and real-world deployment validation [8]. The paper concludes that although AI-driven predictive analytics offers substantial improvements in efficiency and sustainability, future research must prioritize field-validated KPIs and address adoption barriers faced by small- and medium-sized enterprises (SMEs) [7].
Keywords: Predictive Analytics, Vehicle Routing, Traffic Prediction.

1 Introduction

Logistics and transportation systems are inherently data-intensive domains characterized by repeated operational decisions made under complex physical and temporal constraints. By 2026, the industry has fundamentally transitioned from viewing artificial intelligence (AI) as an experimental concept to an everyday operational requirement driven by data. Modern supply chains now rely on the integration of predictive analytics and AI to manage a variety of tasks, including demand forecasting, inventory positioning, and route planning. This shift is further accelerated by the emergence of "Green Logistics," where sustainability and clean energy have become

the new business standard for global organizations. Consequently, logistics software is evolving from purely predictive tools into agentic systems capable of executing autonomous solutions to mitigate risks and disruptions.

1.1 Problem Statement

Despite the potential of AI, several critical challenges persist in the optimization of modern logistics. First, the Capacitated Vehicle Routing Problem (CVRP) and its real-world variants - incorporating time windows, backhaul requests, and distance limits - remain NP-hard and computationally complex to solve efficiently for large-scale networks. In the domain of urban transportation, rising vehicle numbers have led to severe road congestion, which increases greenhouse gas emissions and elevates accident risks. Furthermore, current spatio-temporal models for traffic prediction often suffer from "over-smoothing" in Graph Neural Networks (GNNs), where node-specific characteristics are diminished as modeling layers increase, leading to suboptimal forecasting.

Efficiency bottlenecks are particularly acute in last-mile delivery, which currently accounts for approximately 53% of total shipping costs. While large firms are rapidly adopting AI solutions, small-to-medium enterprises (SMEs) face significant barriers

to entry, including high upfront implementation costs, a lack of specialized technical expertise, and concerns regarding data privacy. Finally, there is a notable "evidence gap" in logistics research; many proposed AI systems rely heavily on simulation or benchmark data, with very few achieving documented field validation in live operational environments.

1.2 Research Motivation

The motivation for integrating AI-driven predictive analytics into logistics is rooted in both economic necessity and technological advancement. From a cost perspective, the integration of Level 5 autonomy in trucking is estimated to reduce total operating costs by 42-45% through optimized fuel consumption and reduced labor expenses. The market for Generative AI in logistics is also experiencing explosive growth, with a projected value of USD 23.1 billion by 2034, highlighting its role in enhancing supply chain visibility and automating repetitive processes.

Sustainability serves as a primary driver, as stricter environmental regulations and rising consumer expectations regarding Environmental, Social, and Governance (ESG) standards force companies to seek leaner, cleaner routes. Innovative frameworks like the Positional-aware Spatio-Temporal Network (PASTN) offer

significant performance incentives, demonstrating up to an 18.45% improvement in RMSE for large-scale traffic prediction. By leveraging AI to standardize unstructured data and optimize resource management, logistics providers can achieve a competitive edge while meeting the modern market's demand for transparency and environmental stewardship.

References

1. Wang, W., Wu, X., Wang, L., Hu, H., Tao, X.: A Unified Knowledge Embedded Reinforcement Learning-based Framework for Generalized Capacitated Vehicle Routing Problems. *arXiv preprint*, (2026).

2. Sadiku, M.N.O., Sadiku, J.O.: Autonomous Vehicles in Logistics. *International Journal of Trend in Research and Development*, (2026).

3. Wadhwani, P., Jaiswal, S.: Generative AI in Logistics Market Size & Share 2025 - 2034. *Global Market Insights Inc.*, (2025).

4. Siam Nistrans Co., Ltd.: Green Logistics 2026: When AI and Clean Energy Become the New Business Standard. *Siam Nistrans Blog*, (2026).

5. Flagship Forwarding LLC: How Artificial Intelligence is Reshaping Global Freight Forwarding in 2026. *Flagship Forwarding Case Study*, (2026).

6.Chen, R.: Positional-aware Spatio-Temporal Network for Large-Scale Traffic Prediction. *arXiv preprint*, (2026).

7. Paul, P.O., et al.: Predictive analytics and AI in sustainable logistics: A review of applications and impact on SMEs. *Magna Scientia Advanced Research and Reviews*, (2024).
8. Ban, B.: Recent Applications of Artificial Intelligence in Logistics: An Evidence-Oriented Operational Review of Studies Published Since 2024. *Preprints.org*, (2026).

https://doi.org./10.58225/mpmma.2026.510

INFLUENCE OF ELASTIC FOUNDATIONS ON NONLINEAR PRIMARY RESONANCE OF LAYERED NANOCOMPOSITE SPHERICAL SHELL SURFACES VIA THE METHOD OF MULTIPLE TIME SCALES

[a,b]*Avey Mahmure,* [b]*Yüce Salim*

[a]Istanbul Gelisim University, Türkiye

[b]Yıldız Technical University, Türkiye

Abstract. This study investigates the influence of elastic foundations on the nonlinear primary resonance behavior of layered nanocomposite spherical surfaces subjected to external excitation. The formulation is developed within the framework of classical shell theory, where nonlinear kinematics, strain–displacement relations, and the corresponding equations of motion are consistently derived to ensure both mathematical rigor and physical accuracy. The structural model incorporates functionally graded nanocomposite (FG-NC) layers with through-thickness material variation, together with viscous damping and a two-parameter elastic foundation (TPEF) model to realistically represent foundation–structure interaction.

The governing nonlinear partial differential equations are reduced to a set of nonlinear ordinary differential equations using the Galerkin method. To capture the nonlinear

primary resonance characteristics, the Method of Multiple Time Scales (MTS) is employed in a systematic and explicit manner, allowing the perturbation procedure to be followed step by step. Through this analytical approach, closed-form expressions describing amplitude–frequency relationships and primary resonance conditions are derived, providing clear insight into the nonlinear dynamic response of the system.

A comprehensive parametric study is conducted to evaluate the effects of foundation stiffness parameters, excitation amplitude, geometric nonlinearity, and layer configuration on the resonance behavior. The results demonstrate how the elastic foundation significantly alters resonance characteristics, including frequency shifts, response amplitude, and stability regions. Furthermore, the interaction between material gradation and foundation parameters is shown to play a critical role in governing the nonlinear vibration response.

Keywords: Applications of differential geometry to engineering, layered nanocomposite shells; nonlinear primary resonance; multiple time scales

https://doi.org./10.58225/mpmma.2026.*512*

ALGORITHM AND STAGES OF TRAINING A TEXT RECOGNITION MODEL FOR THE TURKMEN LANGUAGE USING TESSERACT OCR

Maksud Sharipov, Khikmat J. Rakhimboev, Ikhtiyor Avezmatov
Urgench State University named after Abu Rayhan Biruni, Uzbekistan

Abstract. Enhancing the accuracy of Optical Character Recognition (OCR) models for languages with specific characters, such as the Turkmen language, is of great importance within the field of digital text processing. This paper proposes a complete algorithm and the practical stages for developing and fine-tuning a high-accuracy text recognition model for the Turkmen language using the Tesseract OCR engine. During the training process, the syntactic and morphological rules (langdata, unicharset) of the Turkmen language were formalized on the basis of the related Turkish language, and 6078 clean text–image pairs were prepared and trained within the Tesseract (tesstrain) architecture. The research findings demonstrate that the new model, trained using the Transfer Learning approach on LSTM neural networks, can be effectively applied with high accuracy (97.8%) and a low Character Error Rate (CER) in document

digitization, automated translation, and Natural Language Processing (NLP) systems for the Turkmen language.

Keywords: Turkmen language · Optical Character Recognition (OCR) · Tesseract OCR · Model fine-tuning · LSTM neural networks · Transfer Learning · Natural Language Processing (NLP).

Introduction

Optical Character Recognition (OCR) technologies play a fundamental role in the field of digital text processing and document imaging. In this process, textual images from scanned documents, books, or photographs are automatically converted into editable digital text. The accuracy of this conversion directly determines the quality of every downstream task, from full-text search and archival digitization to machine translation and corpus construction. Over the last decade, handwritten and printed OCR have been studied extensively and surveyed in the literature [8], yet most high-accuracy systems are tuned to high-resource languages, leaving many low-resource languages without reliable recognition tools.

Tesseract OCR is one of the most powerful and widely used open-source OCR engines, particularly distinguished by its Long Short-Term Memory (LSTM) neural-network architecture. However, the Turkmen language possesses unique linguistic and

grammatical characteristics that introduce specific challenges when analyzed through standard OCR models. Specifically, the diacritic and special characters in the Turkmen alphabet — such as Ä, Ö, Ü, Ý, Ň, and Ž — are frequently misread or entirely unrecognized by base models. The agglutinative morphology and rich vocabulary of the Turkmen language require a specialized approach to character and word recognition, necessitating the training of a new model based on the language's precise rules.

For successful text recognition, it is essential to have not only high-quality images but also a deep understanding of the lexical structure of the language, a comprehensive list of unique words, and a reliable dataset (ground truth). This paper explores a complete methodology for developing a high-accuracy text recognition model for the Turkmen language using the Tesseract OCR (tesstrain) architecture. Throughout the paper, the step-by-step processes of gathering 6078 text–image pairs, converting them into the specific Tesseract formats (.tif and .gt.txt), and formulating the morphological rules of the Turkmen language (langdata) on the basis of Turkish language parameters are analyzed in detail. Furthermore, the paper discusses the practical solutions through which the challenge of recognizing specific

Turkmen characters was overcome by training LSTM neural networks with the Transfer Learning approach. The main contributions of this work are: (i) a reproducible pipeline for building Turkmen ground-truth data; (ii) a Turkish-based formalization of the Turkmen unicharset and langdata; and (iii) an empirical evaluation showing a large reduction of the Character Error Rate after fine-tuning.

Literature Review and Theoretical Background

Numerous studies have been conducted globally on developing text-recognition (OCR) and natural-language processing models for low-resource Turkic languages such as Uzbek, Kazakh, and Turkmen. Recent systematic reviews map the available resources, methods, and benchmarks for Uzbek and Turkmen NLP and highlight a clear asymmetry in resource maturity between the two languages [1]. Regarding OCR specifically, R. Smith detailed the open-source architecture of the Tesseract OCR engine, demonstrating its adaptability to various languages [2]. A significant advance in this field occurred with the introduction of LSTM neural networks in the Tesseract 4.0 architecture, which replaced the earlier pattern-based recognizer with a sequence model.

Within the context of Turkic languages, researchers achieved remarkable results by creating dedicated datasets for the Turkish language and fine-tuning Tesseract models [3]. For the Uzbek language, a family of rule-based NLP tools has been developed, including lemmatization through finite-state machines [4], verb and predicate identification [5, 6], and punctuation restoration [7]. These works show that, in the absence of large annotated corpora, carefully engineered linguistic rules and transfer from a closely related language are effective strategies for low-resource Turkic processing. Comprehensive surveys of handwritten and printed OCR confirm that data quality and language-specific modeling are the dominant factors influencing recognition accuracy [8]. However, targeted studies on OCR for Turkmen texts remain relatively sparse, and the Transfer Learning approach proposed in this paper aims to fill this gap.

Tesseract OCR and the LSTM Recognition Model

Tesseract OCR is an advanced computer-vision system designed to analyze characters in images and convert them into digital formats. In its modern versions, the system employs LSTM neural networks, which analyze text line by line and account for the sequential context of characters — a property

that is essential for agglutinative languages whose word forms depend heavily on long affix chains [10]. The theoretical foundation of the recognition model can be expressed as a tuple:

$$M = \langle I, U, W, O \rangle \quad (1)$$

where the four components are defined as follows:

I (Input) — the training image–text pairs in Tesseract format (.tif, .gt.txt).

U (Unicharset) — the set of unique language characters, i.e. the Turkmen alphabet, comprising 129 characters.

W (Weights) — the neural-network weights inherited from the pre-trained Turkish model and updated during fine-tuning.

O (Output) — the fully trained model file (tuk.traineddata) produced at the end of training.

Methodology and Dataset Preparation

In the process of adapting the Tesseract OCR engine to a new language, dataset preparation is the most complex and critical stage, because the quality and consistency of the ground-truth data place an upper bound on the achievable accuracy. In our research, the training process encompassed the following methodological steps.

Gathering and Formatting Ground-Truth Data

To train the neural network, a total of 6078 ground-truth pairs were prepared. Each pair

consists of a high-quality image containing a single line of text (.jpg) and its perfectly matching text file (.txt). Following the stringent requirements of the Tesseract (tesstrain) framework [9], all of these files were standardized using an automated Python script and renamed according to a specific naming convention, such as tuk_00000.tif and tuk_00000.gt.txt. A snippet of the automation code is provided below in Listing 1.

Listing 1. Automated formatting of the ground-truth pairs.

```
def format_ground_truth(source_dir, dest_dir):
    files = os.listdir(source_dir)
    for i, file in enumerate(files):
        if file.endswith('.jpg'):
            base = file.replace('.jpg', '')
            shutil.copy(f"{source_dir}/{file}",
                        f"{dest_dir}/tuk_{i:05d}.tif")

shutil.copy(f"{source_dir}/{base}.txt",

f"{dest_dir}/tuk_{i:05d}.gt.txt")
```

Creating Language Rules and langdata

To enable the new model to recognize its unique alphabet, the text characters from all .gt.txt files were extracted. The comprehensive inclusion of the specific Turkmen characters Ä, Ö, Ü, Ý, Ň, and Ž was explicitly ensured, resulting in a

unicharset dictionary comprising 129 unique characters. Furthermore, based on the existing texts, the essential tuk.training_text and tuk.wordlist files were generated; the latter supplies the recognizer with a dictionary of valid Turkmen word forms, which improves word-level accuracy. Because Turkmen and Turkish share a large part of their phonology and orthography, the Turkish langdata served as a convenient and linguistically motivated starting point, reducing the amount of Turkmen-specific data required to reach competitive accuracy.

Data Splitting

To prevent the neural network from merely memorizing the training data (overfitting) and to verify its true real-world accuracy, the 6078 pairs were divided into three independent subsets, summarized in Table 1:

Train set — 85% (5166 lines). Used directly for adjusting the model's parameters during training.

Validation set — 10% (607 lines). Used to continuously monitor the model's learning progress and Character Error Rate (CER) during training.

Test set — 5% (305 lines). Isolated to independently evaluate the model's ability to recognize completely unseen text once training was fully completed.

Table 1. Partitioning of the 6078 ground-truth pairs.

Subset	Share	Lines	Purpose
Train	85%	5166	Parameter optimization
Validation	10%	607	Progress / CER monitoring
Test	5%	305	Final unseen-data evaluation

Training Process

Baseline Evaluation

Before initiating the training process, a baseline test was conducted to determine the error rate of the pre-existing model. In this step, the validation set (607 lines) was processed using the best available Turkish (tur) model. The resulting baseline CER was notably high, confirming the absolute necessity for specialized fine-tuning and providing a reference point against which the improvements of the new model are measured.

Training Parameters and Procedure

The training of the Tesseract LSTM neural networks was executed using the automated Makefile scripts provided by the tesstrain repository [9]. Utilizing the Transfer Learning method, the training commenced with the linguistic weights of the Turkish language (START_MODEL=tur) rather than from random initialization. This process was

initiated through the terminal using the command shown in Listing 2.

Listing 2. Launching Transfer-Learning training with tesstrain.

```
make training MODEL_NAME=tuk START_MODEL=tur \
    TESSDATA=../tessdata \
    MAX_ITERATIONS=5000 LEARNING_RATE=0.0001
```

The training was configured for MAX_ITERATIONS=5000. A learning rate of 0.0001 was selected to ensure smooth learning and to prevent catastrophic forgetting of the base-language features inherited from Turkish. The entire training process was accelerated using a cloud GPU (NVIDIA T4), ultimately generating the new tuk.traineddata model. The overall sequence of steps — from data collection to the final model — is summarized in the flowchart in Fig. 1.

Fig. 1. Flowchart of the Turkmen OCR model training process.

Results and Discussion

After the training process was completed, the results obtained using the validation (607 lines) and test (305 lines) sets were analyzed in detail. Table 2 presents a comparative analysis of the baseline (Turkish) model and the new (Turkmen) model across three standard metrics: overall accuracy, Character

Error Rate (CER), and Word Error Rate (WER).

Table 2. Comparison of the baseline and fine-tuned models.

Metric	Baseline (tur)	Trained (tuk)	Improvement
Accuracy	74.50%	97.80%	+23.30%
Character Error Rate (CER)	0.26	0.02	-0.23
Word Error Rate (WER)	0.42	0.05	-0.37

As is evident from the table, training via Transfer Learning raised the accuracy to 97.8% and drastically reduced both character- and word-level errors. The reduction of the CER from 0.26 to 0.02 indicates that the diacritic characters that the baseline model previously failed to recognize are now handled correctly in the overwhelming majority of cases. Table 3 shows the dynamics of the error (CER) reduction across the training iterations.

Table 3. CER dynamics across training iterations.

Iteration	Accuracy	CER	Status
0 (Baseline)	74.50%	0.26	Initial
1000	88.20%	0.12	Sharp increase
3000	95.40%	0.05	Stabilization
5000	97.80%	0.02	Converged

The learning curve exhibits the behavior typical of successful Transfer Learning: a sharp accuracy increase during the first thousand iterations, as the model adapts the inherited Turkish weights to the specific Turkmen characters, followed by a gradual stabilization and convergence near iteration 5000. The fact that convergence is reached without overfitting — confirmed by the close agreement between validation and test performance — demonstrates that the prepared dataset is both sufficiently large and sufficiently clean for the task. These results are consistent with prior findings for Turkish [3] and for rule-based and transfer-based approaches to Uzbek [4, 5, 6, 7], reinforcing the conclusion that closely related Turkic languages provide an effective transfer source for one another.

Conclusion

This study focused on developing a comprehensive algorithm and methodology for training and optimizing the Tesseract OCR engine for Turkic languages with unique linguistic features and specific characters, using the Turkmen language as a primary case study. The paper provided an in-depth examination of visual text analysis, the structural components of the recognition system, and the interaction of the training parameters, which together serve as foundational stages of natural-language processing.

Considering the agglutinative nature of the Turkmen language, its relatively free word order, and its morphological complexity, a clean ground-truth dataset comprising 6078 lines was prepared. By applying a Transfer Learning approach within the Tesseract architecture, the baseline Turkish model was fine-tuned. Consequently, the common inadequacies found in standard models — particularly the frequent misrecognition or complete omission of the diacritic characters Ä, Ö, Ü, Ý, Ň, and Ž — were successfully eliminated, and the model achieved an overall accuracy of 97.8%.

Furthermore, the application potential of the developed model in grammar checkers, machine translation, and various NLP systems was explored. This approach enables

automatic and precise textual analysis while faithfully preserving the unique linguistic features of the Turkmen language. The achieved accuracy indicates that the developed parsing and recognition algorithm effectively identifies the visual structure of texts and opens up new opportunities in Turkmen natural-language processing.

In summary, this paper not only proposes an effective framework for automated text recognition (OCR) in the Turkmen language but also serves as a robust foundation for further linguistics and NLP research within the broader context of Turkic languages. The newly established tuk.traineddata model can be deployed freely and with high confidence across software applications requiring high-fidelity text recognition, and the findings will be instrumental in advancing Turkmen machine translation, corpus linguistics, and automated archival digitization. Future work will focus on enlarging the dataset, adding page-level layout analysis, and extending the same Transfer-Learning pipeline to other under-resourced Turkic languages.

References

1. Sharipov, M., Avezmatov, I., Kuriyozov, E., Babayev, S.: Natural Language Processing for Uzbek and Turkmen: a systematic review of resources, methods, and benchmarks (2025).

2.Smith, R.: An overview of the Tesseract OCR engine. In: 9th International Conference on Document Analysis and Recognition (ICDAR), pp. 629–633. Curitiba, Brazil (2007).
3.Dönmez, İ., Adalı, E.: Recognition of Turkish texts with the Tesseract OCR engine. Süleyman Demirel University Journal of Natural Sciences 22(2), 552–558 (2018).
4.Sharipov, M., Avezmatov, I., Adinaev, H.: Development of a rule-based model and algorithm for predicate identification in Uzbek-language texts. In: 10th International Conference on Computer Science and Engineering (UBMK). IEEE (2025).
5.Ruzimboev, K.R., Avezmatov, I.D., Shermatov, B.I.: A Comparative Study of VGG-19 and a Custom CNN for Binary EEG-State Classification Using Composite Time-Frequency Imaging. In: International Conference on Computer Science and Engineering (UBMK), pp. 1513–1518 (2025).
6.Memon, J., Sami, M., Khan, R.A., Uddin, M.: Handwritten optical character recognition (OCR): a comprehensive systematic literature review (SLR). IEEE Access 8, 142642–142668 (2020).
7.Google Tesseract OCR: tesseract-ocr/tesstrain — training workflow for

Tesseract 5 as a Makefile for GNU Make. GitHub (2024).
8.Chomsky, N.: Three models for the description of language. IRE Transactions on Information Theory 2(3

https://doi.org./10.58225/mpmma.2026.528

THE TRANSFORMATION OPERATOR FOR THE PERTURBATED MATHIEU EQUATION

Malaka Mahmudova
Baku State University, Azerbaijan
AzUAC, Azerbaijan

Abstract. The perturbed Mathieu equation $-y''+(chx)y+q(x)y=\lambda y$ on the half-axis $0\le x<\infty$ is considered. By means of transformation operator an integral representation of the Jost - type solution is found. An estimate is obtained with respect to the kernel of the transformation operator. A connection is established between the kernel of the integral representation and the perturbation potential.

Keywords. Perturbed equation, Mathieu equation, Schrödinger equation, transformation operator, additional growing potential, Yost solution

A one-dimensional Schrödinger equation with an additional exponentially growing potential is of particular interest from a physical point of view (see [1]). One such equation is the perturbed Mathieu equation. Note that the Mathieu differential equation often arises in solving scientific and engineering problems (see [2], [3]).

Consider the following perturbed Mathieu equation

$$-y''+(chx)y+q(x)y=\lambda y,\ 0<x<\infty,\quad \lambda\in C$$
, (1)

where the real potential $q(x)$ satisfies the conditions

$$\int_0^\infty x^2 e^x |q(x)|dx<\infty.$$

(2)

It is known [5] that equation (1) with $q(x)=0$ has a special solution $f_0(x,\lambda)$, which can be represented as

$$f_0(x,\lambda)=\left(\sqrt{2}e^{\frac{x}{2}}\right)^{-1} e^{-\sqrt{2}e^{\frac{x}{2}}}\sum_{r=0}^{\infty}(-1)^r c_r\left(\sqrt{2}e^{\frac{x}{2}}\right)^{-r}$$

,

where

$$c_0=1, c_1=\frac{4\lambda+1^2}{8}, c_2=\frac{(4\lambda+1^2)(4\lambda+3^2)}{8^2 2!},$$

$$c_3=\frac{(4\lambda+1^2)(4\lambda+3^2)(4\lambda+5^2)}{8^3 3!}-\frac{4q^2}{3!},$$

$$c_4=\frac{(4\lambda+1^2)(4\lambda+3^2)(4\lambda+5^2)(4\lambda+7^2)}{8^4 4!}-\frac{2q^2}{4!}(4\lambda+13),\ldots$$

Moreover, for each x the solution $f_0(x,\lambda)$ is an entire function with respect to λ. Note that, by virtue of (3), (4), for each fixed λ the function $f_0(x,\lambda)$ belongs to the space

$L_2(0,+\infty)$. Of particular interest is the Jost-type solution of the perturbed equation (1), i.e., solution $f(x,\lambda)$ that satisfies the condition $f(x,\lambda) = f_0(x,\lambda)[1+o(1)], x \to \infty$.

In this work, using the transformation operator, we find an integral representation of the Jost-type solution to equation (1). The transformation operator with a condition at infinity is constructed in [4] for the one-dimensional Schrödinger equation with a rapidly decreasing potential.

Let

$$\sigma_0(x) = \int_x^\infty |q(t)|dt,\ \sigma_1(x) = \int_x^\infty \sigma_0(t)dt$$

.

The main result of the present paper is as follows.

Theorem If the potential $q(x)$ satisfies condition (2), then, for all values of λ , the equation (1) has solution $f(x,\lambda)$ representable as

$$f(x,\lambda) = f_0(x,\lambda) + \int_x^{+\infty} K(x,t)\ f_0(t,\lambda)dt$$

,

where the kernel $K(x,t)$ is a continuously differentiable function and satisfies the following conditions:

$$|K(x,t)| \le \frac{1}{2}\sigma_0\left(\frac{x+t}{2}\right)e^{\sigma_1(x)},$$

$$K(x,x) = \frac{1}{2}\int_x^{+\infty} q(t)dt.$$

References

1. A.D.Alhaydari , Exponential confining potential well, *Theoret. and Math. Phys.*, **206**:1 (2021), 84–96.
2. N.S.Grigoreva, Uniform asymptotic expansions of solutions of the Mathieu equation and the modified Mathieu equation, *Journal of Soviet Mathematics*, **11**:5(1979), 700-721.
3. C. Hunter and B. Guerrieri, The eigenvalues of ME and their branch points, *Studies in Appl. Math.*, vol. **64**(1981), 113-141.
4. B. M. Levitan, *Inverse Sturm–Liouville Problems. Translated from the Russian by O. Efimov*, VSP, Zeist, 1987
5. N.W. McLachlan, *Theory and application of Mathieu functions*, Oxford., 1947.

https://doi.org./10.58225/mpmma.2026.532

THE STUDY OF TRACE PROPERTIES OF FUNCTION $D^{\nu}\left(f(x)-\Phi_{\ell-1}(x)\right)$

Mehraly G. Aliyev[1]

[1] AzUAC, Azerbaijan

Abstract. In this abstract, author give integral representation of functions from Sobolev type spaces $\Lambda_{p_k,\theta_k}^{<m^k,N^k>}(G;\varphi^k)$. Next, with the help of integral representation of function $D^{\nu}\left(f(x)-\Phi_{\ell-1}(x)\right)$ author establish trace theorem for Sobolev type spaces $\Lambda_{p_k,\theta_k}^{<m^k,N^k>}(G;\varphi^k)$.

Keywords: Sobolev type spaces, trace of the functions, traces theorems, integral representations of functions, special type domains.

We define the following class of surfaces $\Gamma_s\ (1<s\le n-1)$. Let the surface $\Gamma_s \subset \overline{G} \subset E_s$ be defined by the following system of equations:

$$\left.\begin{array}{l} x_1 = x_1 \\ x_2 = x_2 \\ \ldots\ldots\ldots\ldots\ldots\ldots \\ x_s = x_s \\ x_{s+1} = g_{s+1}(x_1,\ldots,x_s) \\ \ldots\ldots\ldots\ldots\ldots\ldots \\ x_n = g_n(x_1,\ldots,x_s) \end{array}\right\}, \qquad (1)$$

where the functions $x_k = g_k(x_1,...,x_s)(k = s+1,...,n)$ are defined and continuous in some domain $G_s \subset E_s$. It is assumed that the partial derivatives

$$\frac{\partial}{\partial x_j} g_k(x_1,\ldots,x_s)\,(j = 1,\ldots,s)(k = s+1,\ldots,n)$$

are continuous and bounded in G_s. We denote by Π^1 the class of surfaces satisfying abovementioned condition and condition (1). Let $h = (0,...,0,h_{s+1},...,h_n)$, where $h_k > 0\,(k = s+1,...,n)$. By $\Gamma_s + h$ we denote a surface be defined by the following system of equations:

$$\left.\begin{array}{l} x_1 = x_1 \\ x_2 = x_2 \\ \ldots\ldots\ldots\ldots\ldots\ldots \\ x_s = x_s \\ x_{s+1} = g_{s+1}(x_1,\ldots,x_s) + h_{s+1} \\ \ldots\ldots\ldots\ldots\ldots\ldots \\ x_n = g_n(x_1,\ldots,x_s) + h_n \end{array}\right\}, \qquad (2)$$

where $x_k = g_k(x_1,\ldots, x_s)(k = s+1,\ldots, n)$ are the same functions as in equalities (1). In this case, the vector $h = (0,\ldots,0, h_{s+1},\ldots, h_n)$, $h_k > 0\ (k = s+1,\ldots, n)$ is chosen so that $\Gamma_s + h \subset G.$ Traces of functions $D^\nu(f(x) - \Phi_{\ell-1}(x))$ on the surface $\Gamma_s \subset \overline{G}$ in $L_q(\Gamma_s)(1 < q < \infty)$ are understood as the existence of a limit

$$\left\| D^\nu\left(f - \Phi_{\ell-1}\right)\Big|_{\Gamma_s} \right\|_{L_q(\Gamma_s)} = \lim_{|h|\to 0} \left\| D^\nu\left(f - \Phi_{\ell-1}\right)\Big|_{\Gamma_s} \right\|_{L_q(\Gamma_s + h)}.$$

Under natural assump-tions, after appropriate transformations, we have

$$\left\| D^\nu\left(f - \Phi_{\ell-1}\right)\Big|_{\Gamma_s} \right\|_{L_q(\Gamma_s + h)} \le$$

$$C \left\| D^\nu\left(f - \Phi_{\ell-1}\right)(\ldots; g_{s+1}(\cdot) + h_{s+1},\ldots, g_n(\cdot) + h_n) \right\|_{L_q(G_s)}.$$

Therefore, by evalua-ting the integral

expression on the right-hand side of the last inequality, we get the opportunity to evaluate the integral expression $\left\| D^{\nu}\left(f-\Phi_{\ell-1}\right)\right|_{\Gamma_s+h}\Big\|_{L_q(\Gamma_s+h)}$ for $|h|=\sum_{j=s+1}^{n} h_j \to 0.$ We observe that

$$\left\| D^{\nu}\left(f-\Phi_{\ell-1}\right)(...;g_{s+1}(\cdot)+h_{s+1},...,g_n(\cdot)+h_n)\right\|_{L_q(G_s)} \le$$

$$\le C\sum_{i=1}^{M}\left\| D^{\nu}\left(f-\Phi_{\ell-1}\right)(...;g_{s+1}(\cdot)+h_{s+1},...,g_n(\cdot)+h_n)\right\|_{L_q(\Omega_{s,i})}.$$

Here $\Gamma_s \subset \overline{G}$ and subdomains $\Omega_i \subset G\ (i=1,...,M)$ satisfy "$a(1)$"-horn condition and cover $G \subset E_n$, that is $G \subset \bigcup_{i=1}^{M}\Omega_i$ and $\Gamma_{s,i} \overset{def}{=} \Gamma_s \bigcap \Omega_i\ (i=1,\ldots,M).$ These parts of Γ_s aredefined on the corresponding region $\Omega_{s,i}(i=1,...,M).$ Thus, $G_s \subset \bigcup_{i=1}^{M}\Omega_{s,i}.$ From these considerations and

the above-mentioned inequalities it follows that it is

necessary to estimate the following integral operators:

$$\left\| D^{\nu}\left(f-\Phi_{\ell-1}\right)(\ldots;g_{s+1}(\cdot)+h_{s+1},\ldots,g_n(\cdot)+h_n)\right\|_{L_q(\Omega_{s,i})}$$

for all $i=1,\ldots,M.$ The following integral representation of functions holds:

$$D^{\nu+m}\left(f(x)-\Phi_{\ell-1}(x)\right)=$$

$$=\sum_{k=1}^{n}(-1)^{|\nu-m+m^k|}c_k\int_0^1 w_k(\vartheta)\frac{da_k(\vartheta)}{a_k(\vartheta)}\int_{E_{|E_{N^k}|}}dz\int_{E_n}\left\{\Delta^{N^k}\left(\frac{z}{N^k}\right)D^{m^k}f(x+y)\right\}M_{\delta,k}dy.$$

Here $E_{N^k}=\operatorname{supp}N^k$ is the supports of the corresponding vectors $N^k=\left(N_1^k,\ldots,N_n^k\right)(k=1,\ldots,n)$ and

$$w_k(\vartheta)=\prod_{j\in E_{N^k}}(a_k(\vartheta))^{-1}\times\ \times\prod_{j=1}^{n}(a_k(\vartheta))^{m_j^k-\nu_j-m_j-1}.$$

We observe that $\Phi_{\ell-1}(x)=\Phi_{\ell-1}(x;\ f(x))$ is a polynomial of degree no greater than s_k-1 for each variable $x_k\ (k=1,\ldots,n).$ Moreover, $s_k=N_k^k+m_k^k\ (k=1,\ldots,n).$ In the integral representation, the kernels

$$M_{\delta,k} = M_{\delta,k}\left(\frac{y}{a(\vartheta)};\frac{z}{a(\vartheta)}\right)(k=1,\ldots,n)$$ are sufficiently smooth, compactly supported functions. Under these assumptions we have the following Theorem.

Theorem 1. Let $f \in \bigcap_{k=1}^{n} \Lambda_{p_k,\theta_k}^{<m^k,N^k>}(G;\varphi^k)$ and let the following conditions holds: 1) $1 \le p_k \le \theta_k < \infty, q \ge p_k\,(k=1,\ldots,n);$ 2) an integer non-negative vectors $m^k = (m_1^k,\ldots,m_n^k),\ N^k = (N_1^k,\ldots,N_n^k)$ such that $k \in \operatorname{supp}\{m^k + N^k\}\ \ (k=1,\ldots,n)$; 3) let $G \in c(\bar{a}(\vartheta);1),$ moreover $\bar{a}(\vartheta) = (a_1(\vartheta),\ldots,a_n(\vartheta)),\ \ (0<\vartheta\le 1)$, where $a_k = a_k(\vartheta) > 0,$ and $a_k(\vartheta) \to 0$ at $\vartheta \to 0+;$ $a_k'(\vartheta) > 0,\ k=1,\ldots,n;$ 4) the components of vector-function $\varphi^k(t) = (\varphi_1^k(t_1),\ldots,\varphi_n^k(t_n))$ are positive and continuous and $\varphi_j^k(t_j) \to 0$ $(t_j \to 0)$ for all $j,k=1,\ldots,n.$ Let the components of an integer non-negative

vector $\nu=(\nu_1,...,\nu_n)$ satisfy the conditions $\nu_k<N_k^k+m_k^k,\ \nu_j\geq N_j^k+m_j^k\ \ (j\neq k)$. Then there exists a polynomial $\Phi_{\ell-1}(x;\ f)$ of degree no greater than s_k-1 in each variable $x_k\ \ (k=1,...,n)$ such that $D^{\nu}\left(f-\Phi_{\ell-1}\right)\Big|_{\Gamma_s}\in L_q(\Gamma_s)$ and the following inequality holds:

$$\left\|D^{\nu}\left(f-\Phi_{\ell-1}\right)\Big|_{\Gamma_s}\right\|_{L_q(\Gamma_s)}\leq C\sum_{k=1}^{n}Q_{k,s}(1)\,\|f\|_{\Lambda_{p_k,\theta_k}^{<m^k,N^k>}(G;\,\varphi^k)}.$$

Here $s-1=(s_1-1,...,s_n-1),\ \ s_k=m_k^k+N_k^k$, $C>0$ is a constant independent of f, and

$$Q_{k,s}(1)=\int_0^1\prod_{a_j=1}a_j(\vartheta)^{m_j^k-\nu_j-\frac{1}{p_k}}\prod_{j=1}^{s}\left(a_j(\vartheta)\right)^{\frac{1}{q}}\prod_{j\in E_{N^k}}\varphi_j^k\left(a_j(\vartheta)\right)\frac{da_k(\vartheta)}{a_k(\vartheta)}.$$

References

1.F.G. Maksudov, A.D. Jabrailov. *Method of Integral Representations in the Theory of Function Spaces*. Elm, Baku, 2000.

2. A.D. Jabrailov. *Theory of Spaces of Differentiable Functions*. Elm, Baku, 2005

https://doi.org./10.58225/mpmma.2026.539

COMMUTATORS OF PARABOLIC FRACTIONAL MAXIMAL OPERATORS ON PARABOLIC TOTAL MORREY-GULIYEV SPACES

Mehriban N. Omarova[1,2]

[1] Baku State University, Azerbaijan

[2] Institute of Mathematics, Azerbaijan

Abstract. The main goal is to provide necessary and sufficient conditions for the boundedness of parabolic fractional maximal commutators $M_{b,\alpha}^{P}$ and commutators of the parabolic fractional maximal operator $[b, M_{\alpha}^{P}]$ in parabolic total Morrey-Guliyev spaces $L_{p,\lambda,\mu}^{P}(\mathbb{R}^n)$ with symbols b belonging to parabolic Lipschitz spaces $\dot{\Lambda}_{\beta,P}(\mathbb{R}^n)$, as a result of which some new characterizations of parabolic Lipschitz spaces $\dot{\Lambda}_{\beta,P}(\mathbb{R}^n)$ and non-negative parabolic Lipschitz function spaces are obtained.

Keywords: parabolic total Morrey-Guliyev spaces, parabolic fractional maximal function, commutator, parabolic Lipschitz spaces.

1.Introduction

Morrey spaces, introduced by C. B. Morrey [5], play important roles in the regularity theory of PDE, including heat equations and Navier-Stokes equations. In [2] Guliyev introduce a variant of Morrey spaces called

total Morrey-Guliyev spaces $L_{p,\lambda,\mu}(\mathbb{R}^n)$, $0 < p < \infty$, $\lambda, \mu \in \mathbb{R}$. In [1] the authors was consider the parabolic total Morrey-Guliyev spaces $L^P_{p,\lambda,\mu}(\mathbb{R}^n)$, give basic properties of the spaces $L^P_{p,\lambda,\mu}(\mathbb{R}^n)$ and study some embeddings into the parabolic total Morrey-Guliyev space $L^P_{p,\lambda,\mu}(\mathbb{R}^n)$, see also [4,6].

Let $\mathbb{R}^n$ be the n-dimension Euclidean space with the norm $|x|$ for each $x \in \mathbb{R}^n$. For $x \in \mathbb{R}^n$ and $r > 0$, we denote by $B(x, r)$ the open ball centered at x of radius r.

Let P be a real $n \times n$ matrix, all of whose eigenvalues have positive real part. Let $A_t = t^P$ $(t > 0)$, and set $\gamma = trP$. Then, there exists a quasi-distance ρ associated with P such that

(a) $\rho(A_t x) = t\rho(x)$, $t > 0$, for every $x \in \mathbb{R}^n$;

(b) $\rho(0) = 0$, $\rho(x - y) = \rho(y - x) \geq 0$ and $\rho(x - y) \leq k\big(\rho(x - z) + \rho(y - z)\big)$;

(c) $dx = \rho^{\gamma-1} d\sigma(w) d\rho$, where $\rho = \rho(x), w = A_{\rho^{-1}} x$ and $d\sigma(w)$ is a measure on the ellipsoid $\{w: \rho(w) = 1\}$.

The balls with respect to ρ, centered at x ofradius r, are just the ellipsoids $\mathcal{E}(x, r) = \{y \in \mathbb{R}^n: \rho(x - y) < r\}$ with the Lebesgue measure $|\mathcal{E}(x, r)| = v_\rho r^\gamma$, where v_ρ is the volume of the unit ellipsoid in $\mathbb{R}^n$. If $P = I$, then clearly $\rho(x) = |x|$ and $\mathcal{E}(x, r) = B(x, r)$.

Let $\alpha \in [0,\gamma)$ and $f : \mathbb{R}^n \to \mathbb{R}$ be a locally integrable function, the parabolic fractional maximal function $M_\alpha^P f$ is given by

$$M_\alpha^P f(x) = \sup_{\mathcal{E}\ni x} |\mathcal{E}|^{-1+\frac{\alpha}{\gamma}} \int_{\mathcal{E}} |f(y)| dy.$$

Given any $\alpha \in [0,\gamma)$ and $b \in L_1^{loc}(\mathbb{R}^n)$, the parabolic fractional maximal commutator $M_{b,\alpha}^P$ is defined by

$$M_{b,\alpha}^P f(x) = \sup_{\mathcal{E}\ni x} |\mathcal{E}|^{-1+\frac{\alpha}{\gamma}} \int_{\mathcal{E}} |b(x) - b(y)||f(y)| dy,$$

where the supremum is taken over all parabolic s $\mathcal{E} \subset \mathbb{R}^n$ containing x. If $P = I$, then $M_\alpha \equiv M_\alpha^I$ is the fractional maximal operator and $M \equiv M^I$ is the Hardy-Littlewood maximal operator.

The nonlinear commutators generated by the parabolic fractional maximal operator M_α^P and the locally integrable function b are defined by the formula

$$[b, M_\alpha^P]f = b\, M_\alpha^P f - M_\alpha^P(bf).$$

For a given ellipsoid $\mathcal{E}$, we define the following local fractional maximal function:

$$M_{\mathcal{E},\alpha}^P f(x) := \sup_{\mathcal{E}\supseteq\mathcal{E}'\ni x} |\mathcal{E}'|^{-1+\frac{\alpha}{\gamma}} \int_{\mathcal{E}'} |f(y)|\, dy,$$

where the supremum is taken over all ellipsoid $\mathcal{E}'$ such that $x \in \mathcal{E}' \subseteq \mathcal{E}$.

At first, we give the definition of the parabolic Lipschitz spaces on $\mathbb{R}^n$.

Definition 2.1 Let $0 < \beta < 1$, we say a function b belongs to the parabolic Lipschitz space $\dot{\Lambda}_{\beta,P}(\mathbb{R}^n)$ if there exists a constant C such that for all $x, y \in \mathbb{R}^n$,

$$|b(x) - b(y)| \leq C\rho(x - y)^{\beta}.$$

The smallest such constant C is called the $\dot{\Lambda}_{\beta,P}(\mathbb{R}^n)$ norm of b and is denoted by $\|b\|_{\dot{\Lambda}_{\beta,P}(\mathbb{R}^n)}$.

Definition 2.2 Let $0 < p < \infty$, $\lambda \in \mathbb{R}$, $\mu \in \mathbb{R}$, $[t]_1 = \min\{1, t\}$, $t > 0$. We denote by $L^P_{p,\lambda,\mu}(\mathbb{R}^n)$ the parabolic total Morrey-Guliyev space [1,6] the set of all classes of locally integrable functions f with the finite quasi-norm

$$\|f\|_{L^P_{p,\lambda,\mu}} = \sup_{x\in\mathbb{R}^n,\, t>0} [t]_1^{-\frac{\lambda}{p}} [1/t]_1^{\frac{\mu}{p}} \|f\|_{L_p(\mathcal{E}(x,t))}.$$

We denote by $WL^P_{p,\lambda,\mu}(\mathbb{R}^n)$ the weak parabolic total Morrey-Guliyev space [1,6] the set of all classes of locally integrable functions f with the finite quasi-norm

$$\|f\|_{WL^P_{p,\lambda,\mu}} = \sup_{x\in\mathbb{R}^n,\, t>0} [t]_1^{-\frac{\lambda}{p}} [1/t]_1^{\frac{\mu}{p}} \|f\|_{WL_p(\mathcal{E}(x,t))}.$$

Let us note that if $\lambda = \mu$, then $L^P_{p,\lambda}(\mathbb{R}^n) = L^P_{p,\lambda,\lambda}(\mathbb{R}^n)$ is the parabolic Morrey space, $WL^P_{p,\lambda}(\mathbb{R}^n) = WL^P_{p,\lambda,\lambda}(\mathbb{R}^n)$ is the weak parabolic Morrey space and if $\mu = 0$, then $\widetilde{L^P_{p,\lambda}}(\mathbb{R}^n) = L^P_{p,\lambda,0}(\mathbb{R}^n)$ is the parabolic modified Morrey space, $\widetilde{WL^P_{p,\lambda}}(\mathbb{R}^n) = WL^P_{p,\lambda,0}(\mathbb{R}^n)$ is the weak parabolic modified Morrey space, see [4].

Our main results may be formulated as follows.

Theorem 2.1 [6] Let $0 < \beta < 1$, $0 \le \alpha < \alpha + \beta < \gamma$ and $b \in L^{loc}_1(\mathbb{R}^n)$. Let also $0 \le \mu \le \lambda < \gamma$, $1 < p < \frac{\gamma-\lambda}{\beta}$ and $\frac{\beta}{\gamma-\mu} \le \frac{1}{p} - \frac{1}{q} \le \frac{\beta}{\gamma-\lambda}$. Then, the following statements are equivalent:

(i) $b \in \dot{\Lambda}_{\beta,P}(\mathbb{R}^n)$.

(ii) The operator $M^P_{b,\alpha}$ is bounded from $L^P_{p,\lambda,\mu}(\mathbb{R}^n)$ to $L^P_{q,\lambda,\mu}(\mathbb{R}^n)$.

Applying Theorem 2.1, we obtain the following result.

Theorem 2.2 [6] Let $0 < \beta < 1$, $0 \le \alpha < \alpha + \beta < \gamma$ and $b \in L^{loc}_1(\mathbb{R}^n)$. Let also $0 \le \mu \le \lambda < \gamma$, $1 < p < \frac{\gamma-\lambda}{\alpha+\beta}$ and $\frac{\alpha+\beta}{\gamma-\mu} \le \frac{1}{p} - \frac{1}{q} \le \frac{\alpha+\beta}{\gamma-\lambda}$. Then, the following statements are equivalent:

(i) $b \in \dot{\Lambda}_{\beta,P}(\mathbb{R}^n)$ and $b \ge 0$.

(ii) The operator $[b, M^P_\alpha]$ is bounded from $L^P_{p,\lambda,\mu}(\mathbb{R}^n)$ to $L^P_{q,\lambda,\mu}(\mathbb{R}^n)$.

(iii) There exists a constant $C > 0$ such that

$$\sup_{\mathcal{E}} |\mathcal{E}|^{-\frac{\alpha+\beta}{\gamma}} \frac{\left\| \left(b - M^{P}_{\mathcal{E},\alpha}(b) \right) \chi_{\mathcal{E}} \right\|_{L^{P}_{q,\lambda,\mu}}}{\|\chi_{\mathcal{E}}\|_{L^{P}_{q,\lambda,\mu}}} \leq C. \quad (1)$$

Remark 2.1. Note that in the case of the $P = I \equiv \mathrm{diag}\{1, \dots, 1\}$ the Theorems 2.1 and 2.2 was proved in [3].

References

1. Celik, S., Akbulut, A., Omarova, M.N.: Characterizations of anisotropic Lipschitz functions via the commutators of anisotropic maximal function in total anisotropic Morrey spaces. Trans. Natl. Acad. Sci. Azerb. Ser. Phys.-Tech. Math. Sci. Mathematics 45(1), 25–37 (2025).
2. Guliyev, V.S.: Maximal commutator and commutator of maximal function on total Morrey spaces. J. Math. Inequal. 16(4), 1509–1524 (2022).
3. Guliyev, V.S.: Characterizations of Lipschitz functions via the commutators of maximal function in total Morrey spaces. Math. Meth. Appl. Sci. 47(11), 8669–8682 (2024).
4. Guliyev, V.S., Rahimova, K.R.: Parabolic fractional integral operator in parabolic modified Morrey spaces. Proc. A. Razmadze Math. Inst. 163, 59–80 (2013).
5. Morrey, C.B.: On the solutions of quasi-linear elliptic partial differential equations.

Trans. Amer. Math. Soc. 43, 126–166 (1938).
6. Omarova, M.N.: Commutators of parabolic fractional maximal operators on parabolic total Morrey spaces. Math. Meth. Appl. Sci. 48(11), 11037–11044 (202

https://doi.org./10.58225/mpmma.2026.546

MULTISCALE MATHEMATICAL MODELING OF THE USE OF BIOFILMS IN WASTEWATER TREATMENT

Seynura Hasanova[1] , Messoud Efendiyev[1,2]
[1]AzUAC, Azerbaijan
[2]Marmara University, Helmhotz Center Munich

Abstract. Effective management of organic and inorganic pollutants in wastewater remains a critical challenge in modern environmental engineering. Biofilm-based systems have emerged as a highly efficient and resilient biological treatment technology, though the intricate physical, chemical, and biological mechanisms governing their dynamic behavior are difficult to fully evaluate through experimental means alone. This paper investigates the mathematical modeling of biofilm systems utilized in wastewater treatment, with a specific focus on integrated spatial photocatalytic-biofilm systems. By utilizing partial differential equations, the model quantitatively describes substrate diffusion, pollutant concentration, biomass density, and Darcy velocity within a three-dimensional computational domain. The integration of photocatalysis with biofilm dynamics demonstrates how complex, recalcitrant compounds—such as those found in oil-field produced water—are

sequentially broken down into biodegradable intermediates and mineralized..

Keywords: Biofilm Modeling, Wastewater Treatment, Partial Differential Equations, Photocatalysis, Biomass Dynamics, Environmental Engineering.

1. Introduction

Effective treatment of organic and inorganic pollutants in industrial and domestic wastewater is one of the main problems of modern environmental engineering. As a result of population growth, accelerated industrialization and increasing demand for water resources, environmentally safe treatment of wastewater has become even more relevant. In recent years, biofilm-based systems have attracted special attention among biological treatment technologies due to their high cleaning efficiency, low energy consumption and resistance to various pollutants.

The effective functioning of biofilm systems is determined by the interaction of numerous physical, chemical and biological processes occurring within them. Processes such as diffusion of substrates, proliferation of microorganisms, spatial distribution of biomass, consumption of nutrients and formation of metabolic products shape the dynamic behavior of the system. Since the complete study of these complex mechanisms by experimental methods is difficult both in terms of time and finances, mathematical modeling acts as an important research tool.

Mathematical models allow for the quantitative description of the processes occurring within the biofilm, the assessment of the influence of various parameters on the system and the optimization of treatment devices. In particular, models based on partial differential equations can more realistically express the change in the density of microorganisms, the transport of substrates and the spatial development of biomass. Such models are widely used to determine the formation, thickness changes and long-term steady states of biofilms.

The main objective of this research work is to investigate mathematical models of biofilm systems used in wastewater treatment, describe the main processes occurring in biofilm through differential equations, and study the application possibilities of these models in assessing the cleaning efficiency. At the same time, the factors affecting the dynamics of biofilm development and the significance of the modeling results from the point of view of environmental engineering will be analyzed.

2. Methodology

Mathematical Modeling Biofilms play a crucial role in the mathematical modeling of photocatalytic degradation of organic pollutants, particularly in the treatment of complex industrial effluents like oil-field produced water. The extracellular polymeric substances (EPS) within the biofilm matrix act

as natural sorbents, concentrating hydrocarbon pollutants and other organic contaminants from the aqueous phase. This increases the local concentration of contaminants, thereby enhancing the likelihood of degradation. Photocatalysis first breaks down complex, recalcitrant compounds (e.g., heavy hydrocarbons, phenols) in produced water into smaller, readily biodegradable intermediates.

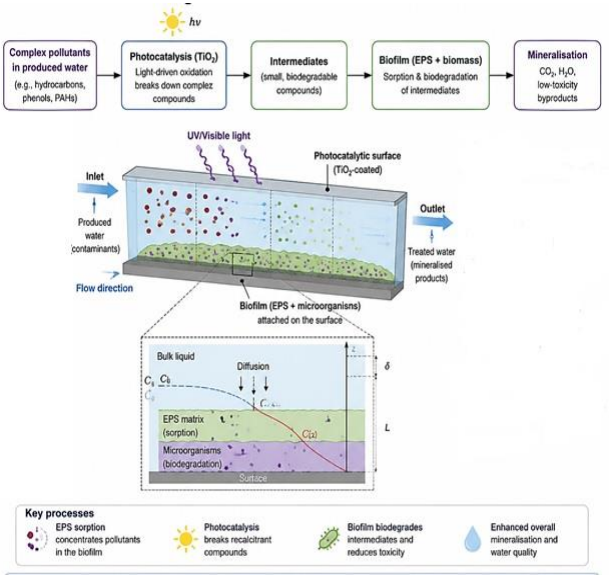


Fig. 1. Integrated Spatial Photocatalytic-Biofilm Systems

$$V = \frac{1}{\mu\rho} A(M) \cdot [F - \nabla P], \; t > 0, \quad x \in \Omega \tag{1}$$

$$\nabla V = 0, \quad t > 0, \quad x \in \Omega \tag{2}$$

$$\partial_t C = \nabla(D_C \nabla C) - V\nabla C + \frac{K_1 CM}{K_2 + C}, \; t > 0, \quad x \in \Omega \tag{3}$$

$$\partial_t M = \nabla\left(\frac{M^a}{(M_{max} - M)^b} \nabla M\right) - K_4 M + \frac{K_3 CM}{K_2 + M}, \quad t > 0, \quad x \in \Omega \tag{4}$$

V=V(t,x): Darcy velocity vector
P=P(t,x): Pressure
C=C(t,x): Concentration of pollutant
M=M(t,x): Biomass density
t≥0: time, x∈Ω: space
□⊂□3: computational domain
Equation (1)-(4) augmental by suitable initial conditions as well as boundary conditions

Conclusion

In this study, a mathematical modeling approach was evaluated to analyze the dynamic behavior and purification efficiency of biofilm systems in wastewater treatment. The integration of partial differential equations allows for a realistic quantitative description of biomass growth, substrate transport, and fluid dynamics within a spatial computational domain. The analysis

underscores the synergy between photocatalytic degradation and biofilm metabolism, particularly for treating complex industrial effluents like oil-field produced water. By decoupling the mechanical and biochemical processes—ranging from extracellular polymeric substances (EPS) sorption to multi-phase mineralization—the model successfully captures the core factors influencing steady-state biofilm thickness and contaminant degradation rates. Ultimately, these mathematical insights offer environmental engineers a predictive tool to optimize bioreactor performance, reduce operational costs, and improve effluent water quality without relying solely on time-consuming empirical trials.

References

1. Author, Messoud Efendiev. Springer book. 265 pp. (2013).
2. Author, S.Hasanova., Mathematical Modeling for Environmental Health Protection . China–Canada–Hungary Joint Workshop on Mathematics of Complexity in Public Health (2026).
3. Author, D., Author, S., Author, L.: A simple and effective method coupling coagulation and UV/TiO_2 photocatalysis for treating real-produced wastewater from oil processing. Chemical Papers (2024).

4.Author, S.: Analysıs of gases produced from photolysıs of heterogeneous phase formed waters under the ınfluence of ultra vıolet radıatıon. Scientific Works Journal. №2 (2024).
5.Author, S.: Compared the efficiency of TiO2 and N-Doped TiO2 to degrade BTEX. Journal, Advanced Physical Research. №3 (2021).

https://doi.org./10.58225/mpmma.2026.553

ON THE BASICITY OF THE WEIGHT SYSTEM EXPONENT WITH EXCEPTION IN BANACH FUNCTIONAL SPACES

Migdad Ismailov[1], Chinara Hasanova[2], Zahira Mammedova[3]

[1]Azerbaijan State Oil and Industry University, Azerbaijan

[2]Ganja State University, Azerbaijan

[3]Landau Secondary School, Azerbaijan

Abstract. In this work, we study the criterion of completeness and minimality of a weighted system of exponentials with an arbitrary element removed in subspaces of Banach functional spaces of functions continuous with respect to a shift. It is shown that in this space the exponent weight system with a remote arbitrary element does not form a Schauder basis.

Keywords: completeness, minimality, Schauder basis, weighted system of exponentials, Banach functional spaces

1. Introduction

For applications in mechanics and mathematical physics, the basic properties of exponential weight systems are of particular interest. The basic properties of the system $\left\{|t|^{\alpha} e^{\text{int}}\right\}_{n\in Z}$ in space $L_2(-\pi,\pi)$ were studied in [1]. In [2] these results were studied for a

general weight function. Note that an equivalent condition for the basicity of a weight system of exponentials in spaces $L_p(-\pi,\pi)$, $p>1$, is that the weight function belongs to the Muckenhoupt class. Along with this, it is of interest to study the defect properties of exponential weight systems. In [3], the completeness and minimality of the system $\left\{t|^{\alpha} e^{\text{int}}\right\}_{n\in Z, n\neq n_0}$, $n_0 \in Z$, were studied, and it was also proved that this system does not form a Schauder basis in the space $L_2(-\pi,\pi)$, and in [4] this issue was studied for a weighted exponential system $\left\{\omega(t)e^{\text{int}}\right\}_{n\in Z, n\neq n_0}$, $n_0 \in Z$, with a general weight function. The indicated question in $L_p(-\pi,\pi)$, $p>1$, spaces for a power weight was studied in [5], and for a weight function of general form in [6] and in grand Lebesgue spaces $L_{p)}(-\pi,\pi)$, $p>1$, in [7]. In the proposed paper, this issue is studied in Banach function spaces of functions.

Defectiveness of the exponent weighing system

Please Let $(M,\Re,\mu)$ be a measurable space with σ-finite measure μ, $F(M)$ be the set of μ-measurable functions $f: M \to R \cup \{\pm\infty\} = \overline{R}$,

$F^{+}(M) = \{f \in F(M): f \geq 0\}$,

$\rho : F^+(M) \to \overline{R}_+$ be a functional norm, $X = X(M)$ be a Banach functional space generated by ρ, i.e. a Banach space equipped with the norm $\|f\|_X = \rho(|f|)$, $X' = X'(M)$ be the associated space to X, and X_a be a subspace of functions with an absolutely continuous norm.

Denote by $X^S(-\pi,\pi)$ the subspace of the space $X(-\pi,\pi)$, consisting of functions $f \in X(-\pi,\pi)$ satisfying the condition $\|T_\delta f(\cdot) - f(\cdot)\|_X \to 0$, $\delta \to 0$, where T_δ is the shift operator, i.e. $T_\delta f(t) = f(t+\delta)$, here $f(t) = 0$, $t \notin [-\pi,\pi]$.

The following statements hold.

Theorem 1. Let $1 \in X_a$, $\omega \in X^S(-\pi,\pi)$ and let $n_0 \in Z$ be any integer. The system $\{\omega(t)e^{\text{int}}\}_{n \in Z \setminus \{n_0\}}$ is complete and minimal in $X^S(-\pi,\pi)$ if and only if $\frac{1}{\omega(t)} \notin \left(X^S(-\pi,\pi)\right)'$ and besides

1) there is a (unique) point $t_0 \in (-\pi,\pi)$ such that $\frac{t-t_0}{\omega(t)} \in \left(X^S(-\pi,\pi)\right)'$;

or

2) $\frac{(t+\pi)(t-\pi)}{\omega(t)} \in \left(X^S(-\pi,\pi)\right)'$.

Theorem 2. Let $1 \in X_a$, $\omega \in X^S(-\pi,\pi)$ and let $n_0 \in Z$ be any integer. The system $\{\omega(t)e^{\text{int}}\}_{n\in Z\setminus\{n_0\}}$ is not a Schauder basis $X^S(-\pi,\pi)$.

Conclusion

Thus, in the paper, a criterion for the completeness and minimality of the system of exponentials $\{\omega(t)e^{\text{int}}\}_{n\in Z, n\neq n_0}$, $n_0 \in Z$, is established in the subspace X^S of the Banach function space X generated by the shift operator. It is also shown that this system does not form a Schauder basis in X^S.

Acknowledgment

This work was supported by the Azerbaijan Science Foundation – Grant No. AEF-MGC-2025-1(54)-20/03/1-M-03.

References

1. Babenko, K.I.: On conjugate functions. Reports of the Academy of Sciences of the USSR, 62(2), 157–160 (1948). (*in Russian*)
2. Gaposhkin, V.F.: “One generalization of the M. Riesz theorem on conjugate functions”. Mat. Sbornik, 46:88(3), 359–372 (1958). (*in Russian*)

3.Golubeva, E.S.: The system of weighted exponentials with power weights. Vestnik Sam. GU, Estestvenno-Nauchnaya Seriya, 2(83), 15–25 (2011). (Russian).
4. Yoon, G.J., Heil, C.: Duals of Weighted Exponential Systems. Acta Appl Math 119, 97-112 (2012).
5. Bilalov, B.T. and Mamedova, Z.V.: "On the frame properties of some degenerate trigonometric systems". Dokl. Nats. Akad. Nauk Azerb., 68(5), 14-18 (2012). (Russian)
6. Shukurov, A. Sh.: On basis properties of weighted exponential systems with excess. Vestnik Samarskogo Universiteta. Estestvenno-Nauchnaya Seriya, 24(1), 14-19 (2018).
7. Ismailov, M.I. and Acar, K.S.: On Banach frameness of degenerate weighted exponential system. Fixed Point Theory, Algorithms, Sci Eng, 1-15 (2025).

https://doi.org./10.58225/mpmma.2026.*558*

LUMP, BREATHER, AND CHAOTIC DYNAMICS OF THE VARIABLE-COEFFICIENT EXTENDED BLMP EQUATION

Muhammad Abubakar Isah[1], brahim Isah[2], Ahmad Muhammad[3]

[1] Istanbul Ticaret University, Türkiye,

[2] College of Arts and Sciences, Qatar University , Qatar.

Abstract. In this work, we investigate the extended Boiti-Leon-Manna-Pempinelli (eBLMP) equation with time-dependent coefficients from two complementary perspectives: integrable soliton solutions and chaotic dynamics. First, starting from the (3+1)-dimensional variable-coefficient BLMP equation, we perform a dimensional reduction to obtain a (2+1)-dimensional extended model. We extend the analysis by allowing the dispersion coefficient $\alpha(t)$ and nonlinearity coefficient $\beta(t)$ to be functions of time. We demonstrate that bilinearization imposes a proportionality condition $\frac{\alpha(t)}{\beta(t)}$ is constant. Under this condition, we construct lump solutions, lump-soliton interaction solutions, and breather solutions using Hirota's bilinear method. Second, through a traveling wave reduction, we obtain a planar dynamical system. Under periodic perturbation, this system exhibits deterministic chaos, characterized by phase

portraits, Poincar\'e maps, a positive Lyapunov exponent $\lambda \approx 0.12$, and sensitivity to initial conditions. The influence of time-dependent coefficients on wave dynamics is analyzed, revealing novel propagation properties. All solutions are presented in explicit form with graphical representations. A critical assessment of the limitations and physical interpretation of the proportionality condition is provided.
Keywords*:* Extended BLMP equation; Variable coefficients; Hirota bilinear method · Lump solutions; Breather solutions; Chaotic dynamics; Lyapunov exponent; Poincaré map

https://doi.org./10.58225/mpmma.2026.*560*

FINITE-PRECISION ANALYSIS OF CHAOTIC MAP-BASED PSEUDORANDOM NUMBER GENERATORS

Muhammed Milani[1]

[1]Bandırma Onyedi Eylul University, Türkiye

Abstract. Due to their nonlinear nature and dependence on initial conditions, chaotic maps have been widely used as part of pseudorandom number generators (PRNGs). However, in digital computers, the complete mathematical representation of continuous chaotic systems is compromised by the limited accuracy of the calculations. In this paper, the effects of limiting numerical accuracy are investigated on three well-known one-dimensional chaotic maps: the logistic map, the tent map, and the piecewise linear chaotic map (PWLCM). Fixed-point digital representations of 8, 12, 16, and 20 bits of accuracy are used. For each generator, a comprehensive search of the seed space is performed and metrics such as transient length, cycle length, maximum observed period, and weak seed ratio are obtained. The destructive potential of their unintentional unpredictability is investigated by comparing two strategies for extracting output bits: threshold-based bit extraction and least significant bit (LSB) extraction. The generated bit sequences are analyzed using

Shannon entropy, autocorrelation, and other statistical tests from NIST SP 800-22. The results of this study show that in practice, the performance of chaotic PRNGs depends not only on the inherent chaos function, but also significantly on the finite-precision format, the initial seed, and the bit extraction mechanism used.

Keywords: Chaotic Maps, Pseudorandom Number Generator, Finite Precision, Logistic Map, Tent Map, PWLCM, Cycle Analysis, Statistical Randomness

1. Introduction

Pseudo-random number generators (PRNGs) play a fundamental role in simulation, cryptography, embedded systems, and stochastic computation. Chaotic dynamical systems are considered excellent candidates for PRNG design due to their sensitivity to initial conditions, topological mixing, and dense periodic circuit properties [1]. Chaotic mappings such as the logistic mapping, the tent mapping, and the piecewise linear chaotic mapping (PWLCM) are theoretically expected to have these properties when the computations are performed exactly on real numbers [2]. However, any digital realization must, of course, partition the state space into a finite set of discrete values. Due to finite-precision arithmetic, the infinite state space of a continuous chaotic system reduces to a finite automaton, and according to the pigeonhole principle, a deterministic finite-

state machine must sooner or later enter a periodic cycle [3]. The duration and distribution of these cycles, and the proportion of seeds that cause very short cycles that can be a threat, are key parameters for measuring the quality of chaotic PRNGs with limited accuracy. Cristea et al. investigated chaotic binary sequences generated through bit-extraction procedures and emphasized that fixed- and floating-point representations can significantly affect the statistical properties of chaotic generators [4]. Li and his colleagues studied the distribution of periods of discrete chaotic maps and showed that the number of discrete cycles increases at a sublinear rate with the size of the state space for many standard maps [5]. This study fills this gap by providing a single, reproducible analysis platform that measures the structural features as well as the statistical quality of three chaotic maps at four different levels of accuracy. Also, this paper also compares two different two-bit extraction methods.

2. Methodology

Three sets of experiments are performed. Experiment A performs comprehensive cycle detection on all seeds for $b \in \{8, 12, 16\}$ and a 10% random sample for $b = 20$. Experiment B evaluates statistical randomness. Experiment C measures the computational power (Mbps) for all generators under identical conditions using

Python with NumPy and time.perf_counter(). The 16-bit cycle length statistics in Table 1 shows that the logistic map provides the highest proportion of weak seeds, a result that is in good agreement with previous studies that showed a near-fixed point collapse to unstable fixed points [3, 5]. The tent map suffers from significant degeneracy: at 8-bit precision, the median cycle length is less than 5% of the state space size; this is due to the bit-shifting nature of the binary fixed-point representation. PWLCM achieves the fairest cycle distribution and has a lower proportion of weak seeds [2].

Table 1. Cycle-length statistics at b = 16 (all seeds enumerated)

Map	Mean Cycle	Median Cycle	Max Cycle	Weak-Seed (%)
Logistic	18,432	12,104	61,247	14.3
Tent	9,817	4,216	55,890	31.7
PWLCM	27,614	23,501	65,002	6.8

Statistical randomness results using threshold extraction are displayed in Table 2; the PWLCM provided entropy values nearest to the theoretical maximum of one bit of entropy per output bit (1.0) and provided the lowest magnitude of autocorrelation; all three chaotic maps passed > 80% of NIST tests

with threshold and failed much lower from results when performing LSB extractions, especially the Tent map (62%). Thus, extraction method is not a trivial implementation detail but rather an important design parameter [6].

Table 2. Statistical quality at b = 20, threshold extraction (30 seeds, 10^6 bits each)

Map	Shannon Entropy	Autocorr. (lag-1)	NIST Pass Rate (%)
Logistic	0.9971	−0.0031	85.7
Tent	0.9904	−0.0087	81.0
PWLCM	0.9988	−0.0011	90.5

Conclusion

This study presents a systematic and repeatable evaluation scheme for finite-precision chaotic PRNGs, which includes cycle length analysis, vulnerability detection, statistical random testing, and throughput measurements. The main result is that finite-precision computation imposes qualitative constraints that cannot be revealed by regular statistical test suites. Among the different schemes analyzed, PWLCM offers the best trade-off between cycle length distribution,

statistical quality, and computational efficiency. In terms of computational cost, the tent scheme is the cheapest option. However, at the same time, it is a scheme that quickly undergoes digital degeneracy with low accuracy.

References

1. Devaney, R. (2018). *An introduction to chaotic dynamical systems*. CRC press.
2. Li, S., Chen, G., & Mou, X. (2005). On the dynamical degradation of digital piecewise linear chaotic maps. *International journal of Bifurcation and Chaos*, *15*(10), 3119-3151.
3. Persohn, K. J., & Povinelli, R. J. (2012). Analyzing logistic map pseudorandom number generators for periodicity induced by finite precision floating-point representation. *Chaos, Solitons & Fractals*, *45*(3), 238-245.
4. Cristea, B. (2008). Statistical properties of chaotic binary sequences. *arXiv preprint arXiv:0805.4405*.
5. Li, C., Feng, B., Li, S., Kurths, J., & Chen, G. (2019). Dynamic analysis of digital chaotic maps via state-mapping networks. *IEEE Transactions on Circuits and Systems I: Regular Papers*, *66*(6), 2322-2335.

6. Rukhin, A., Soto, J., Nechvatal, J., Smid, M., & Barker, E. (2001). *A statistical test suite for random and pseudorandom number generators for cryptographic applications* (No. NISTSP80002).

https://doi.org./10.58225/mpmma.2026.*567*

NONLINEAR ANALYSIS OF CRACK RESISTANCE IN RC SECTIONS

Mukhlis Hajiyev[1] *, Yuriy Vynnykov*[2]
Shirazi Ismayilov[1] *, Tetiana Galinska*[2] *,*
Nazim Polukhov[1]
[1]AzUAC, Azerbaijan.
[2]National University «Yuri Kondratyuk Poltava Polytechnic», Ukraine

Abstract. This paper presents an analytical method for evaluating the crack resistance of rectangular reinforced concrete (RC) sections using a nonlinear deformation model. Concrete behavior in both tension and compression is described by tri-linear stress–strain diagrams, allowing consistent consideration of elastic and inelastic stages up to crack initiation. Based on the plane-sections hypothesis, three deformation cases are defined depending on the stress state in the compression zone. For each case, equilibrium conditions lead to quadratic equations for determining the neutral axis depth, from which closed-form expressions for the cracking moment are derived. Parametric studies show that reinforcement ratio and concrete strength influence the cracking moment in a nonlinear manner. The proposed approach provides a unified, transparent, and efficient tool for analyzing and designing RC members at the serviceability limit state.

Keywords: reinforced concrete; crack resistance; cracking moment; nonlinear deformation model; tri-linear stress–strain diagram

1. Introduction

The prediction of crack initiation in reinforced concrete (RC) members is essential for ensuring serviceability, durability, and structural reliability. However, conventional linear approaches often fail to accurately represent the nonlinear behavior of concrete in both tension and compression near the cracking stage. To address this limitation, this study develops a deformation-based analytical approach using tri-linear stress–strain diagrams for concrete. The model allows a consistent description of material behavior up to crack formation and considers multiple deformation cases within the compression zone. The proposed method provides a unified framework for determining the cracking moment of rectangular RC sections through equilibrium and strain compatibility conditions, improving the accuracy of crack resistance assessment in structural design.

2. Tri-Linear Stress–Strain Models for Concrete in Compression and Tension

In this section, the constitutive behavior of concrete in compression and tension is described using tri-linear (three-segment) stress–strain diagrams, which are suitable for analytical integration within the deformation (strain-based) framework. The conceptual

form of these diagrams is illustrated in Figure 1. The tri-linear representation enables a consistent characterization of concrete behavior across elastic and inelastic stages. In compression, the diagram captures the transition from initial elastic response to nonlinear hardening and ultimate deformation. In tension, it reflects the progression from elastic behavior to microcracking and eventual crack initiation.

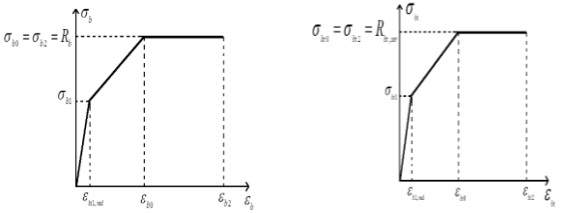


Fig. 1. Tri-linear stress–strain diagrams for concrete (compression, tension)

2. Elastic Behavior of Concrete in the Compression Zone

Traditional approaches distinguish between elastic and nonlinear behavior of concrete in the compression zone. However, such simplifications do not fully represent the actual deformation behavior within a nonlinear framework. In the proposed approach, the compression zone is described using a full tri-linear stress–strain diagram, allowing deformation along any of its segments. At the cracking stage, the tension zone is assumed to fully mobilize all segments of the tri-linear diagram, ensuring a consistent and realistic representation of material behavior. Deformation of

compressible reinforced bars is expressed as the ultimate deformation of concrete under tension $\varepsilon'_s = \frac{x - a'_s}{h - x} \cdot \varepsilon_{bt2}$ (1) based on the hypothesis of flat sections. Then the value of the normal stress arising in this reinforced bars $\sigma'_s = E_s \cdot \varepsilon'_s = \frac{x - a'_s}{h - x} \cdot E_s \cdot \varepsilon_{bt2}$ (2), the normal force generated by these stresses $N'_s = A'_s \cdot \sigma'_s = \frac{x - a'_s}{h - x} \cdot A'_s \cdot E_s \cdot \varepsilon_{bt2}$ (3), and finally the moment of this force relative to the center of gravity of the concrete section will be determined as follows:

$$M'_s = A'_s \cdot \sigma'_s \cdot \left(\frac{h}{2} - a'_s\right) = \frac{x - a'_s}{h - x} \cdot A'_s \cdot \left(\frac{h}{2} - a'_s\right) \cdot E_s \cdot \varepsilon_{bt2}$$

(4)

In this case, deformations develop along the first and second branches of the tri-linear stress–strain diagram, reflecting the initiation of nonlinear behavior in the compression zone. Only the parameters of the compressed concrete are affected, while all other sectional properties remain unchanged. Therefore, the analysis focuses on determining the modified characteristics of the compression zone.

For the case where only the first and second branches of the tri-linear compression diagram are activated, the following condition defines the cracking stage:

$$M_{crc} = M_{b1} + M_{b2} + M_s + M'_s + M_{bt1} + M_{bt2} + M_{bt3}$$
(5)

Conclusion

Analytical expressions for the cracking moment of reinforced concrete sections were developed using tri-linear stress–strain diagrams. The method reduces the determination of the compression zone depth to solving a quadratic equation, providing a unified approach.Results show that the compression zone remains mostly near-elastic at cracking. The cracking resistance depends nonlinearly on reinforcement ratio and concrete strength, highlighting the need for deformation-based models.

References

1. Kolmogorov, A. G., & Plevkov, V. S. (2011). Calculation of reinforced concrete structures according to Russian and foreign standards. Moscow: ASV Publishing House.
2. Gadzhieva, U. M. (2021). Calculation of compression reinforced concrete elements of circular cross-section using a nonlinear deformation model. The Expert: Theory and Practice, (5), 13–20.
3. Sanzharovsky, R. S., & Veselov, A. A. (2001). Theory of calculation of building structures for stability and modern standards. St. Petersburg–Moscow: ASV.
4. Beglov, A. D., & Sanzharovsky, R. S. (2006). Theory of calculation of reinforced concrete structures for strength and stability:

Modern standards and European standards. St. Petersburg–Moscow: ASV.
5. Trekin, N. N., & Kodysh, E. N. (2016). Calculation of the formation of normal cracks based on the deformation model. Industrial and Civil Engineering, (7), 74–78.
6. Karpenko, N. I., & Radaykin, O. V. (2012). Towards improving concrete deformation diagrams to determine the cracking moment and ultimate moment in bent reinforced concrete elements. Construction and Reconstruction, 3(41), 10–15.
7. Veselov, A. A., Hegai, A. O., Hegai, M. O., & Nikolaeva, S. P. (2016). Calculation of reinforced concrete elements for crack formation. Bulletin of Civil Engineers, 3(56), 52–55.
8. Kodysh, E. N., Nikitin, I. K., & Trekin, N. N. (2010). Calculation of reinforced concrete structures made of heavy concrete in terms of strength, crack resistance and deformation. Moscow: Association of Construction Universities Publishing House.
9. SP 63.13330.2018. (2018). Concrete and reinforced concrete structures: Main provisions. Moscow: A.O. SRC Construction, NIIZHB named after A. A. Gvozdev.
10. Hajiyev, M. A., Aeinehchi, S., Bashirzade, S. R., Asadov, E. Z., & Khalilov, H. A. (2024). Structural performance of compressive zone strengthened RC elements.

Scientific and Technical Journal on Engineering Mechanics, 8(2), 56–72.

https://doi.org./10.58225/mpmma.2026.574

COMPUTATIONAL COMPLEXITY OF MACHINE LEARNING ALGORITHMS: A MATHEMATICAL PERSPECTIVE

Murad İsmayılov
Baku State University, Azerbaijan

Abstract. This paper presents a mathematical analysis of the computational complexity of fundamental machine learning algorithms. We examine time and space complexity of linear regression, support vector machines, decision trees, and neural networks, using asymptotic notation as the primary analytical tool. The empirical risk minimization framework and gradient-based optimization are discussed as unifying mathematical foundations. The study demonstrates that algorithm selection must be guided not only by predictive accuracy but also by complexity constraints imposed by the scale of the data. Our analysis draws on established theoretical frameworks and recent empirical comparisons to provide practical guidelines for algorithm deployment in data-intensive settings.

Keywords: computational complexity, machine learning, empirical risk minimization, gradient descent, algorithm analysis.

1 Introduction

Machine learning has become a central discipline within mathematical computer science, offering powerful tools for data analysis and pattern recognition. However, the practical utility of any learning method is inseparable from its computational cost. As the volume of data processed by modern systems continues to grow, a rigorous understanding of how algorithm performance scales with input size becomes increasingly critical.

Computational complexity theory provides the mathematical language for characterizing algorithm efficiency. Time complexity describes how the number of elementary operations grows as a function of input parameters, while space complexity captures memory requirements. These measures are expressed using asymptotic (Big-O) notation, which abstracts away hardware-specific constants and focuses on dominant growth rates [1].

A unifying mathematical framework for supervised learning is Empirical Risk Minimization (ERM). Given a training set of n samples, a hypothesis class, and a loss function l, the goal is to find the parameter vector w that minimizes the empirical risk:

$$L(w) = (1/n) \cdot \sum_{i=1}^{n} l(x_i, y_i)$$

The computational cost of minimizing this objective depends fundamentally on the structure of f and l, and on the optimization

algorithm chosen. Despite the extensive literature on individual algorithms, systematic cross-algorithm comparisons within a unified framework remain underrepresented. The present work addresses this gap through a structured synthesis of existing theoretical results, from which we derive concrete guidelines for complexity-aware algorithm selection.

2 Complexity of Core Algorithms

2.1 Linear Regression

Linear regression is one of the most computationally efficient supervised learning methods. The closed-form ordinary least squares solution requires matrix operations whose cost is polynomial in both n and d. For large datasets, iterative methods such as gradient descent reduce per-iteration cost to O(nd), making them the preferred approach in practice. At each step t, the parameter update takes the form:

$$w_{t+1} = w_t - \eta \cdot \nabla L(w_t)$$

where $\eta > 0$ is the learning rate and $\nabla L(w_t)$ is the gradient of the loss at the current iterate. Convergence to a stationary point is guaranteed under standard smoothness and convexity assumptions [2].

2.2 Support Vector Machines

Support vector machines (SVMs) solve a quadratic programming problem whose standard formulation has worst-case training complexity between $O(n^2)$ and $O(n^3)$, depending on the solver. The prediction phase depends only on the number of support

vectors s and is efficient. The use of kernel functions enables non-linear classification but introduces additional costs tied to kernel evaluations [3].

2.3 Decision Trees

Decision tree induction algorithms such as CART and ID3 build models by recursively partitioning the feature space. The training complexity per split is O(nd), and the total training cost scales as O(nd log n) for balanced trees. Constructing globally optimal decision trees is NP-hard, so practical algorithms rely on greedy heuristics, which sacrifice optimality in exchange for tractability [4].

2.4 Neural Networks

Neural network training via backpropagation has per-epoch complexity that scales linearly with n and with the total number of trainable parameters p. Deep architectures substantially increase p, amplifying both representational power and computational burden. Stochastic gradient descent and its variants address this by processing mini-batches, decoupling iteration cost from dataset size [1, 2].

3 Comparative Analysis and Discussion

The algorithms examined exhibit markedly different complexity profiles. Linear regression offers the most favorable scaling and is well-suited to large, high-dimensional datasets. SVMs provide strong generalization guarantees but are constrained to moderate-scale problems by their cubic training complexity. Decision trees scale efficiently

and are interpretable, though their greedy construction introduces approximation error [4].

A comparative empirical study by Singh (2023) confirmed that theoretical complexity bounds translate to observed runtime behavior across benchmark datasets [3]. The study found that linear models consistently outperformed non-linear methods in wall-clock training time, while neural networks achieved superior predictive accuracy at the cost of substantially higher resource consumption.

These findings underscore the importance of complexity-aware algorithm selection. In deployment scenarios with strict latency or memory constraints, simpler models with favorable complexity bounds may be preferable even if they sacrifice some predictive accuracy. Conversely, for tasks where prediction quality is paramount and computational resources are sufficient, the higher complexity of deep models may be justified.

4 Conclusions

This paper has presented a systematic complexity analysis of four fundamental machine learning algorithms within the empirical risk minimization framework. Our principal contribution is the organization of known complexity bounds into a unified comparative structure, which reveals that no single algorithm dominates across all dimensions. The analysis shows that the choice of method must be guided by the joint

requirements of statistical accuracy and computational feasibility. We further observe that the transition from quadratic to linear complexity — achievable through iterative solvers and mini-batch methods — is the single most impactful factor in scaling learning systems. Future work will extend this analysis to ensemble methods and large-scale neural architectures.

References

1. Shalev-Shwartz, S., Ben-David, S.: Understanding Machine Learning: From Theory to Algorithms. Cambridge University Press, Cambridge (2014).
2. Bottou, L., Curtis, F.E., Nocedal, J.: Optimization Methods for Large-Scale Machine Learning. SIAM Review 60(2), 223–311 (2018).
3. Singh, J.: Computational Complexity and Analysis of Supervised Machine Learning Algorithms. In: Kumar, R., Pattnaik, P.K., Tavares, J.M.R.S. (eds.) Next Generation of Internet of Things. LNNS, vol. 445, pp. 161–171. Springer, Singapore (2023).
4. Breiman, L., Friedman, J., Stone, C.J., Olshen, R.A.: Classification and Regression Trees. Chapman and Hall/CRC, New York (1984).
5. Khalid, S., Khalil, T., Nasreen, S.: A Survey of Feature Selection and Feature Extraction Techniques in Machine Learning.

In: Proc. SAI Intelligent Systems Conference, pp. 372–378. IEEE, London (2014).

https://doi.org./10.58225/mpmma.2026.581

MODELING THE IMPACT OF TOURISM DEMAND ON AIRLINE PROFITABILITY BASED ON PROBABILITY THEORY AND STATISTICAL APPROACHES

Murad Manafli
Vistula University, Poland.

Abstract: The tourism sector plays a significant role in the development of the global aviation industry by directly influencing passenger demand and airline profitability. This study examines the impact of tourism demand on airline financial performance using probability theory and statistical approaches. The research focuses on identifying the relationship between tourism flow, passenger traffic, ticket sales, and airline revenue indicators through mathematical and statistical modeling methods.

The study applies descriptive statistics, regression analysis, and probability-based forecasting techniques to evaluate fluctuations in tourism demand and their effects on airline profitability. Seasonal changes, economic conditions, and travel behavior are considered as key variables affecting airline income. Statistical data related to tourism growth and air transportation are analyzed to determine

patterns and predict future trends in the aviation market.

The results demonstrate that increasing tourism demand positively affects airline profitability by improving passenger load factors and revenue generation. Furthermore, the application of mathematical and statistical models provides more accurate forecasting and supports strategic decision-making in airline management. The research contributes to applied mathematics and transportation economics by presenting a practical analytical framework for evaluating the financial effects of tourism demand on the aviation industry.

Keywords: Tourism Demand, Airline Profitability, Statistical Modeling

1. Introduction and Theoretical Foundations

Tourism demand is a key factor affecting airline profitability through passenger flows and ticket sales. In Azerbaijan, tourism growth and the post-pandemic recovery since 2022 have increased the importance of air transportation and airline revenues (World Tourism Organization, 2023).

Airlines adjust pricing, capacity, and route planning according to tourism demand and seasonal changes (Button, 2017). Therefore, tourism demand directly influences airline financial performance.

This study examines the relationship between tourism demand and airline profitability using

regression analysis and statistical forecasting methods. Recent research shows that predictive models improve airline efficiency and revenue management (Zhang & Zhang, 2020).

2. Technological Approaches and Aviation Experience

The integration of statistical and probabilistic methods into air transport demand forecasting represents a structural change in modern revenue management systems rather than a purely technical improvement (Button, 2017). This process consists of three main stages:

- Data integration: collection of tourism and passenger data from reservation systems, airports, and statistical databases
- Demand optimization: application of regression models and machine learning techniques for forecasting and pricing optimization
- Revenue adaptation: adjustment of strategic decisions based on seasonal variations and demand fluctuations

These approaches increase load factors, improve revenue efficiency, and reduce operational risks (Zhang & Zhang, 2020). In Azerbaijan, companies such as Azerbaijan Airlines (AZAL) apply these methods through digital systems and forecasting tools. The growing tourism inflow further emphasizes the importance of statistical modeling in aviation management (World Tourism Organization, 2023).

Table 1. Passenger Demand Dynamics in Azerbaijan's Aviation Sector (2019–2024)

Year	Passenger Demand (thousand passengers)	Demand Index (x)
2019	1,250	1.00
2020	780	0.62
2021	1,020	0.82
2022	1,480	1.18
2023	1,950	1.56
2024	2,400	1.92

Source: State Statistical Committee (SSC) aviation data and airport traffic reports (2019–2024).

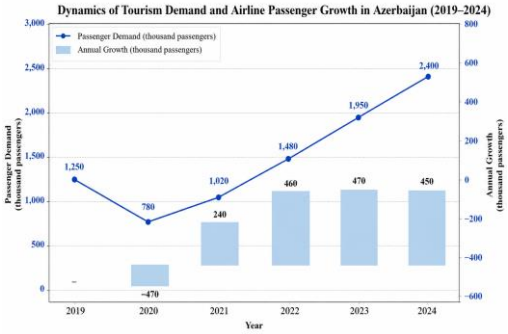


Fig 1. Dynamics of Changes in Tourism Demand and Airline Passenger Growth in Azerbaijan (2019–2024)

Figure 1 shows a strong increase in passenger demand after the pandemic, rising from 780 thousand in 2020 to 2,400 thousand in 2024.

This reflects tourism recovery, improved connectivity, and higher airline capacity utilization.

Conclusion:

The study shows that tourism demand has a direct positive impact on airline passenger growth and profitability in Azerbaijan. The results highlight the importance of statistical forecasting and data-driven decision-making in improving airline efficiency under changing demand conditions.

References

1. Button, K.: Aviation economics and forecasting demand. Transport Policy and Economics 58, 12–25 (2017).
2. State Statistical Committee of the Republic of Azerbaijan: Aviation and passenger transport statistics 2019–2024. Baku: SSC Official Publications (2024).
3. Turkish Airlines: Annual report and operational performance review. Retrieved from https://www.turkishairlines.com (2023).
4. World Tourism Organization (UNWTO): International tourism highlights 2023 edition. Madrid: UNWTO (2023). https://www.unwto.org
5. Zhang, Y., Zhang, A.: Demand forecasting and revenue management in airline industry. Journal of Air Transport Management 85, 101–112 (2020).

https://doi.org./10.58225/mpmma.2026.586

APPROXIMATE SYMBOLIC SOLUTION OF SYSTEMS OF INTEGRO-DIFFERENTIAL EQUATIONS WITH NON-SEPARABLE KERNELS AND NON-LOCAL BOUNDARY CONDITIONS

Nigar Aslanova[1], *Ioannis Parasidis*[2], *Efthimios Providas* [2]

[1] AzUAC, Azerbaijan

[2] University of Thessaly, Greece

Abstract. An approximate symbolic method is proposed for solving systems of ordinary linear Fredholm-type integro-differential equations with non-separable kernels and nonlocal boundary conditions. All non-separable kernels are approximated by truncated power series and the given system is degenerated into the one with separable kernels for which the direct computation method for non-local boundary value problems is applied. The technique can be easily implemented on a computer algebra system using the built-in integration and inverse matrix functions.

Keywords: Integro-differential equations, Non-separable kernels, Non-local boundary conditions.

1.Introduction

We consider the following system of integro-differential equations with generally non-separable

kernels and subject to general multi-point and integral conditions:

$$y'(x) - A(x)y(x) - \int_a^b K(x,s)y(s)ds = f(x), \quad x \in [a,b], \tag{14}$$

$$\sum_{k=1}^{\ell} B_k\, y(x_k) + \int_a^b C(s)y(s)ds = d, \tag{15}$$

where $a, b \in \mathbb{R}$, $y(x)$ is a vector of n unknown functions $y_i(x) \in C^1[a,b]$, $i = 1, \dots, n$, $y'(x) = \frac{dy}{dx}$, $A(x)$ and $C(x)$ are $n \times n$ matrices of given functions $a_{ij}(x)$ and $c_{ij}(x) \in C[a,b]$, $i = 1, \dots, n, j = 1, \dots, n$, respectively, $K(x,s)$ is a $n \times n$ matrix of given kernel functions $K_{ij}(x,s) \in C[a,b] \times [a,b]$, $i = 1, \dots, n, j = 1, \dots, n$, $f(x)$ is a vector of n given forcing functions $f_i(x) \in C[a,b]$, $i = 1, \dots, n$, $B_k, k = 1, \dots, \ell$, are $n \times n$ constant matrices, d is a n-vector of contants, and $a \le x_1 < x_2 < \cdots < x_\ell \le b$ are fixed boundary points.

We consider the case where each non-separable kernel $K_{ij}(x,s)$ is analytic with respect to x and can be expanded into a power series around a point x_0 as follows

$$K_{ij}(x,s) = \sum_{l=0}^{\infty} h_{ij}^{l}(s)(x - x_0)^l, \tag{16}$$

where the functions $h_{ij}^{l}(s) \in C[a,b]$. Truncating the series (3) by taking only the first m terms and substituting them into (1), we obtain the degenerate system

$$\tilde{y}'(x) - A(x)\tilde{y}(x) - \sum_{l=0}^{m-1} G_l(x) \int_a^b H_l(s)\tilde{y}(s)ds = f(x), \quad x \in [a,b], \tag{17}$$

$$\sum_{k=1}^{\ell} B_k \tilde{y}(x_k) + \int_a^b C(s)\tilde{y}(s)ds = d, \tag{18}$$

where $\tilde{y}(x) \in C_n^1[a,b]$ and the $n \times n$ matrices

$$G_l(x) = \begin{bmatrix} (x-x_0)^l & & 0 \\ & \ddots & \\ 0 & & (x-x_0)^l \end{bmatrix},$$

$$H_l(s) = \begin{pmatrix} h_1^l(s) \\ \vdots \\ h_n^l(s) \end{pmatrix} = \begin{bmatrix} h_{11}^l(s) & \cdots & h_{1n}^l(s) \\ \vdots & & \vdots \\ h_{n1}^l(s) & \cdots & h_{nn}^l(s) \end{bmatrix},$$

where the row vectors $h_i^l(s) = (h_{i1}^l(s) \quad \cdots \quad h_{in}^l(s)), i = 1, \dots, n.$

This system can be solved by the direct computation method for non-local boundary value problems. To do this, we first write the system in an operator form.

2. Formulation of the problem

Define the $n \times nm$ matrix G and the $nm \times 1$ vector of integral functionals η as

$$G(x) = [G_0(x) \quad \cdots \quad G_{m-1}(x)], \quad \eta(\tilde{y}) = \begin{pmatrix} \eta_1(\tilde{y}) \\ \vdots \\ \eta_{nm}(\tilde{y}) \end{pmatrix} = \begin{pmatrix} \int_a^b h_1^0(s)\tilde{y}(s)ds \\ \vdots \\ \int_a^b h_n^0(s)\tilde{y}(s)ds \\ \vdots \\ \int_a^b h_1^{m-1}(s)\tilde{y}(s)ds \\ \vdots \\ \int_a^b h_n^{m-1}(s)\tilde{y}(s)ds \end{pmatrix},$$

and the $n \times 1$ vector of boundary functionals as

$$\theta(\tilde{y}) = \begin{pmatrix} \theta_1(\tilde{y}) \\ \vdots \\ \theta_n(\tilde{y}) \end{pmatrix} = \sum_{k=1}^{\ell} B_k \tilde{y}(x_k) + \int_a^b C(s)\tilde{y}(s)ds.$$

Write the system (4), (5) in the matrix form

$$\tilde{y}'(x) - A(x)\tilde{y}(x) - G(x)\eta(\tilde{y}) = f(x), \quad x \in [a,b], \tag{19}$$

$$\theta(\tilde{y}) = d.$$

Furthermore, define the differential operator $\mathcal{A}: C_n[a,b] \to C_n[a,b]$ as

$$\mathcal{A}y = y' - A(x)y, \quad \mathfrak{D}(\mathcal{A}) = \{y \in C_n^1[a,b]\},$$

and the integro-differential operator $\mathcal{B}: C_n[a,b] \to C_n[a,b]$ as

$$\mathcal{B}\tilde{y} = \mathcal{A}\tilde{y} - G(x)\eta(\tilde{y}), \quad \mathfrak{D}(\mathcal{B}) = \{\tilde{y} \in C_n^1[a,b]: \theta(\tilde{y}) = d\}.$$

Write the system (6), (7) in the operator form

$$\mathcal{B}\tilde{y} = f(x), \quad x \in [a,b].$$

3. Existence and construction of the unique solution

Lemma 1. *Let $Z(x)$ be a fundamental matrix of the homogeneous equation $\mathcal{A}y = 0$ and $\hat{\theta}$ be* a *n-vector boundary functional with $\hat{\theta}(Z) = I_n$. Then:*
(i) The restriction $\hat{\mathcal{A}}$ of operator $\mathcal{A}$ on

$$\mathfrak{D}(\hat{\mathcal{A}}) = \{y \in \mathfrak{D}(\mathcal{A}): \hat{\theta}(y) = 0\}$$

is correct and the unique solution of the nonhomogeneous equation $\hat{\mathcal{A}}y = f$ *for any* $f \in C_n[a,b]$ *is given by*

$$y = \hat{\mathcal{A}}^{-1}f = Z(x)\int_{x_0}^{x} Z^{-1}(s)f(s)ds - Z(x)\hat{\theta}\left(Z(x)\int_{x_0}^{x} Z^{-1}(s)f(s)ds\right),$$

where x_0 *is a fixed point in* $[a,b]$.

(ii) In the case that $\hat{\theta}(y) = y(x_0)$,

$$y = \hat{\mathcal{A}}^{-1}f = Z(x)\int_{x_0}^{x} Z^{-1}(s)f(s)ds.$$

The existence, uniqueness and the solution of system (8) are given by the following theorem.

Theorem 1. *Under the assumptions of Lemma 1, the following propositions are true.*

(i) The operator $\mathcal{B}$ *is injective if and only if*

$$detW = det\begin{bmatrix} \theta(Z) & \theta(\hat{\mathcal{A}}^{-1}G) \\ -\eta(Z) & I_m - \eta(\hat{\mathcal{A}}^{-1}G) \end{bmatrix} \neq 0, \quad (22)$$

where W *is a square matrix of order* nm.

(ii) Under (9), the unique solution of the nonhomogeneous problem (8) for any $f \in C_n[a,b]$ *is given by*

$$\tilde{y} = \hat{\mathcal{A}}^{-1}f - [Z(x) \quad \hat{\mathcal{A}}^{-1}G(x)]W^{-1}\begin{pmatrix} \theta(\hat{\mathcal{A}}^{-1}f) - d \\ -\eta(\hat{\mathcal{A}}^{-1}f) \end{pmatrix}.$$

https://doi.org./10.58225/mpmma.2026.591

RESEARCH ON FORCED VIBRATIONS OF A VISCOELASTIC BEAM WITH CLAMPED ENDS

Kurbanov Nabi, Babajanova Vusala, Agamalieva Kamala, Abdullaeva Konul
Sumgayit State University, Azerbaijan

Abstract. This paper investigates the initial-boundary value problem for the integro-differential equation governing the forced vibrations of a viscoelastic beam with clamped ends. This fourth-order linear integro-differential equation of Volterra type with a convolution kernel describes the flexural transverse vibrations of a homogeneous viscoelastic beam under the action of an external force, in the absence of rotational motion during bending.

Using the method of separation of variables and Laplace integral transforms, the problem is solved for arbitrary hereditary functions. The solution to the problem is constructed as a series expansion based on a system of eigenfunctions of a one-dimensional spectral problem, which constitutes an orthogonal and complete function system.

The solution is initially determined in the absence of an external force and under homogeneous boundary conditions, followed by the analysis of the general case involving an external force. In both cases, the solution is constructed as a converging series, where

the first term coincides with the solution obtained by the well-known averaging method, while the subsequent terms provide corrections to these solutions.

The solution is analyzed under specific external influences. It is found that if the forces acting on the system are small, the amplitudes of the true vibrations remain finite at resonance, and the amplitude of the free vibrations decays exponentially over time.

Keywords: clamped beam, forced vibrations, initial and boundary conditions, spectral problem, viscoelasticity, kernel, hereditary function, rheology, analytical solution, convolution of functions

Introduction

Many problems regarding the vibrations of rods, beams, and plates are of great importance in structural mechanics and reduce to solving higher-order Volterra integro-differential equations with a convolution-type kernel. Therefore, methods for solving integro-differential equations are of interest in various fields of science and engineering, such as acoustics, mathematical physics, and the mechanics of deformable bodies.

Consequently, methods for solving these equations are of interest in fields such as acoustics, mathematical physics, and the mechanics of a deformable solid.

Unfortunately, constructing an exact solution for this class of problems involves several difficulties due to non-linear expressions and integrals containing unknown hereditary functions [1, p.12], [2, p.557; 3, p.157]. Therefore, studying the vibrations of a beam with hereditary properties remains an insufficiently explored and highly relevant problem at present.

Problem Formulation

Let us assume that a beam with rheological properties of length ℓ is clamped at both ends by massive vises. We consider the problem of the vibrations of this beam under the influence of an external random load.

This problem reduces to solving a fourth-order Volterra integro-differential equation with a convolution-type kernel, which describes the vibrations of the beam in the following form:

$$EJ\frac{\partial^4 w(x,t)}{\partial x^4} - EJ\int_0^t \Gamma(t-\tau)\frac{\partial^4 w(x,\tau)}{\partial x^4}d\tau + \rho F\frac{\partial^2 w(x,t)}{\partial t^2} = F(x,t) \qquad (1)$$

where $w(x,t)$ - is the transverse displacement, ρ - is the material density of the beam, F - is the cross-sectional area of the beam (assumed to be constant), $F(x,t)$ - is the transverse load, J - is the moment of inertia of the beam's cross-section relative to the neutral axis perpendicular to the plane of vibration, $\Gamma(t)$ – is the relaxation kernel.

The initial conditions are taken in the following form:

$w(x,0) = u_0, \qquad \partial w(x,0) = v_0,$
(2)
where u_0 and v_0 are given constant numbers. These conditions determine the deflection and velocity of the beam at the initial time moment $t = 0$.

In this case, since the ends of the beam are rigidly clamped, the boundary conditions will be:

$w(0,t) = 0, \frac{\partial w(0,t)}{\partial x} = 0, \qquad w(\ell,t) = 0, \frac{\partial w(\ell,t)}{\partial x} = 0.$ (3)

Solution Method

When solving equation (1) with the initial-boundary conditions (2) and (3), we obtain two independent problems.

The First Spectral Problem

$$y^{IV}(x) + \lambda y(x) = 0, 0 < x < \ell$$
(4)

$$y(0) = y'(0) = y(\ell) = y'(\ell) = 0$$
(5)

The solution to this problem does not present any difficulties.

The Second Problem (Cauchy Problem). This is a Cauchy problem for a second-order Volterra integro-differential equation with a convolution-type kernel:

$$\frac{d^2 z(t)}{dt^2} + \omega_k^2 z_k(t) = \omega_k^2 \varepsilon \int_0^t \Gamma(t-\tau)\, z(\tau) d\tau + \omega_k^2 f_k(t)$$ (6)

with the initial condition:

$$z_k(0) = u_0^{(k)}, z_k'(0) = V_0^{(k)}$$
(7)

where $\omega_k^4 = \frac{EJ}{\rho F}\lambda_k^4; f_k(t) = \frac{1}{\omega_k^4 \rho F}\int_0^\ell f(x,t)\, y_k(x)dx.$

Solving the integro-differential equation (6) with the initial conditions (7) constitutes one of the primary difficulties in solving dynamic problems within the theory of viscoelasticity.

Applying the Laplace transform with respect to time t to equation (6), taking into account conditions (7), yields:

$$\bar{z}_k(p) = \frac{pu_0^{(k)} + v_0^{(k)}}{p^2 + \omega_k^2 - \varepsilon\omega_k^2\bar{\Gamma}(p)} + \frac{\omega_k^2 \bar{f}_k(p)}{p^2 + \omega_k^2 - \varepsilon\omega_k^2\bar{\Gamma}(p)} \qquad (8)$$

where p - is the Laplace transform parameter, $\bar{z}_k(p)$ and $\bar{f}_k(p)$ are the images of the respective functions $z_k(t)$ and $f_k(t)$. Let $f_k(t) = 0$. Then, from equation (8), we determine $\bar{\varphi}(p)$, omitting the indices for simplicity of notation:

$$\bar{\varphi}(p) = \frac{pu_0 + v_0}{p^2 + \omega^2 - \varepsilon\omega^2\bar{\Gamma}(p)} = \frac{pu_0 + v_0}{p^2 + \omega^2}\sum_{n=0}^{\infty}\left(\frac{\varepsilon\omega^2\bar{\Gamma}(p)}{p^2 + \omega^2}\right)^n \qquad (9)$$

Using the methodology outlined in [2, p.557], the solution (9) can be represented in the form of a series:

$$\bar{\varphi}(p) = \frac{pu_0 + v_0}{\bar{a}(p)}\left[1 + \varepsilon\omega^2\frac{b}{\bar{a}(p)} + \varepsilon^2\omega^4\frac{b^2}{\bar{a}^2(p)} + \ldots\right] \qquad (10)$$

where $\bar{a}(p) = (p + \frac{1}{2}\varepsilon\omega\Gamma_s)^2 + \omega^2(1 - \frac{1}{2}\varepsilon\Gamma_c)^2; b = \frac{\varepsilon}{4}(\Gamma_s^2 + \Gamma_c)^2$

$$\Gamma_s = \int_0^{\infty} \Gamma(\tau) \sin \omega \tau d\tau;\ \Gamma_c = \int_0^{\infty} \Gamma(\tau) \cos \omega \tau d\tau;\ M(t) = \int_t^0 \Gamma(\tau) \sin \omega (t - \tau) d\tau.$$

The inverse transforms (originals) of the terms in series (10) are found sequentially and take the form:

$$\varphi_1(t) = e^{-\frac{1}{2}\varepsilon\omega_s\Gamma_s t}[u_0 \cos \omega (1 - \frac{1}{2}\varepsilon\Gamma_c)t + \frac{V_0 - \frac{1}{2}\varepsilon\omega\Gamma_s}{\omega(1 - \frac{1}{2}\varepsilon\Gamma_c)} \sin \omega (1 - \frac{1}{2}\varepsilon\Gamma_c)t]$$

$$\varphi_2(t) = e\omega^2 \int_0^t \varphi(\tau)\, \psi(t - \tau) d\tau, \ldots, \varphi_n(t) = \int_0^t \varphi_{n-1}(\tau)\, \psi(t - \tau) d\tau$$

where

$$\psi(t) = \frac{b}{\omega(1 - \frac{1}{2}\varepsilon\omega_c)} e^{-\frac{1}{2}\varepsilon\omega\Gamma_s t} \sin \omega (1 - \frac{1}{2}\varepsilon\omega_c)t$$

It is worth noting that the first approximation is the solution to equation (1) obtained by the well-known averaging method [1, p.12; 3, p.157], whereas accounting for subsequent terms of the series makes it possible to determine the exact solution to the

equation. The solution for $f_k(t) \neq 0$ is found in a similar manner.

Conclusions

1. Using the Laplace integral transform method, solutions to the integro-differential equations of free and forced vibrations of a beam with rheological properties have been constructed in the form of a series for arbitrary rheological functions.
2. It has been demonstrated that the first terms of these series correspond to the solutions obtained by the well-known averaging method, while the subsequent terms provide corrections to these solutions.

References

1. Khvashchevskaya L.F. *Distributed vibration control of a viscoelastic beam.* Irkutsk, Bulletin of IrGTU, 2010, No. 6, pp. 12-15.
2. Kurbanov N.T., Babajanova V.G. *An investigation of the longitudinal fluctuation of viscoelastic cores.* New York, USA, Life Science Journal, 2014, 11 (9), pp. 557-561.
3. Matyash V.I. *Vibrations of isotropic elastic-viscous shells.* Moscow, Polymer Mechanics, 1971, No. 1, pp. 157-164.

https://doi.org./10.58225/mpmma.2026.598

STUDY OF OSCILLATIONS OF CYLINDRICAL SHELLS WITH RHEOLOGICAL PROPERTIES

Nabi Kurbanov[1], Ilham Mardanov[2], Ulviyya Aliyeva[1]

[1] Sumgait State University, Azerbaijan

[2] AzUAC, Azerbaijan

Abstract. A precise mathematical model of cylindrical shell vibrations is constructed, taking into account the rheological properties of the cylinder material under random external influences. The potential of integral Laplace transform methods for solving this class of problems for arbitrary hereditary functions is demonstrated. Using the integral Laplace transform and a small parameter, the solution to the Volterra integro-differential equation with a convolution kernel, describing the cylinder vibrations, is constructed as a series whose first term coincides with the solution to this equation obtained by the well-known averaging method. It is shown that taking subsequent terms of the series into account allows for a more accurate solution to the problem. The resulting solution is investigated under periodic loading. It is found that at resonance, the amplitude of forced vibrations remains finite, while the amplitude of free vibrations decays exponentially over time.

Keywords: integro-differential equation, image, original, kernel, rheology, resonance, amplitude, convolution of functions, Laplace transform, averaging.

Relevance of the topic. Modern load-bearing structures most often employ polymers, composites, and other materials with rheological properties that represent a relatively pliable matrix reinforced with high-strength, high-modulus fibers. These materials are used to create typical structural elements, such as cylindrical shells and panels, whose vibrations are analyzed in this paper. The problem is solved taking into account the viscoelastic properties of the material. Furthermore, the developed mathematical model significantly expands the range of problem solutions and enables more accurate calculations of the dynamic stability of cylindrical shells.

Statement of the problem: As is known, the equation describing the free oscillation of an elastic shell in displacements [1, p . 157] has the form:

$$L_k[u_1, u_2, u_3] = \rho h \frac{\partial^2 u_k}{\partial t^2} (k = 1,2,3) \quad (1)$$

where ρ is the density of the material, h is the thickness of the shell, $u_k(k = 1,2,3)$ and is the displacement of the midplane of the shell. As shown in the work [2, p . 130], the boundary dynamic problem for a viscoelastic body is reduced to a system of integro-

differential equations and boundary conditions using a simple replacement of the constants λ, μ and Eincluded in equation (1) of elasticity theory by operators $\lambda - \lambda^*$, $\mu - \mu^*, E - E^*$defined by the formula

$J^*(z) = z - \int_0^t \omega(t-\tau)\, z(\tau)d\tau.$

In this case, in all equations we can $J^*(z)$ replace with $\varepsilon J^*(z)$, considering it εas a small positive parameter.

In this case, from equation (1) for a viscoelastic shell we obtain [4, p . 163]:

$L_k[J^*(u_1), J^*(u_2), J^*(u_3)] = \rho h \frac{\partial^2 u_n}{\partial t^2}$

(2)

The boundary conditions for equation (2) can be specified in different ways, and the initial conditions are taken as:

$T(t)|_{t=0} = T_0; \left.\frac{dT(t)}{dt}\right|_{t=0} = T_0;$

(3)

Looking for a solution to equation (2) in the form:

$$u_k(\alpha_1, \alpha_2, t) = V_k(\alpha_1, \alpha_2)T_k(t)$$

we get:

$\frac{d^2T_k(t)}{dt^2} + q^2T(t) = \varepsilon q^2 \int_0^t \omega(t-\tau)\, T_k(\tau)d\tau$

(4)

Here the notations $\Gamma(t) = \varepsilon\omega(t)$ and are introduced $0 \le \omega(t) \le 1$. This means that the solution to the stated problem is reduced to solving equation (4) under condition (3) [3, p . 47].

Using the Laplace integral transform, we can represent the solution as a convergent series

(here we omit the indices for simplicity of notation)

$$\bar{T}(p) = \frac{pT_0+T_0'}{p^2+q^2}\sum_{n=0}^{\infty}\left(\frac{\varepsilon q^2\bar{\omega}(p)}{p^2+q^2}\right) \quad (5)$$

After some transformations, the series (5) can be represented as:

$$\bar{T}(p) = \frac{pT_0+T_0'}{\bar{\alpha}(p)}\left[1+\varepsilon q^2\frac{\bar{\beta}(p)}{\bar{\alpha}(p)} + \varepsilon^2 q^4\frac{\bar{\beta}^2(p)}{\bar{\alpha}^2(p)}+\dots\right] \quad (6)$$

Where $\alpha(p) = (p-\frac{1}{2}\varepsilon\omega_s q)^2 + q^2(1-\frac{1}{2}\varepsilon\omega_c)^2; \bar{\beta}(p) = \bar{\omega}(p) + \omega_s\frac{p}{q} + \omega_c + \frac{\varepsilon}{4}(\omega_s^2+\omega_c^2)$

$$\omega_s = \int_0^{\infty}\omega(\tau)\sin\tau\,d\tau;\ \omega_c = \int_0^{\infty}\omega(\tau)\cos\tau\,d\tau.$$

Note that formula (6) is equivalent to formula (5) and is more convenient in terms of handling and application.

The originals of the members of the series (6) are calculated by the following formulas:

$$T_1(t) = e^{-\frac{1}{r}\varepsilon\omega_s qt}\left[T_0\cos q(1-\frac{1}{2}\varepsilon\omega_c)t + \frac{1}{1-\frac{1}{2}\varepsilon\omega_c}\sin q(1-\frac{1}{2}\varepsilon\omega_c)t\right]$$

$$T_2(t) = \varepsilon q^2 T_1(t) * \psi(t) = \varepsilon q^2\int_0^t T_1(\tau)\,\psi(t-\tau)d\tau$$

……

$$T_n(t) = \varepsilon q^2 T_{n-1}(t) * \psi(t) = \varepsilon q^2\int_0^t T_{n-1}(\tau)\,\psi(t-\tau)d\tau \quad (7)$$

where are $\bar{\psi}(p) = \frac{\bar{\beta}(p)}{\bar{\alpha}(p)}$ the originals which look like this:

$$\psi(t) = \omega(t) * e^{-\frac{1}{2}\varepsilon\omega_s qt}\frac{1}{q(1-\frac{1}{2}\varepsilon\omega_c)}\sin q(1-\frac{1}{2}\varepsilon\omega_c)t + Ne^{-\frac{1}{2}\varepsilon q\omega_s t}\sin[q(1-\frac{1}{2}\varepsilon\omega_c)t + \gamma] \quad (8)$$

The following notations are introduced here:
$\gamma = \operatorname{arctg}\frac{\left(1-\frac{1}{2}\varepsilon\omega_c\right)}{\left(m-\frac{1}{2}\varepsilon q\omega_s^2\right)\omega_s^{-2}\varepsilon\omega_c}$; $N = \frac{\omega_s}{q}\sqrt{\frac{\left(1-\frac{1}{2}\varepsilon\omega_c\right)^2}{q^2\left(1-\frac{1}{2}\varepsilon\omega_c\right)^2}} + 1$.

Note that the first approximation $T_1(t)$ is a solution of equation (4) under condition (3) obtained by the well-known averaging method. Taking into account subsequent approximations makes it possible to determine a more accurate solution of the equation [2, p . 157].

Conclusions:

1. A more accurate mathematical model of oscillations of cylindrical shells was constructed taking into account the rheological properties of the material under random influences, and a solution was obtained for arbitrary rheological functions.
2. The solution of the integro-differential equation is constructed in the form of a series, the first term of which coincides with the solution obtained by the averaging method.
3. The solution was investigated under the influence of a periodic load and it was found that at resonance the amplitude of forced oscillations remains finite, and the amplitude of free oscillations decays exponentially over time.

Literature

Matyash V.I. Oscillations of isotropic viscoelastic shells. Moscow. Polymer Mechanics. 1971, no. 1, pp. 157-164.

Ilyushin A.V., Pobedrya B.E. Fundamentals of the Mathematical Theory of Thermoviscoelasticity. Moscow: Nauka, 1970, 280 p.

Abdukarimov R.A., Zhgutov V.I. Mathematical models of problems of nonlinear dynamics of viscoelastic isotropic plates and shells of variable thickness. St. Petersburg Engineering and Construction Journal, 2010, No. 8, pp. 47-55

Eshmatov B.Kh., Khadjayev D.A. Nonlinear Vibration and dynamic stability of a viscoelastic cylindrical panel with concentrated mass. Acta Mechanical-Vienna. 1-4 (190), 2007, p.165-193

https://doi.org./10.58225/mpmma.2026.604

CONSTRUCTİON ASYMPTOTİC SOLUTİONS OF THE PROBLEM FOR A RADİALLY FUNCTİONALLY GRADED TRANSVERSELY İSOTROPİC CYLİNDER OF SMALL THİCKNESS

Natiq Akhmedov, Sevda Akbarova, Yahya Jamalzade

Azerbaijan State University of Economics , Azerbaijan

Abstract. By the method of asymptotic integration of the equations of elasticity theory, the axisymmetric problem of elasticity theory is studied for a radially inhomogeneous, transversely isotropic cylinder of small thickness, when mixed homogeneous boundary conditions are specified on the lateral surfaces. Homogeneous solutions are constructed. It is obtained that the stress-strain state in the cylinder is composed of a penetrating stress-strain state and a boundary effect, analogous to the Saint-Venant boundary effect in the theory of transversely isotropic inhomogeneous plates.

Keywords: axisymmetric problem, equilibrium equation, penetrating solutions.

Let us consider the axisymmetric problem of the theory of elasticity for a radially inhomogeneous, transversely isotropic hollow cylinder of small thickness. We refer

the cylinder to a cylindrical coordinate system r, φ, z:

$$r_1 \le r \le r_2, \quad 0 \le \varphi \le 2\pi, \quad -L \le z \le L$$

In the axisymmetric case, the equilibrium equations take the form [1]:

$$\begin{cases} \dfrac{\partial \sigma_{rr}}{\partial r} + \dfrac{\partial \sigma_{rz}}{\partial z} + \dfrac{\sigma_{rr} - \sigma_{\varphi\varphi}}{r} = 0 \\ \dfrac{\partial \sigma_{rz}}{\partial r} + \dfrac{\partial \sigma_{zz}}{\partial z} + \dfrac{\sigma_{rz}}{r} = 0 \end{cases} \tag{1}$$

Here, $\sigma_{rr}, \sigma_{rz}, \sigma_{zz}, \sigma_{\varphi\varphi}$ are the components of the stress tensor, which are expressed in terms of the displacement vectors $u_r = u_r(r,z)$, $u_z = u_z(r,z)$ as follows [2]:

$$\sigma_{rr} = A_{11}\frac{\partial u_r}{\partial r} + A_{12}\frac{u_r}{r} + A_{13}\frac{\partial u_z}{\partial z}, \quad \sigma_{rz} = A_{44}\left(\frac{\partial u_r}{\partial z} + \frac{\partial u_z}{\partial r}\right),$$

$$\sigma_{zz} = A_{13}\left(\frac{\partial u_r}{\partial r} + \frac{u_r}{r}\right) + A_{33}\frac{\partial u_z}{\partial z}, \quad \sigma_{\varphi\varphi} = A_{12}\frac{\partial u_r}{\partial r} + A_{11}\frac{u_r}{r} + A_{13}\frac{\partial u_z}{\partial z}. \tag{2}$$

Here,

$A_{11} = A_{11}(r), A_{12} = A_{12}(r), A_{13} = A_{13}(r), A_{33} = A_{33}(r), A_{44} = A_{44}(r)$ are arbitrary positive continuous functions of the variable r.

After substituting (2) into (1), we obtain the equilibrium equation in displacements

$$\left(\boldsymbol{L}_0 + \partial_1 \boldsymbol{L}_1 + \partial_1^2 \boldsymbol{L}_2\right)\overline{\boldsymbol{u}} = \overline{\mathbf{O}} \tag{3}$$

.

Here, L_k are matrix differential operators of the form

$$L_0 = \begin{Vmatrix} \partial\left(e^{-\varphi}\left(b_{11}\partial + \varepsilon b_{12}\right)\right) + \varepsilon\left(b_{11} - b_{12}\right)e^{-\varphi}\left(\partial - \varepsilon\right) & 0 \\ 0 & \partial\left(e^{-\varphi}b_{44}\partial\right) + \varepsilon b_{44}e^{-\varphi}\partial \end{Vmatrix};$$

$$L_1 = \begin{Vmatrix} 0 & \varepsilon\left(\partial\left(b_{13}\right) + b_{44}\partial\right) \\ \varepsilon b_{13}\partial + \varepsilon^2\left(b_{13} + b_{44}\right) + \varepsilon\partial\left(b_{44}\right) & 0 \end{Vmatrix};$$

$$L_2 = \begin{Vmatrix} \varepsilon^2 b_{44}e^{\varphi} & 0 \\ 0 & \varepsilon^2 b_{33}e^{\varphi} \end{Vmatrix};$$

$\partial_1 = \dfrac{\partial}{\partial\xi};\ \partial_1^2 = \dfrac{\partial^2}{\partial\xi^2};\ \partial = \dfrac{\partial}{\partial\rho};\ \bar{u} = \left(u_\rho; u_\xi\right)^T;\ u_\rho\left(\rho,\xi\right),\ u_\xi\left(\rho,\xi\right)$ are displacement vector components, $u_\rho = \dfrac{u_r}{r_0}$, $u_\xi = \dfrac{u_z}{r_0}$; $\rho = \dfrac{1}{\varepsilon}\ln\left(\dfrac{r}{r_0}\right)$, $\xi = \dfrac{z}{r_0}$ are new dimensionless variables; $\varepsilon = \dfrac{1}{2}\ln\left(\dfrac{r_2}{r_1}\right)$ is a small parameter characterizing the thickness of the cylinder; $r_0 = \sqrt{r_1 r_2}$, $\rho \in [-1;1]$, $\xi \in [-l;l]$ $\left(l = \dfrac{L}{r_0}\right)$; $b_{ij} = b_{ij}\left(\rho\right)$ are elastic characteristics considered as an arbitrary piecewise continuous function of

the variable $\rho; b_{ij} = \frac{A_{ij}}{A_0}$ are dimensionless quantities; A_0 is some characteristic parameter having the dimension of the modulus of elasticity.

Suppose that the following homogeneous boundary conditions are specified on the lateral surfaces of the cylinder:

$$\bar{\sigma}\big|_{\rho=\pm 1} = \left(M_0 + \partial_1 M_1\right)\bar{u}\big|_{\rho=\pm 1} = \bar{0}, \tag{4}$$

where $\bar{\sigma} = \left(u_\rho, \sigma_{\rho\xi}\right)^T$,

$$M_0 = \begin{Vmatrix} 1 & 0 \\ 0 & \varepsilon^{-1} b_{44} e^{-\varepsilon\rho\partial} \end{Vmatrix}, \; M_1 = \begin{Vmatrix} 0 & 0 \\ \varepsilon b_{44} & 0 \end{Vmatrix}.$$

Let us assume that stresses are specified on the end-faces of the cylinder:

$$\sigma_{\rho\xi}\big|_{\xi=\pm l} = f_{1s}(\rho), \quad \sigma_{\xi\xi}\big|_{\xi=\pm l} = f_{2s}(\rho). \tag{5}$$

Here $f_{1s}(\rho),\ f_{2s}(\rho)\ (s=1,2)$ are sufficiently smooth functions and satisfy the equilibrium conditions; $\sigma_{\rho\xi} = \frac{\sigma_{rz}}{A_0}, \sigma_{\xi\xi} = \frac{\sigma_{zz}}{A_0}$ are dimensionless quantities.

2. We construct homogeneous solutions, i.e., any solutions of the equilibrium equations (3) that satisfy the boundary conditions (4).

Seeking the solutions of the homogeneous systems in the form

$$u_\rho(\rho,\xi)=u(\rho)e^{\alpha\xi};\ u_\xi(\rho,\xi)=w(\rho)e^{\alpha\xi}$$

we obtain the spectral problem

$$\begin{cases}\left(L_0+\alpha L_1+\alpha^2 L_2\right)\bar{a}=\bar{0}\\ \left(M_0+\alpha M_1\right)\bar{a}\big|_{\rho=\pm1}=\bar{0}\end{cases} \tag{6}$$

To construct the solution (6) as $\varepsilon\to 0$ we use the method of asymptotic integration of the equations of elasticity theory, based on three iterative processes [3-5].

The solutions corresponding to the first iterative process have the form:

$$u_\rho^{(1)}=\varepsilon D\left(\frac{d_0}{a_0}\int_{-1}^{\rho}\frac{1}{b_{11}}dx-\int_{-1}^{\rho}\frac{b_{13}}{b_{11}}dx+O(\varepsilon)\right), \tag{7}$$

$$u_\xi^{(1)}=D\xi. \tag{8}$$

Here, $d_0=\int_{-1}^{1}\frac{b_{13}}{b_{11}}d\rho,\ a_0=\int_{-1}^{1}\frac{1}{b_{11}}d\rho.$

The solutions (7) and (8) correspond to the double eigenvalues $\alpha=0.$

Solutions having the nature of a boundary effect and corresponding to the second asymptotic process are absent here.

The solutions corresponding to the third iterative process have the form:

$$u_\rho^{(3)}(\rho;\xi)=\varepsilon\sum_{k=1}^{\infty}F_k\left[-\beta_{0k}^{-3}\left(p_0\psi_k''\right)'+\beta_{0k}^{-1}p_1\psi_k'+\beta_{0k}^{-1}\left(p_2\psi_k\right)'+O(\varepsilon)\right]\exp\left(\frac{\beta_{0k}\xi}{\varepsilon}\right), \quad (9)$$

$$u_\xi^{(3)}(\rho;\xi)=\varepsilon\sum_{k=1}^{\infty}F_k\left[\beta_{0k}^{-2}p_0\psi_k''-p_2\psi_k+O(\varepsilon)\right]\exp\left(\frac{\beta_{0k}\xi}{\varepsilon}\right). \quad (10)$$

Here, ψ_k, β_{0k} are the eigenfunctions and eigenvalues of the generalized Papkovich boundary value problem

$$\begin{cases}\left(p_0\psi''\right)''-\beta_0^2\left[\left(p_1\psi\right)''+p_1\psi''+\left(p_2\psi'\right)'\right]+\beta_0^4p_3\psi=0\\ \left(-\beta_0^{-3}\left(p_0\psi''\right)'+\beta_0^{-1}p_2\psi'+\beta_0^{-1}\left(p_1\psi\right)'\right)\Big|_{\rho=\pm1}=0\\ \psi'\big|_{\rho=\pm1}=0\end{cases} \quad (11)$$

where

$$p_0=b_{11}\theta,\quad p_1=b_{13}\theta,\quad p_2=b_{44}^{-1},\quad p_3=b_{33}\theta,\quad \theta=\left(b_{13}^2-b_{11}b_{33}\right)^{-1}.$$

In contrast to the isotropic case, for a transversely isotropic plate that is inhomogeneous through the thickness, β_{0k} can also take purely imaginary values.

The general solution to (3), (4) will be a superposition of the solutions (7), (9) and (8), (10)

$$u_\rho = u_\rho^{(1)} + u_\rho^{(2)},$$
$$u_\xi = u_\xi^{(1)} + u_\xi^{(2)}.$$
(12)

For the principal vector P of the stresses acting in the section $\xi = const$, we obtain:

$$P = 2\pi\varepsilon D\left(\frac{d_0^2}{a_0} - g_0 + O(\varepsilon)\right),$$
(13)

where $g_0 = \int_{-1}^{1} \frac{\left(b_{13}^2 - b_{11}b_{33}\right)}{b_{11}} d\rho$.

The stress state corresponding to the third group of solutions is self-equilibrated in each section $\xi = const$. The solution (7), (8) corresponding to the first asymptotic process determines the internal stress-strain state of the cylinder. The first terms of its expansion in ε determine the membrane (momentless) stress state.

The third asymptotic process is determined by the solutions (9) and (10), which have the nature of a boundary layer. The first terms of (9) and (10) are equivalent to the Saint-Venant boundary effect of an inhomogeneous transversely isotropic plate. For purely imaginary β_{0k}, the Saint-Venant boundary layer decays very weakly, and the solutions (9) and (10) should be classified as penetrating solutions [2]. Therefore, in this

case, the stress-strain states of the transversely isotropic and isotropic shells differ qualitatively. When β_{0k} are not purely imaginary, the general picture of the stress-strain state is qualitatively similar to the corresponding picture for isotropic radially inhomogeneous cylinders. Quantitatively, they differ in the decay rate of the Saint-Venant boundary layers.

By applying the Lagrange variational principle to determine the arbitrary constants $F_k\left(k=1,2,...\right)$, we obtain an infinite system of linear algebraic equations [2,4,5].

REFERENCES

1.Lure A.I. Theory of Elasticity. Berlin: Springer; 2005.

2.Mekhtiev M.F. Asymptotic analysis of spatial problems in elasticity. Singapore: Springer, 2019.

3.Goldenweiser, A.L. Construction of an approximate theory of shell bending using asymptotic integration of the equations of elasticity theory. Applied Mathematics and Mechanics 1963;27(4): 593-608.

4.Ustinov Y.A. The mathematical theory of transversely non-uniform plates. Rostov-on-Don: OOOTsVVR; 2006.

5.Akhmedov N.K. The asymptotic solution of the elasticity theory problem for a

radially inhomogeneous sylinder. Partial Differential Equations in Applied Mathematics 2024, vol.11. https://doi.org/10.1016/j.padiff.2024.100885

https://doi.org./10.58225/mpmma.2026.613

CONSTRUCTION OF ASYMPTOTIC SOLUTIONS TO THE TORSION PROBLEM FOR A NONHOMOGENEOUS TRANSVERSELY ISOTROPIC CONE

Natiq Akhmedov, Solmaz Hasanova
Azerbaijan State University of Economics , Azerbaijan

Abstract. Using the method of asymptotic integration, torsion problems for a nonhomogeneous transversely isotropic thin-walled cone are investigated. The lateral surface of the cone is assumed to be free of stresses, while boundary conditions maintaining equilibrium are prescribed at the cone ends. The elastic moduli are assumed to be arbitrary continuous functions of the cone opening angle. Two classes of solutions are obtained: penetrating solutions and boundary-layer solutions. It is shown that the penetrating solution determines the internal stress–strain state of the cone. The boundary-layer solutions are localized near the cone ends, and their leading terms are equivalent to the Saint-Venant edge effect in a nonhomogeneous transversely isotropic plate. Asymptotic formulas are derived for determining the stress–strain state of the cone.

Keywords: torsion problem, homogeneous solution, boundary-layer effect

1. A torsion problem is considered for a nonhomogeneous transversely isotropic truncated hollow cone of variable thickness, which is a body bounded by two conical and two spherical surfaces. In the spherical coordinate system r,φ,θ, the region occupied by the cone is denoted by $\Gamma = \{r \in [r_1, r_2], \theta \in [\theta_1, \theta_2], \varphi \in [0, 2\pi]\}$.

The spherical parts of the boundary $(r = r_s)$ will be called the ends of the cone, while the remaining part of the boundary $(\theta = \theta_s)$ will be called the lateral surface $(s = 1,2)$.

The system of equilibrium equations in the absence of body forces in the spherical coordinate system (r, θ, φ) has the form [1]:

$$\frac{\partial \sigma_{r\varphi}}{\partial r} + \frac{1}{r}\frac{\partial \sigma_{\theta\varphi}}{\partial \theta} + \frac{3\sigma_{r\varphi} + 2\sigma_{\theta\varphi} ctg\theta}{r} = 0, \tag{1}$$

where $\sigma_{\varphi\theta}, \sigma_{r\varphi}$ are components of the stress tensor, which are expressed through the displacement-vector component $u_\varphi = u_\varphi(r;\theta)$ as follows [2]:

$$\sigma_{\theta\varphi} = \frac{1}{2}(A_{22} - A_{23})\frac{1}{r}\left(\frac{\partial \upsilon_\varphi}{\partial \theta} - \upsilon_\varphi ctg\theta\right),$$

$$\sigma_{r\varphi} = A_{44}\left(\frac{\partial \upsilon_\varphi}{\partial r} - \frac{\upsilon_\varphi}{r}\right).$$

(2)

Substituting (2) into (1), we obtain:

$$\frac{\partial}{\partial \eta}\left[G\left(\frac{\partial u_\varphi}{\partial \eta} - \varepsilon u_\varphi ctg(\theta_0 + \varepsilon\eta)\right)\right] + 2\varepsilon G\left(\frac{\partial u_\varphi}{\partial \eta} - \varepsilon u_\varphi ctg(\theta_0 + \varepsilon\eta)\right)\times$$

$$\times ctg(\theta_0 + \varepsilon\eta) + \varepsilon^2 G_1 \Delta_0 u = 0,$$

(3)

where $\eta = \frac{\theta - \theta_0}{\varepsilon}, \rho = \frac{r}{r_0}$, are new dimensionless variables, $\theta_0 = \frac{\theta_1 + \theta_2}{2}$ – is the opening angle of the middle surface, $\varepsilon = \frac{\theta_2 - \theta_1}{2}$ – is a small parameter characterizing the thickness of the cone; $r_0 = \sqrt{r_1 r_2}$; $\eta \in [-1;1]$, $u_\varphi = \frac{\upsilon_\varphi}{r_0}$, $b_{ij} = \frac{A_{ij}}{G_0}$ are dimensionless quantities; G_0 is a certain

characteristic modulus;

$$\Delta_0 = \rho^2 \frac{\partial^2}{\partial \rho^2} + 2\rho \frac{\partial}{\partial \rho} - 2;$$

$$G_1 = b_{44}, G = \frac{b_{22} - b_{23}}{2}.$$

It is assumed that the elastic moduli $b_{ij} = b_{ij}(\eta)$ are arbitrary continuous functions of the variable η, whose values may vary within the same order of magnitude.

It is further assumed that the lateral surface of the cone is free from stresses:

$$\sigma^*_{\theta\varphi} = \frac{G(\eta)}{\varepsilon\rho}\left(\frac{\partial u_\varphi}{\partial \eta} - \varepsilon u_\varphi ctg(\theta_0 + \varepsilon\eta)\right)\Bigg|_{\eta=\pm 1} = 0, \tag{4}$$

at the ends (on the spherical parts of the boundary), the stresses are prescribed as

$$\sigma_{\rho\varphi}\Big|_{\rho=\rho_s} = g_{1s}(\eta), \tag{5}$$

where $g_{1s}(\eta)\,(s = 1,2)$ are sufficiently smooth functions satisfying the equilibrium

conditions; $\sigma^*_{\theta\varphi} = \frac{\sigma_{\theta\varphi}}{G_0}$, $\sigma_{\rho\varphi} = \frac{\sigma_{r\varphi}}{G_0}$ are dimensionless quantities.

2. Let us construct a homogeneous solution, i.e., any solution of equation (3) satisfying condition (4).

Seeking solutions of (3), (4) in the form

$$u_\varphi(\rho,\eta) = \rho^{z-\frac{1}{2}} c(\eta), \tag{6}$$

we obtain

$$\begin{cases} \left[G(\eta)(c'(\eta) - \varepsilon c(\eta) ctg(\theta_0 + \varepsilon\eta))\right]' + 2\varepsilon G(\eta)(c'(\eta) - \\ -\varepsilon c(\eta) ctg(\theta_0 + \varepsilon\eta)) ctg(\theta_0 + \varepsilon\eta) + \left(z^2 - \frac{9}{4}\right) \times \\ \times \varepsilon^2 G_1(\eta) c(\eta) = 0, \\ G(\eta)(c'(\eta) - \varepsilon c(\eta) ctg(\theta_0 + \varepsilon\eta))\big|_{\eta=\pm 1} = 0. \end{cases} \tag{7}$$

(8)

As $\varepsilon \to 0$, to solve problems (7), (8), we use an asymptotic method based on three iterative processes [3–6].

The solution corresponding to the first iterative process has the form

$$u_{\varphi}^{(1)}(\rho,\eta) = D\rho^{-2}\sin(\theta_0 + \varepsilon\eta). \tag{9}$$

The solution (9) corresponds to the eigenvalue $z = -\frac{3}{2}$.

The second iterative process, i.e., the solution having the character of an edge effect (boundary-layer effect), is absent in this case.

The solutions corresponding to the third iterative process have the form

$$u_{\varphi}^{(3)}(\rho,\eta) = \sum_{n=1}^{\infty}\left(E_n\rho^{z_n-\frac{1}{2}} + D_n\rho^{-z_n-\frac{1}{2}}\right)c_n(\eta), \tag{10}$$

where E_n, D_n are arbitrary constants.

The general solution of (7), (8) is the superposition of solutions (9) and (10), corresponding to the above iterative processes:

$$u_\varphi(\rho,\eta) = u_\varphi^{(1)} + u_\varphi^{(3)}.$$

(11)

The constant D is proportional to the twisting moment M of the stresses acting on the cross-section $\rho = const$:

$$M = -6\pi D \int_{-1}^{1} G_1(\eta)\sin^3(\theta_0 + \varepsilon\eta)d\eta.$$

(12)

By satisfying the boundary conditions (5), the unknown constants E_n, D_n are determined.

The first part of solution (11) determines the internal stress–strain state of the cone.The stress state corresponding to the third iterative process is self-equilibrated in each cross-section $\rho = const$ and has the character of a boundary layer. The leading terms of its asymptotic expansion are

equivalent to the Saint-Venant edge effect in the theory of nonhomogeneous transversely isotropic plates [2].

REFERENCES

1.Lure A.I. Theory of Elasticity. Berlin: Springer; 2005.

2.Mekhtiev, M.F. Asymptotic analysis of spatial problems in elasticity. Springer. 2019.

3.Goldenweiser,A.L. Construction of an approximate theory of shell bending using asymptotic integration of the equations of elasticity theory. Applied Mathematics and Mechanics 1963;27(4): 593-608.

4.Akhmedov,N.K., Mekhtiev, M.F. Analysis of the three-dimensional problem of the theory of elasticity for an inhomogeneous truncated hollow cone. Applied Mathematics and Mechanics 1993; 57(5): 871-877.

5.Akhmedov N.K. The asymptotic solution of the elasticity theory problem for a radially inhomogeneous sylinder. Partial

Differential Equations in Applied Mathematics 2024, vol.11. https://doi.org/10.1016/j.padiff.2024.100885

6.Ustinov,YA. The mathematical theory of transversely non-uniform plates. Rostov-on-Don: OOOTsVVR; 2006.

https://doi.org./10.58225/mpmma.2026.622

DYNAMIC ANALYSIS OF AN INHOMOGENEOUS HALF-SPACE

Nazila Rassoulova[1] *, Tahmina Mahmudzade*[2]

[1] Institute of Mathematics, Azerbaijan

[2] Baku State University, Azerbaijan

Abstract. The work is devoted to the theoretical and analytical study of the process of propagation of non-stationary waves in elastic piecewise homogeneous bodies. In a particular case, an elastic half-space is considered, inside which a cylinder made of another linear-elastic material is built in and on the end of which a normal impact is applied. A new solution method for spatial problems of elastodynamics, previously presented in [1], was applied, and a version of this method for cylindrical regions and axisymmetric motion was developed here. An interesting result was obtained, scientifically substantiating the so-called phenomenon of reinforced concrete.

Keywords: non-stationary waves, cylinder, half-space.

1. Introduction

The study of dynamic resistance of bodies consisting of different materials is of great interest, but it is accompanied by great mathematical difficulties. The purpose of this work is to find a way to overcome these difficulties and obtain a reliable and analytical

result. Considering that the impact process occurs in a fairly short period of time, the part that describes the initial moment of the process is extracted from the general solution. In the literature on this topic, a work [2] is known, where only the stationary motion of the system is considered - a cylinder and space, and the dispersion characteristics of the process are studied.

2. Mathematical formulation and solution of the problem.

An elastic half-space is considered, occupying the region $z \geq 0,\ a < r \leq \infty$ in a cylindrical coordinate system. In the part of the space $z \geq 0, 0 \leq r < a$ an elastic cylinder made of another material is built in. The impact now $t = 0$ is made only on the end surface of the cylinder. To solve the problem, the Lame equations are considered for the axisymmetric case in the selected cylindrical coordinate system (r, φ, z), the centre of which is located at the centre of the end surface of the cylinder:

$$\nabla \cdot \sigma^{(i)} = \rho_{(i)} \frac{\partial^2 u^{(i)}}{\partial t^2}, i = 1,2, \ldots \quad (2.1)$$

$$u^{(i)} = \begin{bmatrix} u_r^{(i)} \\ u_z^{(i)} \end{bmatrix}, \sigma^{(i)} = \begin{bmatrix} \sigma_{rr}^{(i)} & \sigma_{rz}^{(i)} \\ \sigma_{rz}^{(i)} & \sigma_{zz}^{(i)} \end{bmatrix}$$

$$\sigma^{(i)} = 2\mu_{(i)}\varepsilon^{(i)} + \lambda_{(i)} e^{(i)}, \varepsilon_{rr}^{(i)} = \frac{\partial u_r^{(i)}}{\partial r}; \varepsilon_{\theta\theta}^{(i)} = \frac{u_r^{(i)}}{r}; \varepsilon_{zz}^{(i)} = \frac{\partial u_z^{(i)}}{\partial z}$$

$$\varepsilon_{rz}^{(i)} = \frac{1}{2}\left(\frac{\partial u_r^{(i)}}{\partial z} + \frac{\partial u_z^{(i)}}{\partial r}\right),\ \varepsilon_{z\theta}^{(i)} = \varepsilon_{r\theta}^{(i)} = 0 \qquad (2.2)$$

Initial conditions are zero:

$$\left.\begin{array}{l} u_r^{(i)} = u_z^{(i)} = 0 \\ \frac{\partial u_r^{(i)}}{\partial t} = \frac{u_z^{(i)}}{\partial t} = 0 \end{array}\right\} t = 0; i = 1,2 \qquad (2.3)$$

Here $u_r^{(i)}, u_z^{(i)}$ −are the components of the displacement vector, $\varepsilon_{ij}^{(i)}, \sigma_{ij}^{(i)}$ − are, respectively, the components of the strain and stress tensors in different media, ρ_i −is the density, λ_i and μ_i −are the Lame coefficients, t −time. The quantity with index 1 refers to the cylinder, and with index 2 to the half-space.

On the end surface of the cylinder and around it, the boundary conditions are specified in the following form:

$$\left.\begin{array}{l} \sigma_{zz}^{(1)} = \sigma_0(r)f(t) \\ u_r^{(1)} = 0 \end{array}\right\} z = 0, \quad 0 \le r \le a$$

$$\left.\begin{array}{l} \sigma_{zz}^{(2)} = 0 \\ u_r^{(1)} = 0 \end{array}\right\} z = 0, a < r < \infty \qquad (2.4)$$

because the blow is applied only to the cross-section of the cylinder. As is well known, the corresponding boundary conditions must also be specified here.

The solution is obtained by applying the Laplace transform in time (t) and the Fourier transform in the axial coordinate (z) to the equations of motion. As a result, the original problem is reduced to a system of ordinary differential equations with respect to the radial coordinate:

$$\begin{cases} (\lambda+2\mu)\frac{\partial^2 \bar{u}_r^{(s)}}{\partial r^2}+(\lambda+2\mu)\frac{1}{r}\frac{\partial \bar{u}_r^{(s)}}{\partial r}-(\mu q^2+\rho p^2)\bar{u}_r^{(s)}-(\lambda+2\mu)q\frac{\partial \bar{u}_z^{(c)}}{\partial r} \\ -(\lambda+2\mu)\frac{\bar{u}_r^{(s)}}{r^2}=0 \\ (\lambda+\mu)q\frac{\partial \bar{u}_r^{(s)}}{\partial r}+(\lambda+\mu)q\frac{\bar{u}_r^{(s)}}{r}+\frac{\mu}{r}\frac{\partial \bar{u}_z^{(c)}}{\partial r}-[\rho p^2+(\lambda+2\mu)q^2]\bar{u}_z^{(c)}=\sigma_0 f(p) \end{cases} \quad (2.5)$$

Here $\bar{u}_r^{s(i)}, \bar{u}_z^{c(i)}$ quantities are, respectively, the sine and cosine of the Fourier and Laplace transformations of the displacement components and the primary method employed for determining the inverse Laplace transform is the "First Expansion Theorem" [3]. After performing the above transformations, the transformed potentials can be represented as follows:

$$\phi_1 = -\frac{\sigma_0 f(p)}{q\nu_1^{(1)^2}(\lambda_1+2\mu_1)}+A_0 I_0\left(\nu_1^{(1)} r\right)$$

$$\psi_1 = -\frac{\sigma_0 f(p)}{q^2\nu_2^{(1)^2}\mu_1}+C_0 I_0\left(\nu_2^{(1)} r\right)$$

$$\phi_2 = A_1 K_0\left(\nu_1^{(2)} r\right)$$

$$\psi_2 = C_1 K_0\left(\nu_2^{(2)} r\right) \quad (2.6)$$

The main novelty of this work lies in the fact that the potentials are expressed in terms of the external forces.

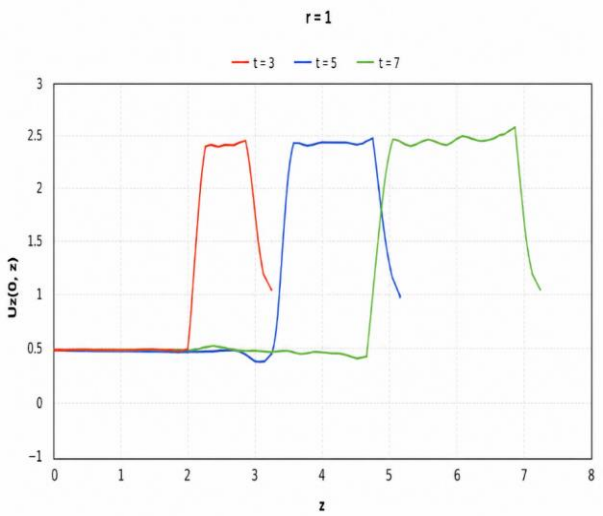


Fig.1. Distribution of the longitudinal velocity along the cylinder fibers for various radii and time instants.

The resulting graphs are quite interesting and exceed all expectations: they show that throughout the entire cross-sectional area of the cylinder, the main energy propagates at the speed of a longitudinal wave of the cylinder material.

It shows that the resistance of the cylinder is greatly increased, and perhaps this event can be called the phenomenon of reinforced concrete and considered the key result of this work.

References

1.Rassoulova, N.B. “On Dynamics of a Bar of Rectangular Cross Section.” Journal of Applied Mechanics (Transactions of the ASME), vol. 68, no. 4, pp. 662–666, (2001)

2. Parnes, R. “Dispersion Relations of Waves in a Rod Embedded in an Elastic Medium.” Journal of Sound and Vibration, vol. 76, no. 1, pp. 65–75, (1981)
3. Ditkin, V.A., and Prudnikov, A.P. Integral Transforms and Operational Calculus. Oxford: Pergamon Press, 529 p. (1965)

https://doi.org./10.58225/mpmma.2026.628

A STURM–LIOUVILLE PROBLEM WITH HERGLOTZ–NEVANLINNA FUNCTION BOUNDARY CONDITIONS AT BOTH ENDPOINTS

Nigar Aslanova[1],Hajar Movsumova[1] , Khalig Aslanov[2]

[1]AZUAC, Azerbaijan

[2] Azerbaijan State Economic University, Azerbaijan,

Abstract. In this paper, we investigate a Sturm–Liouville problem with an unbounded operator coefficient in a separable Hilbert space, where both boundary conditions involve Herglotz–Nevanlinna type functions. To study this problem, we first introduce a new, wider Hilbert space and define an appropriate inner product on it. Then we establish the fundamental concepts and constructions required for the analysis. Considered boundary value problem is transformed into an equivalent eigenvalue problem by means of a suitably defined self-adjoint operator in the underlying space.

Unlike previously studied problems of a similar nature, where either the problem is considered in a different functional setting or only one of the boundary conditions contains a Herglotz–Nevanlinna type function, the present work treats the case in which such functions appear in both boundary conditions. This approach provides a broader

framework for the spectral analysis of Sturm–Liouville problems with eigenparameter-dependent boundary conditions.

Keywords: separabel Hilbert space, Herglotz-Nevanlinna, self-adjoint.

A Sturm–Liouville problem with Herglotz–Nevanlinna Function Boundary Conditions at Both Endpoints

We consider the Sturm-Liouville equation

$$-y''(t) + Ay(t) + q(t)y(t) = \lambda y(t) \quad (1)$$

where A is unbounded operator $A = A^*$, $A > E$ (E is identity operator in separabel Hilbert space H and $A^{-1}\epsilon\sigma_\infty$) with boundary conditions

$$y'(0) = -\left(a\lambda + b - \sum_{k=1}^{n} \frac{b_k}{\lambda - c_k}\right) y(0) \quad (2)$$

$$y'(1) = -\left(a_0\lambda + b_0 - \sum_{k=1}^{N} \frac{d_k}{\lambda - p_k}\right) y(1) \quad (3)$$

where

$$f(\lambda) = a\lambda + b - \sum_{k=1}^{n} \frac{b_k}{\lambda - c_k} \quad a, b, b_k, c_k \epsilon R, \quad k = \overline{1,n}$$

$$F(\lambda) = a_0\lambda + b_0 - \sum_{k=1}^{N} \frac{d_k}{\lambda - p_k} \quad a_0, b_0, d_k, p_k \epsilon R, \quad k = \overline{1,N}$$

are rational functions of Herglotz-Nevanlinna type if and only if $a, a_0 \geq 0$, $b_k, d_k > 0$, $c_1 < c_2 < \cdots < c_n$, $p_1 < p_2 < \cdots <$

p_N , $n \geq 0$, $N \geq 0$ (n and N are finite numbers).

Now we introduce a new Hilbert space (wider) and set up a self-adjoint operator in this space because of the boundary value problem (1)-(3) can be equivalent to the eigenvalue problem for this operator. We consider the Hilbert space $\mathcal{H} = L_2(0,1,H) \oplus H^{2+n+N}$ with the following inner product ($a, a_0 > 0$)

$$(Y,Z)_{\mathcal{H}} = \int_0^1 \big(y(t), z(t)\big)_H dt + \sum_{k=1}^{n} \frac{(y_k, z_k)_H}{b_k} + \frac{(y_{n+1}, z_{n+1})_H}{a} +$$

$$+ \sum_{k=1}^{N} \frac{(y_{n+1+k}, z_{n+1+k})_H}{d_k} + \frac{(y_{n+N+2}, z_{n+N+2})_H}{a_0}$$

where

$$Y = \{y(t), y_1, \cdots, y_{n+1}, y_{n+2}, \cdots, y_{n+N+2}\} \epsilon \mathcal{H}$$

$$Z = \{z(t), z_1, \cdots, z_{n+1}, z_{n+2}, \cdots, z_{n+N+2}\} \epsilon \mathcal{H}$$

$$y(t), z(t)\epsilon C_0^{\infty}(0,1,H_{\infty}), H_{\infty} = \bigcap_{j=1}^{\infty} D\left(A^j\right),$$

$$y_i, z_i \epsilon H, \quad i = \overline{1, n+N+2}.$$

Define operator L_0' as follows

$$D(L_0') = \left\{ \begin{matrix} Y: Y = \{y(t), y_1, \cdots, y_{n+1}, y_{n+2}, \cdots, y_{n+N+2}\} \epsilon \mathcal{H}, y(t) \epsilon C_0^{\infty}(0,1,H_{\infty}) \\ , y_i \epsilon H, i = \overline{1, n+N+2} \ , y_{n+1} = -ay(0), y_{n+N+2} = a_0 y(1) \end{matrix} \right\}$$

$$L_0' Y = \left\{ \begin{matrix} ly, b_1 y(0) - c_1 y_1, \cdots, b_n y(0) - c_n y_n, y'(0) + by(0) - \sum_{k=1}^{n} y_k , \\ p_1 y_{n+2} - d_1 y(1), \cdots, p_N y_{n+N+1} - d_N y(1), y'(1) - b_0 y(1) - \sum_{k=1}^{N} y_{n+1+k} \end{matrix} \right\}$$

In $\mathcal{H}$ closure of L_0' call minimal operator and denote by L_0.

Adjoint of L_0 denoted by L_0^* call a maximal operator.

Theorem. The closure of the operator on C is self-adjoint.

References

1. P.A.Binding, P.J.Browne, B.A.Watson. Sturm-Liouville problems with boundary conditions rationally dependent on the eigenparameter. Journal of Computational and applied mathematics 148, 2002, pp.147-168

2. N. Aslanova, K. Aslanov, L. Kocinac. On some spectral problems for Sturm–Liouville

equation with operator coefficients. Mathematical Methods in the Applied Sciences, 2025
3. N. M. Aslanova , H.F. Movsumova. \ On some spectral properties of differential operator with unbounded operator coefficient ." J. of Contemporary Applied Mathematics 12.1 (2022), pp. 3-16

https://doi.org./10.58225/mpmma.2026.633

AN INNOVATIVE APPROXIMATE SOLUTION FOR THE INTERVAL PARTIALLY BOOLEAN KNAPSACK PROBLEM

Shukurova Nigar Oktay[1]
Mammadov Knyaz Shiraslan[1,2]
Huseynov Saqif Yaqub[2]
[1]Baku State University,İnstitute of Mathematics, Azerbaijan.
[2] Institute of Mathematics, Baku, Azerbaijan.

Abstract. In this paper, optimistic and pessimistic problems are formulated based on the interval-coefficient partially Boolean knapsack problem. Approximate (suboptimal) solutions to these problems are then obtained. Subsequently, the improvement of the derived suboptimal solutions is considered. A program implementing the proposed method has been developed, and extensive comparative experiments have been conducted.

Keywords. Interval partially Boolean knapsack problem, optimistic and pessimistic problems, improved approximate solutions.

1. Introduction

In this paper, we investigate the following problem:

$$\sum_{j=1}^{n}[\underline{c}_j, \overline{c}_j]x_j + \sum_{j=n+1}^{N}[\underline{c}_j, \overline{c}_j]x_j \to \max, \quad (1)$$

$$\sum_{j=1}^{n}[\underline{a}_j, \overline{a}_j]x_j + \sum_{j=n+1}^{N}[\underline{a}_j, \overline{a}_j]x_j \leq [\underline{b}, \overline{b}], \quad (2)$$

$$x_j = 1 \vee 0, \left(j = \overline{1, n}\right), \quad (3)$$

$$0 \leq x_j \leq 1, \left(j = \overline{n+1, N}\right). \quad (4)$$

Here, it is assumed that $0 < \underline{c}_j \leq \overline{c}_j$, $0 < \underline{a}_j \leq \overline{a}_j$, $\left(j = \overline{1, N}\right)$, $0 < \underline{b} \leq \overline{b}$ are given integers. This problem is referred to as the interval partially Boolean knapsack problem.

It should be noted that, in [1], optimistic and pessimistic versions corresponding to this problem were formulated, and several algorithms were developed for obtaining their approximate solutions (suboptimistic and subpessimistic solutions). However, the possibility of further improving the approximate solutions obtained in that study was not investigated.

It should be noted that the concept of an innovatively approximate solution was introduced in [2-4], and methods for obtaining such solutions were proposed for the knapsack

and integer knapsack problems. In the present work, innovatively approximate solution methods are developed for a broader class of problems, namely the interval partially Boolean knapsack problem.

2. Problem Statement

Based on the endpoints of the coefficient intervals in problem (1)–(4), we construct the following problem, referred to as the optimistic and problem.

Optimistic problem:

$$\sum_{j=1}^{n} \overline{c}_j x_j + \sum_{j=n+1}^{N} \overline{c}_j x_j \to \max, \quad (5)$$

$$\sum_{j=1}^{n} \underline{a}_j x_j + \sum_{j=n+1}^{N} \underline{a}_j x_j \le \overline{b}, \quad (6)$$

$$x_j = 1 \vee 0, (j = \overline{1, n}), \quad (7)$$

$$0 \le x_j \le 1, (j = \overline{n+1, N}). \quad (8)$$

First, let us consider the optimistic problem. Without loss of generality, we assume that the coefficients of problem (5)–(8) are ordered as follows:

$$\overline{c}_j / \underline{a}_j \ge \overline{c}_{j+1} / \underline{a}_{j+1}, \left(j = \overline{1, N-1}\right)$$

At this stage, an approximate (suboptimistic) solution can be constructed quite easily. The initial solution is set to $X^{so} = (0,0, \dots ,0)$. Then, using criterion

$$j_* = \arg \max_{j \in I \cup R} \left(\overline{c}_j / \underline{a}_j \right) \quad (9)$$

(9), it is determined whether $x_{j_*} = 1$, $x_{j_*} = 0$, or whether x_{j_*} can take a proper fractional value. Applying this procedure successively for all $j, \left(j = \overline{1, n}\right)$, yields a suboptimal solution.

Here, $I = [1,2, \dots , n]$, $R = [n+1, n+2, . . , N]$ are assumed.

All conducted experiments show that the coordinates at which the obtained suboptimal solution differs from the optimal solution are located in the neighborhood of a certain k-th coordinate. We have proposed a method for determining this index k.

After that, we determine the interval $(k - \delta_1, k + \delta_2)$ containing the k-th

coordinate. In particular, a procedure for determining the parametersδ_1 and δ_2 has been proposed. Then, the values of the variables located within this interval are identified, and new solutions are generated by modifying them one at a time. Among these solutions, the best one is selected as the final innovative suboptimistic solution. Clearly, this solution should be superior to the initial solution obtained at the first stage.

Conclusion.

In this article, an innovative improved approximate solution method for the partially Boolean-variable knapsack problem has been developed. Using this method, the initially obtained solution can be progressively improved.

References

1. Mamedov K. Sh., Mamedli N. O. "Methods for Constructing Suboptimistic and Subpessimistic Solutions of the Partially Boolean Knapsack Problem with Interval Data",Baku: Proceedings of the Azerbaijan National Academy of Sciences (ANAS): Series of Physical-Technical and Mathematical Sciences, Vol. XXXVI, No. 6, pp. 6–13, 2016 (in Russian).

2. Mammadov K.Sh., Niyazova R.R. Innovative improved approximate solution method for the integer knapsack problem, error compression and computational

experiments //Radio Electronics Computer Science Control, No4,pp.64-75, (2024)
3. Mammadov K.Sh., Niyazova R.R., Huseynov S.Ya. Инновативный приближённый метод решения задач о ранце с интервальными коэффициентами. //International Independent Scientific Journal, No 44, pp.8-13, 2022
4. Sigal I. Kh., Ivanova A. P., Introduction to Applied Discrete Programming:
Models and Computational Algorithms, M. Fizmatlit, 2003, 304 p

https://doi.org./10.58225/mpmma.2026.639

PROBABILISTIC-STATISTICAL MODELLING OF NON-STATIONARY HEAT CONSUMPTION REGIMES IN INTELLIGENT RESIDENTIAL BUILDINGS

Nurmammad Mammadov, Jamil Guliev
AzUAC

Abstract. A probabilistic-statistical approach is proposed for modelling non-stationary heat consumption in intelligent residential buildings. The time series is represented as a harmonic function; its four parameters are identified via autocorrelation analysis, spectral density estimation, and cross-spectral decomposition. Python simulation confirmed algorithm validity ($R^2 = 0.9702$, RMSE = 1.88 kW, Cochran $G = 0.1488 \leq G_cr = 0.2945$).

Keywords: heat consumption; non-stationary regime; probabilistic-statistical modelling; autocorrelation; spectral density; intelligent building; energy efficiency.

1. Introductıon

According to the IEA, buildings account for approximately 40% of global final energy consumption, with heating and cooling responsible for nearly half [7]. A building forms a rigid technological chain — outdoor environment, external envelope, indoor air, occupant — in which a change in any

parameter affects all others [1, 2]. The heat consumption regime occurs under unsteady-state conditions owing to significant diurnal climatic fluctuations. Existing deterministic tools (EnergyPlus, TRNSYS) require extensive input data unsuitable for real-time control, while statistical methods (ARIMA, regression) lose accuracy under changing conditions [10, 11]. No precise analytical formulae accounting for all influencing factors have yet been derived.

The present paper proposes a probabilistic-statistical approach to constructing a model of non-uniform heat consumption. Unlike deterministic methods, this approach characterises system behaviour with respect to the entire ensemble of stochastic disturbances rather than a single prescribed input function [5]. Special-purpose hardware correlators enable automatic computation of the correlation function and spectral density in real time, making the approach directly integrable into automatic microclimate control systems of intelligent buildings.

Mathematical Model

Despite the random nature of heat consumption parameters, these can be

described by periodic functions. Let the heat consumption time series be expressed as:

$$Q(t) = Q_0 + A \cdot \cos(\omega t + \varphi_0) \qquad (1)$$

where Q_0 — constant (mean) component; A — amplitude; ω — frequency; φ_0 — initial phase. The mean component Q_0 is the mean-integral value over the observation interval. Considering the zero-mean series $q(t) = Q(t) - Q_0$, its autocorrelation function is $K(\tau) = (A^2/2)\cdot\cos(\omega\tau)$, giving at $\tau = 0$:

The spectral density over a finite correlation interval T_0 is:

The maximum of $S(\omega)$ at $\omega = \omega_0$ (equation 14) yields the oscillation frequency. Since neither the autocorrelation function nor the spectral density contain phase information, the realisation series is divided into two non-overlapping subsets $q_1(t)$ and $q_2(t)$ with identical frequencies but different initial phases:

The cross-correlation function $K_{12}(\tau) = (A^2/2)\cdot\cos(\omega\tau + \Delta\varphi)$, where $\Delta\varphi = \varphi_1 - \varphi_2$ (17). The co-spectrum $C(\omega)$ and quadrature spectrum $Q(\omega)$ are computed over T_0:

After determining Q_0, A, ω, and φ_0, the residual series is tested for randomness using non-parametric criteria. If a non-random component is detected, the procedure is repeated with additional realisations.

2. Algorithm for Constructing the Model

Steps 1–3. Collect time series Q(t); exclude outliers; compute Q_0, variance D, and $A = \sigma\sqrt{2}$. Compute autocorrelation function and spectral density; determine correlation time T_0. Identify frequency ω_0 from the peak of $S(\omega)$.

Steps 4–6. Divide series into two subsets; compute co-spectrum $C(\omega)$ and quadrature spectrum $Q(\omega)$ via (19)–(20); obtain phase $\Delta\varphi$ from (24). Compare RMSD with D; if $RMSD < D$, accept model. Verify equal precision by Cochran's criterion $G = D_max/\Sigma D_i$ (25); accept if $G \leq G_cr$.

3. Simulation Results

A synthetic heat consumption series Q(t) was generated over seven days (T_0 = 168 h, hourly resolution) with true values Q_0 = 50.0 kW, A = 15.0 kW, $\omega = 2\pi/24$ rad/h, $\varphi = \pi/4$ rad, and Gaussian noise σ = 2.0 kW. The identification algorithm recovered all four parameters via FFT-based spectral analysis and least-squares phase fitting. Results are given in Table 1; model adequacy was confirmed by Cochran's criterion ($G = 0.1488 \leq G_cr = 0.2945$, significance level 0.05).

The results confirm $R^2 = 0.9702$ and RMSE = 1.88 kW.

Table 1. Parameter identification results

Parameter	True value	Estimated value	Absolute error
Q_0 (kW)	50.000	49.922	0.078
A (kW)	15.000	15.159	0.159
ω (rad/h)	0.2618	0.2618	0.0000
φ (rad)	0.7854	0.7763	0.009
RMSE (kW)	—	1.877	—
R^2	—	0.9702	—

Discussion

The algorithm recovered all four parameters with high accuracy (ω exact, amplitude error 1.1%, phase error 1.2%). Unlike deterministic tools (EnergyPlus, TRNSYS) requiring extensive input data, and unlike black-box statistical methods, the proposed model characterises system behaviour across the full ensemble of stochastic disturbances while retaining physical interpretability of each parameter.

Compared to data-driven methods, the model retains physical interpretability: Q_0 reflects baseline thermal load, A characterises diurnal variation, ω corresponds to dominant periodicity, and φ defines the temporal alignment. The direct implementability using hardware correlators — without iterative optimisation — makes it suitable for real-time deployment in building automation systems compatible with MPC and IoT-based BMS architectures [9]. Extension to multi-harmonic representations and validation against field data are primary directions for future work.

Conclusions

1. A probabilistic-statistical approach is proposed for modelling non-stationary heat consumption regimes. The time series is modelled as a harmonic function with parameters identified via autocorrelation analysis, spectral density estimation, and cross-spectral decomposition.

2. A four-parameter model $Q(t) = Q_0 + A \cdot \cos(\omega t + \varphi)$ is developed; parameters are identified sequentially and adequacy verified by Cochran's criterion.

3. Python simulation confirmed algorithm validity ($R^2 = 0.9702$, RMSE = 1.88 kW; Cochran $G = 0.1488 \leq G_cr = 0.2945$). The

method is directly implementable with hardware correlators, compatible with MPC and IoT-based BMS architectures, and constitutes a physically interpretable alternative to data-driven methods.

References

1. Tabunshchikov Yu.A., Brodach M.M. Mathematical Modelling and Optimisation of the Thermal Efficiency of Buildings. Moscow: AVOK-PRESS, 2002. 194 p.

2. Mamedov N.Ya. Application of modern information technologies for building microclimate control. Journal "Ecology and Water Management". Baku. 2008, No. 1, pp. 39–43.

5. Bendat J., Piersol A. Measurement and Analysis of Random Data. Moscow: Mir, 1974. 250 p.

6. Korn G., Korn T. Mathematical Handbook for Scientists and Engineers. Moscow: Nauka, 1984. 831 p.

7. IEA. World Energy Outlook 2023. International Energy Agency, Paris, 2023.

9. Afram A., Janabi-Sharifi F. Theory and applications of HVAC control systems — A review of model predictive control (MPC). Building and Environment. 2014. Vol. 72. P. 343–355.

10. Deb C. et al. A review on time series forecasting techniques for building energy consumption. Renewable and Sustainable Energy Reviews. 2017. Vol. 74. P. 902–924.

11. Amasyali K., El-Gohary N.M. A review of data-driven building energy consumption prediction studies. Renewable and Sustainable Energy Reviews. 2018. Vol. 81. P. 1192–1205.

https://doi.org./10.58225/mpmma.2026.647

SEMI-ANALYTICAL SOLUTIONS OF NONLINEAR REACTION DIFFUSION EQUATION IN PACKED-BED REACTORS USING TAYLOR SERIES EXPANSION AND THE ADOMIAN DECOMPOSITION METHOD

Ponraj Jeyabarathi[1] and Lakshmanan Rajendran [1]

[1]AMET, Deemed to be University, India

Abstract. A theoretical model for enzyme-catalyzed isomerization in packed-bed reactors composed of microporous catalyst particles is developed to analyze the coupled effects of diffusion and nonlinear reaction mechanisms within porous media. The system is formulated using finite-range Fickian diffusion combined with Michaelis–Menten kinetics, leading to a nonlinear reaction–diffusion equation that governs substrate transport and conversion inside the particles. The resulting boundary value problem is solved numerically using MATLAB to obtain accurate reference solutions. In addition, approximate analytical solutions are constructed using the Taylor series method and the Adomian decomposition method, yielding explicit expressions for concentration profiles and flux.

Keywords: Nonlinear reaction–diffusion equation; Michaelis–Menten kinetics;

Analytical methods (Taylor series and Adomian decomposition); Numerical simulation.

1. Introduction

Enzymatic reactions are widely used for the conversion of substrates such as glucose into fructose. This process is typically performed in a packed-bed reactor employing immobilized enzymes within microporous particles that possess a distribution of pore sizes. Glucose isomerase, first discovered by Marshall and Kooi [1], enabled the commercial-scale production of fructose through enzymatic catalysis. Dadvar et al. [2] proposed a pore-network model for deactivating microporous biocatalyst particles in a packed-bed reactor and presented preliminary simulation results using two-dimensional network models in their subsequent studies. Ponrani et al. [3] analytically solved the coupled steady-state nonlinear reaction–diffusion equations associated with the pore-network model and

obtained approximate analytical expressions for the concentration and flux in the packed-bed reactor. Ananthasamy and Rajendran [4] derived analytical solutions for the concentration and flux under steady-state conditions using a new homotopy method. Selvi and Hariharan [5] determined the steady-state concentration profiles of immobilized glucose isomerase in a packed-bed reactor by employing a wavelet-based analytical technique. Therefore, the objective of this work is to derive approximate analytical expressions for the steady-state substrate concentration and current using the Adomian Decomposition Method and the Taylor series method.

2. Mathematical Formulation of the Problem.

The enzymatic conversion of glucose to fructose is represented by the reaction scheme

$$G + E \underset{k_{-1}}{\overset{k_1}{\leftrightharpoons}} X \underset{k_{-2}}{\overset{k_2}{\leftrightharpoons}} F + E \quad (1)$$

where G, E, and Fdenote glucose, enzyme, and fructose, respectively, while Xrepresents the

intermediate enzyme–substrate complex. The constants k_1, k_2, k_{-1}, and $k_{-2}$are the forward and backward kinetic rate constants. Based on the model developed by Dadvar and Sahimi [2], the dimensionless steady-state mass transport equation governing the enzymatic reaction in a packed-bed reactor is

$$\frac{d^2c(z)}{dz^2} - \Phi_p^2 \frac{c(z)}{1+\beta c(z)} = 0 \quad (2)$$

subject to the boundary conditions

$$c(0) = 1, \frac{dc}{dz}(1) = 0 \quad (3)$$

where $\Phi_p$is the pore-level Thiele modulus and $\beta$is the dimensionless saturation parameter. The dimensionless concentration is defined as $c(z) = C(z)/C_{z0}$. The corresponding dimensionless current is given by

$$\psi = -\left(\frac{dc(z)}{dz}\right)_{z=0} \quad (4)$$

which represents the substrate flux at the pore entrance.

3.Approximate Analytical Expression of the Concentration and current using Adomian Decomposition Method and Taylor series method.

The analytical expression of a substrate concentration for all dimensionless parameters

can be obtained using ADM method as follows:

$$c(z) = 1 + \frac{\Phi_p^2}{1+\beta}\left(\frac{z^2}{2} - z\right) + \frac{\Phi_p^4}{(1+\beta)^3}\left(\frac{z^4}{24} - \frac{z^3}{6} + \frac{z}{3}\right) \quad (5)$$

The dimensionless current is given by

$$\psi = \frac{\Phi_p^2}{1+\beta} - \frac{\Phi_p^4}{3(1+\beta)^3} \quad (6)$$

The analytical expression of a substrate concentration for all dimensionless parameters can be obtained using TSM method as follows:

$$c(z) = 1 + c'(0)z + \frac{\Phi_p^2}{1+\beta}\left(\frac{z^2}{2}\right) + \frac{\Phi_p^2 c'(0)}{(1+\beta)^2}\left(\frac{z^3}{6}\right) + \frac{\Phi_p^2(\Phi_p^2 - 2\beta(c'(0))^2)}{(1+\beta)^3}\left(\frac{z^4}{24}\right) \quad (7)$$

The dimensionless current is given by

$$\psi = c'(0) \quad (8)$$

Conclusion

The mathematical modeling of immobilized enzymatic reactions in packed-bed reactors based on Michaelis–Menten kinetics has been presented. Approximate closed-form analytical expressions for the concentration and flux in the enzymatic catalytic process were derived using the Adomian Decomposition Method and the Taylor series method. The proposed approach

can be effectively applied to a wide range of nonlinear reaction–diffusion equations in immobilized enzyme reactors involving either reversible or simple Michaelis–Menten kinetics, including systems with substrate or product inhibition effects.

References

1. Marshall, RO.: Kooi, ER.: Enzymatic conversion of D-glucose to D-fructose. Science 125, 648-9 (1957).
2. Dadvar, M.: Sahimi, M.: Pore network model of deactivation of immobilized glucose isomerase in packed-bed reactors. Part III: Multiscale modelling. Chemical Engineering Science 58, 4935 – 4951 (2003).
3. Margret Ponrani, V.: Rajendran, L.: Mathematical modelling of steady-state concentration in immobilized glucose isomerase of packed-bed reactors. Journal of Mathematical Chemistry 50, 1333–1346 (2012)
4. Ananthaswamy, V.: Padmavathi, P.: Rajendran, L.: Simple Analytical Expressions of the Steady State Concentration and Flux in Immobilized Glucose Isomerase of Packed - Bed Reactors. Reviews in Bioinformatics and Biometrics 3, 29-37(2014).

5. Selvi, MSM.: Hariharan, G.: Wavelet-Based Analytical Algorithm for Solving Steady-State Concentration in Immobilized Glucose Isomerase of Packed-Bed Reactor Model. Journal Membrane Biology 249(4), 559-68 (2016).

https://doi.org./10.58225/mpmma.2026.654

STEADY-STATE REACTION DIFFUSION ANALYSIS OF MEDIATOR CONCENTRATION IN BIOELECTROCATALYSIS USING THE ADOMIAN DECOMPOSITION METHOD

Ponraj Jeyabarathi[1] and Lakshmanan Rajendran [1]

[1]AMET, Deemed to be University, India

Abstract. The study investigates the steady-state distribution of mediator concentration in a bioelectrocatalytic system using the Adomian Decomposition Method (ADM). The governing nonlinear reaction–diffusion equation, which represents mediator transport coupled with electrochemical reaction within the catalytic layer, is solved analytically via the ADM framework. The analytical solution demonstrates that ADM is an efficient and systematic technique for handling nonlinearities without requiring linearization or perturbation. Consequently, ADM is well-suited for analyzing nonlinear reaction–diffusion phenomena in bioelectrocatalysis and can be extended to more complex systems or higher-order approximations to improve solution accuracy.

Keywords: Bioelectrocatalysis; Nonlinear reaction–diffusion equation; Adomian Decomposition Method (ADM).

1. Introduction

The present model describes the steady-state behavior of mediator transport and enzymatic reaction in a bioelectrocatalytic system. In such systems, an electroactive mediator facilitates electron transfer between the enzyme and the electrode, enabling efficient oxidation of the substrate. The oxidized mediator participates in the enzymatic reaction within the catalytic layer, while the reduced mediator is regenerated at the electrode surface, establishing a coupled reaction–diffusion process. Bioelectrocatalysis refers to an electrochemical process in which biological materials act as catalysts. The enzyme-catalyzed electrode reaction involving a redox mediator is termed mediated bioelectrocatalysis [1]. Ohgaru et al. [2] determined the steady-state limiting current for mediated bioelectrocatalysis assuming that the substrate concentration is much higher than its Michaelis constant. Under steady-state conditions, the enzymatic kinetics are governed by a Michaelis–Menten-type expression, while the spatial distribution of the oxidized mediator is controlled by diffusion and nonlinear consumption due to the reaction. This coupling produces a second-order nonlinear differential equation governing the mediator concentration within the diffusion layer.

Therefore, approximate analytical techniques such as the Adomian Decomposition Method (ADM) are employed to derive accurate and computationally efficient solutions for the mediator concentration profile and the corresponding current response.

2. Mathematical Formulation of the Problem.

The given reaction scheme represents a two–substrate enzyme-catalyzed redox mechanism, which can be written in a clear kinetic form as [2]:

$$S + M_{ox} \overset{K_M}{\Leftrightarrow} S\,M_{ox} \overset{K_{cat}}{\longrightarrow} P + M_{red} \quad (1)$$

where S denotes the substrate, while $M_{ox}$and M_{red}represent the oxidized and reduced forms of the mediator, respectively. SM_{ox} corresponds to the enzyme–substrate–mediator intermediate complex formed during the reaction process.K_M is the effective Michaelis constant, and K_{cat} is the catalytic rate constant. The enzymatic reaction rate under steady-state conditions is described by the Michaelis–Menten equation

$$v_E = \frac{K_{cat}\,[E]}{1+\frac{K_M}{[M_{ox}]}} \quad (2)$$

The reduced mediator is oxidized at the electrode surface as

$$M_{red} \rightarrow M_{ox} + ne^- \quad (3)$$

The steady-state diffusion–reaction equation for the oxidized mediator concentration is

$$D_M \frac{d^2[M_{ox}]}{dX^2} - \frac{K_{cat}[E]}{1+\frac{K_M}{[M_{ox}]}} = 0, \text{ where } K = \frac{K_{cat}[E]}{K_M}.$$

(4)

The boundary conditions are

$$[M_{ox}]_{X=0} = [M_{red}]^*, [M_{ox}]_{X=\delta} = 0, \left(\frac{d\,M_{ox}}{d\,X}\right)_{X=\delta} = 0$$

(5)

Introducing the dimensionless variables

$$u = \frac{[M_{ox}]}{[M_{red}]^*}, x = \frac{X}{\delta}, k = \frac{K\,\delta^2}{D_M}, \alpha = \frac{[M_{red}]^*}{K_M} \quad (6)$$

the governing equation reduces to the nonlinear dimensionless form

$$u''(x) = k\,u(x)[1 + \alpha u(x)]^{-1}$$

(7)

with boundary conditions

$$u(0) = 1, u(1) = 0, \frac{du}{dx}|_{x=1} = 0 \quad (8)$$

The corresponding dimensionless current is

$$\psi = \frac{i\delta}{nFAD_M[M_{red}]^*} = -\frac{du}{dx}|_{x=0}. \quad (9)$$

3.Approximate Analytical Expression of the Concentration using Adomian Decomposition Method.

The Adomian Decomposition Method efficiently solves nonlinear reaction–diffusion equations through rapidly convergent series

solutions without linearization assumptions. [3,4]. The following expression represents an approximate analytical solution for the mediator concentration $u(x)$, valid for all values of the dimensionless parameters kand α using the boundary conditions $u(0) = 1$ and $u(1) = 0$

$$u(x) = 1 - x + k\left[\frac{x^3}{4\alpha} - \frac{x\log(x)}{\alpha^2} + \frac{\log(1+\alpha-\alpha x)}{\alpha^3} + \frac{x\log(x)}{\alpha^2(1+\alpha)} - \frac{x\log(1+\alpha-\alpha x)}{\alpha^2(1+\alpha)} - \frac{x}{4\alpha}\right] \quad (10)$$

using the boundary conditions $u(0) = 1$ and $\frac{du}{dx}|_{x=1} = 0$

$$u(x) = 1 + \frac{k}{(1+\alpha)}\left[\frac{x^2}{2} - x\right] + \frac{k^2}{(1+\alpha)^3}\left[\frac{x^4}{24} - \frac{x^3}{6} + \frac{x}{3}\right] \quad (11)$$

The corresponding dimensionless current is

$$\psi = -\frac{du}{dx}|_{x=0} = \frac{k}{(1+\alpha)} - \frac{k^2}{3(1+\alpha)^3} \quad (12)$$

Conclusion

In conclusion, the steady-state mediator concentration in a bioelectrocatalytic system was successfully analyzed using the Adomian Decomposition Method. The results demonstrated accurate, rapidly convergent solutions with low computational effort, confirming ADM as an efficient and reliable

method for nonlinear bioelectrocatalytic models.

References

1. Hill, H.: Higgins, I.: Philosophical Transactions of the Royal Society of London Series A. 302, 267–273 (1981).

2. Ohgaru,T.: Tatsumi, H.: Kano, K.: Ikeda, T.: Approximate and empirical expression of the steady-state catalytic current of mediated bioelectrocatalysis to evaluate enzyme kinetics. Journal of Electroanalytical Chemistry 496**,** 37–43 (2001).

3. Jeyabarathi, P.: L. Rajendran, L.: Abukhaled,M.: Semi-analytical expressions for the concentrations and effectiveness factor for the three general catalyst shapes. Reaction Kinetics Mechanisms and Catalysis135, 1739–1754 (2022).

4. Adomian, G.: Solving Frontier Problems of Physics: The Decomposition Method. Kluwer Academic Publishers, (1994).

https://doi.org./10.58225/mpmma.2026.660

APPLICATION OF NONLINEAR DIFFERENTIAL EQUATIONS IN LANGMUIR-TYPE ADSORPTION KINETICS

R. Gayathri[1] , L. Rajendran [1]
[1]AMET University, India.

Abstract. This work presents a mathematical analysis of nonlinear adsorption–desorption kinetics describing surface coverage on heterogeneous interfaces. The governing model is formulated as a nonlinear ordinary differential equation in which the adsorption rate depends on fractional surface coverage through a power-law term, capturing interaction effects among adsorbed species. The kinetics are characterized by adsorption and desorption rate constants k_a and k_d, along with bulk concentration C. The system is solved subject to an initially clean surface, and its asymptotic behavior yields the equilibrium coverage. Analytical investigation is carried out to examine the existence, boundedness, and steady-state behavior of solutions, as well as the influence of the interaction exponent n on system dynamics. The nonlinear structure introduces significant deviations from classical linear models, producing distinct transient regimes and modified equilibrium states. Parametric sensitivity analysis highlights the roles of kinetic constants and

nonlinearity in controlling adsorption rates and stability. The formulation extends the classical Langmuir framework and provides a rigorous mathematical basis for describing cooperative and heterogeneous adsorption phenomena, with relevance to catalytic and electrochemical surface processes.
Keywords: Nonlinear adsorption kinetics, Langmuir-type adsorption model, Mathematical modelling.

1. Introduction

Adsorption processes play an important role in catalytic, electrochemical, and environmental systems. Surface adsorption behavior is described by surface coverage, representing the fraction of occupied active sites. The classical Langmuir model assumes uniform adsorption sites and neglects interactions between adsorbed species [1]. However, practical systems exhibit surface heterogeneity and cooperative adsorption effects, leading to nonlinear adsorption–desorption behavior [2,3]. In this work, a nonlinear adsorption–desorption model with a power-law dependence on surface coverage is investigated. The model incorporates an interaction parameter to describe coverage-dependent effects and adsorption dynamics in catalytic and electrochemical systems [4.5].

2. Methodology

The Rajendran Joy method is an analytical approximation technique used to obtain closed-form solutions of nonlinear differential equations in engineering and physical

sciences. It employs an exponential trial function with unknown constants that satisfies the initial and boundary conditions automatically. Substituting this function into the governing equation and equating similar terms determines the unknown parameters analytically. The method yields accurate approximate solutions for transient and steady-state problems and is widely applied in adsorption–desorption kinetics, catalytic reactions, electrochemical systems, and nonlinear transport phenomena.

3. Mathematical formulation of Langmuir-Freundlich kinetics

Langmuir–Freundlich kinetics models nonlinear adsorption incorporating surface heterogeneity and saturation. Competing adsorption–desorption processes drive surface coverage from an initially clean state toward a finite steady-state equilibrium value. The dimensional kinetic equation is written as [6]

$$\frac{d\theta}{dt} = k_a C(1-\theta)^n - k_d\theta \quad (1)$$

where θ is the fractional surface coverage and n is a heterogeneity parameter, The model incorporates adsorption and desorption processes characterized by the rate constants k_a and k_d respectively.

The initial and boundary condition $\theta(0) = 0$ and $\theta(t_L) = \theta_L$.

The dimensionless equation is

$$\frac{d\theta(\tau)}{d\tau} = (1-\theta(\tau))^n - A\theta(\tau) \quad (2)$$

Initial and boundary conditions are $\theta(0) = \theta_0 = 0, \theta(\infty) = \eta.$ (3)

$(1-\eta)^n - A\eta = 0$

(4)

With the initial condition $\theta(0) = 0$. This is a transcendental/nonlinear algebraic equation for general n. An explicit closed-form solution exists only for special values of n.

4. Result and Discussion

The steady-state surface coverage, denoted by $\eta = \theta(\infty)$, is obtained by setting the time derivative of the governing kinetic equation equal to zero. This reduces the problem to an algebraic equation whose form depends on the reaction order n. The equation is

$\frac{d\theta(\tau)}{d\tau} = (1-\theta(\tau))^n - A\theta(\tau)$

(5)

Initial and boundary conditions are $\theta(0) = \theta_0 = 0, \theta(\infty) = \eta.$

Special case:1 If $n = 1$:

$\eta = \frac{1}{A+1}$

(6)

The exact solution is $\theta(\tau) = \frac{1}{1+A}(1 - e^{-(1+A)\tau})$. (7)

Special case:2. If $= 2$:

$\eta = \frac{(A+2)\pm\sqrt{A^2+4A}}{2}$

(8)

The exact solution is $\theta(\tau) = \frac{\theta_1 - \theta_2\left(\frac{\theta_1}{\theta_2}\right)e^{(\theta_1-\theta_2)\tau}}{1-\left(\frac{\theta_1}{\theta_2}\right)e^{(\theta_1-\theta_2)\tau}}$.

Where $\theta_{1,2} = \frac{(A+2)\pm\sqrt{A^2+4A}}{2}$ (9)

Special case: 3. If $= 3$:

$$\eta^3 - 3\eta^2 + (A + 3)\eta - 1 = 0. \quad (10)$$

The trail solution is,

$$\theta(\tau) = \eta\left[1 - (1 + a_1\tau + a_2\tau^2 + a_3\tau^3 + a_4\tau^4)e^{-b\tau}\right]. \quad (11)$$

When n=3, A=1

$$\theta(\tau) = 0.3177[1 - (1 + 0.4133\tau + 1.3787\tau^2 - 0.8344\tau^3 + 0.5740\tau^4)e^{-3.5612\tau}]. \quad (12)$$

When n=3, A=5

$$\theta(\tau) = 0.1312[1 - (1 - 1.8409\tau + 2.8601\tau^2 - 3.6203\tau^3 + 1.8186\tau^4)e^{-5.7828\tau}]. \quad (13)$$

When n=3, A=10

$$\theta(\tau) = 0.0783[1 - (1 - 2.4709\tau + 4.0234\tau^2 - 4.5906\tau^3 + 1.9654\tau^4)e^{-10.3003\tau}]. \quad (14)$$

4.1. Effect of the parameter

The figures present a comparison between numerical and analytical solutions for the nonlinear adsorption–desorption model under different values of the adsorption parameter A and interaction exponent n. The results demonstrate excellent agreement between both approaches and illustrate the influence of model parameters on transient surface coverage dynamics.

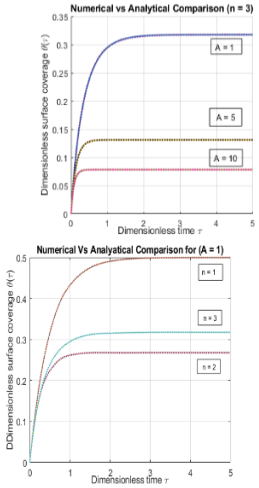


Fig. 1,2. Effects of dimensionless inhibition parameter A and Effect of reaction order / heterogeneity exponent n on fractional surface coverage $\theta(\tau)$.

Fig.1 shows that increasing inhibition parameter A suppresses adsorption, reducing both the rate and equilibrium surface coverage due to stronger site blocking or desorption effects. Fig. 2 indicates that higher heterogeneity exponent n enhances nonlinear interactions, significantly modifying adsorption kinetics and equilibrium levels, reflecting cooperative surface behavior.

5. Conclusion

The nonlinear adsorption–desorption model realistically describes surface coverage dynamics by incorporating interaction effects through the exponent n and kinetic parameters k_a and k_d. Unlike the classical Langmuir model, it captures cooperative and

heterogeneous adsorption behavior observed in practical systems. The model satisfies important physical limits, including clean surface initialization and saturation at equilibrium, providing useful insight into catalytic and electrochemical adsorption mechanisms.

References

1. Azizian, S,: Kinetic models of sorption: A theoretical analysis. Journal of Colloid and Interface Science, 276(1), 47–52(2004).

2. Marczewski, A. W,: Application of mixed-order rate equations to adsorption of methylene blue on mesoporous carbons. Applied Surface Science, 256(17), 5145–5152(2010).

3. Simonin, J. P: On the comparison of pseudo-first-order and pseudo-second-order rate laws in adsorption kinetics. Chemical Engineering Journal, 300, 254–263(2016).

4. Foo, K. Y., & Hameed, B. H: Insights into the modeling of adsorption isotherm systems. Chemical Engineering Journal, 156(1), 2–10(2010).

5. Tran, H. N., You, S. J., & Chao, H. P: Insight into adsorption mechanism of cationic dye onto bio sorbents derived from agricultural wastes. Chemical Engineering Communications, 1020–1036(2017).

6. Azizian, M. Haerifar, J. Basiri-Parsa,: Extended geometric method: A simple approach to derive adsorption rate constants of Langmuir–Freundlich kinetics, Chemosphere 68 2040–2046 (2007).

https://doi.org./10.58225/mpmma.2026.667

APPLICATIONS OF DIFFERENTIAL EQUATIONS IN NONLINEAR ELECTROCHEMICAL REACTION–DIFFUSION PROCESSES

R. Krithiga[1], Lakshmanan Rajendran[1]
[1] AMET University, India,

Abstract. This study focuses on the applications of differential equations in modeling nonlinear electrochemical reaction–diffusion processes occurring in electrode systems. The developed mathematical model describes the coupled interaction between diffusion transport of chemical species and nonlinear electrochemical reaction kinetics at the electrode surface. The governing system consists of nonlinear partial differential equations representing both transient and steady-state behavior of the electrochemical process. Analytical solution techniques are employed to obtain approximate concentration profiles and steady-state distributions. The influence of important physical parameters, including diffusion coefficients, reaction-rate constants, and nonlinear interaction terms, is investigated to understand their effects on concentration evolution and system behavior. The analytical results reveal the significant role of nonlinear reaction–diffusion mechanisms in determining reaction efficiency, mass

transport characteristics, and electrochemical stability. This work demonstrates the importance of differential equation methods in analyzing complex electrochemical systems and provides useful insights for the design, control, and optimization of practical electrode processes in electrochemical engineering applications.
Keywords: Electrochemical reaction kinetics, Electrochemical mass transport, Dimensionless modeling

https://doi.org./10.58225/mpmma.2026.669

FINITE-DIFFERENCE APPROXIMATIONS FOR AN OPTIMAL CONTROL PROBLEM GOVERNED BY AN ELLIPTIC EQUATION WITH PERIODIC BOUNDARY CONDITIONS AND COEFFICIENT-TYPE CONTROL

Rafig Tagiyev[1] *, Aytaj Mammadova*[1]

[1] Baku State University, Azerbaijan

Abstract. An optimal control problem for an elliptic equation with periodic boundary conditions is studied. In the considered problem, the control appears in the state equation as a coefficient multiplying the state variable. The main aim of the work is to construct finite-difference approximations for the problem and to study their convergence properties. For each fixed control, it is proved that the corresponding discrete problem has a unique solution, and a stability estimate is obtained. Error estimates are derived for the difference method with respect to both the state variable and the functional. The convergence rate of the finite-difference approximations for the functional is established. In addition, weak convergence of the approximate controls is proved. To obtain a sequence of controls that converges strongly, a regularization method is applied to the finite-difference approximations. The approach provides a

clear and reliable basis for studying the approximation of the considered optimal control problem.

Keywords: Elliptic Equation, Optimal Control, Difference Approximation.

1.Statement and difference approximation of the problem

Optimal control problems governed by elliptic equations with classical boundary conditions have been widely investigated in the literature. However, analogous problems involving periodic boundary conditions have received comparatively less attention. Such problems arise naturally in many applied fields, including engineering, physics, and medicine. They also occur in inverse problems, such as medical imaging and geophysical exploration, as well as in applications involving optimal shape design and load-distribution control [1], [2].

We consider the following optimal control problem for an elliptic equation:

$$I(v) = \iint_{\Omega} |u(x,v) - u_0(x)|^2 dx \to \min, \tag{1}$$

$$v \in V = \{v = v(x) \in L_2(\Omega): 0 < \mu_1 \le v(x) \le \mu_2, \ \text{a.e.}\ \Omega\}, \tag{2}$$

$$-\sum_{i=1}^{2} \frac{\partial}{\partial x_i}\left(k(x)\frac{\partial u}{\partial x_i}\right) + v(x)u = f(x), \tag{3}$$

$$u|_{x_i=0} = u|_{x_i=l_i}, \qquad i = 1,2,$$

(4)

$$k(x)\frac{\partial u}{\partial x_i}|_{x_i=0} = k(x)\frac{\partial u}{\partial x_i}|_{x_i=l_i}, \qquad i = 1,2.$$

(5)

Here, $l_1, l_2, \mu_1, \mu_2, > 0$ are given numbers, $\Omega = \{x = (x_1, x_2): 0 < x_i < l_i, i = 1,2\}$ is a rectangle in R^2, and $u_0(x), k(x), f(x)$ are given measurable functions satisfying the following conditions:

$$0 < \nu \le k(x) \le \mu, \ \left|\frac{\partial k}{\partial x_i}\right| \le \mu_3, \ x \in \Omega, \ f(x), u_0(x) \in L_2(\Omega), \ i = 1,2,(6)$$

where $\nu, \mu, \mu_3 = \text{const} > 0$.

For each fixed $v \in V$, the solution to the boundary value problem (3)-(5) is understood as a generalized solution in $W_2^1(\Omega)$. It is proved in the work that this problem has a unique solution in $W_2^2(\Omega)$. Furthermore, the optimal control problem (1)-(5) has a solution [3].

We introduce the following grids in the rectangle Ω:

$\underline{\omega}_1 = \{x_{1i} = j_1 h_1: j_1 = 0,1,\dots, N_1, h_1 = l_1/N_1, i = 1,2\}$,

$\underline{\omega}_2 = \{x_{2i} = j_2 h_2: j_2 = 0,1,\dots, N_2, h_2 = l_2/N_2, i = 1,2\}$.

Here, $N_1, N_2 > 0$ are integers, and $h = (h_1, h_2) > 0$ are the grid steps corresponding to the variables $x = (x_1, x_2)$, with $|h|^2 = h_1^2 + h_2^2$. The remaining notation used below is the same as that in [4].

We now define a family of grid optimal control problems corresponding to the problem (1)-(5):

$$I_h(v_h) = \sum_{x \in \omega^+} |y(x, v_h) - u_{0h}(x)|^2 h_1 h_2, \quad (7)$$

$$v_h \in V_h = \{v_h = v_h(x) \in L_2(\omega): 0 < \mu_1 \le v_h(x) \le \mu_2, \ x \in \omega\}, \quad (8)$$

$$\Lambda_h y \equiv -\sum_{i=1}^{2} \left(k^{(-0,5_i)}(x) y_{\underline{x}_i}\right)_{x_i} + v_h(x) y = \varphi_h(x), \quad x \in \omega, \quad (9)$$

$$y|_{x_1=0} = y|_{x_1=l_1}, \quad x_2 \in \underline{\omega}_2, \quad y|_{x_2=0} = y|_{x_2=l_2}, \quad x_1 \in \underline{\omega}_1, \quad (10)$$

$$k^{(-0,5_1)} y_{\underline{x}_1}|_{x_1=h_1} = k^{(-0,5_1)} y_{\underline{x}_1}|_{x_1=l_1}, \quad x_2 \in \omega_2,$$

$$k^{(-0,5_2)} y_{\underline{x}_2}|_{x_2=h_2} = k^{(-0,5_2)} y_{\underline{x}_2}|_{x_2=l_2}, \quad x_1 \in \omega_1, \quad (11)$$

here

$$\varphi_h(x) = S_1 S_2 f(x), \ u_{0h}(x) = S_1 S_2 u_0(x), \ x \in \omega.$$

1 Error estimates for the approximations with respect to the state and the functional. The convergence rate with respect to the functional

Theorem 1. Suppose that the conditions in the statement of problem (1)-(5) are satisfied. Then, the error estimate for the finite-difference approximation with respect to the state is as follows:

$$\|y - u\|_{W_2^1(\omega)} \le C_1\big(|h| + \|v_h(x) - S_1 S_2 v(x)\|_{0,\omega}\big)\|u\|_{W_2^2(\Omega)}.$$

Let $C_j, j = 1,2,\ldots$, denote positive constants independent of the estimated quantities and possible controls.

Theorem 2. Let the conditions of Theorem 1 be satisfied. Then, for arbitrary controls $v \in V$ and $v_h \in V_h$, the following error estimate for the grid functional (7) holds:

$$|I(v) - I_h(v_h)| \le C_2\big[|h| + \|v_h(x) - S_1 S_2 v(x)\|_{0,\omega}\big].$$

To study the relationship between problems (1)-(5) and (7)-(11), we introduce the mapping

$$P_h: W_2^1(\omega) \to W_2^1(\Omega),$$

defined as follows:

$$P_h\big(v_h(\xi)\big) = v(x), \qquad \xi \in e^*(x), \quad x \in \omega.$$

Theorem 3. Let the conditions of Theorem 1 be satisfied. Then, for the convergence of the family of problems (7)-(11) with respect to the functional, the following estimate holds:

$$|I_{h*} - I_*| \le C_3|h|.$$

Here,

$$I_* = \inf \inf \{I(v): v \in V\}, \quad I_{h*} = \inf \inf \{I_h(v_h): v_h \in V_h\}.$$

If the sequence of controls $\{v_{h\varepsilon}\}$ is determined by the conditions

$v_{h\varepsilon} \in V_h,\ I_{h*} \le I_h(v_{h\varepsilon}) \le I_{h*} + \varepsilon_h,\ \varepsilon_h \ge 0,$ $\varepsilon_h \to 0$ as $|h| \to 0,$

then the sequence $\{P_h(v_{h\varepsilon})\}$ satisfies the estimate

$0 \le \{I(P_h(v_{h\varepsilon}))\} - I_* \le C_4|h| + \varepsilon_h$.

To study the strong convergence of the control sequence obtained from approximations (7)-(11) in $L_2(\Omega)$, we apply Tikhonov's regularization method. This method allows us to obtain the convergence of the minimizing sequence of controls with respect to the $L_2(\Omega)$-norm [5].

References

1. Troeltzsch, F.: Optimal Control of Partial Differential Equations: Theory, Methods and Applications. American Mathematical Society, Providence (2010).
2. Isakov, V.: Partial Inverse Problems for Differential Equations. Springer, New York (2006).
1. Ladyzhenskaya, O.A.: Boundary Value Problems of Mathematical Physics. Nauka, Moscow (1973).
2. Samarskii, A.A., Lazarov, R.D., Makarov, V.L.: Difference Schemes for

Differential Equations with Generalized Solutions. Higher School, Moscow (1987).
Vasil'ev, F.P.: Methods for Solving Extremal Problems. Nauka, Moscow (1981

https://doi.org./10.58225/mpmma.2026.676

A RELATIONAL DATABASE FRAMEWORK FOR REAL-TIME MANUFACTURING COST MONITORING: DESIGN AND IMPLEMENTATION

Ramazan Guliyev, Gulnar Mirzayeva
Academy of Public Administration under the President of the Republic of Azerbaijan, Azerbaijan

Abstract. This paper proposes a relational database framework for manufacturing cost monitoring. Eight normalised tables and four SQL analytical views are implemented on Microsoft SQL Server Express. A food-and-beverage case study confirms sub-20 ms query times and direct Power BI integration. The framework separates fixed and variable costs, enforces referential integrity, and is deployable at near-zero licensing cost.

Keywords: relational database, cost monitoring, SQL, ERP, business intelligence.

1 Introduction

Most SMEs in transition economies rely on spreadsheets for cost management [1], preventing real-time visibility. ERP systems are too costly for SMEs [2]. A lightweight relational schema fills this gap by enforcing data consistency, enabling SQL analytics, and connecting to free BI tools. Contributions: (i) normalised eight-table schema; (ii) four

reusable SQL views; (iii) Power BI integration; (iv) real-data evaluation.

2 Related Work

Date's relational model [4] underpins modern RDBMS. Kaplan and Anderson's TDABC [5] requires explicit cost-pool separation — reflected in our schema. Hüseynov [6] identified cost and complexity as key ERP barriers in Azerbaijan; a lightweight schema addresses both.

3 Database Framework Design

3.1 Schema Overview

Eight tables split into reference (Products, Customers, Suppliers, Cost Categories) and transaction (Inventory, Orders, Sales, Cost Events). Foreign-key constraints enforce integrity. A BIT column sabit_mi separates fixed from variable costs.

3.2 Key Table Structures

Table 1. Transaction table structure.

Table	PK	Foreign Keys	Key Attributes
Anbar Stok	stok_id	mehsul_id → Mehsullar	miqdar, min_stok
Sifarisler	sifaris_id	musteri_id, mehsul_id	kemmiyyet, status
Satis	satis_id	sifaris_id, mehsul_id	cemi_satis, menfeet
Xercler	xerc_id	nov_id, mehsul_id (null)	mebleg, sabit_mi

3.3 Analytical Views

Four views feed Power BI directly: vw_AyliqSatis (monthly sales/margin);

vw_StokVeziyyeti (stock alerts); vw_XercAnalizi (fixed/variable breakdown); vw_MusteriXulase (customer totals). Alert logic:

```
CASE WHEN miqdar<=0 THEN 'KRİTİK'
   WHEN miqdar<=min_stok THEN 'AZ STOK'
   ELSE 'NORMAL' END AS status
```

4 Implementation and Evaluation

4.1 Case Study

Deployed on SQL Server Express 2022 with 7 products, 6 customers, 8 orders, 7 sales, and 20 cost events from a food-and-beverage company. Five covering indexes added on date, product, and cost-centre columns.

4.2 Query Performance

Table 2. View execution times.

View	Rows	ms	Index
vw_AyliqSatis	14	12	IX_Satis_Tarix
vw_StokVeziyyeti	7	8	IX_AnbarStok
vw_XercAnalizi	16	15	IX_XercH_Tarix
vw_MusteriXulase	6	9	Full scan

All views execute under 20 ms. Power BI connected via native SQL Server connector; live dashboard operational within 15 minutes.

4.3 Inventory Update

Each sale decrements stock via Python/Flask:
UPDATE AnbarStok SET miqdar=miqdar-:qty WHERE mehsul_id=:id;
A pre-check prevents negative inventory.

5 Conclusion

A lightweight eight-table relational schema for manufacturing cost monitoring was proposed and validated. Sub-20 ms queries and direct Power BI integration were confirmed. The framework offers SMEs a near-zero-cost entry point to digital transformation. Future work will add budget tables for variance reporting and test PostgreSQL portability.

References

1. WEF/C4IR Azerbaijan: IDEA — Investing in the Digital Economy of Azerbaijan (2024).
2. Hüseynov, T.X.: ERP Systems and Enterprise Management. ADA University Press (2022).
3. Monk, E., Wagner, B.: Concepts in Enterprise Resource Planning. Cengage (2013).
4. Date, C.J.: An Introduction to Database Systems. Addison-Wesley (2004).
5. Kaplan, R.S., Anderson, S.R.: Time-Driven Activity-Based Costing. HBR Press (2007).

6. Bəşirov, E.M., Quliyev, R.S.: Fundamentals of Management Accounting. İqtisad Universiteti (2020).
7. Microsoft: SQL Server 2022 Documentation. https://docs.microsoft.com/sql (2025).
8. Microsoft: Power BI SQL Server Connector. https://docs.microsoft.com/power-bi (2025).
9. Coronel, C., Morris, S.: Database Systems. 13th edn. Cengage (2019).
10. Schwab, K.: The Fourth Industrial Revolution. Worl

https://doi.org./10.58225/mpmma.2026.681

APPLICATION OF MACHINE LEARNING METHODS FOR COST FORECASTING IN MANUFACTURING ENTERPRISES: A COMPARATIVE STUDY

Ramazan Guliyev , Gulnar Mirzayeva
Academy of Public Administration under the President of the Republic of Azerbaijan,
Baku, Azerbaijan

Abstract. This paper presents a comparative study of machine learning (ML) algorithms for forecasting production costs in manufacturing enterprises. Five algorithms are evaluated — Linear Regression, Random Forest, XGBoost, LSTM neural network, and an Ensemble method — using 72 months of real financial data (2019–2024) from a global food-and-beverage corporation. The Ensemble model (XGBoost + RF + LSTM stacking) achieves MAPE = 0.76% and R^2 = 98.1%, outperforming all individual models. An anomaly detection subsystem based on Isolation Forest achieves 85.7% sensitivity with a 3.2% false-positive rate. Findings contribute methodological foundations for the digital transformation of Azerbaijani manufacturing enterprises.

Keywords: machine learning, cost forecasting, ensemble methods, LSTM, manufacturing cost management, anomaly detection, digital transformation.

1 Introduction

Accurate cost forecasting is a strategic challenge of modern management accounting. Traditional methods — moving averages, exponential smoothing, ARIMA — model linear patterns well but fall short in capturing non-linear trends, seasonality, and complex multivariate interactions [1]. Rapid ML advancement over the past decade has opened avenues to address these limitations. Existing literature addresses cost forecasting predominantly through single-component studies — energy costs [2] or raw material prices [3] — leaving a gap in multi-component, cross-algorithm comparative analyses on real industrial data. This paper fills that gap by systematically comparing five ML algorithms on authentic financial data, integrating an anomaly detection module, and deriving recommendations for Azerbaijani manufacturing enterprises.

2 Related Work

Deep learning for energy cost forecasting was explored by Cai et al. [2], demonstrating LSTM superiority over classical methods. Kim and Park [3] applied XGBoost to food-industry raw material price prediction, highlighting its advantage in capturing nonlinearity. Breiman's Random Forest [4]

and Chen and Guestrin's XGBoost [5] are widely adopted in industrial forecasting. Ensemble superiority over single learners is confirmed across multiple studies [6]. For anomaly detection, Liu et al.'s Isolation Forest [8] is established as an efficient real-time detector for high-dimensional data [7].

3 Methodology

3.1 Dataset

Monthly cost data (2019–2024, n = 72) from a global food-and-beverage corporation are used, incorporating 8 predictor variables: production volume, raw material price index, energy price index, labour cost index, USD/CHF exchange rate, seasonality index, lagged cost (t−1), and lagged difference. The target variable is monthly total production cost (CHF bn). An 80/20 train-test split is applied.

3.2 Algorithms

(1) Linear Regression (LR) — baseline; (2) Random Forest (RF, n = 200 trees, max_features = $\sqrt{p}$); (3) XGBoost (n = 300, lr = 0.05, depth = 6); (4) LSTM (2 layers × 128 units, Dropout = 0.2, 12-month sliding window); (5) Ensemble — stacking of XGBoost, RF, and LSTM with LR meta-learner.

3.3 Evaluation Metrics

Mean Absolute Percentage Error (MAPE) and coefficient of determination (R^2) are used as primary performance metrics.

4 Experimental Results

4.1 Algorithm Comparison

Table 1 reports MAPE and R^2 on the hold-out test set for all five algorithms.

Algorithm	MAPE (%)	R^2 (%)	Training Time
Linear Regression (LR)	1.42	94.8	< 1 sec
Random Forest (RF)	1.08	96.4	45 sec
XGBoost	0.94	97.1	38 sec
LSTM (2-layer)	0.86	97.6	8 min
Ensemble (XGB+RF+LSTM)	0.76	98.1	10 min

Table 1. Comparative evaluation of cost forecasting algorithms.

The Ensemble model achieves the best accuracy (MAPE = 0.76%, R^2 = 98.1%). Although the difference relative to LR (0.66 percentage points) appears modest, it translates to substantial monetary savings at industrial scale. LSTM outperforms RF and XGBoost individually owing to its capacity to capture long-term temporal dependencies; however, its 8-minute training time may be a constraint for real-time operational deployment.

4.2 Anomaly Detection Results

An Isolation Forest anomaly detection module was applied to the 2024 energy consumption time series. The system correctly identified 6 out of 7 anomaly events in the 24-month test period (sensitivity 85.7%), with a false-positive rate of 3.2% — within acceptable bounds for industrial cost monitoring. Anomalies were flagged when observations exceeded the $+2\sigma$ threshold of the normal consumption range.

5 Discussion

Three key findings emerge. First, ensemble superiority: combining tree-based (XGBoost, RF) and sequence-based (LSTM) learners yields superior generalisation [6], reflecting heterogeneous statistical properties of multi-component production costs. Second, seasonality impact: removing the seasonality index raised MAPE by 0.38 pp for LR and 0.27 pp for XGBoost, confirming that seasonality must be explicitly modelled. Third, the anomaly detector's false-positive rate (3.2%) is operationally acceptable; a three-tier alert scheme — informational / attention / critical — is recommended to prevent alert fatigue. Limitations: the study relies on a single enterprise dataset; generalisability requires additional empirical

work. LSTM's high compute demand may hinder real-time deployment; model compression is suggested for future research.

6 Conclusion

This paper establishes the superiority of ensemble ML methods for manufacturing cost forecasting and demonstrates the operational viability of Isolation Forest-based anomaly detection. A practical adoption pathway is proposed: begin with LR, progress to XGBoost, then advance to the full ensemble as data matures. Integration of anomaly detection with ERP systems is recommended as an immediate step toward intelligent cost governance. Future work will explore Transformer architectures for cost time-series modelling and federated learning for privacy-preserving multi-enterprise training.

References

1.Box G.E.P., Jenkins G.M., Reinsel G.C., Ljung G.M.: Time Series Analysis: Forecasting and Control. 5th edn. Wiley (2015).

2.Cai M., Pipattanasomporn M., Rahman S.: Day-ahead building-level load forecasts using deep learning vs. traditional time-series techniques. Appl. Energy 236, 1078–1088 (2019).

3.Kim J., Park J.: Forecasting Manufacturing Costs Using XGBoost: Application to Food Industry. J. Manuf. Syst. 58, 420–431 (2020).
4.Breiman L.: Random forests. Mach. Learn. 45(1), 5–32 (2001).
5.Chen T., Guestrin C.: XGBoost: A scalable tree boosting system. Proc. 22nd ACM S.IGKDD, pp. 785–794 (2016).
6.Dietterich T.G.: Ensemble methods in machine learning. MCS 2000, LNCS 1857, pp. 1–15 (2000).
7.Chandola V., Banerjee A., Kumar V.: Anomaly detection: A survey. ACM Comput. Surv. 41(3) (2009).
8.Liu F.T., Ting K.M., Zhou Z.H.: Isolation forest. Proc. ICDM 2008, pp. 413–422. IEEE (2008).
9.Hochreiter S., Schmidhuber J.: Long short-term memory. Neural Comput. 9(8), 1735–1780 (1997).
10.McKinsey Global Institute: The Age of AI: A Manufacturing Perspective. McKinsey & Company (2023).
11.WEF / C4IR Azerbaijan: IDEA: Investing in the Digital Economy of Azerbaijan. World Economic Forum (2024).

12.Schwab K.: The Fourth Industrial Revolution. World Economic Forum, Geneva (2016).

https://doi.org./10.58225/mpmma.2026.689

THE STEKLOV PROBLEM FOR AN ORDINARY DIFFERENTIAL EQUATION WITH FRACTIONAL DERIVATIVES

Ramin Zeynalov[1] *, Nihan Aliyev*[2]
[1]Institute of Mathematics, Azerbaijan
[1]AZUAC, Azerbaijan
[2]Baku State University, Azerbaijan

Abstract. In the presented work, for ordinary linear constant coefficient homogeneous fractional order differential equations, the solution of the Steklov problem, where the spectral parameter is involved only in the boundary condition, is investigated. The general solution of the considered equation is sought in the form of a parameter-dependent modified Mittag-Leffler series. The constants included in the general solution are determined from the given boundary conditions, and analytical expressions are obtained for the finite number of eigenvalues and eigenfunctions of the set boundary problem.

Keywords: Mittaq-Leffler series, boundary condition, eigenvalue, eigenfunction.

It should be noted that fractional-order differential equations have been extensively studied in [1,2]. In our previous works [4,5], we investigated solutions to the Cauchy problem and boundary value problems for fractional-order differential equations.

Problem statement

Let us consider the following problem:

$$D^{\frac{2}{7}}y(x) + pD^{\frac{1}{7}}y(x) + qy(x) = 0, \quad x \in (a,b),\ 0 \notin (a,b) \qquad (1)$$

$$y(b) = \lambda y(a), \quad D^{\frac{1}{7}}y(x)|_{x=b} = \lambda D^{\frac{1}{7}}y(x)|_{x=a} \qquad (2)$$

where $p, q \in \mathbb{R}$ are given constants and λ denotes the spectral parameter.

The solution of the problem

Let us find the solution to equation (1) in the form of a modified Mittag-Leffler series:

$$y(x) \equiv y(x,\rho) = \frac{x^{-1+\frac{1}{7}}}{\left(-1+\frac{1}{7}\right)!} + \rho\frac{x^{-1+2\cdot\frac{1}{7}}}{\left(-1+2\cdot\frac{1}{7}\right)!} + \rho^2\frac{x^{-1+3\cdot\frac{1}{7}}}{\left(-1+3\cdot\frac{1}{7}\right)!} + \cdots + = \sum_{k=0}^{\infty}\rho^k\frac{x^{-1+(k+1)\frac{1}{7}}}{\left(-1+(k+1)\frac{1}{7}\right)!} \qquad (3)$$

where ρ is an unknown parameter.
We differentiate (3) as follows:

$$D^{\frac{1}{7}}y(x) = D^{\frac{1}{7}}y(x,\rho) = \frac{x^{-1}}{(-1)!} + \rho\frac{x^{-1+\cdot\frac{1}{7}}}{\left(-1+\frac{1}{7}\right)!} + \rho^2\frac{x^{-1+2\cdot\frac{1}{7}}}{\left(-1+2\cdot\frac{1}{7}\right)!} + \cdots + =$$

$$= \sum_{k=0}^{\infty}\rho^k\frac{x^{-1+k\cdot\frac{1}{7}}}{\left(-1+k\cdot\frac{1}{7}\right)!} = f(x) + \rho\frac{x^{-1+\cdot\frac{1}{7}}}{\left(-1+\frac{1}{7}\right)!} + \rho^2\frac{x^{-1+2\cdot\frac{1}{7}}}{\left(-1+2\cdot\frac{1}{7}\right)!} + \cdots + =$$

$$= \rho\left[\frac{x^{-1+\cdot\frac{1}{7}}}{\left(-1+\frac{1}{7}\right)!} + \rho^2\frac{x^{-1+2\cdot\frac{1}{7}}}{\left(-1+2\cdot\frac{1}{7}\right)!} + \cdots\right] = \rho y(x,\rho),$$

in the same way,

$$D^{\frac{2}{7}}y(x,\rho) = \rho^2 y(x,\rho).$$

If we substitute the obtained expressions into equation (1), we obtain:

$$\rho^2 y(x,\rho) + p\rho\, y(x,\rho) + qy(x,\rho) = 0$$

or

$$\rho^2 + p\rho + q = 0 \quad (4)$$

$$\rho = -\frac{p}{2} \pm \sqrt{\frac{p^2}{4} - q}$$

let's accept that,

$$\rho^2 - 4q > 0, \quad (5)$$

$$\rho_1 = -\frac{p}{2} - \sqrt{\frac{p^2}{4} - q} \in \mathbb{R}, \quad \rho_2 = -\frac{p}{2} + \sqrt{\frac{p^2}{4} - q} \in \mathbb{R}, \quad (6)$$

here,

$$\rho_1 \neq \rho_2$$

Thus, we obtain the following general solution for equation (1):

$$y(x) = C_1 y(x,\rho_1) + C_2 y(x,\rho_2), \quad (7)$$

Let us write the general solution of (7) in terms of boundary conditions (2):

$$\begin{cases} C_1 y(b,\rho_1) + C_2 y(b,\rho_2) = \lambda[C_1 y(a,\rho_1) + C_2 y(a,\rho_2)], \\ C_1\rho_1 y(b,\rho_1) + C_2\rho_2 y(b,\rho_2) = \lambda[C_1\rho_1 y(a,\rho_1) + C_2\rho_2 y(a,\rho_2)], \end{cases} \quad (8)$$

Let's put system (8) into normal form:

$$\begin{cases} [y(b,\rho_1)-\lambda y(a,\rho_1)]C_1+[y(b,\rho_2)-\lambda y(a,\rho_2)]C_2=0, \\ \rho_1[y(b,\rho_1)-\lambda y(a,\rho_1)]C_1+\rho_2[y(b,\rho_2)-\lambda y(a,\rho_2)]C_2=0. \end{cases} \quad (9)$$

The condition for the existence of a non-trivial solution of a system of homogeneous algebraic equations (9) is that its determinant is zero [3].

$$\Delta(\lambda) = \begin{vmatrix} y(b,\rho_1)-\lambda y(a,\rho_1) & y(b,\rho_2)-\lambda y(a,\rho_2) \\ \rho_1[y(b,\rho_1)-\lambda y(a,\rho_1)] & \rho_2[y(b,\rho_2)-\lambda y(a,\rho_2)] \end{vmatrix} = 0,$$

$$[y(b,\rho_1)-\lambda y(a,\rho_1)][y(b,\rho_2)-\lambda y(a,\rho_2)]\begin{vmatrix} 1 & 1 \\ \rho_1 & \rho_2 \end{vmatrix} = [y(b,\rho_1)-\lambda y(a,\rho_1)][y(b,\rho_2)-\lambda y(a,\rho_2)](\rho_2-\rho_1)=0, \quad (10)$$

$$y(a,\rho_1)\neq 0, \quad y(a,\rho_2)\neq 0 \quad (11)$$

$$\lambda_1=\frac{y(b,\rho_1)}{y(a,\rho_1)}, \quad \lambda_2=\frac{y(b,\rho_2)}{y(a,\rho_2)} \quad (12)$$

The expressions (12) represent the eigenvalues of the Steklov problem (1)–(2). Let us now define the corresponding eigenfunctions. From system (9),

$$y(b,\rho_2)-\lambda_k y(a,\rho_2)\neq 0, \quad k=1,2 \quad (13)$$

We get:

$$C_2=-\frac{y(b,\rho_1)-\lambda_k y(a,\rho_1)}{y(b,\rho_2)-\lambda_k y(a,\rho_2)}C_1, \quad (14)$$

$$y_k(x) = C_k\left\{y(x,\rho_1) - \frac{y(b,\rho_1)-\lambda_k y(a,\rho_1)}{y(b,\rho_2)-\lambda_k y(a,\rho_2)}\, y(x,\rho_2)\right\},\quad k = 1,2 \tag{15}$$

Thus, we obtain the following result.

Theorem. If ρ and q are given real numbers , $\rho_1 \neq \rho_2$ are of the form (6), then under the conditions $y(a,\rho_k) \neq 0,\ k = 1,2$ the eigenvalues of problem (1)-(2) are given by (12), and under the conditions (13), the eigenfunctions are given by (15). Here C_k are arbitrary constants. By choosing these constants appropriately, the functions in (15) can be normalized.

Conclusions

Eigenvalues and eigenfunctions have been determined for a linear homogeneous ordinary fractional differential equation with constant coefficients. One can familiarize oneself with such problems in [6].

References

1. Samko, S.G., Kilbas, A.A., Marichev, O.I.: Fractional Integrals and Derivatives: Theory and Applications, Gordon and Breach Science Publishers, Yverdon, Switzerland, 1993, 780 p.

2. Kilbas, A.A., Srivastava, H.M., & Trujillo, J.J.: Theory and applications of

fractional differential equations (2006, Vol. 204). Elsevier.
3. Strang, G.: Introduction to Linear Algebra. Wellesley-Cambridge Press
4. Aliyev, N.A., Zeynalov, R.M.: A boundary value problem for a fractional differential equation. Proceedings of the II Republican Scientific Conference on Differential and Integral Operators. December 3-4, 2024, Baku State University, pp. 62-63.
5. Aliyev, N.A., Rasulov, M.A., Sinsoysal, B.S.: Investigation of the solution of a half-order elliptic type equation with non-local boundary condition (English) Logic Journal of the IGPL, Oxford University Press, Oxford, England, Volume 33, Issue 6, December 2025
6. Home page of Professor Dr. NIHAN Aliev, http://nihan.jsoft.ws

https://doi.org./10.58225/mpmma.2026.695

SOLVING A CUBICALLY NONLINEAR OSCILLATION PROBLEM USING THE OPERATIONAL METHOD

Ramiz Iskanderov[1], Alabbas Akhiev[2]
[1]AzUAC, Azerbaijan
[2]Azerbaijan. Technical University, Azerbaijan

Abstract. The free unsteady oscillations of a mechanical system with a cubically nonlinear differential equation are solved by the operational method. The oscillation frequencies are obtained using precise mathematical methods depending on the nonlinearity parameter and the initial conditions. The solution to the problem is obtained as the sum of two harmonics. It is proved that the obtained solution is accurate. The complexity of solving these problems in comparison with linear ones is due to the lack of theory for constructing exact solutions to nonlinear differential equations. Due to the nonlinearity of the equation, the principle of superposition, widely used in linear theory, is not satisfied. Individual harmonics of vibrations interact with each other, because of which it becomes impossible to individually study the behavior of each harmonic component of vibrations separately. A very effective method for studying nonlinear oscillations is the

methods of asymptotic power expansions of a small parameter. On this basis, nonlinear oscillations and mathematical methods of their research have been greatly developed.

Keywords: Unsteady fluctuations, the operational method, Duffing oscillator, Laplace integral transformations.

1.Introduction.

The foundations of the theory of nonlinear oscillations were laid back in the first half of the twentieth century. The basis for the development of oscillation theory was mechanics, aerohydrodynamics, electricity, quantum electronics, solid-state physics, astrophysics, atmospheric and ocean physics, chemical kinetics, biophysics and many other fields of science. Such a wide range of sciences is because the subject of oscillation theory is determined by the presence of oscillatory movements, regardless of the physical nature of the phenomena under consideration.

2.Statement of problem.

Let us consider a nonlinear differential equation of free oscillations of an elastic system of the form

$$\ddot{x} + \omega_0^2 x + 2\beta x^3 = 0, \quad (1)$$

Where $x(t)$ – is an unknown function, t - the independent variable, the dot at the top indicates the time derivativet, ω_0^2– the square of the natural oscillation frequency of a linear system, β - small parameter of non-linearity If, $\beta > 0$ in the mechanical

interpretation, they speak of the resistance of a “hard” spring, and if they speak of $a\beta < 0$ “soft" spring.

Equation (1) is solved under the following initial conditions $att = 0$:

$$x(0) = x_0, \dot{x}(0) = x_1. \quad (2)$$

The solution of the problem (1), (2) is sought by the operational method. The line at the top indicates the integral Laplace transformations of the functions of the same name, for example

$$\overline{x^3}(p) = \int_0^\infty x^3(t)\, e^{-pt} dt.$$

Where p is the conversion parameter. Applying this transformation to equation (3), we obtain

$$p^2\bar{x} + 2\beta\overline{x^3} + \omega_0^2\bar{x} = x_0 p + x_1.$$

The image of the desired function is in the form

$$\bar{x} = \frac{x_0 p + x_1}{p^2 + 2\beta\overline{x^3}/\bar{x} + \omega_0^2}. \quad (3)$$

Thus, the solution of the problem is reduced to calculating the inverse Laplace transform of the function (3). To do this, we need to find the singular points of the function on the right side, which are the roots of the denominator of the fraction (3), i.e.

$$p^2 + \omega_0^2 + 2\beta\overline{x^3}/\bar{x} = 0. \quad (4)$$

The motion of the system under consideration is approximately represented as

$$x = a\cos(kt+\theta)$$

Calculate the image $\overline{x^3}/\bar{x}$:

$$\frac{\overline{x^3}}{\bar{x}}$$

$$= \frac{a^2}{4}\left(3\frac{p}{p^2+\omega^2}+\frac{p}{p^2+(3\omega)^2}\right)\Big/\frac{p}{p^2+\omega^2}$$

Substituting this into the characteristic equation (4), we obtain

$$\left[p^4+\left(10\omega_0^2+2\beta a^2\right)p^2+9\,\omega_0^4+14\beta a^2\omega_0^2\right](p^2+9\omega_0^2)^{-1}=0. \qquad (5)$$

The zeros of this biquadrate equation will be

$$\omega_1^2 = \omega_0^2+\frac{3}{2}\beta a^2-\frac{3}{32}\beta^2\frac{a^4}{\omega_0^2}-\frac{3}{256}\beta^3\frac{a^6}{\omega_0^4}+\ldots$$

$$\omega_3^2 = 9\omega_0^2+\frac{1}{2}\beta a^2+\frac{3}{32}\beta^2\frac{a^4}{\omega_0^2}+\frac{3}{256}\beta^3\frac{a^6}{\omega_0^4}+\ldots$$

These values are the squares of the frequencies of the fundamental and third harmonics.

The nonlinearity of the oscillation equation will affect the frequency of the first harmonic more than the frequency of the third harmonic. The same effect is exerted by the amplitude of the oscillations or the initial conditions.

At $\beta > 0$ they increase, and at $\beta < 0$ they decrease. However, as the frequency of natural linear

oscillations increases, the frequencies $\omega_1$and $\omega_3$decrease.

Equation (5) is written as

$$(p^2 + \omega_1^2)(p^2 + \omega_3^2)(p^2 + 9\omega_0^2)^{-1} = 0$$

and substitute it into formula (3)

$$\overline{x} = \frac{(x_0 + x_1)(p^2+9\omega_0^2)}{(p^2+\omega_1^2)(p^2+\omega_3^2)}.$$

Decomposing the right side of this equality into the sum of simple fractions, we find the original

$$x(t) = I_1\left[x_0\cos(\omega_1 t) + \frac{x_1}{\omega_1}\sin(\omega_1 t)\right] + I_3\left[x_0\cos(\omega_3 t) + \frac{x_1}{\omega_3}\sin(\omega_3 t)\right] \quad (6)$$

Here

$$I_1 = \frac{9\omega_0^2 - \omega_1^2}{\omega_3^2 - \omega_1^2}, \quad I_3 = \frac{\omega_3^2 - 9\omega_0^2}{\omega_3^2 - \omega_1^2} \quad (7)$$

This formula is an exact solution to the problem (1) - (2). Indeed, let us check the initial conditions: in equation (14) we substitute

$$x(0) = I_1x_0 + I_3x_0 = (I_1 + I_3)x_0 = x_0.$$

Calculating the derivative of (14), we determine the velocity and substitute zero instead of $t = 0$.

$$x'(0) = I_1 x_1 + I_3 x_1 = (I_1 + I_3)\, x_1 = x_1.$$

Thus, solution (6) exactly satisfies the initial conditions (2). We write the solution as

$$x(t) = a\cos\omega_1 t + aI_3(\cos\omega_3 t - \cos\omega_1 t), \quad (8)$$

With an accuracy of up to the square of a small parameter, the harmonic coefficients vanish. Thus, formula (8) satisfies equation (3) and is an exact solution to the problem (1) - (2). The oscillation period of the first harmonic has the form

3 Conclusions

1. Using the well-known trigonometric identity, replacing the cosine cube with the sum of cosines of the first degree in the Laplace image space, we obtain a linear integro-differential equation of the second order equivalent to the cubically nonlinear differential equation of oscillation.

2. A biquadrate characteristic equation is found for determining the frequency of oscillations, which are also the poles of the integrand function of the Mellin–Bromwich integral. Two equations for determining the squares of frequencies by the method of successive approximations are also found.

References

1. Bogolyubov N.N., Mitropolsky Yu.A. Asymptotic methods in the theory of

nonlinear oscillations. Moscow, Nauka, 1974.
2. Panovko Ya.G. Introduction to the theory of mechanical vibrations. Moscow, Nauka, 1991.
3. Dech G. A guide to the practical application of the Laplace transform. Moscow, Nauka, 1965.
4. Eiderman V. Ya. Operational calculus. Fizmatlit, 2002, p256.
5. Kuznetsov A.P., Kuznetsov S.P., Ryskin N.M. Lectures on the theory of oscillations and waves. Nonlinear oscillations. Saratov, 2011.
6. Wolfson I.I. A short course in the theory of mechanical vibrations. Moscow, 2017.
7. R.A.Iskanderov, J.M.Tabatabaei, "Vibrations of fluid-filled inhomogeneous cylindrical shells strengthened with lateral ribs", International Journal on "Technical and Physical Problems of Engineering" (IJTPE), Issue 42, Vol 12, No 1, pp. 121-125, March 2020.

https://doi.org./10.58225/mpmma.2026.702

ALGORITHM FOR SOLVING OPTIMIZATION PROBLEMS OF ELEMENTS OF BENT STRUCTURES, TAKING INTO ACCOUNT THE COMBINED EFFECT OF FORCE LOADS AND AGGRESSIVE ENVIRONMENT

Ramiz Iskanderov , Jamal Mammadov
AzUAC, Azerbaijan

Abstract. Core structures are widely used in construction and many industries, such as chemical, oil refining, gas, metallurgical, agricultural and others, while being influenced not only by thermal force loads, but also by aggressive environments, leading to a significant reduction in load-bearing capacity and shortening their service life. It is obvious from the literature review that, despite the existence of quite extensive results in the direction of optimal design of structures taking into account an aggressive environment, most of the current research is devoted to the consideration of simplified design schemes, and the solution of the applied aspects of the problem is still far from complete, since optimizing the parameters of a real structure operating under extreme external loads requires a number of time-dependent limitations, such as limitations on strength, rigidity, durability,

etc. At the same time, it is particularly difficult to meet the conditions of durability. Difficulties arise due to the need to repeatedly integrate the differential equations of the selected mathematical model of corrosion damage over time for each of the surface points of the structural force element in order to verify the fulfillment of the corresponding constraints at each step of the search algorithm, which leads to both the accumulation of corresponding computational errors and significant complexity of solving the problem as a whole. Thus, the problem of developing a new, more efficient approach to solving such optimal design problems is quite relevant.

Keywords: The Corrosion Wear Model, Cantilever Rod, Section Configuration, Computer Simulation, Displacement Vector, Complex.

Introduction. Core structures are widely used in construction and many industries, such as chemical, oil refining, gas, metallurgical, agricultural and others, while being influenced not only by thermal force loads, but also by aggressive environments, leading to a significant reduction in load-bearing capacity and shortening their service life. It should be noted that increasing the durability of structures operated under the influence of an

aggressive environment is often carried out by increasing their geometric dimensions by introducing an additional, so-called "sacrificial" layer, which, as a result, leads to an overestimation of material costs for the manufacture of structures. Moreover, an increase in corrosion wear is usually assigned based only on the experience of operating the structure in such cases. Therefore, a scientifically based prediction of the durability of structures in such difficult extreme conditions and a rational choice of their basic parameters must be carried out at the design stage. In recent years, much attention has been paid to the problem of optimal (relative to different criteria) design of structural elements undergoing mechanical and chemical destruction, and a number of works have been devoted to its solution. [1, 2-4], which explore ways to reduce the material consumption of structures designed for use in aggressive environments. Mathematical models of the corresponding optimization problems in terms of nonlinear mathematical programming were formulated in [5, 6]. The strength aspects of the problem of interaction of the elements of power structures with aggressive (corrosive) media, as well as the issue of optimizing their parameters, were considered in the works, which provide both

reviews of publications in this field and an analysis of the state of the problem as a whole. In the works . Devoted to the selection of optimal structural parameters, the general case of corrosion was considered, when its rate depends on mechanical stresses. The problem of identifying mathematical models of structural corrosion failure and the computational features of this problem in optimal design were discussed in [7].

Statement of problem. The generally accepted formulation of the problem of weight optimization of structures, taking into account the overall effect of the force load and the aggressive environment, is written as:

$$min\, V\,(\overline{h}(t_0));$$

(1)

$$\sigma_{max}(t,\bar{h}(t),\bar{X}(\bar{x}(t),\bar{y}(t),\bar{z}(t)))\leq[\sigma]\ ;$$

(2)

$$w_{max}\,(t,\ \bar{h}\ (t),\ \bar{X}(\bar{x}(t),\ \bar{y}(t),\ \bar{z}(t)))\leq[\Delta]$$

(3)

$$\overline{h}(t_0)\geq\overline{h}_0;\,(a)\,\overline{h}(t_n)\geq\overline{h}_n;\,(b)$$

(4)

$$t_0 \geq t \geq t_n,$$

(5)

where (1) is the optimality criterion; (2), (3), (4), (5) – accordingly, the limitation of strength, rigidity, structural requirements and durability conditions; $\overline{X}(\overline{x}(t), \overline{y}(t), \overline{z}(t))$ – vector of time-varying coordinates $\overline{x}(t), \overline{y}(t), \overline{z}(t)$ of points on the surface of the power structure; $\overline{h}(t_0)$ - vector of variable variables; t0 – начальный момент времени; tn – the time of exhaustion of the bearing capacity of the structure. It is assumed, however, that the loss of the bearing capacity of the structure occurs if at least one of the requirements is violated. (2), (3), (4, b) at a point in time $t0 \leq t \leq tn$.

A generalized scheme of an iterative optimization algorithm for finding variable $\overline{h}(t_0)$ variables can be represented as:

$$\overline{h}^{k+1}(t_0) = \overline{h}^{k}(t_0) + \Delta\overline{h}^{k}(t_0).$$

(6)

The differences between the existing algorithms, however, as is known, actually consist only in the method of selecting$\Delta\overline{h}^{k}$, where k = 0, 1, 2,.., k is the iteration number

of the search iterative algorithm. A particular difficulty in this case is to verify the fulfillment of constraints (2), (3) for time points (5), since for this it is necessary to repeatedly integrate differential equations describing the corrosion degradation (displacement) in time of the surface points of the power element of the structure for each (both successful and unsuccessful) step of the search algorithm (6). Let us assume that some well-known model is used as a computational model of corrosion damage, taking into account the effect of stress on the rate of corrosion, for example, in the form:

$$\frac{d\overline{d}}{dt} = f(\overline{d}, \overline{\sigma}, \overline{B}, \overline{X}, t); \overline{d}(t_0) = 0. \quad (7)$$

Thus, the proposed approach is a fairly reliable and effective means of solving optimization problems for core structures that are simultaneously influenced by power loads and an aggressive environment.

Conclusions

The main result of the section is a demonstration of the possibilities of an effective algorithm for computer modeling of corrosion degradation of rods, plates and shells of rotation as structural elements in the

oil and gas industry, the use of which allows us to trace the process of corrosion wear and changes in the stress-strain state of such structures from some initial moment in time to its complete destruction in accordance with the well-known mathematical models of V. M. Dolinsky and E. M. Gutman.

Patterns of time-varying configurations of such structural elements have been obtained.

A comparative analysis of the numerical results revealed that the used model of corrosion wear by V. M. Dolinsky leads to smoother and uniform corrosion wear than according to the model of E. M. Gutman.

Reference

1. Gutman E. M. strength of gas-industrial pipes in conditions of corrosion wear / [E. M. Gutman, R. S. Zainulin, A. T. Shatalov et al.]. Moscow: Nedra publ., 1984, 80 p. (in Russian).

2. Gutman E. M. mechanochemistry of metals, and protection from corrosion / E. M. Gutman, 2nd ed., Moscow: Metallurg, 1981, 270 p. (in Russian).

3. Dolinsky V. M. bending of thin plates exposed to corrosion wear / V. M. Dolinsky // dynamics and strength of machines. - Kharkiv. - 1975. - Ed. 21. – P.43-49.

4. Dolinsky V. M. calculation of structural elements exposed to uniform corrosion / V. M. Dolinsky // research on the theory of plates and shells: SB. science. Trudov.

Kazan: Publishing House of the Kazan University, 1976. 7. – p.37-42.
5. Dzyuba A. A., Kolodyazhny A. P. K problemy sravlenie analiza matematicheskikh modeli korrozionnykh iznosya surface bending Rod elements [to the problem of comparative analysis of mathematical models of corrosion wear of curved rod elements]. Teoreticheskie osnovy stroitel'nosti: SB. scientific works / / Theoretical Foundations of Civil Engineering. – Warsaw. – 2007. – №15 – P. 167 – 172.
6. Dzyuba A. P., Vasilenko O. G. algorithm of optimal design for the final level of corrosion damage to structures / A. P. Dzyuba, O. G. Vasilenko // VISN. Dnepropetr. Nat. UN-Tu. - Sir. : Mechanics. - Issue 15, T. 1, №5. – 2011. – P.78-90.
7. Dzyuba A. P., Vasilenko A. G., Dzyuba A. A. Optimization of annular plates at transverse loading / / problems of computational mechanics and structural strength : sat. Scientific works. Dnepropetrovsk: Lira Publ., 2012, Issue 18, Pp. 62-69.

https://doi.org./10.58225/mpmma.2026.*710*

NUMERICAL SOLUTION FOR OPTIMIZATION OF CABLE-STAYED BRIDGE CROSS-SECTION DUE TO EXTERNAL LOADS

Ramiz Iskanderov, Nijat Mastanzade,
Nariman Abdinli
AzUAC, Azerbaijan

Abstract. The paper discusses the problem statement and methods for optimizing a multi-span cable-stayed bridge. The design of the largest multi-span bridge currently under construction in Azerbaijan, located along the Muganly–Ismayilli–Gabala road, was used as a reference project. The self-weight of the structure, as well as traffic loads, were considered as the loads acting on the bridge. The maximum principle of optimal control theory was employed. Based on the obtained analytical expression, an iterative calculation scheme was proposed. At each iteration, the minimum required cross-sectional area of the cables was determined. After each iteration cycle, the strength condition of the cables and the deformability of the bridge girder were verified. The cross-sectional area of the cables and the force transmitted to the pylon were optimized. This resulted in a reduction in both the number of cables and their total cross-sectional area.

Keywords: optimization, dynamic, stiffness, bridge, cable-stayed, tension.

1. Introduction

Due to the active construction of transportation infrastructure and the increase in the mass and dimensional parameters of traffic flows, the need arises to account for the dynamic effects of such loads on bridges. Solutions to problems concerning the impact of moving loads on bridge spans are presented in [1]. The vibrations of suspension and cable-stayed bridges under moving loads are examined in studies [2, 5]. The interaction between railway bridges and rolling stock is discussed in studies [2]. The effects of high-speed, seismic, impact, and wind load on bridges are considered in studies [5–7]. Most of the aforementioned investigations address and describe two-dimensional problems. Three-dimensional vibration problems of bridges subjected to moving loads are presented in studies, where the bridge span structure is modeled as a folded system. Due to the widespread implementation of software systems based on the finite element method in the design practice of complex spatial structures, the application of these systems to problems involving moving loads has become increasingly important. Using the CSI Bridge

software package, it is necessary to obtain a numerical solution for the dynamic response of a cable-stayed bridge subjected to a vertical force moving at a constant speed, with the determination of internal forces in the span structure at each instant of time, and to compare the results with solutions obtained using other numerical methods.

2. Modelling of bridge

The pylon (tower), deck, and stay cables are the three primary components of a cable-stayed bridge. These components are modeled using three-dimensional line elements. A three-dimensional linear frame element is employed to simulate both the deck and the pylon, while the stay cables are modeled using three-dimensional nonlinear cable elements. A commercial finite element (FE) software package, CSI Bridge, was used to develop and analyze the cable-stayed bridge models. It was assumed that the pylon and the girder were rigidly connected at their intersection, ensuring full interaction between the components, and that each level of the pylon was connected to the girder. In the dynamic equation, the force denoted as F_{ext} on the right describes the seismic force. Here, the acting seismic force is determined by the impact of the mass, which is an obstacle, into the impulse of soil occurrence:

$F_{ext} = m\ddot{x_{gr}}$. In addition to seismic forces, the bridge is subjected to various other loads.. The dynamic equation of the bridge can be expressed as follows:

$$M\ddot{u} + C\dot{u} + Ku = f_{eff} \quad (23)$$

Where $\ddot{u}, \dot{u}, u$ are respectively acceleration, velocity and displacement of the bridge's elements – cables and stiffness beam; f_{eff} =-$M\ddot{u}_{gr}$ where $\ddot{u}_{gr}$ is the ground acceleration.
Optimization of bridge cable cross section
If the optimization problem is formulated as an optimal control problem, the governing equation can be written as follows:

$$M\ddot{u}(t) + C\dot{u}(t) + Ku(t) = f_{eff}(t) + Bw(t) \quad (2)$$

Here w is the control function, B is the control coefficient. If $x_1(t) = u(t)$ and $x_2(t) = \dot{u}(t)$ are shown, then the second-order differential equation can be written as two first-order systems of equations:

$$\begin{cases} x_1(t) = x_2(t) \\ x_2(t) = -\frac{K}{M}x_1(t) - \frac{C}{M}x_2(t) + \frac{f_{eff}(t)}{M} + \frac{B}{M}w(t) \end{cases} \quad (3)$$

Then there will be a function of the main criterion

$$I = \int_{t_2}^{t_1}\left(\alpha x_1^2(t) + \beta x_2^2(t) + \gamma w^2(t)\right)dt \to min, \quad (4)$$

Here are α, β, γ weights. Integral expression is a Lagrange function

$$L(x, w, t) = \alpha x_1^2(t) + \beta x_2^2(t) + \gamma w^2(t) \quad (5)$$

Then, according to the maximum principle, the Hamiltonian function can be written as follows:

$$H(x, w, p, \varphi) = L(x, u, t) + p^T(t)\varphi(x, w, t) \quad (6)$$

Here $\varphi(x, w, t)$ is the vector of the right side of the equation $\dot{x} = \varphi(x, w, t)$; $p(t)$ is a vector of connected variables, $p(t) = [p_1(t), p_2(t)]^T$.

To determine the optimal control function, we differentiate *w* and equate to zero:

$$\frac{\partial H}{\partial w} = \frac{\partial}{\partial w}(\gamma w^2) + \frac{\partial}{\partial w}\left(p_2 \frac{b}{M} w\right) = 2\gamma w + \frac{b}{M} p_2 = 0 \quad (7)$$

Therefore, we can get the expression of optimal control:

$$w^* = -\frac{b p_2}{2\gamma M} \to p_2 = -\frac{2\gamma w M}{b} \quad (8)$$

Solution

1) Current design codes and standards for cable-stayed bridges may lead to excessive material consumption and do not explicitly address the optimization of cable cross-sectional areas. Furthermore, the design engineer based on professional experience and engineering judgment typically determines parameters such as the angle of cable inclination relative to the bridge girder, the number of cables within the span, and the spacing between cable anchorage points.
2) Using the maximum principle makes it possible to determine the optimal cross-sectional area of the cables with minimum material consumption and to obtain an analytical expression for the optimization problem.
3) The use of an iterative calculation procedure makes it possible to determine the optimal cross-sectional area of the cables within 3–4 iterations, thereby ensuring minimum steel consumption.

References

1. AASHTO LRFD. Bridge Design Specification. 8th Ed.Sept. 2017

2. Papadopolus P.G., J. Arethas, P. Lazaridis. Numerical study on the behavior of cables of cable-stayed bridges. Earthquake Resistant Engineering. WIT Transaction on the Built Environment, Vol.81. 2005
3. V.Nzapour, S.Gholizadeh. Design optimization of cable-stayed bridges using momentum search algorithm. Int. J. of Optimization in Civil Engineering. 2023, 13(1): 1-16
4. F.L.S.Ferreira, L.M.C.Simoes. Optimum design of a controlled cable-stayed bridge subject to earthquakes. Struct Multidise Optim (2011) 44: 517-528
5. B.Shrestha. Karnali cable-stayed bridge: Development of finite element model and free vibration analysis. J. of the Institute of Engineering. Vol. 10, No. 1, pp. 14-24
6. C.Tie, Z.Ruichuan. Mechanical analysis of stayed bridge. The Open Mechanical Engineering Journal, 2015, 9, 780-785
7. R. A. Iskanderov, N. S. Mastanzade, N. M.Abdinli. Dynamic behavior and optimal design of long-span cable-stayed bridge. Problems of Computational Mechanics and Strength of Structures: Col. of sci. art. / edit. board: A. P. Dzyuba (editor-in chief) and other. – Dnipro: Lira, 2025. – Vol. 40. – 180 p. In Ukr. and Engl.

https://doi.org./10.58225/mpmma.2026.717

COMPARATIVE ANALYSIS OF CENTRALIZED AND OCCUPANCY-BASED HVAC REGULATION

Gasimov Rashad , Mammadov Nurmammad
AzUAC, Azerbaijan

Abstract. This study presents a comparative analysis of centralized and occupancy-based HVAC regulation methods with emphasis on ventilation control using ultrasonic occupancy detection. Conventional centralized systems operate at fixed design conditions regardless of actual room occupancy, resulting in unnecessary energy consumption. In contrast, occupancy-based regulation dynamically adjusts ventilation and heating demand according to the number of occupants detected in real time. A practical case study based on an office floor plan containing a 65-seat assembly hall and a 56-seat dining hall is investigated. Ventilation and heating loads are calculated for both control strategies and compared using analytical methods and MATLAB simulations. Simulation results demonstrate improved indoor air quality control and reduced energy consumption under occupancy-based operation. The obtained results indicate that occupancy-based regulation can reduce total HVAC energy consumption by approximately 39% while

maintaining compliance with ventilation requirements.

Keywords: HVAC regulation; Occupancy-based control; Energy efficiency; Ventilation systems; Ultrasonic sensors

1. Introduction

Heating, ventilation and air-conditioning systems represent one of the largest energy consumers in modern buildings. Conventional HVAC installations are typically designed according to maximum occupancy conditions and operate with fixed airflow rates. However, large spaces such as assembly halls, conference rooms and dining areas rarely remain fully occupied throughout the day. Consequently, substantial energy is wasted by conditioning air for spaces that are only partially occupied.

Recent advances in sensor technologies have enabled occupancy-based HVAC regulation, where airflow and heating demand are adjusted according to the actual number of occupants. Among available sensing technologies, ultrasonic sensors offer a low-cost and privacy-preserving solution for occupancy detection. The objective of this study is to compare centralized and occupancy-based HVAC regulation methods through practical calculations and simulation analysis.

2. Methodology

The investigation considers a real office floor plan containing two major spaces: a 65-seat assembly hall and a 56-seat dining hall. Ventilation requirements were determined using a fresh-air rate of 60 m^3/h per person, consistent with practical HVAC design recommendations.

Two operating scenarios were evaluated:

- entralized regulation: ventilation sized and operated continuously at maximum occupancy.
- ccupancy-based regulation: ventilation adjusted according to actual occupancy levels detected by ultrasonic sensors.

Ventilation thermal load was calculated using:

$$Q = \rho c_p V_s \Delta T = \rho c_p \frac{N \cdot q_i}{3600} \Delta T$$

MATLAB simulations were performed to evaluate:

- O_2 concentration dynamics;
- upply airflow rates;
- VAC energy savings;

-

resh-air delivery relative to ventilation standards.

3. Case Study and Simulation Results

For the centralized scenario, ventilation was supplied according to the full seating capacity of both spaces (121 occupants). For the occupancy-based scenario, average occupancy levels of 26 occupants in the assembly hall and 28 occupants in the dining hall were assumed.

The calculations demonstrated a significant reduction in ventilation thermal energy demand when airflow was adjusted according to occupancy. MATLAB simulations further confirmed these findings.

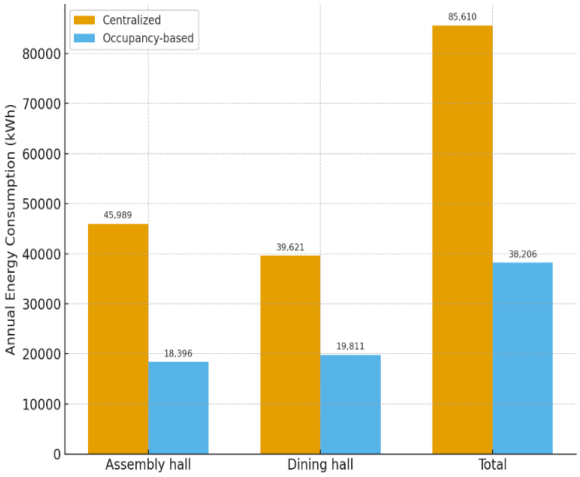


Fig. 1.

Figure 1 presents the comparison of annual HVAC energy consumption for centralized and occupancy-based regulation. The occupancy-based strategy consistently required lower energy input due to the reduction of unnecessary ventilation during low-occupancy periods.

The CO_2 simulations indicated improved indoor air quality control through faster adaptation to occupancy changes. The airflow simulations showed that centralized systems frequently supplied excess fresh air, whereas occupancy-based control-maintained airflow close to the required ventilation standards.

Overall, simulation results indicated approximately 39% HVAC energy savings compared with conventional centralized operation.

Conclusion

This study compared centralized and occupancy-based HVAC regulation methods using practical calculations and MATLAB simulations. The results demonstrated that occupancy-based control significantly improves ventilation efficiency by matching

airflow to real occupancy levels. The proposed approach maintained indoor air quality requirements while reducing unnecessary heating and ventilation loads.

Simulation results showed that occupancy-based regulation can achieve approximately 39% energy savings compared with centralized operation. These findings highlight the potential of ultrasonic occupancy detection as a practical tool for intelligent HVAC management. Future research will focus on integrating occupancy-based regulation with renewable energy systems and AI-assisted predictive control algorithms.

References

1. L. Pérez-Lombard, J. Ortiz, J. F. Coronel, & I. R. Maestre. A review of HVAC systems requirements in building energy regulations. Energy and Buildings, Vol. 43, No. 2-3, pp. 255-268, 2011.

2. I. Korolija, L. Marjanovic-Halburd, Y. Zhang, & V. I. Hanby. Influence of building parameters and HVAC systems coupling on building energy performance. Energy and Buildings, Vol. 43, No. 6, pp. 1247-1253, 2011.

3. W. Guo, & M. Zhou. Technologies toward thermal comfort-based and energy-efficient HVAC systems: A review. In 2009 IEEE international conference on systems, man and cybernetics, pp. 3883-3888, October 2009.
4. A. Beltran, V. L. Erickson, & A. E. Cerpa. Thermosense: Occupancy thermal based sensing for hvac control. Proceedings of the 5th ACM Workshop on Embedded Systems For Energy-Efficient Buildings, pp. 1-8, November 2013.
5. R. Rana, B. Kusy, J. Wall, & W. Hu. Novel activity classification and occupancy estimation methods for intelligent HVAC (heating, ventilation and air conditioning) systems. Energy, Vol. 93, pp. 245-255, 2015.

https://doi.org./10.58225/mpmma.2026.724

APPLICATION OF NONLINEAR DIFFERENTIAL EQUATIONS TO REVERSIBLE ENZYMATIC ISOMERIZATION IN FIXED-BED REACTORS

Regunathan Rajalakshmi[1] and Lakshmanan Rajendran[2]*

[1] Alagappa University, India

[2]AMET University, India

Abstract. The enzymatic isomerization of D-glucose to D-fructose is modeled using a reversible Michaelis–Menten expression to capture nonlinear kinetics. Approximate analytical solutions are obtained via the hyperbolic function method under mixed boundary conditions. Results agree with numerical simulations, validating the model. Parameter analysis highlights the influence of transport and kinetic effects on reactor performance and optimization in fixed-bed systems.

Keywords: Glucose isomerization, Michaelis–Menten kinetics, Packed-bed reactor, IGI catalyst dynamic modelling.

1 Introduction

Solid–liquid enzyme-catalyzed reactions play a key role in biochemical and food industries, with glucose isomerization being especially important for producing low-calorie

sweeteners [1–3]. This reversible process, catalyzed by glucose isomerase, converts glucose into fructose, improving sweetness, viscosity, and product stability [4,5]. Fructose is more suitable for diabetic applications due to its insulin-independent metabolism [6]. Industrially, immobilized glucose isomerase is widely used in packed-bed reactors under optimized temperature conditions to balance conversion and enzyme stability [2,6]. Early batch systems have largely been replaced by continuous reactor configurations [1,4]. Recent studies emphasize improved kinetic modeling and reactor simulation for process optimization [7,8]. In particular, A. M. Dehkordi et al. [9] developed a dynamic packed-bed model integrating experimental data. However, explicit analytical expressions for concentration profiles remain limited. This work derives approximate analytical solutions for glucose concentration and conversion using the hyperbolic function method, providing insights for efficient reactor design and optimization [10-12].

2 Theoretical Formulation

After nondimensionalization, the dimensionless mass balance equations for substrate (glucose) and product (fructose) in a fixed-bed reactor are expressed as:

$$\frac{d^2c(\xi)}{d\xi^2} - Pe_a \frac{dc(\xi)}{d\xi} - \frac{\alpha c(\xi)}{\delta + c(\xi)} = 0. \qquad \frac{d^2f\xi)}{d\xi^2} - Pe_a \frac{df(\xi)}{d\xi} + \frac{\alpha c(\xi)}{\delta + c(\xi)} = 0 \qquad (1)$$

.

Appropriate boundary conditions at the reactor inlet (convective–diffusive type) are:

$$-Pe_a \frac{dc(\xi)}{d\xi}\Big|_{\xi=0} + c(\xi)|_{\xi=0} = 1, \quad - Pe_a \frac{df(\xi)}{d\xi}\Big|_{\xi=0} + f(\xi)|_{\xi=0} = 0. \qquad (2)$$

At the reactor outlet, zero-gradient conditions are imposed:

$$\frac{dc(\xi)}{d\xi}\Big|_{\xi=1} = 0, \quad \frac{df(\xi)}{d\xi}\Big|_{\xi=1} = 0. \qquad (3)$$

Here, $c(\xi)$ and $f(\xi)$ represent the dimensionless concentrations of glucose and fructose, respectively. The parameter Pe_a denotes the axial Péclet number, α is the dimensionless reaction rate constant, and δ is the saturation parameter arising from Michaelis–Menten kinetics. The nonlinear term represents reversible enzyme kinetics governing the glucose–fructose transformation.

3 Methodology

The nonlinear dimensionless reaction–diffusion equations are analytically solved using the Hyperbolic Function Method

(HFM). An assumed solution expressed in hyperbolic functions is substituted into the governing equations. The unknown parameters are evaluated by applying the boundary conditions, reducing the system to an algebraic equation for a key parameter. Solving this equation yields closed-form expressions for substrate and product concentration profiles. This method provides accurate approximate solutions and effectively captures the nonlinear characteristics of the system.

4 Result and Discussion

The Hyperbolic Function Method (HFM) solves nonlinear differential equations in chemical kinetics and transport phenomena using sinh and tanh functions. It provides closed-form solutions with clear physical insight, fast convergence, and flexibility for boundary value problems.

$$c(\xi)=\frac{\cosh[m(1-\xi)]}{Pe_a m\sinh(m)+\cosh(m)}=M\cosh[m(1-\xi)] \;\&$$

$$f(\xi)=1-\frac{\left(\cosh\left((1-\xi)m\right)\right)}{(Pe_a m\sinh(m)+\cosh m)}=1-c(\xi). \qquad (4)$$

where, $M=\frac{1}{(Pe_a m\sinh(m)+\cosh(m))}$. Here, m is obtained from the below equation.

$$m^2+Pe_a m\ \mathrm{Tanh}(0.5m)-\left(\frac{\alpha}{\delta+M\cosh(0.5m)}\right)=0. \quad (5)$$

Using analytical expressions, the fractional conversion χ measures reactant transformation and is defined as: $\chi=1-\frac{C_{out}}{C_{in}}=1-\frac{1}{\cosh(m)}$.

The reaction rate R is given by $R=\frac{\alpha c(\xi)}{(\delta+c(\xi))}$ where $c(\xi)=\frac{\left(\cosh((1-\xi)m)\right)}{(Pe_a m\sinh(m)+\cosh(m))}$. (6)

Zero-Order kinetics ($c(\xi)\ll\delta$) gives constant-rate profiles and First-Order ($\delta\gg c(\xi)$) yields $c(\xi)=1$ and $f(\xi)=0$, highlighting kinetic and transport limits.

1(a)

1(b)

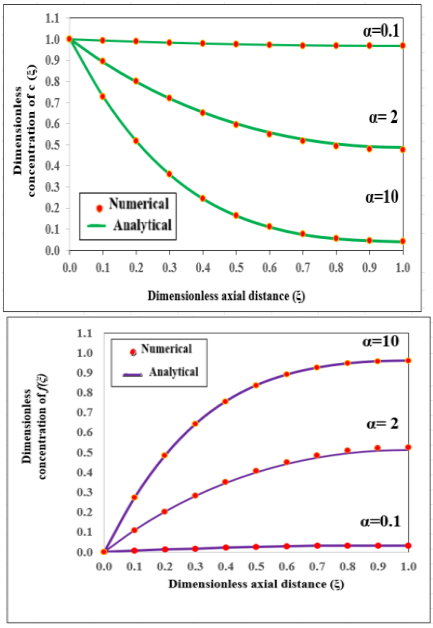


Fig. 1(a-b). Analytical vs. Numerical of glucose and fructose concentration profiles c(ξ) and f(ξ) for varying α under specified conditions.

5 Conclusion

This study analyzes D-glucose to D-fructose isomerization using analytical solutions from the hyperbolic function method. Results agree with simulations, validating the model. Fractional conversion is predicted effectively. Parameters like Péclet number, reaction rate, and saturation influence performance, offering insights into kinetics–transport interaction and aiding optimization

of immobilized enzyme reactors for HFCS production.

References

1. Dehkordi, A.M.: AIChE J. 52(2), 692–704 (2006). https://doi.org/10.1002/aic.10673
2. Faqir, N.M., et al.: Biotechnol. Bioeng. 77, 163–173 (2002). https://doi.org/10.1002/bit.10054
3. Haas, W.R., et al.: AIChE J. 20, 707–712 (1974). https://doi.org/10.1002/aic.690200413
4. Lee, H.S., et al.: J. Biotechnol. 84, 145–153 (2000). https://doi.org/10.1016/S0168-1656(00)00346-2
5. Palazzi, E., et al.: Technol. 28, 246–252 (2001). https://doi.org/10.1016/S0141-0229(00)00315-7
6. Toumi, A., et al.: Chem. Eng. Sci. 59, 3777–3792 (2004). https://doi.org/10.1016/j.ces.2004.05.019
7. Khalilpour, R., et al.: Biochem. Eng. J. 40, 328–336 (2008). https://doi.org/10.1016/j.bej.2008.01.012
8. Al-Muftah, A.E.: Int. J. Chem. React. Eng. 3, A40 (2005). https://doi.org/10.2202/1542-6580.1177
9. Dehkordi, A.M., et al.: AIChE J. 54, 1443–1455 (2008). https://doi.org/10.1002/aic.11477

10. Rajaram, M., et al.: Int. J. Electrochem. Sci. 18, 100023 (2023). https://doi.org/10.1016/j.ijoes.2023.100023
11. Menaka, R., et al.: Math. Model. Eng. Probl. 11, 2132–2140 (2024). https://doi.org/10.18280/mmep.111226
12. Devi, M.C., et al.: React. Kinet. Mech. Catal. 130, 35–53 (2020). https://doi.org/10.1007/s11144-020-01769-4

https://doi.org./10.58225/mpmma.2026.*732*

A CRITICAL REVIEW OF THERMOPHYSICAL PARAMETERS GOVERNING THE PERFORMANCE OF THERMAL INTERFACE MATERIALS IN ADVANCED ELECTRONIC COOLING SYSTEMS

Reyhan Arslan, Bedri Onur Küçükyıldırım, Emel Akyol and Ahmet Selim Dalkılıc
Yildiz Technical University, Türkiye

Abstract. Thermal interface materials (TIMs) are indispensable components in modern electronic systems, where efficient thermal management is required to sustain performance and reliability under increasing power densities. This review provides a critical assessment of the thermophysical parameters governing TIM performance, including thermal resistance, thermal conductivity, viscosity, bond line thickness (BLT), filler characteristics, long-term stability, electrical insulation, and mechanical compliance. Unlike conventional approaches that prioritize thermal conductivity as the primary performance metric, this study emphasizes the dominant role of interfacial phenomena and structural factors in determining effective heat transfer. A comparative evaluation of recent literature reveals that most studies focus on isolated parameter enhancement, while a unified multi-parameter framework remains lacking.

The findings highlight that optimization of TIM performance requires an integrated design approach considering interfacial, structural, and mechanical interactions simultaneously. This work provides a comprehensive perspective for the rational design of next-generation TIMs in advanced electronic cooling applications.
Keywords: Thermal Interface Materials, Interfacial Thermal

Introduction

Thermal management has become increasingly important in modern electronic systems due to rising power densities, device miniaturization, and functional integration. Efficient heat dissipation is essential for maintaining the performance, reliability, and lifetime of CPUs, power electronics, and high-density integrated devices [1,2]. Thermal interface materials (TIMs) enhance heat transfer between contacting surfaces by reducing interfacial thermal resistance caused by surface roughness and trapped air gaps, making them critical components in electronic cooling applications [3]. However, TIM performance depends not only on thermal conductivity but also on factors such as filler dispersion, viscosity, mechanical compliance, thermal resistance, and long-term stability. Although advanced fillers including carbon nanotubes, graphene, and boron nitride have

significantly improved thermal conductivity, recent studies indicate that practical performance is strongly influenced by interfacial phenomena, material structure, and operating conditions [1–4]. Therefore, a comprehensive understanding of the interactions among these thermophysical parameters is essential for the development of next-generation TIMs. This review examines the key factors governing TIM performance and highlights the importance of a holistic design approach for thermal management materials [1–4].

Governing Thermophysical Parameters of TIM Performance

The thermal performance of thermal interface materials (TIMs) is governed by the combined influence of several thermophysical parameters rather than a single material property. Among these, interfacial thermal resistance is one of the primary factors limiting heat transfer between contacting surfaces and can be expressed as:

$$R=\Delta T/Q \quad (1)$$

In addition, the intrinsic heat transport capability of a material is characterized by its thermal conductivity, which follows Fourier's law:

$$q = -k \cdot \nabla T$$

(2)

However, high thermal conductivity alone is insufficient to guarantee superior TIM performance. Practical applications also require appropriate viscosity to ensure adequate spreadability and surface conformity during application. The relationship between shear stress and viscosity is commonly described as:Viscosity determines the application behavior of TIMs [3].

$$\tau = \mu \cdot \dot{\gamma}$$

(3)

Another important parameter is bond line thickness (BLT), which directly affects overall thermal resistance. Excessively thick TIM layers increase heat transfer resistance, whereas excessively thin layers may fail to fill surface irregularities effectively. Therefore, optimal TIM performance requires a balance between minimum thickness and maximum surface conformity.

The type, morphology, loading fraction, and dispersion quality of thermally conductive fillers also play a critical role in determining heat transfer efficiency. Thermal conductivity enhancement in composite TIMs is often described by percolation theory:

$$k \propto (\varphi - \varphi c)^n$$

(4)

Uniform filler dispersion promotes the formation of continuous thermal conduction pathways, while filler agglomeration disrupts heat transfer and reduces overall effectiveness [5,6].

Furthermore, long-term performance depends on maintaining structural stability under thermal cycling conditions. Phenomena such as pump-out, drying, and phase separation may degrade TIM performance over time. Electrical insulation is another key requirement in many electronic applications, making thermally conductive yet electrically insulating fillers, such as boron nitride, particularly attractive. Finally, sufficient mechanical compliance is necessary to accommodate thermal expansion mismatch between contacting surfaces and to preserve interfacial integrity during operation [4,7,8].

Discussion

As summarized in the literature, the majority of studies primarily focus on enhancing thermal conductivity through advanced fillers and composite structures. In contrast, it is evident that interfacial thermal resistance, filler dispersion quality, and mechanical compliance are equally critical in determining real-world performance.

Despite extensive research, a comprehensive framework integrating these interdependent

parameters is still lacking, which limits the effective translation of material-level improvements into system-level performance gains.

Conclusion

This review demonstrates that TIM performance is governed by a complex interaction of thermophysical, interfacial, and mechanical parameters rather than a single dominant factor. While thermal conductivity remains important, interfacial resistance and bond line thickness play a more decisive role in practical applications.

The comparative analysis indicates that current research predominantly focuses on improving individual parameters, often neglecting their coupled effects. This fragmented approach limits the development of truly high-performance TIM systems.

Future research should therefore focus on integrated multi-parameter optimization strategies, combining advanced filler architectures, improved dispersion techniques, and interfacial engineering. Such an approach is essential to bridge the gap between material-level properties and real-world thermal management performance.

References

1.Zhang, M., Zhao, G., Zhao, Y., Chen, X., & Li, Q. (2024).Exploring thermal interface

materials for electronics via molecular dynamics simulations: A review. Materials Today Communications, 41, 110964.

2. Kaur, N. (2026). Thermal interface materials for efficient heat management in electronics. Applied Thermal Engineering, 287, 129415.

3. Lin, C., & Chung, D. D. L. (2009).Rheological behavior of thermal interface pastes. Journal of Electronic Materials, 38(10), 2069–2084.

4. Prasher, R. (2006).Thermal interface materials: Historical perspective, status, and future directions. Proceedings of the IEEE, 94(8), 1571–1586.

5. Wu, X., Tang, B., Chen, J., Shan, L., Gao, Y., Yang, K., Wang, Y., Sun, K., Fan, R., & Yu, J. (2021). Epoxy composites with high cross-plane thermal conductivity by constructing all-carbon multidimensional carbon fiber/graphite networks. Composites Science and Technology, 203, 108610.

6. Sun, Y., Bao, H.-D., Guo, Z.-X., & Yu, J. (2009).Modeling of the electrical percolation of mixed carbon fillers in polymer-based composites. Macromolecules, 42(1), 459–463.

7. Smits, F. M. (1958).Measurement of sheet resistivities with the four-point probe. Bell System Technical Journal, 37(3), 711–71.

8. Mahajan, R., Chiu, C.-P., & Chrysler, G. (2006). Cooling a microprocessor chip. Proceedings of the IEEE, 94(8), 1476–1486.

https://doi.org./10.58225/mpmma.2026.740

RESISTANCE, THERMOPHYSICAL PROPERTIES SPAM DETECTION USING SVM AND TF-IDF FEATURES

Reyyan Oruc and Edip Senyurek
Vistula University, Poland

Abstract. This study focuses on spam email detection using machine learning. The original dataset contained 5,171 emails, and a balanced subset of 1,400 spam and 1,400 non-spam emails was selected. Before training, the email texts were cleaned by converting them to lowercase and removing punctuation marks, unnecessary symbols, and non-informative words. Then, the texts were converted into numerical features using the Term Frequency-Inverse Document Frequency (TF-IDF) method and used to train a Support Vector Machine (SVM) model. The model achieved 98.75% accuracy, showing that TF-IDF and SVM work effectively together for spam email detection.

Keywords: Spam Detection, Support Vector Machine (SVM), Term Frequency-Inverse Document Frequency (TF-IDF), Machine Learning, Email Classification

1 Introduction

The use of spam emails for cyber attacks and online fraud makes this problem very serious. People and companies receive a large

number of emails every day, so it is very important to distinguish normal emails from spam emails. Spam emails are usually different from normal emails in terms of content and writing style. However, traditional rule-based systems are ineffective today. Machine learning and natural language processing (NLP) technologies are used to help computers analyze email texts and determine whether an email is spam. In our previous study [1], we used TF-IDF features and the Naïve Bayes algorithm and achieved a high accuracy rate of 98.86%. In this study, we use a Support Vector Machine (SVM) model with TF-IDF features to further improve the classification results. The dataset used in this research was sourced from Kaggle (https://www.kaggle.com/datasets/venky73/spam-mails-dataset) and contains a total of 5,171 spam and non-spam emails. SVM is used in this study because it can work effectively with large text data and can separate spam and non-spam classes clearly. The main objective of this study is to create a more accurate and reliable spam detection system that can be applied to today's email data.

2 Methodology

2.1 Dataset and Preprocessing

In the spam mail dataset, each email has two main fields: text, which contains the email content, and label, where 1 means spam and 0 means non-spam.

To ensure a balanced study, 1,400 spam and 1,400 non-spam emails were selected randomly from the dataset. Previous studies have shown that class balance can improve the accuracy and stability of text classification models [2]. The email texts were cleaned by converting all texts to lowercase, removing punctuation marks and unnecessary symbols, and filtering common English stop words such as “the,” “a,” and “is.” In addition, the frequently used but non-informative words “houston” and “kaminski” were filtered out to reduce unnecessary noise and improve classification performance [3].

2.2 TF-IDF and SVM

Email texts were converted into numerical features using TF-IDF. TF-IDF gives higher importance to words that appear often in specific emails but less often in the whole dataset. To improve the model’s performance, single words and two-word phrases were used, and very rare words were removed as noise.

After preprocessing, the dataset was mixed and divided into training and test sets. We

used 80% of the data for training (2,240 emails) and 20% for testing (560 emails).

Figure 1 shows the top TF-IDF words in the dataset. These words helped the SVM model classify spam and non-spam emails more effectively.

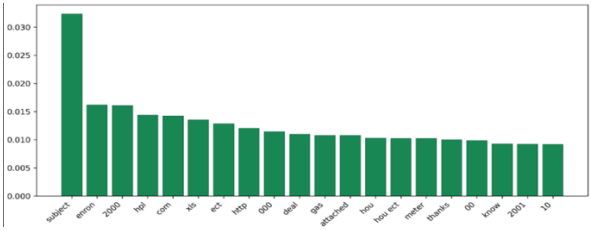


Fig. 1. Top 20 words by TF-IDF score

To calculate the TF-IDF value of terms in mails the following Equation 1 was used:

$$TF - IDF_{(t,d)} = TF_{(t,d)} \times log\left(\frac{N}{1+n_t}\right) \qquad (1)$$

where t is the term (word), d is the document (email), TF(t,d) is the frequency of term t in document d, N is the total number of documents, and n_t is the number of documents containing term t.

Support Vector Machines (SVMs) are machine learning algorithms commonly used for classification tasks such as spam detection. The main goal of SVM is to separate spam and non-spam emails using a hyperplane with the maximum margin between classes.The decision function of a linear SVM can be expressed as Equation (2):

$f(x)=w^Tx+b$ (2)

where the goal is to find the hyperplane that best separates the two classes.

The classification rule is defined in Equation (3):

$\hat{y}=sign(w^Tx+b)$ (3)

where w is the weight vector defining the orientation of the hyperplane, x is the input feature vector representing an email using TF-IDF, b is the bias term that shifts the decision boundary, and ŷ is the predicted class label (1 = spam, 0 = not spam).

When combined with TF-IDF features, SVM provides stable and accurate classification results while reducing the risk of overfitting.

3 Results

In this study, the model's performance was evaluated using Accuracy and F1 Score metrics, which are commonly used in binary classification evaluation [4].

Table 1. Confusion matrix experiment results

	Predicted Non-Spam	**Predicted Spam**
Actual Non-Spam	275 (TN)	5 (FP)
Actual Spam	2 (FN)	278 (TP)

Accuracy was calculated using Equation (4):

$$Accuracy = (TP+TN)/(TP+TN+FP+FN) \quad (4)$$

F1 Score was calculated using Equation (5):

$$F1 = (2 \cdot Precision \cdot Recall)/(Precision+Recall)$$

Model training and testing were performed in Python using the PyCharm Integrated Development Environment (IDE). As shown in Table 1, the confusion matrix shows that the model made only seven classification errors in total. Five non-spam emails were incorrectly classified as spam (false positives), and two spam emails were not detected (false negatives).

4 Conclusion

This study presents a spam detection system that combines Natural Language Processing (NLP) techniques, specifically text cleaning and TF-IDF feature extraction techniques with SVM. The results show that when trained on a balanced and carefully prepared dataset the model can classify spam and normal emails with 98.75% accuracy.

The results show that using TF-IDF in combination with SVM is a clear and effective method for text classification. The model successfully identified unique features such as specific keywords in spam messages distinguishing them from normal emails.

For future work we plan to evaluate the model's performance on imbalanced datasets where the number of non-spam emails is far more than spam emails. This will help us see how the algorithm performs under much more realistic conditions that closely simulate real world email traffic.

References

1. Oruc, R., & Senyürek, E. (2025). Spam Detection With Naïve Bayes And TF-IDF. IOSR Journal of Computer Engineering (IOSR-JCE), 27(4), 47–51.

]2. Nuri, Y., & Şenyürek, E. (2024). Filtering Articles Based on Their Abstracts Using TF-IDF. International Journal of Advances in Engineering and Management, 6(8), 364–368.

3. Alshanik, W., Bhatnagar, R., Rawashdeh, J., & Abuhamdah, A. (2020). A Deep Learning-Based Spam Detection System Using Domain-Specific Stop Words Removal. arXiv preprint arXiv:2012.02294.

4. Chicco, D., & Jurman, G. (2020). The Advantages of the Matthews Correlation Coefficient (MCC) Over F1 Score and Accuracy in Binary Classification Evaluation. BMC Genomics, 21(1), 6.

https://doi.org./10.58225/mpmma.2026.747

EQUATION OF STATE AND LIMIT STATE ZONE AT A CRACK TIP IN UNIDIRECTIONAL COMPOSITE LAMINATES

Roland Duduchava[1], Aleksandr Oleinikov[1],Tatiana Kuzmina[1]

[1]V. Kupradze Institute of Mathematics, University of Georgia, Georgia

Abstract. A new mathematical model of the strength behaviour of a composite is proposed, which is used to assess the size and shape of the fracture process zone near a crack in polymer fibre composites.

Keywords: Composite Laminate, Mathematical Modelling, Equation of State, Fracture Process Zone.

Introduction

The linear fracture mechanics crack theory may lose its effectiveness when applied to composites. Indeed, for composite materials, the surface energy predicted by Griffith's criterion is ten times or more than experimentally measured values. Modelling the behaviour of continuous fibre-layered polymer composites within the fracture process zone, therefore, requires an Equation of State (ES) that accounts for the response of the constituent unidirectionally reinforced

layers. The present work proposes a formulation of such an ES using conical parametric surfaces derived from the matrix ES and based on the extremum principle [1, 2].

Equation of limit state at a crack tip

1. Equations of limit state and their experimental justification

The ES in the fracture process zone near a crack in polymer fibre composites, which considers the directional nature of failure and the principle of minimal destructive forces [3]:

$$\frac{|\sigma_{21}|}{S_{21}} + \frac{\sigma_{22}}{S_{22}^{\pm}}\left(1 - \mathrm{tg}^2\alpha_{*\perp}^{\pm}\right) = 1 \quad \text{at} \quad \left|\frac{\sigma_{21}}{\sigma_{22}}\right| \geq \begin{cases} 2\left|\frac{S_{21}}{S_{22}^{-}}\right| & \text{at } \sigma_{22} < 0 \\ 2\tan^2\alpha_{*\perp}^{+}\left|\frac{S_{21}}{S_{22}^{+}}\right| & \text{at } \sigma_{22} > 0 \end{cases},$$

$$\frac{\sigma_{22}}{S_{22}^{\pm}} + \frac{\sigma_{21}^2}{\sigma_{22}}\frac{S_{22}^{\pm}}{S_{21}^2}\frac{1}{4\mathrm{tg}^2\alpha_{*\perp}^{\pm}} = 1, \quad \text{at} \quad \left|\frac{\sigma_{21}}{\sigma_{22}}\right| < \begin{cases} 2\left|\frac{S_{21}}{S_{22}^{-}}\right| & \text{at } \sigma_{22} < 0 \\ 2\tan^2\alpha_{*\perp}^{+}\left|\frac{S_{21}}{S_{22}^{+}}\right| & \text{at } \sigma_{22} > 0 \end{cases},$$

where $S_{22}, S_{21}, \alpha_{*\perp}$ are given strength characteristics.

Experimental verification of the ES and comparison with known ES for 3D stress

state, plane stress, and uniaxial tension-compression have been performed [2].

4 Limit state zone at crack tip

4.1 Asymptotic solution for the crack

We use asymptotic expansions to study cracks with failure mechanics in composite laminates. The main term in the asymptotic decomposition of stresses for cracks represents the stress state in the pre-fracture zone in which the fracture process begins.

Based on our ES using the asymptotic solutions for the distribution of the stresses on the crack tip [4], the equations of the limit lines for the orthotropic laminates are obtained.

4.2 The fracture process zone for two type cracks and two orientations

Two crack configurations are considered: cracks oriented parallel and orthogonal to the reinforcing fibres. Based on these formulations, the shape and size of the pre-fracture zone near the crack tip are estimated.

Comparison with experiment and discussion and conclusion

The theoretical predictions are compared with experimental observations, demonstrating satisfactory agreement between the model and experimental data.

References

1. Oleinikov, A.I.: Strength criterion variants for unidirectional polymer composites by the fracture condition of the inter-fibre when there is compression perpendicular to the fibers. Mech. Of Solids 57, 1740–1748 (2022).
2. Oleinikov, A.I.: Fracture Criteria for Matrix and Fibers in Unidirectional Polymeric Composites at Static Loadings. Prikladnaâ Matematika I Mehanika 88(2), 255-270 (2024).
3. Oleinikov, A.: Fracture criteria for matrix and fiber in unidirectional polymeric composites. J. of Math. Sci. 290, 722-728 (2025).
4. Sih, G.C., Liebowitz, H.: Mathematical theories of brittle fracture. In: Liebowitz, H. (ed.) Fracture, vol. 2, pp. 67–190. Academic Press, New York (1968).

https://doi.org./10.58225/mpmma.2026.751

RELATIVELY COMPACT SETS IN QUASI GRAND LEBESGUE SPACES

Rovshan Bandaliyev[1,2], Alikhan Mehdiyev[1],Konul Omarova[3]

[1] AzUAC, Azerbaijan

[2] Institute of Mathematics, Azerbaijan

[3]Baku Business University

Abstract. In this abstract, we give an analog of the Kolmogorov-Riesz compactness Theorem in quasi-grand Lebesgue space $L_{p)}(0,1), 0 < p \le 1.$ Also, the authors study some problems of separability in $L_{p)}(0,1).$

Keywords: Quasi-grand Lebesgue space, Kolmogorov-Riesz compactness Theorem, quasi-Banach function space, separability.

Grand Lebesgue spaces have become a natural tool in various applications both in problems of analysis, for example, in the study of the integrability of the Jacobian, see [6], and in the theory of differential equations, for example, in the problem of inverting the p -harmonic operator, see [4]. It is well known that the grand Lebesgue space $L_{p)}(\Omega), 1 < p < \infty,\ \Omega \subset R^n,\ |\Omega| < \infty,$ was introduced in [6] and defined by the norm $\|f\|_{L_{p)}(\Omega)} = \sup\limits_{0<\varepsilon<p-1} \left(\frac{\varepsilon}{|\Omega|} \int\limits_{\Omega} |f(x)|^{p-\varepsilon} dx \right)^{\frac{1}{p-\varepsilon}}.$ The

theory of grand Lebesgue spaces is developed by many mathematicians. In particular, the study of grand Lebesgue spaces has attracted resurgent attentions in recent years. We refer to [3], [8] for some recent work in this vein. But, quasi-grand Lebesgue space $L_{p)}(0,1), 0 < p \le 1,$ was introduced in [1] and defined by the norm

$$\|f\|_{L_{p)}(0,1)} = \sup_{0<\varepsilon<p-1}\left(\varepsilon\int_0^1 |f(x)|^{p-\varepsilon}\right)^{\frac{1}{p-\varepsilon}} = \sup_{0<\varepsilon<p-1}\varepsilon^{\frac{1}{p-\varepsilon}}\|f\|_{L_{p-\varepsilon}(0,1)}.$$

Next, the extension of the definition of grand(quasi-grand) Lebesgue space to the rearrangement invariant Banach function was given in [2]. It is well known that the grand(quasi-grand) Lebesgue spaces are not separable.

Let us note the following well-known useful properties of the quasi-grand Lebesgue space $L_{p)}(0,1).$

Theorem 1.([1]) *Let* $0 < p \le 1$. *The space* $L_{p)}(0,1)$ *is a quasi-Banach function space.*

Lemma 1.([1]) *Let* $0 < p \le 1$ *and let* $0 < \varepsilon < \frac{p}{2}$.

Then the following statements hold

(i) $L_p(0,1) \to L_{p)}(0,1) \to L_{p-\varepsilon}(0,1)$ *for any* $0 < \varepsilon < \frac{p}{2}$;

(ii) if $p_1 \le p_2$, *then* $L_{p_2)}(0,1) \to L_{p_1)}(0,1)$.

It is well known that the closure of compactly supported smooth functions $C_0^\infty(0,1)$ with respect to the grand(quasi-grand) Lebesgue norm does not coincide with the grand(quasi-grand) Lebesgue space. Let us consider a special notation for it, namely, will stand for the closure of $C_0^\infty(0,1)$ with respect to the quasi-grand Lebesgue norm. In the following proposition, it is shown that this closure can be characterized as

$$L_{p)}^0(0,1) = \left\{ f \in L_{p)}(0,1) : \lim_{\varepsilon \to 0+} \varepsilon \int_0^1 |f(x)|^{p-\varepsilon} dx = 0 \right\}.$$

Theorem 2. *Let* $0 < p < 1$. *The space of infinitely differentiable functions with compact support* $C_0^\infty(0,1)$ *in* $(0,1)$ *is not dense in* $L_{p)}(0,1)$. *The closure of the set* $C_0^\infty(0,1)$ *in quasi-grand Lebesgue space norm consists of functions* $f \in L_{p)}(0,1)$ *such that*

$$\lim_{\varepsilon\to 0+}\varepsilon\int_0^1 |f(x)|^{p-\varepsilon}dx=0.$$

Now we give an analog of the Kolmogorov-Riesz compactness Theorem in quasi-grand Lebesgue space. About the history of Kolmogorov-Riesz compactness Theorem,we refer, for example, to the paper [5].

We have the following main theorem.

Theorem 3. *Let* $0<p<1$. *A subset* $\Im\subset L_{p)}^0(0,1)$ *is totally bounded if and only if*

(i) $\Im$ *is uniformly bounded, i.e.* $\sup_{f\in\Im}\|f\|_{L_{p)}(0,1)}<\infty$;

(ii) $\Im$ *is uniformly equicontinuous, i.e.* $\sup_{f\in\Im}\|f(\cdot+h)-f\|_{L_{p)}(0,1)}\to 0$ *at* $h\to 0$.

Remark 1. We observe that an analog of the Kolmogorov-Riesz compactness

Theorem in grand Lebesgue space $L_{p)}(\Omega), 1<p<\infty,\ \Omega\subset R^n,\ |\Omega|<\infty,$ was proved in [9]. Also, the compactness of families of continuous functions in grand Lebesgue spaces was studied in [7].

References

1. R.A. Bandaliyev, K. Safarova. *On Hardy type inequalities in grand Lebesgue spaces*

$L_{p)}(0,1)$ *for* $0 < p < 1$. Linear Multilinear Algebra 70, 6053-6066 (2022).
2. M.R. Formica, E. Ostrovsky and L. Sirota. On grand quasi Lebesgue space. J. Math. Anal. Appl. 504, art.125369 (2021).
3. G. Di Fratta, A. Fiorenza. *A direct approach to the duality of grand and small Lebesgue spaces*. Nonlinear Anal.-Theor., 70, 2582–2592(2009).
4. L. Greco, T. Iwaniec, and C. Sbordone. *Inverting the* p*-harmonic operator*. Manuscripta Math. 92, 249-258(1997).
5. H. Hanche-Olsen, H. Holden. *The Kolmogorov–Riesz compactness theorem*, Expo. Math. 28, 385–394(2010).
6. T. Iwaniec, C. Sbordone. *On the integrability of the Jacobian under minimal hypotheses*. Arch. Rational Mech. Anal. 119, 129-143(1992).
7. R. Katea, Y. Kaya. *On the compactness of families of continuous functions in grand Lebesgue spaces*. AIMS Math. 11, 13647–13659 (2026).
8. V. Kokilashvili, A. Meskhi, H. Rafeiro, and S. Samko. *Integral Operators in Non-standard Function Spaces*. Vol. 2: Variable exponent Hölder, Morrey-Campanato and Grand Spaces. Birkhauser, (2016).

9.H. Rafeiro, A. Vargas. *On the compactness in grand spaces*. Georgian Math. J. 22, 141–152 (2015).

https://doi.org./10.58225/mpmma.2026.757

TWO-WEIGHT NORM INEQUALITIES FOR HAUSDORFF OPERATOR ON MORREY SPACES

Rovshan A. Bandaliyev[1,2], Bahar S. Jafarova[1] and Konul A. Babayeva[1]

[1] AzUAC, Azerbaijan

[2] Institute of Mathematics, Azerbaijan

Abstract. In this abstract, we give necessary condition and sufficient condition for the boundedness of Hausdorff operator on weighted Morrey spaces. In particular, we establish necessary and sufficient conditions for the boundedness of special type of thel Hausdorff operator on weighted Morrey spaces for special type weight functions. Also, we get similar results for important operators of harmonic analysis which are special cases of the Hausdorff operator.

Keywords: Hausdorff operator, weighted Morrey spaces, continuity.

It is well known that Hausdorff operators have a deep root in the study of the Fourier analysis and it has a long history in the study of harmonic analysis. This integral operator is deeply rooted in the study of one-dimensional Fourier analysis and has become an essential part of modern harmonic analysis. In particular, it is closely related to the summability of the classical Fourier

series [8]. Let $x \in R^+ = (0,\infty)$ and let ψ be a fixed kernel defined on $(0,\infty)$ such that $\psi \in L_1^{loc}(R^+)$. Then the one-dimensional Hausdorff operator is defined by a linear operator

$$H_\psi f(x) = \int_0^\infty \frac{\psi\left(\frac{x}{y}\right)}{y} f(y)\, dy.$$

Many important operators in analysis are special cases of the Hausdorff operator,
which can be obtained by taking suitable choice of ψ. For example, the Hardy operator, the adjoint Hardy operator, the Hardy-Littlewood-Polya(Calderon) operator, Cesaro operator and Hardy-Hilbert operator are particular cases of the Hausdorff operator. It is very known that the Sobolev space plays an important role in the theory of partial differential equations, combined with functional analysis. Smoothness of functions is measured by the norm of the Lebesgue space $L_p(R^n)$ if the functions belong to the Sobolev space. The Triebel-Lizorkin space and Besov space are generalizations of the Sobolev space, and they can deal with smoothness of functions more precisely. In recent years it has turned out that the Morrey space is useful to measure the size of

functions and compensate the deficit of the Lebesgue space. We recall the definition of Morrey spaces on R_+. Let ω be a weight function on R_+ and let $B(x,r)=(x-r, x+r)$. Suppose that $|B(x,r)|$ is the length of an open interval $(x-r, x+r)$. Let $1\le p<\infty$, $0\le\lambda\le 1$ and let $f: R_+ \to R$ be a Lebesgue measurable function. Suppose that $f\in L^{loc}_{p,\omega}(R_+)$. We define the weighted Morrey spaces $L_{p,\lambda,\omega}(R^+)$ to be a Banach space equipped with the norm

$$\|f\|_{L_{p,\lambda,\omega}(R^+)}=\sup_{x,r>0}\left(\frac{1}{|B(x,r)|^{\lambda}}\int\limits_{B(x,r)\cap R_+}|f(y)|^p\,\omega(y)\,dy\right)^{\frac{1}{p}}<\infty.$$

We observe that for $\omega=1$, $L_{p,\lambda,\omega}(R^+)$ means unweighted Morrey space $L_{p,\lambda}(R^+)$. Also, for $\lambda=0$, $L_{p,0,\omega}(R^+)$ means weighted Lebesgue space $L_{p,\omega}(R^+)$. A direct check can show that

$$\|f\|_{L_{p,\lambda,\omega}(R^+)}=\max\left\{\sup_{r>0}\frac{1}{(2r)^{\lambda/p}}\|f\|_{L_{p,\omega}(0,2r)};\sup_{\substack{x>r\\ r>0}}\frac{1}{(2r)^{\lambda/p}}\|f\|_{L_{p,\omega}(B(x,r))}\right\}<\infty.$$

Assume that $0<\lambda\le 1$. Let $\omega(x)=x^{\lambda}$ and let

$f(x) = x^{-1/p}$. It is obvious that $x^{-1/p} \notin L_{p,x^{\lambda}}(R_+)$. But $\left\|x^{-1/p}\right\|_{L_{p,\lambda,x^{\lambda}}(R^+)} = \frac{1}{\lambda^{1/p}}$.

Suppose that w and ν be weight functions. We introduce the following quantities:

$$A_{\sup} = \int_0^{\infty} \frac{\psi(t)}{t}\, t^{\frac{1-\lambda}{p}} \left(ess\sup_{x>0} \frac{w(tx)}{\nu(t)} \right)^{1/p} dt < \infty,$$

$$A_{\inf} = \int_0^{\infty} \frac{\psi(t)}{t}\, t^{\frac{1-\lambda}{p}} \left(ess\inf_{x>0} f\, \frac{w(tx)}{\nu(t)} \right)^{1/p} dt < \infty.$$

Theorem 1. Let $0 < \lambda \le 1, 1 \le p < \infty$ and let w and ν be weight functions defined on R_+. Suppose ψ is a fixed positive function on R_+.

Then the following statements hold:

i) If $A_{\sup} < \infty$, then $H_{\psi} : L_{p,\lambda,\nu}(R_+) \to L_{p,\lambda,w}(R_+)$ is bounded and

$$\left\|H_{\psi} f\right\|_{L_{p,\lambda,w}(R_+)} \le A_{\sup} \left\| f \right\|_{L_{p,\lambda,\nu}(R_+)} \qquad (1)$$

ii) If $H_{\psi} : L_{p,\lambda,\nu}(R^+) \to L_{p,\lambda,w}(R^+)$ is bounded, then $\left\|H_{\psi}\right\|_{L_{p,\lambda,\nu}(R_+) \to L_{p,\lambda,w}(R_+)} \ge A_{\inf}$.

Corollary 1. Let $0 < \lambda \le 1, 1 \le p < \infty$ and let w and ν be weight functions defined on R_+. Suppose that there exists $K \ge 1$ such

that $ess\sup_{x>0} \frac{w(tx)}{\nu(x)} \le K\, ess\inf_{x>0} f\, \frac{w(tx)}{\nu(x)}$ for all $t>0$. Let ψ be a fixed positive function on R_+. Then the inequality (1) holds if and only if $A_{\inf} < \infty$.

Remark 1. Recently, two-weight inequalities in the framework of one-dimensional Hausdorff operators were studied in [2] and [9] (see, also [3] and [10]). We observe that in [9] the obtained necessary conditions differ from the sufficient conditions and coincide for the Hardy and Bellman operators. Also, in [2] and [3] the obtained necessary conditions differ from the sufficient conditions. Moreover, in [2], the corresponding boundedness of one-dimensional Hausdorff operators has been studied in the framework of other function spaces as well, namely, grand Lebesgue spaces and variable exponent Lebesgue spaces. Next, in [4], the authors establish necessary and sufficient conditions on monotone weight functions for the boundedness of special kind Hausdorff operators on weighted Lebesgue spaces. Similar problem for the muti-dimensional Hausdorff operators of special kind is studied in [5]. In addition, two-weight norm for Hausdorff operators on

Morrey type spaces were studied in [1], [6], [7] and so on.

References

1.N. An, M.Q. Wei, and F.Y. Zhao. *Sharp constants for multilinear Hausdorff operators on local Morrey-type spaces*. Forum Math. 35, 1133–1154 (2023).

2. R.A. Bandaliyev, P. Górka. *Hausdorff operator in Lebesgue spaces*. Math. Inequal. Appl. 22, 657–676 (2019).

3. R.A. Bandaliyev, K.H. Safarova. *On boundedness of multidimensional Hausdorff operator in weighted Lebesgue spaces*. Tbilisi Math. J. 13, 39–45 (2020).

4.R.A. Bandaliyev, K.H. Safarova. *On two-weight inequalities for Hausdorff operators of special kind in Lebesgue spaces*. Hacet. J. Math. Stat. 50, 1334–1346 (2021) .

5.R.A. Bandaliyev, D.R. Aliyeva. *A characterization of two-weight norm inequalities for multidimensional Hausdorff operators on Lebesgue spaces*. Positivity 28, 13 (2024).

6. V. I. Burenkov, E. Liflyand. *On the boundedness of Hausdorff operators on Morrey-type spaces*. Eurasian Math. J. 8, 97–104 (2017)

7. V. Burenkov, E. Liflyand. *Hausdorff operators on Morrey-type spaces*. Kyoto J. Math. 60, 93–106 (2020).
8.S.N. Lal, S. Ram. *On the absolute Hausdorff summability of a Fourier series*. Pacific J. Math. 42, 439-451(1972).
9. E. Liflyand. *Hardy type inequalities in the category of Hausdorff operators*. Modern Meth. Oper. Theory Harmonic Anal. OTHA 2018. Springer Proc. Math. & Stat. 291, 81–91(2019).
10. E. Liflyand. Hardy type inequalities with power weights for Hausdorff operators. J. Math. Sci. 266, 435-447(2022).

https://doi.org./10.58225/mpmma.2026.764

ON THE CONTINUITY OF HAUSDORFF OPERATOR IN ORLICZ SPACES

Bandaliyev Rovshan[1,2], Vugar Khalilov[2] and Ilhama Alekperova[3,4]

[1] AzUAC, Azerbaijan

[2] Institute of Mathematics , Azerbaijan

[3]Azerbaijan State University of Economics, Azerbaijan

[4]Azerbaijan Technical University, Azerbaijan

Abstract. In this abstract we establish sufficient condition on kernel function related with Young function for the boundedness of Hausdorff operator in Orlicz spaces.

Keywords: Hausdorff operator, Orlicz spaces, boundedness.

It is well known that Hausdorff operators have a deep root in the study of the Fourier analysis and it has a long history in the study of harmonic analysis. This integral operator is deeply rooted in the study of one-dimensional Fourier analysis and has become an essential part of modern harmonic analysis. In particular, it is closely related to the summability of the classical Fourier series [10]. Let $x \in R^+ = (0,\infty)$ and let ψ be a fixed kernel defined on $(0,\infty)$ such that

$\psi \in L_1^{loc}\left(R^+\right)$. Then the one-dimensional Hausdorff operator is defined by a linear operator

$$H_\psi f(x) = \int_0^\infty \frac{\psi\left(\frac{x}{y}\right)}{y} f(y)\, dy.$$

Many important operators in analysis are special cases of the Hausdorff operator,
which can be obtained by taking suitable choice of ψ. For example, the Hardy operator, the adjoint Hardy operator, the Hardy-Littlewood-Polya(Calderon) operator, Cesaro operator and Hardy-Hilbert operator are particular cases of the Hausdorff operator. We recall the definition of Young function. A function $\Phi : [0,\infty) \to [0,\infty]$ is called a Young function if Φ is convex, left-continuous, $\lim_{s\to+0} \Phi(s) = \Phi(0) = 0$ and $\lim_{s\to\infty} \Phi(s) = \infty$. From the convexity and $\Phi(0) = 0$ it follows that any Young function is non-decreasing. If there exists $s \in (0,\infty)$ such that $\Phi(s) = \infty$, then $\Phi(r) = \infty$ for $r \geq s$. By $\Re$ we will denote the set of Young functions such that $0 < \Phi(s) < \infty$ for $0 < s < \infty$. If $\Phi \in \Re$, then Φ is absolutely continuous on every closed interval in $[0,\infty)$

and bijective from $[0,\infty)$ to itself. Also the following Lemma holds.

Lemma [6]. Let Φ be a Young function. Then, as a convex function, Φ is continuous if and only if Φ is finite on $[0,\infty)$.

In particular, $\Phi \in C([0,\infty))$ if $\Phi \in \Re$. For a Young function Φ let $\Psi(r) = \inf\{s \geq 0 : \Phi(s) > r\}$. It is obvious that, if $\Phi \in \Re$, then Ψ is the usual inverse function of Φ. Also, Ψ is non-decreasing and right-continuous function such that $\Psi(0) = 0$. It is easy to see that $\Phi(\Psi(x)) \leq x \leq \Psi(\Phi(x))$ (see, [5]). A Young function Φ satisfies Δ_2-condition if there exists $K \geq 2$ such that $\Phi(2s) \leq K\Phi(s)$ for all $s > 0$. If $\Phi \in \Delta_2$, then $\Phi \in \Re$.

Definition. Let Φ be a Young function. The set

$$L^{\Phi}(R^+) = \left\{ f \in L_1^{loc}(R^+) : \int_0^{\infty} \Phi(k|f(x)|)dx < \infty \text{ for some } k > 0 \right\}$$

is called Orlicz space. $L^{\Phi}(0,\infty)$ is a Banach space with respect to the norm

$$\|f\|_{L^{\Phi}} = \inf\left\{ \lambda > 0 : \int_0^{\infty} \Phi\left(\frac{|f(x)|}{\lambda} \right) dx \leq 1 \right\}.$$

We give the following theorem.

Theorem 1. Let Φ be a Young function on R^+. Suppose that there exists K such that $\Phi(sx) \geq K\,\Phi(s)\Phi(x)$ *for all* $s, x \geq 0$.

Let ψ be a fixed positive function on $(0,\infty)$. Then the inequality

$$\left\|H_\psi f\right\|_{L^\Phi} \leq C \left\|f\right\|_{L^\Phi} \qquad (1)$$

holds if and only if

$$A = \int_0^\infty \frac{\psi(t)}{t}\ \Phi^{-1}(t)\,dt < \infty.$$

Moreover, if $C > 0$ is the best possible constant in (1), then

$$KBA \leq C \leq A$$

where $B = \overline{\lim_{\varepsilon \to +0}} \dfrac{\left\|\Phi^{-1}\left(x^{-1-\varepsilon}\right)\right\|_{L_\Phi\left(\frac{1}{\varepsilon},\ \infty\right)}}{\left\|\Phi^{-1}\left(x^{-1-\varepsilon}\right)\right\|_{L_\Phi(1,\ \infty)}}$.

Remark 1. Recently, two-weight inequalities in the framework of one-dimensional Hausdorff operators were studied in [1] and [11] (see, also [2] and [12]). We observe that in [11] the obtained necessary conditions differ from the sufficient conditions and coincide for the Hardy and Bellman operators. Also, in [1] and [2] the obtained necessary conditions differ from the sufficient conditions. Moreover, in [1], the corresponding boundedness of one-dimensional Hausdorff operators has been

studied in the framework of other function spaces as well, namely, grand Lebesgue spaces and variable exponent Lebesgue spaces. Next, in [3], the authors establish necessary and sufficient conditions on monotone weight functions for the boundedness of special kind Hausdorff operators on weighted Lebesgue spaces. Similar problem for the multi-dimensional Hausdorff operators of special kind is studied in [4]. In [7] the boundedness of Dunkl-Hausdorff operator on weighted Lebesgue spaces has been characterized and for a power type weight function the corresponding operator norm has been obtained. Very recently, in [8], the results of [1] were extended for the Dunkl-Hausdorff operator and the boundedness of one-dimensional Hausdorff operator on the cone of non-increasing functions was proved (see, also [9]).

References

1. R.A. Bandaliyev, P. Górka. *Hausdorff operator in Lebesgue spaces*. Math. Inequal. Appl. 22, 657–676 (2019).

2.R.A. Bandaliyev, K.H. Safarova. *On boundedness of multidimensional Hausdorff operator in weighted Lebesgue spaces*. Tbilisi Math. J. 13, 39–45 (2020).

3. R.A. Bandaliyev, K.H. Safarova. *On two-weight inequalities for Hausdorff operators of special kind in Lebesgue spaces*. Hacet. J. Math. Stat. 50, 1334–1346 (2021) .
4. R.A. Bandaliyev, D.R. Aliyeva. *A characterization of two-weight norm inequalities for multidimensional Hausdorff operators on Lebesgue spaces*. Positivity 28, 13 (2024).
5.O. Blasco, A. Osançlıol. *Notes on bilinear multipliers on Orlicz spaces*. Math. Nachr. 292, 2522-2536(2019).
6. L. Diening, P. Harjulehto, P. Hasto, M. Ruzicka. *Lebesgue and Sobolev Spaces with Variable Exponents*. Lecture Notes in Mathematics, 2017. Springer, Heidelberg, 2011.
7. S. Jain, A. Fiorenza, P. Jain. *Boundedness of Dunkl-Hausdorff operator in Lebesgue spaces*. Rocky Mountain J. Math. 51, 2031–2044(2021).
8. S. Jain, P. Jain. *Hausdorff and Dunkl–Hausdorff operators in Lebesgue spaces for monotone functions and monotone weights*. Positivity 27, 1-14(2023).
9. S. Jain, A.P. Singh, M.Madan, P. Jain. *Boundedness of Dunkl-Hausdorff operator for radially decreasing functions and monotone weights on* R^n. J. Math. Sci. 280, 356-373(2024).

10. S.N. Lal, S. Ram. *On the absolute Hausdorff summability of a Fourier series*. Pacific J. Math. 42, 439-451(1972).
11. E. Liflyand. *Hardy type inequalities in the category of Hausdorff operators*. Modern Meth. Oper. Theory Harmonic Anal. OTHA 2018. Springer Proc. Math. & Stat. 291, 81–91(2019).
12. E. Liflyand. Hardy type inequalities with power weights for Hausdorff operators. J. Math. Sci. 266, 435-447(2022).

https://doi.org./10.58225/mpmma.2026.771

ANALYTICAL SOLUTION OF TWO-DIMENSIONAL GAS DIFFUSION IN CYLINDRICAL FOOD PACKAGING SYSTEMS

Thamizh Suganya[1], Lakshmanan Rajendran[1]
AMET University , India

Abstract. This study presents an analytical investigation of two-dimensional gas diffusion in cylindrical food packaging systems using Fick's second law in cylindrical coordinates. The developed mathematical model describes the radial and axial diffusion behavior of dissolved gas species such as oxygen and carbon dioxide within packaged food compartments. Appropriate initial and insulated boundary conditions were considered to represent realistic storage environments. The governing partial differential equation was solved analytically using the method of separation of variables, where the radial component reduces to Bessel's differential equation and the axial component is represented through cosine eigenfunctions. The obtained analytical solution provides concentration distributions as functions of radial position, axial distance, and time. Eigenvalues were determined from the roots of Bessel functions, and the transient

diffusion behavior was analyzed through exponential decay terms. The proposed model effectively predicts gas transport characteristics in cylindrical geometries and offers a useful mathematical framework for optimizing modified atmosphere packaging systems, improving shelf-life estimation, and enhancing food preservation efficiency in modern packaging applications.
Keywords: Food packaging system; Gas transport; Mass diffusion; Modified atmosphere packaging**1. Introduction**

Food packaging plays a significant role in maintaining food quality, extending shelf life, and minimizing microbial contamination during storage and transportation. Recent developments in food packaging technologies focus on improving gas barrier properties, diffusion control, and sustainable packaging materials for enhanced food preservation. Mathematical modeling based on Fick's second law has become an important approach for studying gas transport mechanisms in cylindrical food packaging systems. Analytical techniques such as separation of variables and Bessel function formulations provide accurate predictions of radial and axial concentration profiles within packaged food products. These diffusion models are

particularly useful in optimizing modified atmosphere packaging (MAP) systems and evaluating oxygen and carbon dioxide migration behavior [1]. Furthermore, recent studies emphasize that advanced nanocomposite and intelligent packaging materials significantly improve diffusion resistance and preservation efficiency in modern food engineering applications [2,3]. Analytical modeling using separation of variables and diffusion equations has significant applications in biosensors and bio trickling filter systems [4].

2. Methodology

The diffusion equation in cylindrical coordinates was formulated using Fick's second law and solved analytically through separation of variables. Bessel and cosine eigenfunctions were applied under insulated initial and boundary conditions to obtain concentration distributions.

The two-dimensional diffusion of dissolved gas species (O_2 and CO_2) in a cylindrical food packaging system is governed by Fick's second law in cylindrical coordinates (r, z). Assuming axial symmetry and neglecting angular variation, the governing equation is [5],

$$\frac{\partial C(r,z,t)}{\partial t} = D\left(\frac{\partial^2 C(r,z,t)}{\partial r^2} + \frac{1}{r}\frac{\partial C(r,z,t)}{\partial r} + \frac{\partial^2 C(r,z,t)}{\partial z^2}\right), 0 < r < R, 0 < z < H, t > 0$$ (1)

The initial condition is, $C(r,z,0) = f(r,z)$ (2)

The BC's are, $\left.\frac{\partial C(0,z,t)}{\partial r}\right|_{r=0} = 0, \left.\frac{\partial C(R,z,t)}{\partial r}\right|_{r=R} = 0, \left.\frac{\partial C(r,0,t)}{\partial r}\right|_{z=0} = 0, \left.\frac{\partial C(r,H,t)}{\partial r}\right|_{z=H} = 0$(3)

Symbol	**Parameter Name**	**Unit**	**Typical Range**
$C(r,z,t$	Gas concentration	$mol\ m^{-3}$	$0.01 - 10$
D	Diffusion coefficient	$m^2 S^{-1}$	$10^{-12} - 10^{-9}$
r	Radial coordinate	m	$0 - R$
z	Axial coordinate	m	$0 - H$
t	Time	s	$0 - 10^6$
R	Radius of cylinder	m	$0.01 - 0.15$
H	Height of cylinder	m	$0.01 - 0.30$

3. Result and discussion

The eqns. (1)-(3) using separation of variables and Bessel functions under insulated boundary conditions and the analytical result is,

$$C(r,z,t) = \sum_{m=1}^{\infty}\sum_{n=0}^{\infty} A_{mn} J_0\left(\frac{\alpha_m r}{R}\right) cos\left(\frac{n\pi z}{H}\right) exp\left[-D\left(\frac{{\alpha_m}^2}{R^2} + \frac{n^2\pi^2}{H^2}\right)t\right] \quad (4)$$

Where, J_0 is Bessel function of first kind, α_m =roots of $J_1(\alpha_m) = 0$ where J_1 is the Bessel function of first order and A_{mn} is determined from the initial condition.

$$J_0(x) = \sum_{k=0}^{\infty} \frac{(-1)^k}{(k!)^2}\left(\frac{x}{2}\right)^{2k}, A_{mn} = \frac{\int_0^R \int_0^H f(r,z) J_0\left(\frac{\alpha_m r}{R}\right) cos\left(\frac{n\pi z}{H}\right) r dz dr}{\int_0^R J_0^2\left(\frac{\alpha_m r}{R}\right) r dr \int_0^H cos^2\left(\frac{n\pi z}{H}\right) dz} \quad (5)$$

The analytical solution successfully predicts radial and axial gas diffusion behavior in cylindrical food packaging systems. Concentration profiles decrease exponentially with time, demonstrating the effectiveness of Bessel-function-based diffusion modeling under insulated boundary conditions.

Conclusion

This study developed an analytical model for two-dimensional gas diffusion in cylindrical food packaging systems using

Fick's second law. The separation of variables method and Bessel functions effectively described concentration distributions, providing useful insights for optimizing modified atmosphere packaging and food preservation applications.

References

1. Mengozzi, A., et al.: Functional properties of food packaging solutions alternative to conventional multilayer systems. Journal of Food Science and Technology, 62, 483–491(2025).
2. Palanisamy, Y., et al.: Recent technological advances in food packaging: Sensors, automation, and application. Sustainable Food Technology, 3(1), 161–180(2025).
3. Bo Peng., et al.: Recent advances in nanomaterials-enabled active food packaging: Nanomaterials synthesis. Food Control, 166, 110542(2024).
4. Anitha, S., et al.: Analytical expression of non-steady-state concentrations and current pertaining to compounds present in the enzyme membrane of biosensor. Journal of Physical Chemistry A, 115, 4299-4306(2011).

5. Anh Khoa Nguyen., et al.: 2D numerical model for gas mass transfers in modified atmosphere packaging systems. Journal of food Engineering, 402,112701(2026).

https://doi.org./10.58225/mpmma.2026.778

MULTI-SUBLINEAR MAXIMAL OPERATORS ON PRODUCT TOTAL MORREY-GULIYEV SPACES

Sabir Hasanov[1]

[1] Gandja State University, Azerbaijan

Abstract. The main goal is to provide sufficient conditions for the boundedness of the multi-sublinear maximal operator $\mathcal{M}$ on product total Morrey-Guliyev spaces $L^{p_1,\lambda_1,\mu_1}(\mathbb{R}^n) \times ... \times L^{p_m,\lambda_m,\mu_m}(\mathbb{R}^n)$ to total Morrey-Guliyev spaces $L^{p,\lambda,\mu}(\mathbb{R}^n)$.

Keywords: total Morrey-Guliyev spaces, multi-sublinear maximal function, commutator, BMO.

1.Introduction

Morrey spaces, introduced by C. B. Morrey [5], play important roles in the regularity theory of PDE. In [1] Guliyev introduce a variant of Morrey spaces called total Morrey-Guliyev spaces $L_{p,\lambda,\mu}(\mathbb{R}^n)$, $0 < p < \infty$, λ, $\mu \in \mathbb{R}$. The total Morrey-Guliyev spaces $L^{p,\lambda,\mu}(\mathbb{R}^n)$, extend the Morrey space $L^{p,\lambda}(\mathbb{R}^n)$ by including the second parameter μ, which can be seen as the intermediate spaces between Lebesgue spaces and Morrey spaces. The total Morrey-Guliyev spaces $L^{p,\lambda,\mu}(\mathbb{R}^n)$ are the set of all locally integrable functions f with the finite norm

$$||f||_{L^{p,\lambda,\mu}} = \sup_{x\in R^n,\, t>0} [t]_1^{-\frac{\lambda}{p}} [1 /t]_1^{\frac{\mu}{p}} |f|_{L^p(B(x,t))},$$

where $[t]_1 = \min\{1, t\}$, $B(x,t)$ denotes the ball centered at x with radius $t > 0$. Total Morrey-Guliyev spaces can be viewed as generalizations of both classical and modified Morrey spaces. In particular, the case where $\lambda = \mu$ corresponds to classical Morrey space, and the case where $\mu = 0$ corresponds to modified Morrey space $\widetilde{L_{p,\lambda}}(\mathbb{R}^n)$.

Let $(\mathbb{R}^n)^m = \mathbb{R}^n \times ... \times \mathbb{R}^n$ be the m-fold product space ($m \in \mathbb{N}$). For $x \in \mathbb{R}^n$ and $r > 0$, we denote by $B(x,r)$ the open ball centered at x of radius r. Let $|B(x,r)|$ be the Lebesgue measure of the ball $B(x,r)$. We denote by $\vec{f}$ the m-tuple $(f_1, f_2, ..., f_m)$, $\vec{y} = (y_1, ..., y_m)$ and $d\vec{y} = dy_1 \cdots dy_m$.

In [4], Lerner et al. introduced the following multi-sublinear maximal function $\mathcal{M}(\vec{f})(x)$ defined as

$$\mathcal{M}(\vec{f})(x) = \sup_{B\ni x} \prod_{i=1}^{m} \frac{1}{|B|} \int_B |f_i(y_i)| dy_i.$$

When $m = 1$, we get $M \equiv M_1$ the classical Hardy-Littlewood maximal operator is given by

$$M(f)(x) = \sup_{B \ni x} \frac{1}{|B|} \int_B |f(y)| dy$$

Theorem 2.2 [3] *Let* p *be the harmonic mean of* $p_1, \dots, p_m > 1$ *and*
$\frac{\lambda}{p} = \sum_{j=1}^{m} \frac{\lambda_j}{p_j}$ for $0 \le \lambda_j < n$, $\frac{\mu}{p} = \sum_{j=1}^{m} \frac{\mu_j}{p_j}$ for $0 \le \mu_j < n$.
(i) *If* $p > 1$, *then the operator* $\mathcal{M}$ *is bounded from product total Morrey space* $L^{p_1,\lambda_1,\mu_1}(\mathbb{R}^n) \times \dots \times L^{p_m,\lambda_m,\mu_m}(\mathbb{R}^n)$ *to total Morrey space* $L^{p,\lambda,\mu}(\mathbb{R}^n)$. *Moreover, there exists a positive constant C such that the following inequality is valid for all* $\vec{f} \in L^{p_1,\lambda_1,\mu_1}(\mathbb{R}^n) \times \dots \times L^{p_m,\lambda_m,\mu_m}(\mathbb{R}^n)$

$$||\mathcal{M}\vec{f}||_{L^{p,\lambda,\mu}} \le C \prod_{j=1}^{m} ||f_j||_{L^{p_j,\lambda_j,\mu_j}}.$$

(ii) *If* $p = 1$, *then the operator* $\mathcal{M}$ *is bounded from product total Morrey space* $L^{p_1,\lambda_1,\mu_1}(\mathbb{R}^n) \times \dots \times L^{p_m,\lambda_m,\mu_m}(\mathbb{R}^n)$ *to weak total Morrey space* $WL^{p,\lambda,\mu}(\mathbb{R}^n)$. *Moreover, there exists a positive constant C such that the following inequality is valid for all* $\vec{f} \in L^{p_1,\lambda_1,\mu_1}(\mathbb{R}^n) \times \dots \times L^{p_m,\lambda_m,\mu_m}(\mathbb{R}^n)$

$$||\mathcal{M}\vec{f}||_{WL^{p,\lambda,\mu}} \le C \prod_{j=1}^{m} ||f_j||_{L^{p_j,\lambda_j,\mu_j}}.$$

In the case $\lambda = \mu$, $\lambda_j = \mu_j$, $j = 1, \dots, m$ from Theorem 2.2 we get the following corollary

Corollary 2.3 [2] *Let p be the harmonic mean of $p_1, \dots, p_m > 1$ and*

$$\frac{\lambda}{p} = \sum_{j=1}^{m} \frac{\lambda_j}{p_j} \text{ for } 0 \le \lambda_j < n. \qquad (2)$$

(i) If $p > 1$, then the operator $\mathcal{M}$ is bounded from product Morrey space $L^{p_1,\lambda_1}(\mathbb{R}^n) \times \dots \times L^{p_m,\lambda_m}(\mathbb{R}^n)$ to Morrey space $L^{p,\lambda}(\mathbb{R}^n)$. Moreover, there exists a positive constant C such that the following inequality is valid for all $\vec{f} \in L^{p_1,\lambda_1}(\mathbb{R}^n) \times \dots \times L^{p_m,\lambda_m}(\mathbb{R}^n)$

$$||\mathcal{M}\vec{f}||_{L^{p,\lambda}} \le C \prod_{j=1}^{m} ||f_j||_{L^{p_j,\lambda_j}}.$$

(ii) If $p = 1$, then the operator $\mathcal{M}$ is bounded from product Morrey space $L^{p_1,\lambda_1}(\mathbb{R}^n) \times \dots \times L^{p_m,\lambda_m}(\mathbb{R}^n)$ to weak Morrey space $WL^{p,\lambda}(\mathbb{R}^n)$. Moreover, there exists a positive constant C such that the following inequality is valid for all $\vec{f} \in L^{p_1,\lambda_1}(\mathbb{R}^n) \times \dots \times L^{p_m,\lambda_m}(\mathbb{R}^n)$

$$||\mathcal{M}\vec{f}||_{WL^{p,\lambda}} \le C \prod_{j=1}^{m} ||f_j||_{L^{p_j,\lambda_j}}.$$

In the case $\mu = \mu_j = 0,\ j = 1, \dots, m$ from Theorem 2.2 we get the following corollary

Corollary 2.4 [2] *Let p be the harmonic mean of $p_1, \dots, p_m > 1$ and satisfy (2).*

(i) If $p > 1$, then the operator $\mathcal{M}$ is bounded from product modified Morrey space $\widetilde{L^{p_1,\lambda_1}}(\mathbb{R}^n) \times \dots \times \widetilde{L^{p_m,\lambda_m}}(\mathbb{R}^n)$ to modified Morrey space $\widetilde{L^{p,\lambda}}(\mathbb{R}^n)$. Moreover, there exists a positive constant C such that the following inequality is valid for all $\vec{f} \in \widetilde{L^{p_1,\lambda_1}}(\mathbb{R}^n) \times \dots \times \widetilde{L^{p_m,\lambda_m}}(\mathbb{R}^n)$

$$||\mathcal{M}\vec{f}||_{\widetilde{L^{p,\lambda}}} \leq C \prod_{j=1}^{m} ||f_j||_{\widetilde{L^{p_j,\lambda_j}}}.$$

(ii) If $p = 1$,then the operator $\mathcal{M}$ is bounded from product modified Morrey space $\widetilde{L^{p_1,\lambda_1}}(\mathbb{R}^n) \times \dots \times \widetilde{L^{p_m,\lambda_m}}(\mathbb{R}^n)$ to weak modified Morrey space $W\widetilde{L^{p,\lambda}}(\mathbb{R}^n)$. Moreover, there exists a positive constant C such that the following inequality is valid for all $\vec{f} \in \widetilde{L^{p_1,\lambda_1}}(\mathbb{R}^n) \times \dots \times \widetilde{L^{p_m,\lambda_m}}(\mathbb{R}^n)$

$$||\mathcal{M}\vec{f}||_{W\widetilde{L^{p,\lambda}}} \leq C \prod_{j=1}^{m} ||f_j||_{\widetilde{L^{p_j,\lambda_j}}}.$$

References

1. Guliyev V.S., Maximal commutator and commutator of maximal function on total Morrey spaces, J. Math. Inequal. 16 (2022), no. 4, 1509-1524.
2. Hasanov S.G. Multi-sublinear rough maximal operator on product Morrey and product modified Morrey spaces, Journal of Contemporary Applied Mathematics, 4, no. 2 (2014), 57-65.
3. Hasanov S.G. Multi-sublinear maximal operators on product total Morrey-Guliyev spaces, Trans. Natl. Acad. Sci. Azerb. Ser. Phys.-Tech. Math. Sci. 46(1) Mathematics (2026), 56-63.
4. Lerner A.K., Ombrosi S., Perez C., Torres R.H., Trujillo-Gonzalez R.: New maximal functions and multiple weights for the multilinear Calder´on-Zygmund theory. Adv. Math., 220 (2009), 1222-1264.
5. Morrey C.B., On the solutions of quasi-linear elliptic partial differential equations, Trans. Amer. Math. Soc. 43 (1938), 126-166.1. Introduction

https://doi.org./10.58225/mpmma.2026.784

THE BOUNDEDNESS OF THE MAXIMAL OPERATOR IN LOCAL " COMPLEMENTARY" GENERALIZED MORREY SPACES

Sevinc Khaligova
Azerbaijan Academy of Labor and Social Relations, Azerbaijan

Abstract. We consider the generalized shift operator, associated with the Laplace-Bessel differential operator. The maximal operator, associated with the generalized shift operator are investigated. We prove that the -maximal operator is bounded from the local" complementary" generalized -Morrey space to where.

Keywords: B-maximal operator, generalized B-Morrey space, local" complementary" generalized B-Morrey space.

1. Introduction

For $x \in R^n$ and $r > 0$, let $B(x,r)$ denote the open ball centered at x of radius r.

Let $f \in L_1^{loc}(R^n)$. The maximal operator M is defined by

$$Mf(x) = \sup_{t>0} |B(x,t)|^{-1} \int_{B(x,t)} |f(y)| dy,$$

where $|B(x,t)|$ is the Lebesgue measure of the ball $B(x,t)$.

Definition 1. *Let* $\omega(r)$ *positive measurable weight function on* $(0,\infty)$ *and* $1 \le p < \infty$. *We denote by* $M^{p,\omega}(R^n)$ *the generalized Morrey spaces, the spaces of all functions* $f \in L_p^{loc}(R^n)$ *with finite quasinorm*

$$\|f\|_{M^{p,\omega}(R^n)} = \sup_{x \in R^n, r>0} \frac{r^{-\frac{n}{p}}}{\omega(r)} \|f\|_{L_p(B(x,r))}.$$

In local "complementary" generalized Morrey spaces ${}^{c}M^{p,\omega}_{\{0\}}(R^n)$ with constant p, the space of all functions $f \in L_p(R^n \setminus B(x_0,r))$, $r>0$ by the norm

$$\|f\|_{{}^{c}M^{p,\omega}_{\{x_0\}}(R^n)} = \sup_{r>0} \frac{r^{\frac{n}{p'}}}{\omega(r)} \|f\|_{L_p(R^n \setminus B(x_0,r))}$$

were introduced and studied.

We denote by the local "complementary" Morrey spaces ${}^{c}L^{p,\lambda}_{\{x_0\}}(R^n)$ with constant p, the space of all functions $f \in L_p(R^n \setminus B(x_0,r))$, $r>0$ with the finite norm

$$\|f\|_{{}^{c}L^{p,\lambda}_{\{x_0\}}(R^n)} = \sup_{r>0} r^{\frac{\lambda}{p'}} \|f\|_{L_p(R^n \setminus B(x_0,r))} < \infty, \ x_0 \in R^n,$$

where $1 \le p < \infty$ and $0 \le \lambda < n$. Note that ${}^{c}L^{p,0}_{\{x_0\}}(R^n) = L_p(R^n)$.

Denote by T^x the generalized shift operator (B–shift operator) acting according to the law

$$T^x f(y) = C_{\gamma,k} \int_0^{\pi} \dots \int_0^{\pi} f((x',y')_\beta, x''-y'') d\nu(\beta),$$

where $(x_i, y_i)_{\beta_i} = (x_i^2 - 2x_i y_i \cos\beta_i + y_i^2)^{\frac{1}{2}}$,

$1 \le i \le k$, $(x,y)_\beta = ((x_i,y_i)_{\beta_1}, \dots, (x_k,y_k)_{\beta_k})$,

$d\nu(\beta) = \prod_{i=1}^{k} \sin^{\gamma_i - 1}\beta_i d\beta_1 \dots d\beta_k$, $1 \le k \le n$ and

$$C_{\gamma,k} = \pi^{-\frac{k}{2}} \prod_{i=1}^{k} \frac{\Gamma\left(\frac{\gamma_i+1}{2}\right)}{\Gamma\left(\frac{\gamma_i}{2}\right)} = \frac{2^k}{\pi^k} \omega(2k,k,\gamma).$$

We remark that the generalized shift operator T^x is closely connected with the Bessel differential operator B.

Let $L_{p,\lambda}(R^n_{k,+})$ be the space of measurable functions on $R^n_{k,+}$ with finite norm

$$\|f\|_{L_{p,\gamma}} = \|f\|_{L_{p,\gamma}(R^n_{k,+})} = \left(\int_{R^n_{k,+}} |f(x)|^p (x')^\gamma dx \right)^{1/p}, \ 1 \le p < \infty.$$

The translation operator T^y generates the corresponding B-convolution

$$(f \otimes g)(x) = \int_{R^n_{k,+}} f(y) \left[T^x g(y)\right] (y')^\gamma dy,$$

for which the Young inequality

$$\|f \otimes g\|_{L_{r,\gamma}} \le \|f\|_{L_{r,\gamma}} \|g\|_{L_{r,\gamma}}, \ 1 \le p,q \le r \le \infty, \ \frac{1}{p}+\frac{1}{q}=\frac{1}{r}+1,$$

holds.

Definition 2. *Let* $1 \le p < \infty, \ 0 \le \lambda \le Q$. *We denote by* $M^{p,\lambda,\gamma}(R^n_{k,+})$ *Morrey space* ($\equiv B-$ *Morrey space), associated with the Laplace-Bessel differential operator the set of locally integrable functions* $f(x), \ x \in R^n_{k,+}$, *with the finite norm*

$$\|f\|_{M^{p,\lambda,\gamma}} = \sup_{t>0, x \in R^n_{k,+}} \left(t^{-\lambda} \int_{E_t} T^y \left[|f| \right]^p (x)(y')^\gamma dy \right)^{1/p}.$$

Consider the $B-$ maximal operator

$$M_\gamma f(x) = \sup_{r>0} |E_r|_\gamma^{-1} \int_{E_r} T^y \left[|f| \right](x)(y')^\gamma dy.$$

2. *B*-maximal Operator in the Spaces ${}^cM^{p,\omega,\gamma}_{\{0\}}(R^n_{k,+})$

Theorem 1. *Let* $1 < p < \infty$ *and* $f \in L_{p,\gamma}(R^n_{k,+} \setminus E(0,r))$ *for every* $r \in (0,\infty)$. *If the integral*

$$\int_0^1 \|f\|_{L_{p,\gamma}(R^n_{k,+} \setminus E(0,r))} \frac{dr}{r}$$

is convergent, then

$$\|M_\gamma f\|_{L_{p,\gamma}(R^n_{k,+} \setminus E(0,r))} \le C \int_0^{2t} \|f\|_{L_{p,\gamma}(R^n_{k,+} \setminus E(0,s))} \frac{ds}{s}$$

for every $t \in (0,\infty)$, *where* C *does not depend on* f, t *and* x.

Theorem 2. *Let* $1 < p < \infty$ *and the functions* ω_1 *and* ω_2 *satisfy condition*

$$\int_0^t s^{-\frac{Q}{p'}} \omega_1(s)\omega_1(s)\frac{ds}{s} \le Ct^{-\frac{Q}{p'}} \omega_2(t),$$

then the operator M_γ *is bounded from* ${}^cM^{p,\omega_1,\gamma}_{\{0\}}(R^n_{k,+})$ *into* ${}^cM^{p,\omega_2,\gamma}_{\{0\}}(R^n_{k,+})$.

References

1. Adams D.R. A note on Riesz potentials. *Duke Math. J.*, 1975, **42** (4), pp. 765-778.

2. Aliyeva L.R., Esen Almali S., Safarov Z.V. Maximal operator in weighted Morrey spaces,

associated with the Laplace-Bessel differential operator. *Baku Math. J.*, 2023, **2** (2), pp.

176- 183.

3. Aykol C., Hasanov J.J. On the boundedness of *B*-maximal commutators, commutators of

B- Riesz potentials and *B*-singular integral operators in modified *B*-Morrey spaces. *Acta*

Sci. Math. (Szeged), 2020, **86** (3-4), pp. 521-547.

4. Chiarenza F., Frasca M. Morrey spaces and Hardy-Littlewood maximal function. *Rend.*

Mat. Appl. (7), 1987, **7** (3-4), pp. 273-279.

5. Gadjiev A.D., Aliev I.A. On classes of operators of potential types, generated by a gener

alized shift. *Reports of Enlarged Session of the Seminars of I.N. Vekua Inst. Appl.*

Math., 1988, **3**(2), pp. 21-24 (in Russian).

https://doi.org./10.58225/mpmma.2026.790

WEIGHTED INEQUALITIES FOR MAXIMAL OPERATORS IN B-MORREY SPACES

Sabina Kasumova
Azerbaijan State Pedagogical University, Azerbaijan

Abstract. In this paper, we prove Calderon-weighted inequalities for maximal operators in B-Morrey spaces.

Keywords: B-maximal operator, generalized shift operator, weighted Lebegue space, Calderon weighted Morrey space.

Let $R^n_{k,+}$ be the part of the Euclidean space R^n of points $x=(x_1,...,x_n)$ defined by the inequalities $x_1>0$, ... $x_k>0$, $1\le k\le n$, $(x')^\gamma = x_1^{\gamma_1}\cdots x_k^{\gamma_k}$, $\gamma=(\gamma_1,...,\gamma_k)$ is a multi-index consisting of fixed positive numbers.

In this paper we realize some estimations of the *B*-fractional maximal operator generated by the generalized shift operator of the form

$$T^y f(x) = C_{\gamma,k}\int_0^\pi\cdots\int_0^\pi f\left((x',y')_\beta, x''-y''\right)d\nu(\beta),$$

where $(x_i,y_i)_{\beta_i} = (x_i^2 - 2x_i y_i\cos\beta_i + y_i^2)^{\frac{1}{2}}$, $1\le i\le k$, $(x',y')_\beta = \left((x_1,y_1)_{\beta_1},\ldots,(x_k,y_k)_{\beta_k}\right)$,

$d\nu(\beta)=\prod_{i=1}^{k}\sin^{\gamma_i-1}\beta_i d\beta_1\cdots d\beta_k$, $1\le k\le n$, and

$C_{\gamma,k}=\pi^{-\frac{k}{2}}\Gamma^{-1}\left(\frac{|\gamma|}{2}\right)\prod_{i=1}^{k}\Gamma^{-1}\left(\frac{\gamma_i+1}{2}\right)$.

Let $L_{p,\varphi,\gamma}(R^n_{k,+})$ be the space of measurable functions on with finite norm

$$\|f\|_{L_{p,\varphi,\gamma}}=\|f\|_{L_{p,\varphi,\gamma}(R^n_{k,+})}=\left(\int_{R^n_{k,+}}|f(x)|^p\,\varphi(x)(x')^{\gamma}dx\right)^{1/p},\quad 1\le p<\infty.$$

For $p=\infty$ the space $L_{\infty,\gamma}(R^n_{k,+})$ is defined using the usual modification

$$\|f\|_{L_{\infty,\varphi,\gamma}}=\|f\|_{L_{\infty,\varphi}}=\operatorname*{ess\,sup}_{x\in R^n_{k,+}}\varphi(x)|f(x)|.$$

Definition 1. The weight function ω belongs to the class $\omega\in C_{p,\gamma}(R^n_{k,+})$ for $1\le p<\infty$, if the following

$$\sup_{x\in R^n_{k,+},r>0}\left\|\frac{\omega}{|\cdot|^{n+|\gamma}}\right\|_{L_{p,\gamma}(R^n_{k,+}\setminus E(x,r))}\left\|\omega^{-1}\right\|_{L_{p',\gamma}(E(x,r))}<\infty$$

is finite.

Consider the *B*-maximal operator

$$M_{\gamma}f(x)=\sup_{r>0}r^{-n-|\gamma|}\int_{B_+(0,r)}T^y|f|(x)(y')^{\gamma}dy,$$

where $B_+(0,r)=\{x\in R^n_{k,+}:T^y|x|<r\}$.

Let $1\le p<\infty$, ω positive measurable function. The local *B*-Morrey space $L_{p,\lambda,\omega,\gamma}(R^n_{k,+})$ is defined by the norm

$$\|f\|_{L_{p,\lambda,\omega,\gamma}(R^n_{k,+})} = \sup_{x\in R^n_{k,+},r>0} r^{-\frac{\lambda}{p}} \left(\int_{B_+(0,r)} \left[T^y \mid f \mid (x) \right]^p \omega^p(y)(y')^\gamma dy \right)^{\frac{1}{p}}$$

.

Theorem 1. *Let* $1 < p < \infty, 0 \le \lambda < n + |\gamma|$, $\omega \in C_{p,\gamma}(R^n_{k,+})$. *Then the operator* M_γ *is bounded from* $L_{p,\lambda,\omega,\gamma}(R^n_{k,+})$ *to* $L_{p,\lambda,\omega,\gamma}(R^n_{k,+})$.

References

1. Aliyeva L.R., Esen Almali S., Safarov Z.V. Maximal operator in weighted Morrey spaces, associated with the Laplace-Bessel differential operator. Baku Math. J., 2 (2), 176-183 (2023).

2. Aykol C., Hasanov J.J. On the boundedness of B-maximal commutators, commutators of B-Riesz potentials and B-singular integral operators in modified B-Morrey spaces. Acta Sci. Math., 86 (3-4), 521-547 (2020).

3. Guliyev V.S., Hasanov J.J. Necessary and sufficient conditions for the boundedness of B-Riesz potential in the B-Morrey spaces. J. Math. Anal. Appl., 347, 113-122 (2008).

https://doi.org./10.58225/mpmma.2026.793

NUMERICAL INVESTIGATION OF THERMO-HYDRAULIC PERFORMANCE OF MULTI-START CORRUGATED COILED TUBES IN TURBULENT FLOWS

Safak Metin Kirkar[1], Alişan Gönül[2] and Ahmet Selim Dalkilic[1,]

[1] Yildiz Technical University, Türkiye

[2] Siirt University, Türkiye

Abstract. This study numerically investigates the thermo-hydraulic performance of multi-start corrugated coiled tubes using computational fluid dynamics. Tubes with one to four corrugation starts are evaluated against a smooth baseline under turbulent flow (10,000 < Re < 50,000). The geometric effects on Nusselt number, friction factor, and Performance Evaluation Criterion (PEC) are systematically analyzed. Results show that while the four-start configuration maximizes heat transfer via intensified secondary flows and boundary layer disruption, it induces a severe pressure drop penalty. Consequently, the three-start configuration provides the optimal thermo-hydraulic balance, achieving a maximum PEC of 1.18 at lower Reynolds numbers.

Keywords: Coiled Tube, Multi-start Corrugation, CFD.

Introduction

Passive heat transfer enhancement techniques, particularly helically coiled tubes, are widely utilized to improve the efficiency of industrial thermal systems [1]. While traditional single-start corrugated tubes effectively improve thermal performance, multi-start profiles have recently emerged to further extend the surface area and distribute the swirl effect more homogeneously. Existing literature on straight tubes demonstrates that multi-start corrugations significantly increase heat transfer, though the optimal number of starts remains debated due to the associated flow resistance penalties [2, 3].

Crucially, the application of multi-start corrugations in helically coiled tubes is scarce in the literature. To address this gap, the present study numerically investigates the thermo-hydraulic performance of helically coiled tubes with one to four corrugation starts using computational fluid dynamics. The enhancements in Nusselt number (Nu_{enh}) and friction factor (f_{enh}), along with the Performance Evaluation Criterion (PEC), are compared against a baseline smooth coiled tube under turbulent conditions ($10{,}000 < Re < 50{,}000$). The primary objective is to

determine the optimum number of corrugation starts that maximizes the PEC for industrial applications.

Numerical Model

Geometric dimensions (tube diameter: 8.32 mm, coil diameter: 150 mm, pitch: 12 mm, 1.23 turns) were kept constant to isolate the effect of surface modification. A baseline smooth coiled tube (SCT) and four corrugated coiled tubes (CCT1-CCT4) were investigated. CCTs have a 2 mm depth and 36.26 mm pitch, altering only in the number of starts (n = 1-4). A hybrid grid of a polyhedral core and prism boundary layers was generated (Fig. 1). y^+ values were maintained below 1 to ensure high resolution in the viscous sublayer. The SST k-ω turbulence model was employed to capture adverse pressure gradients and flow separation. Boundary conditions comprises of varying mass flow inlets at 293.15 K, a zero-gauge pressure outlet, and a no-slip wall with a 50 kW/m² uniform heat flux. Governing equations were discretized via second-order upwind schemes, utilizing the COUPLED algorithm.

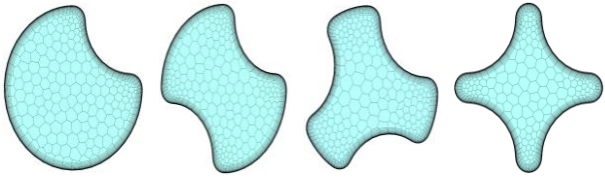


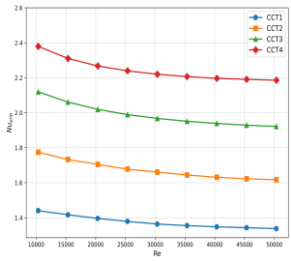
Fig. 1. Mesh structures of the investigated tubes

Results and Discussion

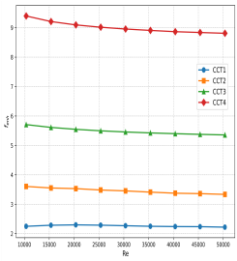
Fig. 2 evaluates the thermo-hydraulic performance of CCT1-CCT4 against the SCT ($10{,}000 < Re < 50{,}000$). As shown in Fig. 2(a), Nusselt number enhancement (Nu_{enh}) exceeds unity for all corrugated coiled tubes, peaking in CCT4. This is due to the continuous thermal boundary layer disruption and intensified Dean vortices [4]. However, this thermal advantage diminishes at higher Re as baseline turbulence dominates.

The hydraulic penalty, which is represented by friction factor enhancement (f_{enh}, Fig. 2b), is highest for CCT4 because of the increased flow resistance, whereas CCT1 and CCT2 revealed moderate increments. Ultimately, the Performance Evaluation Criterion (PEC, Fig. 2c) shows that despite CCT4's superior heat transfer, its greater pressure drop decreases the overall efficiency. Instead, CCT3 provides the optimal balance with a

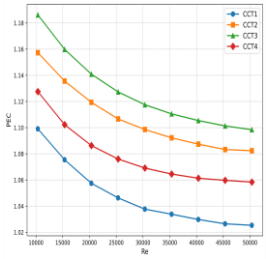
maximum PEC of ~1.18 at lower Reynolds numbers. Across all models, PEC decreases towards unity as Re increases which indicates that these geometries are most effective for relatively low-flow-rate industrial applications.



(a)



(b)



(c)

Fig. 2. Variation of enhancement ratios with Reynolds number for different corrugation starts (CCT1-CCT4): (a) Nu_{enh}, (b) f_{enh} and (c) *PEC*.

Conclusions

This study investigated the thermo-hydraulic performance of multi-start corrugated coiled

tubes under turbulent flow (10,000 < Re < 50,000). Results indicate that while increasing corrugation starts (up to CCT4) maximizes heat transfer via intensified secondary flows, it also produces a higher pressure drop penalty. Consequently, the three-start configuration (CCT3) provides the optimal balance by achieving a maximum PEC of 1.18 at lower Reynolds numbers. Ultimately, combining coiled geometries with three-start corrugations presents the most effective design for industrial heat exchangers.

References

1. Naphon, P., Wongwises, S.: A review of flow and heat transfer characteristics in curved tubes. Renewable and Sustainable Energy Reviews. 10, 463–490 (2006).
2. Qian, J.-Y., Chen, M.-R., Wu, Z., Liu, X.-L., Jin, Z.-J., Sundén, B.: A geometric study on shell side heat transfer and flow resistance of a six-start spirally corrugated tube. Numerical Heat Transfer, Part A: Applications. 73, 565–582 (2018).
3. Harleß, A., Franz, E., Breuer, M.: Experimental investigation of heat transfer and friction characteristic of fully developed gas flow in single-start and three-start corrugated tubes. International Journal of

Heat and Mass Transfer. 103, 538–547 (2016).
4. Yang, C., Chen, M.-R., Qian, J.-Y., Wu, Z., Jin, Z.-J., Sunden, B.: Heat Transfer Study of a Hybrid Smooth and Spirally Corrugated Tube. Heat Transfer Engineering. 42, 242–250 (2021).

https://doi.org./10.58225/mpmma.2026.*800*

MODERN METHODS OF TEXTURE GENERATION IN 3D MODELING: PROCEDURAL, IMAGE-BASED, AND AI APPROACHES

Beknazarova Saida, Abdullayeva Ozoda, Yunusova Dilnoza, Beknazarova Kamilla

[1] TUIT named after Mukhammad al-Khwarazmiy,Uzbekistan

[2] ManTU, Uzbekistan

Abstract. This article analyzes modern approaches to texture generation in 3D modeling, including procedural, image-based, and artificial intelligence (AI)-based methods. The study examines the algorithms used in the texture generation process, their advantages and disadvantages, as well as their effectiveness in achieving realistic visualization. In addition, hybrid approaches for creating photorealistic textures in 3D graphics and their practical applications are discussed.

Keywords: 3D modeling, texture generation, procedural texture, image-based texture synthesis, AI-based texturing, texture mapping, UV mapping, photorealistic visualization, computer graphics, rendering.

Introduction

Nowadays, computer graphics and 3D modeling technologies are rapidly developing and are widely used in various fields such as the film industry, video games, architectural visualization, virtual and augmented reality systems, and scientific simulations. One of the key components of these technologies is the process of texture creation and its application to 3D models. To achieve photorealistic images, the geometric model alone is not sufficient; textures that bring the surface closer to real-world appearance play a crucial role. A texture is a 2D image or a mathematical model applied to the surface of a 3D object, representing its color, light reflection properties, surface structure, and material characteristics. In modern computer graphics systems, texture is considered not only as a visual enhancement but also as an essential component of physically based rendering (PBR) processes [3], [4].In recent years, several main approaches to texture generation have emerged. One of the traditional methods, procedural texture generation, allows the creation of infinite and non-repetitive textures based on mathematical models and algorithmic

functions (such as Perlin noise and fractal models) [1], [5]. The main advantage of this approach is its flexibility and memory efficiency; however, its level of realism can sometimes be limited. Another approach is image-based texture synthesis, which relies on real-world images to generate textures. This method uses techniques such as patch-based algorithms, image quilting, and texture transfer to achieve a high level of visual realism [9], [14]. However, this approach often requires large datasets and complex computational processes. In recent years, artificial intelligence (AI-based texturing) has been rapidly developing. Using neural networks, generative adversarial networks (GANs), and deep learning models, high-quality and photorealistic textures can be generated automatically [15], [16]. Although this method provides superior visual quality compared to traditional approaches, it requires significant computational resources. In addition, the process of texture creation in 3D modeling is not limited to generation alone; it also includes stages such as UV mapping, texture mapping, material parameterization, and rendering. These processes ensure that textures are accurately and seamlessly applied to the surface of 3D models [3], [12]. Therefore, in modern

graphics systems, hybrid methods are often considered the most effective approach. These methods combine procedural, image-based, and AI approaches to produce high-quality textures suitable for real-time systems. This is particularly important in the gaming industry, virtual reality, and scientific visualization. This article provides a comprehensive analysis of modern methods of texture generation in 3D modeling—procedural, image-based, and AI-based approaches—comparing their advantages and disadvantages and examining their practical applications. The process of generating photorealistic images in modern computer graphics and 3D modeling systems consists of several complex stages, one of the most important being texture creation and its proper mapping onto a 3D model. No matter how accurate a geometric model is, without realistic textures, the final visual result will not appear natural. For this reason, texture generation has become a separate research area and is generally divided into three main approaches: procedural (algorithmic), image-based, and artificial intelligence (AI)-based methods. Each approach differs in its mathematical model, computational complexity, and quality of visual results. Furthermore, in practical systems, not only

texture generation but also its application to 3D models (UV mapping), integration with lighting (shading, PBR), and real-time rendering are essential processes.

Literature review

Texture generation in 3D modeling has been an active area of research in computer graphics, with various approaches proposed to improve realism, efficiency, and flexibility. The main directions in this field include procedural methods, image-based techniques, and, more recently, artificial intelligence (AI)-based approaches. Procedural texture generation has its roots in early works on noise functions and fractal geometry. Ken Perlin introduced *Perlin noise*, which became a fundamental tool for generating natural-looking textures such as wood, marble, and clouds. Later studies expanded this concept using fractal models and turbulence functions, enabling the creation of complex and non-repetitive patterns. Researchers have highlighted that procedural methods are highly memory-efficient and suitable for real-time applications, although achieving high photorealism remains a challenge. Image-based texture synthesis methods emerged as

an alternative to procedural techniques, focusing on reproducing real-world surface details. Methods such as image quilting proposed by Alexei A. Efros and William T. Freeman demonstrated how small patches from sample images can be combined to generate larger textures while preserving visual consistency. Subsequent works introduced texture transfer and optimization-based synthesis, improving quality and reducing artifacts. Despite their effectiveness, these methods often require large datasets and significant computational resources. In recent years, AI-based approaches have significantly transformed texture generation. Deep learning models, particularly Generative Adversarial Networks (GANs) introduced by Ian Goodfellow, have enabled the automatic creation of highly realistic textures. Models such as StyleGAN and diffusion-based architectures can learn complex texture distributions from large datasets and generate diverse, high-quality outputs. Studies show that AI-based methods outperform traditional techniques in terms of visual realism, although they require extensive training data and high computational power. Recent research trends focus on hybrid approaches that combine procedural, image-based, and AI techniques.

These methods aim to leverage the strengths of each approach—for example, using procedural methods for base structure, image-based techniques for realism, and AI models for detail enhancement. Such hybrid systems are increasingly used in game engines, virtual reality environments, and digital heritage reconstruction. Overall, the literature indicates that while no single method is universally optimal, the integration of multiple approaches provides the best balance between efficiency, flexibility, and visual quality in modern 3D texture generation.

Methodology

Therefore, modern approaches are often based on hybrid models that combine multiple methods. The following sections discuss these three main approaches—procedural, image-based, and AI-based texture generation methods—their working principles, advantages and disadvantages, and areas of practical application in detail. Among these approaches, procedural texture generation is based on mathematical functions and algorithms and allows the creation of infinite and non-repetitive textures. This method is distinguished by its

memory efficiency and speed, although it may sometimes be limited in achieving highly photorealistic results. Image-based texture synthesis, on the other hand, relies on real images and generates new textures while preserving their statistical and visual characteristics. This approach provides a high level of realism but requires large datasets and computational resources. AI-based texture generation is based on modern deep learning models and automatically produces high-quality and complex textures. Although this approach is the most advanced and flexible, it requires large training datasets and significant computational

3.1. Procedural Texture Generation Method

Procedural texture generation is an approach in computer graphics and 3D modeling where textures are generated without using pre-made images, but instead are based on mathematical functions and algorithmic models. In this method, texture values are defined by spatial coordinates (x,y,z)(x, y, z)(x,y,z), resulting in infinite, non-repetitive, and parametrically controllable surfaces [1], [5].

The fundamental mathematical representation of procedural textures can be expressed in a general form as follows:

$$T(x, y, z) = f(x, y, z)$$

where T(x,y,z) represents the texture intensity or color value, x,y,z are spatial coordinates, and f is an algorithmic function that generates the texture. In the 2D case, the model takes the following form:

$$T(x, y) = f(x, y)$$

One of the most important components in procedural texture generation is noise functions. For example, the Perlin noise model is widely used to generate natural-looking surfaces and can be expressed as:

$$N(x, y) = \sum_{i=1}^{n} a_i \cdot noise(2^i x, 2^i y)$$

where ai are amplitude coefficients and 2i represents the increase in frequency. This approach is used to model complex structures such as wood, stone, clouds, and other natural surfaces. Fractal-based procedural models are also widely used. The Fractal Brownian Motion (fBM) model is defined as:

$$fBM(x, y) = \sum_{i=0}^{n} \frac{1}{2^i} \cdot N(2^i x, 2^i y)$$

where each “octave” represents different frequency and amplitude levels, resulting in multi-scale detailed textures. Trigonometric

functions are also used in procedural textures, where simple periodic structures can be expressed as:

$$T(x, y) = sin(ax + by)$$

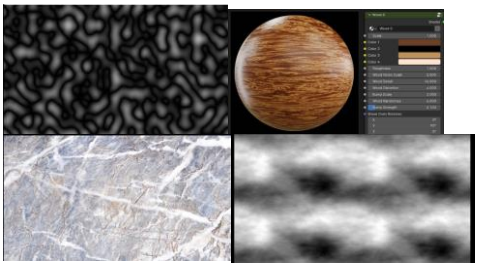
In addition, Voronoi diagram-based models are used to generate geometrically segmented textures, which can be expressed as:

$$T(p) = \min_i \|p - p_i\|$$

The process of procedural texture generation typically consists of several stages: input of coordinate systems, computation of noise functions, application of fractal or combined models, color mapping, and final rendering. This process can also be implemented in real-time graphics systems using shaders [3], [6].

The main scientific significance of the procedural approach lies in its ability to generate textures with infinite detail while minimizing memory usage, as well as providing dynamic control through parameters. Therefore, it is widely used in real-time graphics and large-scale scene modeling.

Figure 1. Examples of procedural textures generated based on noise and fractal models.



• Perlin Noise → clouds, smoke, terrain (landscapes)
• Fractal Brownian Motion (fBM) → natural terrain, rock formations
• Trigonometric models → wave-like surfaces
• Voronoi diagram → cellular structures (cell-like patterns)

3.2. Image-Based Texture Synthesis Method

Image-based texture synthesis is an approach in computer graphics and 3D modeling aimed at generating new textures based on real images (photographs or scanned data). The main idea of this method is to extend and adapt an existing image to larger surfaces or 3D models while preserving its statistical, structural, and local features [14], [9]. From a mathematical perspective, image-based texture synthesis treats an image as a probabilistic and optimization model. In

general form, texture synthesis can be expressed as:

$$T_{out} = arg\min_{T} D(T, T_{ref})$$

where Tout is the generated texture, Tref is the reference (input) image, and D represents a similarity or difference function. One of the most widely used approaches in image-based methods is **patch-based texture synthesis**, which involves dividing the image into small patches and combining them in the most suitable way. This process can be expressed as:

$$T(x) = p_i \; bu \; yerda \; i = arg\min_{j} \|p_x - p_j\|$$

where px is the target patch and pj are patches from the dataset. Another important approach is the **image quilting method**, where patches are combined while minimizing visible boundaries. The optimal cut path is determined as follows:

$$E_{cut} = \sum_{(i,j)\epsilon boundary} \|I_1(i,j) - I_1(i,j)\|^2$$

where Ecut is the matching error between patches, and I1 and I2 are the values of neighboring patches. Statistical models are also used in image-based texture synthesis. In this case, the texture is represented using a probability distribution of pixel values:

$$P(T) = \prod_i p(p_i|N(p_i))$$

where pi is a pixel value and N(pi) denotes its neighborhood. In the approach proposed by Efros and Freeman, **texture transfer** is achieved through the following optimization:

$$T_{out} = arg\min_T(E_{content}(T, T_{ref}) + \lambda E_{smooth}(T))$$

Here:

- Econtent represents structural similarity
- Esmooth represents the smoothness constraint
- λ is a balancing coefficient

The image-based synthesis process typically consists of the following stages: analysis of the input image, division into patches, selection of matching fragments, optimal placement, and seamless blending. During these stages, operations such as segmentation and transformations (rotation, scaling) are also applied. The main scientific significance of this approach lies in its ability to generate highly photorealistic textures from real-world images. Therefore, image-based texture synthesis is widely used in architectural visualization, the film industry, and 3D game graphics [14], [9].

Figure 2. Examples of image-based texture synthesis results.



The image-based approach generates the following real-world textures:

- Brick wall
- Stone surface
- Grass texture
- Fabric patterns

Applied methods: Patch-based synthesis, image quilting, texture transfer.

$$T_{out} = arg\min_{T} D(T, T_{ref})$$

3.3. AI (Deep Learning)-Based Texture Generation Method

Texture generation based on artificial intelligence and deep learning is one of the

most modern and rapidly developing approaches in computer graphics and 3D modeling. In this approach, textures are generated not through traditional mathematical functions or simple image processing techniques, but by neural networks that learn statistical patterns from large-scale datasets [15], [16]. The main objective of deep learning-based texture generation is to produce a new and unique texture distribution similar to the input data X. This process can be expressed as a probabilistic model:

$$T_{gen} \sim P_0(T|X)$$

where Tgen is the generated texture, X is the input data, and Pθ represents the probability distribution learned by the neural network parameters. One of the most popular deep learning approaches is **Generative Adversarial Networks (GANs)**. A GAN consists of two neural networks: a generator G and a discriminator D. The generator creates new textures, while the discriminator evaluates whether they are real or synthetic. The training process is formulated as a minimax optimization problem:

$$\min_{G} \max_{D} V(D,G) = E_{x\sim p_{data(x)}}[logD(x)] + E_{z\sim p_{(z)}}[\log(1-D(G(z)))]$$

In addition, texture synthesis based on **Convolutional Neural Networks (CNNs)** is widely used. In the style-based approach proposed by Gatys et al., texture is represented through content and style components:

$$L_{total} = \alpha L_{content} + \beta L_{style}$$

where:

- Lcontent is the structural similarity loss
- Lstyle is the texture style loss
- α,β are balancing coefficients

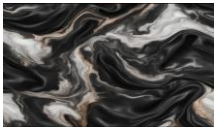
Style features are computed using the Gram matrix:

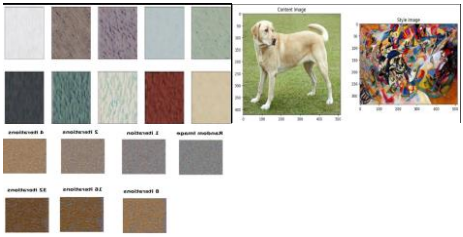
$$G_{ij}^{l} = \sum_{k} F_{ik}^{l} F_{jk}^{l}$$

The deep learning-based texture generation process typically consists of the following stages:

- Preparation of the texture dataset
- Training of the neural network model (GAN/CNN/VAE)
- Generation of new samples in the latent space
- Post-processing (denoising, color correction, sharpening)
- Integration into PBR materials

Figure 3. Examples of textures generated using deep learning models.





The following textures are generated using artificial intelligence:

• Marble and wood textures generated using GANs

• Art-like textures generated using style transfer

• High-resolution textures generated using super-resolution techniques (GAN): $T_{gen} = G(z)$

(Style transfer): $L_{total} = \alpha L_{content} + \beta L_{style}$

Results and Discussion

The experimental results demonstrate that each texture generation approach produces distinct visual and computational characteristics. Procedural methods based on noise and fractal functions generate highly efficient and memory-saving textures. These textures are mathematically consistent and suitable for real-time rendering; however, they often lack fine-grained realism when representing complex natural surfaces. Image-based texture synthesis methods show significantly improved visual realism compared to procedural approaches. Patch-based synthesis and texture quilting successfully preserve local statistical properties of reference images, resulting in more natural and visually convincing textures. Nevertheless, these methods require higher computational resources and are sensitive to input image quality and patch selection strategies. AI-based texture generation methods, particularly those based on deep learning models such as GANs and CNN-based style transfer, provide the highest level of visual realism. The generated

textures exhibit rich detail, structural coherence, and adaptability to different material types. However, the training process is computationally expensive and requires large datasets, which limits their real-time applicability in some systems. The proposed hybrid model combines the advantages of all three approaches. Procedural methods are used to generate the base structural layer of the texture, image-based techniques refine local details using real-world references, and AI-based models further enhance global consistency and visual quality. Experimental observations indicate that this combination produces more stable and visually realistic results compared to any single method.

Proposed Hybrid Model. Recent studies show that achieving the highest quality and most practical results is more effective not through individual methods, but through a hybrid approach that combines them. The proposed model has a three-stage architecture:

Stage 1: Procedural base. The initial structure is generated using mathematical noise and fractal models:

$$T_{base}(x, y) = fBM(x, y)$$

Stage 2: Image-based refinement. Fine details are added using patch-based processing from real images:

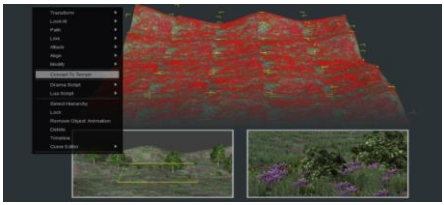
$$T_{detail} = arg\min_{T} D(T, T_{ref})$$

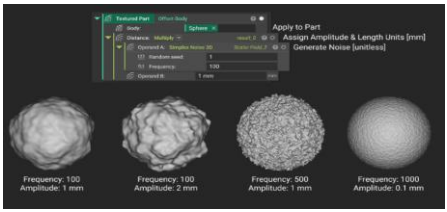
Stage 3: AI optimization. The texture is further enhanced in terms of quality using a neural network:

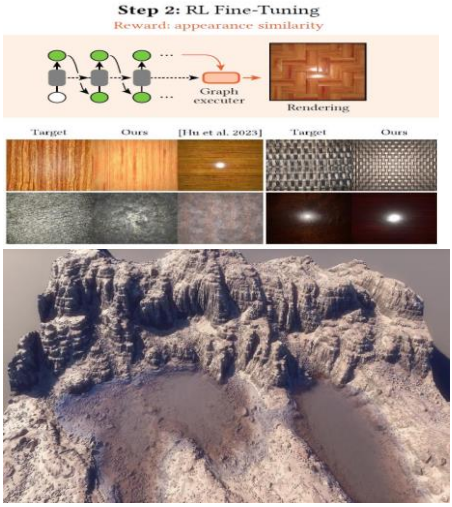
$$T_{final} = G(T_{base,} T_{detail})$$

The main advantage of this hybrid approach is that it combines the speed and stability of procedural methods, the realism of image-based methods, and the high quality and adaptability of AI-based methods. As a result, it enables the generation of photorealistic, optimized textures suitable for real-time systems [1], [14], [15], [16].

Figure 4. Results of hybrid texture generation combining procedural, image-based, and artificial intelligence methods.







The proposed hybrid model produces the following contributions:

- Procedural → basic structure
- Image-based → realistic details
- AI → final quality enhancement

$$T_{final} = G(T_{base}, T_{detail})$$

These examples demonstrate that each approach is effective for generating different types of textures. The highest-quality results are achieved using the hybrid approach, as it integrates the advantages of all three methods. In particular, the hybrid approach improves:

- structural consistency of textures (procedural layer),
- photorealistic detail accuracy (image-based layer),
- overall visual quality and adaptability (AI layer).

A comparative analysis shows that the hybrid model achieves a better balance between computational efficiency and visual realism. While it introduces additional processing stages, the final output quality significantly exceeds that of standalone procedural or image-based methods. Overall, the results confirm that hybrid texture synthesis is a promising direction for modern computer graphics applications, especially in areas requiring real-time rendering and high visual fidelity such as virtual reality, gaming, and digital heritage reconstruction.

Table 1. Comparison of texture generation methods

Method	**Computational Speed**	**Visual Realism**	**Memory Consumption**	**Main Advantages**	**Main Limitations**
Procedural (Noise / Fractal-based)	High (very fast)	Medium	Low	No dataset required, real-time generation, highly scalable	Limited fine detail, less photorealistic results
Image-based (Patch / Quilting)	Medium	High	High	High photorealism, preserves real-world structure	Requires input images, sensitive to data quality, higher computation cost
AI-based (Deep Learning: GAN/ CNN)	Low (training phase), Medium (inference)	Very High	Medium–High	Best visual quality, adaptive texture generation, learns complex patterns	Requires large datasets, expensive training, high computational resources
Hybrid (Proposed Model)	Medium	Very High	Medium	Balanced performance, combines strengths of all methods, improved realism and stability	More complex pipeline, higher implementation complexity

Figure Analysis

Figure 1 illustrates examples of procedural texture generation based on noise and fractal models. As shown in the figure, the generated textures exhibit self-similar patterns and infinite detail scalability. These textures are computationally efficient and suitable for real-time rendering; however, the visual output remains relatively abstract and less realistic compared to natural surfaces. The figure demonstrates that procedural methods are highly effective for generating structured and repeatable patterns such as wood, stone, and cloud-like surfaces.

Figure 2 presents the results of image-based texture synthesis methods. The generated outputs preserve the statistical and structural characteristics of the reference images. Patch-based synthesis and image quilting techniques produce visually coherent textures with high photorealism. However, slight artifacts may appear at patch boundaries depending on the quality of the input image and blending strategy. The figure confirms that image-based approaches are particularly effective for reproducing real-world materials with high fidelity.

Figure 3 shows textures generated using AI-based deep learning models such as GANs

and CNN-based style transfer methods. The results demonstrate significantly improved visual quality, including enhanced detail richness, structural consistency, and realistic material representation. Compared to procedural and image-based methods, AI-generated textures exhibit better adaptability to different material categories, although they require substantial computational resources during training.

Figure 4 illustrates the results of the proposed hybrid texture generation model, which integrates procedural, image-based, and AI-based approaches. The figure clearly shows that the hybrid method produces the most balanced results in terms of structural consistency, fine detail accuracy, and overall realism. Procedural components provide the global structure, image-based methods refine local details, and AI-based optimization enhances the final visual quality. As a result, the hybrid approach achieves superior visual fidelity while maintaining acceptable computational efficiency.

Conclusion

This paper analyzed modern approaches to texture generation in 3D modeling —

procedural, image-based, and artificial intelligence (AI)-based methods — from both scientific and practical perspectives. The mathematical models, working principles, and visual quality of each approach were examined, and their importance in computer graphics systems was justified. The analysis shows that the procedural approach is characterized by high speed and memory efficiency but has limitations in representing complex natural details. The image-based method provides highly photorealistic results due to its reliance on real images, but it requires large datasets and significant computational resources. The AI-based approach is the most advanced, enabling automatic generation of high-quality textures using neural networks, but it is also computationally expensive in terms of training and processing power. Although each of these approaches has its own limitations when used separately, combining them leads to more efficient results. Therefore, the proposed hybrid model integrates procedural, image-based, and AI methods to generate high-quality, photorealistic textures suitable for real-time systems. Overall, the development of texture generation in modern 3D graphics is increasingly moving toward more adaptive,

automated, and AI-driven systems. This trend is expected to further advance the creation of sophisticated graphical models in virtual reality, the gaming industry, and scientific visualization.

References

1. Ebert, D. S., Musgrave, F., Peachey, D., Perlin, K., & Worley, S. (2003). *Texturing and Modeling: A Procedural Approach*. Morgan Kaufmann. https://doi.org/10.1016/B978-155860848-1/50002-3

2. Lagae, A., Lefebvre, S., Drettakis, G., & Dutré, P. (2010). Procedural noise using sparse Gabor convolution. *ACM Transactions on Graphics*, 29(4). https://doi.org/10.1145/1778765.1778803

3 Akenine-Möller, T., Haines, E., & Hoffman, N. (2019). *Real-Time Rendering* (4th ed.). CRC Press. https://doi.org/10.1201/9781315368934

4.Shirley, P., & Marschner, S. (2015). *Fundamentals of Computer Graphics*. CRC Press.

5. Musgrave, F. K. (2012). Fractal terrains and procedural textures. *Computer Graphics and Applications*.

6. Cook, R. L. (2005). Stochastic sampling

in computer graphics. *ACM Transactions on Graphics*.
7. Mandelbrot, B. (2004). *Fractal Geometry of Nature*. W. H. Freeman.
8. Peitgen, H. O., Jürgens, H., & Saupe, D. (2006). *Chaos and Fractals*. Springer.
9.Lefebvre, S., & Hoppe, H. (2006). Appearance-space texture synthesis. *ACM Transactions on Graphics*. https://doi.org/10.1145/1179352.1141920
10.Efros, A. A., & Freeman, W. T. (2001). Image quilting for texture synthesis. *ACM SIGGRAPH Proceedings*. https://doi.org/10.1145/383259.383296
11. Gatys, L. A., Ecker, A. S., & Bethge, M. (2015). Texture synthesis using convolutional neural networks. *arXiv preprint*. https://arxiv.org/abs/1505.07376
12. Goodfellow, I., et al. (2014). Generative adversarial nets. *NeurIPS Proceedings*. https://arxiv.org/abs/1406.26612
13. Kingma, D. P., & Welling, M. (2013). Auto-encoding variational Bayes. *arXiv preprint*. https://arxiv.org/abs/1312.6114
14.Szeliski, R. (2010). *Computer Vision: Algorithms and Applications*. Springer.
15. Turk, G. (2001). Texture synthesis. *ACM SIGGRAPH Course Notes*.
16.Zhang, H., et al. (2017). Deep texture

synthesis with CNNs. *IEEE Transactions on Visualization and Computer Graphics*.

https://doi.org./10.58225/mpmma.2026.*829*

FREE OSCILLATIONS OF A ROD-REINFORCED CYLINDRICAL COVER UNDER THE INFLUENCE OF A COMPRESSIVE FORCE WITH A FLUID.

Salmanov Oktay
AzUAC, Azerbaijan

Abstract. The paper studies asymmetric natural vibrations of a fluid-filled cylindrical shell stiffened with rods subjected to the action of compressive force along the axis. Using the constructive-orthotropic model of the shell, compressive models of fluid and contact conditions, a frequency equation for the system under consideration was structured. The obtained equation is a transcendental equation with respect to the desired frequency parameter. Using the logarithmic derivative of the Bessel function, based on the shell thickness and character of change in the stress-strain of the shell, an analytic expression for the vibration frequency of the system under consideration was obtained and the influence of physical and geometrical parameters characterizing the system on these parameters was studied.

Keywords: compressive force, stiffened with rods, cylindrical shell, vibrations, stress.

The system under consideration consists of a cylindrical shell stiffened with rods and fluid completely filling its inside. Therefore, for studying vibrations of such a system, we will use equations of motion of a cylindrical shell stiffened with rods, of fluid and additional contact conditions.

Fundamentals of theory of deformation of shells stiffened with rods was given by V.Z.Vlasov [1] and A.I.Lourie [2].

It is considered that the coordinate axes coincide with principal curvature lines and rigidly contact with the shell along these lines. Using the Ostrogradsky-Hamilton variation principle, we can derive the system of main equations of the mentioned system. It is considered that the stress-starin state of the cylindrical shell is completely determined by the equations of linear theory of shells, based on Kirchhoff-Liav conjecture. In the calculation of rods the equations based on Kirchhoff-Glebsh theory on for straight axis rods are used.

When the cylindrical shell is under the action of compressive stress σ_x along the axis, its potential energy is determined as follow

$$\Im = \frac{Eh}{2\left(1-\nu^2\right)}\int_0^{\xi_1}\int_0^{2\pi}\left\{\left(\frac{\partial u}{\partial \xi}+\frac{\partial \upsilon}{\partial \theta}-w\right)^2+2(1-\nu)\left[\frac{\partial u}{\partial \xi}\left(\frac{\partial \upsilon}{\partial \theta}-w\right)-\right.\right.$$

$$-\frac{1}{4}\left(\frac{\partial u}{\partial\theta}+\frac{\partial\upsilon}{\partial\xi}\right)^2\Bigg]\Bigg\}d\xi d\theta+\frac{Eh^3}{24\left(1-\nu^2\right)R^2}\int_0^{\xi_1}\int_0^{2\pi}\Bigg\{\left(\frac{\partial^2 w}{\partial\xi^2}+\frac{\partial^2 w}{\partial\theta^2}+\frac{\partial\upsilon}{\partial\theta}\right)^2-$$

$$-2\left(1-\nu\right)\left[\frac{\partial^2 w}{\partial\xi^2}\left(\frac{\partial^2 w}{\partial\theta^2}+\frac{\partial\upsilon}{\partial\theta}\right)-\left(\frac{\partial^2 w}{\partial\xi\partial\theta}+\frac{\partial\upsilon}{\partial\xi}\right)^2\right]\Bigg\}d\xi d\theta+$$

$$+\frac{E_s}{2R}\sum_{j=1}^{k_1}\int_0^{2\pi}\Bigg[F_s\left(\frac{\partial\upsilon}{\partial\theta}-w-\frac{h_s}{R}\frac{\partial^2 w}{\partial\theta^2}\right)^2+\frac{I_{xs}}{R^2}\left(\frac{\partial^2 w}{\partial\theta^2}+w\right)^2+\frac{G_s}{R^2E_s}I_{\kappa p.s}\times$$

$$\times\left(\frac{\partial^2 w}{\partial\xi\partial\theta}+\frac{\partial u}{\partial\theta}\right)^2\Bigg]_{\xi=\xi_j}d\theta-\frac{\sigma_x h}{2}\int_0^{\xi_1}\int_0^{2\pi}\left(\frac{\partial w}{\partial\xi}\right)^2 d\xi d\theta-\frac{\sigma_x F_c}{2R}\sum_{i=1}^{k}\int_0^{\xi_1}\left(\frac{\partial w}{\partial\xi}\right)^2\Bigg|_{\theta=\theta_i}d\xi+$$

$$+\frac{E_c}{2R}\sum_{i=1}^{k_2}\int_0^{\xi_1}\Bigg[F_c\left(\frac{\partial u}{\partial\xi}-\frac{h_c}{R}\frac{\partial^2 w}{\partial\xi^2}\right)^2+\frac{I_{yc}}{R^2}\left(\frac{\partial^2 w}{\partial\xi^2}\right)^2+\frac{G_c}{E_c}I_{\kappa p.c}\left(\frac{\partial^2 w}{\partial\xi\partial\theta}+\frac{\partial\upsilon}{\partial\xi}\right)^2\Bigg]_{\theta=\theta_i}d\xi.$$

In the expressions u,υ,w are displacements of the shell, $E,\nu-$are elasticity modulus and the Poisson ratio of the cylindrical shell, respectively, R,h are radii and thickness of the cylindrical shell, respectively, E_c,E_s are elasticity module of the longtitudinal rod and ring, respectively, F_c,F_s are cross-section

areas of the longitudinal rod and ring, respectively, $I_{yc}, I_{kp.c}$ are enertia moments of the cross section of the longitudinal rod, respectively, $I_{xs}, I_{kp.s}$ are enertia moments of the cross-section of the ring, q_x, q_θ, q_r are the components of stress force acting on the cylindrical shell as viewed from medium, G_c, G_s are elasticity module in shear of the longitudinal rod and ring.

The kinetic energy of the shell stiffened with rods is as follows:

$$K = \frac{Eh}{2(1-\nu^2)} \int_0^{\xi_1} \int_0^{2\pi} \left[\left(\frac{\partial u}{\partial t_1} \right)^2 + \left(\frac{\partial v}{\partial t_1} \right)^2 + \left(\frac{\partial w}{\partial t_1} \right)^2 \right] d\xi d\theta +$$

$$+ \frac{\bar{\rho}_c E_c F_c}{2R\left(1-\nu^2\right)} \sum_{i=1}^{k_2} \int_0^{\xi_1} \left[\left(\frac{\partial u}{\partial t_1} \right)^2 + \left(\frac{\partial w}{\partial t_1} \right)^2 \right]_{\theta=\theta_j} d\xi +$$

$$+ \frac{\bar{\rho}_s E_s F_s}{2R\left(1-\nu^2\right)} \sum_{i=1}^{k_1} \int_0^{2\pi} \left[\left(\frac{\partial v}{\partial t_1} \right)^2 + \left(\frac{\partial w}{\partial t_1} \right)^2 \right]_{\xi=\xi_j} d\theta$$

Using the Ostrogradsky-Hamilton condition of stationarity of action, we can obtain the

equation of motion of a shell stiffened with rods:

$$\delta W = \delta\left(\Im + K\right) = 0$$

References :

1. Bogdanovich A.E., Tamuzh V.P. Parametric vibrations of orthotropic cylindrical shell with viscoelastic filler. - in.: Mekhanika deformiruemykh tel i konstruksiy, Moscow: Nauka, 1975, 71 – 76 – R.J.Mech., 1976, 1976, 4B220.
2. Shvets R.H., Marchuk R.A. Axially symmetric vibrations of fluid-filled orthotropic cylindrical shells. Prikl. Mech. 1985, 21, 8, 46 – 51 – RJ Mech., 1986, 1Г651.
3. Mnev E.H., Persev A.K. Hydroelasticity of shells. –L.: Sudostroeniye, 1970, 365p.- RJ Mech., 1970, 9B319.
4. Amenzade R.A. Asymmetric vibrations of ideal fluid in elastic shell. Dokl. AN SSR, 1976, 229, №3, 566 – 568 – RJ Mech., 1977, 1B422.

https://doi.org./10.58225/mpmma.2026.*834*

TRANSVERSE VIBRATION ANALYSIS OF NON-HOMOGENEOUS STRAIGHT RODS RESTING ON A VISCOELASTIC FOUNDATION

Shakir Mammadov, Jeyhun Musayev, Aytaj Aliyeva

AzUAC, Azerbaijan

Abstract. This paper investigates the transverse vibrations of non-homogeneous straight rods resting on a viscoelastic foundation. The elastic modulus and mass density of the rod are assumed to vary along its length, while the foundation is modeled as a viscoelastic medium. The governing equation has variable coefficients and is solved using an approximate analytical approach. First, the method of separation of variables is applied under the assumption of harmonic motion. Then, the Bubnov–Galerkin method is employed to reduce the problem to a system of algebraic equations and to derive the frequency equation.

Natural frequencies are determined in the first approximation for practical applications. Numerical results show that both material inhomogeneity and foundation properties significantly influence the vibration characteristics of the system.

Keywords: transverse vibrations, non-homogeneous rod, viscoelastic foundation, variable coefficients, Bubnov–Galerkin method, natural frequencies.

Introduction

As is well known, straight rods are widely used in construction and engineering applications. During manufacturing and in various practical situations, their mechanical properties may depend significantly on spatial coordinates.

In such cases, especially when the resistance of the surrounding medium is considered, the governing equations of motion take the form of variable-coefficient equations, which complicates their analytical solution.

It should be noted that the complexity of these equations largely depends on the functions describing the inhomogeneity of the rod and the properties of the supporting foundation [1,2].

In this study, the problem is solved and the results are analyzed for specific distributions of elastic modulus and mass density along the rod, as well as for a chosen mathematical model of the foundation reaction. However, the adopted approximate analytical method remains applicable under more general assumptions.

Let the elastic modulus and mass density vary along the length of the rod according to the following law [3]:

$$E = E_0(1 + \alpha\bar{X}); \qquad \rho = \rho_0(1 + \alpha\bar{X}) \qquad (1)$$

The reaction of the foundation is described by the following model [1]:

$$q = C_1 W + C_2 \frac{\partial^2 W}{\partial t^2} \qquad (2)$$

Here, W is the transverse deflection, t is time, and C_1 and C_2 are experimentally determined coefficients characterizing the properties of the foundation.

The equation of motion for free vibrations, considering relations (1) and (2), can be written as follows [4]:

$$E_0 \frac{\partial^2}{\partial x^2}\left[(1 + \alpha\bar{X})^k \frac{\partial^2 W}{\partial x^2}\right] + C_1 W + C_2 \frac{\partial^2 W}{\partial t^2} + \rho_0(1 + \alpha\bar{X})^q \frac{\partial^2 W}{\partial t^2} = 0 \qquad (3)$$

Equation (3) can be expanded in the following form:

$$E_0(1 + \alpha\bar{X})^k \frac{\partial^4 W}{\partial x^4} + 2K\alpha l^{-1}(1 + \alpha\bar{X})^{k-1} \frac{\partial^3 W}{\partial x^3} + 2K(K - 1)\alpha^2 l^{-2}(1 + \alpha\bar{X})^{k-2} \cdot \frac{\partial^2 W}{\partial x^2} + C_1 W + C_2 \frac{\partial^2 W}{\partial t^2} + \rho_0(1 + \alpha\bar{x})^q \frac{\partial^2 W}{\partial t^2} = 0 \qquad (4)$$

Method of Solution

As can be seen, equation (4) is relatively complex, and obtaining an exact analytical solution is difficult.

Thus, in the first stage, the solution of equation (4) is sought in the following form:

$$W = V(x)l^{i\omega t} \qquad (5)$$

By substituting equation (5) into equation (4), the following expression is obtained:

$$E_0\left[\begin{matrix}(1+\alpha\bar{x})^k\frac{\partial^4 W}{dx^4}+2K\cdot l^{-1}(1+\alpha\bar{x})^{k-1}\frac{\partial^3 W}{dx^3}+2K(K-1)\alpha^2 l^{-2}\\ (1+\alpha\bar{x})\frac{\partial^2 W}{dx^2}\end{matrix}\right]+$$

$$C_1 V + C \qquad (6)$$

$$\omega^2\rho_0^4(1+\alpha\bar{x})^q\, V = 0$$

In the second stage, the solution of equation (6) is constructed using the Bubnov–Galerkin orthogonalization method. The function $V(x)$ can be represented in the form of the following series:

$$V(x) = \sum_{i=1}^{n} a_i \cdot Q_i(x) \qquad (7)$$

Here, a_i are unknown coefficients, and the functions $Q_i(x)$ are chosen such that they satisfy the corresponding boundary conditions.

Based on the orthogonalization procedure, we obtain:

$$\int_0^l \eta_i(x)\theta_p dx = 0; \qquad P = 1{,}2 \qquad (8)$$

It should be noted that, in the general case, the value of ω^2 is determined from a system of homogeneous algebraic equations with respect to the coefficients a_i.

For a non-trivial solution to exist, the determinant of the system coefficients must vanish, i.e.,

$$\|\omega^2\| = 0$$

(9)

Equation (9) represents the frequency equation.

$$\omega^2 = \frac{E_0 \int_0^1 \left\{ \left[\frac{d^4\theta_i}{dx^4} \cdot (1+\alpha\bar{x})^k + 2k\alpha l^{-1}(1+\alpha\bar{x})^{k-1} \frac{d^3\theta_i}{dx^3} + 2k(k-1)\alpha^2 l^{-2}(1+\alpha\bar{x})^{k-2} \right] C_1 a_1 \right\}}{\int_0^1 [C_2 + \rho_0(1+\alpha\bar{x})^q \theta_1^2 d\bar{x}]}$$

(10)

For illustration purposes, the following case is considered:

A) $k = q = 1$ B) $k = q = 2$

$\theta, \sin m\pi\bar{x}$ (11)

In these cases, formula (10) is written as follows:

$$\omega_1^2 = \frac{\int_0^1 E_0 \left[(1+\alpha\bar{x}) \left(\frac{m\pi}{l}\right)^4 sin^2 m\pi\bar{x} - \alpha l^{-1} \left(\frac{m\pi}{l}\right)^3 sin m\pi\bar{x} + sin^2 m\pi\bar{x} \right]}{\int_0^1 [C_2 + \rho_0(1+\alpha\bar{x}) sin^2 m\pi\bar{x} d\bar{x}]}$$

Conclusion

By assigning specific values to α, C_1, C_2, E_0, and ρ_0, the natural frequencies ω^2 can be determined. An efficient approximate solution for engineering

applications is thus provided by the proposed method.

References

1. Kolchin G. B. Design of Structural Elements from Elastic Inhomogeneous Materials. Kishinev, 1971, 172 pp.
2. Rzhanitsyn A. R. Structural Mechanics. Moscow, 1982, 399 pp.
3. Ilyasov M. Kh. Nonstationary Viscoelastic Waves. Baku, 2011, 229 pp.
4. Timoshenko S. P. Vibrations in Engineering. Moscow–Leningrad, 1966, 344 pp.

https://doi.org./10.58225/mpmma.2026.840

THE PROPERTY OF FREDHOLM OF A FOURTH-ORDER INTEGRO-DIFFERENTIAL EQUATION WITH IMPULSE EFFECT

Yusubov Shakir Shixi[1]
Huseynova Minayya Neymat[2,3]
[1] Baku State University, Azerbaijan
[2] National Aviation Academy, Azerbaijan
[3] Azerbaijan Technical University, Azerbaijan

Abstract. In this work, a boundary value problem for a fourth-order integro-differential hyperbolic equation with impulse effect is considered. A special case of the equation under consideration is the Boussinesq-Love equation, which emerges during the transverse vibrations of short thick rods and in the study of wave propagation within periodically layered media. The coefficients of the equation under consideration, along with the functions involved in its right-hand side and boundary conditions, are non-smooth and belong to the class L_p. The solution to the problem is sought within the class of functions possessing discontinuities along the lines parallel to the characteristics of the equation. By utilizing the integral representation of such functions, an adjoint problem

corresponding to the given problem is introduced. The Fredholm property of both the given problem and the corresponding adjoint problem is proved. It is proved that the necessary and sufficient condition for the existence of a fundamental solution to the given problem is that the corresponding homogeneous equation possesses only a trivial solution.
Keywords: Fredholm, integro-differential equation, impulse actions.

İntroduction

Certain natural and engineering processes experience instantaneous changes at specific moments in time. Impulsive differential equations are used for the mathematical modeling of such processes. In recent years, many works [1-9] have been devoted to solving practical problems described by partial differential equations with impulsive effects. In the present paper, a boundary value problem with impulsive effects for an integro-differential equation of hyperbolic type with a dominating fourth-order derivative is investigated. The formulated problem is written in the form of an operator equation and the corresponding adjoint problem is constructed. The Fredholm

property of the original problem and its corresponding adjoint problem is proved. It is proved that a necessary and sufficient condition for the existence of a fundamental solution to the formulated problem is that the corresponding homogeneous equation has only the trivial solution.

Problem Statement. Fundamental solution.

Let us define the sets $G = G_1 \times G_2$, $G_1 = \cup_{k=0}^{1} G_1^k$, $G_1^k = \left(t_1^k, t_1^{k+1}\right), k = 0,1$, $G_2 = (t_2^0, t_2^1)$ and $G^k = G_1^k \times G_2$ on the plane. Here $t_1^k, k = \overline{0,2}, t_2^j, j = 0,1$ are given real numbers, such that $-\infty < t_1^0 < t_1^1 < t_1^2 < +\infty, -\infty < t_2^0 < t_2^1 < +\infty$.

Consider the following integro-differential equation:

$$(l_{22}y)(t) \equiv D_1^2 D_2^2 y(t) + a_1(t)y(t) + a_2(t)D_1 y(t) + a_3(t)D_2 y(t) + a_4(t)D_1 D_2 y(t) + \int_{t_1^0}^{t_1^2} a_5(\xi_1, t)D_1^2 D_2 y(\xi_1, t_2)\, d\xi_1 + \int_{t_2^0}^{t_2^1} a_6(\xi_2, t)D_1 D_2^2 y(t_1, \xi_2)\, d\xi_2 = \varphi_{22}(t), t \in G. \quad (1)$$

Let us investigate the existence of the solution to this equation under the following impulse conditions:

$$(l_{2k}y)(t_1) \equiv D_1^2 D_2^k y(t_1, t_2^0) = \varphi_{2k}(t_1);\ t_1 \in G_1, k = 0,1, \quad (2)$$

$$\left(l_{j2}^i\right)(t_2) \equiv \Delta D_1^j D_2^2 y\left(t_1^i, t_2\right) = \varphi_{j2}^i(t_2); t_2 \in G_2, i = 0,1; j = 0,1, \quad (3)$$

$$l_{jk}^i y \equiv \Delta D_1^j D_2^k y\left(t_1^i, t_2^0\right) = \varphi_{jk}^i, i = 0,1; j = 0,1; k = 0,1. \quad (4)$$

Here

$$\Delta D_1^j D_2^2 y\left(t_1^i, t_2\right) = D_1^j D_2^2 y\left(t_1^i +, t_2\right) - D_1^j D_2^2 y\left(t_1^i -, t_2\right), i = 0,1; j = 0,1,$$

$$\Delta D_1^j D_2^k y(t_1^1, t_2^0) = D_1^j D_2^k y(t_1^1 +, t_2^0) - D_1^j D_2^k y(t_1^1 -, t_2^0),\ j = 0,1; k = 0,1,$$

$$D_2^2 y(t_1^0 -, t_2) \equiv 0,\ D_1 D_2^2 y(t_1^0 -, t_2) \equiv 0,\ t_2 \in G_2,$$

$$D_1^j D_2^k y(t_1^0 -, t_2^0) = 0,\ j = 0,1; k = 0,1.$$

The functions

$a_1(t),\ a_2(t),\ a_3(t),\ a_4(t),\ a_5(\xi_1, t),\ a_6(\xi_2, t),\ \varphi_{22}(t),\ \varphi_{2k}(t_1), k = 0,1,\ \varphi_{j2}^i(t_2),$

$i = 0,1, j = 0,1$ are measurable functions on $G_i \times G$ and satisfy the following conditions:

$$\int_G |a_i(t)|^p dt < \infty, i = \overline{1,4}, \quad \int_G \left(\int_{G_1} |a_5(\xi_1, t)|^q d\xi_1 \right)^{\frac{p}{q}} dt < \infty,$$

$$\int_G \left(\int_{G_2} |a_6(\xi_2, t)|^q d\xi_2 \right)^{\frac{p}{q}} dt < \infty,$$

$\varphi_{22}(t) \in L_p(G), \varphi_{2k}(t_1) \in L_p(G_1), \varphi_{j2}^i(t_2) \in L_p(G_2), 1 < p < \infty,$

$\frac{1}{p} + \frac{1}{q} = 1$ and $\varphi_{jk}^i, i = 0,1; j = 0,1; k = 0,1$ −are constant numbers.

We will seek the solution of the problem (1)-(4) in the space $V_p^{(2,2)}(G)$. Here

$$V_p^{(2,2)}(G) = \left\{ y \in L_p(G) | D_1^i D_2^j y \in L_p(G^k), k = \overline{0,1}, \atop 0 \le i, j \le 2 \right\}.$$

Let us write the problem (1)-(4) in the form of the operator equation:

$$ly = \varphi, \qquad (5)$$

where

$$l = \left(l_{22}, l_{2k}, k = 0,1, l_{j2}^i, i = 0,1; j = 0,1, l_{jk}^i, i = 0,1; j = 0,1; k = 0,1\right),$$

$$\varphi = \left(\varphi_{22}, \varphi_{2k}, k = 0,1, \varphi_{j2}^i, i = 0,1; j = 0,1, \varphi_{jk}^i, i = 0,1; j = 0,1; k = 0,1\right) \in \mathfrak{H}_p^{2,2},$$

$$\mathfrak{H}_p^{2,2} = L_p(G) \times \prod_{k=0}^{1} L_p(G_1) \times \prod_{i=0}^{1} \prod_{j=0}^{1} L_p(G_2) \times \prod_{i=0}^{1} \prod_{j=0}^{1} \prod_{k=0}^{1} \mathbb{R}.$$

The adjoint equation corresponding to the operator equation (5) takes the form

$$l^* f = \psi.$$

The following theorem has been proved:

Theorem. The problem (1)-(4) and its adjoint equation $l^* f = \psi$ are Fredholm. A necessary and sufficient condition for the existence of the fundamental solution is that the corresponding homogeneous problem $ly = 0$ has only a trivial solution.

References

1.Asanova A.T.: On the correct solvability of a nonlocal boundary value problem for systems of hyperbolic equations with impulsive actions. Ukrainian mat. Journal 67(3), 291–303 (2015)

2.Bainov D. D., Minchev E., Myshkis A.: On the correct solvability of a nonlocal boundary value problem for systems of hyperbolic equations with impulsive actions. Commun. Appl. Anal. 1(4), 1-14 (1997)

3.Belarbi A., Benchohra M.: Existence theory for perturbed impulsive hyperbolic differential inclusions with variable times. J. Math. Anal.Appl., vol. 327, 1116-1129 (2007)

4.Кожанов А. И., Шадрина Н. Н.: Исследование влияния параметров на корректность задачисопряжения для дифференциального уравнения Буссинеска — Лява. Челябинский физико-математический журнал, 7(1), 30-42 (2022)

5. Григорьева А. И.: Задачи сопряжения для некоторых аналогов уравнения продольных волн с разрывным коэффициентом. Челяб. физ.-матем. журн., 3(3), 276-294, DOI: 10.24411/2500-0101-2018-13302 (2018)

6.Yusubov Sh. Sh.: On correct solvability and representation of solutions to third-order hyperbolic equations with impulsive action. Bulletin of the Baku University. №1, 124-130, (2000)

7.Юсубов Ш.Ш.: Нелокальная задача с интегральными условиями для трехмерного гиперболического уравнения высокого порядка. Вестник КРАУНЦ. Физ.-мат. науки. 33(4), 51-62, DOI: 10.26117/2079-6641-2020-33-4-51-62 (2020)

8. Yusubov Sh. Sh., Huseynova M. N.: On the Unique Solvability of a Nonlocal Boundary Value Problem for Fourth-Order Hyperbolic Equation with Impulsive Action. In: Institute of Electrical and Electronics Engineers, IEEE DOI: 10.1109/PCI60110.2023.1032591, 5th International Conference on Problems of Cybernetics and Informatics (PCI) (28-30 August 2023), pp. 1–4. (2023)
9. Юсубов Ш.Ш., Гусейнова М.Н.: О корректной разрешимости нелокальной краевой задачи для нагруженного гиперболического уравнения четвертого порядка с импульсными воздействиями. Вестник КРАУНЦ. Физ.-мат. науки. 51(2), 57-72, DOI: 10.26117/2079-6641-2025-51-2-57-72 (2025)

https://doi.org./10.58225/mpmma.2026.848

SEMANTIC NOVELTY DETECTION IN SCIENTIFIC DOCUMENTS USING TRANSFORMER EMBEDDINGS

Bekchanov Shukurla [1] *and Sharipov Alisher* [1]
[1] Urgench State University named after Abu Rayhan Biruni, Uzbekistan

Abstract. The rapid growth of digital document collections has increased the need for effective methods to identify novel information. This paper proposes a semantic novelty detection framework based on text preprocessing, transformer-based embeddings, and cosine similarity. Documents are transformed into dense vector representations, and sentence-level comparison is employed to detect novel information within semantically similar documents. The proposed approach enables automatic identification of repeated and emerging content in large document collections. Experimental results demonstrate its effectiveness in distinguishing novel information from semantically similar documents.

Keywords: Novelty Detection, Semantic Similarity, Telegram Mining, Uzbek Language Processing, Transformer Embeddings.

Introduction

The rapid growth of scientific publications has increased the need for effective methods to identify novel information. Traditional approaches based on lexical similarity often fail to capture semantic relationships between documents. Recent transformer-based models, such as BERT, Sentence-BERT, RoBERTa, and LaBSE, provide powerful semantic representations for document analysis. In this paper, we propose a semantic novelty detection framework that combines text preprocessing, transformer-based embeddings, semantic similarity analysis, and sentence-level comparison to identify novel information in semantically similar documents.

Related Work

Recent advances in transformer-based models, including BERT, Sentence-BERT, RoBERTa, and LaBSE, have significantly improved semantic document representation and similarity analysis. While previous studies mainly focus on document-level similarity, identifying novel information within semantically related documents remains a challenging task. This work

combines transformer embeddings, cosine similarity, and sentence-level comparison for semantic novelty detection.

Proposed Methodology

A Subsection Sample

Before analysis, the documents were preprocessed by removing irrelevant elements, normalizing whitespace, and standardizing the text format to ensure a consistent representation. Let $D = d_1, d_2, \ldots d_n$ denote the collection of documents. The preprocessing operation is defined as $d_i^* = p(d_i)$, where $P(\cdot)$ represents the preprocessing function and d_i^* is the cleaned document.

Semantic Embedding

After preprocessing, each document is transformed into a dense semantic vector using a transformer-based language model. The embedding function is defined as $\mathbb{v}_i = E(d_i^*)$, where $E(\cdot)$ denotes the embedding model and $\mathbb{v}_i$ is the semantic representation of document d_i.

Similar Document Detection

To identify semantically related documents, cosine similarity is employed: $Sim(d_i, d_j) =$

$\frac{\mathbb{v}_i^T \mathbb{v}_j}{|\mathbb{v}_i||\mathbb{v}_j|}$. Documents whose similarity exceeds a predefined threshold (τ) are considered semantically similar: $Sim(d_i, d_j) \geq \tau$.

Novel Information Detection

For each document, the most similar document in the collection is identified. The maximum similarity score is computed as $\max_{j \neq i} Sim(d_i, d_j)$. To determine the amount of new information contained in a document, sentence-level comparison is performed. Let $d_i = s_1, s_2, \ldots, s_m$ be the set of sentences contained in document d_i. For each sentence s_k, the maximum similarity with the sentences of the reference document is calculated: $\max_{r \in d_i} Sim(s_k, r)$. A sentence is considered novel if $M(s_k) < \beta$ where β is a predefined novelty threshold. The set of novel sentences is given by $s_k : M(s_k) < \beta$. The novelty ratio of the document is then calculated as $\frac{|\mathcal{N}(d_i)|}{|d_i|}$, where $|d_i|$ denotes the total number of sentences in the document.

Experimental Setup and Dataset

Dataset

The experiments were conducted on a collection of scientific documents obtained from public academic repositories. Each document contains a title, abstract, and main text. Before analysis, all documents were converted into plain-text format and preprocessed as described in Section 3. Documents with insufficient content and duplicate entries were removed. The resulting corpus is represented as $D = d_1, d_2, \dots d_n$, where d_i denotes the i -th document in the collection.

Experimental Setup

To obtain semantic representations, each document was transformed into a dense vector using a transformer-based embedding model: $\mathbb{v}_i = E(d_i^*)$, where $E(\cdot)$ denotes the embedding model and d_i^* represents the preprocessed document. Semantic similarity between document pairs was computed using cosine similarity: $Sim(d_i, d_j) = \frac{\mathbb{v}_i^T \mathbb{v}_j}{|\mathbb{v}_i||\mathbb{v}_j|}$. Document pairs with similarity values exceeding a predefined threshold were considered semantically related. Subsequently, sentence-level comparison

was performed to identify novel information contained within semantically similar documents.

Evaluation Metrics

The effectiveness of the proposed approach was evaluated using standard information retrieval and classification metrics, including Precision, Recall, and F1-score: $Precision = \frac{TP}{TP+FP}, Recall = \frac{TP}{TP+FN}, F1 = 2 \cdot \frac{Precision \cdot Recall}{Precision+Recall}$. These metrics were used to assess the ability of the framework to correctly identify semantically similar documents and detect novel information within them.

Results and Conclusion

Experimental results demonstrate that transformer-based embeddings effectively capture semantic relationships between documents. Cosine similarity successfully identifies semantically related documents, while sentence-level comparison detects previously unseen information. The proposed framework achieved reliable performance in novelty detection and can be applied to scientific document analysis and digital library monitoring. Future work will focus on multilingual datasets, topic modeling

integration, and advanced language models for improved semantic understanding.

References

1.Madatov, K.A., Bekchanov, S., Khajibaeva, S.: A Technique for Automatic Extraction of Basis Words: A Case Study on "Uzbek Primary School Corpus". In: UBMK 2024 – Proceedings of the 9th International Conference on Computer Science and Engineering, pp. 85–88 (2024).

2. Madatov, K.A., Bekchanov, S.: The Algorithm of Uzbek Text Summarizer. In: International Conference of Young Specialists on Micro/Nanotechnologies and Electron Devices (EDM 2024), pp. 2430–2433 (2024).

3. Madatov, K.A., Bekchanov, S., Vičič, J.: Accuracy of the Uzbek Stop Words Detection: A Case Study on "School Corpus". In: CEUR Workshop Proceedings, vol. 3315, pp. 107–115 (2022).

4. Salaev, U., Matlatipov, G.: Neural Sequence Models for Uzbek Morphological Stemming. In: Proceedings of the 17th International Scientific and Technical Conference Actual Problems of Electronic Instrument Engineering (APEIE 2025).

IEEE, Novosibirsk (2025). DOI: 10.1109/APEIE66761.2025.11289244.

https://doi.org./10.58225/mpmma.2026.856

PRESSURE IN NON-STATIONARY OPERATING MODES OF THE WELL

Shusha Kerimova
Institute of Mathematics, Azerbaijan

Abstract. In this paper, the hydrodynamic processes occurring in the lifting pipe under non-stationary regimes are analyzed, and the behavior of bottomhole pressure variation over time is investigated using experimental indicators. As a result of mathematical modeling and numerical calculations, it is determined that during the transition from one operating mode to another, the well pressure initially exhibits a pulsating character, and after a certain time interval, it dampens, approaches its stationary value, and stabilizes. The study of these regularities is of great importance for the management of gas-lift wells in transient modes and for production forecasting.

Keywords: Gas-lift, Non-stationary mode, Lifting pipe, Laplace transform, Bottomhole pressure, Pulsation.

1. Introduction

In the modern oil and gas production industry, increasing the operating efficiency of wells and optimizing technological

processes require an accurate study of fundamental hydrodynamic regularities. Thermohydrodynamic changes occurring in lifting pipes during non-stationary operating modes of wells directly and significantly affect both bottomhole and wellhead parameters, particularly the well pressure. In recent years, important research has been conducted on the mathematical modeling of transient regimes in gas-lift and lifting pipes, specifically focusing on wavy and pulsating flow dynamics [1,2,3,4]. For this reason, mathematical modeling of the dynamics of multiphase mixtures moving in the lifting pipe and the investigation of the time dependencies of pressure changes represent one of the actual scientific and practical problems.

2. Problem Statement

The gas supplied from the annular space and the fluid coming from the reservoir are mixed into the lifting pipes and ascend through it. In this case, the density of the mixture can be determined by the formula [5]:

$$\frac{1+\xi}{\rho_{mix}} = \frac{1}{\rho_g} + \frac{\xi}{\rho_{oil}}, \qquad \rho_{mix} = \frac{(1+\xi)\rho_{oil}\rho_g}{\rho_{oil} + \xi\rho_g}$$

$\rho_{mix}, \rho_{oil}, \rho_g$ - are the pressures of the mixture, oil, and gas at a given pressure,

respectively. In the first approximation, we consider the mixture to be homogeneous, neglecting the interaction between liquid and gas bubbles. Then, the pressure equations of the mixture .

$$\frac{\partial^2 P}{\partial t^2} = c^2 \frac{\partial^2 P}{\partial x^2} - 2a \frac{\partial P}{\partial t} \qquad (1)$$

will have the same form as equation (1). By placing the origin of the x_1 coordinate axis at the desired end of the pipeline and directing it upward, we can write the initial and boundary conditions in the following form:

$$P|_{t=0} = 0, \quad x_1 \in [0, l] \quad , \quad P|_{x=0} = P_0(t), \quad t \in (0, +\infty) \, ,$$

$$P|_{x1=l} = P_{ycm}(t), \quad t \in (0, +\infty) \qquad (2)$$

We will seek the solution to equation (1), taking into account the boundary conditions(2), in the specified form [2,3]:

$$P = P_w(t) - \frac{P_w - P_{wh}(t)}{l} x_1 + \sum_{i=1}^{\infty} \phi_{1i} \sin \frac{i\pi x_1}{l} \qquad (3)$$

Substituting expression (3) into equation (1), multiplying both sides of the resulting expression by $\sin \frac{i\pi x_1}{l}$ and integrating from 0 to l, we obtain:

$$\ddot{\phi}_{1i} + 2a\dot{\phi}_{1i} + c^2 \frac{i^2\pi^2}{l^2} \phi_{1i} = -\frac{4a\dot{P}_w}{i\pi} + \frac{4a}{i\pi}(-1)^i \dot{P}_{wh} -$$

$$-\ddot{P}_w \frac{2}{i\pi} + \frac{2}{i\pi}(-1)^i \ddot{P}_{wh} \qquad (4)$$

Applying the Laplace transform, from expression (4) we obtain:

$$\overline{\phi_{1i}}(s)=\frac{S}{(s+a)^2+\omega_i^2}\phi_{1i}(0)+\frac{1}{(s+a)^2+\omega_i^2}\dot{\phi}_{1i}(0)+\frac{1}{(s+a)^2+\omega_i^2}2a\phi_{1i}(0)+$$
$$+\frac{1}{(s+a)^2+\omega_i^2}\frac{2}{i\pi}(-1)^i\overline{\dot{P}}_{wh}+\frac{1}{(s+a)^2+\omega_i^2}\frac{4a}{i\pi}(-1)^i\overline{P}_{wh}-$$
$$-\frac{1}{(s+a)^2+\omega_i^2}\overline{\dot{P}}_w\frac{2}{i\pi}-\frac{1}{(s+a)^2+\omega_i^2}\frac{4a\overline{P}_w}{i\pi} \qquad (5)$$

$\varphi_{1i}(0)$ and $\dot{\varphi}_{1i}(0)$ is determined from expression (4) and is given as follows:

$$\phi_{1i}(0)=-\frac{2}{\pi}\left[P_w(0)+P_{wh}(0)\right];\qquad \dot{\phi}_{1i}(0)=0;\qquad c^2\frac{i^2\pi^2}{l^2}-a^2=\omega_i^2;$$

$$\overline{P}=\overline{P}_w(t)-\frac{\overline{P}_w-\overline{P}_{wh}}{l}x_1+\sum_{i=1}^{\infty}\overline{\phi}_{1i}\sin\frac{i\pi x_1}{l} \qquad (6)$$

After substituting expression (5) into formula (6), let us write the resulting expression in the first equation of the following system of equations:

$$-\frac{\partial P}{\partial x}=\frac{\partial Q}{\partial t}+2aQ;\qquad -\frac{\partial P}{\partial t}=c^2\frac{\partial Q}{\partial x},\quad Q=\rho u$$

Applying the Laplace transform to the obtained mathematical expression, we obtain:

$$\overline{Q}_{mix}=\frac{\overline{P}_w(t)}{l(s+2a)}-\frac{\overline{P}_{wh}(t)}{l(s+2a)}-\sum_{i=1}^{\infty}\frac{\overline{\phi}_{1i}(t)}{(s+2a)}\cdot\frac{i\pi}{l}\cos\frac{i\pi x_1}{l}+\frac{Q_{mix}(0)|}{(s+2a)} \qquad (7)$$

here $Q_{smes}(0)$ - is the initial value of the mass flow rate of the mixture.

The continuity equation is:

$$f_k Q_g\big|_{x=l}+Q_{oil}\big|_{r=r_c}=f_T\,Q_{mix}\big|_{x_1=0} \qquad (8)$$

f_T and f_k- are the cross-sectional area of the pipeline and the annular section, respectively.

Applying the Laplace transform, from expression (8) we obtain:

$$f_k \overline{Q}_g\big|_{x=l} + \overline{Q}_{oil}\big|_{r=r_c} = f_T \overline{Q}_{mix}\big|_{x_1=0}$$

(9)

Q_{mix} and Q_g are determined according to the literature [1]. Substituting expressions (8), (9), and (7) into the continuity condition (9) and considering only one term of the series, we obtain an expression to find $\overline{P}_w(t)$ in the first approximation. Returning from this expression to the original domain and using the experimentally obtained parameter values in the calculations, we obtain the following mathematical expression for the variation of the bottomhole pressure of the well $P_c(t)$ over time t:

$$P_w(t) = 8,094995281 - 0,02636096437\exp(-0,0002045376007t) + \\ +8,294617222\cdot 10^{-90}\cdot(-4,515918736\cdot 10^{88}\cos(0,9071083878t)) + \\ +1,157214796\cdot 10^{10}\sin(0,9071083878t))\cdot\exp(-0,03764469709t) + \\ +157,818244\cdot\exp(-29,69372812t)$$

(10)

$\rho_{ат}$ - is the density of the gas at atmospheric pressure g - is the acceleration of free fall;, $P_{ат}$ - is the atmospheric pressure ; $Q_{oil}(0)$ - is

the initial oil inflow entering from the reservoir per unit time. It can be observed from Figure 1 and Figure 2 that the bottomhole pressure $P_w(t)$ initially pulsates when transitioning from one regime to another, and then stabilizes, approaching its stationary value.

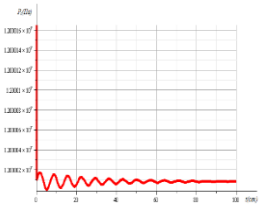


Figure 1. Plot of well pressure versus time at small values of time given by formula (10).

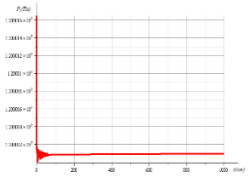


Figure 2. Plot of well pressure versus time at large values of time given by formula (10).

References

1. Kerimova, Sh.A.: Study of well pressure and dynamics of oil production growth in pulsating cases of initial pressure values. *East European Scientific Journal* 2(7(71)), 43–51 (2021).
2. Aydin, M., Aliyev, A.: Transient hydrodynamic modeling of multiphase flow in gas-lift wells during production

onset. *Journal of Petroleum Science and Engineering* 210(109985), 1–12 (2022).
3. Suleimanov, B.A., Shamilov, V.M.: Analytical solution for transient pressure behavior in oil wells using integral transforms. *Journal of Engineering Physics and Thermophysics* 94(4), 987–995 (2021).
4. Wang, K., Liu, Y.: Experimental study on pressure pulsations and flow regime transitions in gas-lift systems. *SPE Production & Operations* 39(02), 145–158 (2024).
5. Bear, J.: Dynamics of Fluids in Porous Media. *Dover Publications*, New York, 250 (2018).

https://doi.org./10.58225/mpmma.2026.863

POTENTIAL OPERATOR ON CARLESON CURVES IN LOCAL GENERALIZED WEIGHTED MORREY SPACES

Suleyman Celik
Firat University, Türkiye

Abstract. In this work we give a strong and weak type Guliyev-Spanne type boundedness criterion for the potential operator $\mathcal{J}^{\alpha}$ in the local generalized weighted Morrey space $LM_{p,\varphi}^{\{t_0\}}(\Gamma,w)$ and the generalized weighted Morrey space $M_{p,\varphi}(\Gamma,w)$ defined on Carleson curves Γ, respectively. For the operator $\mathcal{J}^{\alpha}$ we establish necessary and sufficient conditions for the strong and weak Guliyev-Spanne type boundedness on $LM_{p,\varphi}^{\{t_0\}}(\Gamma,w)$ and the strong and weak Guliyev-Spanne type boundedness $M_{p,\varphi}(\Gamma,w)$.

Keywords: Carleson curve, local generalized weighted Morrey space, potential operator, Guliyev-Spanne type boundedness.

Introduction

The classical Morrey spaces were originally introduced by Morrey in [7] to study the local behavior of solutions to second order elliptic partial differential equations. For the

properties and applications of Morrey spaces. Guliyev, Mizuhara and Nakai [2],[6],[8] introduced generalized Morrey spaces $M^{(p,\varphi)}(R^n)$ (see, also [3],[9]). Recently, Komori and Shirai [5] considered the weighted Morrey spaces $L^{(p,\kappa)}(w)$ and studied the boundedness of some classical operators such as the Hardy-Littlewood maximal operator, the Calderón-Zygmund operator on these spaces. Guliyev [4] gave a concept of generalized weighted Morrey space $M_{((p,\varphi))}(w)$ which could be viewed as extension of both generalized Morrey space $M_{(p,\varphi)}$ and weighted Morrey space $L^{(p,\kappa)}(w)$. In [4] Guliyev also studied the boundedness of the classical operators and its commutators in these spaces $M_{((p,\varphi))}(w)$.

Let $\Gamma=\{t\in C:t=t(s),0\leq s\leq l\leq\infty\}$ be a rectifiable Jordan curve in the complex plane C with arc-length measure $\nu(t)=s$, here $l=\nu\Gamma$="lengths of" Γ.

We denote

$$\Gamma(t,r):=\Gamma\cap B(t,r),t\in\Gamma,r>0,$$

where $B(t,r)=z\in C:|z-t|<r$ .We also denote for brevity $\nu\Gamma(t,r)=|\Gamma(t,r)|$.

A rectifiable Jordan curve Γ is called a Carleson curve if the condition

$$\nu\Gamma(t,r)\leq c_0 r$$

holds for all $t \in \Gamma$ and $r>0$, where the constant $c_0>0$ does not depend on t and r.

Let $f\in L_1^{loc}(\Gamma,w)$. The maximal operator M and the potential operator I^{α} on Γ are defined by holds for all $t \in \Gamma$ and $r>0$, where the constant $c_0>0$ does not depend on t and r.

$$Mf(t)=\left[\left[\sup\right]\right]_{\Gamma(t>0)}(\nu\Gamma(t,r))\left]\right]^{(-1)} \int_{\Gamma(t,r)}|f(\tau)|d\nu(\tau),$$

and

$$I^{\alpha} f(t)=\int_{\Gamma} f(\tau)/|t-\tau|^{(1-\alpha)}\, d\nu(\tau), \quad 0<\alpha<1,$$

respectively.

The main purpose of this work is to establish the boundedness of potential operator I^{α}, $0<\alpha<1$ in local generalized weighted Morrey spaces $LM_{(p,\varphi)}^{(\{x_0 \})}(\Gamma,w)$ defined on Carleson curves Γ. We shall give characterizations the strong and weak Guliyev-Spanne type boundedness of the operator I^{α} from $LM_{(p,\varphi_1)}^{(\{x_0 \})}(\Gamma,w)$ to $LM_{(q,\varphi_2)}^{(\{x_0 \})}(\Gamma,w)$, $1<p<\infty$, $1\vee p-1\vee q=\alpha$ and from the space $LM_{(1,\varphi_1)}^{(\{x_0 \})}(\Gamma,w)$ to the weak space $WLM_{(q,\varphi_2)}^{(\{x_0 \})}(\Gamma,w)$, $1<q<\infty$, $1-1\vee q=\alpha$, see [1].

Theorem 1. [1] Let Γ be a Carleson curve, $0<\alpha<1$, $t_0\in\Gamma$ and $p,q\in[1,\infty)$.

If $1\le p<1/\alpha$ and $1/q=1/p-\alpha$, then the condition

$$\left(\int_r^\infty \left[\left(\left[\operatorname{ess\ inf}\right]_{\tau<s<\infty} \left[\varphi_1(t,s)\left(w^p(\Gamma(t,s))\right)^{1\vee p}\right]\right)\left(w^q(\Gamma(t,\tau))\right)^{1\vee q}\right]\frac{d\tau}{\tau}\right]\le C\varphi_2(t,r) \quad (1)$$

where C does not depend on t and r, is sufficient for the boundedness of the opera I^α from $LM_{(p,\varphi_1)}^{(\{t_0\})}(\Gamma,w)$ to $WLM_{(q,\varphi_2)}^{(\{t_0\})}(\Gamma,w)$.

Moreover, if $1<p<1/\alpha$, the condition (1) is sufficient for the boundedness of the operator I^α from $LM_{(p,\varphi_1)}^{(\{t_0\})}(\Gamma,w)$ to $LM_{(q,\varphi_2)}^{(\{t_0\})}(\Gamma,w)$.

If the function $\varphi_1\in G_p$, then the condition

$$r^a\varphi_1(r)\le C\varphi_2(r) \quad (2)$$

for all $r>0$, where $C>0$ does not depend on r, is necessary for the boundedness of the operator I^α from $LM_{(p,\varphi_1)}^{(\{t_0\})}(\Gamma,w)$ to $WLM_{(q,\varphi_2)}^{(\{t_0\})}(\Gamma,w)$ and $LM_{(p,\varphi_1)}^{(\{t_0\})}(\Gamma,w)$ to $LM_{(q,\varphi_2)}^{(\{t_0\})}(\Gamma,w)$.

Let $1\le p<1/\alpha$ and $1/q=1/p-\alpha$. If $\varphi_1\in G_p$ satisfies the regularity condition

$$\int_r^\infty s^{\alpha-1}\varphi_1(s)ds\le Cr^\alpha\varphi_1(r)$$

for all r>0, where C>0 does not depend on r, then the condition (2) is necessary and sufficient for the boundedness of the operator I^α from LM_(p,φ_1)^(\{t_0 \}) (Γ,w) to WLM_(q,φ_2)^(\{t_0 \}) (Γ,w).

Moreover, if $1<p<q/\alpha$, then the condition (2) is necessary and sufficient for the boundedness of the operator I^α from LM_(p,φ_1)^(\{t_0 \}) (Γ,w) to LM_(q,φ_2)^(\{t_0 \}) (Γ,w).

The research of S. Celik was partially supported by a grant from Kirsehir Ahi Evran University Scientific Research Projects (BAP, Project No: FEF.A1.26.001).

References

Celik, S.: Potential operator on Carleson curves in local generalized weighted Morrey spaces. Azerbaijan Journal of Mathematics 16(1), 1–17 (2026).

Guliyev, V.S.: Integral operators on function spaces on the homogeneous groups and on domains in R^n. Doctoral dissertation. Mat. Inst. Steklov, Moscow (1994).

Guliyev, V.S.: Boundedness of the maximal, potential and singular operators in the generalized Morrey spaces. J. Inequal. Appl. Art. ID 503948, 1–20 (2009).

Guliyev, V.S.: Generalized weighted Morrey spaces and higher order commutators

of sublinear operators. Eurasian Math. J. 3(3), 33–61 (2012).
Komori, Y., Shirai, S.: Weighted Morrey spaces and a singular integral operator. Math. Nachr. 282(2), 219–231 (2009).
Mizuhara, T.: Boundedness of some classical operators on generalized Morrey spaces. In: Igari, S. (ed.) Harmonic Analysis, ICM 90 Satellite Proceedings, pp. 183–189. Springer-Verlag, Tokyo (1991).
Morrey, C.B.: On the solutions of quasi-linear elliptic partial differential equations. Trans. Amer. Math. Soc. 43, 126–166 (1938).
Nakai, E.: Hardy-Littlewood maximal operator, singular integral operators and Riesz potentials on generalized Morrey spaces. Math. Nachr. 166, 95–103 (1994).
Sawano, Y.: A thought on generalized Morrey spaces. J. Indonesian Math. Soc. 25(3), 210–281 (2019).

https://doi.org./10.58225/mpmma.2026.869

ENHANCING ROAD CONCRETE SUSTAINABILITY THROUGH WASTE UTILIZATION AND EXPERIMENTAL PLANNING METHODS

Tahira Hagverdiyev and Khayala Jamalova
AzUAC, Azerbaijan

Abstract. The rapid industrialization of modern society has increased the consumption of natural resources and highlighted the need for utilizing industrial and household wastes in construction materials production. This study investigates the use of sand-like chemical industry waste and plastic bottle waste in concrete production. It was found that finely ground sand-like waste can be used as a mineral additive in concrete mixtures, while plastic bottles can be processed into fibers with improved surface adhesion for fiber-reinforced concrete. Using statistical experimental design, the fiber concrete composition was optimized, resulting in concrete with an average density of 2400 kg/m³ and a compressive strength of 48.35 MPa. The main performance characteristics, including compressive and flexural strength, crack resistance, dynamic stability, tensile strength in bending, abrasion resistance, and water resistance, were evaluated. The results

confirmed the suitability of the developed fiber concrete for road construction applications.
Keywords: Strength, Durable, Concrete, Waste, Modification, Ecology, Mathematical Planning, Impact, Model.

Introduction

The increasing generation of industrial and household waste, together with the depletion of natural resources, has encouraged the use of waste materials in concrete production as a sustainable solution. Research has shown that industrial by-products and recycled materials can improve concrete performance while reducing environmental impacts. Aluminum oxide production waste used as a mineral additive increased the strength of cement-based systems and enabled the production of fiber-reinforced concretes with compressive strengths of up to 48.49 MPa [1]. Recycled PET fibers also enhanced concrete properties and reduced production costs [2]. In addition, limestone dust waste and ultrafine SiO_2-containing mineral additives improved the strength and density of concrete, with compressive strengths reaching 59 MPa [3,4]. These findings demonstrate that the use of waste materials in concrete contributes to sustainable construction, efficient waste

management, and conservation of natural resources [5].

Materials and test methods used. The study utilized CEM II/A-L 42.5 R (Expert) cement produced by the Holcim Azerbaijan Cement Plant, natural aggregates from local deposits, superplasticizer S520, finely ground aluminum oxide production waste, and dense stone dust as mineral additives. All laboratory tests were conducted according to relevant national and international standards. Cement properties were determined in accordance with AZS EN 197.1-2021 and EN 196-2-2013 requirements, while concrete mixture properties were evaluated following BS EN 206-1:2000. Compressive strength was measured on 150×150×150 mm concrete specimens after 28 days of curing using a UTEST UTC-4320 hydraulic press in accordance with EN 12390-2:2019. Crack resistance and friction characteristics were determined according to ГОСТ 29167-2021, ASTM C1018-97, EN 14651:2005+A1:2007, and ГОСТ 13087-2018 standards [6].

Table 6. Mechanical properties of the tested cements.

Test results	**Test results**	
	CEM I 52,5 R	**CEM II/A-L 42,5 R**

	7	28	7	28
	daily, at least	daily, at least	daily, at least	daily, at least
Bending strength limit, MPa	5.98	7.5	4.65	6.2
Compressive strength limit, MPa	31	52.5	20	42.5

The concrete mix design and material consumption for 1 m³ of concrete were determined using a combination of calculations and mathematical statistical analysis of experiments. This method made it possible to evaluate the individual and combined effects of factors with a limited number of experiments and to develop an adequate regression model describing the relationship between mixture components and concrete properties. Based on preliminary studies, three main variable factors and their variation levels were selected, and all factors were investigated at two levels.

Table 2. Indicators of changing factors.

Practice plan indicators	Conventional sign of variable factors		
	X_1	X_2	X_n
Basic level, x_{0i}	x_{01}	x_{02}	x_{0n}

Variation range	Δx_1	Δx_2	Δx_n
High level	X_{max}	X_{max}	X_{max}
Low level	X_{min}	X_{min}	X_{min}

Concrete compositions were optimized using mathematical-statistical experimental design to evaluate the effects of mineral additives and fibers on concrete performance. Dense stone dust and aluminum oxide production waste were found to be effective mineral additives, improving the compressive and flexural strength of cement-based systems, particularly at a dosage of 10% of cement consumption. Increasing the fineness of these additives further enhanced the strength properties of the hardened composites. Fiber-reinforced concretes containing polypropylene and recycled PET fibers were also developed, with an optimum fiber content of 6 kg/m^3. Based on statistical analysis, an optimized fiber concrete composition incorporating aluminum oxide production waste, fibers, and a hyperplasticizer was obtained, achieving a compressive strength of 48.35 MPa and an average density of 2400 kg/m^3. The developed concrete exhibited

satisfactory crack resistance, flexural performance, abrasion resistance, and water resistance, confirming its suitability for road construction applications.

Results. As a result of the conducted research, it was determined that when using dense stone dust waste in an amount of 10% of the cement consumption, the 7-day bending strength of cement-sandstone increased from 6.0 MPa to 6.2 MPa (3.3% higher) in 28 days, and the compressive strength increased from 39.0 MPa to 40.9 MPa (4.87% higher), while using alumina production waste, the bending strength increased from 6.0 MPa to 6.4 MPa (6.66% higher), and the compressive strength increased from 39.0 MPa to 41.4 MPa (6.15% higher).

References

1. T.A.Hagverdiyeva, K.B.Jamalova. Artificial SiO_2-containing mineral-active adhesive material and concrete purchase research. International Journal on Technical and Physical Problems of Engineering (IJTPE), Issue 60, Vol. 16, No. 3, pp. 213-219. 2024.

2. T.A. Hagverdiyeva, K.B.Jamalova. Recycling polyethylene terephthalate waste into functional fibers for sustainable fiber-reinforced concrete. International Journal on Technical and Physical Problems of Engineering (IJTPE), Issue 65, Vol. 17, No. 4, pp. 308-314. 2025.
3. Y.N.Yusifov, I.N.Shirinzade. Sustainable production of high-strength artificial stone using limestone dust waste and hiperplasicizers. International Journal on Technical and Physical Problems of Engineering (IJTPE), Issue 65, Vol. 17, No. 4, pp. 423-427. 2025.
4. K.B.Jamalova, T.A.Hagverdiyeva. Study of Production of Adhesive Material and Concrete Modified With Natural Component Containing SiO_2. 3rd International Conference on Problems of Logistics, Management and Operation in the East-West Transport Corridor (PLMO 2024) pp. 1-7. 2024.
5 .Kamal Kishore, Nakul Gupta. Application of domestic and industrial waste materials in concrete: A review // Journal: Materialstoday proceedings Vol. 26 / p. 2926-2931. 2020.
6. T.A.Hagverdiyeva, K.B.Jamalova. Journal of Scientific Works of AzMIU.

Friction-resistant fiber concrete. 2017, No. 2, 22-24.

https://doi.org./10.58225/mpmma.2026.877

DETERMINING OPTIMAL GAS LIFT REGIME: TRANSITIONING FROM INJECTION RATE TO ENTRY VELOCITY

Terlan Ibadzade
SOCAR, Oil Gas Scientific Research Project İnstitute,
Azerbaijan.

Abstract. In this research, contemporary solutions for optimizing the operational regimes of gas lift wells have been comprehensively reviewed to enhance overall production efficiency. The investigation involves a detailed analysis of complex flow conditions within gas lift systems, specifically focusing on the hydrodynamic process where injection gas displaces liquid in the annulus toward the tubing shoe. A significant part of the study explores the functional interrelationships between the injection gas flow rate, the well's production rate, and the gas entry velocity at the shoe zone.

The study confirms the possibility of determining the optimal operating regime by relying exclusively on surface wellhead parameters. By establishing a robust analytical framework that links surface pressure and flow indicators to downhole

dynamics, the research provides a methodology for real-time optimization in environments where downhole monitoring is limited. This approach enables field engineers to mitigate instabilities and ensure a steady lift mechanism without the need for complex downhole sensory data. Consequently, the proposed model serves as a practical tool for improving the economic and operational performance of gas lift systems through precise wellhead data integration.
Keywords: Gas lift method, optimal operating mode, injection gas rate, injection gas velocity.

1. Introduction

The gas lift technique accounts for a substantial share of global oil recovery. This study evaluates theoretical frameworks and the pivotal task of identifying ideal production settings. Traditionally, the optimal regime is identified using standard $Q = f(V)$ benchmarks [1, 2, 3] and established analytical models [4, 5]. However, departing from conventional methodologies, this research examines the correlation between surface-monitored variables and gas injection metrics. By focusing on wellhead-derived

data, the paper introduces an innovative approach to pinpointing the most efficient operating modes, serving as a viable instrument for real-time production optimization.

2. Determination of the Optimal Gas Lift Regime: A Novel Analytical and Computational Approach

Based on existing research, determining the shoe pressure using wellhead parameters, as described formula in [6], was found to be more effective for accurately representing real field conditions. This methodology was applied to calculate the shoe pressure for the selected gas lift well. Based on the determined shoe pressure and the injection gas flow rate, the gas entry velocity into the second-string production tubing was calculated using the following formula:

$$\upsilon = 1{,}273 \frac{Q_{i.a.}}{d_e^2} \frac{P_0}{T_0} \frac{T_b}{P_b} Z \qquad (1)$$

Where, d_e is equivalent diameter of the annular cross-section; P_{sh} and T_{sh} are pressure and temperature of injection gas at shoe conditions, respectively.

Using wellhead data and formula (1), the shoe pressure and corresponding gas entry velocity were calculated for each injection rate. Based on these results $Q=f(V)$ and υ =

f(V) performance curves were established for the well (Fig. 1).

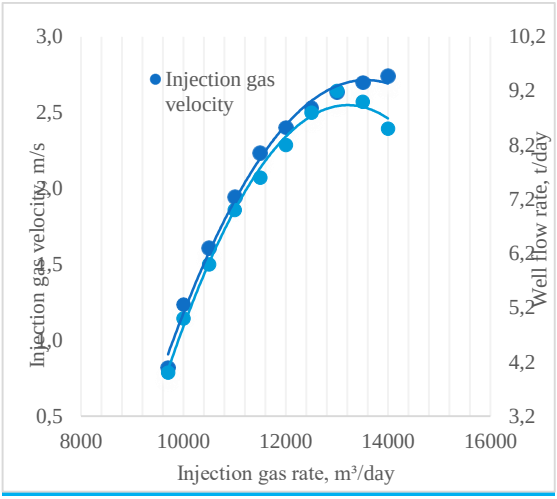


Fig. 1. Performance curves $Q=f(V)$ and $\upsilon = f(V)$ for a gas lift well.

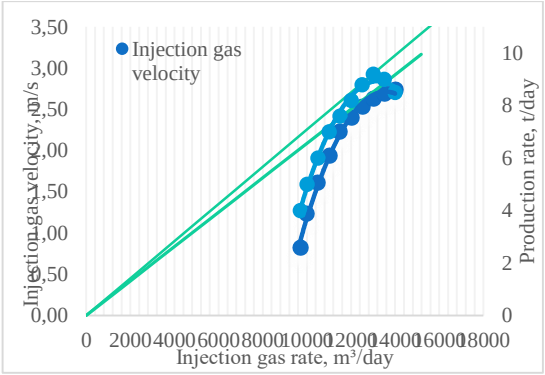


Fig. 2. Determination of the optimal operating regime for a gas lift well based on $Q = f(V)$ and $\upsilon = f(V)$ curves.

Conclusion

1. The gas entry velocity (υ), into the production tubing at the shoe zone was calculated for various operating regimes of one gas lift well. The optimal regime was identified based on Q = *f(V)* and υ = *f(V)* curves, showing nearly identical results on both plots.

2. For determining the optimal operating regime in gas lift wells, the *Q=f(V)* curve can be successfully replaced by the υ = *f(V)* velocity-based curve.

References

1. Guo B., Liu X., Tan X. Petroleum Production Engineering. Second Edition; Gulf Professional Publishing, 2017, p. 88-90.
2. Ali Hernandez, Fundamentals of Gas Lift Engineering / Well Design and Troubleshooting, Gulf Professional Publishing, March 2, 2016.
3. Suleymanov A.A., Ismayilov Sh.Z., Novruzova S.H., Malikov H.Kh., Abdullayev M.Q., Aliyev İ.N., Oil and Gas Well Production Technology – 2022, s. 178-255.
4. Абдуллаев В. Дж., Сравнительное исследование эксплуатационных характеристик наклонных и вертикальных

газлифтных скважин и изучение влияния градиента давления, SOCAR Proceedings No.3, 2020, pages 108-117.
5. Abdullaev V.J., Comparative Study of the Operational Properties of Deviated and Straight Gas-Lift Wells and Sensitivity Analysis of Pressure Gradient, SOCAR Proceedings No.3, 2020, pages 108-117.
6. Абдуллаев В. Дж., Методика расчета башмачного давления в газлифтных скважинах. Известия Академии Наук Азербайджана, Серия «Наук о Земле». Баку, 1995. С. 101-107.

https://doi.org./10.58225/mpmma.2026.883

OPTIMIZATION OF OPERATING PARAMETERS BASED ON TUBING SHOE PRESSURE AND INJECTION GAS VELOCITY DYNAMICS IN GAS LIFT WELLS

Terlan Ibadzade
SOCAR, Oil Gas Scientific Research Project İnstitute,
Azerbaijan.

Abstract. One of the most critical challenges in gas-lift well operations is the occurrence of flow pulsations, which can severely compromise production efficiency. Addressing this phenomenon effectively requires a comprehensive optimization of the dynamic relationship between the injection rate of the lift gas, the operating pressure, and the pressure at the tubing shoe. Detailed empirical dependencies for these three parameters were established across selected wells to identify the stability boundaries.

The study reveals that precise regulation of the velocity and pressure at which the working agent enters the lift string is the key to mitigating instability. By fine-tuning these input variables, it is possible to transition the well from a fluctuating regime to a steady-state flow, thereby ensuring operational reliability. This optimization not only

eliminates harmful oscillations but also maximizes the liquid recovery rate by aligning the hydraulic performance with reservoir capabilities. Consequently, implementing such a controlled injection strategy serves as a robust foundation for maintaining long-term production stability and extending the service life of downhole equipment.
Key words: Mathematical approach to gas lift optimization, shoe pressure, injection velocity, steady-state regime, pulsations

1. Introduction

While numerous models optimize gas-lift performance by analyzing wellhead pressure [1-3] and injection rates [4-7], ensuring operational stability under data-limited conditions remains a significant challenge. Consequently, there is a continuous need for streamlined analytical approaches that utilize basic surface parameters and field data to effectively regulate and stabilize production regimes.

2. Shoe Pressure and Velocity-Based Approach to Operating Parameter Optimization in Gas Lift Wells

To investigate the process in detail, operating parameters were calculated and functional dependencies established for gas lift wells No. 669 and 650. Under various operating modes, the gas entry velocity and shoe pressure (P_{sh}) were determined. The velocity of the injection gas entering the production tubing from the annulus is calculated using the following formula:

$$\upsilon = \frac{4 \cdot P_{st} \cdot Q_{st}}{3.14 \cdot d^2 \cdot P} \cdot \frac{T}{T_{st}} \cdot Z \qquad (1)$$

The shoe pressure was determined analytically based on actual well parameters and [8]. For each well, the correlation between the gas injection velocity and the P_i/P_{sh} ratio was established across various operating regimes. Our analysis indicates that the maximum value for this ratio converges toward $\frac{P_i}{P_{sh}}$ = 1,113 for the subject wells. Fig. 1 illustrates the dependence of the P_i/P_{sh} ratio on the gas entry velocity into the production tubing. As shown, the value of the P_i/P_{sh} ratio increases proportionally with the rise in gas injection velocity (υ).

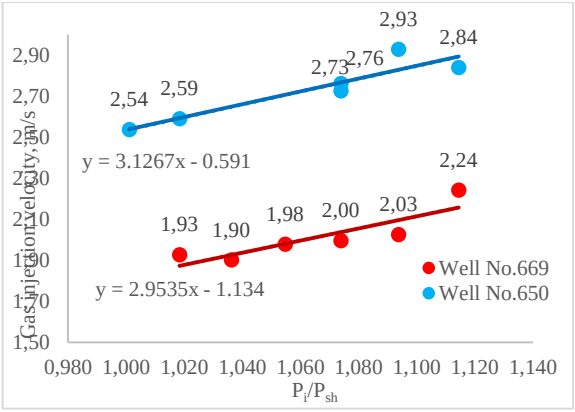


Fig. 1. Gas entry velocity (υ) as a function of injection pressure to shoe pressure ratio (P_i / P_{sh}).

As illustrated in Fig. 1, the $\upsilon = f(P_i/P_{sh})$ dependencies are nearly linear, do not pass through the origin, and can be described by a y = kx + b type equation. Based on the operating parameters of the subject gas lift wells, the $\upsilon = f(P_i/P_{sh})$ equations are as follows:

1) For well No. 650: $\upsilon = 3{,}1267 \cdot P_i/P_{sh} - 0{,}591$;

2) For well No. 669: $\upsilon = 2{,}9535 \cdot P_i/P_{sh} - 1{,}134$.

According to Fig. 1 and the derived formulas, to approach a, P_i/P_{sh} ratio of 1.113, the required gas velocities must be: 1) υ =

2,889 m/s for well No.650; 2) υ = 2,154 m/s for well No.669.

Conclusion

1. The compression ratio at the surface station is a primary factor in gas lift efficiency. Periodic pulsations, which compromise mechanical stability and cause equipment wear, are fundamentally driven by the gas injection rate.

2. A functional relationship was established between injection pressure (P_i), shoe pressure (P_{sh}), and gas entry velocity (υ). While increasing velocity raises the P_i/P_{sh} ratio and may boost production, excessive speeds decrease efficiency. The optimal gas velocity occurs when P_i/P_{sh} =1.113. Beyond this threshold, specific gas consumption increases, rendering the operation inefficient.

3. Results demonstrate that flow-induced complications can be mitigated by optimizing the operating regime using wellhead and field data. Precise control of gas entry velocity and shoe pressure is essential.

References

1. Guo B., Liu X., Tan X. Petroleum Production Engineering. Second Edition; Gulf Professional Publishing, 2017, p. 83-87.
2. Takacs G, Gas lift manual, United States of America, 2005. p.266-271.
3. Абдуллаев В. Дж., Сравнительное исследование эксплуатационных характеристик наклонных и вертикальных газлифтных скважин и изучение влияния градиента давления, SOCAR Proceedings No.3, 2020, pages 108-117.
4. Qingrong W., Zhi Y., Linjuan Z., Anqi D., Yi Ch., Wei L. Research on the Optimization of Continuous Gas Lift Production from Multiple Wells on the Platform. Processes, February 2025, 13, 478. //doi.org/10.3390/pr13020478.
5. Al-Janabi, M., Al-Fatlawi, O. Gas lift optimization: A review. AIP Conference Proceedings, 2443, 030013. 2022. //doi.org/10.1063/5.0091901.
6. Абдуллаев В. Дж., Гамзаев Kh.M., Численный метод определения коэффициента гидравлического сопротивления двухфазного потока в газлифтной скважине, SOCAR Proceedings, 2022, p. 56-60.

7. Abdullayev V.J., New approach for two-phase flow calculation of artificial lift. SOCAR Proceedings, 2021, p. 49-55.
8. Абдуллаев В. Дж., Методика расчета башмачного давления в газлифтныхскважинах. Известия Академии Наук Азербайджана, Серия «Наук о Земле». Баку, 1995. С. 101-107.

https://doi.org./10.58225/mpmma.2026.890

ELECTRICAL TRANSPORT AND OPTICAL RESPONSE IN $In/Ag-AgInS_2$ METAL-SEMICONDUCTOR HETEROSTRUCTURES

Tahir Gadjiev[1] and Rena Cebrayilova[2]

[1] AzUAC & Institute of Mathematics, Azerbaijan

[2] Azerbaijan State Oil and Industry University & AzUAC, Azerbaijan

Abstract. This paper presents a unified theoretical and numerical study of electrical transport and optical response in In/Ag–$AgInS_2$ metal–semiconductor heterostructures. Electrical transport is analyzed using Schottky barrier and thermionic emission models, while optical properties are examined via absorption-based approaches to determine the band gap energy. Simulations reveal the impact of depletion-layer electric fields on near-edge absorption. Analytical scaling relations are established linking Schottky barrier formation to optical behavior, providing a consistent description of electro-optical coupling in $AgInS_2$-based devices.

Keywords: metal-semiconductor heterostructures, electrical transport, optical absorption, Schottky barrier, $AgInS_2$

1 Introduction

Metal–semiconductor junctions are fundamental in optoelectronics [1,3,6]. Interfacial effects remain critical for emerging semiconductors [2]. Optical properties are also important and are analyzed using the Tauc formalism [5]. $\{$Ag$_2$In$_2$S$_3$$\}_2$ is promising for photovoltaics due to its suitable band gap, strong absorption [4,7], and related quaternary systems [8]. However, most studies neglect interface-controlled transport.

We present a theoretical analysis of electrical transport and optical response in In/Ag–$AgInS_2$ heterostructures. Electrical transport is described using Schottky barrier theory and thermionic emission models, while optical properties are also analyzed. This reveals the coupling between interfacial electronic structure and optoelectronic behavior.

2 Electrical and Optical Modeling

2.1 Schottky Barrier and Band Bending

For a metal–n-type semiconductor junction, the Schottky barrier height Φ_B and built-in potential V_{bi} inside the semiconductor are defined by:

$$\Phi_B = \Phi_M - \chi \quad (1)$$

$$V_{bi} = \Phi_B - \frac{kT}{q}\ln\left(\frac{N_C}{N_D}\right) \quad (2)$$

yielding the depletion width W:

$$\frac{d^2\psi(x)}{dx^2} = -\frac{qN_D}{\varepsilon_s} \quad (3)$$

$$W = \sqrt{\frac{2\varepsilon_s}{qN_D}(V_{bi} - V)} \quad (4)$$

where ε_s is the dielectric permittivity of $AgInSS_2$.

2.2 Thermionic Emission Transport

Charge transport follows the thermionic emission model:

$$J(V) = A^*T^2\exp\left(-\frac{q\Phi_B}{kT}\right)\left[\exp\left(\frac{qV}{nkT}\right) - 1\right] \quad (5)$$

$$\Phi_B^{\text{eff}} = \Phi_B - \frac{q\sigma_B^2}{2kT} \quad (6)$$

2.3 Optical Absorption Model

Near the absorption edge, the coefficient $\alpha(\hbar\omega)$ follows :

$$I(x) = I_0\exp(-\alpha x), \quad (7)$$

$$(\alpha\hbar\omega)^2 = C\left(\hbar\omega - E_g\right), \quad (8)$$

2.4 Electro-Optical Coupling via Internal Electric Field

From Eqs. (3)–(4), the electric field is:

$$E(x) = -\frac{d\psi}{dx} = \frac{qN_D}{\varepsilon_s}(W - x), E_{\max} = \frac{qN_D}{\varepsilon_s}W. \quad (9)$$

Within the Franz–Keldysh formalism, the field modifies the band gap as:

$$E_g(E) = E_g - \gamma E^{2/3}$$

[9].

The generalized Tauc relation becomes:

$$[\alpha(\hbar\omega, E)\hbar\omega]^2 = C\left(\hbar\omega - E_g + \gamma E^{2/3}\right). \quad (10)$$

3 Analytical Implications and Limiting Cases

3.1 Barrier-Height Sensitivity and Transport Regimes

From Eqs. (5) and (6), the saturation current density

$$J_0(\Phi_B) = A^* T^2 \exp\left(-q\Phi_B^{\text{eff}}/kT\right)$$

shows exponential dependence on the barrier height. For $qV \ll kT$, the current is linear:

$$J(V) \approx \frac{A^* qT}{nk} \exp\left(-q\Phi_B^{\text{eff}}/kT\right) V.$$

3.2 Bias Dependence and Electro-Optical Scaling

The depletion width variation with voltage is:

$$W(V) = \sqrt{\frac{2\varepsilon_s}{qN_D}\left[\Phi_B - \frac{kT}{q}\ln\left(\frac{N_C}{N_D}\right) - V\right]}, \frac{dW}{dV} = -\frac{\varepsilon_s}{qN_D W}. \quad (11)$$

Near the absorption edge,

$$\frac{d\alpha}{d(\hbar\omega)} \sim \left(\hbar\omega - E_g\right)^{-1/2}$$

Variations in the Schottky barrier affect transport and optical properties.

4 Numerical Results

Numerical simulations at T=300 K validate the model using standard $AgInS_2$ parameters (Table 1).

Table 1: Material and device parameters used in numerical simulations.

Parameter	Value
Franz–Keldysh coefficient, γ	5×10^{-10} eV(m/V)$^{2/3}$
Band gap energy, E_g	1.9 eV
Relative permittivity, $\varepsilon_s/\varepsilon_0$	10
Donor concentration, N_D	1×10^{17} cm^{-3}
Electron affinity, χ	4.0 eV
Richardson constant, A^*	120 A cm^{-2}K^{-2}
Work function (Ag / In)	4.74 eV / 4.12 eV
Temperature, T	300 K

The J–V characteristics show strong dependence on barrier height (0.74 eV for Ag, 0.12 eV for In). At 0.5 V the current density is $\sim 4.1 \times 10^5 \mathrm{Am}^{-2}$ for Ag, and $\sim 10^{16} \mathrm{Am}^{-2}$ for In.

For the $Ag/AgInS_2$ junction, the depletion width is ~80 nm at zero bias and decreases below 40 nm at 0.8 V. The maximum electric field is $\sim 1.5 \times 10^7\ \mathrm{V\,m}^{-1}$ and decreases with forward bias.

The internal field shifts the absorption edge, indicating electro-optical coupling.

5 Conclusion

A unified analytical framework for electrical transport and optical response in $In/Ag-AgInS$ heterostructures has been presented. Current–voltage behavior, depletion width, and electric-field distributions were derived

from Schottky and thermionic emission models, while optical properties were analyzed using absorption-based methods.

The results show exponential sensitivity of transport to the effective barrier height and establish scaling relations linking barrier formation, depletion behavior, and electric field. The choice of metal contact strongly affects current density, while internal electric fields induce measurable shifts in the optical band edge.

References

1. Tung, R. T.: The physics and chemistry of the Schottky barrier height. Applied Physics Reviews 1, 011304 (2014).
2. Therrien, F., Barnett, A. M., Santos, M. B.: Theoretical insights for improving the Schottky-barrier height at β-Ga_2O_3/metal junctions. Physical Review Applied 16, 064064 (2021).
3. Green, M. A.: Intrinsic concentration, effective densities of states, and effective mass in silicon. Journal of Applied Physics 67, 2944–2954 (1990).
4. Nozik, A. J.: Quantum dot solar cells. Physica E: Low-dimensional Systems and Nanostructures 14, 115–120 (2002).
5. Tauc, J.: Optical properties and electronic structure of amorphous Ge and

Si. Materials Research Bulletin 3, 37–46 (1968).
6. Meng, J., Lee, C., Li, Z.: Review: Adjustment methods of Schottky barrier height in one- and two-dimensional semiconductor devices. Science Bulletin 69(9), 1342–1352 (2024).
7. Shishodia, S., et al.: Selected I-III-VI_2 semiconductors: synthesis, properties and applications in photovoltaic cells. Nanomaterials 13(21), 2889 (2023).
8. Uematsu, T., et al.: Facile high-yield synthesis of Ag-In-Ga-S quaternary nanoparticles. Chemistry of Materials (2023).
9. Pankove, J. I.: Optical Processes in Semiconductors. Dover Publications, New York (1971).

https://doi.org./10.58225/mpmma.2026.*897*

ESTIMATES FOR DEGENERATE NON-DIVERGENCE ELLIPTIC EQUATIONS IN INFINITE DOMAINS WITH CONICAL BOUNDARY POINTS

Tahir Gadjiev [1,2], Sevinc Hadiyeva[2] and Konul Memmedova[3]

[1] AzUAC & Institute of Mathematics, Azerbaijan

[2] Sumgait State University & AzUAC, Azerbaijan

[3] Nakhchivan State University, Azerbaijan

Abstract. This paper investigates second-order degenerate linear elliptic equations of non-divergence type whose coefficients are controlled by a Muckenhoupt weight. The problem is studied in an unbounded domain whose boundary contains conical points, a geometric setting that significantly affects the behavior of solutions. For the associated mixed problem, we establish growth estimates and obtain a priori bounds for positive solutions. Using suitably constructed auxiliary functions and comparison principles, we derive estimates that describe both the boundary behavior and the asymptotic properties of solutions at infinity. These results extend classical estimates for uniformly elliptic equations to a degenerate, weighted, and geometrically singular setting.

Keywords: Degenerate elliptic equations, non-divergence form, Muckenhoupt weights, Conical boundary points, Mixed problem, Growth estimates

1 Introduction

Let $\Omega \subset \mathbb{R}^n, n = 2$, be an unbounded domain with boundary $\partial\Omega = \Gamma_1 \cup \Gamma_2$ contains conical points. We consider the mixed problem for a second-order linear elliptic equation of non-divergence type:

$$\sum_{i,j=1}^{n} a_{ij}(x)u_{x_i x_j} + \sum_{i=1}^{n} b_i(x)u_{x_i} + c(x)u(x) = 0 \quad (1.1)$$

$$u|_{\Gamma_1} = 0, \left.\frac{\partial u}{\partial n}\right|_{\Gamma_2} = 0 \quad (1.2)$$

The coefficient matrix $A(x) = \left(a_{ij}(x)\right)$ is real, symmetric, and satisfies the weighted ellipticity condition

$$c\omega(x)|\xi|^2 \leq \sum_{i,j=1}^{n} a_{ij}(x)\xi_i\xi_j \leq c^{-1}\omega(x)|\xi|^2, x \in \Omega, \xi \in \mathbb{R}^n \quad (1.3)$$

where $c \in (0,1]$ is a constant and $\omega \in A_p$ for some $1 < p < \infty$.

Uniformly elliptic second-order equations of non-divergence type have been studied extensively; see [1]-[6]. We also refer to $[7-10]$.

In contrast, we focus on degenerate equations where $\omega(x)$ governs the behavior of solutions in unbounded domains with conical singularities. Our aim is to obtain growth

estimates and a priori bounds for positive solutions of problem (1.1)-(1.2).

To proceed, we impose additional structure on the drift term. Let the coefficients $b_i(x), i = \overline{1,n}$, satisfy the orthogonality condition

$$(b(x), x - x_0) = 0 \qquad (1.4)$$

for all $x \in \Omega$, where $x_0 \neq 0$ is a point exterior to the domain. We introduce the ellipsoidal regions

$$E_R^{x_0}(p) = \left\{ x \in \mathbb{R}^n : \sum_{i=1}^{n} \frac{(x_i - x_{i0})^2}{R^\alpha \omega(x)} < pR^2 \right\} \qquad (1.5)$$

Auxiliary Lemmas

Lemma 1. *Let $z \in \partial E_R^0(\alpha) \cap \bar{\Omega}$, and let $x_0(z) \in \partial E_R^z(\alpha) \cap \partial E_R^0(\beta)$, where $\beta > \alpha$. Then the point x_0 lies outside the domain Ω. Define the auxiliary function*

$$G_S^{(R)}(x) = \left(\sum_{i=1}^{n} \frac{(x_i - x_{i0})^2}{R^\alpha \omega(x)} \right)^{-S/2}.$$

Lemma 2. *Assume that conditions (1.3) and (1.5) hold. Then for any point x_0 belonging to the set $\bigcup_{z \in \Omega \cap \partial E_R^0(\beta)} x_0(z)$, there exists a sufficiently large parameter $S > 0$ such that $L' G_S^{(R)}(x) = 0$ in the corresponding region.*

To normalize the barrier function, let $z \in \Omega \cap \partial E_R^0(\beta), x_0 = x_0(z)$, and $x \in \Omega \cap E_R^0(2\beta)$, and define

$$g_S^{(R)}(x) = \beta R^S G_S^{(R)}(x).$$

Then by construction, $g_S^{(R)}(x) \le 1$ in $\Omega \cap E_R^0(2\beta)$. Finally, denote $\Omega' = \Omega \cap E_R^0(\beta)$, which will serve as the working subdomain in the subsequent comparison arguments.

Theorem 1. *Let $z \in \Omega \cap \partial E_R^0(\beta)$, and let $u(x)$ be a positive solution of problem (1.1)-(1.2) in the region $\Omega' = \Omega \cap E_R^0(\beta)$. Assume that conditions (1.3)-(1.5) hold. Then there exists a constant $\mu > 0$ such that*

$$\sup_{\Omega'} \omega(x)u(x) \ge (1+\mu) \sup_{\Omega' \cap E_R^0(\beta)} \omega(x)u(x). \quad (1.6)$$

Proof. Let $M = \sup_{\Omega'} u^2$ and define

$$U(x) = M\left[1 - g_S^{(R)}(x) + \sup_{\Omega'} g_S^{(R)}(x)\right]$$

It is straightforward to verify that in Ω' :

$$L'(u^2)(x) \ge 0$$

$$,L'(U(x) - u^2(x)) \le 0,\ U(x) - u^2(x) \ge 0$$

Applying the maximum principle yields $U(x) \ge u^2(x)$ in Ω', which implies (1.6).

Theorem 2. *Assume that in the domain Ω the coefficients of the operator L satisfy conditions (1.3)-(1.5). Then any solution $u(x)$ of problem (1.1)-(1.2) satisfies the following dichotomy: either*

$$u(x) \equiv 0 \ \textit{in } \Omega,$$

or

$$\lim_{r\to\infty} r^{-\alpha} M(r) > 0,$$

where $M(r) = \sup_{\Omega\Delta\partial E_R^0(\beta)} (\omega(x)u(x))$ *and* $\alpha > 0$.

Proof. From Theorem 1 we obtain the improvement of supremum:

$$\sup_{\Omega\cap E_R^0(\beta)} \omega(x)u(x) \geq (1+\eta) \sup_{\Omega\cap E_R^0(\beta)} \omega(x)u(x),$$

for some fixed $\eta > 0$. Iterating this estimate, one obtains for $M(r)$ the bound

$$M(r) \geq (1+\eta) \sup_{\Omega\cap E_R^0(\beta^{-m_0})} \omega(x)u(x) \geq (1+\eta)^{m-m_0}\omega(x)u(x)$$

for r sufficiently large. Hence,

$$r^{-\alpha}M(r) \geq c > 0.$$

The alternative $u \equiv 0$ follows from the maximum principle, completing the proof.

Conclusion

We studied second-order degenerate elliptic equations of non-divergence type in unbounded domains with conical boundary singularities, where ellipticity is controlled by a Muckenhoupt weight. Using weighted barrier functions in ellipsoidal regions, we obtained growth estimates for positive solutions of the mixed problem. In particular, Theorem 1 provides an improvement-of-supremum property, leading to the dichotomy in Theorem 2: solutions are either

identically zero or exhibit definite growth at infinity. The method extends classical maximum principle techniques to degenerate weighted settings. Future work may include parabolic analogues and nonlinear generalizations.

References

1. Blokhina, G.N.: Theorems of Phragmen–Lindelöf type for linear elliptic equations of second order. Mat. Sb. (N.S.) 82(124)(4), 507–531 (1970) (in Russian).

2. Bokalo, M.M.: A priori estimation of solution and Phragmen–Lindelöf theorem for some quasi-linear parabolic systems in unbounded domains. Vestnik Lvovsk University, Ser. Mech.-Math. 45, 26–35 (1996) (in Russian).

3. Krylov, N.V., Safonov, M.V.: Some property of solutions of parabolic equations with measurable coefficients. Izv. Akad. Nauk SSSR Ser. Mat. 44(1), 161–175 (1980); Math. USSR-Izv. 16(1), 151–164 (1981).

4. Landis, E.M.: Second Order Equations of Elliptic and Parabolic Types. Nauka Publ., Moscow (1971).

5. Mazya, V.G.: The behavior near the boundary of the solution of the Dirichlet problem for an elliptic equation of the second

order in divergence form. Mat. Zametki 2(2), 209–220 (1967) (in Russian).

6. Safonov, M.V.: Harnack's inequality for elliptic equations and the Hölder property of their solutions. In: Boundary Value Problems of Mathematical Physics and Related Questions in Function Theory, vol. 12, Zap. Nauchn. Sem. LOMI, vol. 96, pp. 272–287. Nauka Publishing House, Leningrad (1980).

7. Gadjiev, T., Rustamov, Y., Yangaliyeva, A.: The behaviour of solutions to degenerate double nonlinear parabolic equations. In: International Conference on Management Science and Engineering Management, pp. 447–459 (2020).

8. Gadjiev, T.: On solutions of mixed boundary-value problems for second order quasilinear elliptic type equations in arbitrary bounded domains. In: Mat. Fizika i Nelineynaya Mekhanika, vol. 5, pp. 56–59. Kiev (1986).

9. Gadjiev, T., Guliyev, V.: Nonlinear elliptic equations with small BMO coefficients in nonsmooth domains in generalized Morrey spaces. Journal of Mathematical Inequalities 15(2), 491–509 (2021).

Eroglu, A., Gadjiev, T., Namazov, F.: Fractional integral associated to Schrödinger operator on the Heisenberg

groups in central generalized Morrey spaces. Journal of Nonlinear Sciences and Applications (JNSA)

https://doi.org./10.58225/mpmma.2026.*905*

QUALITATIVE PROPERTIES AND HARNACK-TYPE ESTIMATES FOR DEGENERATE NON-DIVERGENCE ELLIPTIC EQUATIONS

Tahir Gadjiev[1,3,] *Yasemen Guseynova*[2] *and Aybeniz Yagnaliyeva*[3]

[1] AzUAC & Institute of Mathematics, Azerbaijan

[2]Baku State University, Azerbaijan

[3]Sumgait State University, Azerbaijan

Abstract. This paper is devoted to the qualitative analysis of solutions to degenerate elliptic equations of non-divergence type whose coefficients satisfy weighted ellipticity conditions with a Muckenhoupt weight. We establish local growth estimates and obtain Harnack-type inequalities for positive solutions in domains with nonsmooth boundaries. The results extend classical estimates for uniformly elliptic equations to a degenerate setting and provide new qualitative properties for solutions of weighted non-divergence elliptic problems.

Keywords: degenerate elliptic equations, non-divergence type, Harnack inequality, Muckenhoupt weights, qualitative properties, growth estimates

1 Introduction

Elliptic equations of non-divergence type arise naturally in a wide range of problems in modern physics, mechanics, chemistry, biology, biochemistry, ecology, and many areas of applied science. Their qualitative properties, such as regularity of solutions, solvability of boundary value problems, and the behavior of solutions under degeneracy are central topics in the theory of partial differential equations.

One of the principal results in this theory states that if the coefficients of the equation, the boundary data, and the boundary of the domain are sufficiently smooth, then the solution is also smooth. However, when these assumptions fail, such as when coefficients are discontinuous, the boundary is nonsmooth, or the equation degenerates solutions may develop singularities. The investigation of such degenerate situations remains an active and challenging area of research. A major breakthrough in the non-divergence theory was achieved by Krylov and Safonov, who introduced probabilistic techniques to obtain Hölder continuity and Harnack inequalities for solutions of second-order linear non-divergence elliptic equations with measurable coefficients; see [3]. Their results may be viewed as the non-divergence

analogue of the celebrated De Giorgi-Nash estimates.

Various qualitative and a priori estimates for such equations were obtained in works such as [1], [2], [4]-[9], where weighted Sobolev spaces and Muckenhoupt-type conditions play an essential role. These studies show that degeneracy substantially affects the behavior of solutions and requires refined analytical tools. The purpose of the present work is to investigate qualitative properties of solutions to degenerate non-divergence elliptic equations, in particular to derive Harnack-type inequalities and local inf-sup estimates in bounded domains with nonsmooth boundaries. The results obtained here extend classical regularity theory to a degenerate framework influenced by weighted ellipticity conditions.

2 Formulation of the Problem

We now study the Harnack-type problem for a class of degenerate linear non-divergence elliptic equations. Similar problems arising in mechanics were considered in works such as [2, 7], while various regularity results for degenerate elliptic equations can be found in [1,5,6,8,9]. Let $\Omega \subset \mathbb{R}^n, n \geq 3$, be a bounded domain with a nonsmooth boundary. We

consider the second-order elliptic equation with mixed boundary problem

$$\sum_{i,j=1}^{n} a_{ij}(x)u_{x_i x_j} + \sum_{i=1}^{n} b_i(x)u_{x_i} + c(x)u(x) = 0, \quad (2.1)$$

where the coefficient matrix $A(x) = \left(a_{ij}(x)\right)$ satisfies

$$a_{ij}(x) = a_{ji}(x), i, j = 1, \dots, n,$$

and for every $x \in \Omega$ and $\xi \in \mathbb{R}^n$ the following degenerate ellipticity condition holds:

$$c\omega(x)|\xi|^2 \leq \sum_{i,j=1}^{n} a_{ij}(x)\xi_i\xi_j \leq c^{-1}\omega(x)|\xi|^2 (2.2)$$

where $c \in (0,1]$ is a constant, and $\omega(x) \in A_p$ is a Muckenhoupt weight for some $1 < p < \infty$. The coefficients $b_i(x)$ and $c(x)$ are assumed to be bounded, and moreover $c(x) \leq 0$.

We introduce ellipsoids E_{r,x_0} in the standard way and denote by mes($\cdot$) the Lebesgue measure on Ω.

Lemma 2.1 *Let u be a generalized solution of equation (2.1) belonging to the appropriate weighted Sobolev space. Then there exists a positive constant $\varepsilon > 0$, depending only on the structural parameters of the equation, such that if*

$$mes\left(E_{r,x_0} \cap \{u \geq 0\}\right) \geq \varepsilon mes\left(E_{r,x_0}\right),$$

then

$$\inf_{E_{r,x_0}} u \geq c_1,$$

where $c_1 > 0$ *is a constant depending only on the known data of the problem.* This lemma represents the first step toward establishing a Harnack inequality for positive solutions of the degenerate equation (2.1).

Theorem 2.1. *Let* $u(x)$ *be a positive solution of equation (2.1) in the ellipsoid* E_{r,x_0}*, and assume that all coefficient conditions stated earlier are satisfied. If* $r \leq 1$*, then the following Harnack-type inequality holds:*

$$\sup_{E_{r,x_0}} u(x) \leq c_2 \inf_{E_{r,x_0}} u(x)$$

where $c_2 > 0$ *depends only on the structural constants of the equation.*

Proof. Without loss of generality, normalize the solution so that

$$\sup_{E_{r,x_0}} u(x) = 1$$

Choose a constant K satisfying

$$\frac{1}{r} \leq K < \frac{1}{2r}$$

Let $A = \sup_{E_{r,x_0}} u(x)$ (so that $A = 1$ under our normalization). From the definition of the ellipsoid and standard covering arguments, we obtain

$$\sup_{E_{r,x_0}} u(x) \leq 2^n c_3,$$

for some constant $c_3 > 0$ depending only on the structural data.

Applying the Lemma established earlier to the function $u(x)$ yields

$$\inf_{E_{r,x_0}} u(x) \geq 2^n c_4$$

where $c_4 > 0$ again depends only on the known parameters.

Furthermore, using the monotonicity of the minimum over expanding ellipsoids,

$$\inf_{E_{r,x_0}} u(x) \geq \inf_{E_{2r,x_0}} u(x) > 0.$$

Choosing the constant

$$c_2 = \frac{c_3}{2^n c_4},$$

we obtain the desired inequality

$$\sup_{E_{r,x_0}} u(x) \leq c_2 \inf_{E_{r,x_0}} u(x).$$

This completes the proof.

Conclusion

We studied qualitative properties of positive solutions to degenerate non-divergence elliptic equations with weighted ellipticity conditions of Muckenhoupt type. Despite degeneracy and measurable coefficients, meaningful estimates can be obtained under appropriate weighted assumptions. We proved a measure estimate for the positivity set in ellipsoids and derived a Harnack-type inequality for positive solutions. This result

extends the classical Harnack principle to the considered degenerate setting. Future work may include extensions to nonlinear equations, boundary behavior in nonsmooth weighted domains, and finer regularity properties of solutions.

References

1. Gadjiev, T., Maharramova, T., Suleymanova, K.: Some apriori estimates for the solutions of a degenerate nonlinear elliptic equations. Trans. Natl. Acad. Sci. Azerbaijan Ser. Phys.-Tech. Math. Sci. Mathematics 39(2.1), 54–60 (2019).
2. Gadjiev, T., Aliyev, S., Maharramova, T.: Hölder estimates for the solutions of degenerate nonlinear elliptic equations of non-devergence type. Visnyk Lvivskoho Universytetu. Seriya Prykladna Matematika ta Informatyka 25, 64–67 (2017).
3. Krylov, N., Safonov, M.: A certain property of solutions of parabolic equations with measurable coefficients. Mathematics of the USSR Izvestiya 16, 151 (2007).
4. Liskevich, V., Skrypnik, I.: Harnack inequality and continuity of solutions to elliptic equations with nonstandard growth conditions and lower order terms. Annali di Matematica Pura ed Applicata 189, 335–356 (2010).

5. Gadjiev, T., Rustamov, Y., Yangaliyeva, A.: The behaviour of solutions to degenerate double nonlinear parabolic equations. In: International Conference on Management Science and Engineering Management, pp. 447–459 (2020).
6. Gadjiev, T.: On solutions of mixed boundary-value problems for second order quasilinear elliptic type equations in arbitrary bounded domains. Matematika, Matematicheskaya Fizika i Nelineynaya Mekhanika, Kiev 5(56–59) (1986).
7. Panahov, G., Abbasov, E., Sultanov, B.: Control of capillary instability under hydrodynamic impact on the reservoir. Nafta-Gaz 2, 71–83 (2023).
8. Gadjiev, T., Guliyev, V.: Nonlinear elliptic equations with small BMO coefficients in nonsmooth domains in generalized Morrey spaces. Journal of Mathematical Inequalities 15(2), 491–509 (2021).
Eroglu, A., Gadjiev, T., Namazov, F.: Fractional integral associated to Schrödinger operator on the Heisenberg groups in central generalized Morrey spaces. Journal of Nonlinear Sciences and Applications 11(8) (

https://doi.org./10.58225/mpmma.2026.914

PARTICLE FILTERING FOR HIGH-DIMENSIONAL REACTION DIFFUSION PDE STATE ESTIMATION UNDER NON-GAUSSIAN NOISE

Tahir Gadjiev[1] and Zaur Hajiyev[2]

[1] AzUAC & Institute of Mathematics, Azerbaijan

[2] University of Siena, Italy & AzUAC, Azerbaijan

Abstract. We develop a robust Bayesian filtering framework for state estimation in high-dimensional nonlinear partial differential equations (PDEs) governed by reaction-diffusion dynamics. Traditional filters (EKF, UKF, PF) degrade severely under high-dimensional discretization, sparse sensing, strong nonlinearity, and heavy-tailed noise. To address this, we introduce the Reduced-Order Robust Particle Filter (RO-RPF), combining Proper Orthogonal Decomposition (POD)-based model reduction with a mixture-model robust likelihood. Projecting the full PDE state onto a low-dimensional manifold mitigates particle degeneracy and the curse of dimensionality. Robustness to outliers is enhanced via a heavy-tailed likelihood. Numerical experiments across Gaussian, heavy-tailed, and strongly nonlinear high-

dimensional regimes demonstrate that RO-RPF matches EKF accuracy in low dimensions, while providing vastly superior stability, accuracy, and up to $18\times$ computational speedups over classical PFs in high-dimensional scenarios where standard methods collapse.
Keywords: Particle Filters, Model Reduction, PDE State Estimation, Reaction-Diffusion Systems, Robust Bayesian Filtering, Sparse Sensing

1 Introduction

State estimation for nonlinear and high-dimensional systems is a core challenge in applied mathematics. Classical Bayesian filters, including the Extended and Unscented Kalman Filters (EKF/UKF), rely on local linearization or sigma-point approximations. These fail when underlying dynamics exhibit pronounced nonlinearity or sharp gradients, such as in diffusion-reaction PDEs [1, 2]. The mathematical properties of these PDEs, including degenerate boundaries and generalized Morrey spaces, have been richly studied, highlighting intrinsic structural complexities [3, 4, 5]. Beyond analytical complexity, high-dimensional PDE discretizations aggravate the curse of dimensionality in standard Particle Filters

(PF). Standard PFs require exponentially many particles to prevent weight collapse as state dimensions grow ($M \geq 100$) [6, 7]. Recent research focuses on reduced-order approaches (e.g., Proper Orthogonal Decomposition - POD) to maintain stability while preserving nonlinear expressiveness [8, 9, 11]. Furthermore, real-world measurements often contain outliers, necessitating robust heavy-tailed likelihoods [10, 12]. In this paper, we propose the Reduced-Order Robust Particle Filter (RO-RPF). Our approach integrates POD-based model reduction to project the high-dimensional PDE state into a latent space ($r \ll M$), ensuring tractable sampling, with a robust mixture-based likelihood to attenuate heavy-tailed noise. We validate the framework on a cubic reaction-diffusion PDE under sparse sensing.

2 PDE Model and Analytical Breakdown of EKF

We consider the nonlinear reaction-diffusion PDE with a cubic reaction term on a bounded domain $\Omega = [0, L]$:

$$\frac{\partial u}{\partial t} = \nu \Delta u + u^3, s \in \Omega, t > 0 \qquad (1)$$

with homogeneous Dirichlet boundary conditions. The domain is discretized

uniformly into M nodes. Using central differences for the Laplacian (L) and explicit Euler time-stepping with a saturation operator $\mathcal{S}$ to prevent numerical blow-up, the discrete state propagation is:

$$x_{k+1} = \mathcal{S}\left(x_k + \Delta t\left(\nu L x_k + x_k^{\odot 3}\right)\right) = \mathcal{F}(x_k) \quad (2)$$

The resulting full-order state-space model is:

$$x_{k+1} = \mathcal{F}(x_k) + w_k, w_k \sim \mathcal{N}(0, Q) \quad (3)$$

$$y_k = H x_k + v_k \quad (4)$$

where $H \in \mathbb{R}^{m \times M}$ represents a sparse deterministic sensor array ($m \ll M$) and v_k is the measurement noise. EKF Linearization Failure. To understand why standard methods like the EKF fail in this regime, consider the analytical Jacobian of the unsaturated nonlinear flow:

$$\frac{\partial \mathcal{F}}{\partial x} \approx I + \Delta t\left(\nu L + \mathrm{diag}\left(3\hat{x}_k^{\odot 2}\right)\right). \quad (5)$$

The cubic reaction term induces a quadratic growth in the diagonal elements of the Jacobian. When sharp spatial gradients develop, these diagonal entries become excessively large, causing the covariance matrix update in the EKF to become ill-conditioned and ultimately leading to filter divergence.

3 RO-RPF Methodology

3.1 Dimension Reduction via POD

To mitigate particle degeneracy in $\mathbb{R}^M$, we generate N snapshot solutions $\{x^{(i)}\}$ from the full-order PDE without noise. Singular Value Decomposition of the snapshot matrix yields the reduced basis $\Phi_r \in \mathbb{R}^{M\times r}$ corresponding to the r dominant singular vectors. The state is approximated as $x_k \approx \Phi_r z_k$, where $z_k \in \mathbb{R}^r$. The projected dynamics are:

$$z_{k+1} = \Phi_r^\top \mathcal{F}(\Phi_r z_k) + \tilde{w}_k, \qquad (6)$$

where $\tilde{w}_k \sim \mathcal{N}(0, \Phi_r^\top Q \Phi_r)$. Crucially, the nonlinear operator $\mathcal{F}$ is evaluated in the full-order space before projection to preserve physical fidelity.

3.2 Robust Likelihood Model

To handle non-Gaussian outliers, we adopt a contaminated-Gaussian mixture likelihood:

$$p(y_k \mid x_k) = (1-\epsilon)\mathcal{N}(y_k; Hx_k, R) + \epsilon\mathcal{N}(y_k; Hx_k, \alpha R), \qquad (7)$$

where ϵ is the contamination probability and $\alpha \gg 1$ is the variance inflation factor.

3.3 Algorithm Structure and Complexity

For N_p particles in the latent space $\{z_k^{(i)}\}$:

1. **Prediction:** Propagate $z_{k+1}^{(i)} = \Phi_r^\top \mathcal{F}\left(\Phi_r z_k^{(i)}\right) + \eta_k^{(i)}$.
2. **Robust Update:** Update weights using the robust likelihood: $\tilde{w}_{k+1}^{(i)} = w_k^{(i)} p\left(y_{k+1} \mid \Phi_r z_{k+1}^{(i)}\right)$.

3. **Resampling & Reconstruction:** Resample if the effective sample size N_{eff} is low. Reconstruct the full state: $\hat{x}_{k+1} = \Phi_r \sum_i w_{k+1}^{(i)} z_{k+1}^{(i)}$.

Computational Complexity. A standard Particle Filter in the full state space incurs a computational cost of $\mathcal{O}(N_p M)$ per step. As M grows, N_p must grow exponentially to avoid weight collapse. In contrast, the statistical operations in RO-RPF occur in the latent space $\mathbb{R}^r$, resulting in a sampling complexity of $\mathcal{O}(N_p r)$ with $r \ll M$. This breaks the exponential curse of dimensionality while retaining exact nonlinear physics during propagation.

4 Experiments and Discussion

We evaluate RO-RPF against EKF, UKF, standard PF, and full-space Robust PF (RPF) across three scenarios. Results averaged over 50 Monte Carlo runs.

Scenario 1: Baseline ($M = 50$, Light Noise). Under mild nonlinearity and Gaussian noise, UKF performs best (RMSE 0.008). RO-RPF matches standard PF accuracy (RMSE ~ 0.026) but operates $6\times$ faster.

Scenario 2: High-Dimensional Breakdown ($M = 200$). When the state dimension increases, the classical filters collapse. EKF

diverges due to unstable Jacobian eigenstructure from the cubic term. UKF becomes computationally infeasible (401 nonlinear evaluations per step). PF and RPF suffer complete weight collapse ($N_{\text{eff}} \to 1$) due to the curse of dimensionality [6]. This confirms that dimensionality reduction is essential for large-scale PDEs.

Scenario 3: Full Complexity ($M = 200$, Sparse, Heavy-Tailed). We apply RO-RPF ($r = 8$, capturing $> 99.5\%$ energy, $N_p = 100$) under 7.5% sparse sensing and heavy-tailed noise ($\epsilon = 0.1, \alpha = 50$). Table 1 details the performance.

Table 1: Scenario 3 Quantitative Metrics ($M = 200$).

Filter	RMSE	Time (s)
EKF	0.0337 ± 0.0041	2.82
PF	0.0403 ± 0.0068	298.20
RPF	0.0316 ± 0.0053	312.40
RO-RPF	0.0271 ± 0.0036	**17.48**

RO-RPF achieves the lowest RMSE, successfully filtering heavy-tailed outliers. Furthermore, by evaluating particles in the reduced space, RO-RPF is $\sim 18\times$ faster than standard PF. While EKF is computationally fast, its linearization fails to capture the fine-scale high-frequency spatial oscillations produced by the cubic PDE dynamics, whereas RO-RPF preserves both global and local spatial structures accurately.

5 Conclusion

The proposed RO-RPF provides a highly scalable and robust Bayesian estimation framework for nonlinear, high dimensional PDE systems. By merging a POD-based latent manifold with a heavy-tailed mixture likelihood, RO-RPF overcomes the weight collapse of standard particle filters, the linearization errors of EKF, and the non-Gaussian sensitivity of classical methods. It achieves superior state reconstruction accuracy and order-of magnitude computational speedups in highly complex, sparsely sensed environments.

References

1. Julier, S. J., Uhlmann, J. K.: A new extension of the Kalman filter to nonlinear systems. In: SPIE Proceedings (1997).

2. Wan, E. A., Van der Merwe, R.: The unscented Kalman filter for nonlinear estimation. In: Proceedings of the IEEE AS-SPCC (2000).

3. Gadjiev, T., et al.: The behavior of solutions of nonlinear degenerate parabolic equations in nonregular domains. Trans. Natl. Acad. Sci. Azerbaijan 40, 66–74 (2020).

4. Gadjiev, T., et al.: Solvability of a boundary value problem for degenerate equations. Ukrainian Mathematical Journal 72, 495–514 (2020).
5. Gadjiev, T., et al.: The Dirichlet problem for uniformly elliptic equations in generalized weighted Morrey spaces. Studia Scientiarum Mathematicarum Hungarica 57, 68–90 (2020).
6. Snyder, C., et al.: Obstacles to high-dimensional particle filtering. Monthly Weather Review 136, 4629–4640 (2008).
7. Rebeschini, P., Van Handel, R.: Can local particle filters beat the curse of dimensionality? Annals of Applied Probability 25, 2809–2866 (2015).
8. Berkooz, G., et al.: The proper orthogonal decomposition in the analysis of turbulent flows. Annual Review of Fluid Mechanics 25, 539–575 (1993).
9. Stefanescu, R., et al.: POD/DEIM reduced-order strategies for large-scale PDE systems. Journal of Computational Physics 295, 569–595 (2015).
10. Xu, D., et al.: A robust particle filtering algorithm with non-Gaussian measurement noise. IEEE Signal Processing Letters (2014).
11. Wang, S., et al.: High dimensional ensemble Kalman filter. Quarterly Journal of

the Royal Meteorological Society 147, 1324–1337 (2021).

12. Bai, Y., et al.: A novel adaptive state estimation model: Kalman filter coupled with neural networks. International Journal of Adaptive Control and Signal Processing (2025).

https://doi.org./10.58225/mpmma.2026.*924*

SPECTRAL METHOD FOR STRUCTURES UNDER SHOCK WAVES

Taliat Azizov [1], Dmitro Kochkarev [2], Mukhlis Hajiyev[3] and Tatiana Galinska [4]

[1]National University of Water and Environmental Engineering, Ukraine

[2]Pavlo Tychyna Uman State Pedagogical University, Ukraine

[3]AzUAC, Azerbaijan

[4]National University «Yuri Kondratyuk Poltava Polytechnic», Ukraine

Abstract. This paper presents a simplified spectral method for the analysis of building and structural frames subjected to shock wave loading. Due to the high computational effort required for direct integration of motion equations, a more practical engineering approach is proposed based on spectral analysis. The method reduces multi-degree-of-freedom systems to an equivalent single-degree system and evaluates structural response using dynamic coefficients.

The applicability of the approach is demonstrated by extending dynamic response characteristics from single-mass to multi-mass systems through effective mass coefficients. The procedure also considers modal response combination methods, with

particular emphasis on the SRSS method. The developed methodology is implemented in standard structural analysis software and verified on different structural models. Comparison with the direct integration method shows that the proposed spectral approach provides satisfactory accuracy with significantly reduced computational complexity. The results confirm its suitability for practical engineering analysis of structures under shock wave effects.
Keywords: Spectral method; shock wave; structural analysis; dynamic response; building frames; modal combination; SRSS method; shock loading; structural Dynamics

1. Introduction

The analysis of building and structural frames under shock wave loading is an important task in structural engineering. Determining the correct response of structures to such dynamic воздействия is challenging due to the uncertainty of load magnitude, duration, and impact location. Although the direct integration method provides accurate results, it is computationally intensive and not always practical for engineering applications. Therefore, simplified approaches such as the

spectral method are widely used to estimate structural response with acceptable accuracy. This study focuses on the development and application of a spectral method for analyzing structures subjected to shock waves, providing a balance between accuracy and computational efficiency.

2. Research Methodology

The spectral method for analyzing structures under shock wave loading is based on reducing a multi-degree-of-freedom (MDOF) system to an equivalent single-degree-of-freedom (SDOF) system. This allows the dynamic problem to be solved using simplified analytical relationships.

The equation of motion for an equivalent SDOF system subjected to a dynamic load $P(t)$can be written as:

- with damping

$$m \cdot x'' + c \cdot x' + k \cdot x = P(t); \qquad (24)$$

- without damping

- $m \cdot x'' + k \cdot x = P(t);$ (2)

rütyüsrt

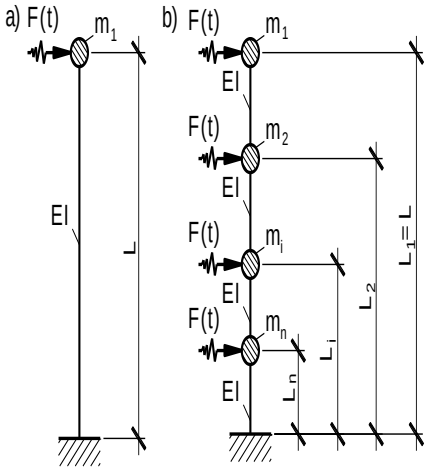


Fig. 1. To determine the coefficient: a) single-mass system; b) multi-mass system.

2. Results and Discussion

The developed spectral method was applied to three types of structural systems: a single-span beam, a multi-storey plane frame, and a spatial frame. The obtained results were compared with those calculated using the direct integration method implemented in SCAD-OFFICE software (figure 2).

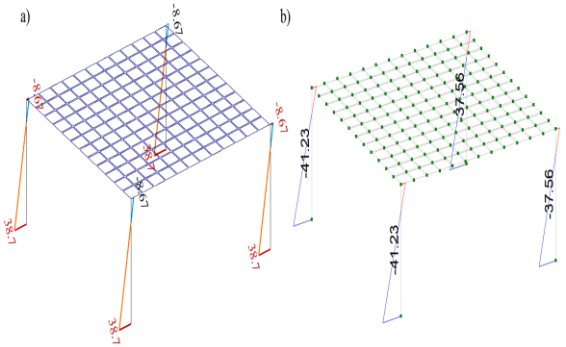


Fig. 2. Fig. 2. Moment diagrams in the columns of the spatial frame: a) Using the spectral method (LIRA-SAPR); b) Using the direct integration method of motion equations (SCAD-OFFICE)

For all considered cases, the spectral method demonstrated good agreement with the reference solution. The comparison of bending moments showed that the discrepancy between the two methods does not exceed approximately 10%, which is acceptable for practical engineering analysis. The smallest deviation was observed for simple systems such as beams, while larger differences occurred in multi-storey and multi-span frames due to their more complex dynamic behavior. The results also confirmed that the SRSS method is the most appropriate approach for combining modal responses in the case of shock wave loading,

since the natural frequencies of vibration are sufficiently separated. Other combination techniques produced less accurate or overly conservative results. In addition, the study showed that the use of dynamic coefficients derived for single-degree-of-freedom systems can be effectively extended to multi-degree systems by introducing appropriate effective mass coefficients. This significantly simplifies the analysis while maintaining reasonable accuracy

Conclusion

A spectral method for analyzing building structures under shock airwave loading has been developed. The applicability of dynamic response functions from single-degree systems to multi-degree systems using effective mass coefficients has been demonstrated. The method has been successfully implemented in modern software packages such as SCAD-OFFICE and LIRA-SAPR.Comparative analysis with the direct integration method on different structural models showed good agreement of results, confirming that the proposed spectral approach is efficient, accurate, and suitable for practical engineering applications.

References

1. Vasilis Karlos, George Solomos. Calculation of blast loads for application to structural components. Luxembourg: Publications Office of the European Union
2. Kingery C. N., Bulmash G., (1984) "Technical report ARBRL-TR-02555: Air blast parameters from TNT spherical air burst and hemispherical burst", AD-B082 713,U.S. Army Ballistic Research Laboratory, Aberdeen Proving Ground, MD.
3. Kinney G. F., Graham K.J., (1985) "Explosive Shocks in Air", Springer, Berlin
4. Kochkarev, D., Azizov, T., Galinska, T. Calculation of Buildings and Structures for Air Blasts Using Explosion Accelerograms. Lecture Notes in Civil Engineering., 2024, 604 LNCE, pp. 245–256
5. L. Wang and D. Kong, "Influence of Ground Impedance on Explosive Shock Wave Test Accuracy," International Journal of Impact Engineering, Vol. 171, p. 104395, Jan. 2023, https://doi.org/10.1016/j.ijimpeng.2022.104395
6. Li, Q., Wang, Y., Li, L., Hao, H., Wang, R., Li, J.: Prediction of BLEVE loads on structures using machine learning and CFD. Process Saf. Environ. Prot. 171, 914–925

(2023).
https://doi.org/10.1016/j.psep.2023.02.008
7. U.S. Department of the Army, (1990) “Structures to resist the effects of accidental explosions”, Technical Manual 5-1300.
8. UFC 04-010-01 , DoD Minimum Antiterrorism Standards For Buildings , U.S. Department of Defense, Washington, DC, 2007.
9. Unified Facilities Criteria (2008), “UFC 3-340-02 Structures to Resist the Effects of Accidental Explosions“, U.S. Army Corps of Engineers, Naval Facilities Engineering Command, Air Force Civil Engineer Support Agency
10. DBN V.2.2-5:2023. (2023) Civil defense protective structures. Kyiv: Ministry of Community, Territories and Infrastructure Development of Ukraine.

https://doi.org./10.58225/mpmma.2026.932

TWO-SCALE FAILURE PROBLEMS OF THE ANISOGRID COMPOSITE LAMINATES

Tatiana Kuzmina and Aleksandr Oleinikov
V. Kupradze Institute of Mathematics,
University of Georgia, Georgia

Abstract. New constitutive equations for direct method to predict failure of anisogrid laminates are presented in the closed formulas for the coupled of meso-macro failure of the composite.

Keywords: Failure, Laminate, Two-Scale Problems, Direct Method, Design Formulas.

Introduction

Failure analysis of plates and shells made of composite laminates is commonly performed using the well-known layer-by-layer approach. This method consists of the sequential analysis of composite failure only at a single level — the ply level. Consequently, the method becomes iterative and multi-stage, requiring repeated recalculation of stresses, strains, and critical loads of the plies after corresponding stepwise changes in their elastic moduli.

A direct coupled meso–macro analysis of laminate failure was apparently first

proposed by R. N. Hadcock in [1]. However, the method presented in [1] allows the determination of failure stresses only for loads acting along the fibre directions of the laminate. Formulas for ultimate uniaxial loads applied at an angle to the fibres were later presented in [2]. The constitutive relations proposed in [1, 2] are based on fibre and matrix failure criteria whose forms have not yet been sufficiently validated [3].

The purpose of this report is to present new constitutive relations for the direct description of failure in anisogrid laminates in the form of closed-form expressions linking meso- and macro-level composite failure.

Direct descriptions of failure in anisogrid laminates

The following Theorem 1 presents the main result of this report and establishes the laminate failure criterion.

Theorem 1 about initial and final failure laminate

Theorem 1. Let multidirectional anisogrid laminate $\left(\pm\psi_{n_1}^{1}, \pm\psi_{n_2}^{2}, \dots, \pm\psi_{n_p}^{p}\right)$ is symmetrical and balanced and is in a state of

plane stress under the action of arbitrarily directed uniaxial loading σ_{φ}.

(a) If

$$\left||\psi| - |\varphi|\right| > \left|B_{T\psi}^{\pm}\right|, \quad (1)$$

then the initial failure laminate criterion is as follows:

$$\sigma_{I\varphi}(\psi_I) = \min_{\psi}\left(\sigma_{m\varphi}^{\psi}\frac{E_{\varphi}^{L}}{E_{\varphi}^{\psi}}\right); \quad (2)$$

(b) If

$$\left||\psi| - |\varphi|\right| \leq \left|B_{T\psi}^{\pm}\right|, \quad (3)$$

then failure final criterion is as follows:

$$\sigma_{II\varphi}(\psi_{II}) = \min_{\psi}\left(\sigma_{f\varphi}^{\psi}\frac{E_{\varphi}^{L}}{E_{\varphi}^{\psi}}\right); \quad (4)$$

(c) If

$$\psi = \varphi \text{ and } \frac{H_{90}}{H_{45}} \leq \frac{1}{2}\left(\frac{S_{11}^{+}}{|S_{11}^{-}|} - 1\right), \quad (5)$$

then failure final criterion is as follows:

$$\sigma_{II\psi}^{k} = -\frac{S_{11}^{-}}{\nu_{\psi,\psi\pm 90}^{L}}\frac{E_{\psi}^{L}}{E_{\psi}^{\psi}}; \quad (6)$$

(d) If

$$\left||\psi| - |\varphi|\right| > \left|B^{\pm}_{T\psi}\right| \text{ and } \psi_I \neq \emptyset, \qquad (7)$$

then the final failure laminate criterion is as follows:

$$\sigma_{II\varphi}(\psi_{II}) = \min_{\psi\setminus\psi_I}\left(\sigma^{\psi}_{m\varphi}\frac{E^{L}_{\varphi}}{E^{\psi}_{\varphi}}\right). \qquad (8)$$

In criteria (2) and (8) of Theorem 1, $\sigma^{\psi}_{m\varphi}$, as well as $\sigma^{\psi}_{f\varphi}$ in criterion (4), denote the projections of the load σ_{φ} onto the axes of the ply-ψ coordinate system, which satisfy the failure criterion of the matrix and fibres, respectively [4, 5]. In criterion (6) $\nu^{L}_{\psi,\psi\pm 90}$ is the Poisson's ratio of an orthotropic body under uniaxial tension in the direction of the ply-ψ fibres. Other designations correspond to [4, 5].

Definition 1. A laminate whose elastic moduli in the direction perpendicular to the fibres and shear moduli in the fibre planes are negligible compared to the elastic modulus in the direction of the fibres will be called *anisogrid*.

Definition 2. Laminate is *a symmetrical* if the alternation of identical layers is mirror symmetric with respect to the median plane

x,y. that is, for each ply-$\psi_{n_k}^{k}$ there is an associated symmetrical ply-$\psi_{n_{k'}}^{k'}$, with respect to the mean plane, the ply-k and ply-k' have the same stiffnesses.

Definition 3. The laminate is termed *balanced* if all ply off-axis x and off-axis y are symmetric with respect to the one and identical:

$\left(+\psi_{n_1}^{1}, -\psi_{n_1}^{2}, \dots, +\psi_{n_{p-1}}^{p-1}, -\psi_{n_{p-1}}^{p}\right)$,

$\left(\pm\psi_{n_i}^{i} \neq 0; 90\right)$.

Corollary 1 about failure of an isogrid laminate

Definition 4. An anisogrid laminate in which all the plies' thicknesses are identical will be called an *isogrid*.

Corollary 1. For all isogrid laminates in which the longitudinal tensile strength of monolayers is three or more times greater than the compressive strength: $S_{11}^{+}/|S_{11}^{-}| \geq 3$, criterion (6) of Theorem 1 is satisfied.

Discussion and conclusion

In conclusion, the proof schemes for Theorem 1 and Corollary 1 are presented, along with a comparison between theory and experiment and a discussion of the results.

References

1.Hadcock, R.N.: Design and analysis of advanced composite structures. In: Lubin (ed.) Handbook of Composites, pp. 533–563. G. Van Nostrand Reinhold Company, New York (1984).

2. Polilov, A.N., Tatus', N.A., Plitov, I.S.: Estimating the effect of misorientation of fibers on stiffness and strength of profiled composite elements. Journal of Machinery Manufacture and Reliability 42(5), 390–397 (2013).

3.Kaddour, A.S., Hinton, M.J., Soden, P.D.: A comparison of the predictive capabilities of current failure theories for composite laminates: additional contributions. Composite Science and Technology 64, 449–476 (2004).

4. Oleinikov, A.I.: Strength criterion variants for unidirectional polymer composites by the fracture condition of the inter-fibre when there is compression perpendicular to the fibers. Mechanics of Solids 57, 1740–1748 (2022).

5. Oleinikov, A.I.: Fracture criteria for matrix and fibers in unidirectional polymeric composites at static loadings. Prikladnaâ Matematika i Mehanika 88(2), 255–270 (2024)

https://doi.org./10.58225/mpmma.2026.938

BEM MODELLING OF AN ADAPTIVE MECHANISED WING LEADING EDGE

Tatiana Kuzmina
V. Kupradze Institute of Mathematics,
University of Georgia, Georgia

Abstract. The growing use of composite materials in modern engineering structures requires reliable mathematical and computer methods for their design and analysis. This study aims to improve the accuracy and reliability of numerical methods for analysing composite structures. The research is based on numerical modelling using the Boundary Element Method (BEM). The accuracy of the method was verified by comparing the numerical results with known exact solutions from elasticity. A computer program was developed to calculate stress distribution in composite structures, providing an effective tool for engineering analysis.

Keywords: Composite Material, Computer Modelling, BEM.

Introduction

Composite structures are widely implemented in aerospace engineering, particularly in aircraft wing components,

where structural efficiency, safety, and aerodynamic performance are critically dependent on accurate prediction of stress–strain behaviour. One of the most promising directions in aircraft design is the development of adaptive or morphing wing structures capable of changing their geometry according to flight conditions [1]. The accuracy of such simulations directly determines the practicability and safety of adaptive aerospace components.

The present work focuses on the development and validation of a numerical modelling approach for analysing stress distribution in composite adaptive wing leading edges using the Boundary Element Method (BEM). The primary objective of the study is to enhance the reliability and computational efficiency of mathematical modelling techniques applied to composite structures. In this research, a deformable leading edge configuration with a single force application point is investigated.

Differential and integral formulation of the problem

The mathematical formulation of the problem is based on the classical elasticity theory. Equilibrium equations describing stress

balance within an elastic body are combined with Cauchy strain–displacement relations and Hooke's constitutive laws linking stresses and deformations. Boundary conditions include prescribed surface tractions and displacements acting on different parts of the structure boundary. Within the BEM framework, stresses and displacements inside the domain are expressed through boundary integral representations involving influence functions [2] that satisfy the governing differential equations:

$$\sigma_{ij}(Q) = \int_G H_{ij;k}(Q, q_0) f_k(q_0) dl, \quad (25)$$

$$u_i(Q) = \int_G I_{i;k}(Q, q_0) f_k(q_0) dl.$$

A singular boundary integral equation is derived by introducing fictitious boundary loads associated with identified singularities:

$$\frac{1}{2} f_k(q) + \int_G H_{ij;k}(q, q_0) n_j(q) f_k(q_0) dl_{q_0} = t_k^0(q).$$

Numerical solution method and computer program

The unknown boundary quantities are determined through the discretisation of the structure boundary into finite segments.

Numerical integration is performed using rectangular quadrature formulas, transforming the integral formulation into a system of linear algebraic equations. The resulting matrix system is diagonally dominant, enabling a stable numerical solution using the Gauss elimination method.

An original computational algorithm and computer program were developed to implement the proposed modelling procedure.

Validation and verification

Verification and validation of numerical models are essential to ensuring their applicability to real engineering problems. To confirm the accuracy of the developed BEM implementation, the classical Kirsch problem was selected, as the exact analytical solution is known [3]. The obtained numerical results demonstrate strong agreement between calculated and analytical stress distributions. The validation results indicate that the developed program reliably captures high stress gradients and concentration effects, which are critical for composite aerospace structures. The developed modelling framework can be

extended to analyse more sophisticated morphing wing concepts.

Conclusion and perspective

In conclusion, this work presents a computational methodology for the stress analysis of adaptive mechanised wing leading edges using the Boundary Element Method. The results confirm the accuracy, stability, and computational effectiveness of the proposed approach for modelling composite structures. The proposed modelling approach supports reliable prediction of stress distribution in adaptive composite components and can assist in reducing experimental costs during the design process.

References

1. Kintscher, M., Wiedemann, M., Monner, H. P., Heintze, Ol., Kühn, T.: Design of a smart leading edge device for low speed wind tunnel tests in the European project SADE. International Journal of Structural Integrity 2(4), 383–405 (2011).
2. Love, A.E.H.: A treatise on the mathematical theory of elasticity.

CAMBRIDGE: University Press, Cambridge (1906).
3. Lekhnitskii, S.G.: Anisotropic plates. Gordon and Breach Science Publishers, New York (1984).

https://doi.org./10.58225/mpmma.2026.944

VALIDATION OF THE EXPERIMENTAL AND NUMERICAL SPLITTER PLATES OF THE CONDENSER TUBE BANKS DURING CROSS FLOW OF AIR

Tayip Türk[1] , Umut Melikoğlu[1]
[1], Tolga Tani[1] , Yunus Emre Dündar[1,2],
Furkan Yıldırım[1,3], Hüseyin Onur Dağlı[1],
Alişan Gönül[4] , Ahmet Selim Dalkılıç[1,]
[1] Yildiz Technical University, Türkiye
[2] Yeditepe University, Türkiye
[3] İstanbul Gedik University, Türkiye
[4] Siirt University, Türkiye

Abstract. The validation of the developed model by commercial software is performed for both experimental and numerical data of the cross-flow condenser tube bank in staggered arrangements with and without the splitter plate. The Reynolds number's range is 5500-14500, and the splitter plate's L/D is 1. Mesh types are selected as polyhedral and triangular, and node number is 15,480,342. The RNG k-e model with the enhanced wall treatment approach is used. Validation results point out that the developed model has better outputs than the numerical solution in the literature for the prediction of experimental data at specific Reynolds numbers.

Keywords: Tube Bank, Splitter Plate, Nusselt number, Pressure Drop.

Introduction

Heat exchangers find diverse uses in thermal management in power production and air conditioning. Crossflow tube heat exchangers are preferred because of their ease of construction, mechanical strength and large area of heat transfer. However, flow around cylindrical tubes may affect the performance of the system especially at low to medium Reynolds numbers. In this range [1] boundary layer separation and wake generation can lead to increased pressure losses and weakened heat transfer. Flow separation can also generate vortex shedding, which can contribute to vibration and noise concerns in tube bank systems [2]. So, passive solutions based on surface geometry or extra flow-control features, and active methods which need the input of external energy were examined to improve the thermohydraulic performance [3]. The knowledge of the flow around a single cylinder is significant for the enhancement of the crossflow heat exchanger performance, as circular cylinders are the fundamental elements of tube bundles.

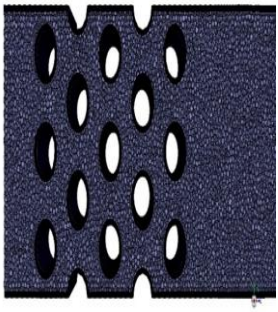
Using experimental and numerical techniques, staggered condenser tube banks with splitter plates and crossflow air have been examined by Mangrulkar et al. [4]. Their investigation was performed in the Reynolds number range of 5500 to 14,500 and indicated that the splitter plate attachments resulted in an increase in Nusselt number, enhancement of heat transmission, and a decrease in pressure drop in comparison with bare cylinders. They also noted a 60–82% overall thermal performance improvement. In the present numerical work, ANSYS Fluent 2023R2 was used. The consistency of the present results, especially at higher Reynolds numbers, was checked by comparing the Nusselt number and pressure drop results with the experimental and numerical results of Mangrulkar et al. [4].

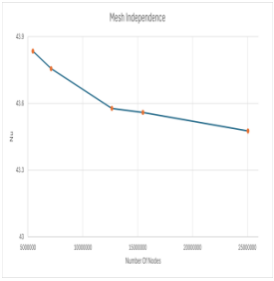
Numerical Model

By using the method of computational fluid dynamics, the simulations of heat transfer of fixed temperature coiled tubes are conducted employing the commercial software ANSYS Fluent. Reynolds-averaged Navier-Stokes (RANS) equations are obtained by considering the time average of velocity and

other quantities, and the RANS equations are solved by employing a turbulence model.

A study investigates mesh independence for bare and splitter plate arrangements, focusing on boundary conditions like average wall temperature, inlet

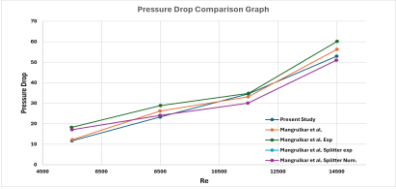


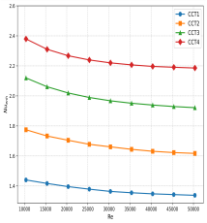


velocity, and pressure outlet. Polyhedral mesh is chosen for the domain. The findings indicate that the optimal mesh configurations contain 15,480,342 elements for splitters, and a certain number for bare tube banks, aimed at balancing computational efficiency and electricity consumption, as higher element counts do not significantly impact numerical results.

Fig. 1. Detailed view of mesh on the tube bank with splitter plate (a), mesh independency graphic (b)

Fig. 2. Graphs of





Nu for all (a) - Pressure Drop for all (b)

Figures 2a and 2b show that obtained numerical outputs have better accuracy than Mangrulkar et al. [4]' ones for their experimental data regarding Nusselt number and pressure drop at some specific Reynolds numbers, in turn.

Conclusion

The usage of the splitter plate enhances the Nusselt number for fluid flow, leading to increased heat transfer and decreased pressure drop within the tube bank compared to a bare cylinder. In this study, The data base on the experimental and numerical findings related to the Nusselt number and pressure drop regarding the bare and splitter plate usage scenarios during cross-flow for the condenser tube bank in staggered arrangements were incorporated into new numerical model, indicating tolerable average errors and trend lines displaying closer compatibility with the numerical one in the literature, especially at higher Reynolds numbers.

References

1. Batista, J., Trp, A., & Lenic, K. (2022). Heat Transfer Enhancement of Crossflow Air-to-Water Fin-and-Tube Heat Exchanger by Using Delta-Winglet Type Vortex Generators. *Energies 2022, Vol. 15, 15*(6). https://doi.org/10.3390/EN15062070

2. Kaushik, S., Singh, H., Kumar, A., Kishore, C., Pati, P. R., Chamoli, S., Giri, J., & Kanan, M. (2026). Fluid–structure interaction and thermal performance: a numerical study on crossflow heat exchangers with aerodynamically optimised splitter elements. *Scientific Reports 2026 16:1*, *16*(1), 9798-. https://doi.org/10.1038/s41598-026-38542-3

3. Bhattacharyya, S., Vishwakarma, D. K., Srinivasan, A., Soni, M. K., Goel, V., Sharifpur, M., Ahmadi, M. H., Issakhov, A., & Meyer, J. (2022). Thermal performance enhancement in heat exchangers using active and passive techniques: a detailed review. *Journal of Thermal Analysis and Calorimetry 2022 147:17*, *147*(17), 9229–9281. https://doi.org/10.1007/S10973-021-11168-5

4. Mangrulkar, C. K., Dhoble, A. S., Chakrabarty, S. G., & Wankhede, U. S. (2017). Experimental and CFD prediction of heat transfer and friction factor

characteristics in cross flow tube bank with integral splitter plate. *International Journal of Heat and Mass Transfer, 104, 964-978.*

https://doi.org./10.58225/mpmma.2026.*951*

BASISNESS OF EIGENFUNCTIONS OF A DIFFERENTIAL OPERATOR WITH A DISCONTINUITY POINT IN WEIGHTED LEBESGUE SPACES

Telman Gasymov, Zahra Aliyeva
Baku State University, Azerbaijan

Abstract. The paper considers the spectral problem for a second-order differential operator with a discontinuity point. The eigenvalues and eigenfunctions of spectral problem are found and it is shown that, if the weight function satisfies the kind of Muckenhoupt condition, the system of eigenfunctions forms a basis in the corresponding weighted Lebesgue spaces.

Keywords: Spectral problem; basis; eigenvalue; eigenfunction; weight function.

The following spectral problem is considered:

$$-y''(x)=\lambda y(x), \qquad x\in\left(0;\frac{1}{2}\right)\cup\left(\frac{1}{2};1\right) \tag{1}$$

,

$$\begin{cases} y(0) = y(1) = 0\,, \\ y\left(\frac{1}{2} - 0\right) = ay\left(\frac{1}{2} + 0\right)\,, \\ y'\left(\frac{1}{2} - 0\right) = by'\left(\frac{1}{2} + 0\right), \end{cases}$$

(2)

where λ is spectral parameter, a and b are an arbitrary complex numbers satisfying condition $a+b \neq 0$. The basis properties of the eigenfunctions of this type spectral problems were studied more generally in works [1,4]. A similar issue was considered in [2]. In this paper, theorem on basis property of the system of eigunfunctions of the spectral problem (1),(2) in weighted Lebesgue spaces are proved.

Let us denote $Z^+ = N \cup \{0\}$. The eigenvalues of problem (1) , (2) are of the form $\lambda_n = (\pi n)^2$, $n \in Z^+$. The eigenfunctions corresponding to the eigenvalues of λ_{2k}, $k \in N$

$$y_{2k}(x) = \begin{cases} b\sin 2\pi kx, & x \in \left(0; \frac{1}{2}\right), \\ \sin 2\pi kx, & x \in \left(\frac{1}{2}; 1\right), \end{cases}$$

are in the form, the eigenfunctions corresponding to the eigenvalues of λ_{2k+1}, $k \in Z^+$

$$y_{2k+1}(x) = \begin{cases} a\sin(2k+1)\pi x, & x \in \left(0;\frac{1}{2}\right), \\ \sin(2k+1)\pi x, & x \in \left(\frac{1}{2};1\right), \end{cases}$$

are in the form.

Suppose that, $L_{p,w}(0,1)$, $1 < p < \infty$ is a weighted Lebesgue space given by the norm:

$$\|f\|_{L_{p,w}} = \left(\int_0^1 |f(x)|^p w(x)dx\right)^{\frac{1}{p}}.$$

Let J be any finite or infinite interval of the number axis. If the weight function $w(x)$ satisfies the condition

$$\sup_{I \subset J} \frac{1}{|I|} \int_I w(x)dx \left(\int_I w(x)^{-(p-1)}dx\right)^{\frac{1}{p-1}} < \infty$$

then we say that the weight function $w(x)$ belongs to the Muckenhoupt class $A_p(J)$ [3];

where $|J|$ is the length of the interval and the supremum is taken over all intervals $I \subset J$.

We denote the class $A_p\left(0,\frac{1}{2}\right)\cup\left(\frac{1}{2},1\right)$ of weight functions given in the interval $(0,1)$, such that their contractions to the intervals $\left(0,\frac{1}{2}\right)$ and $\left(\frac{1}{2},1\right)$ belong to the Muckenhoupt classes $A_p\left(0,\frac{1}{2}\right)$ and $A_p\left(\frac{1}{2},1\right)$ respectively. It is clear that $A_p(0,1)\subset A_p\left(0,\frac{1}{2}\right)\cup\left(\frac{1}{2},1\right)$, the converse is not true in general (see, for example, [5]) .

Theorem 1. Suppose that, the weight function $w(x)$ satisfies $w(x)\in A_p\left(0,\frac{1}{2}\right)\cup A_p\left(\frac{1}{2},1\right)$. System of eigenfunctions $\{y_n(x)_{n\in Z^+}\}$ of problem (1), (2) forms basis in weighted Lebesgue spaces $L_{p,w}(0,1), 1<p<\infty$.

This work was supported by the Azeirbaijan Science Foundation – **Grant AEF-MCG-2023-1(43)_13/06/1-M-06.**

References

1.T.B.Gasymov, Fractional powers of discontinious quasidifferensial operators and basis theorems , Dep.VINITI 16.12.1987, 8902, 74p .

2.T.B.Gasymov, Z.E. Aliyeva, A differential operator with intersection point and summable potential equivalent basis in Lebesgue and weighted Lebesgue spaces, Modern Problems of Mathematics and Mechanics XII International Scientific Conference , 2025, p.149-151

3.R. Hunt , B. Muckenhoupt, R.Wheeden, Weighted norm inequalities for the conjugate function and Hilbert transform // Trans. of AMS V.176(1973), p.227-251

4.L.A.Muravei, Riesz basis in $L_2(-1,1)$, boundary value problems for differential equations, Steklov Inst. Math., 1967, 91(1967), 117-136

5.S.S.Pukhov , Bases of exponentials in weighted spaces generated by zeros of the Fourier-Stieltjes transform. Math Notes 95, 820-832 (2014). https:doi.org/10.1134/S0001434614050277

https://doi.org./10.58225/mpmma.2026.956

NON-ITERATIVE SPECTRAL EVALUATION OF FLUID-FILLED CYLINDRICAL SHELLS

Tukazban Hasanova
AzUAC, Azerbaijan

Abstract. This study investigates the free radial vibrations of an infinite thin-walled cylindrical shell filled with compressible fluid using an inverse method. The approach reformulates the problem of determining natural frequencies, traditionally requiring solutions of transcendental equations, by expressing the shell's frequency without fluid explicitly through the system's frequency. This transformation enables both analytical and graphical exploration of the frequency spectra. The novelty of the work lies in the inverse formulation, which simplifies the spectral analysis and allows direct construction of frequency graphs, facilitating identification of critical points such as stability thresholds and inflection zones. The research highlights how compressible fluid interaction alters the dynamic behavior of the shell, revealing nonlinear dependencies and frequency shifts across modes.

Keywords: Cylindrical shell vibrations; Compressible fluid interaction; Inverse

method analysis; Natural frequency determination; Dynamic stability; Fluid-structure interaction

1. Introduction

The study examines free vibrations of thin-walled cylindrical shells interacting with compressible fluid. Classical shell theories [1], [2] established the foundation, later extended to account for fluid compressibility and shell anisotropy. However, determining natural frequencies of shell–fluid systems remains difficult due to transcendental governing equations requiring iterative numerical solutions. This work proposes an inverse analytical method that reformulates the frequency equation, expressing the shell's frequency without fluid through the system's frequency. The approach enhances transparency in analyzing resonance phenomena and stability conditions, offering a framework suitable for spectral analysis and practical applications in structural mechanics.

2. Methodology

The methodology outlines the mathematical modeling of the acoustic-structural coupling between an elastic cylindrical boundary and an internal compressible medium. The

steady-state radial eigenfrequencies of an infinitely long, thin-walled cylindrical shell containing a fluid characterized by non-zero compressibility are investigated. The internal fluid domain is treated using potential flow theory, where convective acceleration terms are neglected due to the small amplitude of the oscillations. The interacting boundary conditions at the fluid-structure interface are defined via the velocity potential and expressed mathematically through cylindrical Bessel functions. To describe the dynamic behavior of the structural component, the governing differential equations from the technical theory of thin elastic shells are applied:

$$\frac{1}{Eh}\nabla^4\Psi - \nabla_k^2 W = 0$$
$$\nabla_k^2\Psi - D\nabla^4 W - Z = 0 \quad (1.1)$$

where

$$\nabla^2 = \frac{1}{AB}\left[\frac{\partial}{\partial\alpha}\left(\frac{B}{A}\frac{\partial}{\partial\alpha}\right) + \frac{\partial}{\partial\beta}\left(\frac{A}{B}\frac{\partial}{\partial\beta}\right)\right]$$
$$\nabla_k^2 = \frac{1}{AB}\left[\frac{\partial}{\partial\alpha}\left(\frac{B}{A}\frac{1}{R_2}\frac{\partial}{\partial\alpha}\right) + \frac{\partial}{\partial\beta}\left(\frac{A}{B}\frac{1}{R_1}\frac{\partial}{\partial\beta}\right)\right]$$

W—radial displacement of a part of the shell; A, B—coefficients of the first quadratic form of the middle surface of the shell;

α, β— orthogonal coordinates; R_1, R_2— radii of curvature of the lines; E—Young's modulus; ν—Poisson's ratio;h—shell thickness; Z—normal to the surface mass and external forces per unit volume and per unit area, respectively.

$$Z = -q\frac{\partial^2 W}{\partial t^2} + p \quad (1.2)$$

p—fluid pressure; q—mass of the shell material per unit area of the middle surface;B— constant; J_1— Bessel function of the first order.

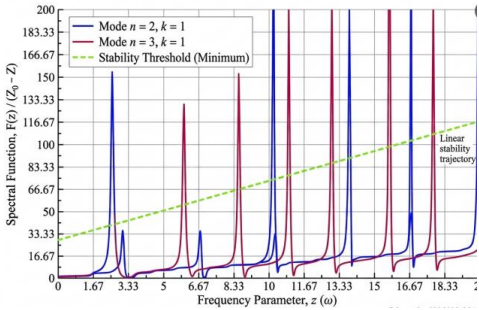


Figure 1. Frequency spectrum curves F(z) versus z for the cases n = 2, n=3 and the stability Threshold.

Conclusion

The inverse method reveals nonlinear effects of fluid compressibility on shell dynamics, simplifying spectral analysis compared to direct transcendental solutions. It enables

efficient construction of frequency graphs, identification of stability thresholds, and analysis of resonance phenomena. Fluid–structure interaction significantly alters natural frequencies, producing nonlinear shifts across modes.

This novel analytical framework avoids iterative numerical techniques by expressing the empty-shell frequency through the coupled system frequency. The explicit relations and graphical mapping provide practical tools for design optimization, resonance prediction, and stability assessment. The findings are highly relevant for aerospace hulls, marine tanks, pipelines, and other thin-walled structures operating in compressible fluid environments.

References

1. Vlasov, V.Z.: *Stroitel'naya mekhanika tonkostennykh prostranstvennykh sistem* [Structural Mechanics of Thin-Walled Spatial Systems]. Stroyizdat, Moscow (1949), 435 pp.
2. Filipkov, A.P.: *Kolebaniya deformiruemykh sistem* [Oscillations of Deformable Systems]. 2nd edn. Mashinostroenie, Moscow (1970), 734 pp.

3. Mamasoliev, K., Ismoilov, E.A.: Analysis of the deformation state of a transverse isotropic cylindrical shell under longitudinal-radial vibrations. *Universum: Tekhnicheskie Nauki* 11(140), 181–190 (2025). DOI: 10.32743/UniTech.2025.140.11.21154.

4. Khudoynazarov, Kh., Mamasoliev, K., Ismoilov, E.A., Ovchinnikov, E.V.: Non-stationary influence of a transverse-isotropic cylindrical shell with a viscous compressed fluid. In: *AIP Conference Proceedings*, vol. 3177, 050005, pp. 1–7. AIP Publishing, Melville, NY (2025). DOI: 10.1063/5.0294882.

5. Bochkarev, S.A., Matveenko, V.P.: Free vibration analysis of a cylindrical shell of variable thickness partially filled with a fluid. *Trudy Instituta Matematiki i Mekhaniki UrO RAN* 29(4), 27–40 (2023).

6. França Júnior, D. O., Ribeiro, P. M. V., Pedroso, L. J. (2019). *Simplified expressions for dynamic behavior of cylindrical shells uncoupled and coupled with liquids.* Latin American Journal of Solids and Structures, 16(6).

7. Ventsel, E., Naumenko, V., Strelnikova, E., Yeseleva, E. (2010). *Free vibrations of shells of revolution filled with a fluid.*

Engineering Analysis with Boundary Elements, 34(10), 856-862.

https://doi.org./10.58225/mpmma.2026.*963*

ANALYSIS OF THE LIMITED CAPACITIES OF PUBLIC TRANSPORT IN THE TRANSPORT SYSTEM IN AZERBAIJAN

Tunzala Alifova Hakim , Hamil Babazada Jahangir

Mingachevir State University

Abstract. The article extensively analyzes the limited capabilities of public transport in the transport system in Azerbaijan. Studies show that the main part of passenger transportation in the country falls on automobile transport, and its indicator varies in the range of approximately 60–70%. Bus transport accounts for 20–25% of total transportation, and the metro accounts for only 8–10%. The share of other modes of transport remains at the level of 3–5%. These figures indicate the existence of a serious structural imbalance in the public transport system and clearly reveal the uneven distribution between modes of transport. In particular, the fact that the metro network operates only in Baku and the almost complete absence of rail transport infrastructure in the regions creates serious restrictions on the development of public transport. As a result, the level of traffic jams in urban areas is approximately 30–40%

higher, and environmental pollution is 20–25%. This situation negatively affects both economic efficiency and the daily quality of life of the population. The research results show that the introduction of multimodal transport systems and the expansion of the metro and rail transport networks can significantly increase the efficiency of public transport. Overall, high dependence on road transport complicates the formation of a sustainable transport system and necessitates structural reforms in this area.
Keywords: Public transport, Car dependency, Rail transport, Transport infrastructure Sustainable development

1. Introduction

In modern times, the transport system is one of the main factors of socio-economic development of countries. Ensuring population mobility, efficient organization of economic activities and development of interregional relations depend on the level of transport infrastructure. In particular, public transport plays an important role in the development of cities and regions, expanding the population's access to work, education and other services. Although important projects have been implemented in

Azerbaijan in recent years towards the development of transport infrastructure, certain problems remain in the public transport system. Carrying out the majority of passenger transport by road increases the load on the road network, causes traffic jams, increases fuel consumption and deepens environmental problems (Aliyeva & Aliyev, 2025). Especially in Baku, the increase in the number of vehicles limits the capabilities of the existing system. High-speed rail transport in the country is mainly limited to the Baku Metro. The lack of metro, tram and other rail transport in the regions increases the population's dependence on road transport and weakens transport accessibility. International experience shows that the integration of metro, bus, suburban train and other modes of transport is important for the formation of a sustainable transport system. In this regard, the analysis of the current state of public transport in Azerbaijan, the investigation of the problems caused by high dependence on automobile transport and the preparation of proposals for the expansion of rail transport infrastructure are of urgent scientific and practical importance. The current situation is considered one of the important issues in terms of ensuring sustainable urban mobility and increasing the

efficiency of the transport system (Ismayilov, 2025).

2. Methodology

Metro network operating only in Baku – Metro is only available in Baku and there is no mass rapid transit system in other major cities. Lack of rail transport in the regions. The lack of development of trams, light metro and suburban trains increases the population's dependence on automobile transport. High dependence on automobile transport – Since the main part of passenger and freight transportation is carried out by automobile transport, the load on the road infrastructure increases. Increased traffic jams – The increase in the number of vehicles, especially in Baku and Absheron, leads to traffic jams, loss of time and additional costs. Increased environmental problems –

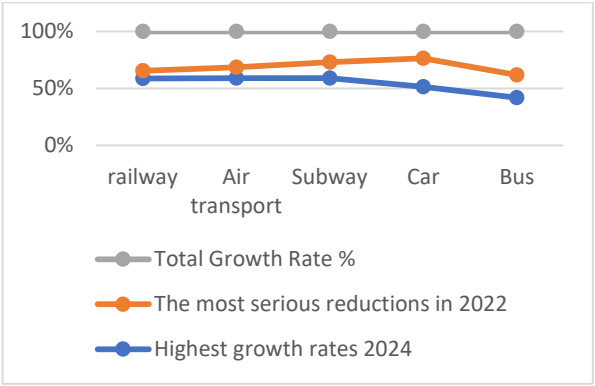


Fig. 1.

The widespread use of automobile transport increases air pollution and greenhouse gas emissions. Limited alternative modes of transport – The insufficient development of alternatives such as metro, tram, bicycle and electric transport reduces passenger choices. Interregional transport differences – The uneven development of transport infrastructure weakens accessibility in some regions and increases regional development. In 1991–2024, an overall growth trend was observed in passenger transportation, a sharp decrease occurred in 2020 due to the pandemic, and in 2021–2024, a rapid recovery was recorded, especially in metro (231.3%), air (198.9%) and railway (181.8%) transport. In 2020, a significant decrease in passenger transportation was observed as a result of the impact of the pandemic.

Conclusion

Statistical analyses conducted show that Azerbaijan's transport system demonstrates a certain sensitivity to global crises such as the pandemic. The sharp decline in passenger transport in 2020 showed that the transport

sector was directly affected by economic and social changes. However, a recovery process was recorded starting in 2021, and high growth rates were observed in 2022. According to the results of the analysis, the highest growth was recorded in metro (231.3%), air transport (198.9%) and railway (181.8%) transport. These indicators indicate that rail and air transport have high passenger transport potential. The growth in bus (127.9%) and automobile (125.5%) transport was relatively low, which indicates that the road infrastructure is under additional load (Natera Orozco, L. G., et al. (2021). The results show that for the sustainable development of the transport sector, it is important to expand the metro and other rail transport networks, create alternative transport systems in the regions, and strengthen the integration of various transport modes. This approach can make a significant contribution to increasing economic efficiency, social well-being, and environmental sustainability.

References

1. Aliyeva, R. T., & Aliyev, F. Z. (2025). Economic assessment of transport and logistics system’s contribution to national

economic growth. *Economics of Transport Complex*, *46*, 233–253. https://doi.org/10.30977/ETK.2225-2304.2025.46.233

2. UNECE. (2025). *Sustainable transport action plan for Azerbaijan: Improving sustainable urban mobility*. United Nations Economic Commission for Europe. https://unece.org/info/publications/pub/406110

3. Ismayilov, A. (2025). Moving sustainably towards conscious mobility chain: The case of Baku. *ResearchGate*. https://www.researchgate.net/publication/391078017

4. Salayev, E. (2025). Assessing the risk of public transport in southern cities of Azerbaijan using the bow tie method. *Transport Journal*, 2(1). https://www.researchgate.net/publication/391271758

5. Natera Orozco, L. G., et al. (2021). Multimodal urban mobility and multilayer transport networks. *arXiv*. https://arxiv.org/abs/2111.02152

https://doi.org./10.58225/mpmma.2026.*970*

NUMERICAL VALIDATION OF AIR-SIDE THERMAL-HYDRAULIC PERFORMANCE IN A BAR AND PLATE HEAT EXCHANGER

Ulaş Kayaoğlu, Celal Melih Eriş, Melih Gökay Uslu, Ahmet Selim Dalkılıç
Yildiz Technical University, Turkiye

Abstract. The present work investigates the air-side thermal-hydraulic performance of a cross-flow bar and plate heat exchanger under laminar flow conditions. Using experimental correlations and Computational Fluid Dynamics (CFD) simulations, the study analyzes air as the working fluid at an inlet temperature of -10°C and explores six different flow conditions with inlet velocities from 1 to 3.5 m/s. The CFD simulations were performed in the ANSYS Fluent environment to assess the thermal and flow characteristics of the heat exchanger. Following the simulations, the researchers calculated the Colburn j-factor and Fanning friction factor (f) based on the numerical results, comparing them with empirical correlations from Kays and London for a geometrically similar plate-fin surface across various Reynolds numbers. The study found that the deviation between CFD-based and experimental Colburn j-factor values ranged

from 11% to 21%, while the deviations for the Fanning friction factor ranged from 8% to 22%. Despite these discrepancies, the results demonstrated an acceptable agreement with the reference experimental data, suggesting that the empirical correlations used are reliable for the tested conditions. The findings validate the developed numerical model and indicate that CFD simulations can effectively predict the air-side thermal-hydraulic performance of bar and plate heat exchangers, serving as a valuable tool for performance evaluation and design studies.
Keywords: Bar and Plate Heat Exchanger, CFD, Colburn j-Factor; Fanning Friction Factor

Introduction

Bar and plate heat exchangers are extensively utilized for compact thermal systems because of their large heat transfer surface density and good thermo-hydraulic properties [1,2]. In these arrangements, precise prediction of air-side performance is crucial to design optimization and energy efficiency improvements. For this reason, the complicated interaction between flow and heat transfer is often studied through a

combination of numerical and experimental methods. In this work, numerical investigation of a bar and plate heat exchanger in cross-flow is conducted for six various input velocities related to different Reynolds numbers with air at -10°C as the working fluid. The flow and heat transfer behaviors are modeled with a conjugate heat transfer technique in ANSYS Fluent . The k-w turbulence model is employed. The computational domain mesh, consisting of around 13.3 million elements, is used to resolve intricate flow structures at adequate resolution. The Colburn j-factor and Fanning friction factor are extracted from the CFD data for evaluation of the thermal-hydraulic performance and are compared with conventional experimental correlations of Kays and London for similar geometries [1]. The comparison is intended to assess the numerical model consistency and the reference correlations applicability for the present operating conditions. The results demonstrate that the proposed CFD framework offers a sound description of the air-side behavior of bar and plate heat exchangers, facilitating its application in design-oriented studies.

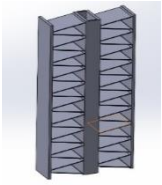


Fig.1. Design view of the model created as the computational domain

Analytical Equations and Numerical Modelling

The air-side thermal-hydraulic performance of the system was evaluated based on the CFD findings for the necessary performance parameters. In this work, the Colburn j-factor and Fanning friction factor were determined numerically from the extracted temperature and pressure fields of the simulations, and the respective governing equations. These results were then utilized to characterize the heat transfer and pressure drop characteristics of the heat exchanger under the operating circumstances examined.

$$D_h = \frac{4.A_{free\ flow}.L_{flow}}{A_{heat\ transfer\ area}}$$

$$m = \rho \cdot V \cdot A \qquad Re = \frac{(\rho \cdot V \cdot D_h)}{\mu}$$

$$Q = m \cdot c_p \cdot (T_{out} - T_{in})$$

$$\Delta T_{lm} = \frac{[(T_{wall} - T_{in}) - (T_{wall} - T_{out})]}{[\ln(T_{wall} - T_{in})/(T_w - T_{out})]}$$

$$Q = h \cdot A \cdot \Delta T_{lm} \qquad Nu = \frac{h \cdot D_h}{k}$$

$$j = \frac{Nu}{Re \cdot Pr^{1/3}} \qquad f = \frac{(P_{in} - P_{out}) \cdot D_h}{2 \cdot \rho \cdot L \cdot V^2}$$

The results were obtained by applying the specified boundary conditions and setting up a parametric study. A mesh independence analysis was performed based on outlet temperature and pressure values, and it was concluded that the solution should be carried out using a mesh consisting of 13.3 million elements. The maximum skewness value of the mesh was found to be 0.88.

Results and Discussion

The numerical study was performed for the plate-fin surface under laminar flow conditions (Re<2000). The performance of the geometry was evaluated using the Fanning friction factor f and the Colburn heat transfer factor j. The numerical results were validated against the Kays and London data for the 1/8-16.12(T) surface, where $St.Pr^{2/3}$ was directly taken as the Colburn j factor. Both f and j decreased with increasing

Reynolds number, consistent with the reference trend. [3]

Table 1. The performance coefficients and corresponding error rates with respect to Reynolds number

5 Conclusion

Mesh independence was reached at around 13.3 million elements. The numerical model was validated by contrasting the numerical results with the experimental data for the thermal-hydraulic performance on the air-side of the bar and plate heat exchanger. The little differences show that the model is able to forecast the air-side heat transfer and pressure-drop features adequately.

Reynolds Number	**j Kays& London**	**$j_{present\ work}$**	**j % error**	**f Kays&London**	**$f_{present\ work}$**	**f % error**
300	0,02190	0.02524	15.29	0.10030	0.09146	-8.81
450	0,01670	0.01992	19.26	0.07755	0.06760	-13.53
600	0,01395	0.01687	20.97	0.06440	0.05478	-14.94
750	0,01268	0.01480	16.82	0.05750	0.04713	-18.03
900	0,01174	0.01334	13.71	0.05240	0.04181	-20.21
1050	0,01103	0.01227	11.24	0.04880	0.03784	-22.45

References

1. Kays, W. M., & London, A. L. Compact Heat Exchangers. 3rd edn. Scientific International Pvt. Ltd., New Delhi, 2018.
2. Melwanki, R. M., & Umale, S. S. Analysis of Plate Type Offset Fin Compact Heat Exchanger - A Review. 1st National Conference on Mechanical Engineering in Next Decade (NC-MEND 2017), 326-330, 2017.
3. Yang, K., Zhang, X., & Yang, H. Performance prediction of plate fin heat exchangers: A CFD and NTU-based approach. International Communications in Heat and Mass Transfer, 169, 109618, 2025.

https://doi.org./10.58225/mpmma.2026.977

ON A OPTIMAL CONTROL PROBLEM FOR A LOADED PARABOLIC EQUATIONS

Vagif Abdullayev [1,2,3] *Soltanali Jafarli* [1]

[1]Azerbaijan State Oil and Industry University, Azerbaijan

[2]Institute of Mathematics, Azerbaijan

[3]AZUAC, Azerbaijan

Abstract. We consider an approach to the optimization of loading points and the corresponding reaction functions for loaded partial differential equations. In these problems, it is required to restore the loading points and the functions of reaction on them from the available information on the observations of the process state. The choice of loading points and reaction functions under the condition of minimizing the functional of the root-mean-square deviation from the observed state values leads to the parametric optimal control problem. To solve the problem we have derived formulas for the gradient of the functional with respect to optimizable loading parameters.

Keywords: optimal control, loaded differential equation, gradient of the functional.

1. Introduction

The states of many objects (processes) can be represented by loaded differential equations, either with ordinary or partial derivatives [1]–[11]. Load points affect the change in the state of the entire object. Consequently, the design of such systems, in particular the determination of optimal load points and their associated response functions, plays a crucial role in ensuring the overall efficiency and performance of the object [8].

The paper presents the formulation and a numerical solution approach to the optimization problem of determining load points and the corresponding reaction functions for objects described by loaded partial differential equations, illustrated through the example of a rod heating process described by a loaded parabolic differential equation. The optimization of load points and reaction functions is performed under the condition of minimizing a prescribed functional that assesses the quality of the process. For solving the problem analytical expressions for the gradient of the functional with respect to the optimized parameters and functions are derived. The results of computing experiments are carried out on examples of solving test problems.

2.Problem Statement

The functioning of the process (object) described by the loaded parabolic equations

is considered:

$$W_t(x,t) = a^2 W_{xx}(x,t) + \sum_{s=1}^{L} Q^s(x,t) W(\xi_s,t) + f(x,t) \quad (1)$$

$$(x,t) \in \Omega = (0,l) \times (0,T],$$

under the initial and boundary conditions

$$W(x,0) = \varphi(x), x \in [0,l], \quad (2)$$

$$W(0,t) = \mu_1(t), \ t \in [0,T], \quad (3)$$

$$W(l,t) = \mu_2(t), t \in [0,T]. \quad (4)$$

In this process $W(x,t)$ is a function characterizing the state of the object at the point $x \in [0,l]$ of the rod at the time $t \in [0,T]$. a, T, $l-$ the given numbers and $T > 0$, $l > 0$; $\xi = (\xi_1, \xi_2, \dots, \xi_L)^T -$the load points from the segment $[0,l]$.

And, $Q = Q(x,t) = (Q^1(x,t), Q^2(x,t), \dots, Q^L(x,t) -$the corresponding reaction functions at the load points; $\varphi(x) \in L_2[0,l], \mu_1(t), \mu_2(t) \in L_2[0,T]$ and $f(x,t)$ are given functions. The task is to determine the optimized load points $\xi_s \in [0,l], s = 1,2,3,\dots,L$ and the corresponding continuous reaction functions $Q^s(x,t), s = 1,2,3,\dots,L$ minimizing (that minimize) the given functional:

$$J(Q,\xi) = \alpha_1 \int_0^T \int_0^l f^0\big(x,t,W(x,t),Q(x,t),\vartheta(\xi,t)\big)dxdt +$$

$$+\alpha_2 \int_0^l f^1\big(x, W(x,T)\big)dx + $$

$$+\alpha_3 \sum_{s=1}^{L} \left\| Q^s(x,t) - \widetilde{Q}^s(x,t) \right\|^2_{L_2(\Omega)}$$

$$+ \alpha_4 \sum_{s=1}^{L} \left\| \xi_s - \widetilde{\xi}_s \right\|^2_{R^L} . \qquad (5)$$

Here $f^0(x,t,W,Q,\vartheta)$ is a given function which is continuous in x,t and differentiable by W,Q,ϑ; $f^1(x,W(x,T))$ is a given function and continuous in x and differentiable by$W$; $\alpha_1,\alpha_2$are weight coefficients,α_3, α_4, $\widetilde{Q}^s(x,t),\widetilde{\xi}_s, s = 1,2,3,\dots L$ the regularization parameters, $\vartheta(\xi,t) = \big(W(\xi_1,t), W(\xi_2,t), \dots, W(\xi_L,t)\big) = = (\vartheta_1,\vartheta_2,\dots,\vartheta_L) = \vartheta.$

On optimized load points and functions $Q^s(x,t), s = 1,2,3,\dots,L$ any conditions can be imposed, in particular, of the (following) form:

$$\underline{\xi}_s \le \xi_s \le \overline{\xi}_s, \underline{\xi}_s, \overline{\xi}_s \in [0,l], s = 1,2,3,\dots,L, \qquad (6)$$

$$\underline{Q}^s \le Q^s(x,t) \le \overline{Q}^s, s = 1,2,3,\dots,L, (x,t) \in \Omega. \qquad (7)$$

We will assume that for the given admissible load points ξ and the functions $Q(x,t)$ the considered problem (1)–(4) has a unique

solution.

The problems (1)–(7) under consideration may occur in the context of optimal design and synthesis of stationary systems with loading [4]. The inverse problems that arise in the mathematical modeling of loaded systems (processes), which are encountered, in particular, in underground fluid dynamics, etc., have the same formulation [6, 7, 9].

Note that for the given admissible values of optimized ξ and $Q(x,t)$ to solving loaded boundary value problems (1)–(4) there are numerical methods based on the use of grid method schemes [10]. The approach is based on the property of superposition of systems of linear algebraic equations and uses special parametric representations of systems of linear algebraic equations solutions with specific structures obtained as a result of applying methods of difference approximation of boundary value problems with respect to loaded equations. In [11] an approach to the numerical solution of loaded linear and nonlinear differential equations with ordinary derivatives was proposed and studied. Using the method of lines, the approach was extended to the solution of linear partial differential.

References

1. Nakhushev, A. M.: Loaded Equations and Applications. Nauka, Moscow, (2012). [in Russian].

2. Abdullayev, V. M., Jafarli, S. S.: On a Loaded Optimal Control Problem with Multipoint Conditions . 2023 5th International Conference on Problems of Cybernetics and Informatics (PCI), 1-3 (2023).
3. Parasidis, I. N., Providas, E. : Closed-form solutions for some classes of loaded difference equations with initial and nonlocal multipoint conditions, T. Rassias and N.J. Daras, eds., Springer, (2018).
4. Abdullayev, V. M., Aida-zade, K.R.: Numerical Solution of the Problem of Determining the Number and Locations of State Observation Points in Feedback Control of a Heating Process. Comput. Math. and Math. Phys. 58(1), 78–89 (2018).
5. Abdullayev, V.M., Aida-zade, K.R. Approach to the Numerical Solution of Optimal Control Problems for Loaded Differential Equations with Nonlocal Conditions . Comput. Math. and Math. Phys.59(1), 696–707 (2019).
6. Dzhenaliev, M. T.: Optimal control of linear loaded parabolic equations // Diff. Uravn.1989. Vol. 25. No. 4, 641–651.
7. Kozhanov, A. I.: Nonlinear loaded equations and inverse problems. Comput. Math. and Math. Phys. 44(4), 657–678 (2004).
8. Abdullayev, V.M.: Identification of the Functions of Response to Loading for

Stationary Systems. Cybern. Syst. Anal. 53(3), 417–425 (2017).
9. Aida-Zade, K.R., Abdullayev, V.M.: Numerical Method for Solving the Parametric Identification Problem for Loaded Differential Equations. Bull. Iran. Math. Soc. 45(6), 1725–1742 (2019).
10. Abdullayev, V. M., Aida-zade, K.R.: Finite-difference methods for solving loaded parabolic equations. Comput. Math. and Math. Phys. 56(1), 93–105 (2016).
11. Abdullaev, V.M., Aida-zade, K.R.: Numerical method of solution to loaded nonlocal boundary value problems for ordinary differential equations. Comput. Math. and Math. Phys. 54(7), 1096–1109 (2014).

https://doi.org./10.58225/mpmma.2026.984

ADVANCED ALGEBRAIC AKBARI-GANJI MODELING FOR VOC TRANSPORT IN BIOFILTRATION

Vanaja Ramalingam[1] and R. Shanthi[2]

[1] Saveetha Institute of Medical and Technical Sciences, India

[2]Meenakshi Academy of Higher Education and Research,India

Abstract: This study presents 3rd-order algebraic Akbari-Ganji Method (AGM) to model the biofiltration of hydrophilic and hydrophobic volatile organic compounds. We analytically solve non-linear differential equations for methanol and α-pinene concentration profiles. Compared to existing Adomian decomposition and Taylor series methods, this algebraic AGM approach provides rapid convergence and high accuracy for analyzing VOC transport.

Keywords: Biofiltration, Volatile Organic Compounds, Akbari-Ganji Method, Non-linear Differential Equations, Mathematical Modeling.

Introduction :

Biological methods, specifically biofiltration, are increasingly utilized for treating air polluted by volatile organic compounds

(VOCs) like methanol and α-pinene due to their cost-effectiveness and low secondary pollution. Biofilters operate by passing contaminated air through a porous medium where microorganisms immobilized in a biofilm degrade the pollutants. While previous studies have successfully used techniques like the Adomian Decomposition Method (ADM) and Taylor Series Method (TSM) to understand the complex, non-linear mass transfer and degradation kinetics in these systems, obtaining highly accurate and easily computable analytical solutions remains critical for parametric optimization. Recently, the Akbari-Ganji Method (AGM) has proven effective in providing semi-analytical approximations without requiring linearization. This paper introduces a novel approach by applying a 3rd-order algebraic AGM to evaluate the concentration profiles of mixed VOCs, offering an advanced mathematical tool for optimizing biofilter performance.

Methodology

The nonlinear governing equations of the model were first formulated and transformed into a dimensionless form. The Advanced Algebraic Akbari-Ganji Method (AAGM) was then applied to obtain analytical

solutions. An algebraic polynomial trial function with unknown coefficients was assumed. The boundary conditions were imposed on the assumed function to establish coefficient relationships. The trial solution was substituted into the governing equations to form residual equations. The unknown coefficients were determined by solving the resulting algebraic system. Finally, the obtained analytical results were validated through comparison with numerical and existing analytical solutions

The transport of VOCs in the biofilm is mathematically described by non-linear differential equations for methanol (ζ_m) and α-pinene (ζ_p).
The dimensionless governing equations are

$$\frac{d^2\zeta_m}{d\eta^2}=\phi\left(\frac{\zeta_m}{1+\beta\zeta_m}\right) \quad (1)$$

$$\frac{d^2\zeta_p}{d\eta^2}=\alpha\phi_1\left(\frac{\zeta_p}{1+\beta_1\zeta_p}\right) \quad (2)$$

Boundary conditions are

$$\zeta_m=1, \zeta_p=1 \text{ at } \eta=0$$

(3)

$$\frac{d\zeta_m}{d\eta}=\frac{d\zeta_p}{d\eta}=0 \text{ at } \eta=1$$

(4)

Analytical expression of the concentrations using Akbari-Ganji's method

Assume that the solution of equation (1) is given by:

$$\zeta_m(\eta)= a_0+a_1\,\eta+a_2\eta^2+a_3\eta^3$$

(5)

where a_0, a_1 and a_2 are constants. Applying the boundary conditions the analytical expression product is

$$\zeta_m(\eta)=1-\frac{2\varnothing\,(1-\beta)}{2+\varnothing\,(1+\beta)}\,\eta+\frac{\varnothing\,(1-\beta)}{2}\,\eta^2+\frac{a_1\,\varnothing\,(1-\beta)}{6}\,\eta^3$$

(6)

Similar to equation (5), we assume that the solution to equation (2) has the form:

$$\zeta_p(\eta)= b_0+b_1\eta+b_2\eta^2+b_3\eta^3$$

(7)

the analytical expression for the product is

$$\zeta_p(\eta) = 1 - \frac{\alpha\varphi_1(1-\beta)}{2+\alpha(1-\beta)}\,\eta + \left(\frac{1-\beta}{2}\right)\alpha\varphi_1\,\eta^2 + \left[\frac{(1-\beta)b_1}{6}\right]\alpha\varphi_1\,\eta^3 \quad (8)$$

Conclusion

This study successfully introduces a novel 3rd-order algebraic Akbari-Ganji Method to analytically solve non-linear VOC biofiltration models. The derived polynomial expressions offer a straightforward, highly accurate theoretical tool for predicting methanol and α-pinene concentration profiles. This computationally efficient approach facilitates superior parameter optimization for industrial biofilter designs, demonstrating significant potential for broader applications in environmental engineering and multiphase bioreactor modeling.

References

1. Li GW, Hu HY, Hao JM, Zhang HQ. Environ Sci 2002; 23(5):13–18.
2. Sun YM, Quan X, Yang FL, Chen JW, Lin QY. J Appl Environ Biol 2005;11(1):82–5.
3. Yang CP, Suidan MT, Zhu XQ, Kim BJ. Environ Prog 2003;22(2):87–94.
4. Mohseni M, Allen DG. Chem Eng Sci 2000;55(9):1545–58.

5. Adomian G, Rach R. J Math Anal Appl 1993;174:118–37.
6. Biazar J, Babolian E, Islam R. Appl Math Comput 2004;147:713–19.
7. Meena V, Rajendran L, Kumar S, Rani PGJ. Egypt J Basic Appl Sci 2014;1:71–6.
8. Sivasundari SAS, Rani RU, Lyons MEG, Rajendran L. Int J Electrochem Sci 2022;17:220447.
9. Ottengraf SPP. Tibtech 1987;5:132–6.
10. Wani AH, Branion RMR, Lau AK. J Environ Sci Health A 1997;32:2027–55

https://doi.org./10.58225/mpmma.2026.990

SECTIONS OF LAURENT GENERATING SERIES FOR SOLUTIONS OF TWO-DIMENSIONAL DIFFERENCE EQUATIONS WITH CONSTANT COEFFICIENTS

Vitaly Alexeev and Alexander Lyapin
Siberian Federal University, Russia

Abstract. We study sections of Laurent generating series associated with solutions of two-dimensional linear difference equations with constant coefficients in simplicial cones of the integer lattice. The generating series is decomposed into families of one-dimensional sections along subcones generated by the edges of the cone. Using projection and shift operators, we derive recurrence relations satisfied by these sections. In contrast to previous works, the support of the difference operator is not restricted to the generators of the cone and may be arbitrary inside the cone. It is shown that the order of the obtained recurrence relation is determined by the width of the Newton polytope of the characteristic polynomial in a fixed direction. Several examples are considered, including equations related to lattice path enumeration and Schröder paths. The proposed approach provides a convenient tool for the study of multidimensional difference equations, D-

finite discrete generating series, and symbolic computation methods in discrete analysis and enumerative combinatorics.

Keywords: difference equations; Laurent generating series; simplicial cones; Newton polytope; recurrence relations; lattice paths.

We study sections of Laurent generating series associated with solutions of two-dimensional linear difference equations with constant coefficients in simplicial cones of the integer lattice [9, 11-12]. The theory of generating series for multidimensional difference equations goes back to the works of E. K. Leinartas [1-2] and his collaborators and is closely related to problems of combinatorics, symbolic computation, and discrete analysis. In recent years, special attention has been paid to D-finite generating series [7-8] and recurrence relations satisfied by their sections [3-6].

Let a^1 and a^2 be linearly independent vectors with integer coordinates generating a simplicial cone $K = \langle a^1, a^2 \rangle$. Consider the Cauchy problem for a two-dimensional difference equation

$$\sum_{\alpha=\Omega}^{n} c_\alpha f(x+\alpha) = g(x), x \in M,$$

where Ω is a finite subset of the cone K and c_α are constant coefficients. The main object of our study is the Laurent generating series c_α.

We represent this series as a family of sections along one-dimensional subcones

$$c_\alpha$$

where $K_1 = \langle a^1 \rangle$ and y belongs to the complementary cone $K_2 = \langle a^2 \rangle$. Similar sections may also be considered along K_2.

The principal goal of the paper is to derive recurrence relations satisfied by the sections of the Laurent generating series. In contrast to previous papers devoted to equations directly associated with generators of the cone, we consider a more general situation where the support Ω of the difference operator is arbitrary inside the cone. Every point $\alpha \in \Omega$ can be uniquely represented in the form $\alpha = r_\alpha\, a^1 + s_\alpha\, a^2$,which allows us to separate shifts along different directions f the cone. Using projection operators and shift operators, we construct a combined operator c_α.

The main theorem establishes that the sections satisfy a recurrence relation of the form c_α.

We show that the order of this recurrence relation is equal to the width of the Newton polytope of the characteristic polynomial along the direction a^2. Thus, geometric properties of the Newton polytope determine analytic properties of the sections [10].

Several examples are considered. In particular, we study a difference equation whose support consists of four lattice points inside a simplicial cone. Explicit recurrence relations for the corresponding sections are obtained. We also discuss an example related to Schröder lattice paths. In this case the generating functions arise naturally in enumerative combinatorics, and the recurrence relations for sections provide an effective way to describe the structure of the solutions.

The proposed approach can be useful in the study of D-finite discrete generating series, multidimensional recurrences, and symbolic algorithms for difference equations. The obtained recurrence relations reduce multidimensional problems to one-dimensional recurrences for sections, which may simplify both theoretical analysis and computer algebra computations.

This research is supported by the Russian Science Foundation and Krasnoyarsk

Regional Science Foundation, project no. 25-21-20076.

References

1. Leinartas, E.K.: Multiple Laurent Series And Difference Equations. Sib. Math. J. 45(2), 321–326 (2004).
2.Leinartas, E.K.: Multiple Laurent Series And Fundamental Solutions Of Linear Difference Equations. Sib. Math. J. 48(2), 268–272 (2007).
3.Akhtamova, S.S., Grishunov, V.Y., Lyapin, A.P., Tikhomirov, S.A.: On Sections Of Generating Series In Lattice Path Problems. Applied Mathematics & Physics 52(2), 146–151 (2020).
4.Lyapin, A.P., Akhtamova, S.S.: Recurrence Relations For The Sections Of The Generating Series Of The Solution To The Multidimensional Difference Equation. Vestn. Udmurtsk. Univ. Mat. Mekh. Komp. Nauki 31(3), 414–423 (2021).
5.Lyapin, A.P., Cuchta T.: Sections of the generating series of a solution to the multidimensional difference equation. Bulletin of Irkutsk State University-Series mathematics 42, 75–89 (2022).
6.Akhtamova, S., Alekseev, V., Lyapin, A.: D-Finite Discrete Generating Series and

Their Sections. Mathematics 13(20), 3259 (2025).
7.Stanley, R. P.: Differentiably finite power series. Eur. J. Comb. 1, 175–188 (1980).
8.Lipshitz, L.: D-Finite Power Series. J. Algebra 122, 353–373 (1989).
9.Bousquet-Melou, M., Petkovsek, M.: Linear recurrences with constant coefficients: the multivariate case. Discrete Mathematics 225, 51–75 (2000).
10.Forsberg, M., Passare, M., Tsikh, A.: Laurent determinants and arrangements of hyperplane amoebas. Advances in mathematics 151(1), 45-70 (2000).
11.Kostić, M.: Almost Periodic Type Solutions to Integro-Differential-Difference Equations. De Gruyter, Berlin (2025)
12.Abbas, S., Fedorov, V.E., Kostić, M.: Fractional partial difference operators and multidimensional Z-transform. Comput Math Model (2026).

https://doi.org./10.58225/mpmma.2026.996

MECHANICAL ANALYSIS OF FUNCTIONALLY GRADED CYLINDRICAL ELEMENTS UNDER PURE TORSION FOR ITER-TYPE TOKAMAK REACTORS

Vusal Aliyev

Baku State University ,Azerbaijan

Abstract. Layered inhomogeneous materials used in ITER-type tokamak reactors often fail under torsion because stress jumps at the boundaries accelerate structural damage. We resolved this problem by deriving a clean, closed-form shear stress expression for a hollow cylinder with a power-law functionally graded material (FGM) profile. This framework transitions smoothly from a ductile metal base to a thermal ceramic shield. By defining a simple modulus ratio (k), we managed to collapse the entire grading system into a single parameter, making the analytical integration of the torsion formula straightforward. Our results for typical metal-ceramic and metal-tungsten pairs show that $k$directly shapes the internal stress curves while the baseline material stiffness cancels from the normalized stress formulation. The stress field is perfectly smooth across the whole section, which provides an exact mathematical guideline for

selecting robust materials for fusion shield design.

Keywords: functionally graded materials, pure torsion, ITER tokamak, shear stress, power-law grading.

1 Introduction

The ITER First Wall endures neutron flux and cyclic heat shocks up to 1.0 MW/m^2, causing stress jumps at bonding interfaces that trigger delamination and fatigue cracks [1, 2]. Functionally graded materials (FGMs) eliminate sharp boundaries by continuously blending material properties across the wall [3, 4]. This study presents an analytical torsion model for an FGM hollow cylinder to evaluate material combinations for ITER blankets (see Fig. 1).

2 Model and Analytical Formulation

We analyze a graded hollow cylinder bounded by an inner radius $R_1 = 10$ mmand an outer radius $R_2 = 20$ mm. The component experiences a steady torque M_b along its centerline. The shear modulus $G(r)$ transitions from the inner to the outer radius based on a standard power-law layout:

$$G(r) = G_m \left[1 + (k-1)\left(\frac{r}{R_2}\right)^n\right], k = \frac{G_c}{G_m}$$

Here, G_m represents the shear modulus of the starting metal substrate, G_c is the modulus of the outer ceramic phase, and k acts as our structural stiffness ratio.

For pure torsion, the local shear stress follows the relation $\tau(r) = G(r) \cdot r \cdot (d\phi/dx)$, where $d\phi/dx$ is the twist rate per unit length. Balancing the total internal torque across the cross-section yields:

$$M_b = 2\pi \frac{d\phi}{dx} \int_{R_1}^{R_2} r^3 \, G(r) \, dr$$

When we extract $d\phi/dx$ from this equilibrium and plug it back into the main stress equation, the base term G_m cancels out completely. This leaves us with a normalized shear stress distribution:

$$\tau(r) = \frac{M_b \cdot r \left[1 + (k-1)\left(\frac{r}{R_2}\right)^n\right]}{2\pi \int_{R_1}^{R_2} r^3 \left[1 + (k-1)\left(\frac{r}{R_2}\right)^n\right] dr}$$

We integrated the denominator analytically to get the exact closed-form solution:

$$\int_{R_1}^{R_2} r^3 \left[1 + (k-1)\left(\frac{r}{R_2}\right)^n\right] dr = \frac{R_2^4 - R_1^4}{4} + \frac{k-1}{R_2^n} \cdot \frac{R_2^{n+4} - R_1^{n+4}}{n+4}$$

This formula expands earlier classical models [5]. By isolating k as a direct design factor, it proves mathematically that the actual shape of the stress curve does not depend on the absolute stiffness values of the chosen phases.

3 Results and Discussion

Three FGM pairs were evaluated at $n = 2$: Al_2O_3–Ti ($k = 3.45$), W–Cu ($k = 3.33$), and SiC–Steel ($k = 2.37$), with $R_1 = 10$ mm, $R_2 = 20$ mm (see Fig. 2). Shear stress increases monotonically from inner to outer radius in all cases. Al_2O_3–Tireaches ~ 105 MPa at the outer boundary; SiC–Steel remains lowest, consistent with k values. No discontinuities appear across any profile, confirming FGM structures prevent interface shearing failure (see **Fig. 2**).

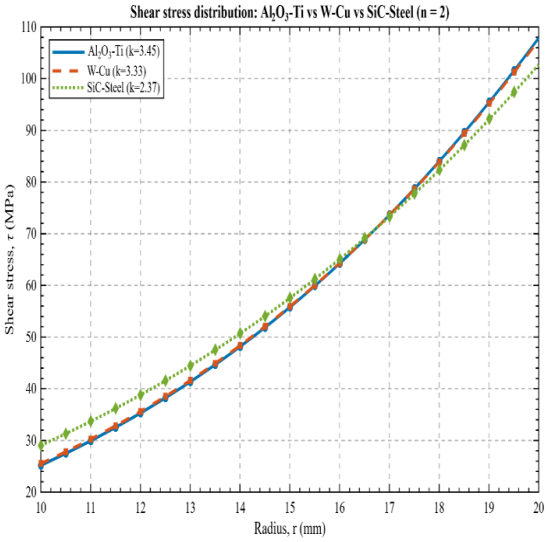


Fig. 2. Shear stress distribution for $Al_2O_3 - Ti$, $W - Cu$, and $SiC - Steel$ FGM pairs at $n = 2$.

Conclusion

This work presents a reliable closed-form equation for the shear stress field in a power-law graded hollow cylinder under pure torsion. We tested the model against three primary FGM candidates proposed for ITER First Wall shields. The analysis shows that the modulus ratio $k = G_c/G_m$ is the key

factor controlling the normalized stress distribution for any selected exponent n.

References

1. Aymar, R., et al.: The ITER design. Plasma Phys. Control. Fusion 44(5), 519–565 (2002).
2. Federici, G., et al.: Plasma-wall interactions in ITER. Nucl. Fusion 41(12R), 1967–2137 (2001).
3. Grüner, D., et al.: Functionally graded tungsten/steel composites. J. Nucl. Mater. 367–370, 1219–1223 (2007).
4. Suresh, S., Mortensen, A.: Fundamentals of Functionally Graded Materials. IOM Communications, London (1998).
5. Akhmedov, N.K., Piriev, S.A., Rustamova, M.A.: Mech. Solids 59(3), 1603–1613 (2024).

https://doi.org./10.58225/mpmma.2026.1002

INVESTIGATION OF NECESSARY OPTIMALITY CONDITIONS IN A NON-SMOOTH BOUNDARY CONTROL PROBLEM FOR GOURSAT-DARBOUX SYSTEMS

Vusala Suleymanova

Sumgait State University, Azerbaijan

Abstract. This paper investigates an optimal control problem for a quasi-linear hyperbolic system of Goursat-Darboux partial differential equations under a non-smooth quality criterion. The distinctive feature of the problem formulation is that the boundary conditions on one of the characteristics are determined by the trajectory of a dynamic system governed by a Cauchy problem for ordinary differential equations, which directly contains the control action. Utilizing needle-like control variations, the formula for the functional increment is derived in terms of directional derivatives. A general constructive first-order necessary optimality condition is established in the form of a variational inequality. It is demonstrated that under smoothness assumptions on the problem parameters, the derived condition reduces to an analogue of the Pontryagin maximum principle.

Keywords: Goursat-Darboux system, non-smooth optimal control, necessary optimality conditions, directional derivative, boundary control, Cauchy problem, variation of functional.

The thesis investigates the problem of minimizing functionality

$$S(u) = \varphi(a(t_1)) + G(z(t_1, x_1)) \tag{1}$$

subject to the constraints

$$u(t) \in U \subset R^r, \quad t \in T = [t_0, t_1], \tag{2}$$

$$z_{tx} = f(t, x, z, z_t, z_x),$$

with the boundary conditions

$$z(t,x_0)=a(t), t\in[t_0,t_1],$$
$$z(t_0,x)=b(x), x\in[x_0,x_1],$$
$$a(t_0)=b(x_0)=a_0. \tag{3}$$

Here, $f(t,x,z,z_x)$ – is a given n-dimensional vector-function, continuous in $D\times R^n\times R^n$ together with its partial derivatives with respect to z and z_x, $b(x)$- is a given absolutely continuous n-dimensional vector-function in $[x_0,x_1]$ n -dimensional vector function, $a(t)$ –absolutely continuous vector function, determined from the Cauchy problem

$$\dot{a} = F(t,a,u), t \in [t_0,t_1],$$

$$a(t_0) = a_0,$$

(4)

by means of choosing an r - dimensional control function $u = u(t)$. Here, $F(t,a,u)$ – is a given n-dimensional vector-function, continuous in $[t_0,t_1] \times R^n \times R^r$ together with its derivative $F_a(t,a,u)$. It is assumed that the control function $u(t)$ is piecewise continuous (with a finite number of points of discontinuity of the first kind) and takes its values from a given non-empty and bounded set U, i.e.,

$$u(t) \in U \subset R^n, \qquad t \in [t_0,t_1].$$

(5)

Such control functions will be called admissible. On the absolutely continuous solutions of the boundary value problem (2)–(3) generated by all possible admissible controls, we define the functional. The problem consists in minimizing the functional (1) subject to constraints (2)–(5).

An admissible control $u(t)$, providing a minimum to the functional (1) under constraints (2)–(5), will be called an optimal control, and the corresponding process $(u(t),a(t),z(t,x))$ – an optimal process.

The increment formula for the functional is established using needle-like variations of the

control. From the expansion of the increment, the following relation is derived:

$$S(\bar{u}(t;\varepsilon))-S(u(t))=\left[\frac{\partial\varphi(a(t_1))}{\partial T(\theta,v)}+\frac{\partial G(z(t_1,x_1))}{\partial Q(\theta,v)}\right]+o(\varepsilon) \quad (6)$$

From this expansion, the validity of the following relation follows:

$$\frac{\partial\varphi(a(t_1))}{\partial T(\theta,v)}+\frac{\partial G(z(t_1,x_1))}{\partial Q(\theta,v)}\geq 0 \quad (7)$$

Theorem. For the optimality of an admissible control $u(t)$ in problem (1)–(5), it is necessary that inequality (7) holds for all $\theta\in[t_0,t_1)$, and $v\in U$.

Inequality (6) is a rather general necessary condition for optimality expressed in terms of directional derivatives. In the case of a smooth quality criterion, an analogue of the Pontryagin maximum principle for the problem under consideration can be obtained from it. The obtained results allow conducting a constructive analysis of optimality in boundary control problems for hyperbolic systems without the preliminary requirement of differentiability of the target functional.

References

1. Egorov A.I. Necessary optimality conditions for systems with distributed parameters // Matematicheskii Sbornik. vol. 69, No. 3, pp. 371-421. (1966),
2. Gasanov K.K. On optimal control in systems with distributed parameters with a functionally perturbed argument // Uchenye Zapiski Az. GU, Ser. Fiz.-Mat. Nauk. No. 1, pp. 28-35. (1972).
2. Mansimov K.B. On a scheme for investigating a singular case in Goursat-Darboux systems // Izv. AN Azerb. SSR. Ser. Fiz.-Tekhn. i Mat. Nauk, No. 2, pp. 100-104.(1981).
3. Melikov T.K. Investigation of singular processes in certain optimal systems / Author's abstract of the dissertation for the degree of Candidate of Physical and Mathematical Sciences. Baku. - 17 p. (1976).
4. Plotnikov V.I., Sumin V.I. Stability problems of non-linear Goursat-Darboux systems // Differents. Uravneniya. No. 5, pp. 845-856.(1972).
5. Mansimov K.B., Mardanov M.J. Qualitative theory of optimal control of Goursat-Darboux systems. Baku: ELM. 363 p. (2013).

6. Suleymanova V.A. On multipoint necessary optimality conditions for singular, in the classical sense, controls in a boundary value problem of control of Goursat-Darboux systems. Journal of Baku Engineering University, mathematics and computer science,volume 3, No. 1, Bakı, pp. 36-48. (2019).

https://doi.org./10.58225/mpmma.2026.1008

ON GENERALIZATION OF MITEV'S INEQUALITIES

Yagub Aliyev[1], Zamina Guliyeva[1], Narmin Aliyeva[2]

[1] ADA University, Azerbaijan

[2] Baku State University, Azerbaijan

Abstract. In the current work we are studying an optimization problem involving symmetric functions. We focus on several means such as, arithmetic mean A_n, harmonic mean H_n, and quadratic mean Q_n. We find maximum and minimum of the ratio of differences $A_n - H_n$ and $Q_n - H_n$. We prove that the maximum of this ratio is $\sqrt{n-1}/\sqrt{n}$ and the minimum is $1/\sqrt{n}$. This result generalizes the earlier results by T. Mitev about cases n=3, n=4 etc. Our approach is based on the idea of reducing the number of variables and solving one variable optimization problem. On the other hand, we need to find multivariable limit at the singular point, where all the variables are equal, and redefinition of a discontinuous function at this removable discontinuity point to be able to use well-known theorem from analysis about the existence of the maximum and the minimum of a continuous function in a compact set. In addition to this, the single variable optimization problem

itself required L'Hôpital type monotonicity lemma. The proved result can also be interpreted in the context of mathematical statistics and probability.

Keywords: Inequality, symmetric polynomials, best constant, approximation.

Introduction

We consider the inequality

$$\frac{\sqrt{\mathrm{n\text{-}1}}}{\sqrt{\mathrm{n}}} \geq \frac{\mathrm{A_n\text{-}H_n}}{\mathrm{Q_n\text{-}H_n}} \geq \frac{1}{\sqrt{\mathrm{n}}} \qquad (1)$$

where A_n is arithmetic mean, H_n is harmonic mean and Q_n is quadratic mean.

Let P_α be the power mean of nonnegative real numbers $x_1, \dots, x_n$:

$$P_\alpha\,(x_1, \dots, x_n) = \left(\frac{\Sigma_{i=1}^{n} x_i^\alpha}{n}\right)^{\frac{1}{\alpha}}$$

except when (i) $\alpha = 0$ or (ii) $\alpha < 0$ and one or more of x_i are zero. If $\alpha = 0$, then we assume that $P_\alpha = G_n$, where $G_n = (\Pi_{i=1}^{n} x_i)^{\frac{1}{n}}$ is the geometric mean of numbers $x_1, \dots, x_n$. If $\alpha < 0$ and there is an i such that $x_i = 0$, then we assume that $P_\alpha = 0$. In particular, if $\alpha = -1, 1, 2$, then we obtain

familiar harmonic, arithmetic, and quadratic means:

$$H_n = \frac{n}{\Sigma_{i=1}^{n} \frac{1}{x_i}}, \quad A_n = \frac{\Sigma_{i=1}^{n} x_i}{n}, \quad Q_n = \sqrt{\frac{\Sigma_{i=1}^{n} x_i^2}{n}}$$

In [1] and [2] the best constants for the inequalities $C_1 \leq \frac{A_n - H_n}{Q_n - H_n} \leq C_2$ are studied for the cases $n = 3, 4, 5$. In [1] and [2] it was shown that if $n = 3$, then $C_1 \leq \frac{\sqrt{3}}{3}$ and $C_2 \geq \frac{\sqrt{6}}{3}$. Similarly, if $n = 4$, then $C_1 \leq \frac{1}{2}$ and $C_2 \geq \frac{\sqrt{3}}{2}$. Finally, if $n = 5$, then $C_1 \leq \frac{\sqrt{5}}{5}$ and $C_2 \geq \frac{2\sqrt{5}}{5}$.

In the current study, we generalize these results by considering all the cases $n \geq 3$ in a unified way. We also study the more general question about the best constants for the inequalities $C_1 \leq \frac{A_n - H_n}{P_\alpha - H_n} \leq C_2$ for all possible values of α. In particular, the following result is obtained.

The following result was used to remove the discontinuity point.

Lemma about a limit

$$\lim_{(x_1,x_2,\ldots,\, x_n)\to(x,\, x,\, \ldots,\, x)} \frac{A_n - H_n}{Q_n - H_n} = \frac{2}{3} \tag{2}$$

3.1 Lemma about optimization

Let $x, y,$ and z be positive real numbers such that, $x+y+z=\beta$ and $\frac{1}{x}+\frac{1}{y}+\frac{1}{z}=\alpha$. Without loss of generality, we can sort the variables in such a way that, $x \leq y \leq z$. The sum $x^2+y^2+z^2$ is decreasing when y is increasing staying between x and z.

The following graph illustrates the intersection of the plane and the surface in lemma 1.2. Here, we took $y = t$ and got the equations $x + z = \beta - t$, $\frac{1}{x}+\frac{1}{z} = \alpha - \frac{1}{t}$. Then we found the coordinates of A, B, C and D using the constraints. We prove that the sum $x^2+y^2+z^2$ is decreasing from D to C.

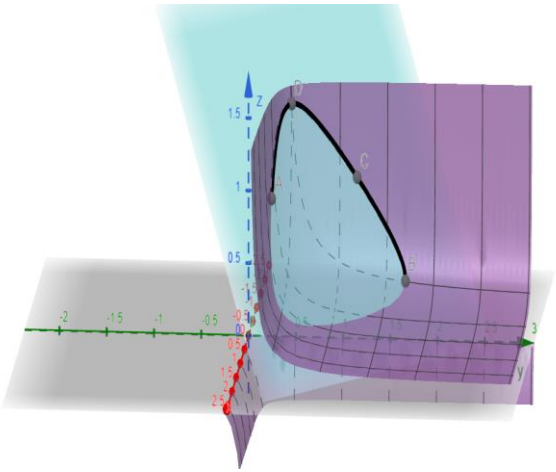


Fig. 3. The graph of the parametric curve (black) representing the intersection of the plane (blue) $x+y+z=\beta$ and surface (purple) $x+y+z=\beta$.

References

1. T.P. Mitev, Some new inequalities among the arithmetic, geometric, harmonic and quadratic means (in Bulgarian), Mathematics and Informatics, Bulgarian Journal of Educational Research and Practice, **59** (2016), no. 6, 626-656.
2. T.P. Mitev, Some Holder approximations among the arithmetic, harmonic and quadratic means (in Bulgarian), Proceedings of University of Ruse, **58** (2019), Book 6.1, 22-28.

3. Aliyev, Y.: The Extremal Values of the Ratio of Differences of Means. Mediterranean Journal of Mathematics, (2025).
4. Lord, N.: More on the Relative Location of Means II. The Mathematical Gazette 85(502), 114–116 (2001).

https://doi.org./10.58225/mpmma.2026.1014

NECESSARY AND SUFFICIENT CONDITIONS FOR STURM-LIOUVILLE PROBLEMS WITH A BOUNDARY CONDITION DEPENDING LINEARLY ON AN EIGENPARAMETER

Yagub Aliyev and Narmin Aliyeva

[1] ADA University, Azerbaijan

[2] Baku State University, Azerbaijan

Abstract. In this paper, a spectral problem known as the Sturm–Liouville equation is considered. The eigenfunctions and associated functions of the problem are determined, and several results concerning the eigenfunctions and associated functions are obtained. The boundary value problem contains the spectral parameter both in the differential equation and in one of the boundary conditions, which leads to a nonselfadjoint spectral problem. The characteristic function of the problem is introduced and the relationship between its zeros and the eigenvalues is studied. Conditions under which the eigenvalues are simple, double, or triple are established. For multiple eigenvalues, the corresponding first- and second-order associated functions are constructed and their defining relations are derived. The structure of the root function

system generated by the eigenfunctions and associated functions is investigated. It is shown that, under appropriate assumptions, this system forms a basis in the space $L_p(0,1)\ (1 < p < +\infty)$, with the exception of certain cases associated with multiple eigenvalues. The obtained results extend known basis properties of Sturm–Liouville operators with eigenparameter-dependent boundary conditions and contribute to the spectral theory of nonselfadjoint differential operators.

Keywords: Sturm–Liouville, associated functions, eigenfunctions.

https://doi.org./10.58225/mpmma.2026.*1016*

ON A LINEAR INVERSE BOUNDARY VALUE PROBLEM FOR THE EQUATION OF FLEXURAL VIBRATIONS OF A ROD

Yashar Mehraliyev, Sevdimaliyev Yusif , Ferecova Sona

Baku State University, Azerbaijan

Abstract. This paper investigates a linear inverse boundary value problem for the equations of flexural vibrations of a rod. The essence of the problem is the need to determine the right-hand side along with its solution. To solve this problem, a transition is made from the original inverse problem to an auxiliary inverse problem. The existence and uniqueness of the solution to the auxiliary problem are proven. A transition is then made to the original inverse problem, resulting in a conclusion regarding the solvability of the original inverse problem.

Keywords: Inverse boundary value problem, classical solution, uniqueness, existence, Fourier method, equation flexural vibration.

IntroductionIn modern technology, it is necessary to regulate vibration processes in one-dimensional distributed systems, and the relevance of these problems is increasing. For shafts, which are the basic

elements of mechanical transmission, dangerous transverse vibrations are not allowed [1]. In aircraft such elements are constructed simultaneously by bending and torsional vibrations. One of the objectives of the project is to prevent shaft vibrations with an adjustable speed [2,3]. For such problems, mathematical models of transverse vibrations of rods are built on the basis of a refined theory [4].

2. Methodology

This paper investigates a linear inverse boundary value problem for the equation of bending oscillations of a rod.

Consider the equation

$$u_{tt}(x,t)+u_{xxxx}(x,t)=a(t)g(x,t)+f(x,t) \quad (1)$$

in the domain $D_T=\{(x,t):0\le x\le 1,\ 0\le t\le T\}$ in the domain of an inverse boundary value problem with initial conditions

$$u(x,0)=\varphi(x),u_t(x,0)=\psi(x) \quad (0\le x\le 1) \quad (2)$$

the boundary conditions

$$u(0,t)=u_x(1,t)=u_{xx}(0,t)=u_{xxx}(1,t)=0 \quad (0\le t\le T) \quad (3)$$

and with the additional conditions

$$u(1,t)=h(t) \quad (0\le t\le T)$$

(4)

where $f(x,t),\ g(x,t),\varphi(x)$, $\psi(x)$, $h(t),$ – given functions, $u(x,t)$ and $a(t)$- desired functions. Denote

$$\tilde{C}^{4,2}(D_T)=\left\{u(x,t):u(x,t)\in C^{2,2}(D_T),u_{xxxx}(x,t)\in C(D_T)\right\}$$

Definition. The classical solution of the inverse boundary value problem (1)-(4) is the pair $\{u(x,t),a(t)\}$ of functions $u(x,t)\in\tilde{C}^{4,2}(D_T)$ and $a(t)\in C[0,T]$ satisfying equation (1) in D_T , condition (2) in $[0,1]$ and conditions (3)-(4) in $[0,T]$.

The following theorem is true.

Theorem 1. Assume that $f(x,t),g(x,t)\in C(D_T),\ \varphi(x),\psi(x)\in C[0,1],$ $h(t)\in C^2[0,T]$ $g(0,t)\neq 0\ (0\le t\le T)$, and the compatibility condition $\varphi(1)=h(0),\ \psi(1)=h'(0)$ holds. Then the problem of finding a classical solution of (1)-(4) is equivalent to the problem of determining the functions $u(x,t)\in\tilde{C}^{4,2}(D_T)$ and $a(t)\in C[0,T]$, satisfying the conditions (1)-(3) and the relation

$$h''(t)+u_{xxxx}(1,t)=a(t)g(1,t)+f(1,t)$$

(5)

After applying the formal scheme of the Fourier method, finding the first component

$u(x,t)$ of any solution $\{u(x,t),a(t)\}$ to problem (1)-(3), (5) reduces to solving the following integro-differential equation:

$$u(x,t)=\sum_{k=1}^{\infty}\left\{\varphi_k\cos\lambda_k^2 t+\frac{1}{\lambda_k^2}\psi_k\sin\lambda_k^2 t+\frac{1}{\lambda_k^2}\int_0^t F_k(\tau;a)\sin\lambda_k^2(t-\tau)d\tau\right\}\sin\lambda_k x. \quad (6)$$

where

$$F_k(t;a)=a(t)g_k(t)+f_k(t),$$

$$f_k(t)=2\int_0^1 f(x,t)\sin\lambda_k x dx,$$

$$g_k(t)=2\int_0^1 g(x,t)\sin\lambda_k x dx,$$

$$\varphi_k=2\int_0^1\varphi(x)\sin\lambda_k x dx \quad \psi_k=2\int_0^1\psi(x)\sin\lambda_k x dx,$$

$$\lambda_k=\frac{\pi}{2}(2k-1)$$

Further, using equation (6), from condition (5) to determine the second component of any solution $\{u(x,t),a(t)\}$ of problem (1)-(3), (5) we obtain the following nonlinear integral equation:

$$a(t)=[g(1,t)]^{-1}\left\{h''(t)-f(1,t)+\right.$$

$$\left.+\sum_{k=1}^{\infty}\lambda_k^4\left[\varphi_k\cos\lambda_k^2 t+\frac{1}{\lambda_k^2}\psi_k\sin\lambda_k^2 t+\frac{1}{\lambda_k^2}\int_0^t F_k(\tau;a)\sin\lambda_k^2(t-\tau)d\tau\right]\right\} \quad (7)$$

Thus, the solution of problem (1)-(3), (5) was reduced to the solution of system (6),(7),

with respect to the unknown functions $u(x,t)$ and $a(t)$.

The following theorem can be proven:

Theorem 2. Assume that the data of problem (1)-(3), (5) satisfy the following conditions:

1. $\varphi(x) \in C^4[0,1]$, $\varphi^{(5)}(x) \in L_2(0,1)$, $\varphi(0) = \varphi'(1) = \varphi''(0) = \varphi'''(1) = \varphi^{(4)}(0) = 0$;

2. $\psi(x) \in C^2[0,1]$ $\psi'''(x) \in L_2(0,1)$, $\psi(0) = \psi'(1) = \psi''(0) = 0$;

3. $f(x,t)$, $f_x(x,t)$, $f_{xx}(x.t) \in L(D_T)$, $f_{xxx}(x,t) \in L_2(D_T)$, $f(0,t) = f_x(1,t) = f_{xx}(0,t) = 0 \quad (0 \le t \le T)$;

4. $g(x,t), g_x(x,t), g_{xx}(x,t) \in C(D_T)$, $g_{xxx}(x,t) \in L_2(D_T)$ $g(0,t) = g_x(1,t) = g_{xx}(0,t) = 0$, $g(1,t) \ne 0$ $(0 \le t \le T)$;

5. $h(t) \in C^2[0,T]$

Then problem (1)-(3), (5) has a unique solution, and $u(x,t) \in \tilde{C}^{4,2}(D_T)$, $a(t) \in C[0,T]$,

By virtue of Theorem 1, the unique solvability of problem (1)-(4) immediately follows from Theorem 2.

Theorem 3. Let all conditions of Theorem 2 be satisfied, $\varphi(1) = h(0)$, $\psi(1) = h'(0)$.

Then problem (1)-(4) has a unique classical solution, and $u(x,t) \in \tilde{C}^{4,2}(D_T)$, $a(t) \in C[0,T]$,

References

1. Bolotin V.V. Nonlinear oscillations of shafts beyond critical rotation speeds. Collection of Problems of Strength in Mechanical Engineering. Issue 1, Publishing House of the USSR Academy of Sciences, 1958.
2. Robertson D, Hysteretic influences on the whirling of the rotors, Proc. Inst. Mech. Eng. 131(1935)
3. Kapitsa P.L. Stability and transitions through critical speeds of rapidly rotating rotors in the presence of friction, Zhurn. tech. phys. 9, No. 2 (1939)
4.Erofeev V.I., Kazhaev V.V., Semerikov N.P.Waves in rods. Dispersion. Dissipation. Nonlinearity-M.: Fizmatlit, 2002.-208s.

https://doi.org./10.58225/mpmma.2026.*1022*

NUMERICAL METHOD FOR ANALYZING FLUID FLOW IN INTERCONNECTED PIPELINE NETWORKS

Yegana Ashrafova
Baku State University, Institute of Mathematics, Azerbaijan

Abstract. This paper presents numerical method for analyzing transient fluid flow processes in interconnected pipeline networks with complex topological structures. The mathematical model is formulated as a system of hyperbolic partial differential equations describing the unsteady flow of a compressible fluid in individual pipeline segments. Particular attention is devoted to the treatment of coupling conditions at network junctions, where the flow variables satisfy conservation laws derived from Kirchhoff-type principles. An implicit finite-difference scheme is developed for the numerical solution of the governing equations. To efficiently solve the resulting algebraic systems, a generalized sweep algorithm is constructed for interconnected pipeline sections. Computational experiments performed on pipeline networks with multiple branches and loops demonstrate the accuracy,

stability, and computational efficiency of the proposed approach. The obtained results confirm the applicability of the developed numerical methods for the simulation and analysis of transient hydraulic regimes in large-scale pipeline networks and provide a useful tool for improving the operational reliability of fluid transport systems.

Keywords: pipeline network, transient flow, hyperbolic equations, grid method, sweep method, numerical simulation.

Mathematical Model

Consider a pipeline network consisting of several linear sections connected at nodes. The unsteady motion of fluid in each section is described by a system of hyperbolic partial differential equations representing conservation of mass and momentum. For clarity and simplicity in presenting the numerical schemes, let us consider an oil pipeline consisting of five sections, the structure of which is shown in Fig. 1. The arrows in the figure formally indicate the assumed (not necessarily actual) direction of crude oil flow.

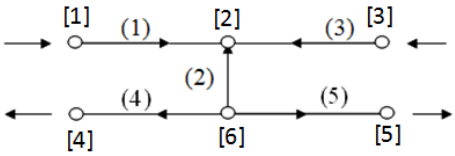


Fig. 4. Scheme of the oil pipeline with five sections

The numbers in square brackets correspond to the numbers of the vertices (nodes), while the numbers in parentheses denote the section numbers; the set of these sections will be denoted by K.

The linearized system of differential equations describing the unsteady isothermal laminar flow of a liquid with constant density ρ in the k-th linear section of an oil pipeline of length l_k and diameter d_k can be written in the following form [1]:

$$\begin{cases} -\dfrac{\partial P^k(x,t)}{\partial x} = \dfrac{\rho}{S_k}\dfrac{\partial Q^k(x,t)}{\partial t} + 2a_k\dfrac{\rho}{S_k}Q^k(x,t), \\ -\dfrac{\partial P^k(x,t)}{\partial t} = c^2\dfrac{\rho}{S_k}\dfrac{\partial Q^k(x,t)}{\partial x}, x \in (0,l_k), t \in (0,T], k \in K = \{1,...,5\}, \end{cases}$$

(1)

where $P^k(x,t)$ and $Q^k(x,t)$ are respectively the pressure and the flow rate of the fluid at time t at point $x \in (0,l_k)$ of the k-th pipeline section; c is the speed of sound in the medium; and S_k – is the cross-sectional area of the pipeline section.

Assume that the kinematic viscosity coefficient γ does not depend on pressure; then the corresponding condition $2a = \frac{32\gamma}{d^2} = const$ is sufficiently accurate for the laminar flow regime.

At the four ends of the oil pipeline—nodes [1], [3], [4], and [5]—there are pumping stations that ensure the required pumping regime:

$$P^1(0,t) = u_1(t),\ P^3(0,t) = u_3(t),$$
$$P^4(l_4,t) = u_4(t),\quad P^5(l_5,t) = u_5(t). \quad (2)$$

Similarly, four conditions can also be specified, for example, for the flow rates of the crude oil,

$$Q^1(0,t) = u_1(t),\ Q^3(0,t) = u_3(t),$$
$$Q^4(l_4,t) = u_4(t),\quad Q^5(l_5,t) = u_5(t),$$

or mixed boundary conditions involving both flow rate and pressure can be imposed.

At the connection nodes of the network [2] and [6], boundary conditions are derived from Kirchhoff's conservation law, which requires that the algebraic sum of flows entering a node must be equal to zero.

$$Q^1(l_1,t) + Q^2(l_2,t) + Q^3(l_3,t) = 0,\quad t \in [0,T], \quad (3)$$

$$Q^2(0,t) + Q^4(0,t) + Q^5(0,t) = 0,\quad t \in [0,T], \quad (4)$$

Additionally, pressure continuity conditions are imposed at the same nodes.

$$P^1(l_1,t) = P^2(l_2,t) = P^3(l_3,t), \tag{5}$$

$$P^2(0,t) = P^4(0,t) = P^5(0,t). \tag{6}$$

Initial conditions specify the distribution of pressure and flow along each pipeline section at $t = 0$ the starting time of the simulation:

$$Q^k(x,0) = Q_0^k(x),\ P^k(x,0) = P_0^k(x),\ \ x \in [0, l_k],\ k \in K,$$

The functions $Q_0^k(x), P_0^k(x),\ k \in K$ are assumed to be given. We will assume that the functions defining the initial state of the process and the boundary conditions satisfy all the conditions required for the existence and uniqueness of the solution of the corresponding boundary value problem.

For the numerical solution of the formulated boundary value problem with non-separated boundary conditions of the form (3) – (6) an approach based on the application of the grid method is proposed and investigated below. For this approach, the corresponding formulas are derived and algorithms are developed based on the scheme analogous to the method of transferring boundary conditions proposed in [2]. Numerical

experiments are carried out, and an analysis of the obtained results is presented.

Conclusion

The obtained results show that the proposed numerical method provides an effective tool for analyzing transient processes in complex pipeline networks. The use of an implicit grid scheme ensures numerical stability even for relatively large time steps. Another advantage of the method is the possibility of extending it to networks with arbitrary topology. By appropriately defining the node connectivity and boundary conditions, the same computational framework can be applied to large-scale pipeline systems.

The algorithm can also be integrated with monitoring and control systems used in modern pipeline operations. Such integration would allow real-time prediction of hydraulic regimes and early detection of potentially dangerous conditions.

References

1. I.A. Charny *Unsteady Motion of Real Fluid in Pipes*. Moscow: Nedra, 199 p. (1975).

2. A.A. Samarskii, A.V. Gulin. *Numerical Methods*. Moscow: Nauka, 428 p. (1989).K. R. Aida-zade and Ashrafova E. R. Localization of the points of leakage in an oil main pipeline under non-stationary conditions. //Journal of Engineering Physics and Thermophysics, Vol. 85, No. 5, pp. 1148-1156 (2012)
3. Xiao, Jz., Kong, Wc., Wang, Xl. *et al.* Numerical modeling and assessment of natural gas pipeline separation in China: the data from Henan Province. *Pet. Sci.* **17**, 268–278 (2020). https://doi.org/10.1007/s12182-019-00400-5
4. Guo, W.; Wang, B.; Zhao, L. A Visual Software Implementation of Numerical Simulation for Transient Process of Pipeline Network System of Water Supply Project. Energies , 14, 4606. (2021). https://doi.org/10.3390/en14154606
5. S.M. Ahmadi, M.N. Behbahani, Y. Shekari, Transient modeling of natural gas in pipeline networks by two non-iterative explicit and implicit finite volume methods, Applied Mathematics and Computation, Vol. 478, (2024). https://doi.org/10.1016/j.amc.2024.128793

https://doi.org./10.58225/mpmma.2026.1029

NUMERICAL VALIDATION OF THERMAL PERFORMANCE IN A DOUBLE-PIPE HEAT EXCHANGER

Yusuf Oflaz, Yusuf Ogunc and Ahmet Selim Dalkili

Yildiz Technical University , Türkiye

Abstract. This study investigates the thermal-hydraulic properties of a 0.45 m counter-flow double-pipe heat exchanger under turbulent flow using theoretical correlations and Computational Fluid Dynamics (CFD) simulations. Hot water (0.125 kg/s, 355 K) flows through the inner tube, and cold water (0.215 kg/s, 305 K) flows through the annulus. Following the theoretical analyses, the correlations of Petukhov-Kirillov and Gnielinski were used for the inner and annulus sides, respectively, to calculate the system's heat transfer coefficients and outlet temperatures considering the Ɛ-NTU method. The results obtained were compared with data from CFD analyses carried out via commercial software. Finally, the theoretical calculations give an estimate of the deviation of 0.13% for the cold-water outlet temperature of 308 K with respect to the CFD results (308.4 K). Similarly, a deviation of 0.69% was found in the theoretical calculation of the hot water

outlet temperature of 350 K with respect to the numerical result (352.4 K). The deviation rates indicate that the selected empirical correlations yield applicable and reliable results under the given boundary conditions and confirm that the developed model works properly.
Keywords: Heat Transfer, Heat Exchanger, Ɛ-NTU, CFD, Validation

Introduction

The double pipe heat exchanger (DPHE) is one of the most important heat exchanger in many industries due to its simplicity and versatility. It works by heat transfer through two pipes, which enhances the thermal efficiency of countercurrent flow arrangements. Recently there has been an interest in improving the efficiency of such heat exchangers to reduce energy consumption and environmental impact [1, 2]. Computational Fluid Dynamics (CFD) simulations are a common tool for optimizing performance, but it is necessary to validate the numerical models with the analytical correlations that have already been established. The Petukhov and Kirillov correlations [3] for turbulent internal flows and the Gnielinski correlation [4] for annular

sections are important references that guarantee accuracy [5]. The aim of this work is to show the concordance between the theoretical and CFD methods in predicting the outlet temperatures of a turbulent flow counter-flow heat exchanger which was used as a reference and modelled in the ANSYS environment [6].

Theoretical Correlations and Numerical Modelling

To verify the accuracy of the outlet temperatures of the system under consideration, a scenario was considered in which the outlet temperatures of both fluids were unknown. Accordingly, the system was solved using the Ɛ-NTU method, and the Ɛ value was obtained from Ɛ-NTU diagrams accepted in the literature and developed for counterflow and double-pipe systems [7]. To calculate the convective heat transfer coefficients (h) by Nusselt (Nu) numbers, the Petukhov-Kirillov (Nu_P) [3] and Gnielinski (Nu_G) correlations [4] were used for water flowing in the inner and annulus sides, respectively.

$\varepsilon = \frac{Q}{Q_{MAX}}$ $Q = C_1(T_{1i} - T_{1o})$

$= C_2(T_{2o} - T_{2i})$ $C_1 = \dot{m}_1 c_{p1}$

$C_2 = \dot{m}_2 c_{p2}$

$Q_{max} = C_{min}(T_{1i} - T_{2i})$

$\varepsilon = \frac{C_1(T_{1i} - T_{1o})}{C_{min}(T_{1i} - T_{2i})}$

$NTU = \frac{UA}{C_{min}}$

$$Nu_P = \frac{(\frac{fp}{8})\, RePr}{1.07 + \frac{900}{Re} - \frac{0.63}{1+10Pr} + 1.27(\frac{fp}{8})^{1/2}(Pr^{3/2} - 1)}$$

$f_P =$

$(0.79 ln Re - 1.64)^{-2}$

$$Nu_G = \frac{\left(\frac{f_{ann}}{8}\right) RePr}{k_1 + 1.27\left(\frac{f_{ann}}{8}\right)^{\frac{1}{2}}\left(Pr^{\frac{3}{2}} - 1\right)} \left[1 + \left(\frac{Dh}{L}\right)^{\frac{2}{3}}\right] F_{ann}\ K$$

$k_1 = 1.07 + \frac{900}{Re} - \frac{0.63}{(1+10Pr)}$

$\frac{1}{U} = \frac{1}{h_P} + \frac{1}{h_G}$

$Nu = \frac{hD_h}{k}$

$K = (\frac{Pr}{Pr_{wall}})^{0.11}$

where the other related correlations are shown below:

$f_{ann} = (1.8 * log_{10}^{Re*} - 1.5)^{-2}$,

$R_e* = Re \frac{(1+a^2)ln(a) + (1-a^2)}{(1-a^2)ln(a)}$,

$a = Di / D_o$,

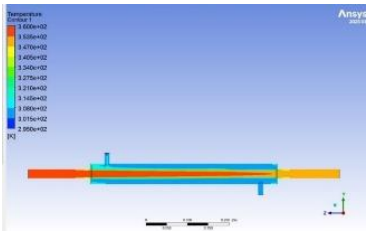
$F_{ann} = (0.9 - 0.15a^{0.6})$

The inlet temperatures used in the reference system's boundary conditions were maintained in the ANSYS CFD simulation. The system was meshed using the mesh independence method with 0.9 million, 2.2 million, and finally 4,053,359 mesh elements, respectively. Based on ANSYS criteria, the 4-million element mesh achieved excellent skewness (0.20) and very satisfactory orthogonality (0.80). The CFD method was applied within these parameters.

Results and Discussion

Theoretical analyses indicate Reynolds numbers of Re = 19,716.36 (NuP = 142.063) for fluid inside the pipe, and Re = 27,296.58 (NuG = 234.984) for the fluid in the annular cross-section, confirming turbulent flow. Temperature variations under specified boundary conditions are depicted accompanying in Figure 1 and Figure 2. Theoretical calculations forecast hot and cold-water outlet temperatures of 350 K and 308 K, respectively, while a 4-million-element ANSYS simulation produced 352.4 K and 308.4 K, resulting in discrepancies of only 0.13% for cold and 0.69% for hot water

outlet temperatures, showcasing the reliability of the ANSYS CFD calculation.



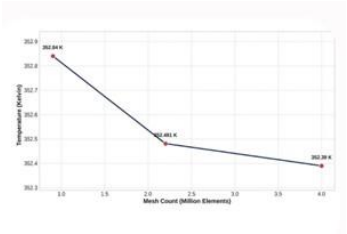


Fig. 1. Change in temperature Based on mesh count.

Fig. 2. Temperature distribution in the investigated heat exchanger

obtained by the ANSYS simulation.

Conclusion

A tetrahedral mesh was generated with parameters that can be considered "very good" and "excellent", according to ANSYS, and the mesh resolution reached four million mesh cells. In the validation process, the comparison between theoretical and numerical analyses showed that the differences in cold and hot water outlet

temperatures were very low and the simulation was reliable. For future studies, it is recommended to maintain these low deviations when investigating ways to improve heat transfer and efficiency at the same level of accuracy by adding dimples or fins to the tubes of the same length.

References

1. Grand View Research, https://www.grandviewresearch.com/industry-analysis/heat-exchangers-market, last accessed 2026/05/20.

2. Ali, M.A., Shebab, S.N.: Numerical Analysis of Heat Convection Through a Double-Pipe Heat Exchanger: Dimpled Influence. Journal of Engineering Research 11, 100016 (2023).
3. Petukhov, B.S., Kirillov, V.V.: On heat exchange at turbulent flow of liquid in pipes. Teploenergetika 4(4), 63–68 (1958).
4. Gnielinski, V.: Heat transfer coefficients for turbulent flow in concentric annular ducts. Heat Transfer Engineering 30(6), 431–436 (2009).

5. Haw, W., Oan, C.S., Lau, E.V.: Thermal-Hydraulic and Hydrodynamic Analysis of Twisted Fins in a Double-Pipe Heat

Exchanger. Results in Engineering 26, 104642 (2025).

6. Mohan, A., Ganesh, P.S., Ramesh, S., Sathish, M.: CFD Analysis of Double-Pipe Heat Exchanger With and Without Dimples. [International Research Journal of Engineering and Technology (IRJET)] 5(10), 2395-0056 (2018).
7. Nguyen, D.K., San, J.Y.: Heat transfer and exergy analysis of a spiral heat exchanger. Heat Transfer Engineering 37(12), 1013–1026 (2016).

https://doi.org./10.58225/mpmma.2026.1037

ASSESSMENT OF THE SPATIOTEMPORAL DYNAMICS OF SOIL SALINIZATION BASED ON SPECTRAL DATA

Zakir Zabidov [1], Aydin Shukurov [1] M.Kh. Kuliev[2]

[1] Institute of Mathematics, Azerbaijan

[2] Odlar Yurdu University, Azerbaijan

Abstract. The primary objective of this study is to assess the spatiotemporal variability and dynamics of soil salinization using multispectral remote sensing data and spectral index analysis. The study area, the Kura–Araks lowland, represents one of the most vulnerable regions to salinization processes due to its arid climate, high evaporation intensity, shallow groundwater table, and extensive irrigation practices that often contribute to secondary salinization. These environmental and anthropogenic factors make the region an ideal case for investigating salinity dynamics.

Keywords: soil salinization, remote sensing, spectral indices, NDVI, NDSI, COSRI, spatiotemporal analysis, land degradation monitoring.

1. Introduction

Soil salinization is recognized as one of the most extensive and environmentally

detrimental forms of land degradation, posing a serious threat to sustainable agricultural development, soil health, and ecosystem resilience on a global scale. The excessive accumulation of soluble salts in the soil profile adversely affects plant physiological processes by disrupting nutrient uptake, and deteriorating soil structure. As a consequence, salinization leads to significant declines in crop productivity, land usability, and ecological stability, particularly in arid and semi-arid regions where evapotranspiration rates exceed precipitation.

Traditional methods for assessing soil salinity are predominantly based on field surveys, soil sampling, and laboratory-based physicochemical analyses, such as electrical conductivity (EC) measurements. Although these approaches provide high accuracy at specific locations, they are often constrained by their labor-intensive nature, high cost, and limited spatial and temporal coverage. These limitations hinder their applicability for continuous monitoring and large-scale assessments, especially in regions characterized by heterogeneous landscapes and rapidly evolving degradation processes.

In this context, remote sensing technologies have emerged as an effective

and efficient alternative for monitoring soil salinity and associated environmental changes. The integration of multispectral satellite imagery with geospatial analysis techniques allows for the indirect estimation of soil salinity through the interpretation of surface reflectance patterns and vegetation responses. Spectral indices derived from different wavelength bands provide valuable proxies for detecting salinity-induced stress in vegetation and bare soil conditions, enabling comprehensive spatiotemporal analysis.

2. Methodology

For the analysis, Sentinel-2 satellite imagery covering the period from 2018 to 2025 was utilized. Sentinel-2 provides high-resolution multispectral data across several bands, including Blue, Green , Red , Near-Infrared , and Shortwave Infrared , which are particularly sensitive to variations in soil moisture, salinity levels, and vegetation condition. Based on these spectral bands, several widely used indices were computed, including the Normalized Difference Vegetation Index (NDVI), which reflects vegetation vigor and biomass; the Normalized Difference Salinity Index (NDSI), which is sensitive to salt-affected

soils; and the Combined Optical Salinity Response Index (COSRI), which integrates multiple spectral responses to improve salinity detection accuracy.

The analysis was conducted for 17 georeferenced sampling sites distributed across the study area. These sites were previously investigated through detailed field studies carried out by the Institute of Soil Science and Agrochemistry of the Azerbaijan National Academy of Sciences, providing essential ground-truth data for validation and calibration of remote sensing results. The combination of satellite-derived indices and in situ observations enabled a more robust assessment of salinity patterns and their temporal evolution.

The results demonstrated substantial spatial heterogeneity and temporal fluctuations in the calculated spectral indices, indicating dynamic changes in both vegetation cover and soil salinity levels over the study period. Areas exhibiting low NDVI values in conjunction with high NDSI and COSRI values were identified as zones of increased salinity stress. Temporal analysis further revealed trends associated with seasonal variations, irrigation practices, and climatic factors influencing salinity accumulation and redistribution.

Three observation points (6, 16, and 17) were selected for detailed analysis within the study. These points were characterized by different dynamics of the NDVI, NDSI, and COSRI spectral indices over time. The different dynamics of the spectral indices are presented graphically in the following images.

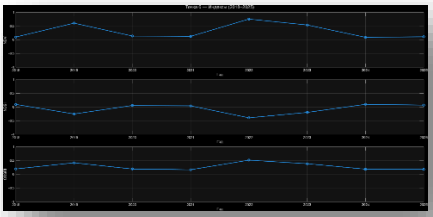


Figure 1. Change in spectral indices (NDVI, NDSI, COSRI) for the 6th study point over the period 2018–2025.

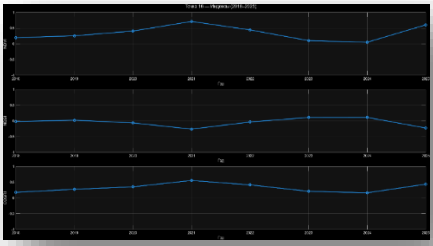


Figure 2. Change in spectral indices (NDVI, NDSI, COSRI) for the 16th study point over the period 2018–2025.

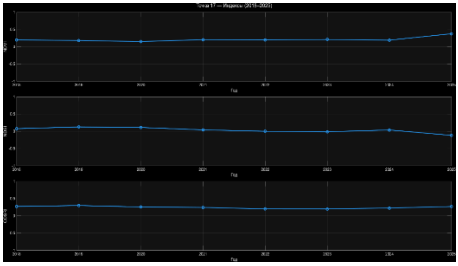


Figure 3. Change in spectral indices (NDVI, NDSI, COSRI) for the 17th study point over the period 2018–2025.

Conclusion

Overall, the findings confirm that remote sensing-based spectral analysis is a reliable and cost-effective approach for large-scale monitoring of soil salinization. The integration of multispectral data with ground-based measurements enhances the accuracy of salinity assessment and provides valuable insights for land management, agricultural planning, and environmental protection strategies

Acknowledgment. This research was supported by the Azerbaijan Science Foundation (Grant No. AEF-MGC-2025-1(54)-20/02/1-M-02).

References

1. Guidelines for the Management of Salt-Affected Soils: Implementation Plan of

the Eurasian Soil Partnership. Published by Food and Agriculture Organization of the United Nations and Lomonosov Moscow State University, Rome, 153 p. (2017).

2. Konyushkova, M. V. Mapping of Soil Cover and Soil Salinity of the Solonetz Complex Based on Digital Analysis of Satellite Imagery (Case Study of the Dzhanybek Research Station Area). PhD Dissertation, Moscow, 155 p. (2010).

3. Babayev M., Orucova N., Mustafayev M., et al. Restoration of Fertility of Soils Affected by Floodwaters. Baku, 118 p. (2013).

4. John P. Snyder Map Projections: A Working Manual. Washington, D.C.: United States Geological Survey, 383 p. (1987).

5. Remote Sensing of Soil Salinization: Impact on Land Management Metternicht, G., Zinck, J. A. Remote Sensing of Soil Salinization: Impact on Land Management. Boca Raton: CRC Press, 308 p. (2003).

https://doi.org./10.58225/mpmma.2026.*1044*

SOIL SALINITY CLASSIFICATION BASED ON MULTISPECTRAL IMAGERY

Zakir Zabidov , Khayala Gadirova
Institute of Mathematics, Azerbaijan

Abstract. Soil salinity is a major factor significantly affecting agricultural productivity. Modern remote sensing technologies are widely used to assess soil properties. In particular, multispectral images reflect the physicochemical properties of the soil surface at different wavelengths. This paper analyzes an algorithm developed for assessing soil salinity using multispectral imagery. The algorithm divides land plots into three main salinity classes based on data obtained from the visible and near-infrared (IR) spectral ranges: highly saline, moderately saline, and slightly or non-saline areas. Sentinel-2 satellite data are used for the analysis. The proposed method provides a simple classification approach based on spectral thresholds and also explores methods for addressing identification issues that arise when applying this classification approach.

Keywords: Brightness; Spectral image; Soil salinity; Monitoring

References

1. Guidelines for the Management of Salt-Affected Soils: Implementation Plan of the Eurasian Soil Partnership. Published by Food and Agriculture Organization of the United Nations and Lomonosov Moscow State University, Rome, 153 p. (2017).

2. Konyushkova, M. V. Mapping of Soil Cover and Soil Salinity of the Solonetz Complex Based on Digital Analysis of Satellite Imagery (Case Study of the Dzhanybek Research Station Area). PhD Dissertation, Moscow, 155 p. (2010).

3. Karavanova, E.I. Optical Properties of Soils and Their Nature. Moscow, 153 p. (2003).

https://doi.org./10.58225/mpmma.2026.*1046*

THE NUMERICAL MODELING OF NONLINEAR WAVE PROCESSES IN TWO-PHASE SYSTEMS

Musraddin Tağıyev[1], *Reshad Tağıyev*[2]

[1]Baku State University , Azerbaijan.

[2]Azerbaijan State Oil and Industry University, Azerbaijan.

Abstract. The nonlinear evolution equation describing the processes of nonlinear waves Propagation in two-phase continuums is derived. At that passing on to moving coordinates with scalable time and spaces the wave evolution from perturbation source is investigated. At the first approximation it is obtained the dispersion equation for the velocity of stationary travelling linear waves, at the second approximation the nonlinear evolution equation whose measure of nonlinearity effects strongly depends on rate of wave dispersion, energy dissipation, rheology of solid particles and forces of interfacial interaction.

Keywords: liquid phase, solid phase, medium, viscosity, wave, perturbation, non-linear equation, dispersion relation, evolution equation.

İntroduction

In the papers [1-2] the theoretical study of nonlinear wave propagation within the bounds of models of two-phase continuum at small portion of volume of dispersed phase has been led. At that in each phase the durability effects are absent and therefore one of phases is present in the form of separate monodisperse inclusions (as solid particles, bubbles, resins), whose immediate interaction that is neglected. The viscous fluid model describes the carrier phase and the forces of viscous resistance are led only to the effective force [3-5]. The system of the equations describing this process is completed by the thermodynamic equations constituting the phases [3;4].

In the model of two-phase continuum the both phases have been considered in [4-5] as two interpenetrating compressible media that mechanically interact. At the small Reynolds numbers averaged by the range of motion equation the Reynolds stresses are neglected as against the remain der terms/ The solid phases are composed of viscoelastic particles resulting of some smaller particles having inertia force and viscoelastic ity property. Depending on concentration and strength of solid phase there may exist a lot of intermediate states of two-phase continuum

(media), in particular, two limit forms: the first one is the motion of the single solid particle [5], the second one is that the solid particles form the closely packed (durable) matrix [3].

2.Methodology.

The mathematically posed problem for one-dimensional and isothermic case is led to the solution of the mass and momentum conservation equation [3].

$$\frac{\partial(\alpha_i\rho_i)}{\partial t}+\frac{\partial(\alpha_i\rho_i\vartheta_i)}{\partial x}=0,\qquad \alpha_1+\alpha_2=1,\quad i=\overline{1,2}$$

(1)

$$\frac{\partial(\alpha_i\rho_i\vartheta_i)}{\partial t}+\frac{\partial(\alpha_i\rho_i\vartheta_i\vartheta_i)}{\partial x}=\delta_{1i}\frac{\partial\sigma}{\partial x}+\alpha_i\frac{\partial P}{\partial x}-(-1)^i R_{12}.$$

(2)

We take the connection between stress and deformation of solid phase in the form

$$\left(b_0+\sum_{l=1}^{m}b_l\frac{D^l}{Dt^l}\right)(\sigma+\gamma P)=\left(a_0+\sum_{l=1}^{n}a_l\frac{D^l}{Dt^l}\right)e_1.$$

(3)

The system of equations (1)-(3) is completed by the thermodynamic equation of phase states

$$\rho_1=\rho_1(\sigma,P),$$

$$\rho_2=\rho_2(P).$$

(4)

The parameters of solid and fluid phases are denoted here by indices 1 and 2, respectively. We can give the force of interfacial resistance in the form [3].

$$R_{12} = (\vartheta_2 - \vartheta_1) f\left(\left|\vec{\vartheta}_2 - \vec{\vartheta}_1\right|\right) = K_v(\vartheta_2 - \vartheta_1) + K_v b(\vartheta_2 - \vartheta_1)\left|\vec{\vartheta}_2 - \vec{\vartheta}_1\right|. \quad (5)$$

The domains of correctness of law (5) and linear connection $(when\, b = 0)$ are defined by the Reynolds inner number

$$\mathrm{Re} = ul\rho_2 / \nu = (\rho_2 / \nu)\left|\vec{\vartheta}_2 - \vec{\vartheta}_1\right|\sqrt{k/\alpha_2}$$

and its critical value Re_{kr} after that the linear connection get broken, where ν is the dynamic fluid viscosity, k is a permeability coefficient of the porous medium.

The equations (1)-(4) are completed by the following kinematic relation

$$\frac{\partial e_1}{\partial t} + \frac{\partial e_1 \vartheta_1}{\partial x} = \frac{\partial \vartheta_1}{\partial x}.$$

Using the length and time rescaling [1]

$$X = \eta x,\ \tau = t - c^{-1}x, \quad (6)$$

By using the length and time scaling given in expression (6), the transition to new variables is carried out, and the desired solution is sought in the form of a series with respect to a small parameter. In the first approximation, the following dispersion relation for the velocity of linear stationary waves is obtained:

$$\alpha_1^{(0)}\rho_1^{(0)}b_0\left[\alpha_1^{(0)}\rho_2^{(0)}(L_1-D_1\gamma)+\rho_1^{(0)}\alpha_2^{(0)}B_1\right]c^4+$$
$$+\left[\alpha_1^{(0)}\rho_2^{(0)}(\alpha_1^{(0)}a_0D_1-a_0L_1+\alpha_1^{(0)}\rho_1^{(0)}b_0-\gamma\rho_1^{(0)}b_0)+\right.$$
$$\left.+\alpha_2^{(0)}\rho_1^{(0)}(\alpha_1^{(0)}\rho_1^{(0)}b_0-a_0B_1)\right]c^2-\alpha_2^{(0)}\rho_1^{(0)}a_0=0. \quad (7)$$

Equation (7) characterizes two roots corresponding to longitudinal wave propagation in the solid and fluid phases. In the second approximation, the nonlinear evolution equation is obtained:

$$X=\eta x,\ \vartheta=-\eta R_1\vartheta_1^{(1)},\ T=c^{-1}x-t,$$

we obtain the following non-linear evolution equation:

$$\frac{\partial\vartheta}{\partial x}+\vartheta\frac{\partial\vartheta}{\partial T}-R_2\vartheta\left(1+\frac{b}{|R_1|}\left|1-\frac{\alpha_1^{(0)}\rho_1^{(0)}-a_0/(b_0c^2)}{\rho_1^{(0)}(\alpha_1^{(0)}-\gamma)}\right|\frac{\vec{\vartheta}}{|\vartheta|}\right)+$$
$$+R_3\sum_{l=1}^{n}(-1)^{l+1}A_{l+1}\frac{\partial^{l+1}\vartheta}{\partial T^{l+1}}=0 \quad (8)$$

where

$$A_{l+1}=\Gamma_{m-l}\frac{a_0b_l}{b_0}-\Gamma_{n=l}a_l,\ \Gamma_{n-l}=1,\ n\geq l,\ \Gamma_{n-l}=0,\ n<l$$

.

The nonlinear equation (8) describes the propagation process of nonlinear waves in two-phase continuums and at $K_\nu=0$ is simplified and gets the form [6].

Conclusion: On the basis of the suggested model there are discovered new effects holding at analysis and regulation of development of oil-and-gas deposits as well as for forecasting consequences of accepted technological measures on influence upon stratum and stimulation of oil production. The results obtained in the paper allow to study seismic fields of deposits at wave transmission from focal zones.

References

1. Ramazanov T. K. *Nonlinear waves in two-phase systems.* Intern.sci/ journ., Applied Mechanics, Kiev, 1995, v.31, №9, pp.38-45. (Russian).
2. Ramazanov T. K. *Nonlinear waves in suspension with antisymmetric stresses. 15th* IMACS, Berlin, august, 1997, v.3. Computational physics, Chemistryand Biolog, pp.387-390.
3. Nikolaevskii V. N. *Geomechanics and fluid dynamics.* M.: «Nedra», 1996, 448p. (Russian)
4. Grishin A. M., Fomin V. M. *adjoint and nonstationaey problems of mechanics of agents.* Novosibirsk , «Nauka», Sibir depart., 1984, 318p. (Russian)
5. Immich H. *Impulsive motion of a suspension: effect of antisymmetric*

stresses and particle rotation. Int. J. Multiphase Flow, 1980, v.6, pp.441-471.

6. Nikolaevskii V. N. *Nonlinear waves in grounds and fractured rocks. Physical technical problems of development of mineral wealths.* 1988, №6, pp.31-38. (Russian)

https://doi.org./10.58225/mpmma.2026.*1053*

STRESS-STRAIN STATE OF DOMAINS WITH PARTIAL CRACKS UNDER EXTERNAL LOADING

Etimad Eyvazov
AzUAC, Azerbaijan

Abstract. When designing engineering problems, designers often encounter various defects in structures, including cracks, which in turn lead to the failure of machinery and equipment. This paper examines the uniaxial stress state of an infinite sheet weakened by holes with linear cracks. Since conformal mapping functions for such complex domains with linear cracks were unknown, this problem has not been considered in previous studies due to the lack of conformal mapping functions for complex domains. In the presented article, a plane problem of elasticity theory with a complex geometric configuration weakened by two elliptical holes with straight cuts was solved using the theory of functions of a complex variable and applying comfortable mapping functions.

Keywords: analytical functions, elliptical holes, intensity factor, conformal mapping functions, stress components

https://doi.org./10.58225/mpmma.2026.1054

NONLOCAL NAVIER—STOKES EQUATIONS AND THEIR APPLICATIONS

Veli Shakhmurov[1] *, Rishad Shahmurov*[2]

[1]Antalya Bilim University, Türkiye,

[2]University of Alabama

The Cauchy problem for the stationary and instationary nonlocal incompressible abstract Navier-Stokes equation is considered. The equation involve a convolution term and an abstract operator function $A = A(x)$ in a Fourier type Banach space E . First, the existence, uniqueness and coercive estimates of corresponding Stokes equation is derived in L^p spaces. Then the existence and uniqueness of Navier-Stokes equation is obtained. We can obtain different classes of Stokes and Navier-Stokes equations by choosing the space E and the linear operator A which occur in a wide variety of physical systems. In application the existence, uniqueness and L^p -regularity properties to solution of initial value problems for nonlocal degenerate Stokes equations and the existence and uniqueness of nonlocal Navier Stokes equations with discontinuous coefficients are established.

Key Word: Navier-Stokes systems, Elliptic and parabolic equations, Semigroups of operators, Boundary value problems,

Abstract differential equations, Maximal L^p regularity

First Section

We consider the Cauchy problem for the nonlocal Navier-Stokes(N-S) equation

$$\frac{\partial u}{\partial t} - a * \Delta u + A * u + (u.\nabla)u + \nabla\varphi = f(x,t),$$

$$\text{div}\, u = 0,\ u(x,0) = u_0(x),\ x \in \mathbb{R}^n,\ t \in (0,T),$$

where $A = A(x)$ is a linear operator function in a Banach space E ,

$$u = (u_1(x,t), u_2(x,t), \ldots, u_n(x,t)),\ \varphi = \varphi(x,t),\ u_0 = u_0(x)$$

are an E -valued vector solution, unknown pressure and data functions, respectively. Moreover,

$$f = (f_1(x,t), f_2(x,t), \ldots, f_n(x,t))$$

is a given E -valued inhomogenity vector function, $a_k = a_k(x)$ are complex-valued functions,

$$a = a(x) = (a_1(x), a_2(x), \ldots, a_n(x)),$$

$$a * u = (a_1 * u_1, a_2 * u_2, \ldots, a_n * u_n),$$

where $a_i * u_i$ denotes the convolution of the functions a_i and u_i defined by

$$a_i * u_i = \int_{\mathbb{R}^n} a_i(y) u_i(x - y, t) dy.$$

First we will investigate the corresponding instationary Stokes problem

$$\frac{\partial u}{\partial t} - a * \Delta u + A * u + \nabla \varphi = f(x,t), x \in \mathbb{R}^n, t \in (0,T),$$

$$\frac{\partial u}{\partial t} - a * \Delta u + A * u + \nabla \varphi = f(x,t), x \in \mathbb{R}^n, t \in (0,T),$$

and we prove the $L^p(0,T;\mathbb{X}_q)$ -well-possedeness of the problem (2) , where $L^q(\mathbb{R}^n;E)$ denotes E -valued L^q space and

$$\mathbb{X}_q = (X_q)^n, X_q = L^q(\mathbb{R}^n;E).$$

Then by using the maximal regularity properies of the linear problem (2) , we

obtain the existence, uniqueness local and global solution of N-S problem (1) . This problem is characterized with the presence of an abstract operator A and the convolution terms $a * \Delta u, \quad A * u$. We obtain the well-posedeness of the problem (1) in E -valued L^p space.

Note that, the existence of weak or strong solutions and regularity properties for the classical N-S problems extensively studied e.g. in $[1\text{-}8]$.

First of all, we consider the corresponding stationary Stokes problem:

$$-a * \Delta u + A * u + \nabla\varphi + \lambda u = f(x), \ \mathrm{div}\, u = 0, x \in \mathbb{R}^n,$$

$$u(x,0) = u_0(x), x \in \mathbb{R}^n, t \in (0,T).$$

Let

$$u(x,0) = u_0(x), x \in \mathbb{R}^n, t \in (0,T).$$

We show that, for $f \in \mathbb{X}_q$, $\varphi \in H^{1,p}(\mathbb{R}^n;E)$, $\lambda \in S_\psi$ problem (3) has a unique solution $u \in \mathbb{Y}^{q,2}$,

$\varphi \in H^{1,p}(\mathbb{R}^n;E)$ and the following coercive uniform estimate holds

$\varphi \in H^{1,p}(\mathbb{R}^n;E)$

Consider the operator $O = O_q$ in $L^q_\sigma(\mathbb{R}^n;E)$ generated by problem (3). From the estimate (4), we obtain that O is a dissipative operator in $\mathbb{X}_q$ and also is a generator of an analytic semigroup in $\mathbb{X}_q$. By using this fact, the well posedness of (2), the existence of maximal regular solution, and uniqueness of Navier-Stokes problem (1) are obtained in the space $\mathbb{X}_q$.

Referances

Y. Giga and H. Sohr, Abstract L_p estimates for the Cauchy problem with applications to the Navier-Stokes equations in exterior domains. J. Funct. Anal., (1991)102, 72-94.

D. Fujiwara and H. Morimoto, An L_r - theorem of the Helmholtz decomposition of vector fields, J. Fac. Sci. Univ. Tokyo, Sec. (1977) (I) 24, 685-700.

R. Farwing and H. Sohr, Generalized resolvent estimates for the Stokes system in

bounded and unbounded domains, J. Math. Soc. Japan, (46) 4(1994), 607--643.

T. Kato, Strong L_p -solutions of the Navier-Stokes equation in R^m , with applications to weak solutions. Math. Z., (1984)187, 471--480.

O. A. Ladyzhenskaya, The mathematical theory of viscous incompressible flow, Gordon and Breach, New York, 1969.

V. Solonnikov, Estimates for solutions of nonstationary Navier-Stokes equations, J. Sov. Math., 1977, 8, 467-529.

P. E. Sobolevskii, Study of Navier-Stokes equations by the methods of the theory of parabolic equations in Banach spaces, Soviet Math. Dokl. (1964)(5), 720-723.

V. B. Shakhmurov, Navier-Stokes problems with small parameters in half space and application, Siberian Mathematical Journal, (64) 1, (2023) 181--201.

https://doi.org./10.58225/mpmma.2026.1060

INVESTIGATION OF STRESS CONCENTRATION IN A UNIFORMLY ROTATING PLATE WEAKENED BY AN ELLIPTICAL HOLE AND TWO STRAIGHT CRACKS

Huseyn Mammadsadygov[1], *Jeyhun Musayev* [2]
AzUAC, Azerbaijan

Abstract. The stress concentration problem in a uniformly rotating isotropic circular plate weakened by a central elliptical hole and two straight cracks is investigated. The plate rotates with a constant angular velocity, and additional inertia forces caused by attached point masses are taken into account. The analytical solution is obtained using the superposition principle, complex variable methods, and conformal mapping techniques. Stress intensity factors and critical rotational loads are evaluated. Numerical examples demonstrate the influence of crack length, cavity geometry, and attached masses on the stress distribution and fracture resistance of the rotating plate.

Keywords: rotating plate; stress concentration; elliptical hole; crack; stress intensity factor; critical load.

Introduction. Consider an isotropic circular plate weakened by a centrally located elliptical cavity with two straight

cracks. Two-point masses m are attached on the imaginary axis OY at distances $\pm id$ from the center of the plate. The plate rotates with a constant angular velocity ω about an axis passing through its center, which is taken as the origin of the coordinate system.

The straight cracks emanating from the elliptical boundary are symmetrically located along the real axis OX. The coordinates of the crack tips are denoted by $\pm e$.

Such a plate can be modeled as being subjected to body forces (inertia forces) given by

$$X = \rho\,\omega^2 x, \quad Y = \rho\,\omega^2 y \tag{1}$$

as well as to two concentrated forces

$$P = md\omega^2,$$

applied at the points $\pm id$ on the imaginary axis OY. These concentrated forces are assumed to be uniformly distributed over the plate thickness, i.e., the forces P are considered per unit thickness $2h$.

The solution of the problem under consideration is obtained by superposition of the solutions to two auxiliary problems: 1) The problem of the stress–strain state of a uniformly rotating circular plate with an elliptical hole and two straight cracks, without attached point masses. 2) The

problem of the stress state of a circular plate with an elliptical cavity and two straight cracks subjected to two concentrated tensile forces P, applied at the points $\pm id$ on the imaginary axis OY.

As is well known, the problem of the stress–strain state of a uniformly rotating plate reduces to determining the stress function F, which satisfies the biharmonic equation:

$$\Delta\Delta F = \alpha \tag{2}$$

were,

$$\alpha = 2(1-\nu)\,\rho\,\omega^2 \tag{3}$$

Here, ρ is the material density of the plate, ω is the angular velocity, and ν is Poisson's ratio.

The solution of the differential equation (3) is sought in the form:

$$F = F_0 + F_1 \tag{4}$$

where F_0 is a particular solution of equation (3), and F_1 is the general solution of the corresponding homogeneous equation

$$\Delta\Delta F = 0. \tag{5}$$

The general solution F_1 of the homogeneous (biharmonic) equation (5) can be represented in the form [1–3, 7, 8]:

$$F_1 = \mathrm{Re}[\bar{z}\,\phi(z) + \psi(z)] \quad (6)$$

Here, $\phi(z)$ and $\psi(z)$ are analytic functions regular within the domain S of the plate.

Results and Discussion

The developed analytical model makes it possible to evaluate stress concentration near crack tips for different geometric and loading parameters. Numerical calculations show that increasing crack length causes a significant rise in stress intensity factors and a corresponding reduction in the critical rotational load. The presence of attached point masses produces an additional stress field and further increases the stress concentration near the crack tips. Consequently, crack propagation may begin at lower rotational speeds than in the case without attached masses.

The obtained results agree with classical solutions available in the literature for limiting cases, confirming the validity of the proposed analytical approach.

Conclusion

An analytical investigation of a uniformly rotating circular plate weakened by an elliptical hole and two straight cracks has been presented. The influence of attached point masses was incorporated through additional inertia forces. The solution was obtained using complex variable methods, conformal mapping, and the superposition principle. The results indicate that both geometric parameters and attached masses strongly affect the stress distribution and fracture behavior of the plate. The developed model can be applied in the design and safety assessment of rotating engineering components containing defects.

References

1. Savin, G.N. Stress Distribution around Holes. Kyiv: Naukova Dumka, 1968.
2. Kuliyev, S.A. Stress State of a Polygonal Plate with a Central Circular Hole and Two Linear Cracks. Engineering Fracture Mechanics, 27(6), 1987, 601–613.
3. Sih, G.C., Paris, P.C., Erdogan, F. Stress Intensity Factors for Cracks in Plates under Plane Tension and Bending. Journal of Applied Mechanics, 29(2), 1962, 102–108.

4. Mamedsadygov, H.H., Aliyev, R.D. Free Vibrations of a Circular Plate Weakened by an Elliptical Hole with Two Straight Cracks. Theoretical and Applied Mechanics, 2017, 10–15.

https://doi.org./10.58225/mpmma.2026.1066

A SMART TASK AND ISSUE MANAGEMENT SYSTEM WITH GEOSPATIAL PROBLEM MAPPING

Sonay Arzimanli
University of Lodz, Republic of Poland

Abstract
Urban infrastructure management requires efficient task allocation, issue tracking, and real-time communication. This platform enables administrators to assign tasks, workers to complete them, and all users to interact via real-time chat. Additionally, a city problem mapping module helps visualize reported issues, improving efficiency and transparency in maintenance operations.

Keywords: Urban Infrastructure, Task Allocation, Issue Tracking, Real-time Communication, City Maintenance, Administrators, Workers, Interactive Map, Problem Mapping, Efficiency, Transparency, Public Infrastructure, Potholes, Streetlight Issues, Workforce Management, Collaboration, Technology Integration, Smart Cities, Web Application, GIS (Geographic Information System).

Introduction

The modern urban environment requires rapid and structured issue resolution mechanisms to maintain city infrastructure effectively. Traditional methods of task management, which often rely on paper-based processes or disconnected digital

solutions, lead to inefficiencies, delays, and miscommunication between administrators and field workers. The Smart Task and Issue Management System is designed to overcome these challenges by integrating task management, real-time chat functionality, and geospatial mapping into a single web-based solution.

The core objectives of this system include:

1. Efficient Task Assignment – Administrators can create and assign tasks to specific workers, set deadlines, and track progress.
2. Geospatial Problem Visualization – Issues such as potholes or damaged infrastructure are displayed on an interactive map, enabling efficient resource allocation.
3. Real-Time Communication – A built-in chat system allows workers and administrators to discuss assignments and report urgent issues.
4. Status Tracking and Feedback – Workers can mark tasks as completed, and administrators can provide feedback for continuous improvement.

The Need for Digital Task Management in City Maintenance

Urban management systems require structured communication channels to assign, track, and complete maintenance tasks efficiently. Traditional maintenance workflows often involve manual reporting,

phone calls, or email exchanges, which can lead to delays, data inconsistencies, and a lack of centralized monitoring. Studies indicate that implementing digital task management systems can reduce task completion times by up to 40%, enhancing accountability and efficiency in public works projects.

Integration of Geospatial Data in Urban Maintenance

Geospatial data plays a crucial role in modern infrastructure management. Many cities now use GIS (Geographic Information Systems) to track urban issues, such as road damage, lighting failures, and public safety hazards. By incorporating a mapping feature, our system ensures that city officials and maintenance teams can visualize problem areas, prioritize repairs based on geospatial clustering, and enhance decision-making.

The Importance of Real-Time Communication in Field Operations

A real-time chat system is essential for coordinating field workers efficiently. Studies in workforce collaboration show that instant communication reduces task resolution delays by over 50%, enabling real-time problem-solving and faster response times.

Advantages of the System

The Smart Task and Issue Management System offers multiple advantages:

1. Improved Efficiency in Task Assignment

The platform eliminates delays caused by manual reporting and tracking. Administrators can assign, monitor, and manage tasks in real-time.

2. Geospatial Insights for Better Decision-Making

The map-based issue visualization helps in prioritizing repairs and allocating resources effectively. City maintenance teams can identify clusters of problems and address them strategically.

3. Scalability and Flexibility

The system is scalable to accommodate more workers and administrators as needed. Additional features such as emergency alerts, push notifications, and AI-based task recommendations can be incorporated in future versions.

4. Data-Driven Maintenance Planning

Administrators can analyze historical task data to identify recurring issues in specific city zones, leading to proactive infrastructure maintenance planning.

Conclusion

The Smart Task and Issue Management System is a comprehensive digital solution designed to optimize city maintenance operations. By integrating task management, real-time communication, and geospatial issue mapping, the platform enhances efficiency, collaboration, and decision-making among maintenance teams.

The system reduces delays in task completion, improves transparency in communication, and helps officials strategically address infrastructure problems. As urban centers continue to expand, smart infrastructure management solutions like this system will play a vital role in maintaining and improving city services efficiently.

Literatur:

1. "Spatial Database Systems: Design, Implementation and Project Management" by Albert K.W. Yeung and G. Brent Hall

2. "Geospatial Technologies for Resources Planning and Management" edited by Chandra Shekhar Jha, Ashish Pandey, V.M. Chowdary, and Vijay Singh

3. "Geospatial Technology and Smart Cities" edited by Poonam Sharma

https://doi.org./10.58225/mpmma.2026.*1071*

NORMALIZING KHOREZM DIALECT SPEECH TRANSCRIPTS INTO STANDARD UZBEK: A FINE-TUNED NLLB-200 APPROACH

Maksud Sharipov , Ruzikajon Kurbonova, Lola Kurbanova

Urgench State University named after Abu Rayhan Biruni, Uzbekistan

Abstract. The Khorezm dialect differs so much from the Uzbek literary language that the usual rules of literary language are not always applicable to understanding or analyzing it. We consider the translation task of Khorezm dialect transcripts into standard Uzbek and specify the NLLB-200 model, which already includes Uzbek among its languages, on a manually aligned corpus of 2932 dialect-standard sentence pairs from the Khorezm region. The zero-hit model achieved 16.6 BLEU and 51.7 ChrF on the test set; after refinement, it reached 50.3 BLEU and 76.8 ChrF. The increase of almost 34 BLEU scores indicates that a few thousand sentence pairs combined with a model that already knows the target language are sufficient to create a working dialect-literary system. We derive the corpus and model as a basis for similar work on other Uzbek dialects.

Keywords: Khorezm dialect, dialect normalization, parallel corpus, NLLB-200,

neural machine translation, Uzbek, low-resource languages.

1 Introduction

Although more than 39 million people speak Uzbek, existing language programs and technologies are designed to meet only one standard — the official literary language. As a result, the living speech (dialects) that people use in everyday life and across different regions receive little attention from artificial intelligence and language technologies. The current literary language standard was created in the 20th century based on the dialects of the capital and its surrounding regions, and it can meet the needs of official agencies, education, and the press, but it cannot fully cover all regional dialects. Today, as digital services move from text to live speech — voice assistants and dictation systems — this gap is becoming a serious obstacle: systems that recognize only the literary language cannot serve the large population of people who speak dialects in everyday life. Furthermore, while recent advancements have introduced specialized tools for the official language standard, such as the UzMorphAnalyser, which focuses on morphological analysis using standard inflectional endings, these models are inherently constrained by literary norms and fail to capture the diverse, non-standard morphological variations present in regional dialects [1].

Khorezm is a region with a unique linguistic system, historically distinct among the Uzbek-speaking regions, formed by the interaction of Turkic and Iranian languages. The dialect used here is not just a deviation from the standard language but a coherent structure with deep historical roots and millions of speakers. Therefore, it is scientifically wrong to view dialectal speech as simply an "incorrect form". The goal of normalization in this study is not to eliminate the dialect, but to ensure its integration with digital tools for the standard language. This approach is crucial for the correct formulation and assessment of the task, and for scientifically justifying the decision to preserve the dialect features in their original state, without artificially adapting them to the standard during transcription in the source part of the corpus, without errors.

The Khorezm region is a clear example. Its dialect belongs to the Oghuz branch of the Turkic languages, not to the Karluk core from which the literary norm originates [2]. This difference is so great that speech recognition (SCR) or machine translation systems adapted to standard Uzbek make serious errors when encountering Khorezm speech [3]. Although the two linguistic systems are mutually intelligible at the human level, linguistic features that a listener would easily perceive—vowel shifts, unusual verb endings, and local vocabulary—are

completely incomprehensible and distorted by statistical models trained solely on the standard language.

These differences are not merely superficial lexical peculiarities, but affect the entire grammatical system. There are phonetic substitutions that are not reflected in the standard spelling rules; verb affixes differ significantly (for example, the suffix -yotir of the present continuous tense in the dialect takes the place of -yaptı in the standard language); lexical units belonging to the Oghuz and Old Persian layers are not found in standard dictionaries at all. However, the fact that these features are not accidental, but strictly systematic, is both a source of difficulty and a solution to the problem: a model that has received enough information can learn regular correspondences (regular patterns) and apply them to new sentences that the system has not encountered before.

We approach this problem not as a simple graphical correction (spelling correction), but as a full-fledged translation task: here, the source language is the Khorezm dialect, and the target language is the standard Uzbek literary language. Considering the process not as a rule-based rewriting system but as machine translation frees us from the obligation to manually program each change and allows the model to infer (map) patterns in the data itself. This approach is fully compatible with the sequence-to-sequence model in the

Transformer [4] architecture and allows us to effectively use large multilingual models (LLMs) that include Uzbek.

In our study, we work with the distilled 600M-parameter NLLB-200 model [1]. Since NLLB has been trained on Uzbek (uzn_Latn) among two hundred languages, it can already produce perfect text in standard Uzbek. Therefore, the corpus we have built is sufficient to train the model not on the language itself, but only on the rules of transition from dialect to standard. Previous multilingual models, such as mBART-50, completely excluded Uzbek, forcing researchers to use close variants of other Turkic languages; NLLB overcomes this limitation. A similar recent study used the same methodology for Southern Uzbek [5]; however, to our knowledge, our work is the first systematic study to combine transfer learning, automatic assessment metrics, and a parallel corpus specifically for the Khorezm dialect.

This study seeks to answer two important questions. Practical question: Can a research team with limited resources (only a few thousand identified sentences and a single GPU) create a dialect-normalizing system that works in real life, rather than just a theoretical idea? Scientific question: How important is the choice of the right base model? If the model already knows the target language perfectly, how much can the system produce before domain-specific data is

added, and how much does the parallel corpus contribute to this? While the difference between the zero-shot and fine-tuned states of the model directly answers the second question, the magnitude of this difference indicates the solution to the first question.

Beyond Uzbek, this work is also relevant to general global patterns in language technologies. The world's writing systems and standards only partially capture the live speech of people. Language variants excluded from digital resources often belong to the least technologically advanced groups, further deepening the digital divide. Therefore, methods that can turn even small, hand-crafted corpora into working systems are essential for any language: they lower the minimum threshold needed to support dialects with few resources. The Khorezm dialect is a vivid illustration of this broader argument, and the figures below should be interpreted as evidence that the limits of research have been sufficiently lowered, rather than as a conclusion about dialects.

This paper presents the following scientific contributions:

- A hand-adapted original Khorezm-standard parallel corpus of 2932 sentence pairs;
- The first BLEU and ChrF benchmarks were computed for this dataset;

- Empirical evidence that fine-tuning the NLLB-200 model can increase the BLEU score from 16.6 to 50.3;
- A reproducible universal methodological procedure that can be applied to other regional dialects of the Uzbek language.

The rest of the article is organized as follows: Section 2 reviews prior research on the topic; Section 3 describes the parallel corpus; Section 4 outlines the methodology; Section 5 reports the results and their discussion; and Section 6 concludes with directions for future research.

2 Related Work

2.1 Dialect-to-standard translation

The practice of dialect-to-standardization (normalization) is well-developed in the case of Arabic. In particular, the MADAR corpus [6], which includes 25 urban dialects, has served as a basis for many Transformer-based normalization systems and has yielded BLEU scores between 20 and 30. The linguistic situation in Arabic is similar in important respects to that of Uzbek: alongside the authoritative written standard (literary language), there are also spoken forms of speech (a dialect continuum) that are at varying distances from it. Therefore, the normalization process here is not simply a matter of correcting errors, but also of aligning one legal linguistic variant

with another. The methodology that has proven itself in this area—the approach of formulating the task as a direct translation and relying on large pre-trained models rather than training the system from scratch—translates naturally to our research context.

The experience with Swiss German is also useful for our research in another respect: in an environment with no strictly defined spelling rules, transcription conventions themselves become part of the problem, as is the case with our transcripts [7]. In the absence of a single agreed-upon spelling standard in a dialect, a single spoken form can be written in multiple ways, and the model must learn to accept these diverse variants as equivalent inputs that correspond to a single standard target. The Khorezm dialect has exactly this feature, since its speakers lack standardized rules for writing; therefore, the transcription choices made by our annotators are not merely neutral transcriptions but important design decisions for the project. The main conclusion to be drawn from this literature is that, given a strong multilingual base model, it is possible to achieve a practical and efficient result with just a few thousand parallel pairs. This paper is based on this scientific hypothesis.

At the heart of all the systems considered is the Transformer [4] encoder-decoder architecture, which is widely regarded as a standard recipe for neural

machine translation (NMT). Today, this architecture is implemented using the pre-trained weights of large multilingual models rather than random weights. The transition to pre-trained multilingual models has made it practically possible to work with low-resource language and dialect pairs. Because such a basic model brings its general linguistic competence to the task, while the small domain-specific corpus serves only to fine-tune it for a specific purpose. Our work is a vivid example of applying this global methodology to the intra-lingual environment. Here, the source and target are not two separate languages but two different versions of the same language. This configuration turned out to be unusually convenient and efficient for the model: since the bulk of the sentences (stems and general lexicon) is distributed equally between the input and output, the model is required to rewrite only the divergent parts.

2.2 Language technology for Uzbek

Digital resources created for Uzbek are mainly aimed at covering the fundamental needs of the language, and include: an open-source Uzbek speech corpus of approximately 100 hours [3], an Uzbek-Kazakh parallel corpus [8], a lexical database based on the WordNet model [9], a semantic similarity assessment dataset [10], a transliteration tool for Latin-Cyrillic graphics [11], and an initial sentiment analysis dataset [12]. Each of these resources serves to fill a

specific gap, and together they have brought Uzbek from the category of low-resource languages to the level of a language with the initial building blocks that can be used in digital technologies. The practice of automatic text generation (neural text generation) in standard Uzbek using neural networks has developed in parallel, starting from sequence-to-sequence (seq2seq) models [13] to studies comparing LSTM and mT5-small models [14]. These studies have shown that modern architectures can be successfully trained and evaluated on Uzbek texts and have shown results close to those in more resource-rich languages.

However, a common feature of these studies is that they are focused exclusively on the literary standard (official language). Existing benchmarks for speech recognition, morphological analysis, or text generation refer only to standard Uzbek, while regional dialects are almost completely left out of the digital map. The only exception to this is a recent study of South Uzbek, a language spoken by the Afghan population, which included parallel translation resources and a fine-tuned NLLB model [5]. Although this effort and our study share a common strategy—that is, the creation of a parallel corpus and the refinement of an NLLB model—they address completely different linguistic systems at two opposite poles of the Uzbek language range and do not cover each other in content. No sentence-level

parallel corpus has been created for the Khorezm dialect, and no machine translation results have been published; our study aims to fill this serious scientific and technical gap.

2.3 Positioning of the present work

Read together, the prior work establishes two points. First, treating dialect normalization as low-resource translation on top of a multilingual model is a sound and repeatedly validated strategy [5], [6], [7]. Second, the approach has not yet been applied to the Khorezm dialect, and no automatic scores for it have been reported. The present paper closes that particular gap, and in doing so, contributes a reusable recipe and a public benchmark that later work on other Uzbek dialects can build on directly.

3. The Corpus

3.1 Why the dialect is hard, and why that helps

Because the dialect is Oghuz while the standard is Karluk, the two diverge in regular, describable ways that a model can learn to undo: phonetic alternations that surface in transcription, an Oghuz/Persian vocabulary stratum absent from standard dictionaries, and rule-governed inflectional substitutions such as -yotir for -yapti. It is worth stressing the word regular. Each of these divergence types is, for the most part, systematic: a given dialectal ending

corresponds to a given standard ending, a given sound alternation recurs in the same phonological environment. A model does not have to memorize each sentence; it has to learn a comparatively small set of correspondences and generalize them. This is precisely the kind of structure that sequence-to-sequence models capture well, which is why a corpus of only a few thousand sentences can go a long way.

The harder residue is lexical. Where a dialect word has no standard counterpart in the training data, or appears only once or twice, the model has little to generalize from, and these rare items account for a disproportionate share of the errors that survive fine-tuning. This observation shapes both our error analysis in Section 5 and our recommendations for future data collection.

It is useful to make the three types of divergence concrete. Phonetic alternations include the voicing of stops and shifts in vowel quality that the dialect carries, but the standard spelling does not; when an annotator writes the dialect as it sounds, these surface directly in the text and become a regular input-side pattern. Inflectional divergences are exemplified by the present-continuous, where the dialectal ending differs from the standard one in a fully predictable way, so that the model can learn the substitution from a handful of examples and apply it everywhere. Lexical divergences are the least regular: an Oghuz or Persian-

derived word may map to a quite different standard form, and unless that pairing appears in training, the model has no principled way to recover it. The first two types are where fine-tuning delivers most of its gains; the third is where the residual errors live.

3.2 Data collection and annotation

We gathered speech from native speakers across the Khorezm region in conversation and guided sessions, transcribed it through annotators who speak the dialect, and paired each sentence with a standard Uzbek equivalent written by a bilingual linguist. The guided sessions were designed so that common grammatical constructions — the divergent verb forms in particular — would be well represented rather than left to chance. At the same time, the conversational material kept the corpus close to natural usage. Using annotators who are themselves speakers of the dialect mattered: it ensured that the transcriptions preserved the dialect's sound and vocabulary instead of quietly standardizing them on the page, which would have erased the very phenomena the model needs to learn.

A second annotator checked the pairs and removed any personal information. This second pass served two purposes at once. It improved consistency by resolving cases where the first annotator's standard rendering was debatable, and it served as a privacy safeguard by discarding any sentence that

contained identifying details. The finished corpus holds 2,932 pairs, split 80/10/10 (Table 1). The split is performed once with a fixed random seed, ensuring the same partition can be reproduced exactly; the development portion is reserved for model selection, and the test portion is left untouched until final evaluation.

Table 1. Corpus statistics.

Item	Value	Note
Total sentence pairs	2,932	Manually aligned
Train / Dev / Test	2,346 / 293 / 293	80 / 10 / 10 %
Annotation passes	2	Second-annotator check

4 Method

4.1 Model and language tags

We fine-tune NLLB-200-distilled-600M [1]. It already produces grammatical standard Uzbek, so the corpus only supplies the dialect-to-standard mapping; the distilled size also fits a single GPU, aiding reproducibility. The choice of the distilled 600M variant rather than a larger NLLB checkpoint is deliberate: it keeps training and inference within the reach of a single mid-range GPU, which matters for a research setting without large compute budgets and makes the results easier for others to

reproduce. Both source and target tags are set to Uzbek (uzn_Latn), since input and output share the same base and differ only in the dialectal layer. Tagging both sides as the same language signals to the model that most of each sentence should pass through unchanged, and that its job is to rewrite the dialectical portions rather than to translate wholesale.

4.2 Tokenization and training

Text was tokenized using NLLB's SentencePiece model, whose subword units are well-suited to agglutinative Uzbek. Subword segmentation is especially valuable here because Uzbek words often carry several stacked suffixes; splitting them into reusable pieces lets the model handle inflected forms it has not seen as whole words, which is important when the dialect and the standard differ precisely in their endings. Training used a learning rate of 5×10^{-5} with a 500-step warm-up, an effective batch of 16 (batch 8 × 2 gradient-accumulation steps), AdamW with 0.01 weight decay, gradient checkpointing, and up to 20 epochs, keeping the checkpoint with the best development BLEU. Gradient accumulation lets us reach an effective batch size of 16 without exceeding memory limits, and gradient checkpointing trades a little extra computation for a smaller memory footprint, which allows the model to be trained on a single device. Keeping the best development checkpoint, rather than the final

one, guards against the mild overfitting that appears in the last few epochs.

4.3 Baseline and evaluation

A zero-shot run of the unmodified model gives the baseline. Because NLLB already covers Uzbek, this baseline is a meaningful comparison rather than a formality: it measures how much of the dialect the model can handle on the strength of its pretraining alone, thereby isolating the contribution of our corpus. Quality is measured with sacreBLEU using BLEU [15] and the character-level ChrF [16], the latter being fairer to a morphologically dense language. Reporting both metrics matters because they reward different things: BLEU is sensitive to whole-word and phrase matches, while ChrF gives partial credit for getting most of a long inflected word right, which is common when only a suffix differs between dialect and standard.

4.4 Implementation and reproducibility

The entire pipeline is built on widely available open-source components, which keeps the work reproducible and inexpensive to repeat. The model and tokenizer are loaded from their public checkpoints, training is driven by a standard sequence-to-sequence trainer, and evaluation uses a community-maintained implementation of the metrics to ensure scores are comparable to those reported elsewhere. Randomness is controlled by a fixed seed governing the data split and initialization, so that a second run

reproduces the same partition and closely similar scores. Because the distilled model fits comfortably on a single GPU and the corpus is small, a full cycle — zero-shot evaluation, fine-tuning, and final testing — completes in a matter of hours rather than days, making iteration practical and putting replication within reach of any group with modest hardware.

5 Results and Discussion

5.1 Overall scores

Table 2 reports the headline results. Fine-tuning lifts BLEU from 16.6 to 50.3 (+33.7) and ChrF from 51.7 to 76.8.

Table 2. Test-set results.

System	BLEU	ChrF
NLLB-200-distilled-600M, zero-shot	16.6	51.7
NLLB-200-distilled-600M, fine-tuned (ours)	50.3	76.8

The baseline is already non-trivial — NLLB recognizes much of the input before adaptation, as expected of a model that knows standard Uzbek and its Turkic neighbors [17] — and development BLEU scores exceed 40 within three epochs, indicating that systematic dialect features are learned quickly, while later epochs handle rarer cases. This learning curve is consistent with the picture drawn in Section 3: the regular correspondences, being frequent and rule-like, are absorbed first and account for

most of the gain, after which the model spends its remaining capacity on the long tail of infrequent words and constructions, where progress is necessarily slower.

5.2 Error analysis

Manual inspection shows the remaining errors concentrate in rare vocabulary (words seen once or twice), code-switched Russian or Persian material, and phonetic variants absent from the transcription. Table 3 illustrates the range: a frequent form is rendered exactly, a rare lexical item is mangled, and a longer sentence is recovered fluently and faithfully. The first example, a high-frequency verb form, is normalized correctly, which is the expected outcome for the mapping's systematic part. The second fails because the dialectal word is rare in the training data, leaving the model with too little evidence to recover the standard equivalent; instead, it produces a near-phonetic guess. The third shows the system at its best on a longer input, returning a fluent and faithful standard sentence, which indicates that the model handles sentence-level reordering and agreement, not merely word-for-word substitution.

Table 3. Example outputs of the fine-tuned model.

Khorezm dialect	Model output (standard)	Comment
Galyotirman	Kelayapman	Correct
Novvi bo’ldi	Navvi boldi	Rare word,

Khorezm dialect	Model output (standard)	Comment
		mangled
Nishab zo’tamiz indi	Qanday qilib tuzatamiz endi?	Fluent, faithful

Because the trouble lies in data sparseness rather than the architecture, the clearest next step is more data with wider lexical coverage. This is an encouraging diagnosis: it means the path to better results does not require a larger or fundamentally different model, only a larger and lexically richer corpus, which is a matter of annotation effort rather than computation.

5.3 Discussion

The 50.3 BLEU figure sits above the twenties-to-thirties band typical of comparable Arabic work [6], an advantage attributable to NLLB’s native Uzbek coverage [17], the same edge the Southern Uzbek effort relied on [5]. The comparison should be read with care, since scores are not strictly comparable across languages, corpora, and test sets; what it suggests is not that our system is better than the Arabic ones in any absolute sense, but that starting from a model which already knows the target language gives a real and measurable head start. The wide gap between a respectable zero-shot baseline and a much stronger fine-tuned result is the central finding: when the

base model already speaks the target language, a modest, carefully built parallel corpus is enough to bootstrap a genuinely useful dialect-normalization system, and the bulk of the work is done by data that a small team can realistically collect.

5.4 Broader implications

The result carries a message that extends past the single dialect studied here. The decisive factor was not a novel architecture or an unusually large corpus but the alignment between the base model's pretraining and the target of the task: because NLLB already produced standard Uzbek, the corpus could devote all of its signal to the dialect-to-standard mapping. This suggests a practical heuristic for other under-resourced varieties — choose a base model that already covers the target standard, and the parallel data needed to adapt it drops sharply. Where no such model exists, the same logic argues for first investing in coverage of the standard, since that investment pays off across every dialect of the language. The strong showing of a compact, distilled model also indicates that useful dialect normalization need not wait for the largest available systems, which broadens the set of groups that can realistically take on this kind of work.

Finally, the gap between the zero-shot and fine-tuned scores is itself a useful measurement, independent of the absolute numbers. It quantifies how much of the dialect a general multilingual model already

handles versus how much must be taught, and tracking that gap across dialects would give a principled way to prioritize annotation effort: varieties with a small gap need little data, while those with a large gap are where new corpora would yield the greatest return. The Khorezm figures provide one data point on that map, and the methodology makes it straightforward to add others.

6 Conclusion and Future Work

A corpus of fewer than three thousand sentence pairs, fine-tuning a model that already knows the target language, is enough to convert Khorezm dialect transcripts into standard Uzbek well: NLLB-200 moved from 16.6 to 50.3 BLEU and from 51.7 to 76.8 ChrF, giving the first benchmarks for this pair. Beyond the headline numbers, the study offers a template — collect a few thousand carefully aligned pairs, fine-tune a multilingual model that covers the target language, evaluate against a zero-shot baseline — that other groups working on under-resourced varieties can follow with modest resources.

The corpus and model also support dialect-aware spell checking, ASR rescoring [3], dictionary building, and heritage preservation. A normalizer of this kind can sit behind a speech recognizer to clean up its output, feed a semi-automatic pipeline for compiling dialect dictionaries, or help bring

archived recordings of folklore and oral history into a form that search and analysis tools can handle. In each case, the practical value comes from the same source: lowering the cost of working with dialectal material so that it is no longer excluded by default from the language technology built around the standard.

Several limitations temper these conclusions and frame the work ahead. The corpus, while sufficient to demonstrate the approach, is small by the standards of mainstream machine translation, and its coverage of the dialect's vocabulary is necessarily partial; the rare-word errors documented above are a direct consequence. The evaluation rests on automatic metrics, which approximate but do not replace human judgment of fluency and adequacy, and a human evaluation would give a fuller picture of where the system succeeds and fails. Finally, the present pipeline operates on transcripts rather than audio, so any phonetic information the transcription does not capture is lost before the model ever sees the input. Each of these limitations points to a concrete improvement, and none undermines the central result.

Future work will expand the corpus beyond 10,000 pairs, add a dialect-tuned speech front-end for end-to-end spoken normalization, and extend the recipe to the Fergana and Kashkadarya dialects. Enlarging the corpus, with particular attention to the

rare vocabulary that drives the residual errors, should narrow the remaining gap; coupling the normalizer with a speech recognizer fine-tuned on dialect audio would turn it into a complete spoken-to-standard pipeline; and applying the same procedure to other Uzbek dialects would test how far the approach generalizes across the dialect continuum. Taken together, these steps point toward Uzbek language technology that reflects the language as it is actually spoken, not only as it is written.

References

[1]U. Salaev, “UzMorphAnalyser: A Morphological Analysis Model for the Uzbek Language Using Inflectional Endings,” in AIP Conference Proceedings, 2024. doi: 10.1063/5.0241461.
[2]N. Abdurakhmonova, G. Astanova, A. Akhmedov, D. Mengliev, B. Ibragimov, and A. Abdullayev, “Development of a lexical dataset and a rule-based algorithm for the analysis of Khorezm dialects of the Uzbek language,” Data Brief, vol. 63, p. 112216, 2025, doi: https://doi.org/10.1016/j.dib.2025.112216.
[3]M. Musaev and others, “USC: An Open-Source Uzbek Speech Corpus and Initial Speech Recognition Experiments,” in International Conference on Speech and Computer (SPECOM 2021), in Lecture

Notes in Computer Science, vol. 12997. Springer, 2021, pp. 437–448.
[4]A. Vaswani et al., “Attention Is All You Need,” in Advances in Neural Information Processing Systems (NeurIPS), 2017, pp. 5998–6008.
[5]M. Mamasaidov, A. Aral, A. Shopulatov, and M. Inomjonov, “Filling the Gap for Uzbek: Creating Translation Resources for Southern Uzbek,” in Proceedings of the Tenth Workshop on Statistical Machine Translation (WMT), 2025, pp. 1081–1087.
[6]H. Bouamor et al., “The MADAR Arabic Dialect Corpus and Lexicon,” in Proceedings of the Eleventh International Conference on Language Resources and Evaluation (LREC), 2018, pp. 3387–3396.
[7]Y. Scherrer and N. Ljubešić, “Automatic Normalization of Swiss German Dialect Text,” in Proceedings of the Joint Workshop on Language Technology for Closely Related Languages, Varieties and Dialects (KONVENS / VarDial), 2016.
[8]B. Allaberdiev, G. Matlatipov, E. Kuriyozov, and Z. Rakhmonov, “Parallel Texts Dataset for Uzbek-Kazakh Machine Translation,” Data Brief, vol. 53, p. 110194, 2024.
[9]A. Agostini and others, “UzWordNet: A Lexical-Semantic Database for the Uzbek Language,” in Proceedings of the 11th Global WordNet Conference, 2021, pp. 8–19.
[10] U. Salaev, E. Kuriyozov, and C. Gómez-Rodr\’\iguez, “SimRelUz: Similarity

and Relatedness Scores as a Semantic Evaluation Dataset for Uzbek," in Proceedings of the International Workshop on Special Interest Group on Under-resourced Languages (SIGUL), 2022, pp. 199–206.
[11] U. Salaev, E. Kuriyozov, and C. Gómez-Rodr\'\iguez, "A Machine Transliteration Tool Between Uzbek Alphabets," in CEUR Workshop Proceedings, 2022.
[12] E. Kuriyozov and S. Matlatipov, "Building a New Sentiment Analysis Dataset for Uzbek Language and Creating Baseline Models," in MDPI Proceedings, 2019, p. 37.
[13] M. Sharipov, R. Qurbanova, and L. Kurbanova, "An LSTM-Based Model and Algorithm for Uzbek Language Text Generation," in Proceedings of the International Conference on International Conference on Computer Science and Engineering (UBMK), 2025, pp. 505–508. doi: 10.1109/UBMK67458.2025.11206897.
[14] M. Sharipov, R. Kurbonova, and O. Sobirov, "Conditional Text Generation for Uzbek: A Comparative Study with LSTM and mT5-small," in Proceedings of the International Conference on Actual Problems of Electronic Instrument Engineering (APEIE), 2025. doi: 10.1109/APEIE66761.2025.11289441.
[15] K. Papineni, S. Roukos, T. Ward, and W.-J. Zhu, "BLEU: a Method for Automatic Evaluation of Machine Translation," in

Proceedings of the 40th Annual Meeting of the Association for Computational Linguistics (ACL), 2002, pp. 311–318.
[16] M. Popović, “chrF: character n-gram F-score for automatic MT evaluation,” in Proceedings of the Tenth Workshop on Statistical Machine Translation (WMT), 2015, pp. 392–395.
[17] M. R. Costa-jussà, others, and NLLB Team, “No Language Left Behind: Scaling Human-Centered Machine Translation,” arXiv preprint arXiv:2207.04672, 2022.

TABLE OF CONTENTS

PLENARY

Messoud Efendiev

Frontiers of Biomathematics: Biofilms vs Public Health……...……....6

Ljubiša D. R. Kočinac, K. Demirci, F. Dirik, S. Yildiz.

Karamata Theory and Statistical Convergence…….……7

Kamil Aida-Zade

Computational problems in hydraulic networks……..…9

Man Wah Wong

An Asymptotic Expansion of the Eigenvalue Counting Function for the Twisted Bi-Laplacian……...……...11

Abdullah H. Sofiyev, Aziz Sencan, Ali Deniz, Yusif N. Hasanov, Zihni Zerin, Nuri Kuruoğlu

Analysis of Influences of Different Environments on Buckling Hydrostatic Pressure of Shear Deformable Multilayer Nanocomposite Cylindrical Shells……...12

Bilal Bilalov

The Latest Developments in the Direction of $\boldsymbol{X}$-Valued Elliptic Equations…….……14

Dongmei Xiao

Stability and Complexity of Ecological Communities with Energy Landscapes…….…….……20

Roland Duduchava

Spectral properties of convolution integro differential equations on the submonoid M = [0, 1)…….22
Vagif Guliyev
Characterization of **BMO** and Lipschitz Functions Via the Commutators of Fractional Maximal Function in Total Morrey Spaces on Stratified Lie Groups…….....25

SESSIONS

Nigar Aslanova, Khalig Aslanov
On two type extensions of minimal symmetric operator in exit space:with resolvents from $\boldsymbol{\sigma_p}$ and with continuous spectrum.....31
Mukanov A.B., Mukanov Zh.B.
Lorentz-type theorems in Lipschitz classes……..34
A.B.Sazairov, Z.M.Khalilov, M.A.Rustamova, A. Kh.Aliyeva
On a Torsion Problem of a Composite Prismatic Bar With a Doubly Connected Cross Section……..…….38
A.H. Guliyev, P.H. Mammadov, V.H. Kerimov, X.R. Necimbeyli, V.A. Alquluyev, I.V. Khurshudov
Application of Artificial Intelligence in Lean Manufacturing…….……44
A.H.Sofiyev, S.A.Piriyev, M.A.Rustamova
Mathematical Modeling of the Bending Durability of a Functionally Graded Prismatic Beam……..…….51
A.K. Babadjanova, G. Eshchanova, J. Xudayberganov·

Short pulse equation with a dissipative term…….64
A. Marimuthu, R. Krithiga, Sheng Zhang , Lakshmanan Rajendran, K. K. Viswanathan
Applications of Coupled Differential Equations for Biofilm Nitrification Models……..……..68
A.B. Sazairov, M. A. Rustamova
Elastic–Plastic Bending of a Rectangular Beam Made of a Non-Hardening Material……...73
Alexander Goncharov
Spaces without the bounded approximation property. New examples…..……78
Aynura Khudiyeva
Impact of stiffener count and deformatıon on the non-linear frequencies of a cylindrical shell containing liquid…….....79
Aynura Khudiyeva
Analytical and Numerical Investigation of Dispersion and Phase Velocity of Harmonic Waves……..84
Abbas Guvalov, Rafig Shirinov
Effect of Multi-Walled Carbon Nanotubes on the Properties of Low-Density Non-Autoclaved Aerated Concrete…….……90
Abbas Quvalov, Saida Abbasova
Reducing the environmental impact through the reuse of concrete scrap…..……96
Abdullah Yener
Doubly Nonlinear Parabolic Problems Related to Greiner Operator……103
Aytekin E. Abdullayeva

Approximation of the Bernstein-Chlodowski polynomial in Lebesgue space with a weighted modulus of continuity……106
Adnan Ahmad Mahmud, Longjun Zhan, Haci Mehmet Baskonus
On the soliton properties of the generalized (3+1)-dimensional P-type nonlinear wave equation…….110
Ahmad Muhammad, Muhammad Abubakar Isah
QSER Decomposition of Predator-Prey Dynamics: Separating Source from Environment……..……113
Alexander Guterman
Permanent function: an instrument to solve algebraic and combinatorial problems…..115
Ali Akbulut, Suleyman Celik, Esra Takan, Tunahan Takan
Adams Theorem for the $\boldsymbol{B}$-Riesz Potential in Total $\boldsymbol{B}$-Morrey Spaces…….……120
Kamil R. Aida-zade, Vugar A. Hashimov
Synthesis of Control of the Movement of Measurement Points of the State and Power of Heat Sources at the Ends of the Rod……..……126
Ali Khalilov , Hilala Jafarova
Automatic Transcription and Classification of Customer Call Recordings for CRM Analytics: A Whisper-Based Web System……...……132
Alik M.Najafov Ahmet Eroglu , Nilufer R.Rustamova

On interpolation type theorems in grand grand besov spaces with dominant mixed derivatives…….……140
Alik M. Najafov, Aygun T. Omarova , Sain T.Alekberli
On the smoothness of solutions of hypoelliptic type equations……...145
Alik M.Najafov, Sain T.Alekberli , Leyla Sh.Gadimova
On the solution of hypoelliptic type equations in grand Sobolev spaces with dominant mixed derivatives……..149
Amir Rahmanparast, Muhammed Milani, Ahmet Selim Dalkilic
Machine Learning-Based Thermal Comfort Classification in Buildings……153
Anar Hummatov ,Vusala Hummatova
Study of optimization of seawater use based on linear programming model……...161
Mammadova Arzu Imamverdi , Sevda Mammadjafar Hajizada ,Kharimova Sevinj Fuzuli
Integral Representations of Smooth Functions of Several Variables at Points…….169
Asef Rusanov , Samira Mustafayeva
Computational Modelling of Biological Systems Under Climate Change Conditions…….177
P.H.Mammadov , Vasif.H. Kerimov*, I.V. Khurshudov, X.R.Necimbəyli , K.K. V.A.Alquluyev Shiraliyev
Application of AI in the optimization of production planning……..……183

Guliyeva Aygun
Dynamic Analysis of an Auger Drilling System Used in Pile-Driving Machines……..…….188
Aygun Gurbanova
Integration of Artificial Intelligence in STEAM Education: A Data-Driven Framework for Primary and Secondary Schools……..……197
Azer Kasimzade, Reyhan Akbarli, Emin Nematli
Next-Generation Structural Seismic Protection: An Industrial Application for the Tallest Building in the Caucasus…...……202
Bahar Milani
Comparative Statistical and Computational Evaluation of Chaotic-Based Pseudorandom Number Generators……...207
Bekchanov Shukurla, Babadjanova Malika
A Framework for Semantic Document Similarity Detection Based on Automatic Text Summarization and Transformer Embeddings……..…….213
Beknazarova Saida, Yunusova Dilnoza,
3D texture modeling based on procedural models, splines, and artificial intelligence methods ……....219
Buğra Avcı, Kaan Erşahin , Ahmet Selim Dalkılıç, Burak Uğuz
Performance Prediction of Carrier Fan Coil Units Using Artificial Neural Networks.....225
Büşra Selenay Önal ,Ahmet Selim Dalkılıç

Examination of the Impact of Industrial Heat Pumps on Energy Efficiency…….……230
Cihan Sezer , Kenan Kaya , Mahdi Tabatabaei Malazi , Ahmet Selim Dalkılıç
Numerical Investigation of Red Blood Cell Diameter Effect on Cell-Free Layer Formation in a Converging Microtube…….….237
Dilek Çağlı Gel , Ahmet Selim Dalkılıç
Thermo-Hydraulic Performance Analysis of Propylene Glycol in a Type E Shell-and-Tube Heat Exchanger with Baffles……...……243
Roland Duduchava, Aleksandr Oleinikov,Tatiana Kuzmina
Equation of State and Limit State Zone at a Crack Tip in Unidirectional Composite Laminates.....249
Abbasov E.M., Darishova A.O.
Modeling the dynamics of gas-liquid mixtures considering Phase Transformations of Heat Exchange with the external environment……...……253
Abbasov E.M., Darishova A.O.
Modeling of Fluid Flow Dynamics in a Complex-Geometry Pipe considering Heat Exchange with the Surrounding Environment…….……259
Elchin M. Mamedov
On Qualitative Properties of a Fourth-Order Nonlinear Wave Equation with Internal Dissipation and Nonlinear Boundary Damping……265
Elif Demir, Yusuf Zeren, Alpaslan Demirci

Comparative Evaluation of Quantum-Inspired Metaheuristics for Welded Beam Design Optimization…….270
Elif Demir,Yusuf Zeren, Mehmet Zeki Sarıkaya , Alpaslan Demirci
A Composite Fractional-Integral Inspired Nonlocal Loss Function for Image Denoising……...……...276
Imamaliyev Elman Bahlul, Mirzeyeva Fatima Elman
Artificial Intelligence and Digital Twin Framework for Hazardous Buildings Assessment……282
Eray Karakaser, Safak Metin Kirkar, Ahmet Selim Dalkilic
Investigation of the Effect of Corrugation Depth on Heat Transfer Performance in Spherical Corrugated Pipes……...290
F. A. Seyfullayev, A.B. Garayev, N.Hasanov
Dynamics of Filled Cylindrical Envelopes Under Axial Compression and Sliding Friction……..……296
Farhad Guliyev, Cavid Islamov,Salahzade Salah , Racab Darchınov
Mechanics of Supersonic Flight: Aerodynamic Analysis, Wave Drag, and Thermal Loading……...……303
Farida Iachachene Hanane Cheradi, Ahmet Selim Dalkılıç
Optimal Porosity Selection for Enhanced Melting and Solidification Performance in Metal Foam-Enhanced PCM Storage Systems…….……308

Fatih Kumru, Erman Aslan
Mean-Line Modelling and Frozen-Geometry Performance Mapping of Axial and Radial Turbines for Internal Combustion Engine Exhaust-Energy Recovery……...……..314
Ferecova Sona
Wave Propagation in a Transversely Isotropic Homogeneous Eccentric Hollow Cylinder……...……..321
G.R.Mirzayeva
Pure Bending Of An Isotropic Plate Weakened By A Doubly Periodic System Of Circular Holes And Straight Cracks Along The Coordinate Axes……..…326
Gadir Ahmadov , Michael Holik, Daniyar Berikov, Sebuhi Nuruyev, Farid Ahmadov, Azer Sadigov, Arzu Mammadli, Ramil Akbarov
Angular Correlations and Decay Spectroscopy of Short-Lived Light Fragments in the Quaternary Fission of ^{252}Cf…….332
Imamguliyeva Gunel Salim
The Impact of the Food and Goods Sector on Economic Growth in the Manufacturing Industry…….……337
Haakan Hedenmalm
Liouville phenomenon for the Klein-Gordon equation in 1+1 dimensions……344
Halil Tugra Basancelebi, Umit Ozkas, Atlas Gerelioglu, and Ahmet Selim Dalkılıc
Thermal and Mechanical Design Analysis of a Small Shell-and-Tube Heat Exchanger Using Kern and Bell-Delaware Methods……346

Vaqif Abdullayev , Efthimios Providas
Numerical Methods for Solving Coefficient Inverse Problems for Ordinary Differential Equations with Nonlocal Conditions…..…353
Halil Tugra Basancelebi , Umit Ozkas , Atlas Gerelioglu, and Ahmet Selim Dalkılıc
CFD Validation of Heat Transfer Performance of Double Pipe Heat Exchangers as Household Machines Used for Heat Recovery…….....360
Hamit Caglar Calisgan, Suleyman Celik, Vagif Guliyev, Nisanur Polat
Commutator of the maximal function in total morrey-guliyev spaces in the dunkl setting……..……..366
Huseyn Mirzayev, Gulnar Salmanova
Validation of stress tensor models for spur gear root stress via finite element analysis…….…….373
Hasanova T.J., Rustamova M.A.
Integral–Analytıcal Modelıng Of Wave Propagatıon In An Elastıc Membrane Under Oblıque Impact.....379
I.H.Mammadova
Investigation of the Effects of Ultradisperse Plagiogranite Powder on Ceramic Material Properties via Mathematical Modeling……..385
Elshan Ibayev and Konul Omarova
On the Laplace–Stieltjes Transform of the Distribution of a semi-Markov process……..……391

Ibrahim M. Nabiev, Aygun R. Latifova, Leyla I. Mammadova , Jalala A. Osmanli.
On the uniqueness of recovery of the Dirac operator with a boundary condition linearly depending on the spectral parameter……397
Ibrahim Suleymanov, Kamran Huseynov, Aysu Huseynova, Elmeddin Mohubbetov, Nicat Ahmadov, Rahman Karimli
Cost-Effective Hybrid Sensor Network Optimization for Flood Monitoring in Resource-Constrained Environments Using Genetic Algorithms……..……405
M.Ariyanatchi, I.Paulraj Jeyasimman
Fractional-Order Optimal Control of Drug-Resistant Tuberculosis: Model Analysis and Numerical Validation……...408
Shirinzade Irada Nusrat
Study of The Influence of Chemical Composition on the Properties of Clay-Dolomite Composite Materials Using Mathematical Modeling……..……415
Isa Muradov , Irana Akhundova
Mathematical modeling of seasonal changes in Tourism Economics.....422
Aslanov Jamaladdin Nuraddin, Huseynli Zenfira Seyidi, Babazadah Jalal Fikrat
Analysis of Failure Problems in the Sealing Units of Centrifugal Pumps.....429
Jamila Imamaliyeva
Evaluation of Damaged Buildings with Smart Technologie.....435
Javanshir Azizov, Vagif Guliyev

Some Sructural Properties of Discrete Morrey Spaces over ℤ……...443
Kamila Majidli
Ecological Modelling of Sustainable Hydropower Development Potential in the Hakari River Basin, Azerbaijan……449
Kamran Khan
A Comprehensive Mathematical Framework for Hydrostatic Pressure Behavior, Stress Analysis, and Integrity Assessment in Gas Pipeline Hydrotesting…….……..…466
Khalid Mammadov, Lalazar Ahmadova
Contact Interaction of Thin-Walled Elastic Shells with Deformable Foundations: An Approximate Method…….....471
Khayala Seyfullayeva
An Optimal Control Approach To The Inverse Problem For Nonlinear Vibrations of a Plate And its Study……...476
Mamedov Knyaz Shiraslan , Niyazova Rayiha Rasim
The Dual Problem Corresponding to the Boolean Programming Problem and Its Lagrangian-Type Approximate Solution……483
Levent Sıvakcı, Ali Kuruçay , Ahmet Selim Dalkılıç
Verification Analysis of the Thermal Performance of Cylindrical Solid Pin-Fin and Cylindrical Perforated Pin-Fin Heatsinks Using CFD……...…...….490
Leyla Mammadova
On some properties of eigenvalues of a second-order differential operator with a

boundary condition containing a spectral parameter……..……497
Mahammad Zeynalov
AI-Driven Predictive Analytics for Logistics and Transportation Systems.....504
Avey Mahmure, Yüce Salim
Influence of Elastic Foundations on Nonlinear Primary Resonance of Layered Nanocomposite Spherical Shell Surfaces via the Method of Multiple Time Scales……...…….510
Maksud S. Sharipov, Khikmat J.Rakhimboev, Ikhtiyor D. Avezmatov
Algorithm and Stages of Training a Text Recognition Model for the Turkmen Language Using Tesseract OCR…….512
Malaka Mahmudova
The Transformation Operator For The Perturbated Mathieu Equation……..528
Mehraly Aliyev
The study of trace properties of function $D^{\nu}\left(f(x)-\Phi_{\ell-1}(x)\right)$ ……...……532
Mehriban Omarova
Commutators of Parabolic Fractional Maximal Operators on Parabolic Total Morrey-Guliyev Spaces…….…….……..539
Seynura Hasanova , Messoud Efendiyev
Multiscale mathematical modeling of the use of biofilms in wastewater treatment.....546
Migdad I. Ismailov, Chinara M. Hasanova, Zahira V. Mammedova
On the basicity of the weight system exponent with exception in Banach functional spaces……..553

Muhammad Abubakar Isah, brahim Isah, Ahmad Muhammad
Lump, Breather, and Chaotic Dynamics of the Variable-Coefficient Extended BLMP Equation……..…..558
Muhammed Milani
Finite-Precision Analysis of Chaotic Map-Based Pseudorandom Number Generators……560
Mukhlis Hajiyev , Yuriy Vynnykov, Shirazi Ismayilov, Tetiana Galinska, Nazim Polukhov
Nonlinear Analysis of Crack Resistance in RC Sections.....567
İsmayılov Murad Hacı oğlu.
Computational Complexity of Machine Learning Algorithms: A Mathematical Perspective……..…….574
Murad Manafli
Modeling the Impact of Tourism Demand on Airline Profitability Based on Probability Theory and Statistical Approaches……...581
N.M. Aslanova, I.N. Parasidis and E. Providas
Approximate symbolic solution of systems of integro-differential equations with non-separable kernels and non-local boundary conditions……..……...586
Kurbanov Nabi, Babajanova Vusala, Agamalieva Kamala, Abdullaeva Konul
Research on Forced Vibrations of a Viscoelastic Beam With Clamped Ends……..591

Nabi Kurbanov, Ilham Mardanov, Ulviyya Aliyeva
Study of Oscillations of Cylindrical Shells With Rheological Properties.....598
Natiq Akhmedov, Sevda Akbarova, Yahya Jamalzade
Construction asymptotic solutions of the problem for a radially functionally graded transversely isotropic cylinder of small thickness……...……604
Natiq K. Akhmedov, Solmaz A. Hasanova
Construction of asymptotic solutions to the torsion problem for a nonhomogeneous transversely isotropic cone……...…613
Nazila B. Rassoulova and Tahmina M. Mahmudzade
Dynamic Analysis of an Inhomogeneous Half-Space……..…..622
Nigar Aslanova, Hajar Movsumova, Khalig Aslanov
A Sturm–Liouville problem with Herglotz–Nevanlinna Function Boundary Conditions at Both Endpoints.....628
Shukurova Nigar Oktay,Mammadov Knyaz Shiraslan, Huseynov Saqif Yaqub
An Innovative Approximate Solution for the Interval Partially Boolean Knapsack Problem……633
Nurmammad Mammadov, Jamil Guliev
Probabilistic-Statistical Modelling of Non-Stationary Heat Consumption Regimes in Intelligent Residential Buildings.....639
Ponraj Jeyabarathi and Lakshmanan Rajendran

Semi-analytical solutions of nonlinear reaction diffusion equation in packed-bed reactors using Taylor series expansion and the Adomian decomposition method……647
Ponraj Jeyabarathi and Lakshmanan Rajendran
Steady-State Reaction Diffusion Analysis of Mediator Concentration in Bioelectrocatalysis Using the Adomian Decomposition Method.....654
R. Gayathri , Lakshmanan Rajendran
Application of Nonlinear Differential Equations in Langmuir-Type Adsorption Kinetics……...….660
R. Krithiga, Lakshmanan Rajendran
Applications of Differential Equations in Nonlinear Electrochemical Reaction–Diffusion Processes…….….667
Rafig Tagiyev , Aytaj Mammadova
Finite-Difference Approximations for an Optimal Control Problem Governed by an Elliptic Equation with Periodic Boundary Conditions and Coefficient-Type Control…..……669
Ramazan Guliyev, Gulnar Mirzayeva
A Relational Database Framework for Real-Time Manufacturing Cost Monitoring: Design and Implementation.....676
Ramazan Guliyev and Gulnar Mirzayeva
Application of Machine Learning Methods for Cost Forecasting in Manufacturing Enterprises: A Comparative Study…...…681
Ramin Zeynalov and Nihan Aliyev

The Steklov problem for an ordinary differential equation with fractional derivatives.....689
Ramiz Iskanderov, Alabbas Akhiev
Solving a Cubically Nonlinear Oscillation Problem Using The Operational Method…….695
Ramiz Iskanderov, Jamal Mammadov
Algorithm For Solving Optimization Problems Of Elements Of Bent Structures, Taking Into Account The Combined Effect Of Force Loads And Aggressive Environment……..……702
Ramiz Iskanderov, Nijat Mastanzade and Nariman Abdinli
Numerical Solution for Optimization of Cable-Stayed Bridge Cross-Section Due to External Loads……..…710
Gasimov Rashad, Mammadov Nurmammad
Comparative Analysis Of Centralized And Occupancy-Based Hvac Regulation.....717
Regunathan Rajalakshmi and Lakshmanan Rajendran
Application of Nonlinear Differential Equations to Reversible Enzymatic Isomerization in Fixed-Bed Reactors……...……724
Reyhan Arslan, Bedri Onur Küçükyıldırım, Emel Akyol and Ahmet Selim Dalkılıç
A Critical Review of Thermophysical Parameters Governing the Performance of Thermal Interface Materials in Advanced Electronic Cooling Systems…….……732
Reyyan Oruc and Edip Senyurek

Resistance, Thermophysical Properties Spam Detection Using SVM and TF-IDF Features……....740
Roland Duduchava and Aleksandr Oleinikov and Tatiana Kuzmina
Equation of State and Limit State Zone at a Crack Tip in Unidirectional Composite Laminates.....747
Rovshan A. Bandaliyev, Alikhan G. Mehdiyev and Konul K. Omarova
Relatively compact sets in quasi grand Lebesgue spaces……..…751
Rovshan A. Bandaliyev, Bahar S. Jafarova and Konul A. Babayeva
Two-weight norm inequalities for Hausdorff operator on Morrey spaces……..……771
Bandaliyev Rovshan, Vugar Khalilov and Ilhama Alekperova
On the continuity of Hausdorff operator in Orlicz spaces……..764
S. Thamizh Suganya, L. Rajendran
Analytical Solution of Two-Dimensional Gas Diffusion in Cylindrical Food Packaging Systems……....771
Sabir G. Hasanov
Multi-sublinear maximal operators on product total Morrey-Guliyev spaces……...……778
S.Z. Khaligova
The Boundness of the Maximal Operator in Local "Complementary" Generalized Morrey Spaces……..…784
Sabina H. Kasumova
Weighted inequalities for maximal operators in B-Morrey spaces……..……790

Safak Metin Kirkar, Alişan Gönül and Ahmet Selim Dalkilic
Numerical Investigation of Thermo-Hydraulic Performance of Multi-Start Corrugated Coiled Tubes in Turbulent Flows……793
Beknazarova Saida, Abdullayeva Ozoda, Yunusova Dilnoza, Beknazarova Kamilla
Modern Methods of Texture Generation in 3D Modeling: Procedural, Image-Based, and AI Approaches……800
Salmanov Oktay Shirin
Free oscillations of a rod-reinforced cylindrical cover underthe influence of a compressive force with a fluid……..829
Sh.A. Mammadov, J.E. Musayev, A.Kh. Aliyeva
Transverse Vibration Analysis of Non-Homogeneous Straight Rods Resting on a Viscoelastic Foundation……...834
Yusubov Shakir Shixi , Huseynova Minayya Neymat
The property of Fredholm of a fourth-order integro-differential equation with impulse effect……..…840
Bekchanov Shukurla and Sharipov Alisher
Semantic Novelty Detection in Scientific Documents Using Transformer Embeddings……..848
Sh.A.Kerimova
Pressure in Non-Stationary Operating Modes of the Well.....856
Suleyman Celik

Potential Operator on Carleson Curves in Local Generalized Weighted Morrey Spaces……..……863
T.A.Hagverdiyeva and K.B.Jamalova
Enhancing Road Concrete Sustainability through Waste …….....869
Terlan Ibadzade
Determining Optimal Gas Lift Regime: Transitioning from Injection Rate to Entry Velocity……..……..877
Terlan Ibadzade
Optimization of Operating Parameters Based on Tubing Shoe Pressure and Injection Gas Velocity Dynamics in Gas Lift Wells…….……883
Tahir Gadjiev, Rena Cebrayilova
Electrical Transport and Optical Response in $In/Ag-AgInS_2$ Metal-Semiconductor Heterostructures……890
Tahir Gadjiev, Sevinc Hadiyeva and Konul Memmedova
Estimates for Degenerate Non-Divergence Elliptic Equations in Infinite Domains with Conical Boundary Points.....897
Tahir Gadjiev, Yasemen Guseynova and Aybeniz Yagnaliyeva
Qualitative Properties and Harnack-Type Estimates for Degenerate Non-Divergence Elliptic Equations……..905
Tahir Gadjiev and Zaur Hajiyev
Particle Filtering for High-Dimensional Reaction Diffusion PDE State Estimation under Non-Gaussian Noise……...……914

Taliat Azizov, Dmitro Kochkarev, Mukhlis Hajiyev and Tatiana Galinska
Spectral Method for Structures under Shock Waves.....924
Tatiana Kuzmina and Aleksandr Oleinikov
Two-Scale Failure Problems of the Anisogrid Composite Laminates……932
Tatiana Kuzmina
BEM Modelling of an Adaptive Mechanised Wing Leading Edge.....938
Tayip Türk , Umut Melikoğlu, Tolga Tani, Yunus Emre Dündar, Furkan Yıldırım, Hüseyin Onur Dağlı, Alişan Gönül, Ahmet Selim Dalkılıç
Validation of the Experimental and Numerical Splitter Plates of The Condenser Tube Banks During Cross Flow of Air……944
Telman Gasymov, Zahra Aliyeva
Basisness of Eigenfunctions of a Differential Operator with a Discontinuity Point in Weighted Lebesgue Spaces.....951
Tukazban Hasanova
Non-Iterative Spectral Evaluation of Fluid-Filled Cylindrical Shells.....956
Tunzala Alifova Hakim , Hamil Babazada Jahangir
Analysis of the Limited Capacities of Public Transport in the Transport System in Azerbaijan.....963
Ulaş Kayaoğlu, Celal Melih Eriş, Melih Gökay Uslu, Ahmet Selim Dalkılıç

Numerical Validation of Air-Side Thermal-Hydraulic Performance in a Bar and Plate Heat Exchanger……970
V. M. Abdullayev and S. S. Jafarli
On a optimal control problem for a loaded parabolic equations……...…977
Vanaja Ramalingam, R. Shanthi
Advanced Algebraic Akbari-Ganji Modeling for VOC Transport in Biofiltration ……...…984
Vitaly Alexeev and Alexander Lyapin
Sections of Laurent Generating Series for Solutions of Two –Dimensional Difference Equations With Constant Coefficients….990
Vusal Aliyev
Mechanical Analysis of Functionally Graded Cylindrical Elements Under Pure Torsion for ITER-Type Tokamak Reactors……996
Vusala Suleymanova Abdulla
Investigating of Necessary Optimality Conditions in a Non –Smooth Boundary Control Problem For Goursat-Darboux Systems.....1002
Yagub Aliyev, Zamina Guliyeva, Narmin Aliyeva
On generalization of Mitev's inequalities……1008
Yagub N. Aliyev and Narmin N.Aliyeva
Necessary and sufficient conditions for Sturm-Liouville problems with a boundary condition depending linearly on an eigenparameter……...……1014
Yashar Mehraliyev, Sevdimaliyev Yusif, Ferecova Sona

On a Linear Inverse Boundary Value Problem For The Equation of Flexural Vibrations of a Rod……..……1016
Yegana Ashrafova
Numerical Method for Analyzing Fluid Flow in Interconnected Pipeline Networks…..1022
Yusuf Oflaz, Yusuf Ogunc and Ahmet Selim Dalkilic
Numerical Validation of Thermal Performance in a Double-pipe Heat Exchanger……...……1029
Z.J. Zabidov , A.Sh.Shukurov and M.Kh. Kuliev
Assessment of the Spatiotemporal Dynamics of Soil Salinization Based on Spectral Data……...…....1037
Z.J. Zabidov , Kh.M. Gadirova
Soil Salinity Classification Based on Multispectral Imagery……...……1044
Musraddin Tağıyev, Reshad Tağıyev
The numerical modeling of nonlinear wave processes in two-phase systems……..…1046
Etimad Eyvazov
Stress-strain state of domains with partial cracks under external loading..……..…1053
Veli Shakhmurov, Rishad Shahmurov
Nonlocal navier—stokes equations and their applications ……1054
Huseyn Mammadsadygov, Jeyhun Musayev
Investigation of stress concentration in a uniformly rotating plate weakened by an

elliptical hole and two straight cracks…….....1060
Sonay Arzimanli
A Smart Task and Issue Management System with Geospatial Problem Mapping …….....1066
Maksud Sharipov , Ruzikajon Kurbonova, Lola Kurbanova
Normalizing Khorezm Dialect Speech Transcripts into Standard Uzbek: A Fine-Tuned NLLB-200 Approach ……..……1071